Deutsches Zentrum für Luft- und Raumfahrt e.V.
in der Helmholtz-Gemeinschaft

MAX-PLANCK-INSTITUT FÜR CHEMIE

iup

RAL Space

Royal Netherlands Meteorological Institute
Ministry of Infrastructure and the Environment

S5P/TROPOMI
Science Verification Report

document number	:	S5P-IUP-L2-ScVR-RP
CI identification	:	CI-D500-ScVR
issue	:	2.1
date	:	2015-12-22
status	:	final

Document approval record

	digital signature
prepared:	Andreas Richter and the Verification Teams
checked:	<digital signature> or n/a
approved PM:	<digital signature> or n/a
approved QA:	<digital signature> or n/a
approved CM:	<digital signature> or n/a
approved client:	<digital signature> or n/a

Document change record

issue	date	item	comments
0.0.1	2014-02-24	All	Initial draft version
0.0.2	2014-03-10	All	revised based on comments from the prototyping teams
0.0.3	2014-03-18	NO2, clouds	fixed broken links, replaced stratospheric NO2 results
0.0.4	2014-05-13	All	revised by verification groups
0.0.5	2014-05-28	All	revised by verification groups after internal review by prototyping teams
0.0.6	2014-06-02	Ozone Column	included missing update by verification team
0.0.7			minor updates after ESA review
0.0.8	2014-09-22	All	major revisions by verification teams after ESA review and further verification work
1.0.0	2014-09-30	All	major revisions and restructuring by verification teams after internal review
1.0.1	2015-05-02	All	major additions of verification results
1.0.2	2015-05-13	All	updates in response to internal review, addition of cloud verification results
1.9	2015-10-22	All	major updates by verification groups
2.0	2015-11-03	All	major updates and restructuring after internal review
2.1	2015-12-22	NO2, clouds	minor edits

Contents

1 Introduction

1.1 Motivation

Within the S5P L2 project, a strong component of verification exists which consists of an independent retrieval algorithm for each operational prototype. This approach is based on similar settings used in the SCIAMACHY SQWG context, but integration into the project prior to launch is a novel development in the S5P L2 project.

There are several reasons for following the concept of verification already during prototype development:

- Independent verification retrievals were used for critical evaluation of the prototype algorithms by applying both retrievals to predefined sets of test data and comparing the results. This helpes to validate the operational prototypes.
- As most of the verification retrievals use different approaches than the prototype, algorithms or data bases used in the verification algorithms that turned out to be advantageous for the quality of the product could still be implemented in the prototype algorithms.
- Independent verification retrievals are not limited by the constraints of an operational environment (such as computational time, strict software engineering and delivery schedule) and can continue to develop novel approaches and ideas, allowing further development of the algorithms which can be used for future improvements of the operational processor.

Regular communication and iteration between the developers of the prototype algorithms and those of the verification algorithms (different algorithm, different institute) ensured continuing exchange of expertise which contributed to making the prototype algorithms and their operational counterpart state of the art at S5P launch.

As mentioned above, the verification algorithms are operated by groups not involved in the development of the respective prototype algorithms, ensuring a large degree of independence for the verification. An overview over the different verification algorithms and the project partners responsible is given in Table 1.1.

Table 1.1: Overview of the verification algorithms

Product	Team	Algorithm	Heritage	Prototype
O3-TC	KNMI	OE	OMI	DLR / IASB
O3 trop. C.	KNMI	OE	OMI	IUP / DLR
O3 profile	IUP / RAL	OE	GOME / SCIA / GOME-2	KNMI
NO2-TC	DLR	DOAS	GOME-2	KNMI
NO2 trop C.	IUP	DOAS	GOME / SCIA / GOME-2	KNMI
NO2 strat. C.	MPIC	STREAM	SCIA	KNMI
SO2	MPIC	DOAS	GOME / SCIA / GOME-2	IASB
SO2	DLR	DOAS	GOME-2	IASB
HCHO	IUP	DOAS	GOME / SCIA / GOME-2	IASB
XCH4	IUP	BESD	SCIA	SRON
CO	IUP	BESD	SCIA	SRON
CTH, COT	IUP	SACURA	GOME / SCIA / GOME-2	DLR
CF	MPIC	HICRU	GOME / SCIA / GOME-2	DLR
CCH	KNMI	FRESCO	GOME / SCIA / GOME-2	DLR
AOD	IUP	BAER	SeaWiFs	KNMI
AAI	MPIC	UVAI	GOME / SCIA / GOME-2	KNMI

1.2 Approach to Verification

The overall approach to verification is similar for all products. It relies on direct comparison of results from the prototype algorithms in several steps

Comparison of fundamental quantities used such as modelled radiances, air mass factors, data bases and retrieval parameters

Comparison of intermediate and final results retrieved on a small set of synthetic data based on the CAMELOT scenarios

Comparisons of results obtained on data from existing instruments, OMI where possible and GOME-2 or SCIAMACHY where needed (OMI is not covering all relevant wavelengths). Data sets are selected according to the needs of the individual products but are homogenized as much as possible.

The main aim of verification is not to enforce consistency between prototype and verification algorithm but to provide estimates of the uncertainties in the prototype results and an understanding of the differences observed and their origins.

As this aim is best achieved in close cooperation between verification and prototyping groups, all results shown in this report have been obtained in cooperation between both groups, the results have been iterated and the report been reviewed by the prototyping teams. By this approach it was guaranteed that any need for adaptations of the prototype was realised at an early stage and tests are repeated with the latest versions of the algorithms.

1.3 Scope of Document

The intention of this document is to collect information on the verification within the S5P L2 project. This includes details of all the verification algorithms used, their settings and the main differences to the operational prototype algorithms. It also includes information on the set-up of the various verification activities on synthetic data based on a small number of simple scenarios, real data from other sensors and realistic S5P data. Finally, it summarises the results from the pre-launch verification activities.

1.4 Document Overview

The main part of the document is divided into sections covering one product each. In some cases, several related quantities are covered in one section, for example in the part on clouds (cloud fraction, cloud top and bottom height, cloud albedo, cloud optical thickness and cloud optical centroid top pressure). In some cases verification algorithms are provided by different groups for one product, which can lead to some overlap in the descriptions.

1.5 Document Summary

As the results and conclusions of the verification differ between the various products, a summary of verification results is given at the end of each chapter and will not be repeated here.

2 Applicable and reference documents

2.1 Applicable documents

[AD1] GMES Sentinel-5 Precursor – S5P System Requirement Document (SRD);
source: ESA/ESTEC; **ref**: S5P-RS-ESA-SY-0002; **issue**: 4.1; **date**: 2011-04-29

[AD2] Sentinel-5P Level 2 Processor Development – Statement of Work -;
source: ESA; **ref**: S5P-SW-ESA-GS-053; **issue**: 1; **date**: 2012-03-02

[AD3] GS Requirements Document, S5P-RS-ESA-GS-092

[AD4] GMES Sentinels 4 and 5 Mission Requirements Traceability Document, EO-SM/2413/BV-bv, iss 1.0

[AD5] GS Master Schedule, S5P-PL-ESA-GS-069

[AD6] S5P/TROPOMI Level 2 Product Development Plan, S5P-KNMI-L2CO-0010-PL

2.2 Standard documents

There are no standard documents

2.3 Reference documents

[RD1] Terms, definitions and abbreviations for TROPOMI L01b data processor;
source: KNMI; **ref**: S5P-KNMI-L01B-0004-LI; **issue**: 1.0.0; **date**: 2011-05-18

[RD2] Terms, and symbols in the TROPOMI Algorithm Team;
source: KNMI; **ref**: SN-TROPOMI-KNMI-049; **date**: 2011-09-28

[RD3] S5P/TROPOMI Static input for Level 2 processors;
source: KNMI; **ref**: S5P-KNMI-L2CO-0004-SD; **date**: 2013-04-11

[RD4] Algorithm theoretical basis document for TROPOMI L01b data processor.
source: KNMI; **ref:** S5P-KNMI-L01B-0009-SD; **issue:** 1.0.0; **date:** 2013-03-27

[RD5] TROPOMI Instrument Performance Analyses Report.
source: Dutch Space; **ref:** TROP-DS-0000-RP-0060; **issue:** 6.0; **date:** 2011-05-18.

2.4 Electronic references

There are no electronic references.

3 Terms, definitions and abbreviated terms

3.1 Acronyms and abbreviations

AAI	Absorbing Aerosol Index
AOD	Aerosol Optical Depth
BAER	Bremen AErosol Retrieval
BESD	Bremen Optimal Estimation DOAS
CCD	Convective Cloud Differential
CINDI	Cabauw Intercomparison campaign for Nitrogen Dioxide measuring Instruments
DISCOVER-AQ	Deriving Information on Surface Conditions from Column and Vertically Resolved Observations Relevant to Air Quality
DISAMAR	KNMI tools for Level 2 simulations
DOAS	Differential Optical Absorption Spectroscopy
ECMWF	European Centre for Medium-Range Weather Forecasts
FRESCO	Fast REtrieval Scheme for Clouds from the Oxygen A band
FURM	FUll Retrieval Method
GMES	Global Monitoring of the Environment and Security
GODFIT	GOME Direct-FITting
HITRAN	High Resolution Transmission
HICRU	Heidelberg Iterative Cloud Retrieval Utilities
ICARTT	**I**nternational **C**onsortium of **A**tmospheric **R**esearch on **T**ransport and **T**ransformation
IPA	Independent Pixel Approximation
L2WG	Level-2 Working Group
LEO	Low Earth Orbit
LIDORT	LInearized Discrete Ordinate Radiative Transfer
LUT	Look Up Table
MERIS	MEdium Resolution Imaging Spectrometer
NDACC	Network for the Detection of Atmospheric Change
OCRA	Optical Cloud Recognition Algorithm
OE	Optimal Estimation
ROCINN	Retrieval Of Cloud Information using Neural Networks
RT(M)	Radiative Transfer (Model)
SACURA	Semi-Analytical CloUd Retrieval
SCD	Slant Column Density
SCI	SCattering Index

SCIATRAN	IUP Bremen radiative transfer model
SES	Stratospheric Estimation Scheme
STREAM	STRatospheric Estimation Algorithm from Mainz
SZA	Solar Zenith Angle
TCCON	Total Carbon Column Observation Network
TOGOMI	Total Ozone algorithm for GOME using the OMI algorithm
TROPOMI	TROPOspheric Monitoring Instrument
UVAI	UV Aerosol Index
VCD	Vertical Column Density
VIIRS	Visible/Infrared Imager Radiometer Suite
WFDOAS	Weighting Function DOAS
WFMDOAS	Weighting Function Modified DOAS

4 TROPOMI Instrument Description

4.1 Sentinel-5 Precursor Mission

The Sentinel-5 Precursor (S5P) mission is a low Earth orbit polar satellite system to provide information and services on air quality, climate and the ozone layer in the timeframe 2016-2023. The S5P mission is part of the Global Monitoring of the Environment and Security (GMES) space component programme. The S5P mission consists of a satellite bus, the payload consisting of the TROPOspheric Monitoring Instrument (TROPOMI), and a ground system. In this section a description of the mission is provided with emphasis on those aspects that are relevant for the L1-2 algorithms. A comprehensive description of the mission can be found in [RD4].

4.2 Orbit

The orbit definition of the S5P mission plays an important role in the operational aspects. Both instrument operations and data processing use a (coordinated) orbital scenario. This orbital scenario is also linked to in-flight calibration of the instrument. S5P will fly a sun-synchronous polar orbit, in close formation with the U.S. Suomi NPP mission. The orbital parameters for S5P are given in Table 4.1.

Each S5P orbit has a day (lit) side and a night (dark) side (Figure 4.1). On the day side the spacecraft flies from south to north; on the night side it flies from north to south. Spacecraft midnight is defined as the time halfway the nadir day-night terminator and the nadir night-day terminator; spacecraft noon is the time halfway the nadir night-day terminator and the nadir day-night terminator. Both the instrument operations as well as data processing will use the spacecraft midnight as the start and end points of an orbit. This convention has the advantage that the orbits are defined without any seasonal dependency. Due to seasonal variation, the position of the equator with respect to the spacecraft midnight will change. As a result, spacecraft midnight is not at a fixed latitude.

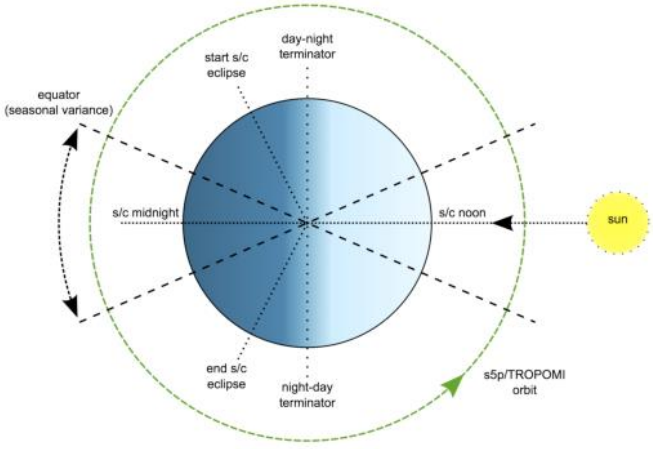

Figure 4.1: S5P orbit overview.

Table 4.1: Parameters of the S5P reference orbit.

Operational parameter	Value
Repeat Cycle	17 days
Cycle Length	241 orbits
Semi-Major Axis	7205.919 km
Eccentricity	0.001148
Inclination	98.7462 deg
Argument of Perigee	90.00 deg
Mean Local Solar Time of Ascending Node Crossing	13:35 hrs
Orbital period	6094.6 s

4.3 Suomi NPP Formation Flying

The S5P satellite will fly in so-called loose formation with the NOAA/NASA Suomi NPP satellite. Loose formation means that the overpass time between S5P and NPP will be less than 5 minutes. The main driver for the formation flying is the cloud clearing for the CH_4 product using the high spatial resolution data from the Visible/Infrared Imager Radiometer Suite (VIIRS) aboard Suomi NPP.

4.4 TROPOMI

The payload of the S5P mission is the TROPOspheric Monitoring Instrument (TROPOMI) that will measure key atmospheric constituents including O_3, NO_2, SO_2, CO, CH_4, CH_2O and aerosol properties. TROPOMI is a push broom imaging spectrometer with a wide field of view that provides daily global coverage with high spatial resolution.

The measurement principle of TROPOMI is illustrated in Figure 4.2. The instrument images a strip of the Earth on a two dimensional detector for a period of 1 second during which the observed swath satellite moves by about 7 km over the Earth's surface. This strip has dimensions of approximately 2600 km in the direction across the track of the satellite and 7 km in the along track direction. After the 1 second measurement a new measurement is started. In this way, the instrument scans the Earth as the satellite moves. The two dimensions of the detector are used to detect the ground pixels in the across track direction and for the wavelengths along track. The collected light is separated in the different wavelengths using grating spectrometers. TROPOMI has four spectrometers, covering non-contiguous wavelength bands from the ultraviolet to the shortwave infrared.

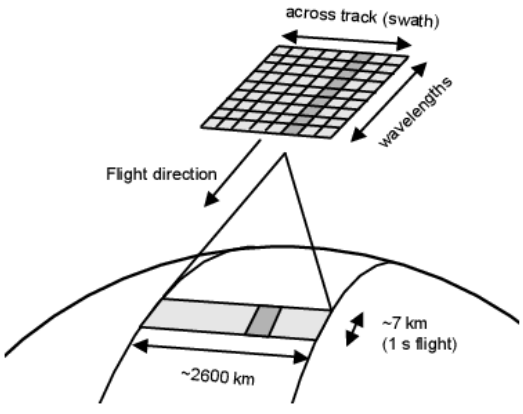

Figure 4.2: TROPOMI measurement principle. The dark-grey ground pixel is imaged on the two-dimensional detector as a spectrum. All ground pixels in the 2600 km wide swath are measured simultaneously.

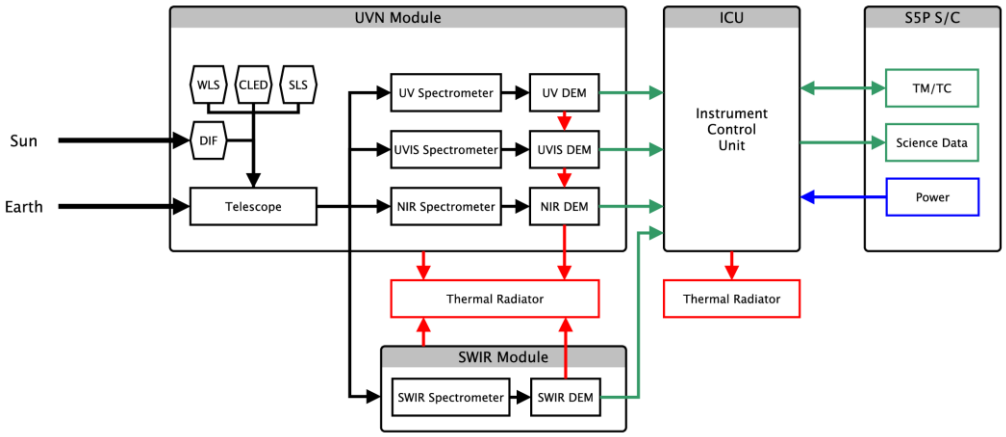

Figure 4.3: Functional diagram of TROPOMI.

A functional block description of the TROPOMI architecture is given in Figure 4.3. Light enters the telescope from the Earth, the Sun via one of the diffusers (DIF), or one of the on-board calibration sources (spectral line source (SLS), common LED (CLED) or white light source (WLS)). The solar diffusers and the calibration sources are part of the calibration (CAL) unit. From the telescope the light goes to the three UVN spectrometers (UV, UVIS, NIR) and the SWIR spectrometer. The detector electronics modules (DEMs, one per spectrometer) collect the spectra and send the data to the Instrument Control Unit (ICU). The ICU provides the data interfaces with the S5P spacecraft (S/C). The spacecraft supplies TROPOMI with power. The UVN and SWIR modules are cooled using a two-stage thermal radiator. The ICU is cooled using a separate thermal radiator.

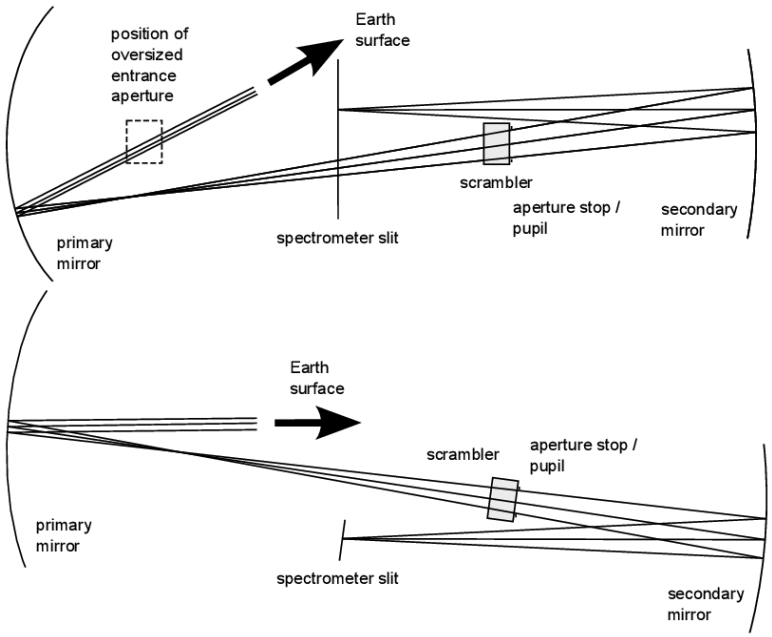

Figure 4.4: Cross-section of the TROPOMI telescope in the across track (top) and along track (bottom) direction.

In the remainder of this section the main blocks of the instrument will be described.

4.4.1 Telescope

The telescope (see Figure 4.4) is a two-mirror reflective telecentric telescope. It has a large field-of-view in the across track direction (swath, across flight, or spatial direction), and a small field-of-view in the along track direction (along flight or spectral direction). This is shown at the top and bottom of Figure 4.4. The two telescope mirrors are referred to as primary and secondary mirror, in the order in which light from the Earth passes through the telescope. A strip on the Earth's surface is imaged by the first mirror. The intermediate image, located close to the primary mirror, is re-imaged by the secondary mirror on the entrance slit of the spectrometer system. At the same time, the entrance pupil is imaged to infinity. Both mirrors are concave and aspherical. In the optical path between the two mirrors, coincident with the intermediate pupil, there is a polarization scrambler preceded by a rectangular aperture. The latter determines the telescope's throughput.

The telescope has different f-numbers in the along and across track directions. This has been achieved by dimensioning the aperture stop (pupil) to a rectangular shape. The focal length in the two directions is also different, which has been achieved by making the secondary mirror aspherical. The telescope has a large field-of-view (108 degrees) across track and a small field-of-view along track. In the spectral direction the field-of-view is defined by the width of the slit.

The light for the UVIS and NIR spectrometers passes through the slit. Light destined for the UV and the SWIR spectrometers is reflected from the sides of the slit. Both the SWIR and the UV spectrometers include another slit. A consequence of this arrangement is that the UV and the SWIR are not co-registered with the UVIS and the NIR. The light detected in the UV and SWIR originates from another position than the light detected in the UVIS and NIR. The difference in flight time between the two positions is two seconds, which corresponds to two read-outs in the baseline configuration.

4.4.2 UVN Spectrometers

The three UVN spectrometers are conceptually almost the same: they all image a slit on a detector, dispersing the light by means of a grating. As an example, Figure 4.5 shows the optical layout of the UVIS spectrometer. The UVIS and NIR spectrometers share the same 280 µ-wide slit. Light for the UV and SWIR spectrometers first reflects off the UVIS-NIR slit and then, after passing through a dichroic that directs the shortwave component of the light towards the SWIR relay optics, is imaged on a second slit on a conjugate plane to the focal plane of the telescope. This slit is 696 µ wide on its conjugate plane, which corresponds to a virtual slit with a width of 560 µ. Using cylindrical optics, the slit is imaged only in the spectral dimension. This removes the strict requirement on the sharpness of the slit edges in the spatial dimension.

At the end of the spectrometer, the light falls onto a charge coupled device (CCD). One direction of the CCD corresponds to the spatial (across track) dimension, the other direction corresponds to the spectral (along track or flight) dimension. The CCD pixel size is 26µ x 26µ, and the total number of pixels in the imaging area is 1024 x 1024. The image of the slit in the across track direction is about 862 pixels wide, the remaining pixels being used for calibration and monitoring purposes. During data acquisition, pixels can be binned in the spatial direction to decrease noise at the cost of resolution.

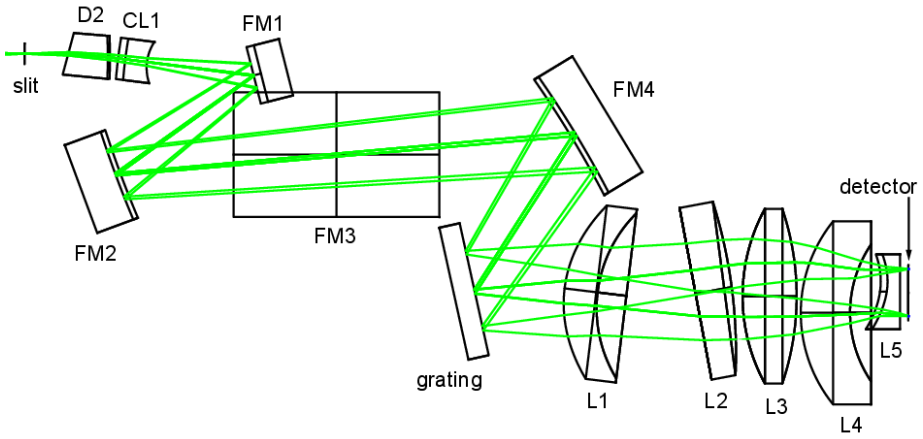

Figure 4.5: Optical layout of the UVIS (320–490 nm) spectrometer. The UVIS light passes the slit, a dichroic (D2) and collimation optics (CL1). Via folding mirrors (FM1–4) the light is guided to the grating. The diffracted light is then imaged by a system of lenses (L1–L5) onto the UVIS detector.

4.4.3 SWIR Spectrometer

Functionally, the SWIR spectrometer is similar to the UVN spectrometers. The optical layout of the SWIR spectrometer is shown in Figure 4.6. The SWIR entrance pupil is formed by the UVN telescope and SWIR relay optics, and it forms the optical interface between the UVN and SWIR subsystems. The SWIR spectrometer receives its input from the main UVN optics and focuses it on a slit prism. The slit delimits the spatial extent of the image, defining the along track field-of-view, as well as the spectral resolution (in combination with the collimator and the immersed grating). The collimator then transfers the image of the slit to an immersed grating that causes spectral separation. A final imager forms an image of the scene on the SWIR detector.

The SWIR detector is a CMOS detector. This is a HgCdTe (or MCT, Mercury Cadmium Telluride) pixel array hybridized on a silicon read-out integrated circuit (ROIC). The detector has 1000 x 256 square pixels (30µ pitch). The SWIR detector will be operated at a temperature of approximately 140K.

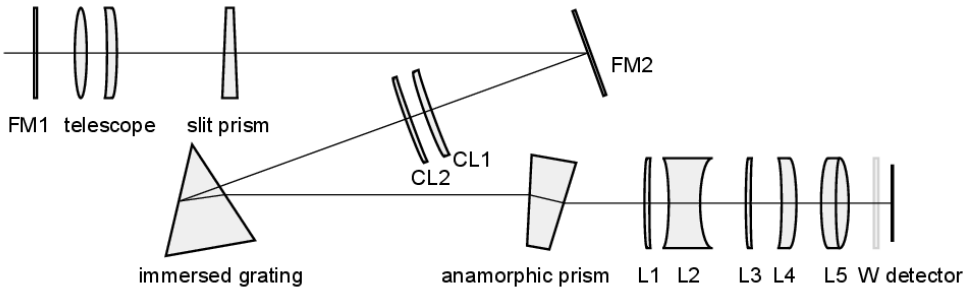

Figure 4.6: Optical layout of the SWIR spectrometer. The light entering the SWIR spectrometer is guided by the folding mirror FM1 through the telescope onto the slit prism. Via another mirror (FM2) and a collimator (CL1 and CL2) the light reaches the immersed grating. The diffracted beam is re-shaped by the anamorphic prism and imaged onto the detector by the lenses L1–L5. A window (W) decouples the detector unit from the optical bench.

4.4.4 TROPOMI performance

Table 4.2 shows the instrument performance parameters of TROPOMI most relevant for the Level 1-2 development. This table is an update of the information provided in [RD5]. Figure 4.7 shows an analysis of the signal-to-noise ratio for the four spectrometers, which is compliant with the signal-to-noise requirements given in Table 4.2

The spectral resolution and sampling ratio (spectral resolution divided by the spectral sampling) is given in Table 4.2. An example of the modeled instrument response function (slit function) is shown in Figure 4.8. It is noted that the instrument response will vary both with wavelength as well as with the across track position. The actual slit function may differ considerably from the example in Figure 4.8 as it can be asymmetrical, and it may contain multiple maxima. The instrument response function will be measured during the on-ground calibration. These data are an important input for the Level 1-2 algorithms.

The spectral registration will differ from ground-pixel to ground-pixel due to thermal variations over the orbit as well as due to inhomogeneous filling of the slit in the flight direction. The Level 1B data will contain a spectral assignment, however, an accurate spectral calibration based on the Fraunhofer lines needs to be performed by the Level 1-2 algorithms.

As described above the TROPOMI spectrometers use two-dimensional detectors where one dimension is used for the across track (or swath) information and the other dimension for the spectral information (see Figure 4.2). To increase the signal-to-noise and to reduce the data rate, the UVN detectors perform on-chip binning in the swath direction. For the Bands 2-5 the binning factor for nadir viewing direction is 4, for Band 1 it is 16 and for Band 6 it is 2. The binning factor determines the across-track spatial sampling. If a constant binning factor is used over the swath, the pixel size will increase substantially. To reduce this effect a variable binning factor is implemented. For a variable binning factor the binning decreases towards the end of the swath, e.g. for Bands 2-5 it is 4 around nadir, and reduces to 2 and 1 when going towards the end of the swath. The effect of the constant and variable binning scheme on the across-track track spatial sampling is shown in Figure 4.9. It is noted that reducing the binning will also reduce the signal-to-noise of the observation. For the SWIR spectrometer (Band 7-8) there is no binning, thus the variable binning scheme is not applicable to the SWIR observations.

Table 4.2: Performance parameters most relevant for the TROPOMI instrument

Spectrometer	**UV**		**UVIS**		**NIR**		**SWIR**	
Band ID	1	2	3	4	5	6	7	8
Full Range [nm]	270 – 320		310 - 495		675 - 775		2305 - 2385	
Performance range [nm]	270-300	300-320	320-405	405-495	675-725	725-775	2305-2345	2345-2385
Performance range [nm]	270-300	300-320	320-405	405-495	675-725	725-775	2305-2345	2345-2385
Spectral Resolution FWHM[nm]	0.48	0.49	0.54	0.54	0.38	0.38	0.25	0.25
Spectral Sampling [nm]	0.071	0.073	0.22	0.22	0.14	0.14	0.10	0.10
Spectral Sampling Ratio [1]	6.8	6.7	2.5	2.5	2.8	2.8	2.5	2.5
Slit Width (μm)	560	560	280	280	280	280	560	560
Spectral magnification	0.327	0.319	0.231	0.231	0.263	0.263	TBD	TBD
Spatial Sampling at nadir [km^2]	28x7	7x7	7x7		7x7	3.5x7	7x7	
Required Signal-to-noise	100-800 [2,3]	90-700 [2]	800-1000 [2]		100-500 [2,4]		100-120 [5]	

[1] The spectral sampling ratio is defined as the spectral resolution divided by the spectral sampling.
[2] The minimum signal to noise is specified for a reference scene with a surface albedo of 2% and the Sun in zenith.
[3] The signal to noise for Band 1 is specified for a ground pixel size of 21x28 km^2.
[4] The signal to noise for Band 6 is specified for a ground pixel size of 7x7 km^2.
[5] The signal to noise is specified for a reference scene with a surface albedo of 5% and solar zenith angle of 70°.

As shown in Table 4.2, the spatial sampling varies between the different bands of TROPOMI. Most of the bands have a sampling of 7 x 7 km^2 at nadir, except for Band 1, which has a sampling of 28 x 7 km^2 (across x along track) and Band 6, which has a sampling of 3.5 x 7 km^2. The L1B will report the spectra on these sampling, hence algorithms that combine different bands have to combine them in the Level 1-2 processing. The use of variable binning further complicates this for algorithms that combine UVN and SWIR bands, because the variable binning only applies to the UVN bands. As a consequence, the number of UVN pixels that are covered by a SWIR pixel varies from 1 in nadir to 4 at the end of the swath for Bands 2-5 and from 2 to 8 for Band 6.

In addition to the difference in spatial sampling, the area observed on Earth does not fully overlap between bands. This effect is described by the inter band co-registration error. These errors can be substantial (up to 50%) but analyses indicate that they will be stable in orbit. The inter band co-registration will be measured during on-ground calibration. The co-registration errors need to be compensated in the Level 1-2 processing when combining spectra from different spectrometers.

Besides inter band co-registration errors, there are also intra band co-registration errors. Intra band co-registration errors describe the difference in area observed on Earth for the different spectral channels within a spectrometer. Table 4.3 shows the intra-band co-registration errors for the along and the across track direction. It is noted that these numbers are for the entire spectrometer, for a spectral window that covers only a part of the spectrometer the errors will be smaller. Furthermore, these errors describe a worst case scenario which will probably occur at the ends of the swath. Closer to nadir these errors are expected to be much smaller. Co-registration errors are not corrected for in the L0-1B processor, but will be quantified using on-ground measurements. If these errors are affecting the L2 products significantly, they have to be addressed in the Level 1-2 processing steps.

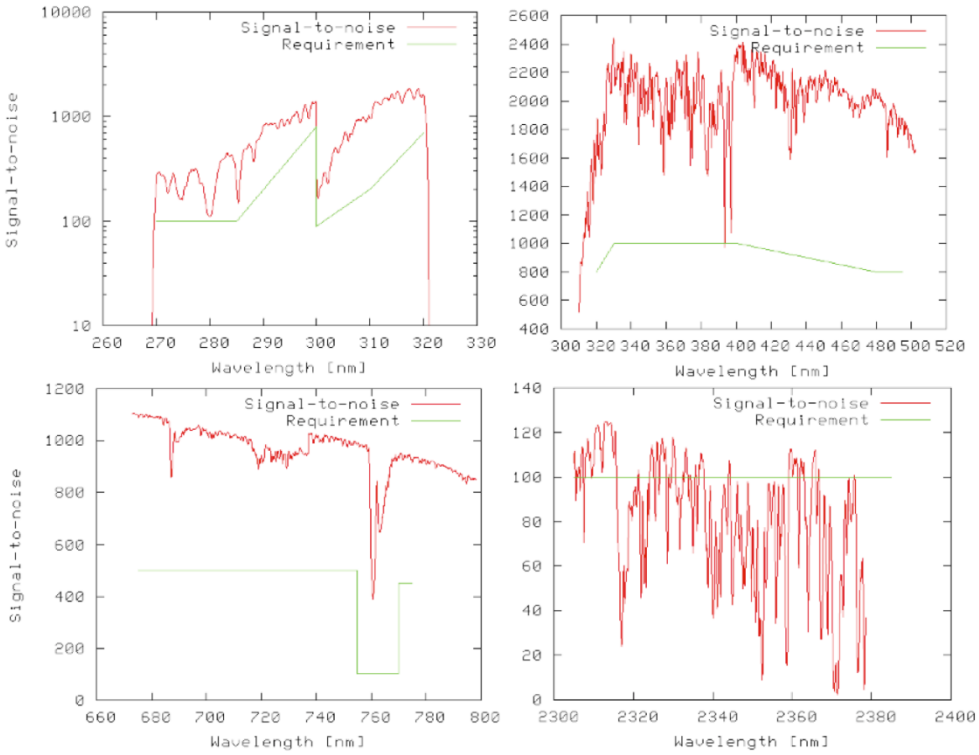

Figure 4.7: End-of-life signal-to-noise for reference scenes for the UV spectrometer (top-left), the UVIS spectrometer (top-right), the NIR spectrometer (bottom-left) and the SWIR spectrometer (bottom-right). The reference has a surface albedo of 2% and the Sun in the zenith for the UVN spectrometers and a surface albedo of 5% and solar zenith angle of 70° for the SWIR spectrometer. The green lines indicate the requirements, which are also given in Table 4.2. Source: [RD5]

Futhermore, it should be noted that each along-track row has a different wavelength grid, which is indicated by the term ‘spectral-smile’. This should normally be accounted for by using the correct wavelength assignment.

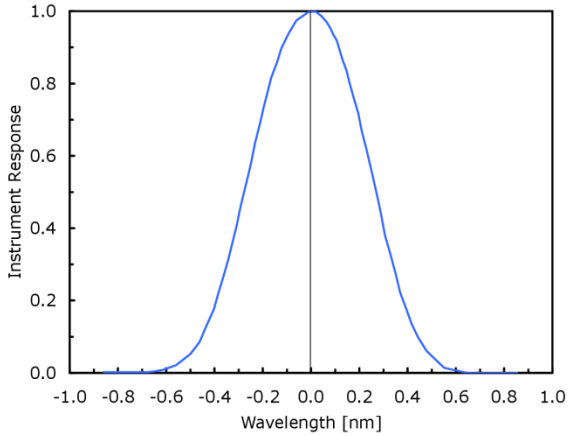

Figure 4.8: Example of a modeled instrument response function.

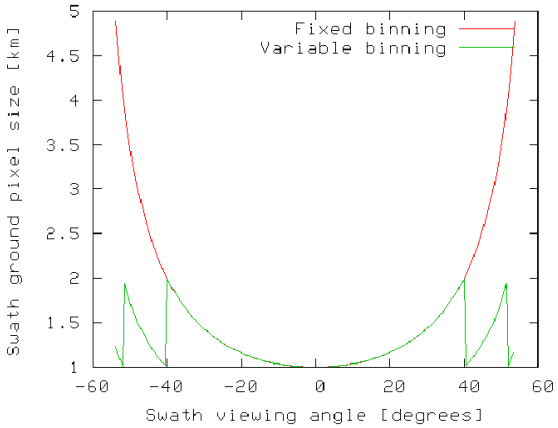

Figure 4.9: Across-track ground pixel size as a function of the viewing angle. The across-track size is given as increase compared to the nadir viewing direction. The red line indicates the ground pixel size with a constant binning factor, the green line indicates the ground pixel size with a variable binning factor, where the binning factor is reduced by a factor 2 and 4 at the point in the swath where the ground pixel size has double that of the nadir pixel size. [RD5]

Spectrometer	**UV**	**UVIS**	**NIR**	**SWIR**
error in across-track direction	20%	20%	10%	5.3%
error in along-track direction	12.5% (1%)	12.5% (1%)	12.5% (<1%)	5.3%

Table 4.3: Intra-band co-registration errors. Numbers in brackets indicate current best estimates.

4.4.5 Instrument Operations

For TROPOMI instrument operations, an orbital scheduling approach is used. An orbit is defined from spacecraft midnight to spacecraft midnight. This convention has the advantage that the orbits are defined without any seasonal dependency.

Earth radiance measurements will be performed on the day-side of the orbit. At the north side of the orbit, near the day-night terminator, the Sun is visible in the instrument's solar port. Approximately once a day, a solar irradiance measurement is performed. The night side of the orbit is used for calibration and background measurements.

To accommodate regular, fixed repetition intervals for the calibration measurements, a scheme of 360 orbits is used. As 360 is divisible by many numbers, it is possible to accommodate many different repetition intervals. For sake of simplicity, the 360 orbits are divided into 24 blocks of 15 orbits, each block corresponding to approximately 25 hours, or roughly to a day. A `week' is therefore defined to be 6 of these 15-orbit blocks and a `month' as 4 of these weeks. This allows for easy definition of calibration measurements that have (roughly) daily, weekly, biweekly or monthly repetition cycles.

4.4.6 Instrument modes

The TROPOMI instrument has many configurable parameters. For example, the exposure time, co-addition period, gains and (for UVN-DEMs) the binning factors can be varied. As a result the instrument can be operated in many different modes or configurations. Each combination of instrument settings is referred to as instrument configuration and is identified by an instrument configuration ID, a number in the range [1,65535]. This instrument configuration ID, or IcID, is primarily used by the instrument, where it identifies an entry in the instrument configuration tables. On ground the IcID is used to determine the intended purpose of a measurement and is used in the L01b data processing to determine the processing path.

For each IcID it is possible to have multiple versions, identified by the instrument configuration version or IcVersion. The combination of IcID and IcVersion uniquely identifies the set of configuration settings of the instrument. At a given time only one IcVersion of an IcID can be active within the instrument.

5 O3 Total Column

Authors: Johan de Haan (KNMI), Christophe Lerot (BIRA-IASB), Nan Hao (DLR)

5.1 Document changes

Changes in issue 2.0:

- Section added comparing ozone columns from prototype NRT (GDOAS) and offline chains (GODFIT).

5.2 Verification approach

In order to verify the retrieval algorithm for the total ozone column, synthetic spectra were generated using the software package DISAMAR developed at KNMI. For this purpose the European background profile from CAMELOT (with an integrated ozone column of 301.1 DU) was used and a Lambertian surface albedo of 0.05 (wavelength independent). There are no clouds or aerosols present in the atmosphere. Apart from the radiance spectra, detailed information was provided on the solar irradiance, (Rayleigh) scattering optical thickness, absorption optical thickness, depolarization factor, absorption cross-section of ozone, degree of polarization (if relevant) and filling-in to describe rotational Raman scattering (when relevant). The fitting window used by the prototype teams being 325-335 nm, the synthetic spectra have been generated between 320 and 340 nm to have some flexibility. Absorption by trace gases other than ozone was ignored.

Radiances and sun-normalized radiances were calculated for the following four cases:

- Case 1: polarization and rotational Raman scattering (RRS) ignored
- Case 2: polarization included and RRS ignored
- Case 3: RRS included and polarization ignored
- Case 4: polarization and RRS included

Here, we focus on just one geometry, namely nadir viewing and a solar zenith angle of 60 degrees.

It is interesting to note that filling-in [using the definition of Joiner: $(I_{inelastic} - I_{elastic}) / I_{elastic}$, where $I_{elastic}$ is the radiance for Rayleigh scattering, i.e. without RRS] differs when polarization is taken into account or not. Figure 5.1 shows the filling-in for these two cases.

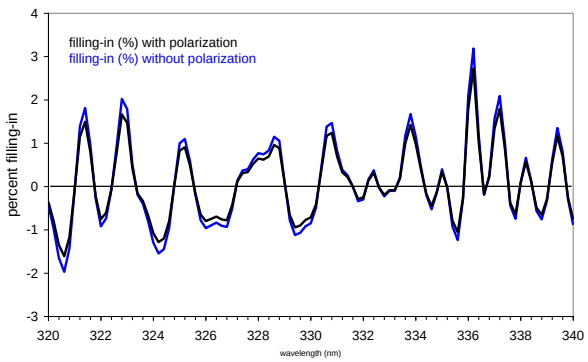

Figure 5.1: Difference in filling-in when polarization is included in the calculations or not.

This impact of polarization on the amplitude of the filling-in is well understood from the physics involved. Ideally, corrections for RRS should be based on Ring spectra (or filling-in) calculated when polarization is taken into account. In practice, very few radiative transfer codes exist that include both polarization and RRS. Therefore, the results obtained by DISAMAR are not well tested, as there is hardly any reference material available.

In the total ozone prototype algorithms, corrections for Ring (i.e. for RRS) are based on calculations ignoring polarization. This may lead to a bias in the retrieved ozone column, which is expected to be relatively small, in the light of the filing-in amplitude change simulated with DISAMAR when polarisation is included.

Initial results for the verification were obtained by Christophe Lerot (BIRA-IASB) and Nan Hao (DLR-IMF), for the offline and near-real time algorithms respectively. They reported good agreement when polarization and RRS were ignored in the calculations, but they found significant biases when polarization and RRS were included in the calculation of the synthetic spectra. Therefore the set of synthetic spectra was extended to the four cases mentioned above in order to try to identify the problem more precisely.

Total ozone columns from the prototype NRT (GDOAS) and offline (GODFIT) algorithms have also been compared in Section 5.5 in order to better illustrate the expected differences between the two approaches.

5.3 Results based on GODFIT (offline algorithm)

For this verification exercise, the same a-priori ozone and temperature profiles have been used as for generating the synthetic spectra (i.e. the European background scenario from CAMELOT). Therefore, the T-shift procedure available in the prototype algorithm has not been used. The same ozone cross-sections (DBM) have been used as in DISAMAR and they have been convolved with the specified instrumental function (a Gaussian with a FWHM of 0.55 nm). The Ring cross-section required in the empirical correction of GODFIT has been generated using the irradiance spectrum provided by KNMI.

GODFIT has two different closure modes to account for broadband structures not taken into account explicitly in the forward model:

- External closure mode: the simulated radiance is multiplied by an adjustable polynomial at each iteration. The albedo is fixed to the true value (0.05).
- Internal closure mode: An effective wavelength-dependent albedo is fitted simultaneously to the ozone column.

These two modes are tested in this verification exercise. The results are given in Table 5.1 - Table 5.4 below for each of the four spectra/cases provided by KNMI.

Table 5.1: No Polarization - no RRS case: Retrieved total ozone column and albedo and fit residuals RMS with internal or external closure. The closure degree is 0 (1 parameter).

	External closure	**Internal closure**
Tot. O3 (DU) **(Percent Error)**	300.5 (-0.2)	300.5 (-0.2)
Albedo (325nm)	NA	0.050
RMS (x1e-3)	0.16	0.16

Table 5.2: With Polarization - no RRS case: Retrieved total ozone column and albedo and fit residuals RMS with internal or external closure. The closure degree is 0 (1 parameter).

	External closure	**Internal closure**
Tot. O3 (DU) **(Percent Error)**	301.2 (0.0)	301.0 (0.0)
Albedo (325nm)	NA	0.051
RMS (x1e-3)	0.16	0.17

For the two first cases (without RRS), the retrieved column is very close to the true value with differences less than 0.2%. The fit residuals RMS are also very small. GODFIT is based on the scalar RT model LIDORT. To take atmospheric polarization into account, pre-tabulated correction factors are applied to the simulated radiances. From the computational point of view, this procedure is much more efficient than using a vector RT code such as VLIDORT. The excellent agreement we have for case #2 confirms that this procedure works well, at least for this scenario. Note also that the agreement is excellent with both internal and external closures, independently of the degree.

Table 5.3: No Polarization - with RRS case: Retrieved total ozone column and albedo and fit residuals RMS with internal or external closure. The closure degree is 0 (1 parameter).

	External closure	**Internal closure**
Tot. O3 (DU) **(Percent Error)**	308.3 (+2.4)	307.5 (+2.1)
Albedo (325nm)	NA	0.053
RMS (x1e-3)	1.34	1.31

When RRS is included in the simulations, the differences with respect to the true column are significantly larger (> 2%). Also the fit residuals are much larger as illustrated in Figure 5.2. Figure 5.3 compares the filling-in factors simulated by DISAMAR, the GODFIT forward model, LIDORT_RRS and also from simulations realized with a third RT model, i.e. SCIATRAN. Note that the filling-in factors in GODFIT are not produced directly from a radiative transfer model but are based on an empirical formulation, built to reproduce accurately filling-in factors computed by LIDORT_RRS. The general features are consistently reproduced by the four models. However, it is clear that the filling-in factors from DISAMAR slightly differ from the three other spectra, which agree excellently. Figure 5.4 shows the differences between the filling-in factors of GODFIT, LIDORT_RRS and SCIATRAN with respect to those from DISAMAR. It appears that the DISAMAR amplitude is larger, and also a slope is visible in the filling-in factor differences.

Table 5.4: With Polarization - with RRS case: Retrieved total ozone column and albedo and fit residuals RMS with internal or external closure. The closure degree is 0 (1 parameter).

	External closure	**Internal closure**
Tot. O3 (DU) **(Percent Error)**	307.5 (+2.1)	306.4 (+1.8)
Albedo (325nm)	NA	0.053
RMS (x1e-3)	1.14	1.11

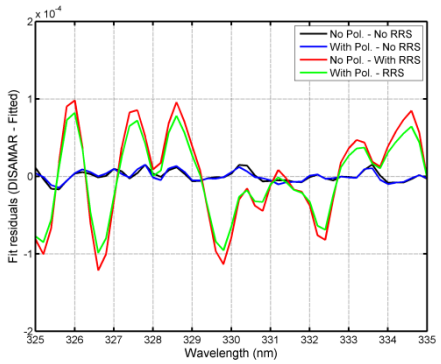

Figure 5.2: Fit residuals in the fitting window used for GODFIT total O_3 retrievals. Those correspond to the differences between the sun-normalized radiances simulated by DISAMAR and by the GODFIT forward model in the last iteration. These residuals are much larger when RRS is included in the two models.

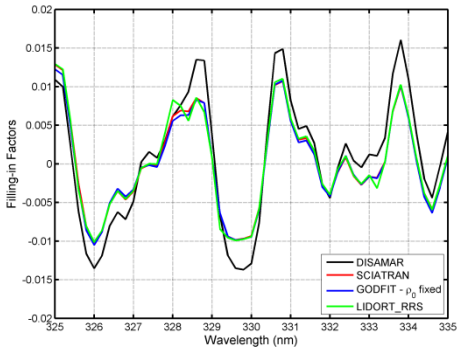

Figure 5.3: Comparison of the filling-in factors simulated by DISAMAR (KNMI), LIDORT_RRS, SCIATRAN and by the empirical formulation used in GODFIT.

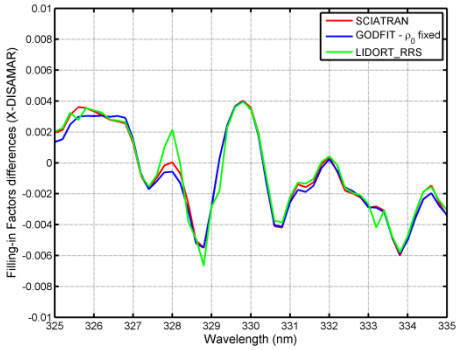

Figure 5.4: Absolute differences between the filling-in factors simulated by the GODFIT forward model, by LIDORT_RRS and by SCIATRAN on one hand and by DISAMAR (KNMI) on the other.

As a sanity test, we have used the DISAMAR filling-in factors instead of the nominal ones within the GODFIT retrieval procedure. Doing this for the case with RRS and no polarisation led to a retrieved column of 300.5 DU. The fit residuals were also significantly reduced. This confirms that the differences between the retrieved columns and the true value originate from differences in the simulations of the RRS signature.

Similarly, if we use the SCIATRAN filling-in factors (their amplitude being fitted) to correct the LIDORT elastic radiances for RRS within the fit procedure, we obtain an ozone column of 309.3 DU, consistent with the results shown in Table 5.3.

Finally we have tested the GODFIT algorithm on synthetic spectra generated with SCIATRAN for the same scenario. These tests have been done for the cases #1 (No polarization and no RRS) and #3 (No polarization and RRS) and the results are given in Table 5.4 for the external closure mode (results are similar for the internal closure mode). The agreement between the retrieved and the true columns is excellent for the two cases. Note also that the residuals RMS are smaller than those obtained using the DISAMAR spectra, even for the elastic case.

In summary, the total ozone columns retrieved with GODFIT from the DISAMAR synthetic spectra are in excellent agreement with the true column for this simple scenario as long as inelastic processes are neglected. The correction for polarization in GODFIT appears to be accurate enough. When RRS is included in the simulations, the retrieved columns deviate significantly from the “truth”. However, comparisons with filling-in factors from a third radiative transfer model SCIATRAN and additional GODFIT retrievals from SCIATRAN synthetic spectra indicate that the cause for these deviations is to be found in the DISAMAR verification forward model.

Table 5.5: SCIATRAN simulations: Total ozone column and fit residuals RMS of GODFIT retrievals from SCIATRAN simulations. The closure degree is 0 (1 parameter).

	No polarization - No RRS	**No polarization - With RRS**
Tot. O3 (DU) **(Percent Error)**	302.3 (+0.4)	301.5 (+0.1)
RMS (x1e-3)	0.08	0.25

Investigation has been carried out at KNMI to determine the source of uncertainties in the DISAMAR filling-in factor simulations. It has been found that the convolution with the rotational Raman lines in DISAMAR was inaccurate. This procedure has been improved in the verification forward model and new synthetic spectra have been generated for cases #3 and #4. Figure 5.5 is the same as Figure 5.3, except that filling-in factors computed by the improved version of DISAMAR are also compared to those from other models. The overall consistency of the filling-in factors from DISAMAR with those from LIDORT_RRS, SCIATRAN and from the empirical model used in GODFIT is improved, even if some differences remain. The total ozone columns retrieved with GODFIT from these new spectra are now in excellent agreement with the "true" column with differences less than 0.5% for cases #3 and #4 (see Table 5.6). This clearly demonstrates that the discrepancies previously observed originated from the inaccurate DISAMAR simulations of the RRS filling-in factors.

Also, additional spectra have been produced for case #3, but altering successively different parameters including SZA, surface albedo and ozone content as listed below:

- Case 3a: SZA=0°, albedo=0.05, Total ozone= 301.1 DU.
- Case 3b: SZA=80°, albedo=0.05, Total ozone= 301.1 DU.
- Case 3c: SZA=60°, albedo=0, Total ozone= 301.1 DU.
- Case 3d: SZA=60°, albedo=0.6, Total ozone= 301.1 DU.
- Case 3e: SZA=60°, albedo=0.05, Total ozone= 0.01 DU.

Table 5.6 presents the results of the analyses of these new sub-cases by GODFIT. The agreement with the true column is excellent for all these scenarios, the differences being always less than 0.5%. At the present time, it can be concluded that the verification and prototype algorithms present very similar performance in terms of accuracy for the retrieval of total ozone under the geophysical conditions covered by these scenarios. Some differences still remain between the DISAMAR RRS filling-in factors and those from the prototype algorithm GODFIT, which in turn agree very well with a third RT model SCIATRAN. It is therefore likely that the source of these discrepancies is in DISAMAR.

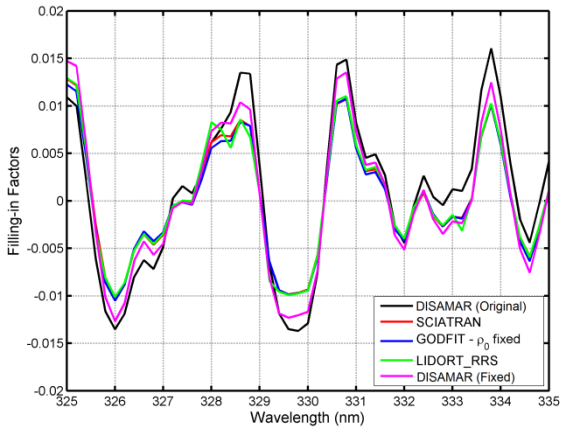

Figure 5.5: Comparison of the filling-in factors simulated by the improved version of DISAMAR (KNMI), LIDORT_RRS, SCIATRAN and by the empirical formulation used in GODFIT.

Table 5.6: Total ozone columns and fit residuals RMS of GODFIT retrievals from improved DISAMAR simulations. The closure degree is 0 (1 parameter).

	Tot. O3 (DU) (Percent Error)	**RMS (x1e-3)**
Case 3	300.1 (-0.3)	0.25
Case 4	300.5 (-0.2)	0.23
Case 3a	300.9 (-0.1)	0.17
Case 3b	301.5 (+0.1)	0.99
Case 3c	300.1 (-0.3)	0.26
Case 3d	299.9 (-0.4)	0.31
Case 3e	-0.5 NA	0.14

5.4 Results based on GDOAS (near-real-time algorithm)

The GDP algorithm employs the two-step Differential Optical Absorption Spectroscopy (DOAS) method, with slant column fitting followed by Air Mass Factor (AMF) conversion to the vertical column density (VCD). Ozone slant column density (SCD) is retrieved over the 325-335 nm fitting window using QDOAS developed at BIRA-IASB (http://uv-vis.aeronomie.be/software/QDOAS/). The fitting includes the effective temperature of the ozone absorption and scaling factors for interference due to the Ring effect (only used for the RRS cases). For this verification test, DBM ozone cross-sections at 243 K and 218 K used in DISAMAR have been convolved with the instrumental slit function (a Gaussian with a FWHM of 0.55 nm). The Ring cross-section has been calculated from the irradiance spectrum provided by KNMI and by folding rotational Raman cross-sections at a fixed temperature with a high-resolution Fraunhofer spectrum (Chance and Kurucz, 2010) respectively. The first 'Exact' Ring cross-sections are calculated using formula:

$$Ring = \log\left(\frac{I^{elastic} + I^{inelastic}}{I^{elastic}}\right) \quad (1)$$

which are fully consistent with the simulated scenes. The second 'Franhofer' Ring cross-section does not include telluric contribution which has been corrected using a molecular Ring correction since GDP 4.0. The molecular Ring correction is calculated by the following formula

$$M_{ring} = E_{ring} \cdot \sigma_{ring} \cdot \left(1 - \frac{\sec(\theta_0)}{A}\right) \quad (2)$$

where A is the ozone AMF, θ_0 the viewing zenith angle, E_{ring} the SCD of Ring and σ_{ring} the average Ring cross-section calculated over 325-335 nm.

For the second step, LIDORT v3.6 and VLIDORT v2.6 have been used to calculate AMFs at 325.5 nm for cases without polarization and with polarization, respectively. The ozone and temperature profiles (the European background scenario from CAMELOT) provided by KNMI were interpolated into 13 layers.

The results are given in Table 5.7 for case 1 and 2 and

Table 5.8 for case 3 and 4. The two Ring cross-sections are tested for the RRS case. The SCD retrieval and AMF calculation will be discussed separately.

As seen from Table 5.7 and

Table 5.8, the retrieved SCD without RRS and with RRS cases are the same when 'Exact' Ring cross-sections are included in fitting for RRS cases. Also the RMS remains small for both cases as expected. However, this 'Exact' Ring cross-section is not available for the real process of satellite data retrieval. We have to use the 'Fraunhofer' Ring cross-section following by a molecular Ring correction in the operational processing (default setting for GDP). As shown in Figure 5.6, the RMS increases when RRS is included in the simulation. The O_3 SCD decrease by about 6.6% and 5.7% for cases without polarization and with polarization, respectively, compared to using the 'Exact' Ring cross-section. It was found that neglecting the telluric Ring effect leads to systematic underestimated of ozone total columns by up to 10% (Van Roozendael et al., 2002). Our results are consistent with this finding. After the application of the molecular Ring correction, the underestimation with respect to using 'Exact' Ring cross-section is partly compensated. However, the differences between using 'Fraunhofer' and 'Exact' Ring cross-section are still quite large (-4.2% and -4.0% for the cases without polarization and with polarization).

Table 5.7: No RRS case: slant column density (SCD), DOAS fitting residual (RMS), AMF calculated at 325.5 nm, vertical column density (VCD)

	No Polarization **No RRS**	**With Polarization** **No RRS**
SCD	2.29E+19	2.27E+19
RMS	1.20e-3	1.18e-3
AMF (325.5 nm)	2.85	2.83
VCD (DU) **(Percent Error)**	299.0 (-0.7%)	298.5 (-0.9%)

Table 5.8: RRS case: slant column density (SCD), DOAS fitting residual (RMS), AMF calculated at 325.5 nm, vertical column density (VCD)

	No Polarization **With RRS**	**With Polarization** **With RRS**	**No Polarization** **With RRS using 'Fraunhofer' Ring Correction**	**With Polarization** **With RRS using 'Fraunhofer' Ring Correction'**
SCD	2.29E+19	2.27E+19	2.14E+19	2.14E+19
SCD_{corr} with M_{ring}			2.21E+19	2.20E+19
RMS	1.20e-3	1.18e-3	1.46e-3	1.36e-3
AMF (325.5 nm)	2.85	2.83	2.85	2.83
VCD_{corr}(Percent Error)	299.0 (-0.7%)	298.5 (-0.9%)	288.6 (-4.2%)	289.3 (-4.0%)

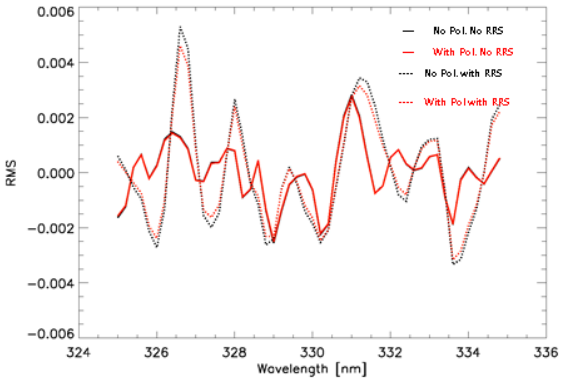

Figure 5.6: DOAS Fit residuals in the fitting window for the four cases. 'Faunhofer' Ring cross-section is used for ozone fit. These residuals are much larger when RRS is included.

Similar as in section 5.3, we also tested the QDOAS algorithm on synthetic spectra generated with SCIATRAN for the scenario: No polarization and no RRS and no polarization and RRS. The results are given in Table 5.9. The agreement between the retrieved and the true columns is excellent for these two cases. The differences of O_3 SCD between using 'Exact' Ring cross-section and 'Fraunhofer' Ring cross-section changed from -2.2% to -0.7% after using the molecular Ring correction. The results are consistent with our previous study using LIDORT-RRS model. Also Van Roozendael et al. (2006) showed that the systematic underestimation of using 'Fraunhofer' Ring cross-section is largely compensated by the molecular Ring correction (see Figure 8 in this reference). For this verification study, the incomplete achievement of the molecular Ring correction might be related to the differences in the simulations of the RRS signature for DISAMAR and LIDORT-RRS which has been discussed in section 5.3.

After correcting the convolution with the rotational Raman lines in DISAMAR, the new synthetic spectra have been analyzed using the GDP algorithm. The total ozone columns are now in better agreement with the "true" column than before, showing differences within 2% for no polarization (cases 3) and with polarization (case 4, see Table 5.10). The agreement with the "true column" is also good (within 2%) for the other scenarios (case 3a, 3c, 3d and 3e) except for SZA equal 80 (case 3). Part of this large difference (3.5%) is probably related to the single wavelength AMF calculation and partially to the differences between the DISAMAR RRS filling-in factors and those from other radiative transfer models.

The AMF calculated from DISAMAR for 325 nm is 2.802 and 2.776 without and with polarization, respectively. To verify the AMF calculation, we also used LIDORT and VLIDORT to calculate the AMF at 325 nm. The AMF difference between using DISAMAR and using LIDORT, VLIDORT AMF is about -1.5% and -1.8% for cases without and with polarization.

Table 5.9: SCIATRAN simulations: slant column density (SCD), DOAS fitting residual (RMS), AMF calculated at 325.5 nm, vertical column density (VCD)

	No Polarization No RRS	**No Polarization With RRS**	**No Polarization With RRS using 'Fraunhofer' Ring Correction**
SCD	2.31E+19	2.31E+19	2.26E+19
SCD_{corr} with M_{ring}			2.29E+19
RMS	1.17e-3	1.17e-3	1.43e-3
AMF (325.5 nm)	2.85	2.85	2.85
VCD_{corr}(Percent Error)	301.6 (0.2%)	301.6 (0.2%)	299.0 (-0.7%)

Table 5.10: RRS case: slant column density (SCD), DOAS fitting residual (RMS), AMF calculated at 325.5 nm, vertical column density (VCD)

	No Polarization With RRS	**With Polarization With RRS**	**No Polarization With RRS using 'Fraunhofer' Ring Correction**	**With Polarization With RRS using 'Fraunhofer' Ring Correction'**
SCD	2.32E+19	2.30E+19	2.20E+19	2.19E+19
SCD_{corr} with M_{ring}			2.35E+19	2.32E+19
RMS	3.43e-4	3.25e-4	4.98e-4	4.35e-4
AMF (325.5 nm)	2.85	2.83	2.85	2.83
VCD_{corr}(Percent Error)	302.95 (0.6%)	302.46 (-0.5%)	306.8 (1.9%)	304.7(1.2%)

In summary, the ozone VCD differences with respect to the true column are within 1% for the case without RRS. When RRS is included in the simulations, the differences are within 2% for SZA smaller than 80. One reason for larger differences at SZA > 80° is that the molecular Ring correction cannot fully compensate the effect of neglecting the telluric Ring effect when we use 'Fraunhofer' Ring cross-section. Another reason is the difference of AMF calculation using DISAMAR and using LIDORT, VLIDORT.

5.5 Comparison of GDOAS and GODFIT total ozone columns

A subset of OMI data (one day/month in 2006) has been processed using both the prototype NRT (GDOAS) and the offline (GODFIT) total ozone algorithms in order to illustrate the expected differences between the two approaches.

Figure 5.7 shows typical relative differences between the total ozone columns retrieved using the NRT prototype algorithm based on the DOAS approach and the offline prototype algorithm using a direct-fitting approach for one day of OMI data. In general, ozone columns from the two approaches agree well at low and mid-latitudes and differences become larger at high latitudes. Those differences result mostly from

(1) The more realistic forward model of the direct-fitting approach in which the radiative transfer is simulated at every wavelength of the fit window. In DOAS, the radiative transfer simulation is performed at one single wavelength, leading to systematic biases at high solar zenith angles and/or large ozone optical depth.

(2) The fit of an effective albedo simultaneously to the ozone column in the direct-fitting approach. This removes errors introduced by the use (as done in DOAS) of highly uncertain climatological albedo values, especially at high latitudes.

The combination of those two aspects may lead to a few percent differences in Polar Regions (sometimes up to 10 percent under extreme conditions). Figure 5.8 shows the seasonal dependence of the zonal mean total ozone differences between the DOAS and direct-fitting approaches. It illustrates clearly the larger differences at high latitudes and the associated seasonality related to solar zenith angle variation. Figure 5.9 shows more explicitly the dependences of the DOAS/direct-fitting differences as a function of the solar zenith angle on one hand, and of the differences between albedo from a climatology or retrieved with GODFIT, on the other. Again, the largest albedo differences are expectedly found at high latitudes, which combined with the large SZA there may lead to very high differences.

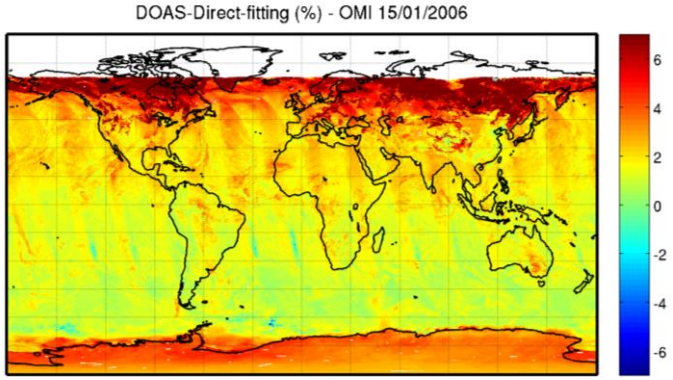

Figure 5.7: Relative differences between total ozone columns retrieved with the NRT (DOAS) and offline (Direct-fitting) algorithms from one day of OMI level-1 data

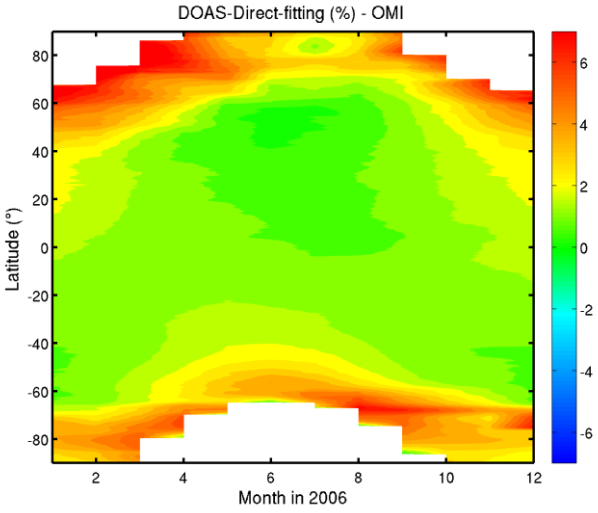

Figure 5.8: Zonal mean DOAS/Direct Fitting total ozone relative differences plotted as a function of the month.

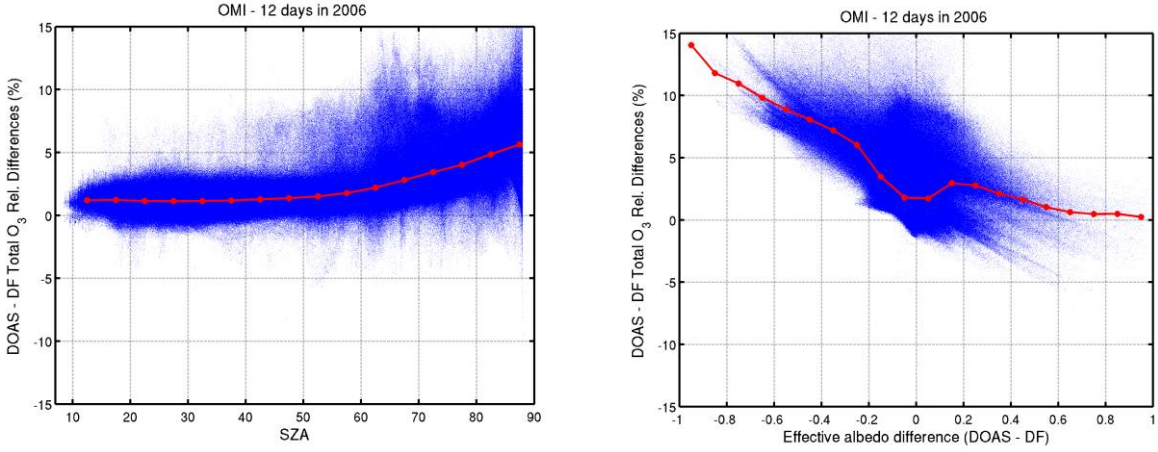

Figure 5.9: DOAS/Direct-Fitting total ozone relative differences as a function of solar zenith angle (left panel) and of the albedo differences (right panel).

The approach for the cloud correction is also slightly different between the two prototype algorithms. While the DOAS approach relies on the classical Independent Pixel Approximation, GODFIT uses a simple effective scene located at a level located in between the cloud and the ground, of which the effective albedo is fitted during the retrieval (see total ozone ATBD for more details). Systematic differences are visible for high clouds, for which DOAS ozone columns are on average a few percent larger than GODFIT columns. This is illustrated in Figure 5.10 showing mean total ozone relative differences as a function of the cloud top pressure provided by the OMI O_2-O_2 cloud product.

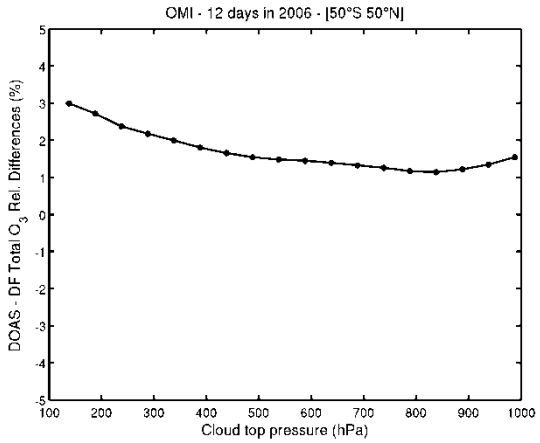

Figure 5.10: DOAS/Direct fitting total ozone differences for latitudes between 50°S and 50°N as a function of the O_2-O_2 cloud top pressure.

5.6 Summary of verification results

- The verification algorithm did produce inaccurate RRS filling-in factors. This has been fixed and now produces results consistent with those from the offline prototype algorithm GODFIT and from SCIATRAN.
- The total ozone columns retrieved with the offline prototype algorithm agree very well with the true column used for generating synthetic spectra with the improved version of DISAMAR.
- The total ozone columns retrieved with the near-real time prototype algorithm agree well with the true column in most cases for the new synthetic spectra.
- Differences between the total ozone columns retrieved from the NRT and offline prototype algorithms are mostly significant at high latitudes and result from the combination of systematic biases in DOAS at large SZA and of uncertain climatological albedo values.

5.7 References

Chance K and Kurucz R. L. (2010) An improved high-resolution solar reference spectrum for Earth's atmosphere measurements in the ultraviolet, visible, and near infrared. JOURNAL OF QUANTITATIVE SPECTROSCOPY & RADIATIVE TRANSFER Volume: 111 Issue: 9 Special Issue: SI Pages: 1289-1295.

Van Roozendael, M., Soebijanta, V., Fayt, C., and Lambert, J.-C.: Investigation of DOAS issuesaffecting the accuracy of the GDP version 3.0 total ozone product, in: ERS-2 GOME GDP30 3.0 Implementation and Delta Validation, edited by: Lambert, J.-C., ERSE-DTEX-EOAD-TN-02-0006, ESA/ESRIN, 97–129, Eur. Space Agency, Frascati, Italy, 99–131, 2002.

Van Roozendael, M., Loyola, D., Spurr, R., Balis, D., Lambert, J.-C., Livschitz, Y., Valks, P., Ruppert, T., Kenter, P., Fayt, C., and Zehner, C.: Ten years of GOME/ERS-2 total ozone data-The new GOME data processor (GDP) version 4: 1. Algorithm description, J. Geophys. Res., 111, D14311, doi:10.1029/2005JD006375, 2006.

6 O3 profile (including troposphere)

Authors: Richard Siddans (RAL), Georgina Miles (RAL), Mark Weber (IUP-UB), Stefan Bötel (IUP-UB)

6.1 Document changes

Changes in issue 2.0:

- Minor changes in most sections, leading to some changes in section numbering.
- Inclusion of new linear and non-linear retrievals from prototype scheme, and comparison to vertification schemes.
- Update of section 6.6.6
- Inclusion of Figure 6.16, Figure 6.17 and Figure 6.18
- Inclusion of Table 6.8, Table 6.9, Table 6.10, and Table 6.11

6.2 Verification approach

The verification of the prototype algorithm for the retrieval of ozone profiles is based on two different verification algorithms. As both verification algorithms are very different they will be described separately and their performance will also be evaluated separately.

The basic joint verification approach is as follows:

- Comparison of basic retrieval diagnostics for the reference conditions.
- Comparison of retrieved profiles from non-linear retrievals applied to simulated measurements.
- Comparisons using retrievals from real satellite measurements have also been made between the two verification algorithms.

6.3 Description of Verification Algorithm - RAL Ozone Profile Algorithm

The RAL profile scheme (Munro, (1997), Siddans (2000), Miles (2015)) is an optimal estimation method (OEM) algorithm which uses a three step approach to retrieve ozone profile information spanning troposphere and stratosphere:

- “B1 fit”: Fit ozone profile to the sun-normalised radiance in the Harley band (in GOME Band 1) from 265-307nm.
- “Albedo fit”: Fit effective surface albedo for the Huggins bands from a narrow region (where ozone absorption is low) around 334nm (assuming the B1 ozone to be correct).
- “B2 fit”: Add information on ozone from the differential absorption spectrum in the Huggins bands between 322 and 334nm. I.e., retrieve ozone taking the B1 result to define the prior state and errors. Here measurements are fit to very high precision (better than 0.1%), to extract tropospheric information from the temperature dependent structure. A differential absorption approach is used to prevent broad-band instrumental artefacts from degrading the quality of the fit.

Each step of the RAL retrieval is performed using optimal estimation (Rodgers, 2000). The standard equations apply.

In order to fit the Huggins bands to the required accuracy it is necessary to model the Ring effect and the effect of under-sampling / wavelength mis-registration between direct-sun and back-scattered spectra. This model relies on accurate knowledge of the slit-function and the wavelength registration relative to the solar reference spectrum used in the model. These parameters are derived by fitting measured solar spectra to a high-resolution reference spectrum, optimising wavelength calibration parameters and the width of the instrument slit-function. For GOME-2, the on-ground measured slit functions are used as the basis for this fit. For GOME-1, a Gaussian shaped slit-function is assumed.

The B1 and B2 retrievals both make use of the estimated random error on measurements provided by appropriate instrument noise model. However, in both steps noise-floors (upper limits on the fitting precision) are imposed. The noise-floor values are arrived at empirically by inspection of fitting residuals and comparison of retrievals with climatology and validation data. In B1 the noise floor is set to 0.01 in sun-normalised radiance units. In B2 the value varies with solar zenith angle, but is typically 0.05% (0.0005 in units of the natural log of the sun-normalised radiance).

Since the absolute sun-normalised radiance is used in the B1 fit, and this is subject to degradation over time (which varies from instrument to instrument). An empirical correction scheme is used to correct the level1 data in the B1 range (265-307nm) used. This is based on modelling observed radiances based on climatological ozone distributions and fitting a polynomial in time (sufficient to capture seasonal variations) and wavelength (4th order over the band) which captures the deviations of the observations from the climatological predictions.

6.3.1 Main differences to Prototype

The three step procedure, in particular the use of differential absorption spectra in the Huggins bands, is distinct from the operational approach. This provides significantly different sensitivity to tropospheric ozone and instrumental artefacts which should be informative for the prototype algorithm development. It is also notable that differences in ozone prior error also influence the estimated precision of retrieved profile error, and the two schemes use characteristically different approaches in this respect which cannot be harmonised without impacting the algorithms' behaviour. The RAL scheme requires a more relaxed prior error for ozone in order for it to be sensitive to the real state. This arises from the high precision fit in the Huggins bands that the RAL scheme is optimised for, which is required to capture the temperature-dependent structure that yields information for tropospheric ozone. The approach is different for the prototype algorithm, where a tighter prior constraint is assumed.

6.3.2 Forward model

Temperature and pressure profiles are taken from meteorological analysis. Usually ECMWF ERA-Interim profiles are used, though Met Office stratospheric analyses have been used in the past.

A background aerosol profile taken from MODTRAN is assumed.

Cloud may be ignored (in which case it is fitted via the retrieved surface albedos) or modelled according to information either from GOME (O_2 A-band retrieval) or co-located imagery (AATSR for GOME-1 and AVHRR for GOME-2).

To perform the radiative transfer the scheme uses a version of the GOMETRAN++ (Rozanov et al., 1997) but with a number of processing speed improvements implemented at RAL.

6.3.3 Inverse Algorithm

6.3.3.1 Iterations and convergence

The standard Marquardt-Levenberg approach is used.

Convergence is judged to occur if (a) the cost function (absolute value, not normalised by the number of elements in the state vector) changes by <1 (b) at this point a Newtonian iteration (i.e., a step without applying the Marquardt-Levenberg damping) also results in a change in cost of <1. This 2nd criterion ensures retrievals do not appear to converge due to a high value of the Marquardt-Levenberg damping parameter.

6.3.3.2 State vector

Ozone retrieval levels are defined to be pressure levels of 1000, 422, 177, 100, 56, 32, 18, 10, 5.6, 3.2, 1.8, 1.0, 0.56, 0.32, 0.18, 0.10, 0.056, 0.032, 0.018, 0.01 hPa, i.e., approximately 0, 6, 12 km, then at 4 km intervals up to 80 km. These are chosen to over-sample the resolution expected on the basis of averaging kernel analysis. The forward model performs radiative transfer calculations at a finer vertical resolution than the retrieval levels, varying from 1 to 2km, the output of which is interpolated onto the retrieval grid.

State vector elements in the B1 fit other than the ozone profile are as follows:

- Leakage Current: A leakage current in binary units is fitted in B1, to correct for imperfect prediction of this at level1. A single parameter is fit for the band, unless the Band1A/Band1B boundary occurs below 307nm, in which case one parameter is fitted for each sub-band. The leakage current in binary units (BU) is assumed constant with wavelength.
- Lambertian effective surface albedo: A single, wavelength independent albedo is retrieved.
- Ring effect: Two parameters are fitted, namely:
    - Scaling factor for the single-scattering Ring effect filling-in factor (as modelled via the approach of Joiner(1995);
    - Wavelength shift of the pattern relative to the nominal wavelength calibration.
- Wavelength shift of the absorption cross-section: A single parameter represents a shift of the GOMETRAN modelled spectrum (before Ring effect or slit-function convolution are simulated), with respect to the measured sun-normalised radiance. The magnitude of the retrieved shift is such that it can be considered to pertain effectively to the trace-gas absorption cross-sections, since the scattering coefficient varies relatively weakly with wavelength.

State vector elements in the B2 fit other than the ozone profile are as follows:

- Ring effect: A single scaling parameter is fitted (to represent approximately the expected number of scattering events). No wavelength shift is fitted in this case; the mis-registration / under-sampling correction makes the shift of the filling-in spectrum redundant.
- Wavelength shift of the absorption cross-section: The parameter has the same meaning as the corresponding B1A state-vector element. In this case a 2nd order polynomial fit to the wavelength shift is fitted across the measurement vector range.
- Wavelength mis-registration between solar and back-scattered spectrum: Parameters in 3rd order polynomial expansion (as above) of the wavelength shift between the GOME solar irradiance and back-scattered spectra used to form the sun-normalised radiance.
- Column amounts of NO_2, formaldehyde, and BrO, with a fixed climatological profile shape.
- Residual scaling factor: A single scaling factor for the systematic residual.

6.3.4 Error Characterization

A quite complete study of the errors pertaining to the profile retrieval is reported in (Siddans 2003). This was based on performing retrieval simulations for a set of basic geo-physical scenario which had been defined for the GOME-2 Error Study (Kerridge 2002), which also contains a detailed error budget. For these conditions basic retrieval diagnostics such as averaging kernels and solution covariances were computed. A large number of additional error sources were also considered. These included an assessment of errors on retrieved ozone introduced by the presence of aerosols, incorrect surface pressure, errors in the prescribed temperature profile, scan mirror degradation, polarisation and radiometric calibration. While this error study was appropriate for the retrieval scheme as before some of the more recent developments outlined above were implemented, it may be considered as providing a baseline characterisation of the retrieval error. The main results are summarised here:

- The retrieval provides useful information on the ozone profile below 50km.
- Retrieval precision, accounting for measurement noise and other quasi-random errors is expected to be generally in the few-percent range in the stratosphere increasing to a few 10s of percent in the lowest retrieval levels.
- Retrieved quantities should be interpreted as estimates of layer-averaged number density, taking into account the shape of the averaging kernels, and the influence of the a priori.
- The instrumental and RTM errors are generally relatively small, compared to the climatological variance and, in most cases, the estimated standard deviation (ESD). Exceptions are radiometric gain errors including scan-mirror degradation (which has most impact above 40 km) and possibly imperfect knowledge of slit-function shape (expected to cause a significant negative bias in the troposphere, though the magnitude is difficult to quantify). These errors are currently addressed in the real scheme by the empirical degradation correction factor, but still represent a significant issue for long-term quality of the retrieved profiles.
- High perturbations in aerosol and errors in the assumed temperature profile give rise to retrieval errors in the troposphere of order 10-20%. (The temperature error is larger at high solar zenith angle.)
- Radiative transfer model approximations in the retrieval scheme are seen to be adequate.
- It was also noted that for GOME-1 a significant error source was lack of pre-flight measurement of the slit-function. Pre-flight characterisation of GOME-2 has much reduced uncertainties for that instrument at the beginning of life but in-orbit changes may mean this source of error is important for GOME-2 as well.

An evaluation of the quality of the estimate of retrieval errors using real measurements against ozonesondes was performed in Miles (2015), which showed them to be a good estimate of the true error.

6.3.5 Prior Information

The *a priori* covariance is used to constrain the profile shape. An *a priori* correlation length of 6km is imposed for the Harley band fit (B1).

The values of the *a priori* and corresponding errors are taken from the McPeters-Labow climatology, but the errors are subsequently modified to allow the retrieval sufficient sensitivity to information from the measurements for all cases.

For the B2 fit, the *a priori* is taken from the B1 retrieval, on the same levels. Instability in the retrieval at UT/LS altitudes was encountered when the full solution covariance, from the B1 retrieval was taken to define the *a priori* covariance for the B2 retrieval. This instability was reduced by using a Gaussian *a priori* covariance with 8km correlation length and *a priori* standard deviation equal to that from the B1 fit.

To avoid too tight an *a priori* constraint, and to avoid spurious effects in the retrieval due to the imperfect sampling of the tropospheric variance by the climatology, the relative *a priori* errors are set to the larger of the climatological standard deviation and the following minimum values:

- 0-12km: 100%
- 16km: 30%
- 20-50km: 10%
- 56km: 50%
- 60-80km: 100%

Figure 6.1 shows an example of simulated averaging kernels for the RAL algorithm (with S5 settings currently). Differences between these simulations and those based on S5P settings are expected to be small. The figure indicates the expected improvement upon prior uncertainty and sub-column retrieval error for a reference atmospheric case using the CAMELOT European background profile. These will be updated with settings for Sentinel 5 Precursor (such as a realistic noise estimate) when they become available.

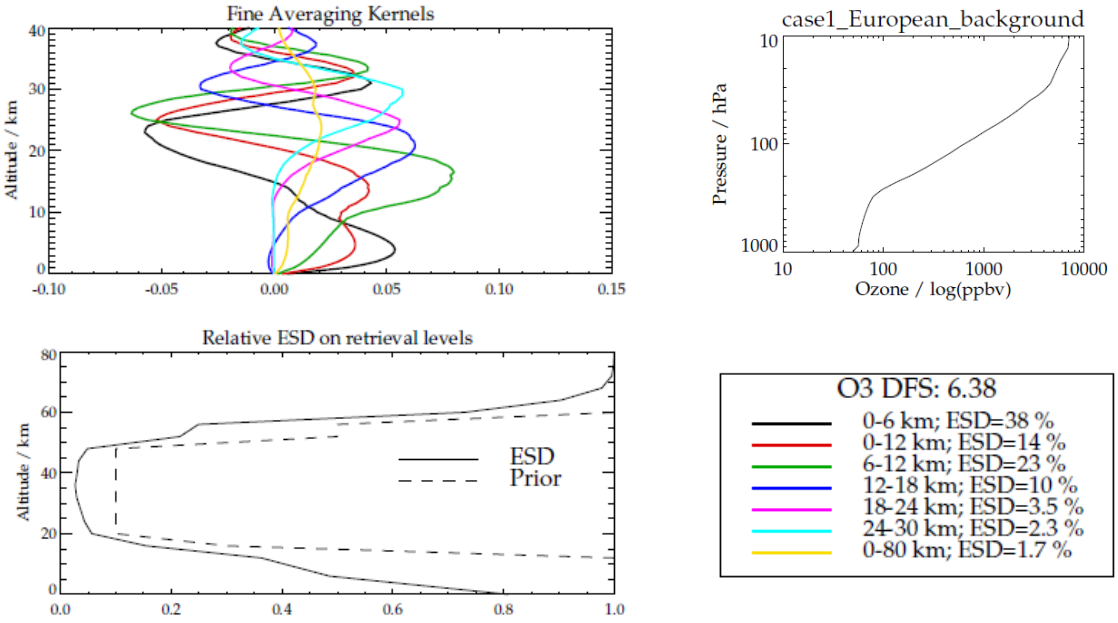

Figure 6.1: Simulated fine averaging kernels in number density units (top left) for CAMELOT European background profile (top right) with SZA 30°, nadir view and a surface albedo of 0.02. The ESD (see text) is the estimated retrieval error, as compared to the prior error profile (bottom left), and retrieved sub-columns (bottom right), where the Degrees of Freedom for Signal (DFS) is also indicated.

6.3.6 Model Errors

Here we use the estimated standard deviation (ESD) which can be used as an estimate of the expected retrieval error. It is the standard deviation of the diagonal of the simulated retrieval covariance matrix for ozone.

6.3.7 Instrumental errors

Comparisons of the sensitivity to instrumental errors of the RAL and S5P prototype scheme have been carried out in a parallel ESA study to define requirements for Sentinel 5.iterative (and to an extend non-iterative) retrieval simulations can not be performed until an adequate or reasonable noise model can be agreed upon or provided.

- Noise
- radiometric calibration
- stray light
- spectral calibration
- slit function

6.3.8 Algorithm Validation

See section below, entitled “Validation”, or else Miles et al 2015.

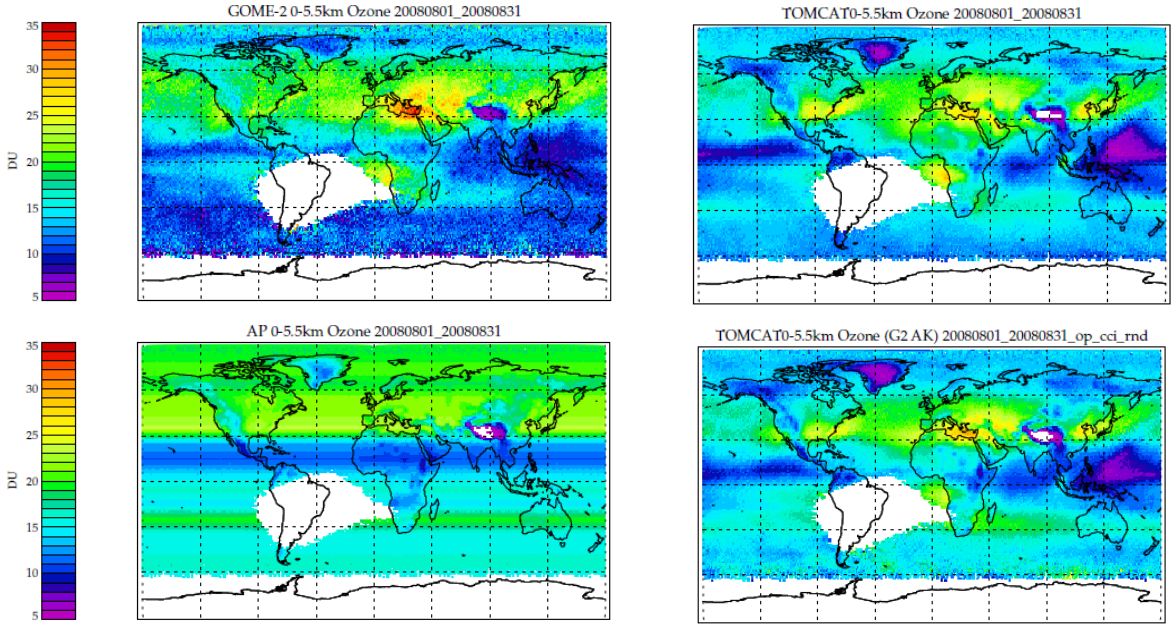

Figure 6.2: August 2008 monthly mean of 1000-450hPa sub-column ozone retrieved by GOME-2 (top left), a priori used (bottom left) and output from the Chemistry Transport Model TOMCAT (U. Leeds) as sampled by GOME-2 (top right) and with GOME-2 averaging kernels applied (bottom right). The GOME-2 data has not been cloud cleared.

6.3.9 Application to real data

The scheme has been extensively applied to process GOME-1 and GOME-2 datasets. It is one of the candidate algorithms being assessed in the ESA CCI Ozone project, alongside KNMI’s OPERA scheme. Subsets of SCIAMACHY data have also been processed (Siddans, 2007). The scheme was also used in the ESA Camelot study (Veefkind, 2009) to define observational requirements for Sentinels 4 and 5.

The RAL ozone profile algorithm has been applied to GOME, SCIAMACHY and GOME-2 data. An example is shown in Figure 6.2, of the mean of one month of lower tropospheric ozone from GOME-2. The *a priori* used in the retrieval is also indicated. Output from the Chemistry Transport Model TOMCAT [Richards et al., 2013] is shown for the same period, with and without GOME-2 averaging kernels applied. The TOMCAT is a tropospheric CTM so the model stratosphere has been replaced by with the ECMWF Operational ozone product. The GOME-2 data has not been cloud cleared in the case shown here for the sake of being comprehensive, but in the case of high/thick cloud this can lead to an underestimate of lower tropospheric ozone, which is particularly evident in the southern hemisphere oceans in the tropics and extra-tropics.

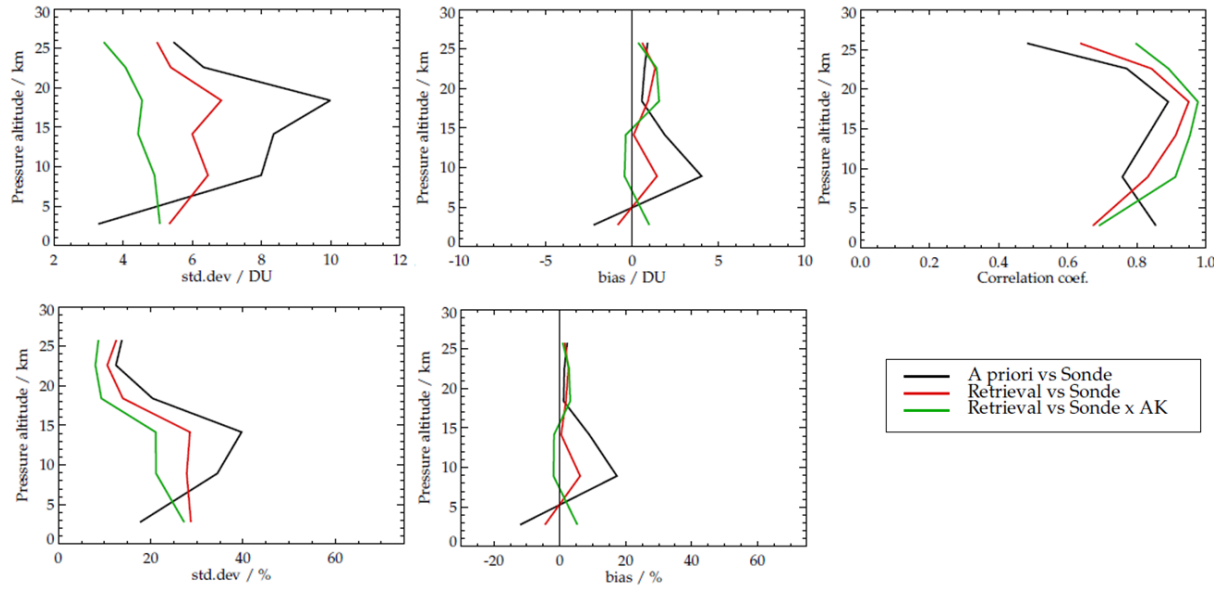

Figure 6.3: Statistical comparison of RAL GOME-2 ozone profiles with ozonesondes sampled worldwide for 2007-2008 (WOUDC [Fioletov et al., 2008] and SHADOZ [Thompson et al., 2003]). Collocation criteria 2 hours and 200km. The standard deviations (left) and biases (centre) in GOME-2 minus ozonesonde values are in absolute (DU) units and as % of sonde value in the top and bottom rows, respectively. The top right panel shows the correlation coefficient. Points denote the mid-point of each sub-column. In each case, results are shown for the a priori vs sonde and for the retrieval vs sonde with and without application of AKs to the ozonesonde profiles. Statistics have been derived from percentage difference calculated with respect to each individual ozonesonde. Figure taken from Miles et al 2015.

6.3.10 Validation

The RAL ozone profile algorithm was described and validated in Miles (2015). It also underwent a full and extensive validation by (Keppens (2014)). An interim validation was also performed under the auspices of the ESA CCI ozone ECV project in the form of a round robin exercise where the RAL algorithm (v2.1) was compared with the GOME-2A Operational algorithm from OPERA, from KNMI. The round robin validation results are summarised in the Draft Product Validation and Selection Report (PVASR) (http://www.esa-ozone-cci.org/?q=webfm_send/58).

Figure 6.3 shows 2 years of global average GOME-2 ozonesonde agreement (2007-2008) from the RAL ozone profile product. The bias and precision for ozone profiles are height and latitude dependent, and Figure 6.4 shows the same information as a function of latitude. Globally for GOME-2, a bias of between 5 and 20% is found in the troposphere and typically less than -10% in the lower stratosphere with respect to ozonesondes in 2008. The standard deviation is found to be between 15 and 30% in the troposphere and 20% in the lower stratosphere. The global tropospheric bias is primarily driven by particularly challenging ozone profile conditions at high latitudes in Northern Hemisphere spring, where the stratospheric ozone concentration is very high, the tropopause altitude is relatively low and the ozone profile has considerable vertical structure in this region. Outside of these conditions the profile bias and standard deviation with respect to ozonesondes are reduced.

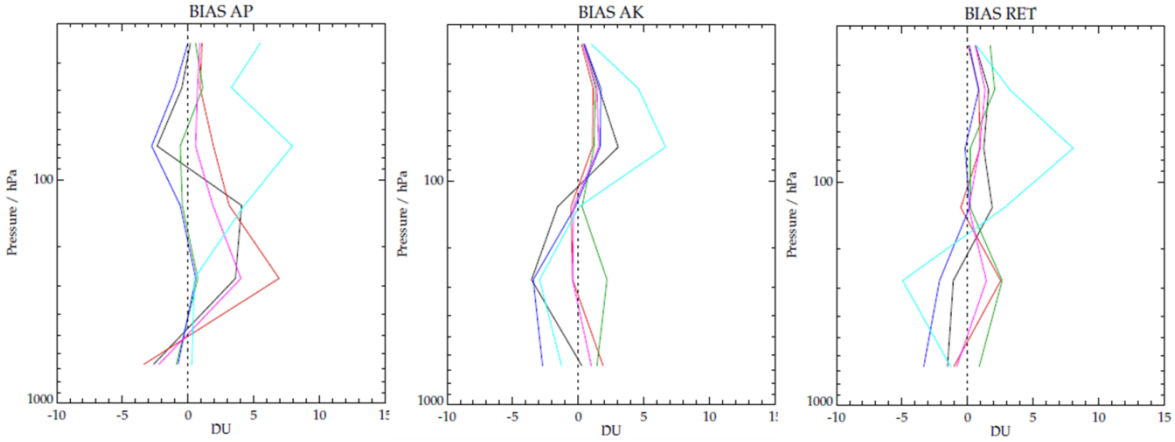

Figure 6.4: Bias with respect to ozonesondes as a function of latitude and pressure for sub-columns in Dobson units for the *a priori* (left) and retrieved profile (centre) and with GOME-2 AKs applied to the sonde (right). The pink lines indicate the averages over all latitude bands, for comparison to the black and green lines in the left hand panel of Figure 6.3, which depict the same *a priori* and retrieval biases as % differences from the ozonesondes. *Figure taken from Miles et al 2015.*

6.4 Description of Verification Algorithm – IUP Ozone Profile Algorithm

6.4.1 Forward Model

The used forward model is the radiative transfer model (RTM) SCIATRAN version 3.0 of which a detailed description is given in Rozanov et al. (2014). As such only the chosen parameters for SCIATRAN will be highlighted here.

6.4.1.1 Absorption Cross-section

While the ozone absorption cross-section measured at the IUP (Gorshelev et al. 2013; Serdyuchenko et al. 2013) is intended to be used for actual retrievals from TROPOMI spectra, we here use the absorption cross-sections from Malicet et al. (1995) for consistency with the other retrieval algorithms.

6.4.1.2 Pressure and Temperature

Pressure and temperature profiles are generally taken from the ECMWF ERA-Interim dataset (Simmons et al. 2007). In the case of comparisons with pre-defined test cases the temperature and pressure from these test cases were used.

6.4.1.3 Ground Albedo

In the applied algorithm the ground albedo will usually be specified as weighted average of spectral albedos for the specific ground type. The ground types are taken from (Matthews 1985). For verification purposes a constant albedo was however assumed depending on the verification scenarios.

6.4.1.4 Treatment of Clouds

Currently clouds are treated by calculating an effective scene height and an effective albedo from the cloud top height and the cloud fraction. This treatment may need to be adjusted due to the fine spatial resolution of TROPOMI though the actual effect on the ozone profiles retrieval with its relatively coarse ozone profile pixels still needs to be investigated.

6.4.1.5 Scattering

The scattering is assumed to be Rayleigh scattering and is calculated according to Rozanov et al. (2014). 303 nm is taken as the boundary from single to multiple scattering. The ring effect is treated by simulated rotational Raman scattering for a large number of scenarios.

6.4.1.6 Wavelength Window

The algorithm uses three wavelength windows. The first wavelength window extends through the complete range of band 1, i.e., from 270 – 300 nm with the second wavelength window extends from 300 – 320 nm. The third wavelength window starts at 320 nm in the performance of band 3 and extends to 335 nm. Depending on the actual performance of band 3 the boundary between the second and third wavelength window might be pushed towards 315 nm to utilise the higher signal-to-noise ratio of band 3.

6.4.1.7 Altitude Grid

SCIATRAN operates on geometric altitudes. In this algorithm we use the altitude grid defined in Table 6.1 below. This altitude grid is also used as the retrieval altitude grid.

Level	1	2	3	4	5	6	7	8	9	10	11	12	13	14	15	16	17	18	19	20
Altitude [km]	0	2	4	6	8	10	11	12	13	14	15	16	17	18	19	20	21	22	23	24
Level	21	23	22	24	25	26	27	28	29	30	31	32	33	34	35	36	37	38	39	40
Altitude [km]	25	26	27	28	29	30	31	32	33	34	35	36	37	38	39	40	41	42	43	44
Level	41	42	43	44	45	46	47	48	49	50	51	52	53	54	55	56	57	58		
Altitude [km]	45	46	47	48	49	50	51	52	53	54	55	57	59	62	65	70	75	80		

Table 6.1: Altitude grid for SCIATRAN and as the retrieval altitude grid

6.4.2 Retrieval Algorithm

The retrieval of ozone profiles from nadir are primarily based on the optimal estimation retrieval technique as described in Rodgers (2000) and depend largely on the increased penetration depth of ultraviolet photons through the atmosphere with increased wavelength. These retrieval problems are usually ill-posed and require some form of regularisation. A good overview about these techniques is given by Hasekamp and Landgraf (2001). For this retrieval we use a Phillips-Tikhonov regularisation as proposed in Rodgers (2000).

They also require good knowledge of the absolute radiances for a good performance. The algorithm used here to test the effects of the proposed calibration is largely based on the Full Retrieval Method (FURM) by Hoogen et al. (1999) with SCIATRAN (Rozanov et al. 2014) used as the forward model instead of GOMETRAN (Rozanov et al. 1997). The FURM retrieval was validated for GOME (Hoogen et al. 1999; Bramstedt et al. 2002).

6.4.3 Error Characterisation

As with the prototype algorithm the error characterisation follows Rodgers (Rodgers 2000) closely leading to ozone profile errors primarily due to

- measurements errors
- forward model errors
- a priori errors
- smoothing errors

These errors will be explained further in the following sections. As this discussion follows Rodgers (2000) the same nomenclature will used. In this case $\hat{x}$ is the state vector, $\vec{y}$ denotes the measurement vector and R is the retrieval method such that the retrieval is given by

$$\hat{x} = R\left(\vec{y}, \hat{b}, \overrightarrow{x_a}, c\right) \tag{3}$$

where $\hat{b}$ are the estimated forward function parameters, $\overrightarrow{x_a}$ is the a priori of $\vec{x}$ and c is a set of additional parameters.

6.4.3.1 Measurement Errors

All measurement errors are included in their covariance matrix. Its diagonal contains the measurement errors while the off-diagonal elements include errors due to the radiometric and spectral calibration. The measurement errors can be approximated from the expected signal-to-noise ratio and the resulting noise level. Errors in the radiometric and spectral calibration are much harder to identify and will probably only be addressed once they are estimated during the calibration of the actual instrument. Its covariance matrix is given by

$$S_e = G_y S_y G_y^T \tag{4}$$

6.4.3.2 Forward Model Errors

The forward model error is given by

$$E_{fm} = G_y[f(\vec{x}, b, b') - F(\vec{x}, b)] \tag{5}$$

where

$$G_y = \frac{\partial R}{\partial \vec{y}} \tag{6}$$

is the sensitivity of the retrieval to the measurement, f is the forward function, F is the forward model and b' is the set of parameters which have an influence on how the measured quantity is derived from the state of the atmosphere, but are not included in the forward model.

6.4.3.3 A Priori Errors

Errors due to a wrong a priori depend largely on the sensitivity of the retrieval to the a priori which is given by

$$\frac{\partial R}{\partial \overrightarrow{x_a}} = I_n - A \tag{7}$$

where I_n is the identity matrix of size n and

$$A = G_y K_y \tag{8}$$

is the averaging kernel matrix with

$$K_x = \frac{\partial F}{\partial \vec{x}} \tag{9}$$

giving the sensitivity of the forward model to the state vector.

6.4.3.4 Smoothing Errors

Smoothing errors are in general given by their covariance matrix

$$S_s = (A - I_n) S_e (A - I_n)^T \tag{10}$$

6.4.3.5 Output Quantities

Most of the above mentioned quantities will not be output for each retrieval for performance and storage reasons. They will only be output for testing and error estimation purposes. During normal retrievals only the averaging kernel matrix, the fit residual, and the degrees of freedom will be output. The averaging kernel matrix is necessary for the comparison of retrieved profiles with other profiles and gives information on the vertical resolution and contribution of each layer to the surrounding layers. The degrees of freedom provide information on the number of actually independent pieces of information, i.e., the number of actually retrievable layers. The fit residual can be used to improve the retrieval in general by identifying structures due to absorbers not treated in the retrieval, imperfections in the calibration etc. Additionally it is a measure of the fit quality.

6.4.4 Main differences to prototype algorithm

The retrieval outlined above is largely very similar to the prototype algorithm. Primary differences occur due to the inherent differences between the forward models DISAMAR and SCIATRAN. These differences should however be small as simulated radiances from both radiative transfer models are similar for a set of test-cases (Section 6.6.1.1). Additional differences can occur due to the different a priori, particularly in layers with low information content. These differences can be mostly eliminated by using the same a priori for all algorithms or changing the a priori to a common one as outlined in Rodgers (2000).. As the performance of the retrieval does however depend to a certain extent on the a priori information a number of scenarios have to be compared where the a priori information is obtained as if it were an actual retrieval from real data in order to fully evaluate the performance of the algorithm. Additionally, differences can originate from SCIATRAN working on altitude levels while DISAMAR uses pressure levels. This will also have an impact on all prior profile information taken from ECMWF. This may also lead to additional inconsistencies when attempting to use harmonized a priori information.

6.5 Description of Synthetic Data Used

Comparisons are based on the geophysical scenarios defined in the ESA CAMELOT study. Radiances for the 16 cases have been simulated at specific viewing geometries by KNMI, using the forward model of the prototype scheme, DISAMAR. These profiles are used to estimate the linear retrieval diagnostics (errors, averaging kernels) from each scheme and the simulated measurements are used in non-linear retrieval tests.

6.5.1 Radiative transfer settings and program used

In the radiative transfer calculations 10 streams are used in DISAMAR, 6 are used in the RAL algorithm. Sensitivity tests have been performed with the RAL algorithm to show that no notable improvement is found (for this algorithm specifically) for the cost of increasing the number of streams in the radiative transfer calculation. As discussed in the algorithm description, the RAL algorithm uses a version of GOMETRAN++ to perform radiative transfer calculations.

6.6 Presentation and Discussion of Results

6.6.1 Comparison of results for different groups

6.6.1.1 RTM comparison

Before comparing output from different retrieval algorithms, it was recognised that an important initial step would be to establish that their radiative transfer models were consistent. This is to ensure that differences in algorithm simulations or retrieval outcomes could not be attributed solely to differences in radiative transfer model used by the algorithms. To do this, monochromatic simulations were performed for DISAMAR, GOMETRAN(RAL), and LIDORT for a reference atmospheric case (CAMELOT European background) for a range of viewing geometries and surface albedos. The differences between the results are shown in detail in Figure 6.5, which include a comparison to SCIATRAN, which is used in the alternative ozone profile verification algorithm. The performances of SCIATRAN, GOMETRAN and DISAMAR are shown to agree very well, which minimises any difference that might be found in the verification process that could be attributed to differences in the RTM.

Here, sun normalised radiance is defined as:

$$SNR = \pi \frac{I}{I_0} \tag{11}$$

Where *I* is the radiance and I_0 the irradiance. The RTMs were run to have as similar settings as possible, using the same ozone absorption cross-sections (Malicet et al. (1995) for 210 K, 250 K, and 290 K) and ozone-only atmospheric profiles, which can be found along with the temperature and pressure profile in Table 6.12 in the Appendix (Section 6.8). Additional scattering parameters for the entire atmosphere are given in Table 6.12 in the Appendix (Section 6.8. While small (~1%) difference remain, the results indicate that the RTM performances are comparable, and agree to an acceptable level.

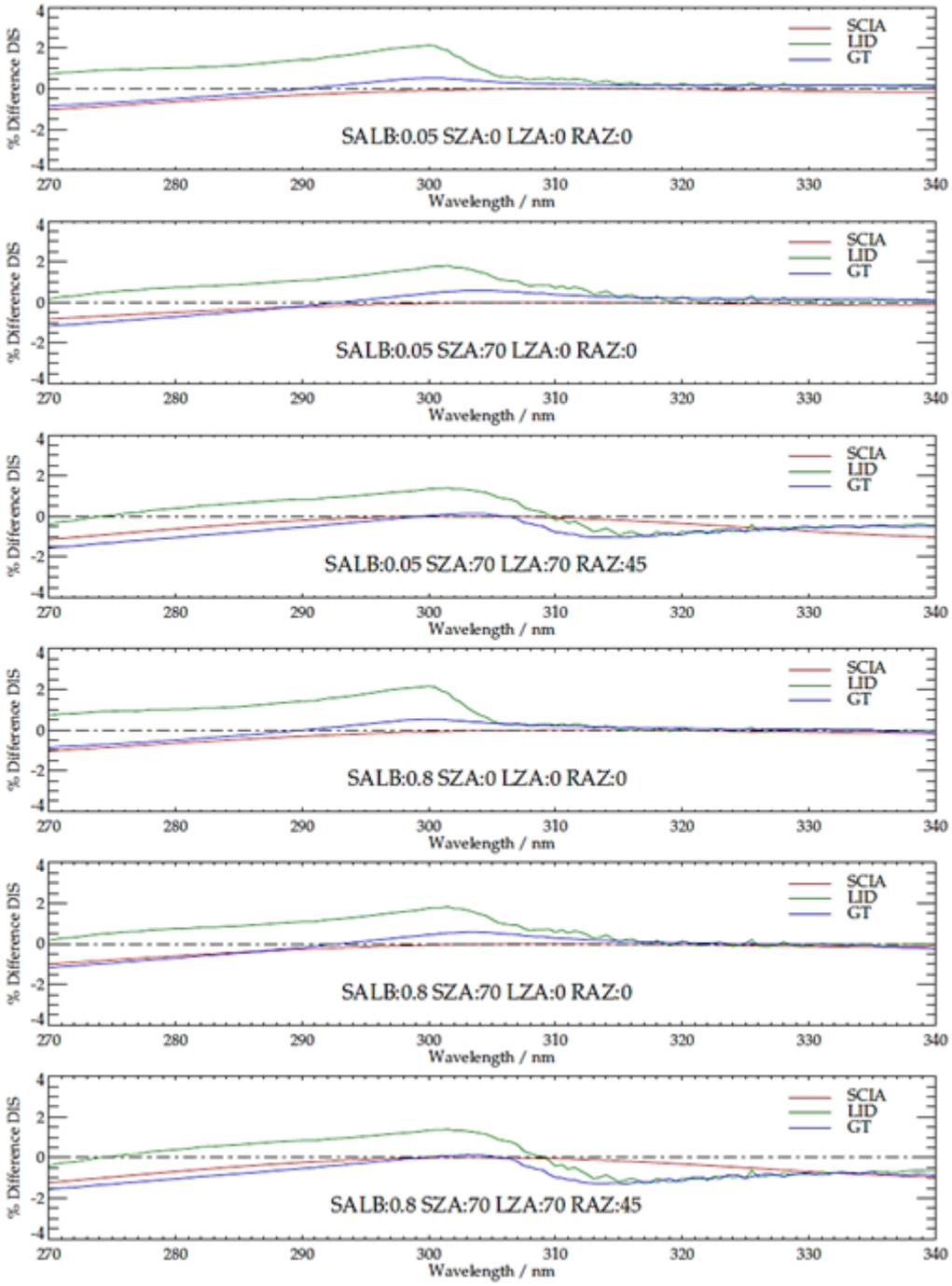

Figure 6.5: Relative differences in sun-normalised radiance for CAMELOT European Background scenario (ozone only) for 6 viewing geometries/surface albedo cases as simulated by radiative transfer models used in verification algorithms. Results are shown relative to DISAMAR/KNMI: LIDORT(BIRA), SCIATRAN(Bremen), GOMETRAN(RAL).

6.6.2 Linear Simulations – RAL Algorithm

In order to establish the expected performance of a verification algorithm it is necessary to estimate the error on a retrieved ozone profile. Furthermore, it is important for these to be understood in terms of the user requirements as set out in the MRTD. In the case of the tropospheric column and ozone profile products, these are defined as is relative errors in sub-column amount.

Sub-column errors are computed as follows:

The error covariance of the solution from an OEM retrieval is given by

$$\boldsymbol{S_x} = \left(\boldsymbol{S_a^{-1}} + \boldsymbol{K^T S_y^{-1} K}\right)^{-1} \quad (12)$$

Where $\boldsymbol{K}$ is the weighting function matrix which contains the derivatives of the FM with respect to each element of the (solution) state vector. The square-roots of the diagonal elements of this matrix are referred to as the *estimated standard deviation* (ESD) of each element of the state vector. In the RAL scheme the state vector consists of a set of volume mixing ratios defined on pressure levels.

$\boldsymbol{S_x}$ can be divided into two terms:

$$\boldsymbol{S_x} = \boldsymbol{S_n} + \boldsymbol{S_s} \quad (13)$$

Where $\boldsymbol{S_n} = \boldsymbol{G\, S_y\, G^T}$ describes the uncertainity due measurement errors (characterised by $\boldsymbol{S_y}$**)** and $\boldsymbol{S_s}$ describes the smoothing error, i.e. departue from the true state caused by the imposed prior constraint. This uses the gain matrix ***G***, which characterises the sensivity of the retrieval to perturbations in the measurement:

$$\boldsymbol{G} = \boldsymbol{S_x K^T S_y^{-1}} \quad (14)$$

The error covariance for sub-column amounts can be computed using matrix ***M*** which contains the weights needed to integrate the profile between the required set of levels:

$$\boldsymbol{S_{x:c}} = \boldsymbol{M\, S_x M^T} \quad (15)$$

Estimates of the error due to noise can also be estimated applying the same equation to $\boldsymbol{S_n}$ in place of $\boldsymbol{S_x}$.

ESDs and noise errors are estimated for a range of CAMELOT scenarios at specific viewing geometries, named in Figure 6.6, which shows the sun normalised radiance simulated by the prototype algorithm.

Figure 6.7 shows the estimated sub-column error for the range of CAMELOT scenarios predicted by the simulations. The contribution of noise (instrumental) is given by Figure 6.8. In these simulations the *a priori* errors used in the RAL scheme were set to 20% in order to be as consistent as possible with the prototype scheme. Corresponding results for the IUP and KNMI prototype scheme are shown in the following sections.

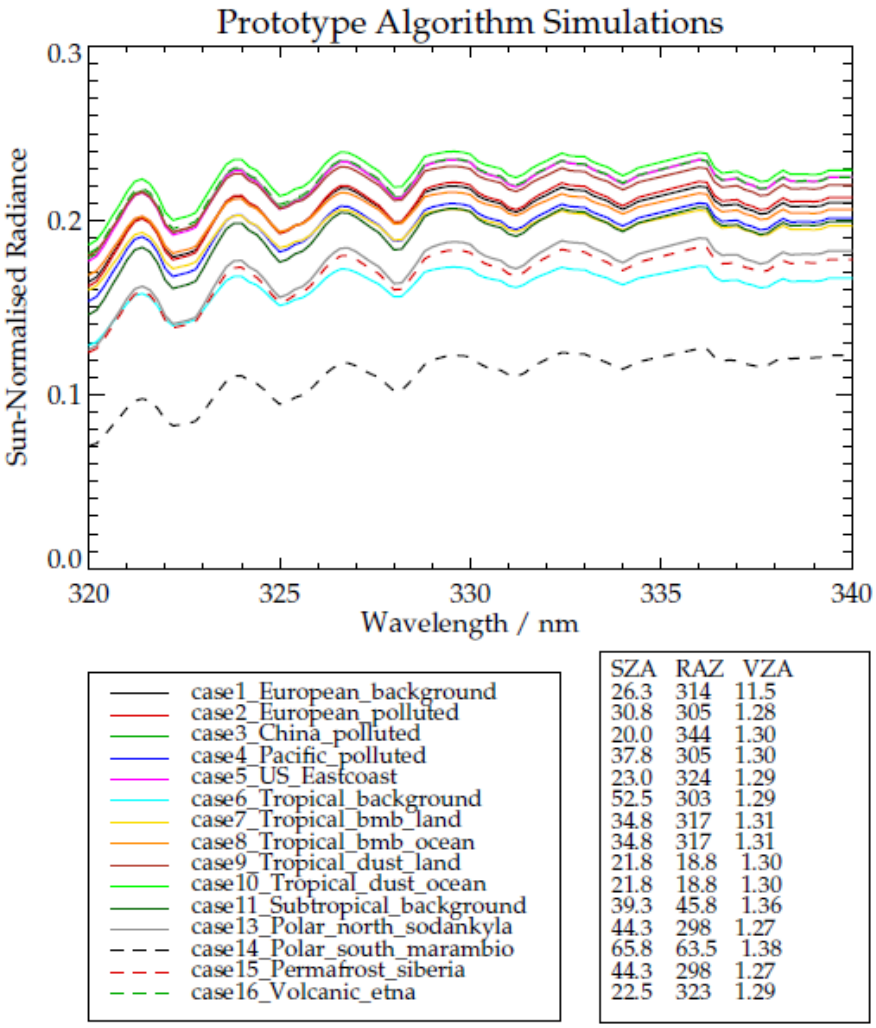

Figure 6.6 Sun-normalised radiance simulated by prototype algorithm DISAMAR for the range of CAMELOT atmospheric scenarios with specific viewing geometry, and a surface albedo of 0.02 [assumed].

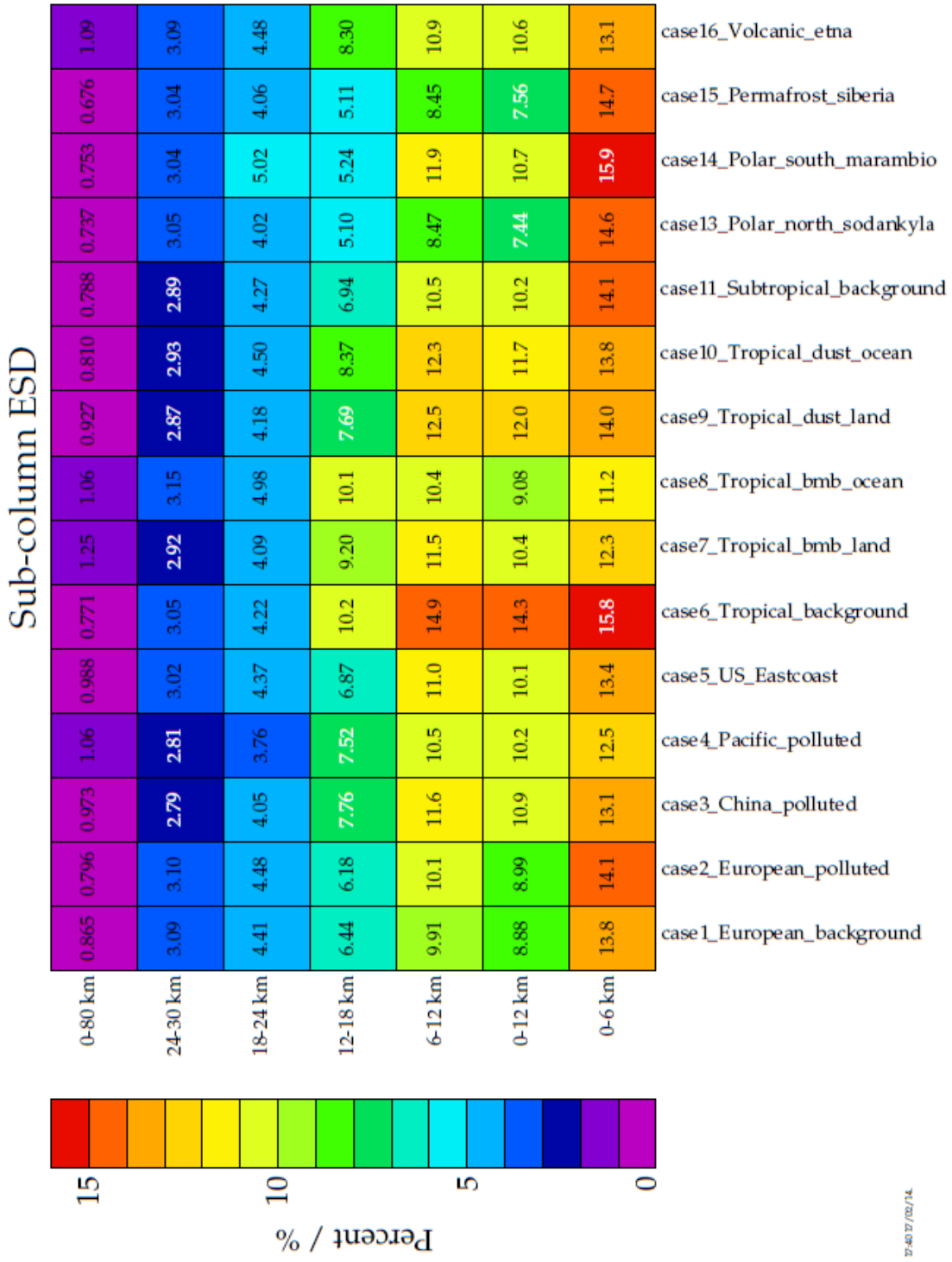

Figure 6.7: Estimated sub-column retrieval error from RAL ozone profile algorithm. The viewing geometry used for each scenario is giving in Figure 6.6

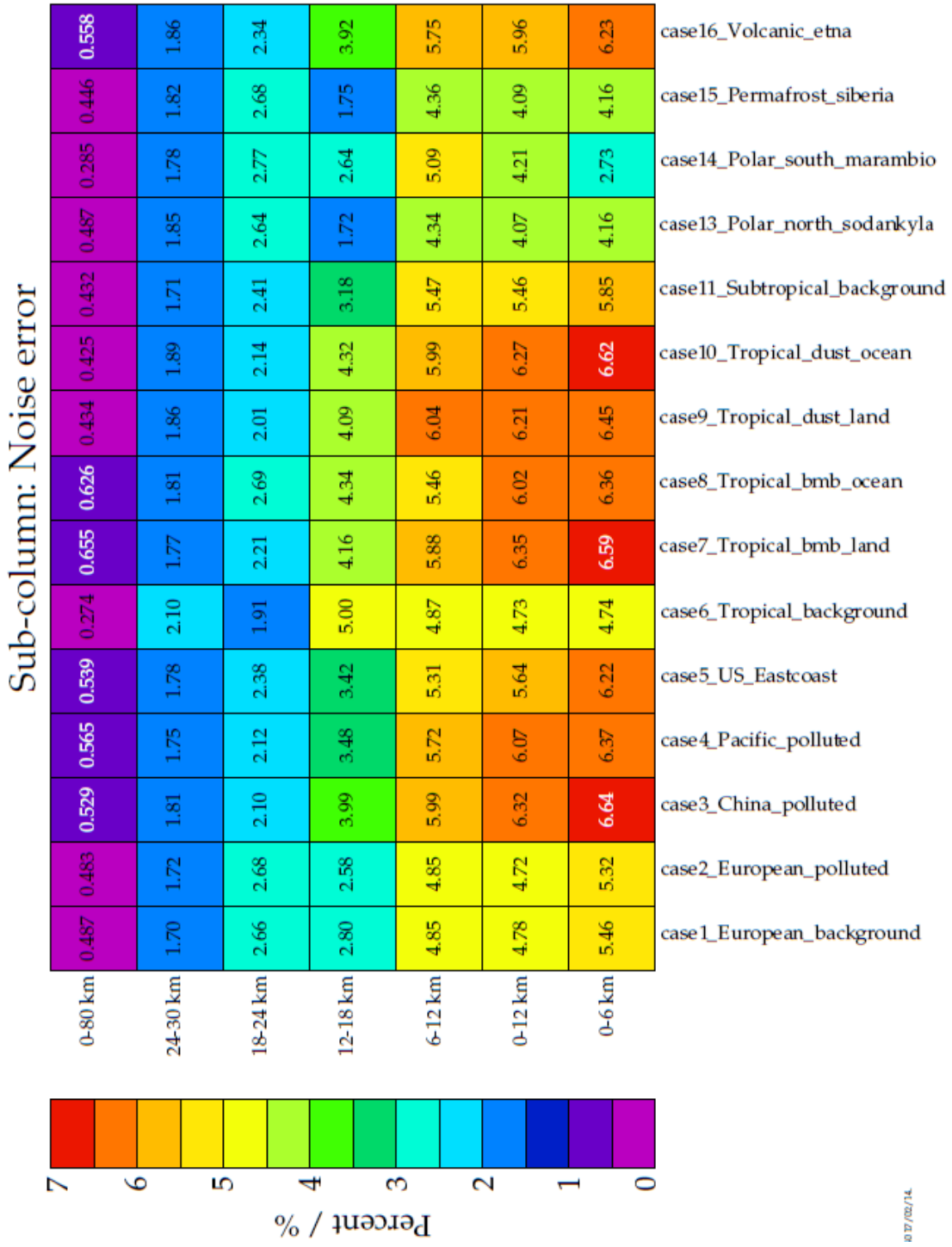

Figure 6.8: Estimated noise contribution to sub-column retrieval error linearly mapped using simulated gain matrix from RAL ozone profile scheme (S5 noise). The viewing geometry used for each scenario is giving in Figure 6.6

6.6.3 Linear Simulations IUP

6.6.3.1 Retrieval Testing on Synthetic Data

In this section the retrieval is tested on a number of synthetic spectra in order to assess the performance of the IUP ozone profile retrieval. To achieve this, spectra were simulated for a number of conditions. Gaussian noise with the minimum and maximum estimated signal-to-noise ratio was then applied to the spectra. Ozone retrievals were then performed as outlined in section 6.1. To assess the performance, the accuracies for the sub columns 0-6 km, 6-12 km, 12-18 km, and 18-50 km were calculated.

6.6.3.2 Testing on IUP-generated Spectra

Spectra were simulated in 10° latitude steps from 0° to 90° N for January, April, July and October from the TOMS V8 climatology (Wellemeyer et al. 2004). The ozone profile was then scaled to fit a total column of 300 DU to 500 DU in steps of 50 DU. As pressure and temperature profiles, averaged profiles from ECMWF ERA-Interim data for the 15th of each month were used. Additionally, no clouds or aerosols were taken to be present. The surface albedo was taken to 0.02 with a solar zenith angle of 0°. A-priori ozone profiles were taken from either the IUP climatology scaled to the correct ozone column ± 10 DU or the 1976 standard atmosphere.

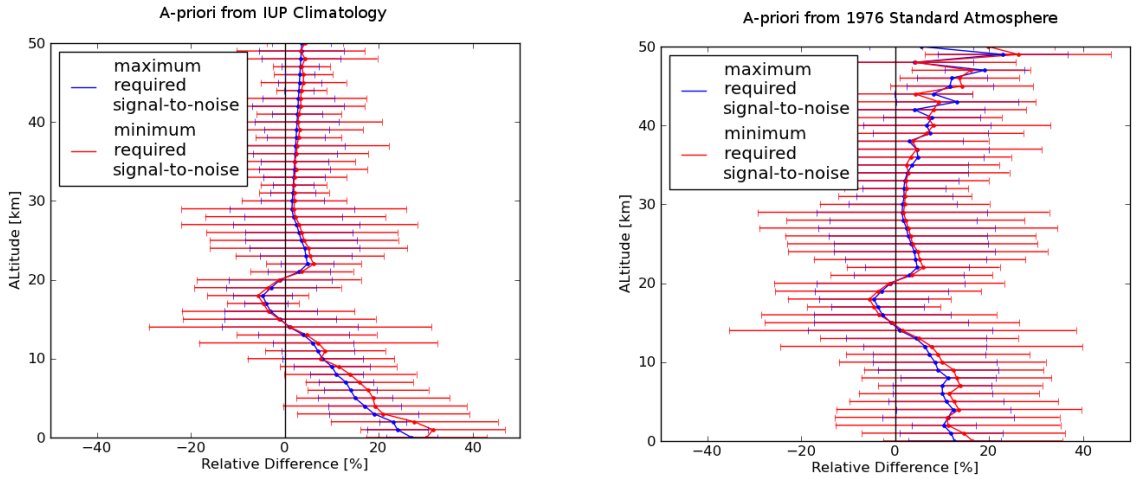

Figure 6.9: Relative differences for retrievals applied to synthetic spectra generated at the IUP using the IUP climatology for a-priori ozone profiles (left) and the 1976 standard atmosphere for a-priori ozone profiles (right). Error-bars indicate the standard deviation at the 2 σ level.

The relative differences shown in Figure 6.9 show very good agreement in middle altitudes with larger differences below 10 km. These larger differences can be attributed to lower sensitivity of the algorithm at lower altitudes and the subsequently higher contribution of the a-priori profile to the retrieved profile.

Table 6.2: Accuracies in % for sub columns as determined from the set of synthetic spectra generated at the IUP

	A-prior from IUP climatology		**A-priori from 1976 std atmosphere**	
Altitude	Max SNR	Min SNR	Max SNR	Min SNR
0km-6km	20	23.8	11.4	12.9
6km-12km	10.7	12.8	9.4	11.7
12km-18km	3.2	4.7	3.1	3.9
18km-50km	2.3	2.7	2.6	2.9

The accuracies determined for these test spectra in Table 6.2 show generally good agreement and algorithm performance within the requirements. In addition it was decided to perform a comparison of retrievals and estimated sub-column errors for a selected small set of conditions from the CAMELOT test scenarios with solar zenith angles of 0° and 70° with an albedo of 0.05 and a signal-to-noise ratio of 1000. The scenarios used were the CAMELOT scenarios "European background" and "China polluted" as well as a scenario based on the "European background" scenario with considerably increased ozone loading in the boundary layer. The used ozone profile is given in Table 6.14. For this purpose radiance spectra were generated at RAL, KNMI, and IUP and sub-column errors were then estimated from these radiances and for the IUP radiances using the IUP retrieval can be found in Table 6.2.

Table 6.3: Estimated sub-column errors for the CAMELOT cases "European background" and "China polluted" as well as the "European background" case with increased boundary layer ozone concentration at a solar zenith angle of 0° and 70°.

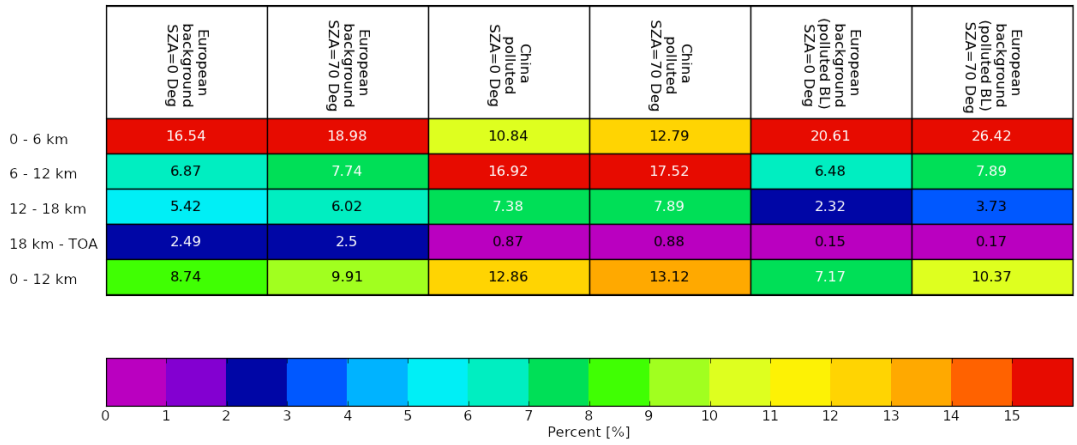

6.6.3.3 Testing on CAMELOT Spectra

For this part of the algorithm testing CAMELOT scenarios were used. Gaussian noise was applied to create 50 distinct radiance spectra. All retrievals were then conducted as outlined in section 6.4.Tests were performed for all CAMELOT cases.

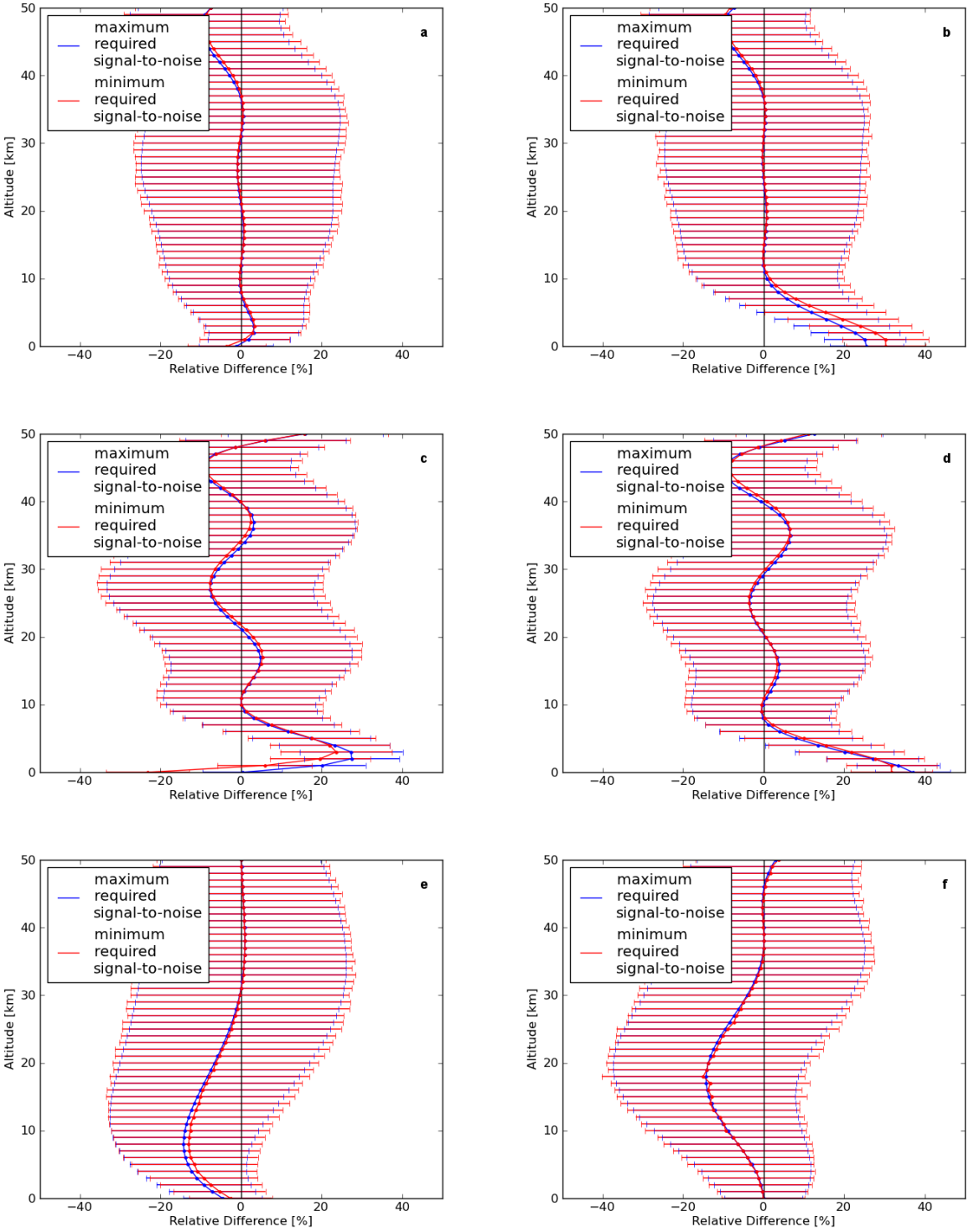

Figure 6.10: Relative differences for the CAMELOT scenarios a: European background, b: European polluted, c: polar south Marambio, d: polar north Sodankyla, e: China polluted, f: Etna volcanic. Error-bars indicate the standard deviation at the 2 σ level.

Figure 6.10 shows generally good agreement between profiles used for forward modelling and the final retrieved profiles with higher differences in regions with lower sensitivity. Additionally it can be seen that the retrieval performs better at mid-latitudes than at very high latitudes.

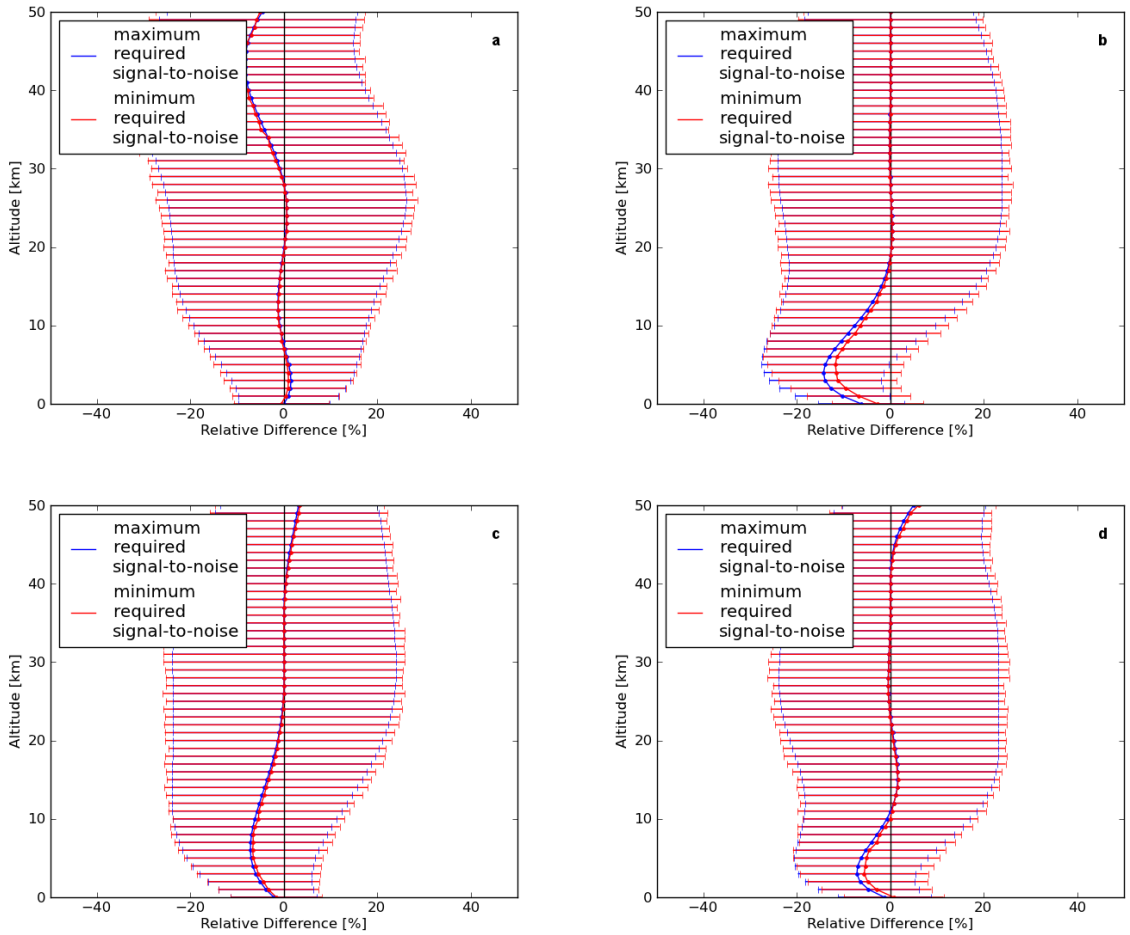

Figure 6.11: Relative differences for the CAMELOT scenarios a: subtropical background, b: US east coast, c: tropical biomass burning background, d: tropical biomass burning ocean. Error-bars indicate the standard deviation at the 2 σ level.

Similar features can be seen in additional cases shown in Figure 6.11 Table 6.4 shows that the retrievals perform very close to the requirements even at high latitudes. It can however be seen that the estimated sub column differences are large in Polar Regions at low altitudes. This is however expected due to the higher solar zenith angle in combination with the low tropopause height. Additionally, the polluted cases 3 and 4 show higher differences up to 18 km. This is not the case for case 2. In order to further investigate the influence of pollution in this scenario the additional test case with increased pollution in the boundary layer (see Table 6.3) was added which shows higher differences at altitudes from 6 - 18 km. In addition it can be seen that cases with enhanced aerosol loading such as case 16 and 9 show higher differences in middle altitudes. This effect can be seen with both maximum and minimum SNR though as expected differences are mostly larger for minimum SNR. In Table 6.6 and Table 6.7 it can be seen that about 50% of the sub column differences can be attributed to noise. This figure is of course larger in the case of minimum SNR.

Table 6.4: Accuracies in % for sub columns as determined from the set of synthetic spectra from CAMELOT scenarios assuming maximum SNR

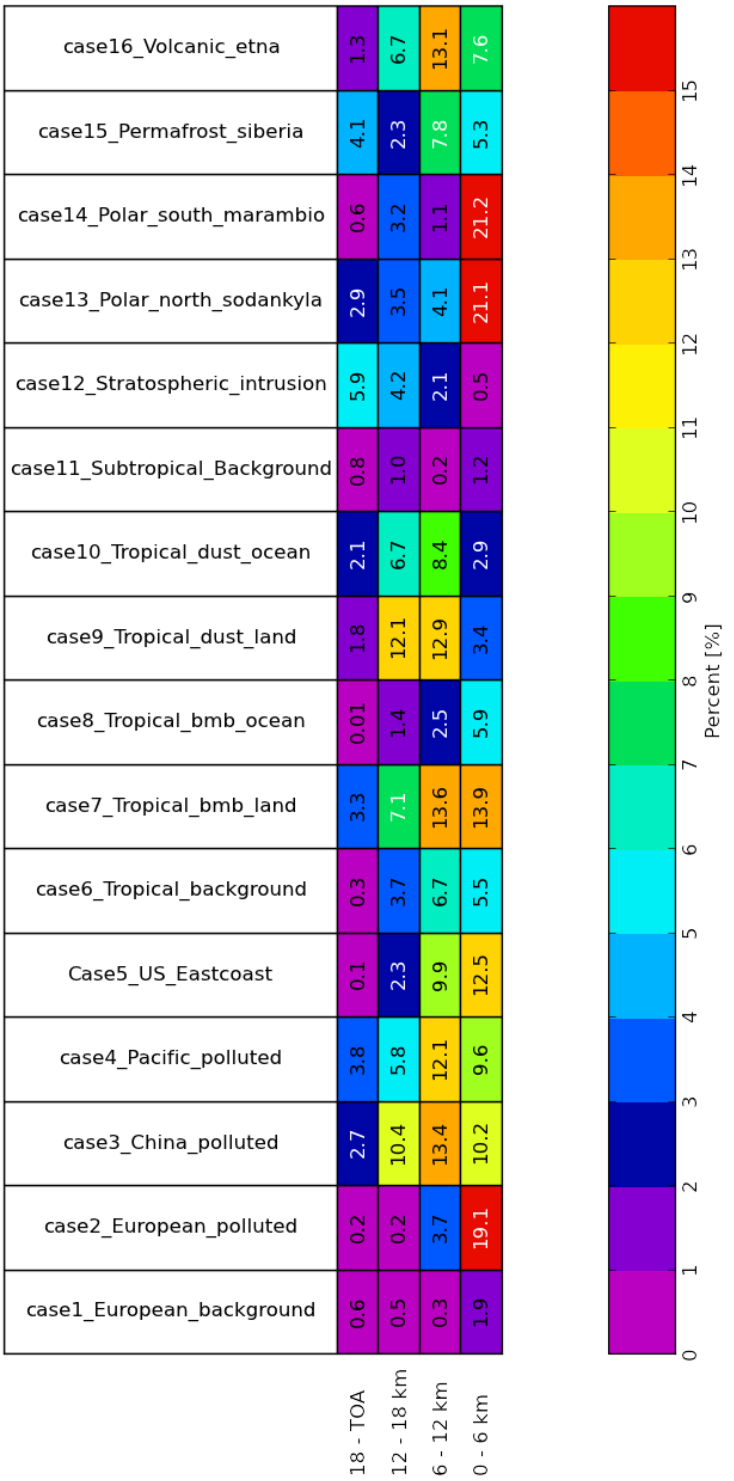

Table 6.5: Accuracies in % for sub columns as determined from the set of synthetic spectra from CAMELOT scenarios assuming minimum SNR

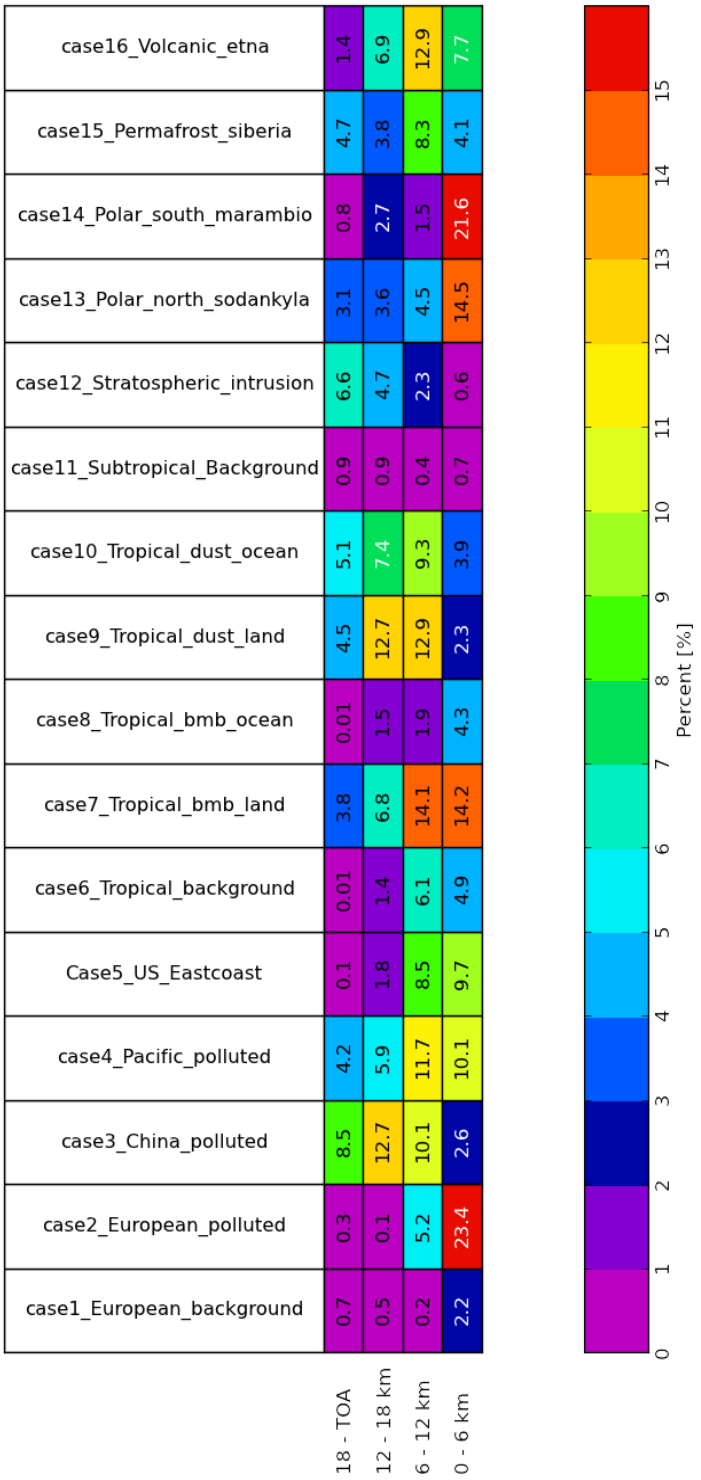

Table 6.6: Contribution of noise to retrieval error in % for sub columns as determined from the set of synthetic spectra from CAMELOT scenarios assuming maximum SNR

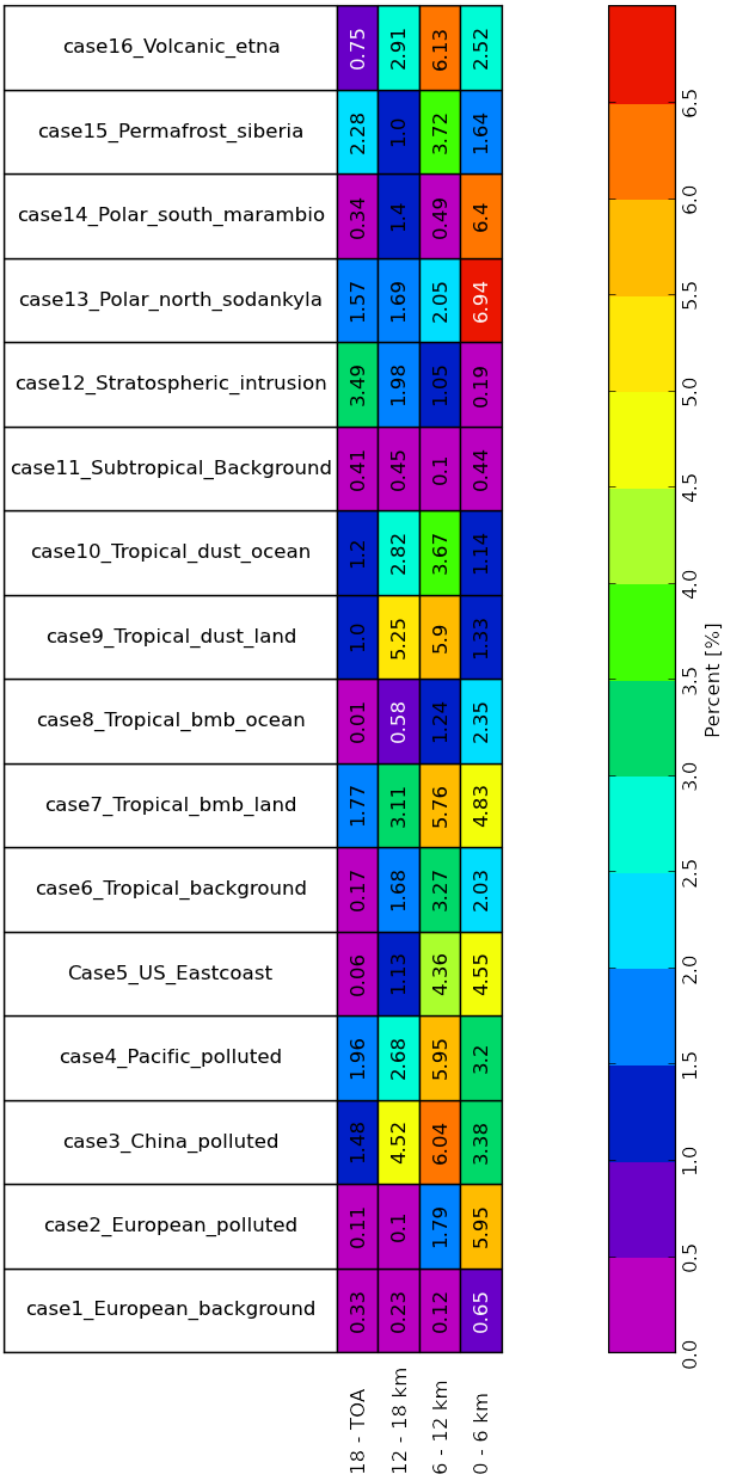

Table 6.7: Contribution of noise to retrieval error in % for sub columns as determined from the set of synthetic spectra from CAMELOT scenarios assuming minimum SNR

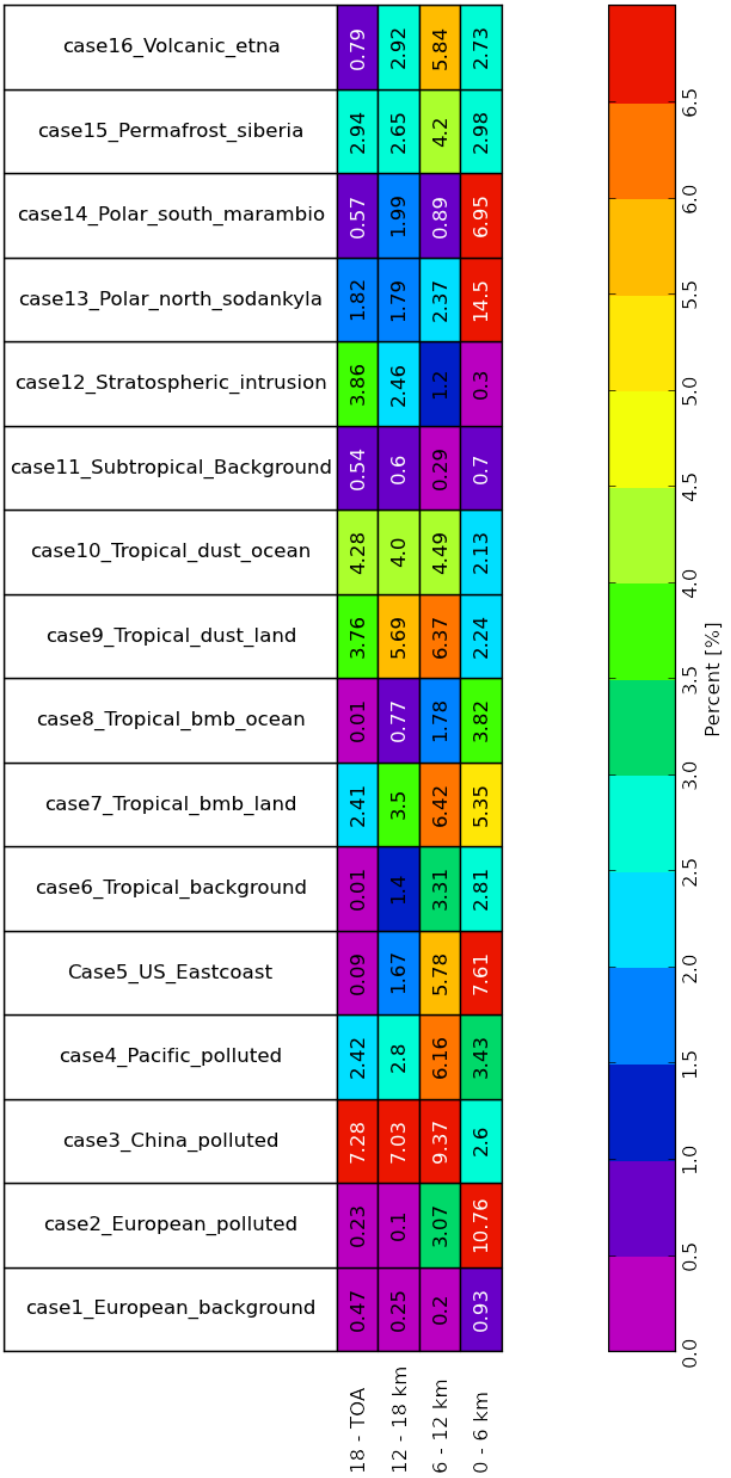

6.6.4 Linear Simulations KNMI (prototype scheme)

Results for ESD and noise errors from the the proptotype scheme, provided by KNMI are shown in figures Figure 6.12 and Figure 6.13, respectively. Agreement with the RAL estimated errors is considered acceptable, with KNMI values being somewhat smaller due to the use of a broader spectral coverage. (The RAL scheme omits wavelength ranges in order to avoid regions found to be problematic in analysis of GOME data.)

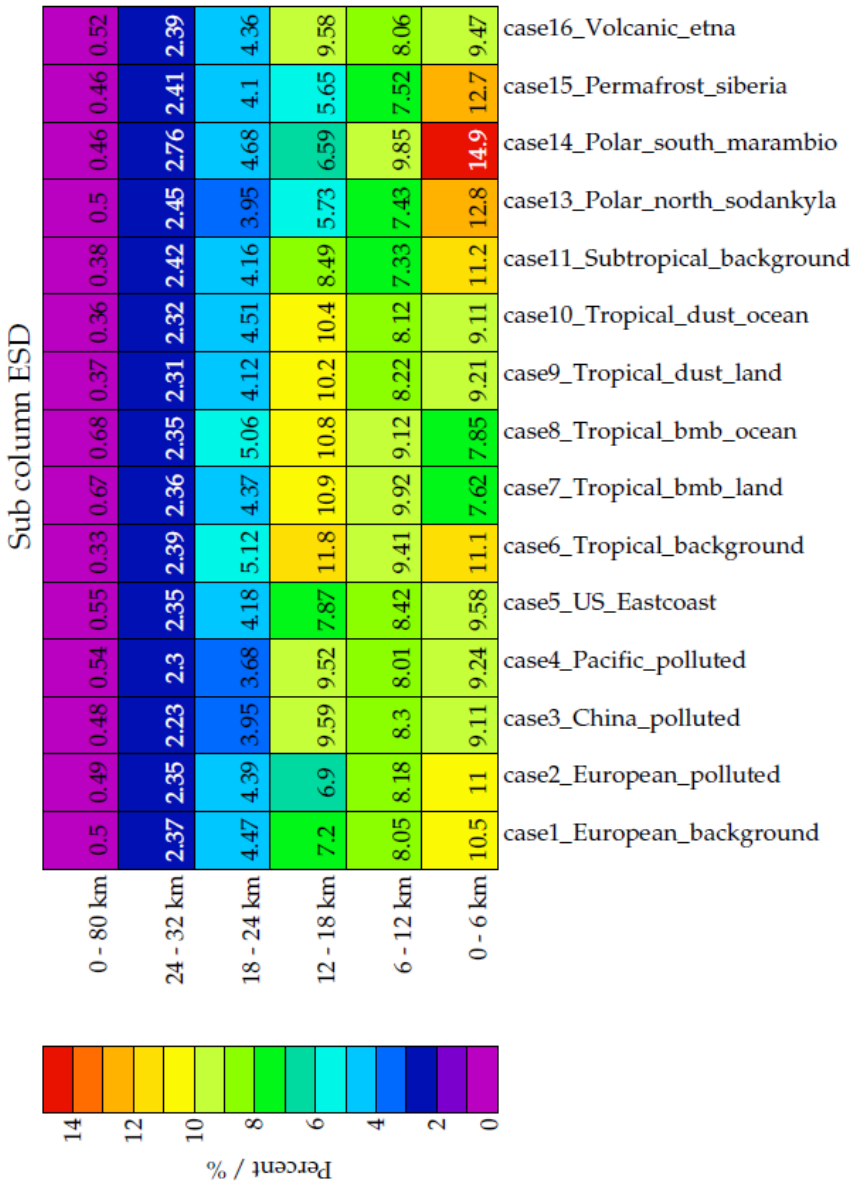

Figure 6.12: Estimated sub-column retrieval total error from KNMI prototype algorithm. The viewing geometry used for each scenario is giving in Figure 6.6

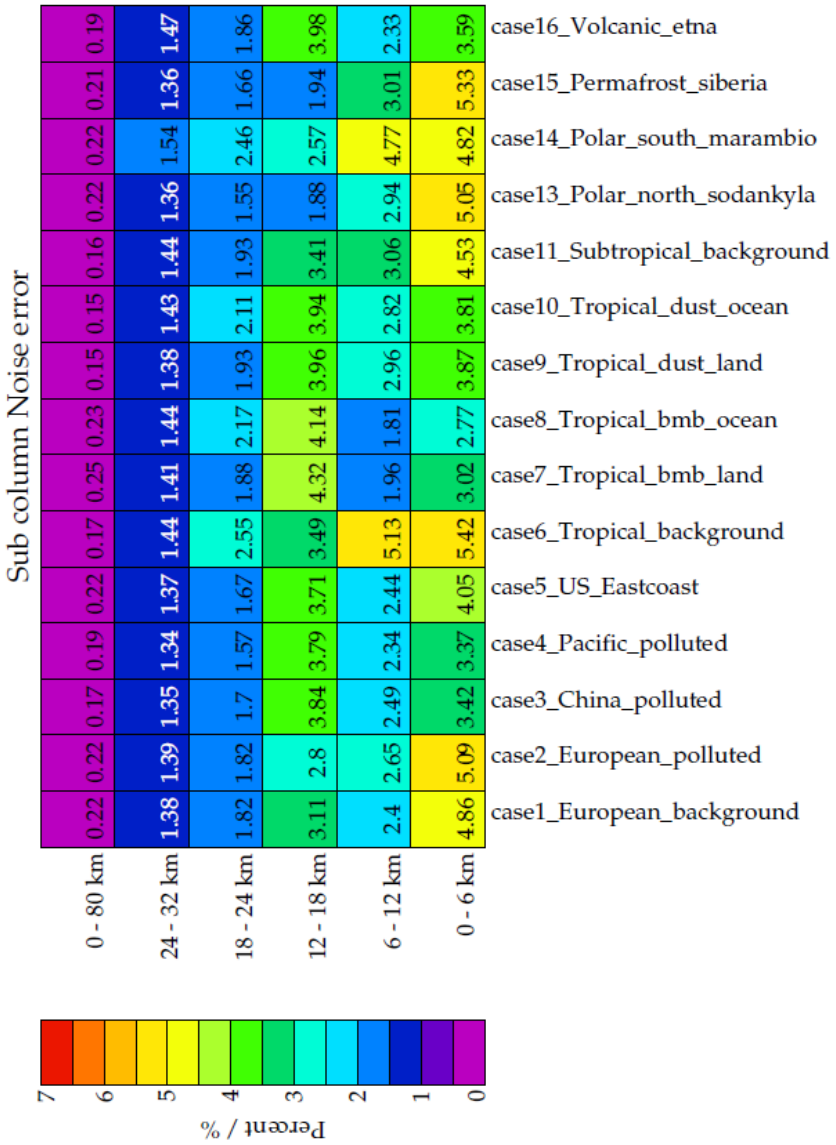

Figure 6.13: Estimated sub-column retrieval noise error from KNMI prototype ozone profile algorithm. The viewing geometry used for each scenario is giving in Figure 6.6

6.6.5 Non-Linear Retrieval simulations (RAL)

The full RAL retrieval scheme (with its standard *a priori* constraint) was applied to simulated radiance spectra generated by KNMI for the CAMELOT geophysical scenarios. Results for the sub-column amounts are shown in Figure 6.14. As well as comparing retrieval with the true sub-column amounts (derived from the CAMELOT) profiles, we show also the true sub-columns after accounting for retrieval smoothing, computed from profiles estimated using:

$$\hat{\boldsymbol{x}}_{\boldsymbol{t}} = (\boldsymbol{I} - \boldsymbol{A})\boldsymbol{a} + \boldsymbol{A}_{\boldsymbol{f}}\boldsymbol{x}_{\boldsymbol{t}} \quad (16)$$

Where,

- **A** is the retrieval averaging kernel matrix
- **a** is the *a priori* state**.**

- $\mathbf{A_f}$ is the fine-scale averaging kernel, which contains the sensitivity of the retrieved profile to perturbations in the true state on a finely resolved vertical grid (i.e. finer than the retrieval spacing, commensurate with the grid on which the CAMELOT profile is defined).
- $\mathbf{x_t}$ is the true, CAMELOT profile
- $\hat{\boldsymbol{x}}_{\boldsymbol{t}}$ is the expected retrieved state.

Figure 6.15 shows some a statistical summary of the results. Even though based on a small sample of cases, these show behaviour generally similar to that which would be based expectations and the actual performance of the RAL scheme against ozone-sondes: The prior is already in reasonably good agreement with the truth, however the retrieval improves over the prior in all layers, and the improvement is stronger when the effect of retrieval smoothing is taken into account.

It is noted that the RAL retrieval is biased low in the lowest retrieval layer, which is presumably caused by a systematic difference in radiative transfer or instrument modelling between the KNMI simulated measurement and the assumptions in the RAL scheme. The bias is only partly explained by retrieval smoothing. Apart from this bias, results are commensurate with user requirements on the ozone profile, in particular the 25% requirement on tropospheric ozone.

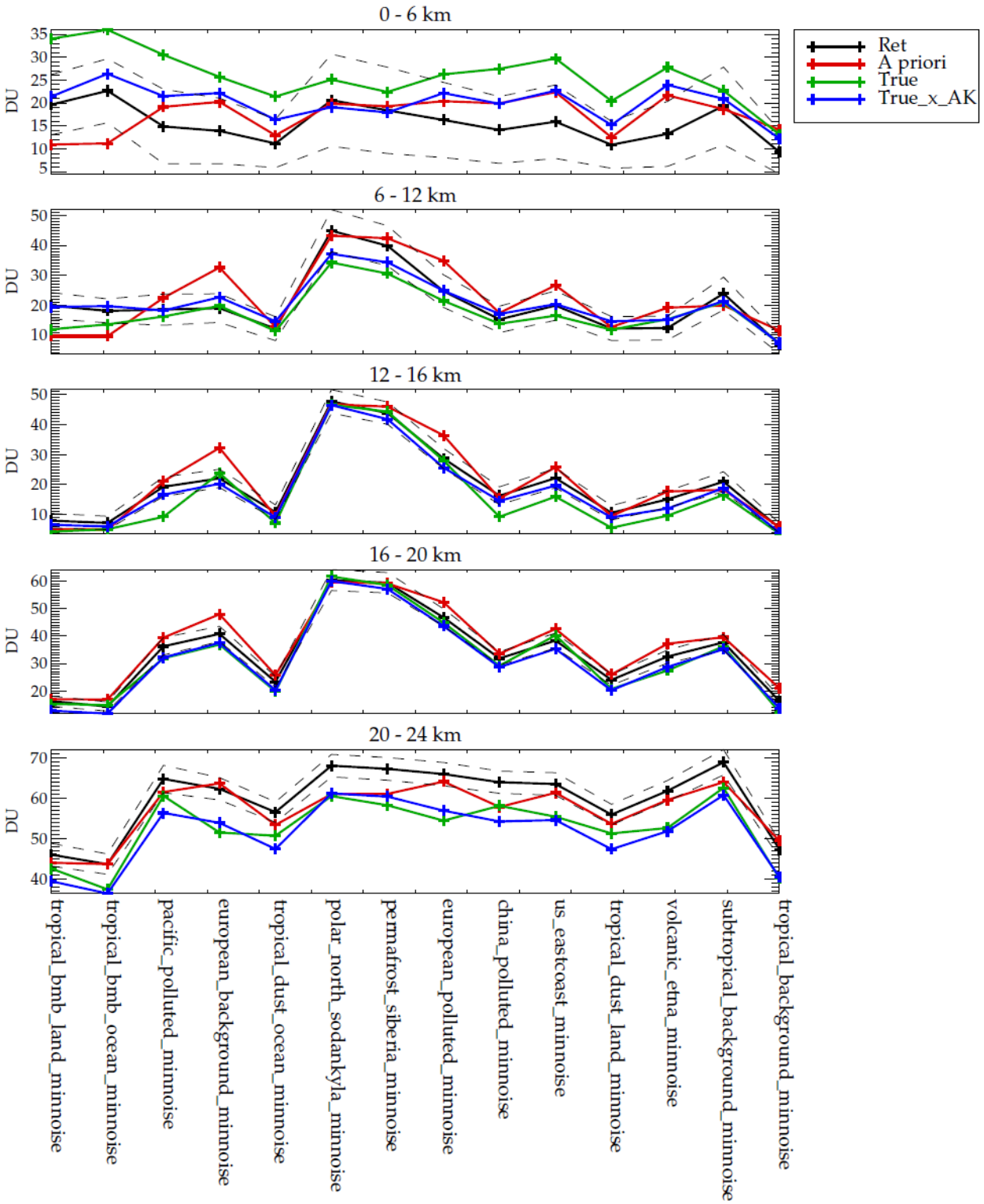

Figure 6.14: Non-linear retrieval results for CAMELOT study cases from the RAL scheme. Each panel shows results for a specific sub-column amount. Black lines show the retrieved sub-column; Red shows the a priori; Green shows the true amount based on the CAMELOT profile; Blue shows sub-columns derived applying the retrieval averaging kernels to the true profiles, i.e. accounting for smoothing by the retrieval. Dashed lines indicate the retrieval +/- estimated standard deviation.

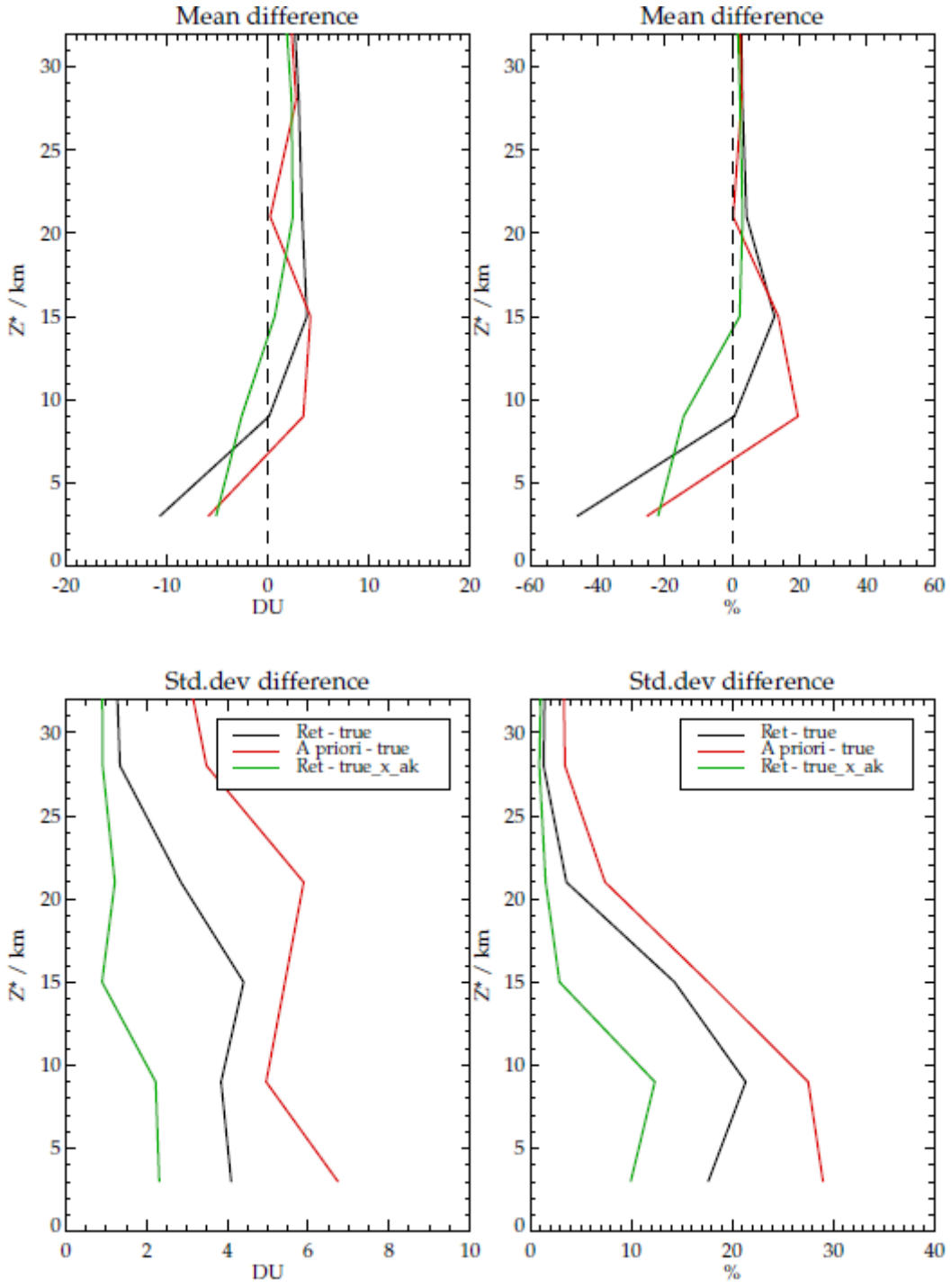

Figure 6.15: Summary of non-linear retrieval results for CAMELOT study cases from the RAL scheme. Upper panels show the mean differences over all cases, in terms of Dobson units(left) and percent (right); Bottom panels show the standard deviation in the differences.

6.6.6 Non-linear Retrieval simulations (IUP)

Non-linear retrievals have been performed for all CAMELOT cases and the resulting relative differences are shown in figures Figure 6.16 - Figure 6.18. ESDs and corresponding noise contribution are shown in Table 6.8 and Table 6.9 for the maximum required SNR and in Table 6.10 and Table 6.11 for the minimum required SNR. The described algorithm has been successfully applied to measurements by the GOME-2 instrument on MetOp A, with certain instrument specific differences (e.g. slit function, spectral windows boundaries etc.). It was then compared to WOUDC (http://www.woudc.org/) ozonesonde measurements (Section 0). In addition direct comparisons have been conducted between the retrieved profiles for 2008 with the profiles retrieved at RAL and submitted to the ESA Ozone CCI (Section 6.6.6.4). In order to facilitate the verification based on OMI measurements the IUP algorithm has in addition been applied to OMI level1 data and directly compared to WOUDC ozonesondes (Section 6.6.6.5).

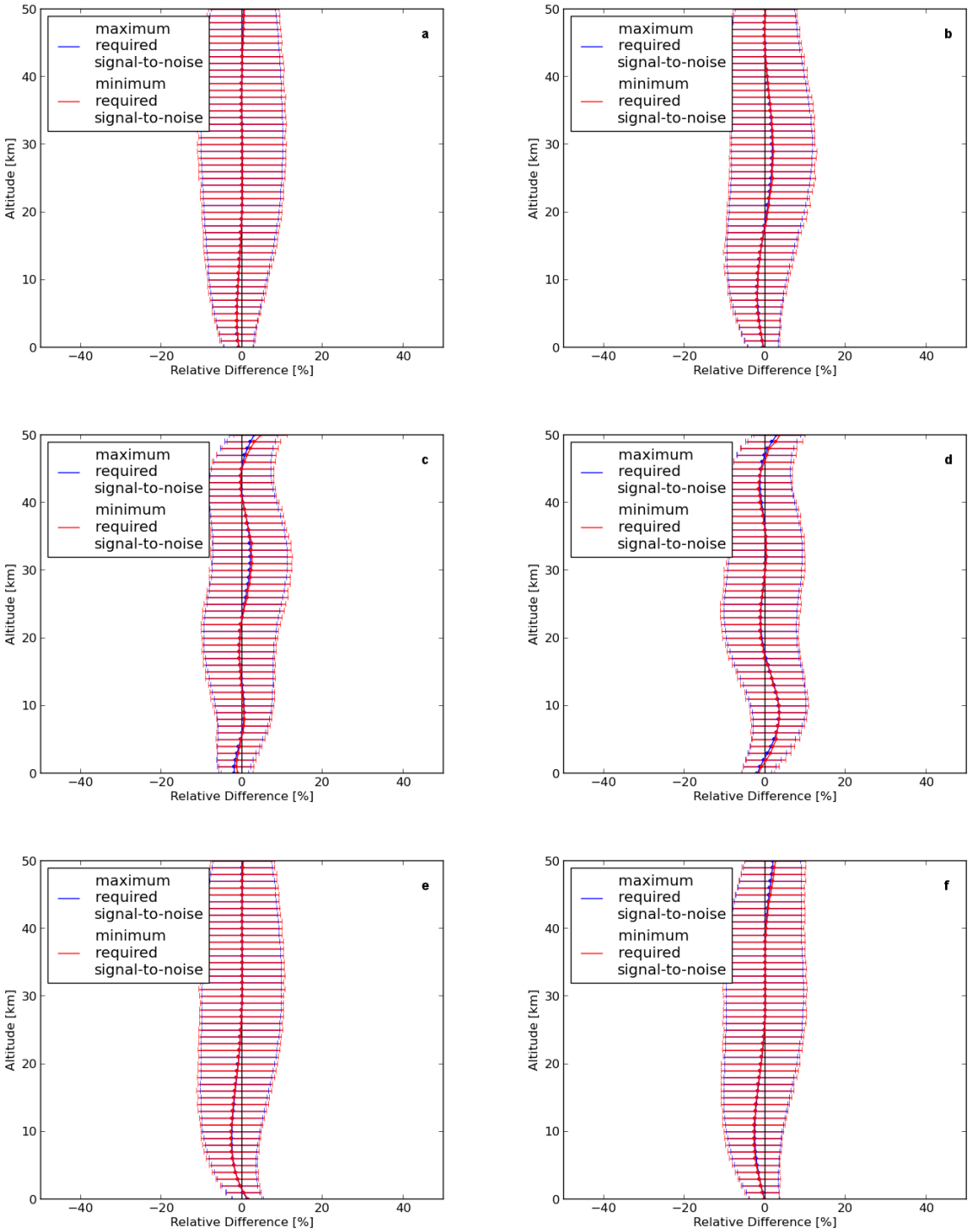

Figure 6.16: Relative differences for the CAMELOT scenarios a: European background, b: European polluted, c: polar south Marambio, d: polar north Sodankyla, e: China polluted, f: Etna volcanic. Error-bars indicate the standard deviation at the 2 σ level

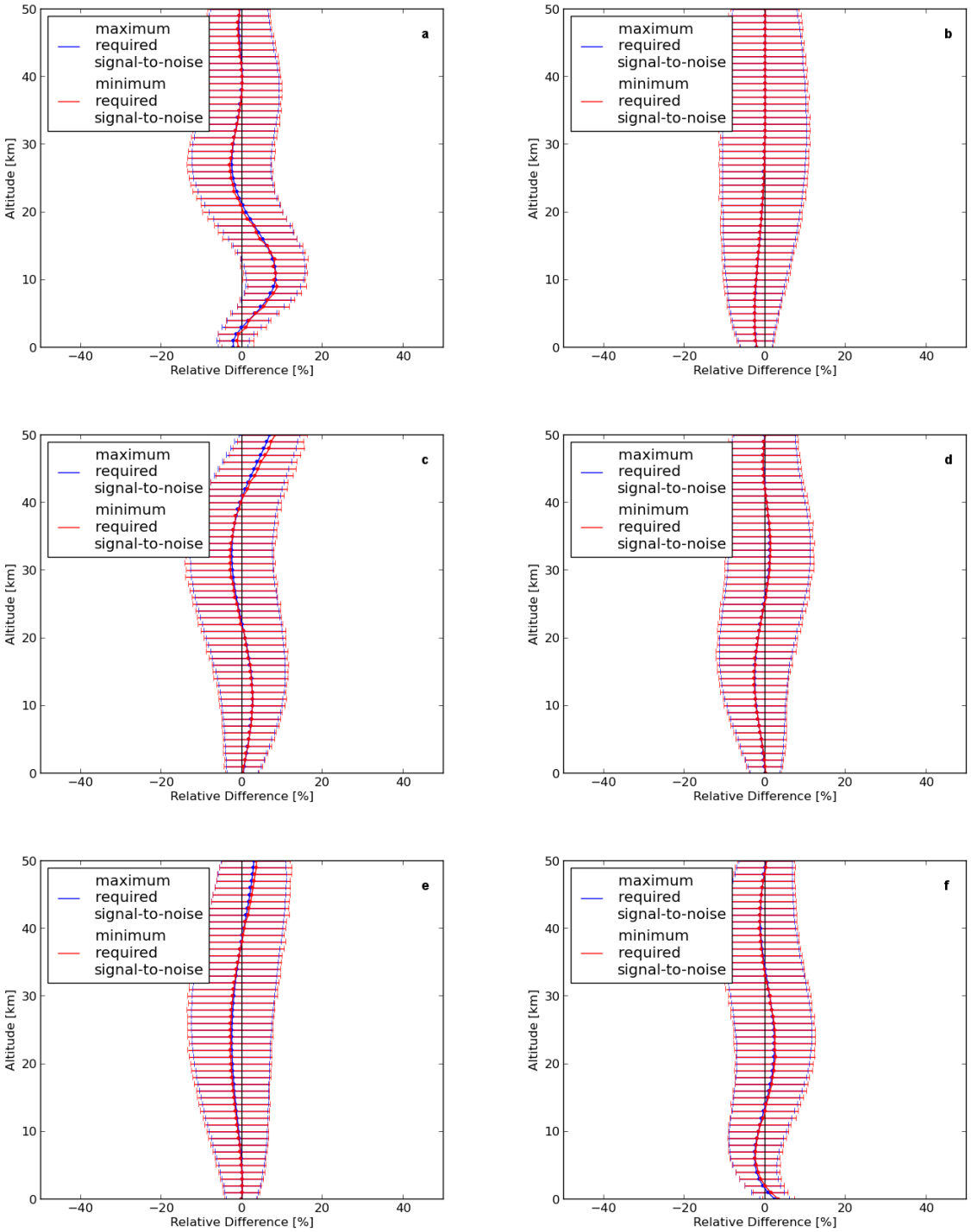

Figure 6.17: Relative differences for the CAMELOT scenarios a: Pacific polluted, b: Tropical bmb land, c: Tropical dust land, d: Tropical dust ocean, e: Stratospheric intrusion, f: Permafrost Siberia. Error-bars indicate the standard deviation at the 2 σ level

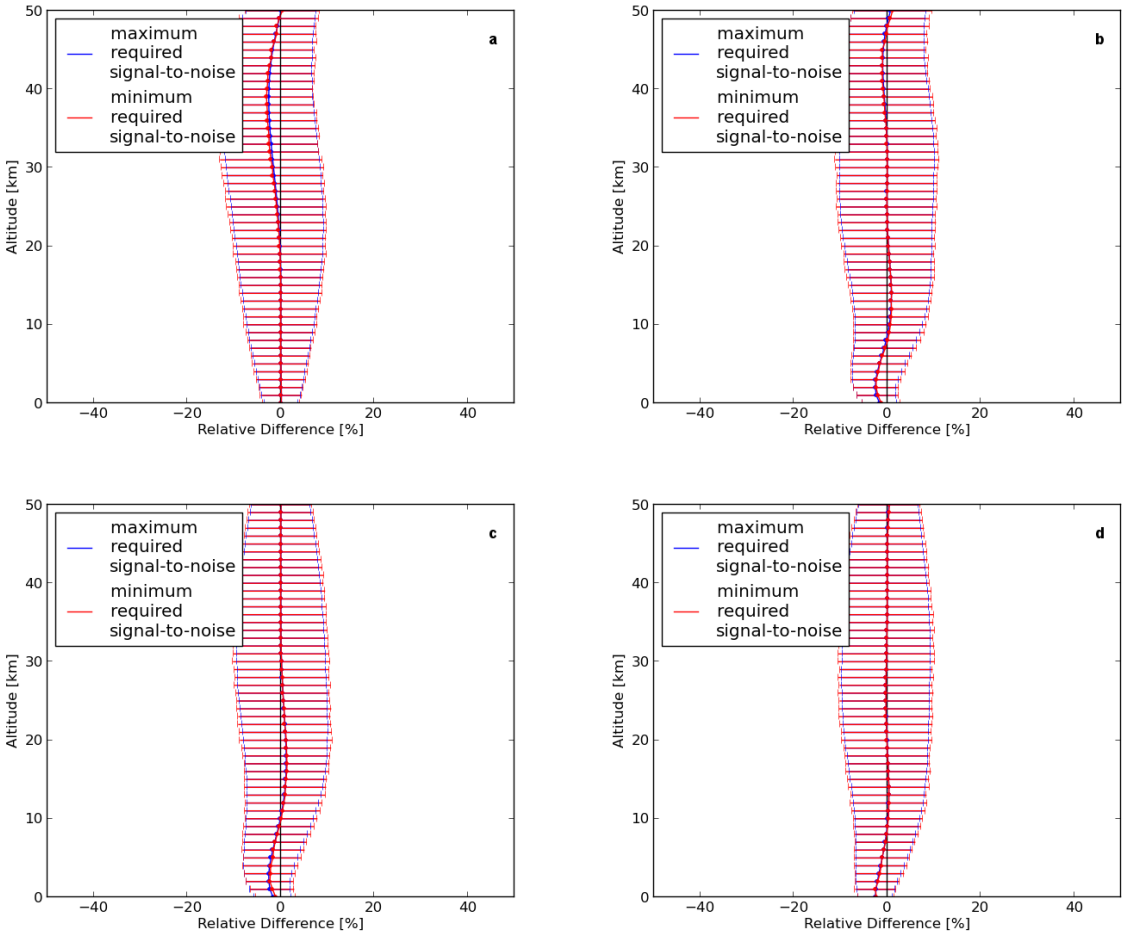

Figure 6.18: Relative differences for the CAMELOT scenarios a: subtropical background, b: US east coast, c: tropical biomass burning background, d: tropical biomass burning ocean. Error-bars indicate the standard deviation at the 2 σ level.

Table 6.8: Accuracies in % for sub columns as determined from the set of synthetic spectra from CAMELOT scenarios assuming maximum SNR

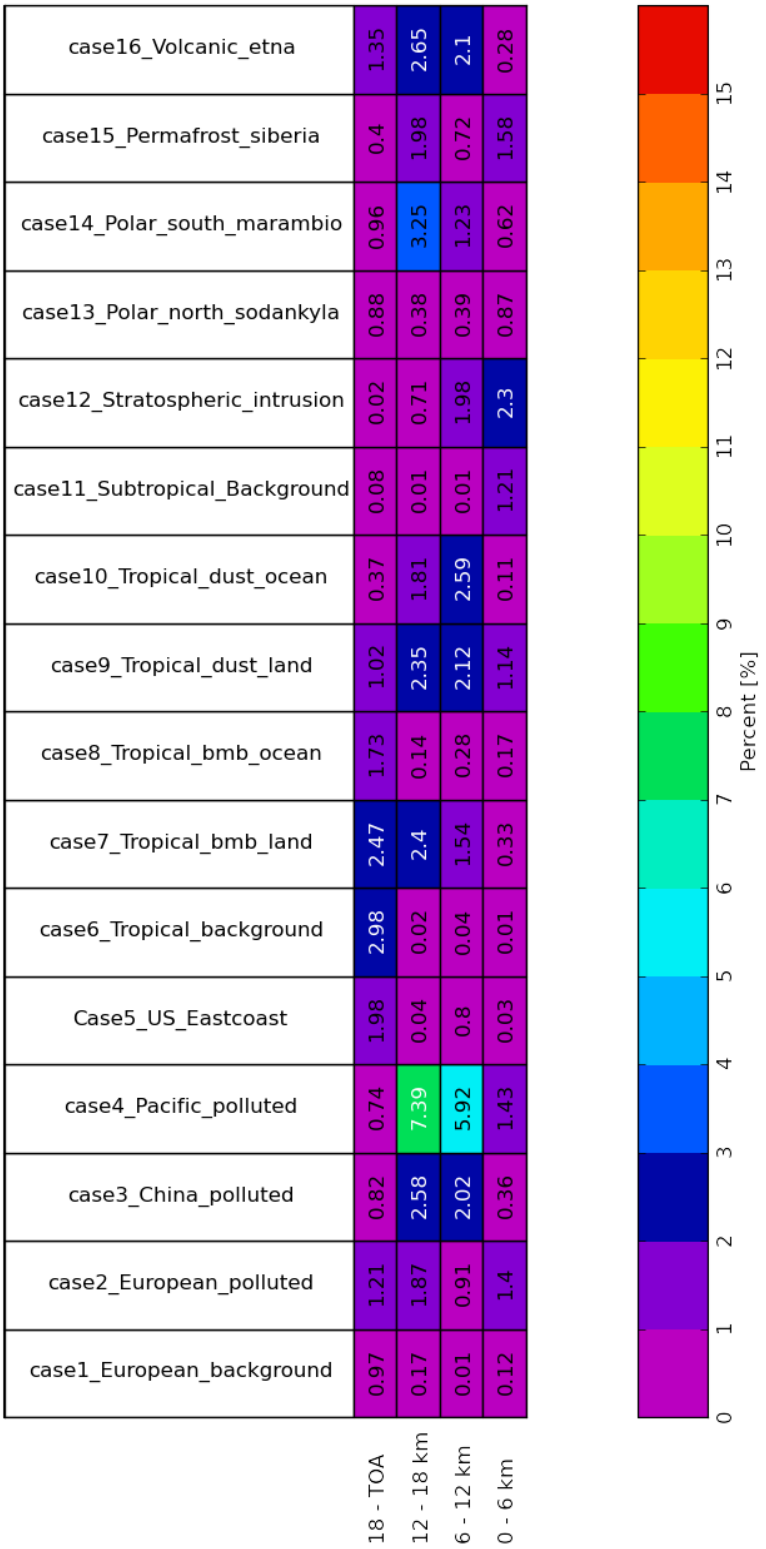

Table 6.9: Contribution of noise to retrieval error in % for sub columns as determined from the set of synthetic spectra from CAMELOT scenarios assuming maximum SNR

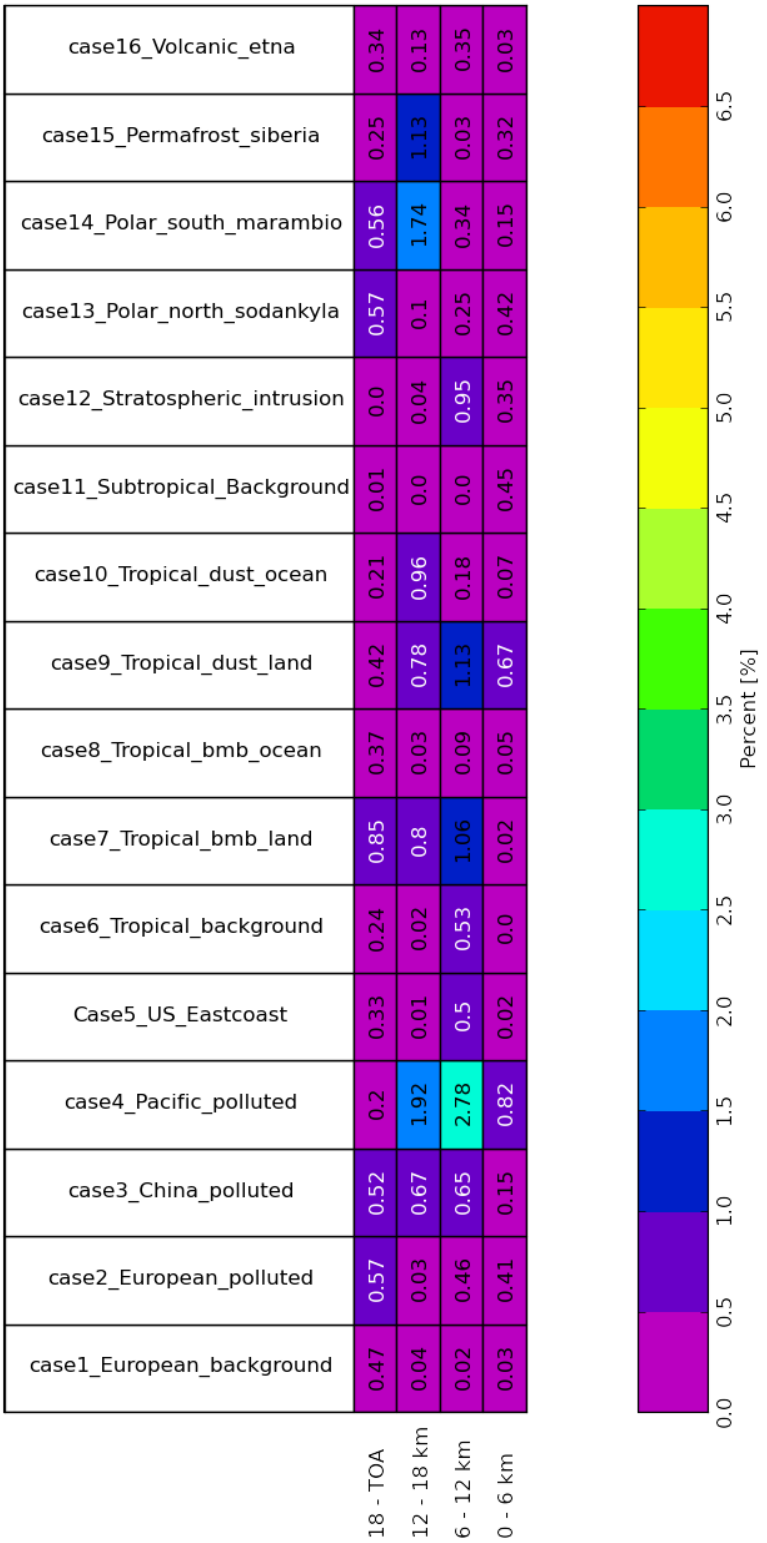

Table 6.10: Accuracies in % for sub columns as determined from the set of synthetic spectra from CAMELOT scenarios assuming minimum SNR

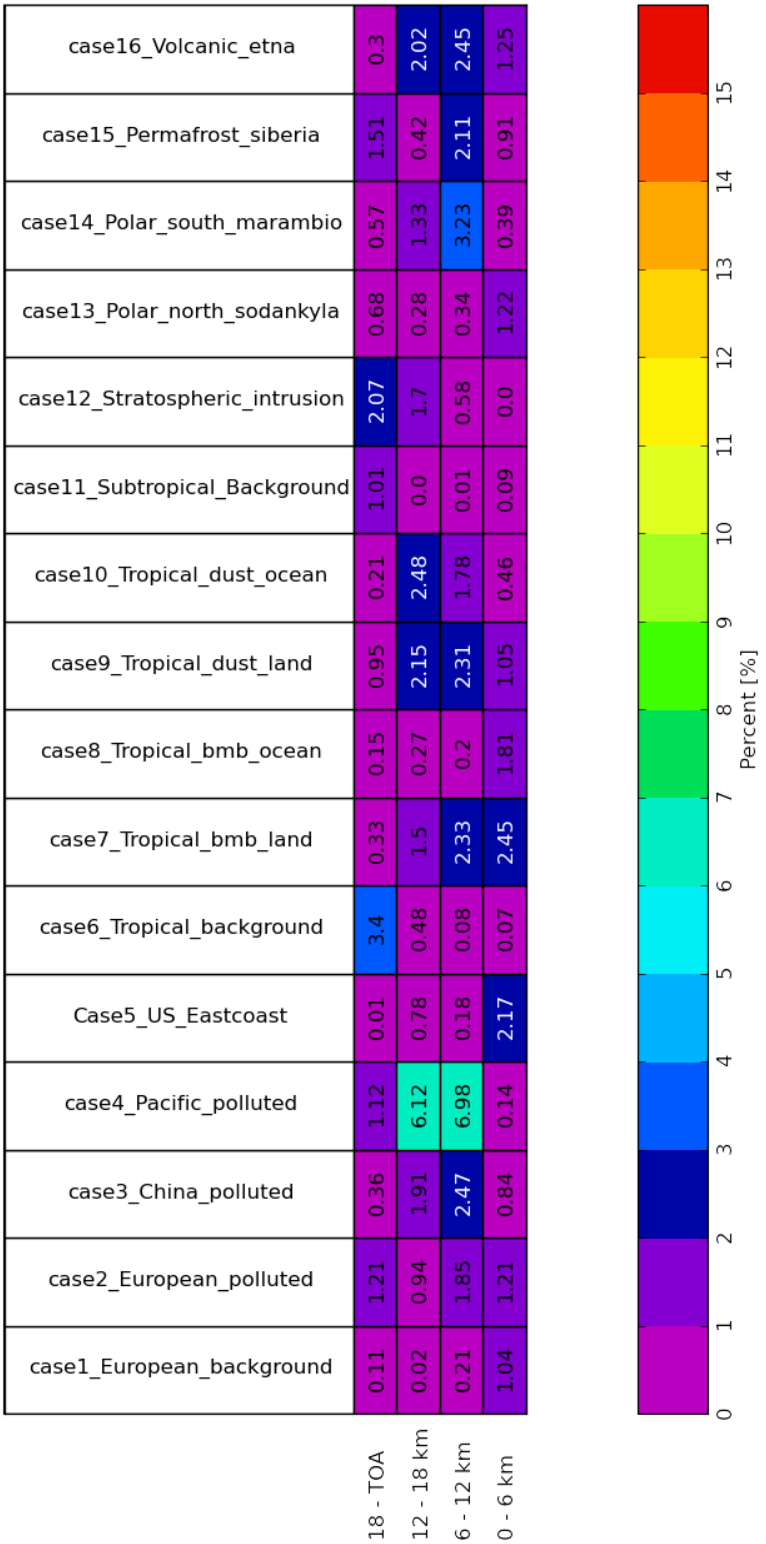

Table 6.11: Contribution of noise to retrieval error in % for sub columns as determined from the set of synthetic spectra from CAMELOT scenarios assuming minimum SNR

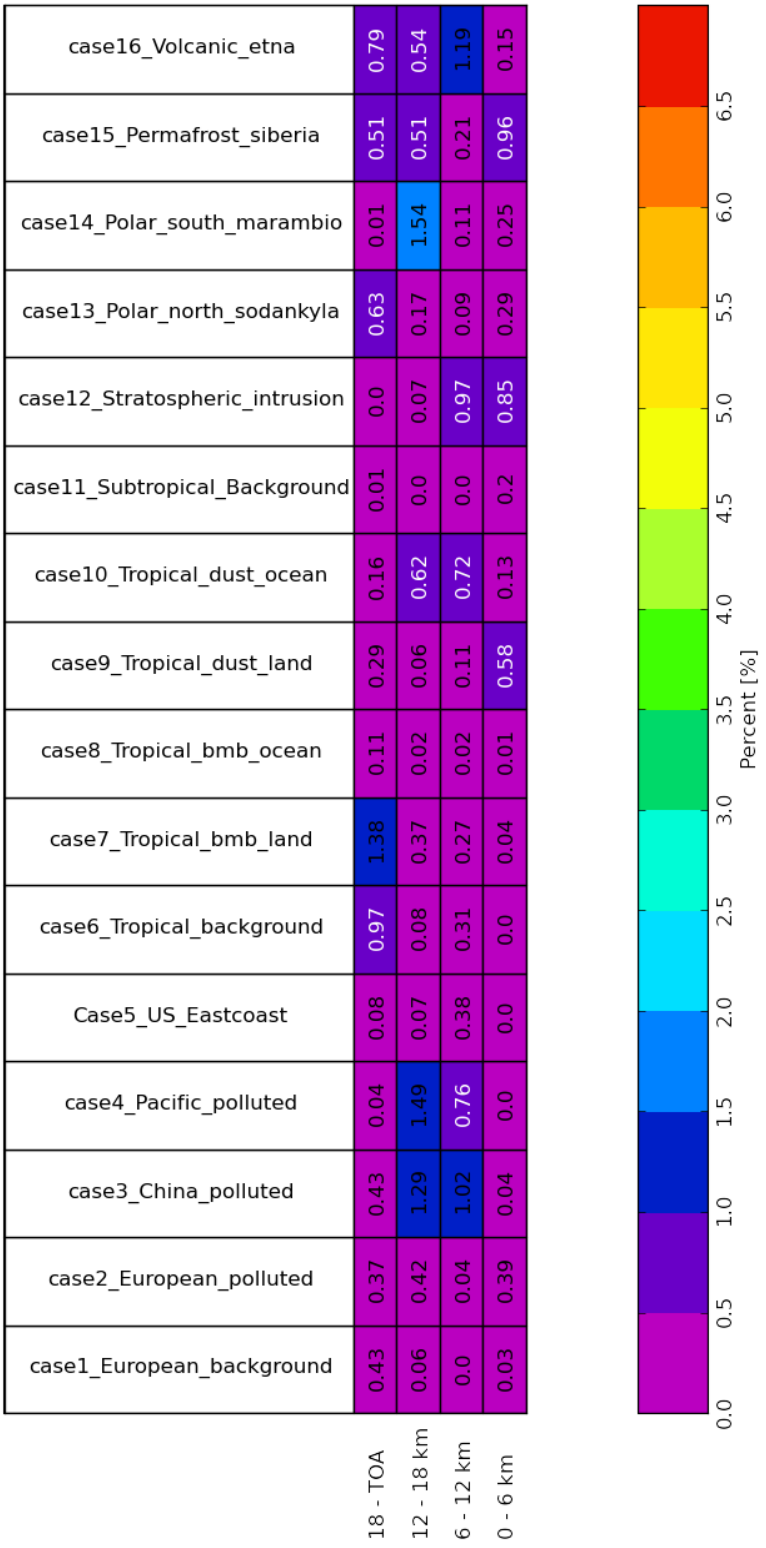

6.6.6.1 Direct comparisons with ozonesondes

A set of single retrievals compared to sonde measurements are shown in the appendix (Section 6.8) in Figure 6.29.

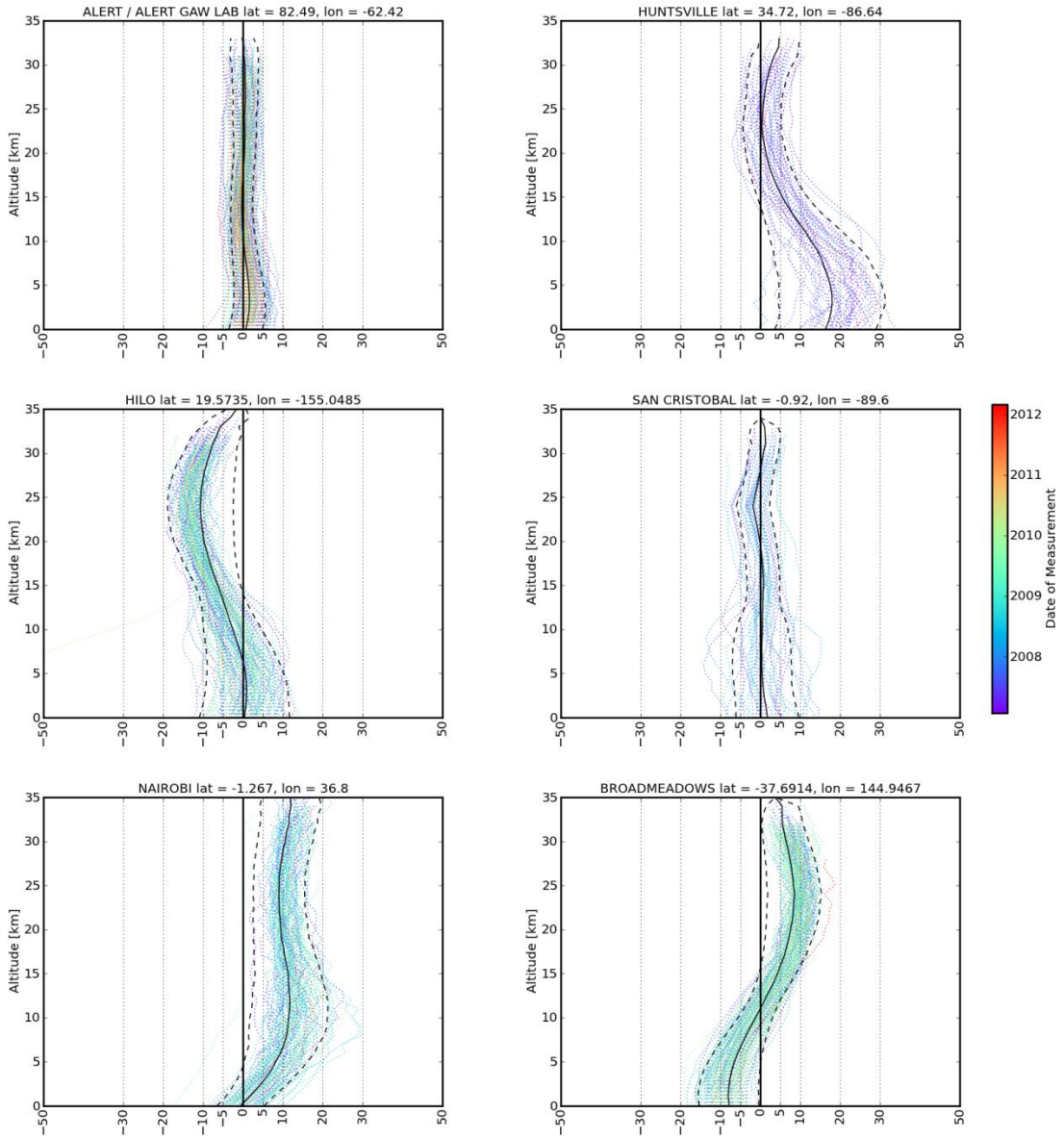

Figure 6.19: Relative differences in percent between ozone profiles retrieved from GOME-2 (A) UV spectra and ozone profiles from WOUDC ozonesondes launched on the same day. Colour indicates the launch date of the ozonesondes while black lines show then mean relative difference and the standard deviation at the 2 σ level.

A summary of retrieved profiles compared to sonde measurements taken on the same day is shown in Figure 6.19. Profiles were retrieved for the closest cloud-free pixel within 300 km of the ozonesonde launch location on the day of the ozonesonde launch. The set of used ozonesonde measurements comprises all ozonesondes for each location within the WOUDC database between from the beginning of 2007 to the end of 2012. The agreement is in general very good with larger differences at low altitudes where the contribution of the a priori profile is higher.

6.6.6.2 Direct Comparisons with NDACC Lidar Profiles

Direct comparisons between NDACC (Network for the Detection of Atmospheric Composition Change www.ndsc.ncep.noaa.gov) lidar profiles and profiles retrieved for GOME-2/A with a collocation criterion of 12 h and 300 km are shown in Figure 6.20 and Figure 6.21. Overall it can be seen that the retrieval performs within the requirements.

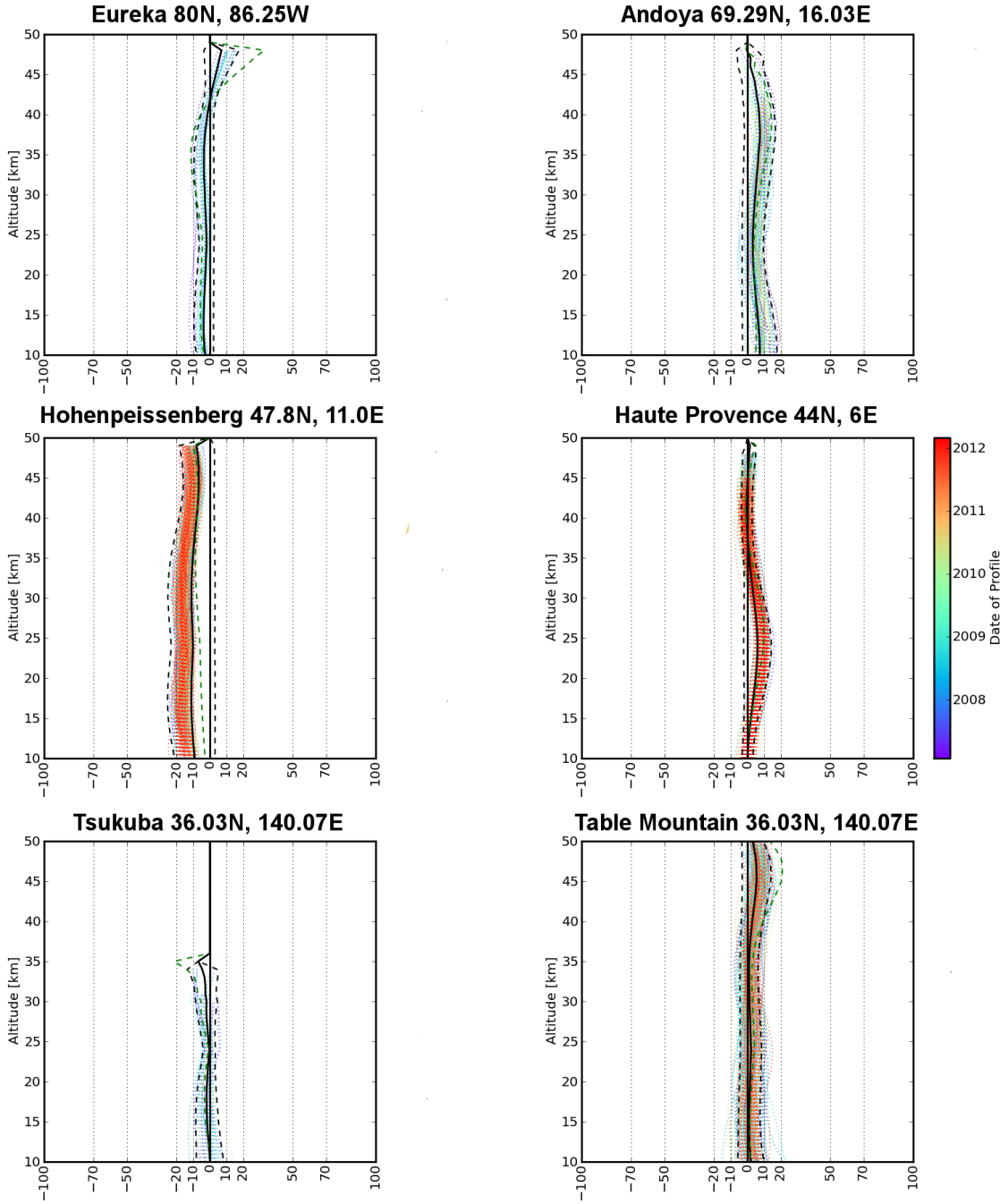

Figure 6.20 Relative differences in percent between ozone profiles retrieved from GOME-2/A UV spectra and ozone profiles from NDACC lidars measured on the dame day. Colour indicates the measurement date while black lines show the mean relative difference and the 2 σ level. The mean a priori contribution is shown as the green dashed line.

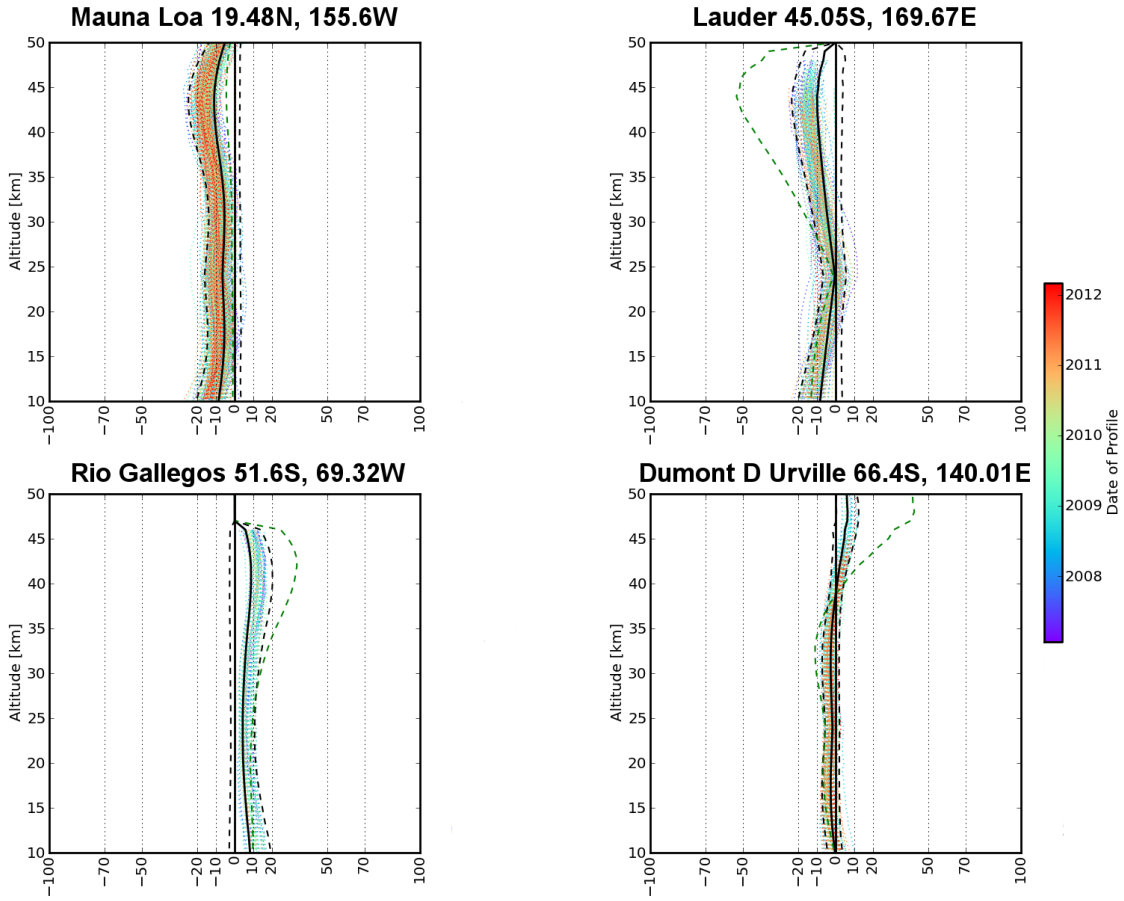

Figure 6.21 Relative differences in percent between ozone profiles retrieved from GOME-2/A UV spectra and ozone profiles from NDACC lidars measured on the dame day. Colour indicates the measurement date while black lines show the mean relative difference and the 2 σ level. The mean a priori contribution is shown as the dashed green line.

6.6.6.3 Intercomparison between GOME-2/A and GOME-2/B

Ozone profiles have been retrieved for 2014 for GOME-2/A and GOME-2/B. Mean relative differences for ground scenes fulfilling the collocation criterion of 12 h and 1000 km are shown in Figure 6.22. The retrievals from both instruments agree within the requirements.

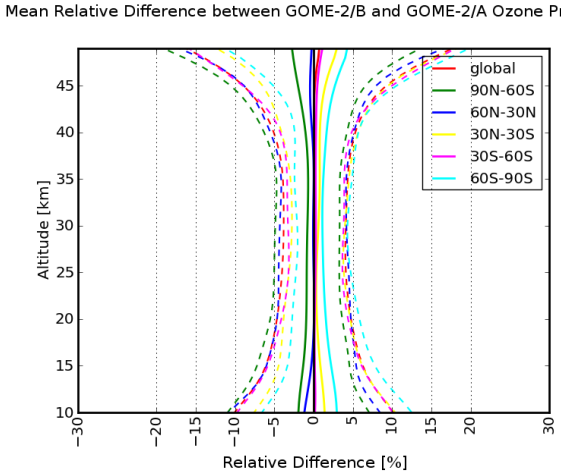

Figure 6.22 Mean relative difference between GOME-2/B and GOME-2/A relative to GOME-2/A for 2014 for different latitude bands. 2 σ levels are shown as dashed lines.

6.6.6.4 Direct comparison with RAL profiles

Ozone profiles from GOME-2 on MetOp-A have been retrieved for 2008 on the same altitudes used by RAL as part of the Ozone CCI project. A comparison for a sample day is shown in Figure 6.30, Figure 6.31, and Figure 6.32 in the appendix (section 6.8). These retrievals have been performed at IUP using the a priori used by RAL. Overall both datasets agree very well with generally slightly higher values retrieved using the IUP algorithm. The relative difference of both retrievals (relative to the RAL retrievals) has been averaged in 1° latitude bins and is plotted for three altitudes in Figure 6.23, Figure 6.24, and Figure 6.25. Overall the differences are below 10% in all cases with smaller differences at higher altitudes. This can probably be attributed to the additional retrieval step used at RAL with a focus on the tropospheric ozone. Differences are generally larger in December in the northern hemisphere and in February in the southern hemisphere. A more detailed comparison and a comparison of retrieval diagnostics still need to be conducted.

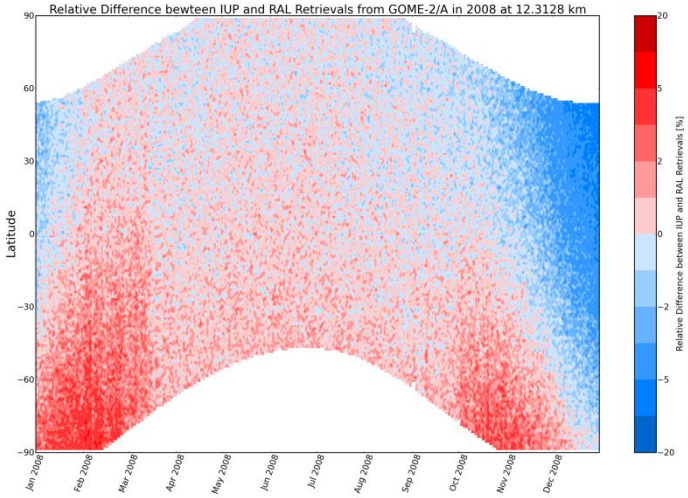

Figure 6.23 Relative differences between IUP and RAL retrieved O_3 concentrations relative to RAL retrieved O_3 concentrations averaged in 1° latitude bins at 12.3128 km

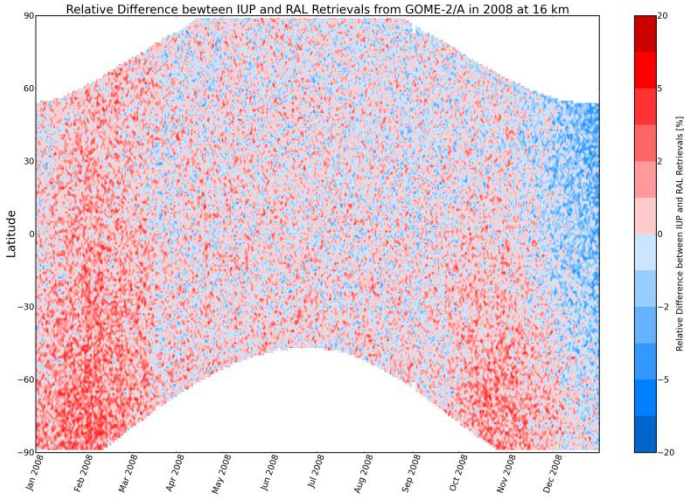

Figure 6.24 Relative differences between IUP and RAL retrieved O_3 concentrations relative to RAL retrieved O_3 concentrations averaged in 1° latitude bins at 16 km

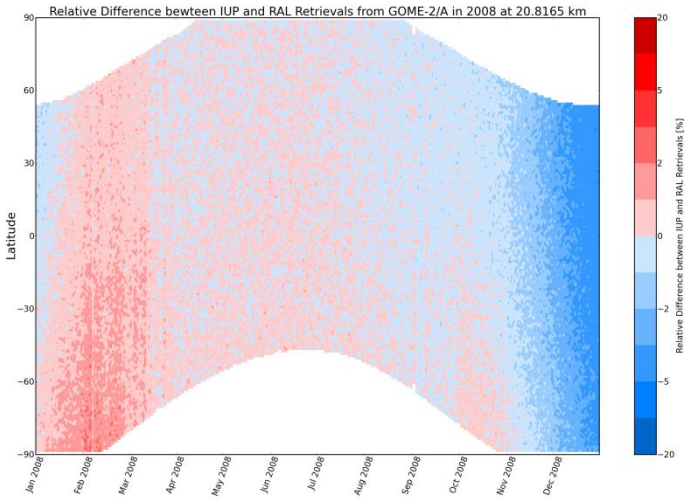

Figure 6.25 Relative differences between IUP and RAL retrieved O_3 concentrations relative to RAL retrieved O_3 concentrations averaged in 1° latitude bins at 20.8165 km

6.6.6.5 Direct Comparison of IUP Algorithm applied to OMI with Ozonesondes

In order to better understand results from a verification effort based on OMI spectra reformatted to the TROPOMI data format the IUP ozone profile retrieval algorithm was applied to OMI spectra and compared with WOUDC ozonesondes. Relative differences for 4 WOUDC stations are shown in Figure 6.26. Overall the agreement is very good at lower latitudes with an apparent underestimation at higher latitudes.

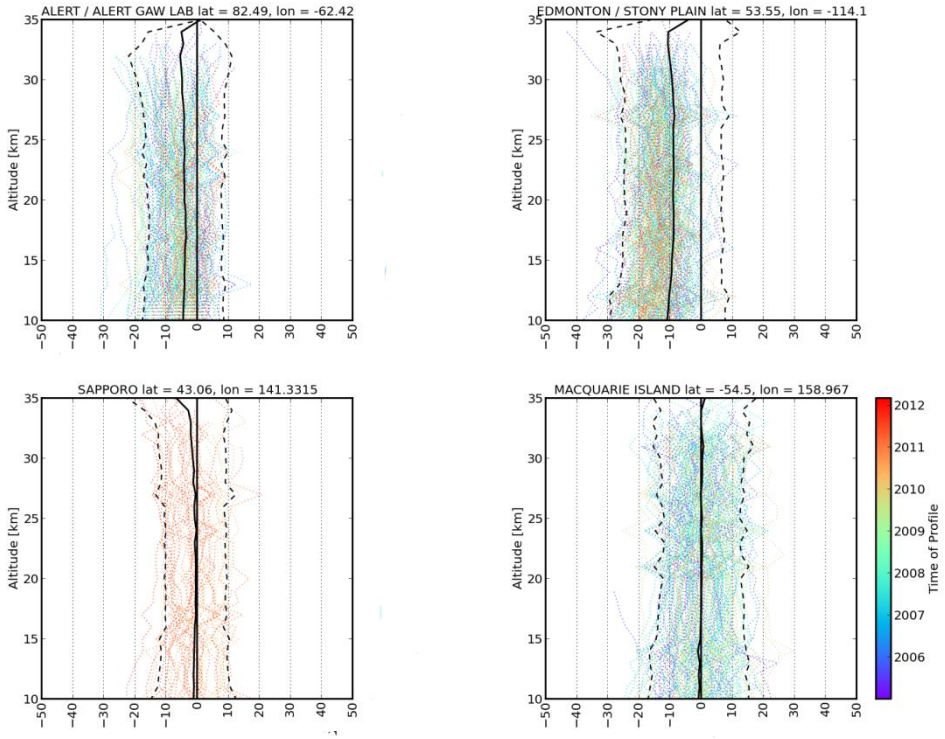

Figure 6.26: Relative differences in percent between ozone profiles retrieved from OMI UV spectra and ozone profiles from WOUDC ozonesondes. Colour indicates the measurement date while black lines show the mean relative difference and the 2 σ

6.6.7 Non-Linear Retrieval simulations (KNMI)

Non-linear retrieval results for the KNMI prototype scheme are shown in a form similar to the RAL results in Figure 6.27 and Figure 6.28. Results indicate agreement within 10% for bias and 20% for standard deviation, which are commensurate with requirements. Retrievals strongly improve over the prior. Results are somewhat better than for the RAL scheme. This may be due to use of more spectral coverage or due to better consistency in RTM modelling with the simulated radiances (the DISAMAR model being used in both cases). The use of different prior profiles and constraints in the two cases will also contribute to the differences. (The prototype algorithm uses the TOMS v8 ozone climatology. The RAL scheme uses the McPeters et al., (2007) climatology, but with a relaxed constraint in the troposphere.). Nevertheless, the fact that both RAL and KNMI schemes give agreement broadly within requirements for the same measurements provides a strong indication that the prototype scheme is functioning as it should.

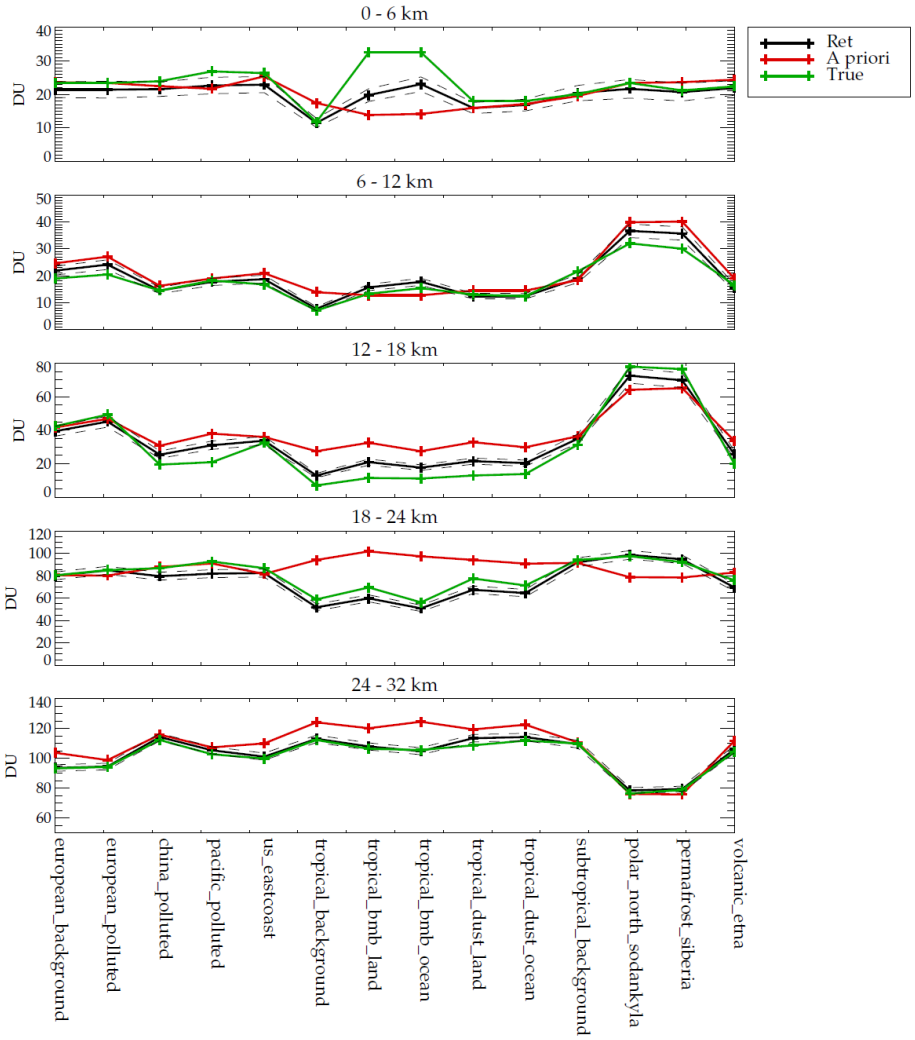

Figure 6.27: Non-linear retrieval results for CAMELOT study cases from the KNMI prototype scheme. Each panel shows results for a specific sub-column amount. Black lines show the retrieved sub-column; Red shows the a priori; Green shows the true amount based on the CAMELOT profile.

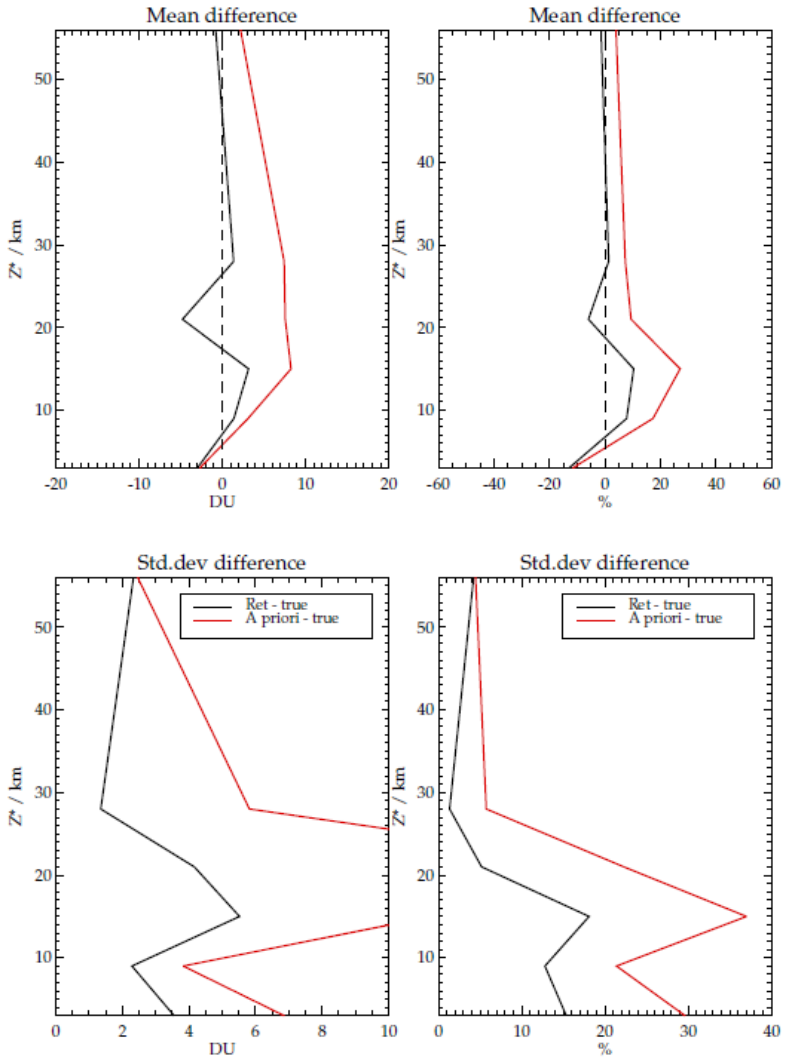

Figure 6.28: Summary of non-linear retrieval results for CAMELOT study cases from the KNMI prototype scheme. Upper panels show the mean differences over all cases, in terms of Dobson units(left) and percent (right); Bottom panels show the standard deviation in the differences.

6.6.8 Summary of Verification Results

The RTMs have been established as being broadly consistent. Discrepancies were found at the 1-2 % level, which remain to be fully explained. Nevertheless these differences do not seem to impact ozone profile retrievals performed by the verification schemes strongly (with the exception of the bias found in the lowest layer in the case of the RAL scheme).

Linear retrieval simulations, have shown a similar estimated errors for sub-column amounts from both prototype and verification algorithms.

Non-linear retrievals from both prototype and verification algorithms, performed based on simulated spectra by the forward model used in the prototype algorithm, have demonstrated good agreement with the true profiles, providing confidence in the correct implementation of the prototype algorithm.

The performance of the verification schemes on real data has also been established. Further verification based on common application of both prototype and verification schemes to the same set of (GOME-2) data was planned, however this work was not completed within the time available.

6.7 References

Bhartia, P. K., McPeters, R. D., Mateer, C. L., Flynn, L. E., and Wellemeyer, C.: Algorithm for the estimation of vertical ozone profiles from the backscattered ultraviolet technique, J. Geophys. Res., 101, 18793–18806, 1996.

Bracher, A., M. Weber, K. Bramstedt, S. Tellmann, J. P. Burrows, Long-term global measurements of ozone profiles by GOME validated with SAGE II considering atmospheric dynamics, J. Geophys. Res. 109, D20308, doi 10.1029/2004JD004677, 2004.

Bramstedt, K., K.-U., Eichmann, M., Weber, V. V., Rozanov, J. P., Burrows. GOME ozone profiles: a global validation with HALOE measurements. Advances in Space Research, 29(11), pp.1637–1642. 2002.

Bremer, H., M. von König, A. Kleinböhl, H. Küllmann, K. Künzi, K. Bramstedt, J. P. Burrows, K.-U. Eichmann, M. Weber, A. P. H. Goede, Ozone depletion observed by ASUR during the Arctic Winter 1999/2000, J. Geophys. Res. 107, 8277, doi:10.1029/2001JD000546, 2002.

Eichmann, K.-U., M. Weber, K. Bramstedt, and J.P. Burrows, Ozone depletion in the NH winter/spring 1999/2000 as measured by GOME-ERS2, J. Geophys. Res. 107, 8280, doi:10.1029/2001JD001148, 2002.

Fiotov, V.E., Labow, G.J., Evans, T., Hare, E.W., Köhler, U., McElroy, C. T., Miyagawa, K., Redonda, A., Savastiouk, V., Shalamyansky, A. M., Staehelin, J., Vanicek, K., and Weber, M.: Performance of the ground-based total ozone network assessed using satellite data, J. Geophys. Res., 113, D14313 doi:10.1029/2008JD009809, 2008.

Gorshelev, V., A., Serdyuchenko, M., Weber, W., Chehade, J. P., Burrows High spectral resolution ozone absorption cross-sections – Part 1: Measurements, data analysis and comparison with previous measurements around 293 K. Atmos. Meas. Tech. Discuss., 6(4), pp.6567–6611. 2013.

Hansen, G., K. Bramstedt, V. Rozanov, M. Weber, and J.P. Burrows, Validation of GOME ozone profiles by means of the ALOMAR ozone lidar, Annales Geophysicae 21, 1879-1886, 2003.

Hasekamp, O. P. and Landgraf, J.: Ozone profile retrieval from backscattered ultraviolet radiances: The inverse problem solved by regularization, J. Geophys. Res., 106, 8077–8088, 2001.

Hasekamp, O. P. and Landgraf, J.: Tropospheric ozone information from satellite-based polarization measurements, J. Geophys. Res., 107, 4326, doi:10.1029/2001JD001346, 2002.

Hoogen, R., V. V., Rozanov, K., Bramstedt, K.-U., Eichmann, M., Weber, J. P. Burrows. O3 profiles from GOME satellite data—I: Comparison with ozonesonde measurements. Physics and Chemistry of the Earth, Part C: Solar, Terrestrial & Planetary Science, 24(5), pp.447–452. 1999.

Hoogen, R., V.V. Rozanov and J.P. Burrows, Ozone profiles from GOME satellite data: Algorithm description and first validation, J. Geophys. Res. 104, 8263-8280, 1999.

Joiner, J., P.K. Barthia, R.P. Cebula, E. Hilsenrath, R.D. McPeters, and H. Park. Rotational Raman scattering (Ring effect) in satellite backscatter ultraviolet measurements. Applied Optics, 34(21), 4513-4525., 1995

Keppens, A., Lambert, J.-C., Granville, J., Miles, G., Siddans, R., van Peet, J. C. A., van der A, R. J., Hubert, D., Verhoelst, T., Delcloo, A., Godin-Beekmann, S., Kivi, R., Stübi, R., and Zehner, C.: Round-robin evaluation of nadir ozone profile retrievals: methodology and application to MetOp-A GOME-2, Atmos. Meas. Tech. Discuss., 7, 11481-11546, doi:10.5194/amtd-7-11481-2014, 2014.

Kerridge, B.J.K. , R. Siddans, B.L. Latter, J.P. Burrows, M. Weber, R. De Beek, I. Aben, and W. Hartman. GOME-2 Error Assessment Study. Final Report EUMETSAT Contract No EUM/CO/01/901/DK, 2002.

Levelt, P. and Veefkind, P., ESA CAMELOT study: Challenges in future operational missions for GMES atmospheric monitoring, sentinel 4 and 5. In EGU General Assembly Conference Abstracts. p. 8911. 2009.

Levenberg, A. "A method for the solution of certain non-linear problems in least squares." Q. Appl. Math. , 2, 1944: 164-168.

Liu, X., Chance, K., Sioris, C. E., Spurr, R. J. D., Kurosu, T. P., Martin, R. V., and Newchurch, M. J.: Ozone profile and tropospheric ozone retrievals from Global Ozone Monitoring Experiment: Algorithm description and validation, J. Geophys. Res., 110, D20307, doi:10.1029/2005JD006240, 2005.

Liu, X., Bhartia, P. K., Chance, K., Spurr, R. J. D., and Kurosu, T. P.: Ozone profile retrievals from the Ozone Monitoring Instrument, Atmos. Chem. Phys., 10, 2521-2537, doi:10.5194/acp-10-2521-2010, 2010.

Malicet, J., D., Daumont, J., Charbonnier, C., Parisse, A., Chakir, J., Brion. Ozone UV spectroscopy. II. Absorption cross-sections and temperature dependence. Journal of Atmospheric Chemistry, 21(3), pp.263–273. 1995.

Marquardt, D. W. "An algorithm for least-squares estimation of nonlinear parameters." J. Soc. Ind. Appl. Math., 1963: 431-441.

Matthews, E., 1985. Atlas of archived vegetation, land-use and seasonal albedo data sets.

McPeters, R. D., Lebow, G. J., and Logan, J. A.: Ozone climatological profiles for satellite retrieval algorithms, J.Geophys. Res.,112, D05308, doi:10.1029/2005JD006823, 2007.

McPeters, R. D. and G. J. Labow (2012), Climatology 2011: An MLS and sonde derived ozone climatology for satellite retrieval algorithms, J. Geophys. Res., 117, D10303, doi:10.1029/2011JD017006

Meijer, Y. J., Swart, D. P. J., Baier, F., Bhartia, P. K., Bodeker, G. E., Casadio, S., Chance, K., Del Frate, F., Erbertseder, T., Felder, M. D., Flynn, L. E., Godin-Beekmann, S., Hansen, G., Hasekamp, O. P., Kaifel, A., Kelder, H. M., Kerridge, B. J., Lambert, J. C., Landgraf, J., Latter, B., Liu, X., McDermid, I. S., Pachepsky, Y., Rozanov, V., Siddans, R., Tellmann, S., van der A, R. J., van Oss, R. F., Weber, M., and Zehner, C.: Evaluation of Global Ozone Monitoring Experiment (GOME) ozone profiles from nine different algorithms, J. Geophys. Res., 111, D21306, doi:10.1029/2005JD006778, 2006.

Miles, G. M., Siddans, R., Kerridge, B. J., Latter, B. G., and Richards, N. A. D.: Tropospheric ozone and ozone profiles retrieved from GOME-2 and their validation, Atmos. Meas. Tech., 8, 385–398, 2015 www.atmos-meas-tech.net/8/385/2015/ doi:10.5194/amt-8-385-2015MSC, NOAA-CMDL, MeteoSwiss, ABM, World Ozone and Ultraviolet Radiation Data Centre (WOUDC) [Data]. Retrieved January 16, 2012, from http://www.woudc.org.

Munro, R., R. Siddans, W.J. Reburn, and B.J.K. Kerridge. Direct measurement of tropospheric ozone distributions from space. Nature 392 (6672): 168-171, 1998

NOAA-CMDL, MeteoSwiss, ABM, World Ozone and Ultraviolet Radiation Data Centre (WOUDC) [Data]. Retrieved January 16, 2012, from http://www.woudc.org.

Richards, N.A.D., Arnold, S.R., Chipperfield, M.P., Rap, A., Monks S.A., Hollaway, M.J., Miles, G., Siddans, R., The Mediterranean summertime ozone maximum: Global emission sensitivities and radiative impacts, Atmospheric Chemistry and Physics, 13, 2331-2345. doi: 10.5194/acp-13-2331-2013

Rodgers, Clive D. Inverse Methods for Atmospheric Sounding: Theory and Practice. World Scientific, 2000.

Rozanov, V.V., D. Diebel, R.J.D. Spurr, and J.P. Burrows. GOMETRAN: A radiative transfer model for the satellite project GOME - the plane-parallel version. . J. Geophys. Res. 102 (d14) , 16683-16695., 1997.

Rozanov A., V. Rozanov, M. Buchwitz, A. Kokhanovsky and J.P. Burrows, SCIATRAN 2.0 - A new radiative transfer model for geophysical applications in the 175-2400 nm spectral region, Adv. Space Res., 36, 1015-1019, doi:10.1016/j.asr.2005.03.012, 2005.

Rozanov, V. V. A. V., Rozanov, A. A., Kokhanovsky, J. P. Burrows. Radiative transfer through terrestrial atmosphere and ocean: Software package SCIATRAN. Journal of Quantitative Spectroscopy and Radiative Transfer, 133(0), pp.13–71. 2014.

Serdyuchenko, A., V., Gorshelev, M., Weber, W., Chehade, J. P., Burrows. High spectral resolution ozone absorption cross-sections–Part 2: Temperature dependence. Atmospheric Measurement Techniques 7.2 (2014): 625-636. 2014.

Siddans, R. Height Resolved Ozone Retrievals from the Global Ozone Monitoring Experiment, PhD Thesis, Univesity of Reading, 2003.

Siddans, R., C Poulsen, B. Latter, A. Waterfall, B. Kerridge, S. Migliorini, A. Kaiser-Weiss, G. Bergametti, G. Foret, A. Ung, Study on the Exploitation of the SEVIRI IR 9.7um Channel. Final Report, 2007

Simmons, A., S., Uppala, D., Dee, S., Kobayashi., ERA-Interim: New ECMWF reanalysis products from 1989 onwards. ECMWF newsletter, 110(110), pp.25–35. 2007.

Tellmann, S., V.V. Rozanov, M. Weber, and J.P. Burrows, Improvements in the tropical ozone profile retrieval from GOMEUV/vis nadir spectra, Adv. Space Res. 34, 739-743, 2004.

van Peet, J.C.A., R.J. van der A, A.T.J. de Laat, O.N.E. Tuinder, G. Koenig-Langlo and J. Wittig, Height resolved ozone hole structure as observed by the Global Ozone Monitoring Experiment 2, Geophys. Res. Lett., 36, doi:10.1029/2009GL038603, 2009.

Thompson, A. M., Witte, J. C., McPeters, R. D., Oltmans, S. J., Schmidlin, F. J., Logan, J. A., Fujiwara, M., Kirchhoff, V.W.J.H., Posny, F., F., Coetzee, G. J. R., Hoegger, B., Kawakami, S., Ogawa, T., Johnson, B. J., Vomel H., and Labow, G. J.: Southern Hemisphere Additional Ozonesondes (SHADOZ) 1998–2000 tropical ozone climatology: 1. Comparison with Total Ozone Mapping Spectrometer (TOMS) and ground-based measurements, J. Geophys. Res., 108(D2), 8238, doi:10.1029/2001JD000967, 2003.

van der A, R. J., van Oss, R. F., Piters, A. J. M., Fortuin, J. P. F., Meijer, Y. J., and Kelder, H. M.: Ozone profile retrieval from recalibrated GOME data, J. Geophys. Res., 107, 4239, doi:10.1029/2001JD000696, 2002.

Veefkind, J.P. (editor) CAMELOT Final Report, RP-CAM-KNMI-050, Issue 1, 30 November 2009, ESA CONTRACT NO: 21533/07/NL/HE

Wellemeyer, C. G., P. K., Bhartia, S. L., Taylor, W., Qin, C., Ahn, Version 8 Total Ozone Mapping Spectrometer (TOMS) algorithm. In Proceedings of the XX Quadrennial Ozone Symposium. 2004.

6.8 Appendix

wavelength (nm)	τ sca	τ abs	depolarization
270	1,85938	63,89732	0,034434
271	1,829318	58,47912	0,034358
272	1,799875	56,96401	0,034283

wavelength (nm)	τ sca	τ abs	depolarization
273	1,771036	52,75148	0,034209
274	1,742785	48,59459	0,034136
275	1,715109	46,85972	0,034064
276	1,687992	42,60919	0,033993
277	1,661421	39,95868	0,033924
278	1,635383	36,70022	0,033855
279	1,609864	34,01719	0,033787
280	1,584851	31,93354	0,033721
281	1,560333	28,83624	0,033655
282	1,536297	25,42282	0,03359
283	1,512732	23,62358	0,033527
284	1,489627	21,423	0,033464
285	1,46697	19,47814	0,033402
286	1,444751	17,64057	0,033341
287	1,42296	15,79947	0,03328
288	1,401586	13,63862	0,033221
289	1,38062	12,3082	0,033163
290	1,360053	10,9531	0,033105
291	1,339874	9,864617	0,033048
292	1,320076	8,445073	0,032992
293	1,300648	7,662499	0,032937
294	1,281584	6,534889	0,032882
295	1,262874	5,889447	0,032829
296	1,244511	5,06493	0,032776
297	1,226487	4,492731	0,032723
298	1,208794	3,804038	0,032672
299	1,191424	3,429759	0,032621
300	1,174371	2,910987	0,032571
300,5	1,165961	2,750118	0,032546
301	1,157627	2,540663	0,032521
301,5	1,149369	2,324822	0,032497
302	1,141186	2,24135	0,032472
302,5	1,133077	2,09504	0,032448
303	1,125041	1,891609	0,032424
303,5	1,117077	1,766405	0,0324
304	1,109185	1,722175	0,032377
304,5	1,101364	1,604087	0,032353
305	1,093613	1,437874	0,03233
305,5	1,085931	1,311129	0,032307

wavelength (nm)	τ sca	τ abs	depolarization
306	1,078317	1,277646	0,032283
306,5	1,070771	1,238473	0,032261
307	1,063293	1,120868	0,032238
307,5	1,05588	0,988147	0,032215
308	1,048533	0,961542	0,032193
308,5	1,041251	0,902886	0,03217
309	1,034033	0,8763	0,032148
309,5	1,026879	0,771408	0,032126
310	1,019787	0,697801	0,032104
310,5	1,012758	0,685762	0,032083
311	1,00579	0,636412	0,032061
311,5	0,998882	0,636513	0,03204
312	0,992035	0,5441	0,032018
312,5	0,985248	0,492061	0,031997
313	0,978519	0,46053	0,031976
313,5	0,971849	0,48568	0,031955
314	0,965236	0,436744	0,031934
314,5	0,95868	0,353057	0,031914
315	0,952181	0,338371	0,031893
315,5	0,945738	0,369359	0,031873
316	0,93935	0,321532	0,031853
316,5	0,933016	0,275329	0,031832
317	0,926737	0,259304	0,031812
317,5	0,920511	0,257475	0,031793
318	0,914338	0,248803	0,031773
318,5	0,908218	0,193571	0,031753
319	0,90215	0,165087	0,031734
319,5	0,896133	0,21526	0,031714
320	0,890166	0,220238	0,031695
320,5	0,884251	0,163308	0,031676
321	0,878385	0,117103	0,031657
321,5	0,872568	0,112609	0,031638
322	0,8668	0,150793	0,031619
322,5	0,86108	0,137888	0,031601
323	0,855408	0,134824	0,031582
323,5	0,849784	0,079245	0,031564
324	0,844206	0,058498	0,031545
324,5	0,838675	0,074972	0,031527
325	0,833189	0,129644	0,031509

wavelength (nm)	τ sca	τ abs	depolarization
325,5	0,827749	0,096325	0,031491
326	0,822354	0,067611	0,031473
326,5	0,817004	0,04434	0,031455
327	0,811697	0,03878	0,031438
327,5	0,806434	0,054822	0,03142
328	0,801215	0,097104	0,031403
328,5	0,796038	0,057901	0,031385
329	0,790903	0,031971	0,031368
329,5	0,785811	0,022157	0,031351
330	0,78076	0,021954	0,031334
330,5	0,77575	0,048926	0,031317
331	0,77078	0,04636	0,0313
331,5	0,765851	0,042321	0,031284
332	0,760962	0,022546	0,031267
332,5	0,756112	0,013843	0,031251
333	0,751302	0,01714	0,031234
333,5	0,74653	0,020003	0,031218
334	0,741797	0,035615	0,031202
334,5	0,737101	0,019064	0,031186
335	0,732443	0,011922	0,031169
335,5	0,727822	0,007657	0,031154
336	0,723239	0,006793	0,031138
336,5	0,718691	0,014951	0,031122
337	0,71418	0,013959	0,031106
337,5	0,709705	0,024123	0,031091
338	0,705265	0,012732	0,031075
338,5	0,70086	0,006664	0,03106
339	0,69649	0,004979	0,031045
339,5	0,692155	0,006058	0,031029
340	0,687853	0,00795	0,031014

Table 6.12: Scattering and absorption parameters for the entire atmosphere used in the DISAMAR RTM to simulate sun-normalised radiances

altitude (km)	pressure (hPa)	temperature (K)	O_3 (ppbv)
0	977,52	291,238	50,34
0,9975	868,598	285,652	56,62
1,9934	770,37	281,145	56,75
2,993	681,566	275,872	57,95
3,9882	601,81	269,839	59,83
4,987	529,615	263,398	62,12
5,9913	464,238	256,462	64,92
6,9906	405,708	249,084	68,32
7,9768	353,748	241,396	72,66
8,9718	306,683	233,52	78,9
9,9877	263,809	226,217	97,34
10,977	226,86	220,586	132,6
11,961	194,665	217,339	190,3
13,01	165,124	216,582	264,9
13,946	142,548	216,343	345,3
15	120,739	215,062	465,3
15,932	104,169	213,829	591
17,017	87,66	213,43	812
17,917	75,955	213,033	1033
18,966	64,29	213,927	1404
19,935	55,155	215,096	1808
20,896	47,417	216,332	2270
22,034	39,697	217,712	2863
22,745	35,553	219,092	3456
23,534	31,483	220,472	4049
24,438	27,412	221,95	4617
27,512	17,236	226,706	5766
29,495	12,863	231,462	6916
32,161	8,758	236,814	7215
34,682	6,139	242,335	7271
36,929	4,508	248,033	7016
40,109	2,941	254,088	6129
41,755	2,371	260,144	5242
43,9	1,801	263,478	4362
46,861	1,232	259,99	3500
51,533	0,671	256,502	2639
56,567	0,345	250,249	1356
61,51	0,177	245,957	696,7
66,374	0,091	240,1	358,6

71,066	0,046	218,1	180,2
80,868	0,01	215	150

Table 6.13: Pressure, temperature and ozone profile for the European background CAMELOT case

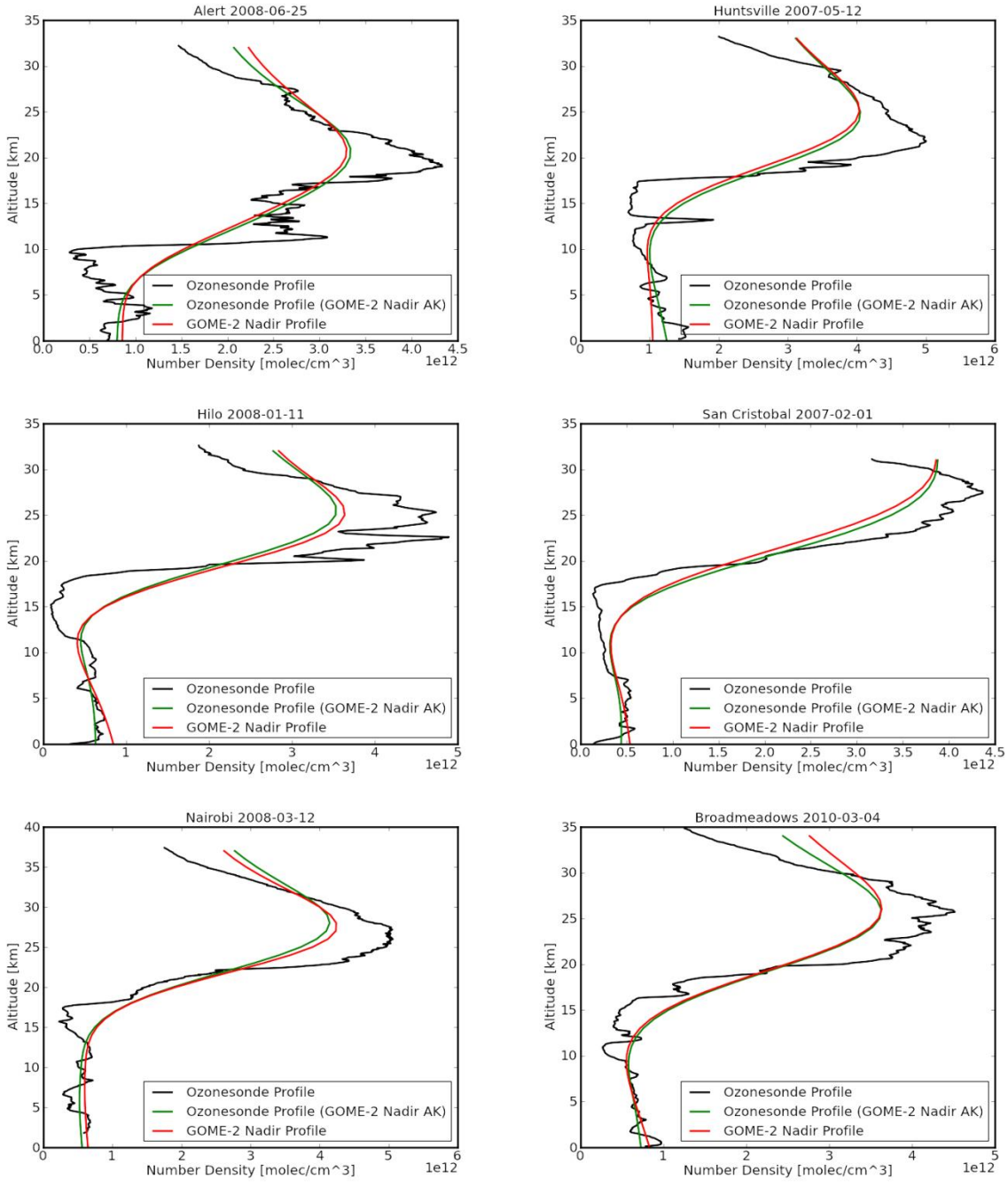

Figure 6.29: Sample set of single retrievals from GOME-2 data with corresponding WOUDC ozonesonde measurements

Table 6.14: Ozone profile used for the highly polluted CAMELOT scene

Pressure [hPa]	vmr [ppmv]
1050.0000	0.30000
977.5200	0.20000
868.5980	0.10000
770.3700	0.05675
681.5660	0.05795
601.8100	0.05983
529.6150	0.06212
464.2380	0.06492
405.7080	0.06832
353.7480	0.07266
306.6830	0.07890
263.8090	0.09734
226.8600	0.1326
194.6650	0.1903
165.1240	0.2649
142.5480	0.3453
120.7390	0.4653
104.1690	0.5910
87.6600	0.8120
75.9550	1.0330
64.2900	1.4040
55.1550	1.8080
47.4170	2.2700
39.6970	2.8630
35.5530	3.4560
31.4830	4.0490
27.4120	4.6170
17.2360	5.7660
12.8630	6.9160
8.7580	7.2150
6.1390	7.2710
4.5080	7.0160
2.9410	6.1290
2.3710	5.2420
1.8010	4.3620
1.2320	3.5000
0.6710	2.6390
0.3450	1.3560
0.1770	0.6967
0.0910	0.3586
0.0460	0.1802

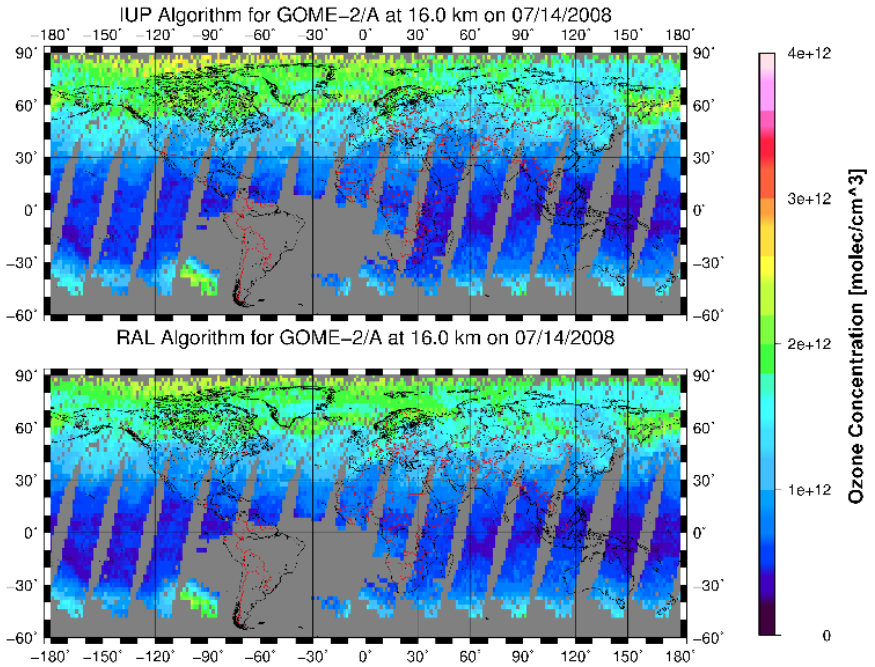

Figure 6.30: IUP and RAL O_3 concentration at 12.3128 km on 14th July 2008

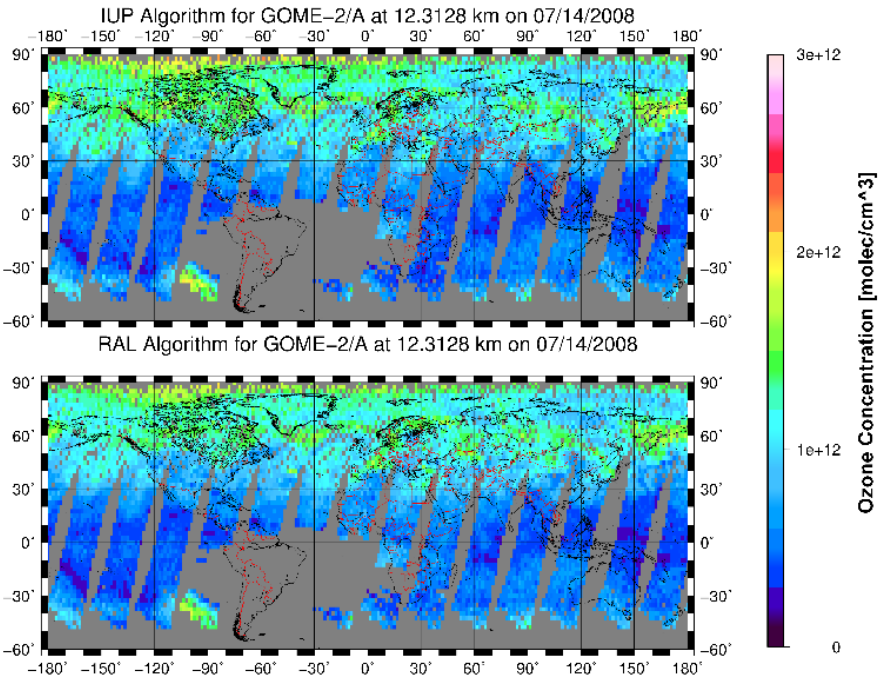

Figure 6.31: IUP and RAL O_3 concentration at 16 km on the 14th of July 2008

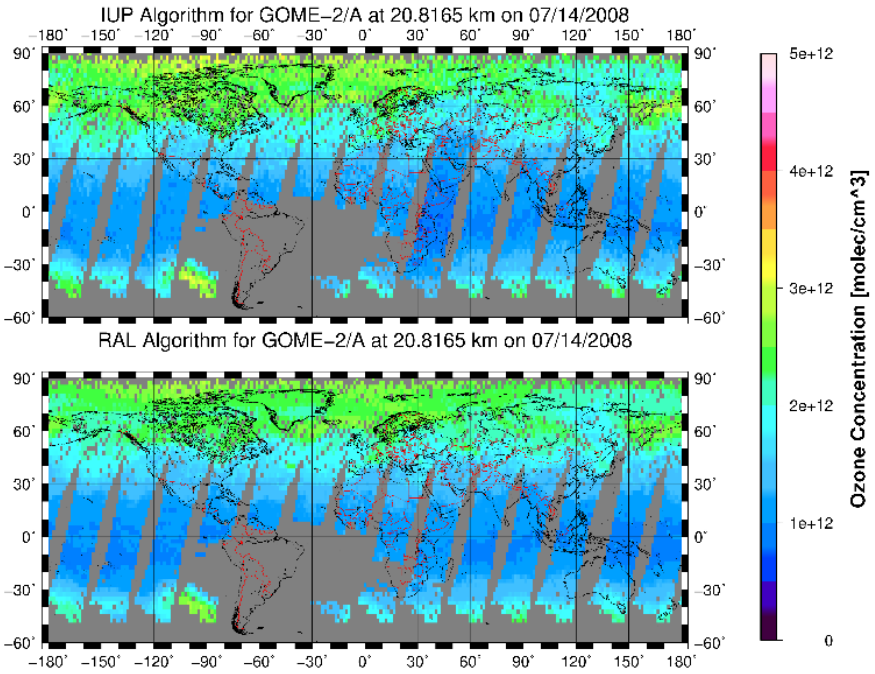

Figure 6.32: IUP and RAL O_3 concentration at 20.8165 km on 14th July 2008

7 O3 Tropospheric Column

Authors: Elpida Leventidou, Mark Weber (IUP UB)

7.1 Document changes

Changes in issue 2.0:

- An outlier data screening scheme has been developed for the CCD-IUP algorithm.
- The verification algorithm was run using GOME-2 GDP V4.6 AND V4.7 data. The results have been compared with the prototype using the same GOME-2 dataset.

7.2 Verification approach

- A convective clouds differential algorithm (CCD-IUP) has been developed in order to create a dataset of monthly mean tropical tropospheric ozone columns.
- Results from the verification CCD-IUP algorithm are compared with the prototype S5P_TROPOZ_CCD results using the same input data. Both models are furthermore compared with collocated tropospheric ozone columns from ozonesondes and nadir ozone profile data up to 200 hPa height.

7.3 Description of Verification Algorithm

The Global Ozone Monitoring Experiment-2 (GOME 2) instrument onboard EUMETSAT's Meteorological Operational Satellites (METOP-A and METOP-B) can measure ozone columns as well as other atmospheric constituents and cloud properties in nadir mode. DLR generates the operational GOME-2/METOP level 2 products in the framework of EUMETSAT's Satellite Application Facility on Ozone and Atmospheric Chemistry Monitoring (O3M-SAF). The GOME Data Processor (GDP) operational algorithm is the baseline algorithm for the trace gas column retrievals from GOME/ERS-2 and GOME-2/MetOp. DOAS slant columns are converted to ozone vertical columns using the Air Mass Factor (AMF) conversion (Valks et al., 2013). Cloud information used in the trace gas retrieval is obtained with the OCRA and ROCINN algorithms (Loyola et al., 2007).

The Tropical Tropospheric Columns of Ozone (TTCO) can be retrieved with the Convective Clouds Differential (CCD) technique (Ziemke et al., 1998) by using total column of ozone and cloud information from satellite data (see Figure 7.2). To use the CCD technique, one assumes that the stratospheric column above deep convective clouds (ACCO) is identical to all stratospheric columns in the same latitude band, which is a valid assumption only in the Tropics. But it is known that in the tropical region on monthly time scales, a zonal variability (see Figure 7.1) on the order of ~5 DU exists (Ziemke et al., 2010). This zonal ACCO is then subtracted from clear-sky ozone column measurements to yield the tropical tropospheric column of ozone.

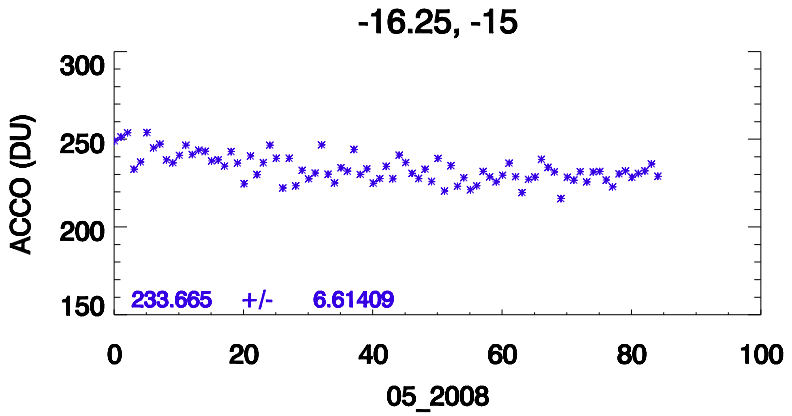

Figure 7.1: Ozone column above deep convective clouds in the area of the Western Pacific Ocean (70°E-170°W, 20°S-20°N) for the latitude band [-16.25°S; 15°S] (cf>0.8 and ctp <200hPa) vs. count per latitude band for GOME-2 GDP V4.5 (OCRA/ROCINN) in May 2008. The monthly mean above cloud ozone is 233.7 DU and the deviation 6.6 DU.

Another basic assumption for the CCD method is that the tropopause (~100 hPa) lies close to the top of the deep convective clouds (DCC), which are high, thick and bright clouds with highest occurrence rates over the ITCZ, the western Pacific, and the Indian Ocean (Sassen et al., 2009; Hong et al., 2007). It is known that DCC tops only reach the bottom of the tropical tropopause layer or the 'tropical transition layer' (TTL) (Sherwood and Dessler, 2001; Gettelman and Forester, 2002; Fueglistaler et al., 2009), which is well below the thermal (cold point) tropopause (~150 hPa). Only in rare occasions, DCCs overshoot beyond the top of the TTL (Hong et al., 2007; Fueglistaler et al., 2009).

Additionally, the original CCD method assumes that the UV measuring instruments only measure the ozone above the tops of the Deep Convective Clouds. This is not true as solar UV radiation penetrates deeply into the clouds for many km (Valks et al., 2003). Despite this fact, the method works well in the Western Pacific, because very low ozone concentrations of 4-7ppbv are present inside and above DCCs (Valks et al., 2014) due to vertical convection of O_3 poor oceanic air from the marine boundary layer into the Upper Troposphere. Thus the error from ozone below the thermal tropopause is minimal if the retrieved ACCOs are taken from that region (Ziemke et al., 2009).

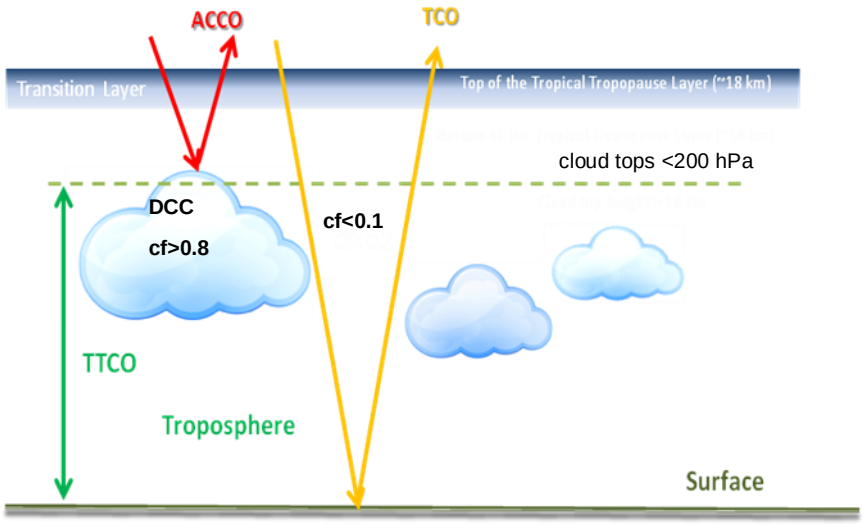

Figure 7.2: Illustration of the Convective Clouds Differential (CCD) technique. DCC are the deep convective clouds, cf is the cloud fraction, ACCO is the above cloud column of ozone, TCO is the total column of ozone and TTCO is the tropical tropospheric column of ozone.

7.3.1 Above cloud column

As seen in Figure 7.3 and Figure 7.4 the most frequent deep convective clouds can be found in the area of the Western Pacific (70°E – 170°W). Therefore, this area is selected for the Above Cloud Ozone Columns (ACCO) calculation. The ACCOs were determined for each 1.25° latitude band by averaging over all cloudy scenes in the Western Pacific and Indian Ocean (70°E-170°W, 20°S-20°N) for cloud fraction cf>0.8, cloud albedo a_c>0.8, and cloud top pressure p_c<300hPa. The choice of these criteria is due to sampling reasons. The cloud properties are determined by the OCRA and ROCINN algorithms (Loyola et al., 2007). A small correction is then applied to the ACCO between the actual cloud-top and the top of the Tropical Transition Layer at 200hPa (Valks et al., 2014). This correction is taken from climatological values and added to the ACCO for the cases where the retrieved clouds are below the 200hPa (higher cloud top pressures, lower heights) and subtracted when the effective cloud top pressure is lower than the 200hPa. In the future the correction value could be determined with the cloud slicing technique.

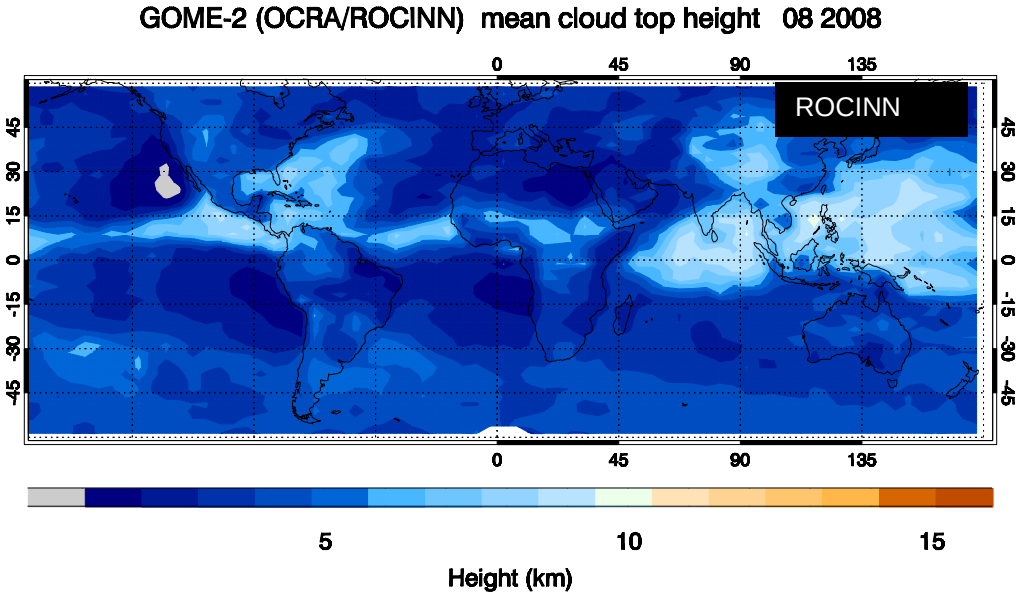

Figure 7.3: Global distribution of cloud top height for ROCINN (GOME-2) in August 2008.

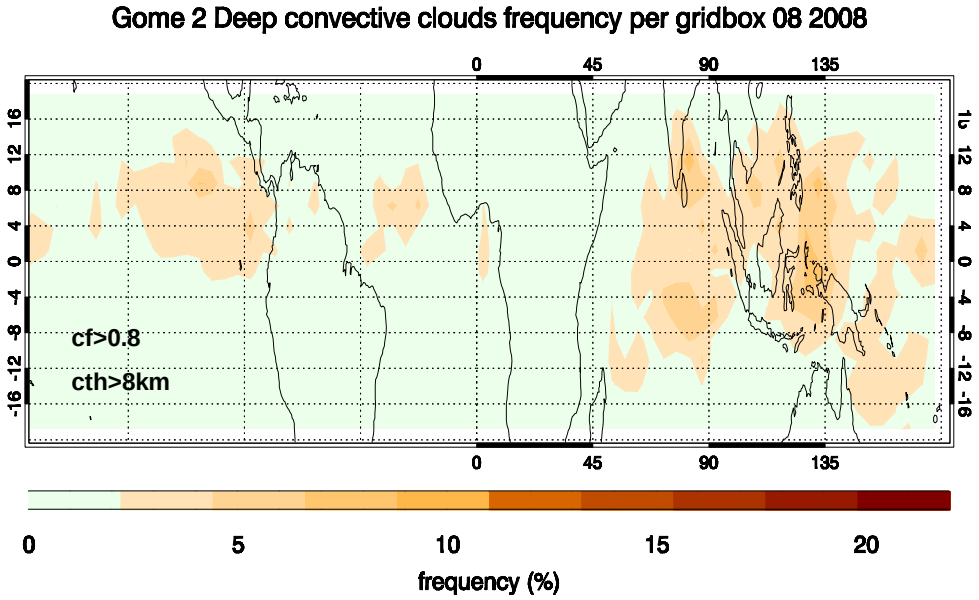

Figure 7.4: Frequency of Deep Convective Clouds in the Tropics from GOME-2 data, determined using *cf*>0.8 and *cth*>8km (~350hPa) for August 2008.

First, the variation of the above cloud column of ozone with the cloud height and cloud fraction was tested (see Figure 7.5) and it was concluded that the ACCO does not change significantly with cloud height, for clouds with cloud tops less than 9km (300hPa) and cloud fraction greater than 0.8. Then, the latitude dependence of the ACCO was investigated. As seen in Figure 7.5 - Figure 7.7, the ACCO has a notable latitudinal variation. Consequently, a latitude dependent ACCO was computed.

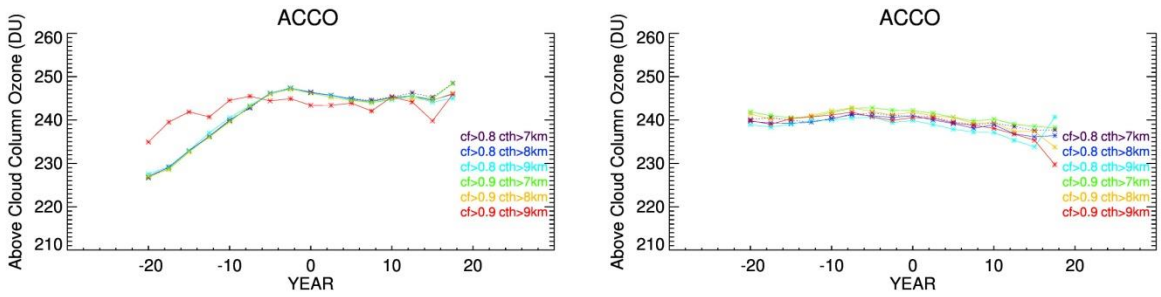

Figure 7.5: Above cloud ozone column for 1.25° latitude bands in the Indian Ocean (70°E-170°W) for different cloud fractions and cloud top heights using GOME-2 (OCRA/ROCINN) data, on May (up) and October (down) 2012.

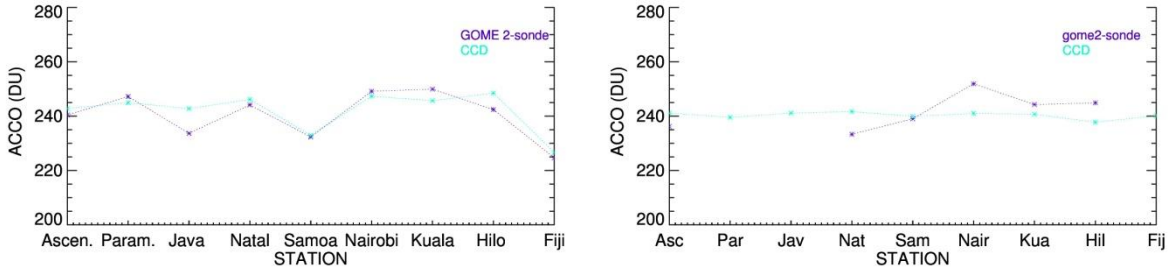

Figure 7.6: Above cloud ozone column retrieved with CCD technique (light blue) using cloud fraction > 0.8 and cloud top height > 8km, and Sonde/GOME-2 until 200hPa (blue) for 7 ozonesonde stations, on May (up) and October (down) 2012.

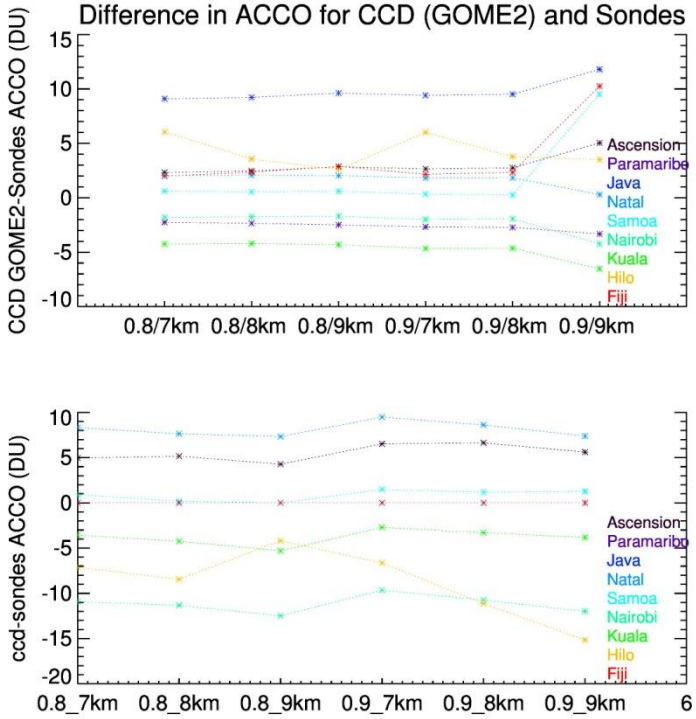

Figure 7.7: Difference in above cloud ozone column retrieved with CCD using different cloud fraction and cloud top heights and Sondes/GOME-2 stratospheric column until 200hPa, over 7 ozonesonde stations, on May (up) and October (down) 2012.

7.3.2 Tropospheric column of Ozone

The cloud-free total ozone columns from scenes with *cf*≤0.1 were monthly averaged in grid boxes of 1.25°x2.5° between 20°N and 20°S. Finally, the monthly mean ACCO from the same latitude band was subtracted from each gridded clear-sky total ozone column (TCO) covering the same latitude bands resulting in monthly mean gridded tropical tropospheric column of ozone (TTCO).

7.3.3 Error Analysis

In all the averages, for both cloudy and cloud free measurements, a weighted average has been applied. The weight for the averaging was the retrieval error of the total column. This error has been propagated to the tropospheric column of each grid box.

$$\textit{Tropospheric } O_3 \textit{ column error} = \{(\textit{total, cloud free } O_3 \textit{ column error})^2 + (\textit{above cloud } O_3 \textit{ column error of the appropriate latband})^2\}^{1/2}$$

The ACCO error per latitude band refers only to the errors of the ozone column above cloudy scenes. Propagation of the cloud products errors which is much more complicated has not been applied here. With this way an error for the tropospheric O_3 column has been calculated which in most of the cases is around 5-8 DU.

7.4 Main differences to prototype algorithm

The main differences with the prototype algorithm originate from the sorting of the outlier data. In the verification CCD-IUP algorithm all the daily above cloud ozone measurements with standard deviation more than 4 DU per grid-box and measurements that differ more than 8 DU from the neighbouring grid-boxes are sorted out.

7.5 Verification results

7.5.1 Application to real data and validation

The results of the prototype S5P_TROPOZ_CCD and of the verification CCD-IUP algorithm where compared with each other and with collocated tropospheric ozone columns below 200hPa (Bottom of the Tropical Transition Layer), derived from the Southern Hemisphere ADditional OZonesondes (SHADOZ) network (Thompson et al., 2003). The sonde sites shown here are Ascension (8°S, 14.4°W), Java (7.6°S, 111°E), Samoa (14.4°S, 170.6°W) , Paramaribo (5.8°N, 55.2°W), Natal (5.4°S, 35.4°W) and Nairobi (1.4°S, 36.8°E) from 2008-2012 for CCD tropospheric ozone columns validation.

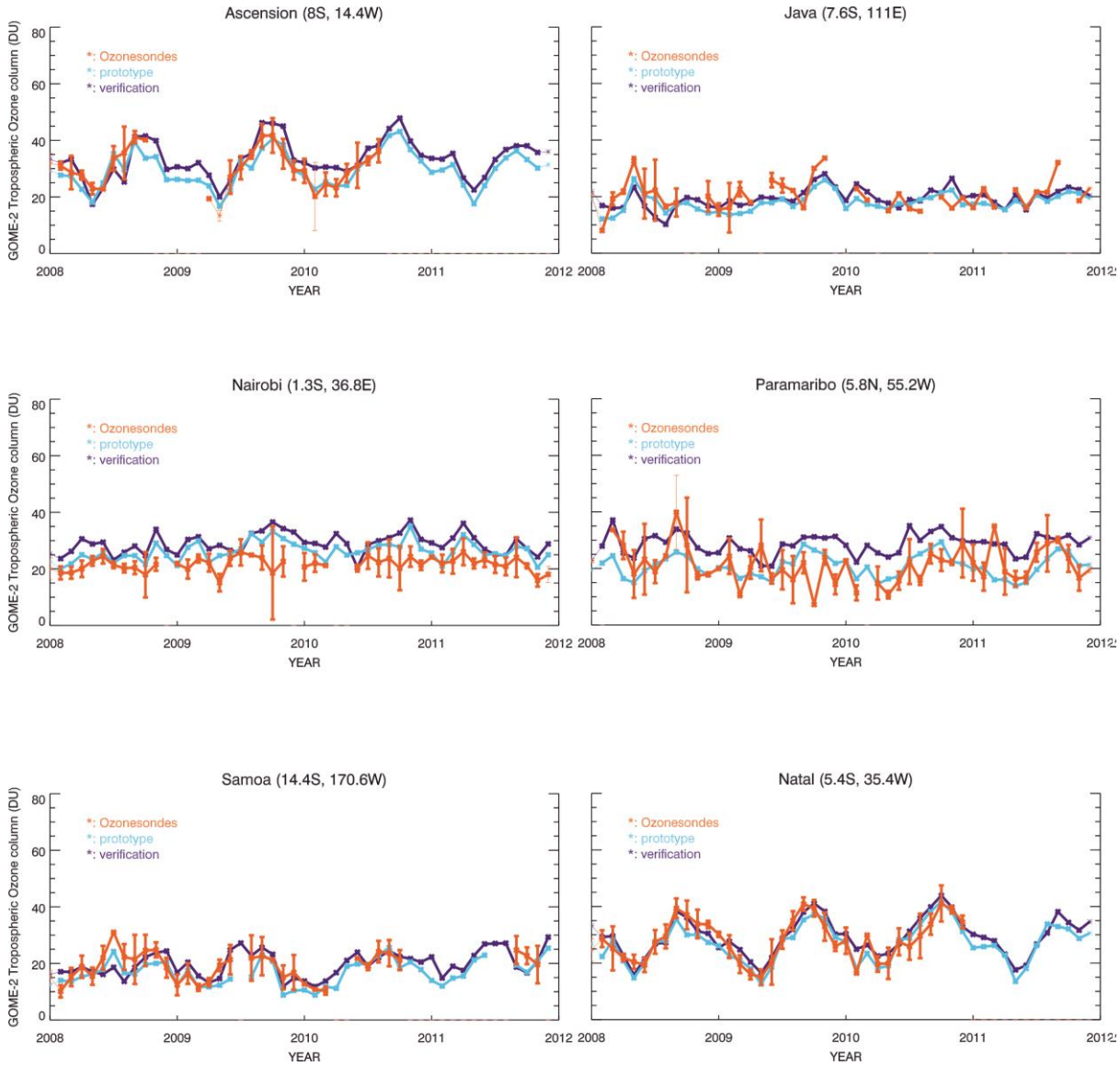

Figure 7.8: Validation of CCD-IUP tropospheric ozone columns with six ozonesonde stations from the SHADOZ Network. Red lines are tropospheric ozone from sondes integrated up to the bottom of the TTL, 200hPa. Blue lines are S5P_TROPOZ_CCD GOME-2 TTCOs and light blue are CCD-IUP GOME-2 TTCOs.

Figure 7.8 shows the comparison for the seven sonde sites for verification and prototype tropospheric O_3 columns. On average there were 3-5 sonde launches per month, except from Java where there is only one in most cases. Both the prototype and verification TTCOs follow the seasonality of tropospheric ozone columns from ozonesondes for most of the stations with the exception of Nairobi, where both algorithms overestimate the ozone. According to Table 7.1, the root mean square (RMS) of the verification algorithm is between 4-9DU and the bias is less than 2 DU, with the exception of Nairobi (8 DU), which still is within the RMS values. The prototype has better correlations (R>0.9) for most sites, reaching R=0.99 at Natal, whereas the correlation with ozonesondes for the verification algorithm is better than the prototype at Ascension (R=0.99). The two algorithms show the worst correlation in Paramaribo (R=0.9), which is the station with the generally lowest correlation for the CCD-IUP verification algorithm (R=0.66).

Table 7.1: Statistical comparison between GOME 2 and ozonesondes SHADOZ sites. Information presented here: the ozonesonde site, the mean TTCO for GOME/SCIAMACHY and for ozonesondes, the bias and the RMS difference between CCD-IUP TTCO and sondes and finally the correlation coefficient. The values are in DU.

Sonde site (2008-2012)	*TTCO Verification (DU)*	*TTCO Prototype (DU)*	*TTCO Sondes (DU)*	*Relative Difference (DU)*	*RMS Verif. Vs prot. (DU)*	*R verification vs sondes*	*R Prototype vs sondes*	*R Verif. vs prot.*
Ascension	33.7	29.8	30.8	2.9	5.0	0.99	0.99	0.98
Java	19.6	18.1	20.6	-1.1	4.8	0.89	0.92	0.96
Samoa	18.4	16.2	18.7	-0.3	4.1	0.93	0.96	0.96
Paramaribo	28.7	20.7	21.3	7.3	9.5	0.66	0.59	0.90
Natal	29.6	27.0	28.2	1.4	3.8	0.97	0.98	0.99
Nairobi	28.9	26.1	21.5	7.4	8.1	0.91	0.92	0.97

The CCD-IUP results have been compared with the S5P verification nadir ozone profile data until 200hPa for the full year of 2012 (see Figure 7.9). The comparison shows that the ozone profile data agree better with ozonesondes whereas the differences are not more than 7 DU in most of the cases.

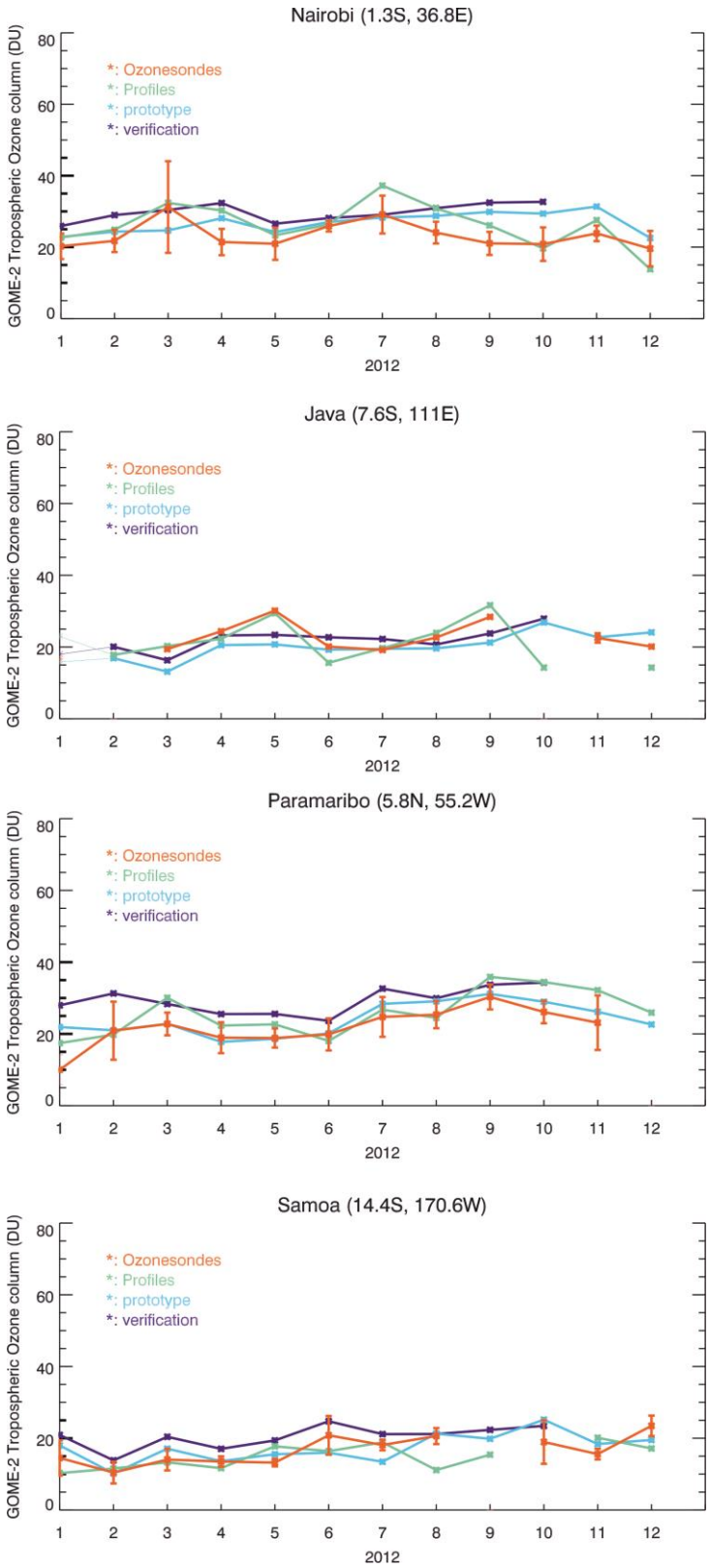

Figure 7.9: TTCO for January to December 2012 calculated with prototype S5P_TROPOZ_CCD algorithm (Light blue), verification CCD-IUP algorithm (Blue), ozone profile data until 200 hPa (Green) and ozonesonde data until 200 hPa (Orange).

7.5.2 Presentation and discussion of Results

Monthly averaged tropospheric ozone columns have been calculated using the CCD method for the tropical region for May 2013. Figure 7.10 presents the comparison of the TTCO between prototype and verification algorithms using GDP 4.7. Both algorithms exhibit the same patterns with absolute differences less than 5 DU.

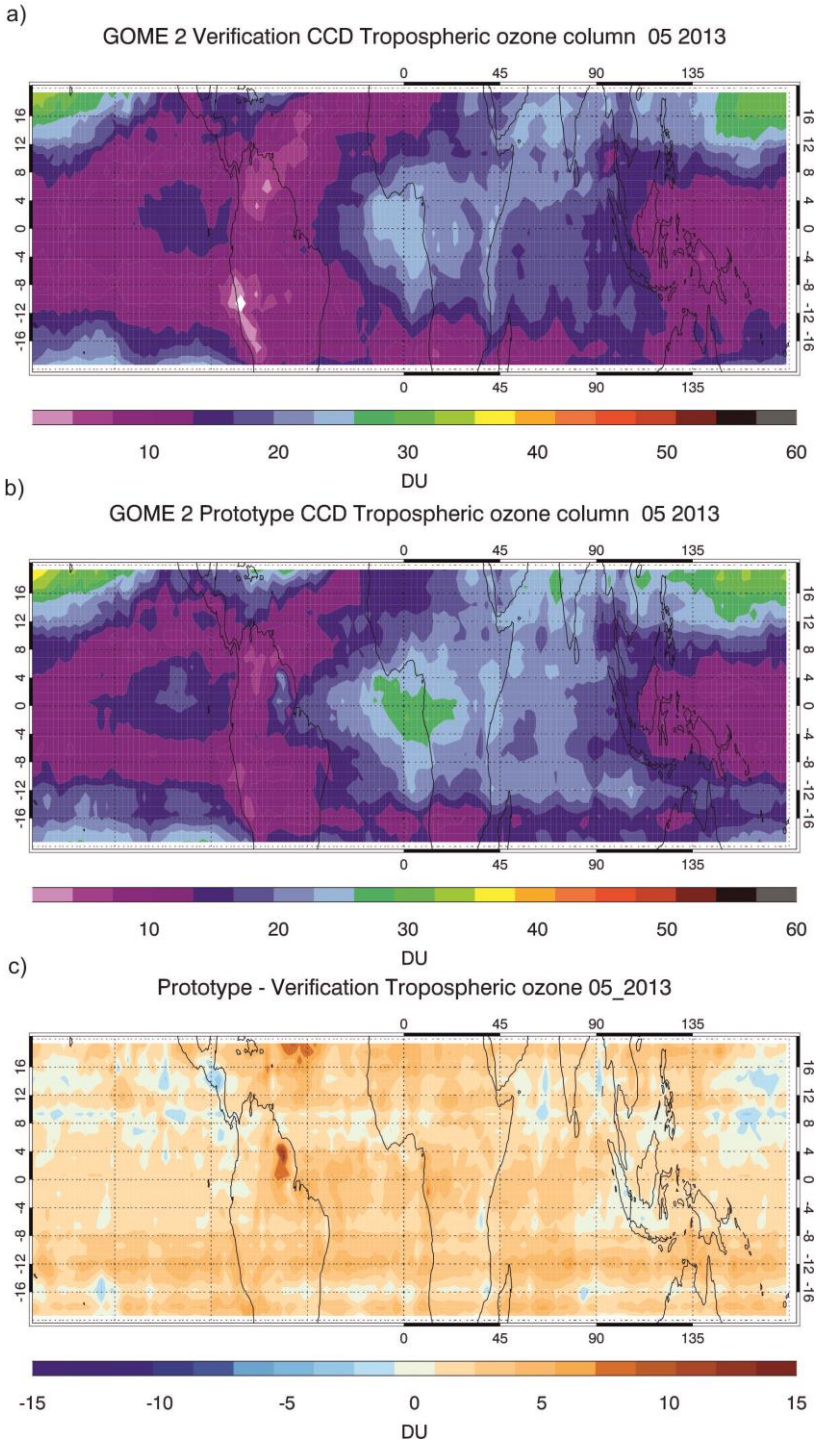

Figure 7.10: Tropical tropospheric ozone column (TTCO) derived with the convective cloud differential technique for May 2013 with (a) CCD-IUP (GOME-2 GDP 4.7), (b) S5P_TROPOZ_CCD (GOME-2 GDP 4.7), and (c) the absolute differences between the two algorithms.

7.6 Summary of verification results

- Tropospheric ozone columns derived with the CCD-IUP verification algorithm have been compared with the S5P_TROPOZ_CCD prototype algorithm. The agreement between them is very good ($0.9 < R < 0.99$, RMS between 4 and 9 DU and the biases less than 2 DU in most of the cases).
- The comparison with ozone sondes showed that the prototype correlates slightly better to them, whereas the comparison with the ozone profile data gave moderate agreement of both algorithms with it.

7.7 References

Fueglistaler, S., A. E. Dessler, T. J. Dunkerton, I. Folkins, Q. Fu, and P. W. Mote (2009) Tropical tropopause layer, Rev. Geophys., 47, RG1004, doi:10.1029/2008RG000267.

Gettelman, A. and P. Forster (2002) Definition and climatology of the tropical tropopause layer, J. Met. Soc. Japan, 80, 911-924.

Hong, G., P. Yang, B-C. Gao, B. A. Baum, and Co authors (2007) High cloud properties from three years of MODIS Terra and Aqua collection-4 data over the tropics. J. Appl. Meteor. Climatol., 46,1840–1856

Loyola, Diego and Thomas, Werner and Yakov, Livschitz and Ruppert, Thomas and Peter, Albert and Hollmann, Rainer (2007) Cloud Properties Derived From GOME/ERS-2 Backscatter Data for Trace Gas Retrieval. IEEE Transactions on Geoscience and Remote Sensing, 45 (9), pp. 2747-2758. DOI: 10.1109/TGRS.2007.901043.

Rex, M., Wohltmann, I., Ridder, T., Lehmann, R., Rosenlof, K., Wennberg, P., Weisenstein, D., Notholt, J., Krüger, K., Mohr, V., and Tegtmeier, S.: A tropical West Pacific OH minimum and implications for stratospheric composition, Atmos. Chem. Phys., 14, 4827-4841, doi:10.5194/acp-14-4827-2014, 2014.

Sassen, K., Z. Wang, and D. Liu (2009) Cirrus clouds and deep convection in the tropics: Insights from CALIPSO and CloudSat, J. Geophys. Res., 114, D00H06

Sherwood, Steven C., Andrew E. Dessler (2001) A Model for Transport across the Tropical Tropopause. J. Atmos. Sci., 58, 765–779.

Thompson, A.M., et al. (2003), Southern Hemisphere Additional Ozonesondes (SHADOZ) 1998-2000 tropical ozone climatology 2. Tropospheric variability and the zonal wave-one, J. Geophys. Res., 108, 8241, doi:10.1029/2002JD002241.

Valks, P., Koelemeijer, R., Van Weele, M., and Coauthors: Variability in tropical tropospheric ozone: Analysis with Global Ozone Monitoring Experiment observations and a global model. Journal of Geophysical Research 108, 2003

Valks,P, D. Loyola, N. Hao, P. Hedelt, S. Slijkhuis, M. Grossi, Algorithm Theoretical Basis Document for GOME-2 Total Column Products of Ozone, Tropospheric Ozone, NO2, tropospheric NO2, BrO, SO2, H2O, HCHO, OClO, and Cloud Properties (GDP 4.5 for O3M-SAF OTO and NTO), DLR/GOME- 2/ATBD/01, Iss./Rev. 2/H, 2013.

Valks, P., Hao, N., Gimeno Garcia, S., Loyola, D., Dameris, M., Jöckel, P., and Delcloo, A.: Tropical tropospheric ozone column retrieval for GOME-2, Atmos. Meas. Tech. Discuss., 7, 727-768, doi:10.5194/amtd-7-727-2014, 2014.

Ziemke J. R., Chandra S., and Bhartia P. K.(1998) Two new methods for deriving tropospheric column ozone from TOMS measurements: The assimilated UARS MLS/HALOE and convective-cloud differential techniques", J. Geophys. Res., 103, 22,115-22,127

Ziemke J. R., and S. Chandra (1999), Seasonal and interannual variabilities in tropical tropospheric ozone, J. Geophys. Res., 104(D17), 21425–21442.

Ziemke J. R., Joiner J., Chandra S., Bhartia P. K. et al. (2009) Ozone mixing ratios inside tropical deep convective clouds from OMI satellite measurements, Atmos. Chem. Phys., 9, 573-583.

Ziemke, J. R., Chandra, S., Oman, L. D., and Bhartia, P. K. (2010) A new ENSO index derived from satellite measurements of column ozone, Atmos. Chem. Phys. Discuss., 10, 2859-2887, doi:10.5194/acpd-10-2859-2010.

8 Verification set-up for NO2, SO2, and HCHO spectral analysis

Authors: Andreas Hilboll and Andreas Richter (IUP-UB)

8.1 Document changes

Changes in issue 2.0:

- none

8.2 Introduction

As all three products NO_2, SO_2, and HCHO use DOAS-based algorithms, it was decided to use a common set of scenarios and synthetic data for the verification. The overall set-up of the tests and the input used are described in this section while the results are reported in the respective product chapters (sections 9.3.4.1 and 11.5).

All radiative transfer simulations are performed using the radiative transfer model (RTM) SCIATRAN, version 3.2.5 [Rozanov et al. 2014]. Both TOA radiance spectra and slant column densities have been simulated to yield input data and reference results for the operational and verification algorithms, respectively.

Due to the large similarities between the OMI and TROPOMI instruments, true satellite measurements from OMI are used for verification additionally to simulated spectra. In order to test the retrieval algorithms in a wide array of possible conditions, one day of each month from one year is used as test dataset. Here, the year 2005 is chosen as at that time, the OMI measurements were not contaminated by the “row anomaly” yet.

8.2.1 Spectral specification of the simulation

8.2.1.1 Wavelength range

In order to verify all DOAS-type retrievals, the wavelength range from 310nm–498.54nm is covered by the simulations.

8.2.1.2 Spectral resolution

The spectral sampling of the S-5P instrument in the UVIS channels (channels 3+4) will be 0.22nm, the spectral resolution FWHM will be 0.54nm [van Geffen et al. 2013][1] .

8.3 Description of input data

8.3.1 Solar irradiance spectrum

The solar irradiance spectrum has been taken from Chance and Kurucz [2010][2] ; it has been convolved with a Gaussian of FWHM 0.54nm to match the spectral resolution of the S-5P instrument.

[1] While the different available S-5P documents contain contradicting information, the Lv2 NO2 ATBD apparently has the correct information (Maarten Sneep, pers. comm.)

[2] The spectrum was downloaded on 09 Dec 2013 from http://www.cfa.harvard.edu/atmosphere/links/sao2010.solref.converted.

8.3.2 Absorption cross-sections

The absorption cross-sections listed in Table 8.1 have been included in the radiative transfer simulations. Where necessary, an air-to-vacuum conversion of the wavelength axis has been performed, as indicated by the column Air_to_Vac. Those cross-sections measured at high spectral resolution have been convolved with a Gaussian of FWHM 0.54nm and interpolated to the S-5P wavelength grid using Akima interpolation [Akima 1970]; those cross-sections measured at a spectral resolution similar to the spectral sampling of S-5P have only been interpolated to the S-5P wavelength grid. Absorption at those spectral points of the S-5P wavelength grid which are not covered by the original cross-sections has been set to 0.0.

Table 8.1: Absorption cross-sections used in the simulations.

Absorber	Reference	Temperatures (K)	Air_to_Vac	Convol.
O_3	Serdyuchenko et al 2011, Gorshelev et al. 2013, Serdyuchenko et al. 2013	193, 203, 213, 223, 233, 243, 253, 263, 273, 283, 293	raw[3]	+
NO_2	Vandaele et al. 1998	220, 294	pre[4]	+
BrO	Fleischmann et al. 2000	203, 223, 243, 273, 298	raw	+
SO_2	Bogumil et al. 2003	203, 223, 243, 274, 293	raw	+
HCHO	Meller and Moortgat 2000	223, 293	pre	+
O_4	Greenblatt et al. 1990	296	pre	-
H_2O_{vap}	Rothman et al. 2009	273	pre	+

8.3.2.1 Pre-processing of the SO_2 absorption cross-section

The SO_2 cross-section has been derived from the measurements by Bogumil et al. [2003], which are used as baseline, and the measurements by Hermans et al. [2009]. The Bogumil et al. cross-sections have been measured with the SCIAMACHY instrument. Before using them in our simulations, it is therefore necessary to de-convolve them with the SCIAMACHY instrument's slit function and then to convolve them with the TROPOMI slit function. The cross-sections cover the wavelength range form 238.9581–395.0267nm, falling into SCIAMACHY channels 1–3. Therefore, they are subject to different spectral resolutions, depending on the wavelength in question. According to Bogumil et al. [2003], the spectral resolution is 0.22nm FWHM below 312.5nm and 0.21nm FWHM above 312.5nm.

There are however further complications involving the SO_2 cross-sections by Bogumil et al. Firstly, apparently the cross-section measured at a temperature of 273K shows unwanted artifacts; when compared to the other temperatures, it seems to consistently over-estimate the actual absorption cross-section [J. van Gent, pers. comm.]. To correct this, the Bogumil et al. cross-section measured at 273K is discarded and a new cross-section for 273K is computed by linear interpolation between 243K and 293K. An example is shown in Figure 8.1.

[3] Original data files contain the wavelength in vacuum.

[4] The cross-section has been pre-processed within IUP-UB to convert to wavelength in vacuum.

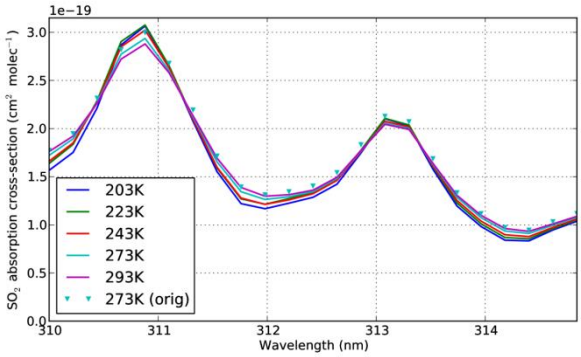

Figure 8.1: Temperature interpolation for the SO_2 absorption cross-section by Bogumil et al. [2003]. The value for 273K has been linearly interpolated from the cross-sections at 243K and 293K. Exemplarily, this plot shows the SO_2 absorption bands between 310–315nm.

Furthermore, the measured SO_2 absorption bands between 360–390nm are very noisy in the Bogumil et al. data. As the retrieval of very large SO_2 columns is not reliably possible with these noisy data [J. van Gent, pers. comm.], the original Bogumil et al. cross-sections are replaced by a linear extrapolation of the cross-sections measured by Hermans et al. [2009]. The resulting absorption cross-sections are shown in Figure 8.2 alongside the original Bogumil et al. and Hermans et al. data. While the resulting cross-sections show jumps at 360nm and at 390nm, this is not considered as a problem because these wavelengths are only used in the SO_2 retrieval at extremely high absorber columns, and the respective retrieval covers exactly the 360–390nm range [J. van Gent, pers. comm.].

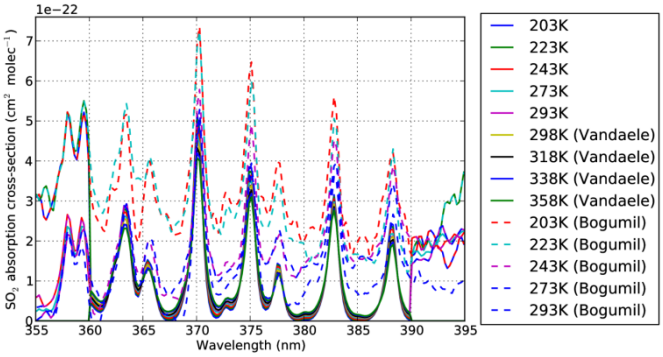

Figure 8.2: Extrapolation of the SO_2 absorption cross-section between 360–390nm using the high-temperature measurements by Hermans et al. [2009].

8.3.2.2 Notes

- The O_4 cross-section has been corrected manually by Jim Burkholder, NOAA, Boulder (wavelength axis) and Andreas Richter, IUP-UB (additional manual corrections to remove sampling artefacts).
- The wavelength resolution of the O_4 cross-section is quite low (0.1nm) so that convolution with the S-5P slit function is not advisable.

8.3.3 Surface reflectance / albedo

In the course of this study, a spectrally constant Lambertian equivalent reflectance model is assumed. As data base, the OMI surface reflectance climatology has been used [Kleipool et al. 2008]. For each atmospheric scenario, the albedo has been calculated by simply averaging all wavelengths for the appropriate geolocation and month.

8.3.4 Absorber profiles / atmospheric scenarios

As a first data set, atmospheric scenarios have been compiled using the vertical profiles from the CAMELOT project, which are available of the S-5P FTP server at ftp://ftppro.knmi.nl/Testdata/Scenarios/. The solar zenith angles have been computed assuming a satellite overpass on the 15th of the month at 13:45 LT. An overview of these scenarios is given in Table 8.2.

Table 8.2: Overview of CAMELOT atmospheric scenarios used in the comparison study.

CAMELOT scenario	Month	Lat (°)	Long (°)	SZA (°)	Albedo
Case0_mozart	06	56	2	30.338	0.056
Case1_European_background	06	45	2	30.338	0.056
Case1_European_background_TM4plusCHIMERE	06	45	2	30.338	0.056
Case2_European_polluted	06	51	7	34.244	0.039
Case2_European_polluted_TM4plusCHIMERE	06	51	7	34.244	0.039
Case3_China_polluted	06	31	116	24.412	0.061
Case4_Pacific_polluted	03	31	140	40.181	0.061
Case4_US_Eastcoast	06	40	-75	27.652	0.066
Case6_Tropical_background	10	-10	-180	29.425	0.081
Case7_Tropical_bmb_land	01	5	20	35.015	0.044
Case8_Tropical_bmb_ocean	01	5	5	35.007	0.064
Case9_Tropical_dust_land	06	20	-10	24.503	0.143
Case10_Tropical_dust_ocean	06	20	-30	24.501	0.070
Case11_Subtropical_background	10	-30	90	35.122	0.066
Case12_Stratospheric_intrusion	1	40	-73	65.117	0.055
Case13_Polar_north_sodankyla	6	68	26	47.468	0.038
Case14_Polar_south_marambio	10	-64	-57	59.489	0.198
Case15_Permafrost_siberia	6	67	146	46.651	0.040
Case16_Volcanic_etna	7	38	15	27.379	0.047

The geolocations of these scenarios are presented in Figure 8.3.

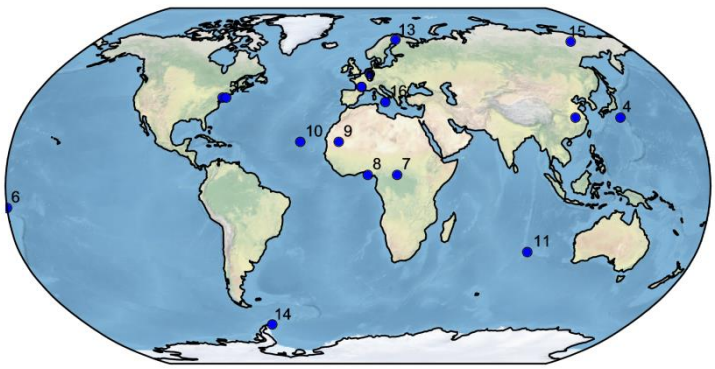

Figure 8.3: World map showing the geolocations of the CAMELOT atmospheric scenarios.

8.3.4.1 Notes

- The longitude for scenario 14 seems to be given incorrectly as 57°E in the original CAMELOT file; for this study, it has been changed to 57°W.
- Scenario case12_Stratospheric_intrusion contains only ozone, water vapor, and BrO.

8.3.4.2 BrO vertical profiles

Table 8.3: Overview of BASCOE BrO climatological scenarios.

BASCOE scenario	Month	Lat (°)	Solar zenith angle (°)
Prof_Tropic	06	0	20
Prof_NorthMLMarch	03	45	50
Prof_NorthMLJuly	07	45	35
Prof_NorthHLMarch	03	67.5	70
Prof_NorthHLJuly	07	67.5	50
Prof_SouthMLSept	09	-45	60
Prof_SouthMLJan	01	-45	35
Prof_SouthHLSept	09	-67.5	75
Prof_SouthHLJan	01	-67.5	55

Table 8.4: Assignment of BASCOE and CAMELOT scenarios.

CAMELOT scenario	BASCOE scenario
Case0_mozart	Prof_NorthMLJuly
Case1_European_background	Prof_NorthMLJuly
Case1_European_background_TM4plusCHIMERE	Prof_NorthMLJuly
Case2_European_polluted	Prof_NorthMLJuly
Case2_European_polluted_TM4plusCHIMERE	Prof_NorthMLJuly
Case3_China_polluted	Prof_NorthMLJuly
Case4_Pacific_polluted	Prof_NorthMLMarch
Case4_US_Eastcoast	Prof_NorthMLJuly
Case6_Tropical_background	Prof_Tropic
Case7_Tropical_bmb_land	Prof_Tropic
Case8_Tropical_bmb_ocean	Prof_Tropic
Case9_Tropical_dust_land	Prof_Tropic
Case10_Tropical_dust_ocean	Prof_Tropic
Case11_Subtropical_background	Prof_SouthMLSept
Case12_Stratospheric_intrusion	Prof_NorthMLMarch
Case13_Polar_north_sodankyla	Prof_NorthHLJuly
Case14_Polar_south_marambio	Prof_SouthHLSept
Case15_Permafrost_siberia	Prof_NorthHLJuly
Case16_Volcanic_etna	Prof_NorthMLJuly

As the CAMELOT scenarios do not contain information about BrO, climatological vertical profiles derived from the BASCOE CTM are used (Theys et al. [2009], Nicolas Theys, pers. comm.). The available scenarios are described in Table 8.3.

As the available months and latitudes do not exactly match the CAMELOT scenarios, the BASCOE scenarios are matched to the CAMELOT scenarios according to Table 8.4.

8.3.4.3 SO_2 vertical profiles

In order to perform realistic tests of the SO_2 retrieval for volcanic eruptions, the CAMELOT scenarios do not contain sufficiently high SO_2 concentrations. Therefore, as a first workaround, the scenario case16_Volcanic_etna has been scaled uniformly with factors 10, 50, 100, 300, 500, and 1000. The corresponding simulations are then called case16x*n*_Volcanic_etna, where *n* stands for the scaling factor.

As the evaluation of the modified volcanic CAMELOT scenarios showed significant discrepancies to the expected “real” VCDs for both the prototype and verification algorithm, for the current verification report (1.0.0) additional synthetic SO_2 box-profile scenarios were provided in order to optimize the algorithms.

The synthetic SO_2 box-profiles are based upon the original volcanic CAMELOT16 scenario with respect to the measurement geometries and general atmospheric components. However, instead of the original SO_2 profile, homogeneous SO_2 layers of 1km thickness at altitudes of 1-2km, 5-6km and 10-11km were included for the calculation of the synthetic spectra. The SO_2 VCD was varied from $1\cdot10^{16}$ molec/cm² to $1\cdot10^{17}$ molec/cm² (in steps of $1\cdot10^{16}$ molec/cm²), $1\cdot10^{17}$ molec/cm² to $1\cdot10^{18}$ molec/cm² (in steps of $1\cdot10^{17}$ molec/cm²) and $1\cdot10^{18}$ molec/cm² to $1\cdot10^{19}$ molec/cm² (in steps of $1\cdot10^{18}$ molec/cm²). For each given SO_2 VCD, 200 spectra with Gaussian noise at a SNR of 1000 were provided.

8.4 Setup of the radiative transfer simulations

All radiative transfer simulations are performed with the RTM SCIATRAN, vers. 3.2.5 [Rozanov et al. 2014].

8.4.1 Vertical grid

The radiative transfer calculations cover an altitude range from the surface to 100km. The vertical spacing of the altitude grid is described in Table 8.5.

Table 8.5: Vertical grid of the radiative transfer simulations.

Altitude (km)	Vertical spacing (km)
0.0–10.0	0.1
10.0–62.0	1.0
62.0–100.0	2.0

8.4.2 Viewing geometry

The TROPOMI instrument will have a swath angle of 108° [Kleipool 2013, p. 19]. The Sentinel-5 Precursor satellite platform will fly at an altitude of 817km [Kleipool 2013, p. 19].

The SCIATRAN RTM requires the measurement geometry to be defined in the platform reference frame. To cover the full swath width in the present study, 28 viewing directions have been defined for each atmospheric scenario. The viewing zenith angle (defined at the satellite) has been varied from -54° to +54° in steps of 4°. The solar zenith angle (also defined at the satellite) has been kept constant, approximately representative of the location and time of the atmospheric scenario.

To derive approximate relative azimuth angles, the sample geometries from the test data file trl01b.v0.5.12.refdata.short_orbit.tgz (specifically, the therein contained file l1b_ra_bd3.nc) have been used. In a first step, the viewing azimuth angle and solar azimuth angle have been averaged along the scan line direction. Then both viewing and solar azimuth angles have been interpolated from these two arrays, assuming they both represent 316 evenly spaced line-of-sight angles between -54° and +54°. Here, the relative azimuth angle is defined as the difference between the viewing azimuth and the solar azimuth angles. A value of 0° means the instrument is pointed into the solar direction, and the value of 180° means anti-solar direction.

The two approximations used in this approach, namely that

- the solar zenith angle does not vary with the line-of-sight angle for one atmospheric scenario
- the solar azimuth angle at the surface equals that at the platform

are assumed to not negatively influence the representativeness of the performed simulations.

8.4.3 Rotational Raman Scattering

Rotational Raman scattering is included in the RT calculations using wavelength bins of 0.01nm [Rozanov and Vountas 2014]. Thus, the "Ring effect" is accounted for in the RTM.

8.4.4 Synthetic noise

To simulate real, i.e., noisy, measurements, normally distributed uncorrelated noise with a signal-to-noise ratio of 1000 (which is the upper limit of the range 800–1000 given by van Geffen et al. [2013] in their Table 2) has been added to the measurements. To this end, the standard deviation of the normal distribution has been calculated for each wavelength individually, as $\sigma(\lambda) = \frac{I(\lambda)}{SNR}$ where $I(\lambda)$ is the simulated intensity at wavelength λ. Random numbers are generated with a Mersenne Twister as implemented by NumPy [Oliphant 2006]. To ensure reproducibility of the results, the random number generator is seeded with the name of the spectrum's CAMELOT scenario plus the sequential number of the noise realization.

8.5 References

Akima, H.: A new method of interpolation and smooth curve fitting based on local procedures, Journal of the ACM, 17(4), 589-602, 1970.

Bogumil, K., Orphal, J., Homann, T., Voigt, S., Spietz, P., Fleischmann, O., Vogel, A., Hartmann, M., Kromminga, H., Bovensmann, H., Frerick, J., and Burrows, J. P.: Measurements of molecular absorption spectra with the SCIAMACHY pre-flight model: instrument characterization and reference data for atmospheric remote-sensing in the 230–2380 nm region, Journal of Photochemistry and Photobiology A: Chemistry, 157, 167–184, 2003.

Chance, K. and Kurucz, R.: An improved high-resolution solar reference spectrum for earth's atmosphere measurements in the ultraviolet, visible, and near infrared, Journal of Quantitative Spectroscopy and Radiative Transfer, 111, 1289–1295, 2010.

Fleischmann, O. C., Hartmann, M., Orphal, J., and Burrows, J. P.: UV absorption cross-sections of BrO for stratospheric temperatures (203-293K) recorded by a Time-resolved Rapid Scan FTS method, Tech. rep., Institute of Remote Sensing, University of Bremen, Bremen, URL http://www.iup.physik.uni-bremen.de/gruppen/molspec/bro2_page.html, 2000.

Gorshelev, V., Serdyuchenko, A., Weber, M., Chehade, W., and Burrows, J. P.: High spectral resolution ozone absorption cross-sections – Part 1: Measurements, data analysis and comparison with previous measurements around 293 K, Atmospheric Measurement Techniques Discussions, 6, 6567–6611, 2013.

Greenblatt, G. D., Orlando, J. J., Burkholder, J. B., and Ravishankara, A. R.: Absorption measurements of oxygen between 330 and 1140 nm, Journal of Geophysical Research, 95, 18 577–18 582, 1990.

Hermans, C., Vandaele, A. C., and Fally, S.: Fourier transform measurements of SO2 absorption cross-sections:: I. Temperature dependence in the 24 000–29 000 cm-1 (345–420 nm) region, Journal of Quantitative Spectroscopy and Radiative Transfer, 110, 756–765, 2009.

Kleipool, Q.: Algorithm theoretical basis document for the TROPOMI L01b data processor, Tech. Rep. S5P-KNMI-L01B-0009-SD, Issue 2.0.0, KNMI, De Bilt, Netherlands, URL http://dev.knmi.nl/dmsf_files/84, 2013.

Kleipool, Q. L., Dobber, M. R., Haan, J. F. d., and Levelt, P. F.: Earth surface reflectance climatology from 3 years of OMI data, 2008.

Meller, R. and Moortgat, G. K.: Temperature dependence of the absorption cross-sections of formaldehyde between 223 and 323 K in the wavelength range 225–375 nm, Journal of Geophysical Research: Atmospheres, 105, 7089–7101, 2000.

Oliphant, T. E.: Guide to NumPy, Trelgol Publishing, USA, URL http://numpy.scipy.org/, 2006.

Rothman, L., Gordon, I., Barbe, A., Benner, D., Bernath, P., Birk, M., Boudon, V., Brown, L., Campargue, A., Champion, J.-P., Chance, K., Coudert, L., Dana, V., Devi, V., Fally, S., Flaud, J.-M., Gamache, R., Goldman, A., Jacquemart, D., Kleiner, I., Lacome, N., Lafferty, W., Mandin, J.-Y., Massie, S., Mikhailenko, S., Miller, C., Moazzen-Ahmadi, N., Naumenko, O., Nikitin, A., Orphal, J., Perevalov, V., Perrin, A., Predoi-Cross, A., Rinsland, C., Rotger, M., Šimečková, M., Smith, M., Sung, K., Tashkun, S., Tennyson, J., Toth, R., Vandaele, A., and Vander Auwera, J.: The HITRAN 2008 molecular spectroscopic database, Journal of Quantitative Spectroscopy and Radiative Transfer, 110, 533–572, 2009.

Rozanov, V. V. and Vountas, M.: Radiative transfer equation accounting for rotational Raman scattering and its solution by the discrete-ordinates method, Journal of Quantitative Spectroscopy and Radiative Transfer, 133, 603–618, 2014.

Rozanov, V. V., Rozanov, A. V., Kokhanovsky, A. A., and Burrows, J. P.: Radiative transfer through terrestrial atmosphere and ocean: Software package SCIATRAN, Journal of Quantitative Spectroscopy and Radiative Transfer, 2014.

Serdyuchenko, A., Gorshelev, V., Weber, M., and Burrows, J. P.: New broadband high-resolution ozone absorption cross-sections, Spectroscopy Europe, 23, 14–17, 2011.

Serdyuchenko, A., Gorshelev, V., Weber, M., Chehade, W., and Burrows, J. P.: High spectral resolution ozone absorption cross-sections – Part 2: Temperature dependence, Atmospheric Measurement Techniques Discussions, 6, 6613–6643, 2013.

Theys, N., Van Roozendael, M., Errera, Q., Hendrick, F., Daerden, F., Chabrillat, S., Dorf, M., Pfeilsticker, K., Rozanov, A., Lotz, W., Burrows, J. P., Lambert, J.-C., Goutail, F., Roscoe, H. K., and De Mazière, M.: A global stratospheric bromine monoxide climatology based on the BASCOE chemical transport model, Atmos. Chem. Phys., 9, 831–848, 2009.

van Geffen, J. H. G. M., Boersma, K. F., Maasakkers, J. D., and Veefkind, J. P.: TROPOMI ATBD of the total and tropospheric NO2 data products, Tech. Rep. S5P-KNMI-L2-0005-RP, Issue 0.5.0, KNMI, De Bilt, Netherlands URL http://dev.knmi.nl/dmsf_files/18, 2013.

Vandaele, A., Hermans, C., Simon, P., Carleer, M., Colin, R., Fally, S., Mérienne, M., Jenouvrier, A., and Coquart, B.: Measurements of the NO2 absorption cross-section from 42 000 cm-1 to 10 000 cm-1 (238–1000 nm) at 220 K and 294 K, Journal of Quantitative Spectroscopy and Radiative Transfer, 59, 171–184, 1998.

9 NO_2 Tropospheric and Total Column

Authors: Andreas Richter, Andreas Hilboll, and Enno Peters (IUP-UB), Steffen Beirle (MPIC), Mathias Begoin (DLR), Alba Lorente Delgado (Wageningen University)

9.1 Document changes

Changes in issue 2.0:

- More consistent overall structure
- Tropospheric NO_2 verification:
  - Verification of AMF added
- Stratospheric NO_2 verification:
  - Final settings for Algorithm based on sensitivity studies
  - Algorithm validation for synthetic input and SCIAMACHY limb measurements
  - Final verification against DOMINO v2.
- Total NO_2 verification:
  - Changed to row dependant slit function/cross-section
  - Updated SCD results
  - Total column comparison

9.2 Verification approach

The retrieval of NO_2 total columns can be separated in different parts – the tropospheric NO_2 columns and the stratospheric NO_2 column. The total column is then the sum of the two. However, the different quantities are interlinked with each other, and errors in the stratospheric column can lead to errors in the tropospheric and total columns. On the other hand, systematic errors in the slant columns often cancel when computing tropospheric columns as they affect both quantities in similar ways.

For the verification, three independent retrievals are used to evaluate the different aspects of the product:

- NO_2 total column (DLR) (see section 9.5)
- NO_2 stratospheric column (MPIC) (see section 9.4)
- NO_2 tropospheric column (IUP-UB) (see section 9.3)

While this involves some overlap, it also provides additional cross-check opportunities of the operational prototype NO_2 product.

The verification of NO_2 slant columns includes two steps:

- First, a limited set of synthetic data based on the CAMELOT scenarios is produced and slant columns are computed by verification and prototyping groups and the results are compared
- Second, the exercise is repeated on a limited set of OMI data from different seasons using the first day of each month in 2005.

The expected result is a quantification of the level of agreement on the slant column level and a better understanding of the factor responsible for remaining differences.

The verification of stratospheric NO_2 columns follows different approaches:

- comparison of stratospheric fields and the resulting tropospheric residues amongst the TROPOMI prototype and verification algorithms: consistency and plausibility checks, quantification of differences
- a “successful” stratospheric correction can partly be judged by the tropospheric residues T: negative average T, or a high standard deviation of T over clean regions indicate algorithm shortcomings.
- comparison to other stratospheric correction algorithms
- comparison to independent datasets: SCIAMACHY limb measurements
- comparison to chemical transport models

The outcome of the stratospheric verification is a quantification of agreement in stratospheric columns (which can directly be converted to uncertainties in tropospheric and total columns) and identification of regions or geophysical conditions leading to problems (systematic biases) of the stratospheric correction in the prototype algorithm.

The verification of the vertical tropospheric and total columns follows a three step approach:

- First, box AMFs are computed and compared for simplified scenarios to establish consistency between the radiative transfer models.
- Second, AMFs are computed for individual OMI orbits and compared between verification and prototyping algorithms.
- Third, individual orbits / days of OMI data are compared end to end.

The outcome of this exercise is a quantification of uncertainties in the AMF part of the prototyping algorithm and a better understanding of the driving parameters.

9.3 Tropospheric column

9.3.1 Algorithm description

9.3.1.1 Slant Column Retrieval

The verification retrieval for NO_2 is based on the Differential Optical Absorption Spectroscopy (DOAS) approach and as such very similar to that of the S5P prototype algorithm. However, the **fitting window** used is larger (425 – 497 nm) and more extended to the visible part of the spectrum. This has three advantages:

- As more spectral points and NO_2 bands are included, the signal to noise ratio of the retrieved NO_2 columns is superior to that obtained in smaller fitting windows. This was demonstrated for GOME-2 data in Richter et al. 2011, and is again apparent in the synthetic S5P data when comparing to results from the fitting window of 425 – 450 nm employed for GOME and SCIAMACHY. The difference to the fitting window selected for the prototype algorithm (405 – 465 nm) is small in synthetic data but appears to be significant in real measurements. An additional benefit of a large fitting window is the better applicability of spike removal algorithms, see section 9.3.1.3.
- As the importance of scattering in the atmosphere decreases with wavelength, the sensitivity to NO_2 in the boundary layer (BL) increases with wavelength, improving the sensitivity to NO_2 in the troposphere. This is shown in Figure 9.1 for part of an orbit of GOME-2 data over China, clearly indicating the enhanced pollution signal in the fitting window extending to longer wavelengths.

- In cases of very large NO_2 pollution, the wavelength dependence of the air mass factor can be detected in the fit, and a simple flag indicating a large BL signal can be provided. This is shown in Figure 9.4 for GOME-2 data, again over China. More details on this approach are given in section 9.3.1.2.

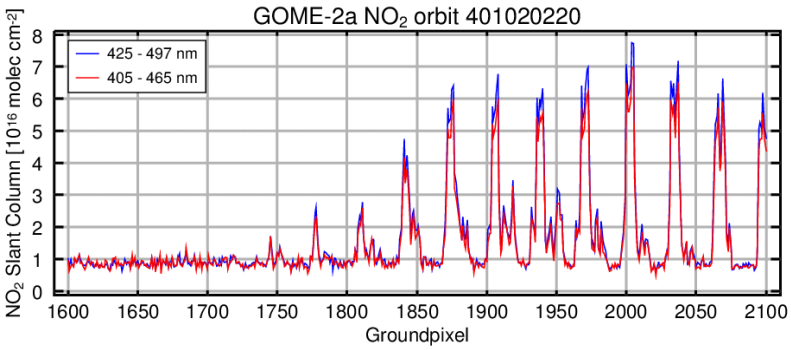

Figure 9.1: Example of NO_2 slant columns from different fitting windows for one orbit of GOME-2 data over China. The larger sensitivity for pollution NO_2 in the window proposed for verification can be seen from the larger NO_2 columns.

Using a larger NO_2 fitting window also has some disadvantages which need to be taken into consideration:

- More spectral points increase the time needed for analysis of a full orbit. As DOAS retrievals are relatively fast, this is not considered to be a serious problem but will have to be kept in mind for a possible operational application.
- Using a larger fitting window increases the requirements on the consistency of spectral and radiometric calibration as well as for the cross-sections used.
- The wavelength dependence of the AMF which contains additional information is at the same time also a challenge if not considered properly, in particular if surface reflectance changes with wavelength as well.
- With the extension of the fitting window to longer wavelengths, surface spectral reflectance effects become more relevant for the DOAS fit, including a spectral feature of bare soils and absorption of liquid water over oceanic regions having clear water. In addition to these two interferences which were already discussed in Richter et al., 2011, there is indication for other surface effects from vegetation and over some desert regions. These effects need to be taken into account for the 425-497 nm window and can potentially impact on the NO_2 column retrieved. In smaller spectral fitting windows, the polynomial used in the DOAS fit can compensate such effects to a large degree.

Table 9.1; Overview over cross-sections used in the NO_2 retrieval

Quantity	**cross-section verification**	**cross-section prototype**
O3 (243K)	Serdyuchenko et al., 2013	Bogumil et al., 2003
NO2 (220K)	Vandaele et al., 1998	Vandaele et al., 1998
NO2_AMF	empirical	--
O4	Greenblatt et al., 1990, adapted	Thalman et al., 2013
H2O	HITRAN 2009	HITRAN 2012
Ring	SCIATRAN	DISAMAR
Ring wavelength	empirical	--

dependence		
Liquid Water	Pope and Frey, 1997, interpolated to TROPOMI resolution	Pope and Frey, 1997, interpolated to TROPOMI resolution
Surface properties	empirical	--
Vibrational Raman, Straylight, Ring deficiencies	intensity offset	

The need for additional correction terms is reflected in the selection of the NO_2 cross-sections used which is listed in Table 9.1. For comparison, the choices made in the prototype are also included.

For the Ring effect (filling in of lines from **Rotational Raman Scattering**), a spectrum simulated by SCIATRAN (Rozanov et al., 2014) is used together with a second spectrum which was scaled by wavelength to account for variations of the Ring effect with wavelength depending on viewing geometry as well as cloud, aerosol, and surface properties. This simple approach could in principle be improved by the eigenvector approach proposed by Vountas et al., 1998, who used the first two eigenvectors of a Principle Component Analysis of a large number of SCIATRAN simulations of the Ring effect. However, in practice the simple approach proved to be equally efficient. An important consideration is the choice of absorbers in the Ring calculations. Here, the Ring spectrum is calculated for an atmosphere without NO_2 in order to exclude the effect of molecular filling in. While this introduces a small error in the calculations, it avoids the uncertainty of scaling of the NO_2 filling in with the Ring effect which is dominated by telluric filling-in. This aspect will have to be investigated in more detail further in the project.

Vibrational Raman Scattering in liquid water also creates discernible spectral features in scattered light spectra over clear water bodies (Vountas et al., 2003). These effects can be simulated by SCIATRAN and considered as a pseudo-absorber in the fit. However, experience shows that including an intensity offset in the retrieval can also partly account for the effect and at the same time help to compensate possible instrumental straylight and inaccuracies in the Ring spectra.

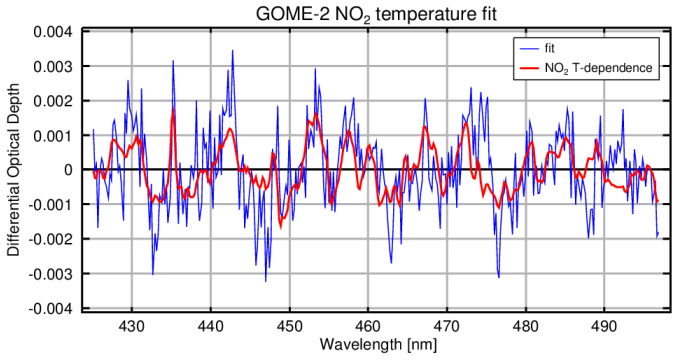

Figure 9.2: Example of spectral detection of the NO_2 temperature dependence in a GOME-2 retrieval over China. The red curve shows the cross-section of the temperature effect, scaled with its fitting coefficient while the blue line includes in addition the RMS from the fit. Even for very large NO_2 columns, the effect is small.

The **temperature dependence** of the NO_2 absorption cross-section is significant in the spectral region used for the fit but is in first approximation a linear scaling factor. The current approach is therefore to use only one NO_2 cross-section in the retrieval and to correct the tropospheric columns for the temperature effect in the air mass factor application (Boersma et al., 2004). At very large NO_2 absorption signals, deviations from the simple scaling approach become apparent and inclusion of an additional cross-section at a higher temperature, orthogonalised to the first cross-section can improve the residuals (see Figure 9.2) However, the effect is considered to be small for most scenarios and the temperature effect cross-section is therefore not included in the verification algorithm.

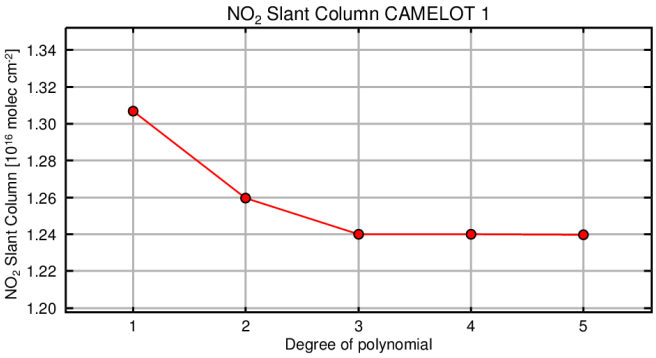

Figure 9.3: Dependence of NO_2 slant column in the 425 – 497 nm window as a function of degree of polynomial (number of coefficients) for the synthetic data computed for the scenario camelot1_European_background_TM4plusCHIMERE

The **choice of polynomial order** is often critical in DOAS retrievals but NO_2 with its many absorption bands is not as sensitive as other target gases. As shown in Figure 9.3, a polynomial degree of 3 is sufficient for the verification fitting window in synthetic data not taking surface effects into account. Experience with real data from the GOME, SCIAMACHY, and OMI instruments shows that interference from surface effects and calibration issues can often be reduced by choosing a larger polynomial order. Therefore, the current baseline is a polynomial degree of 4 (5 coefficients).

Experience with data from previous satellite sensors shows that excellent **spectral calibration** is an important issue for DOAS retrievals, even for relatively strong absorbers such as NO_2. Therefore, the verification algorithm applies two wavelength calibration steps; first a calibration of the solar irradiance measurement used as background spectrum on the Kurucz Fraunhofer atlas (Chance et al., 2010) and then for each earth-shine spectrum on the solar irradiance. In each case, the calibration is performed via a non-linear Levenberg-Marquardt fit allowing for a shift and a stretch of the wavelength axis. The linearized correction as suggested by Beirle et al., 2013 has also been implemented and has been successfully tested on GOME-2 and OMI data. Therefore, the linearized DOAS fit will become the default in the verification processor for reasons of computational speed.

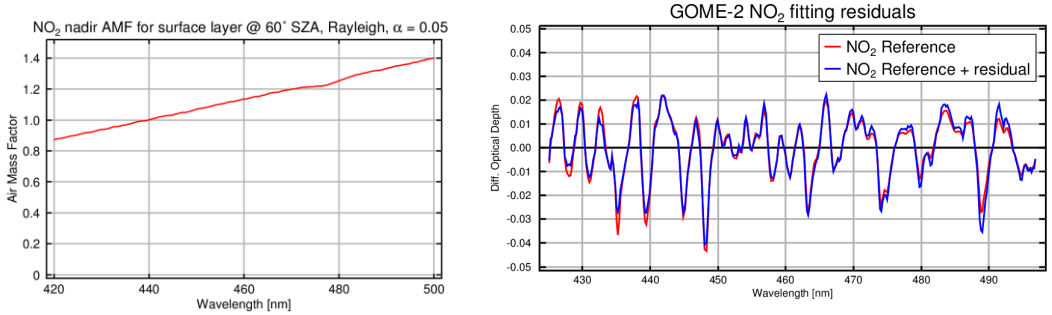

Figure 9.4: Effect of wavelength dependent AMF (left for NO_2 in a 1 km thick layer at the surface) on the retrieval over a very polluted scene (right, NO_2 reference in red, NO_2 fit result in blue)

9.3.1.2 Boundary Layer NO_2 flag

As result of the strong wavelength dependence of Rayleigh scattering, the sensitivity to NO_2 absorption in the boundary layer increases with wavelength. This is illustrated in Figure 9.4 for 60° SZA, nadir view and a wavelength independent surface albedo of 5%. As the fitting window used in the verification algorithm covers nearly 75 nm, this effect can be detected in the residuals of fits over regions with large NO_2 pollution (see Figure 9.5 for an example from GOME-2/MetOp-A data).

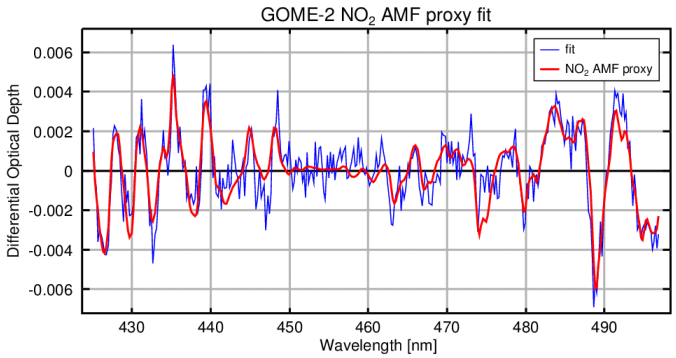

Figure 9.5: Orthogonalised scaled NO_2 cross-section used as NO_2 air mass factor proxy and example for a fit on GOME-2a data during the January 2013 pollution episode in China

In principle, this effect can be used to estimate the vertical distribution of NO_2 by using radiative transfer calculations and an appropriate inversion scheme. The information content of such an inversion is currently being investigated using a range of scenarios covering varying SZA, viewing azimuth angle, vertical NO_2 distribution, NO_2 tropospheric column amounts, surface reflectance and aerosol conditions. Depending on the outcome of this study, a more quantitative treatment including a link to the selection of appropriate AMF could be considered but preliminary results indicate that due to SNR limitations, this will only be possible for situations with very large NO_2 columns.

In the current version of the verification algorithm, a simple and fast flag is being computed by introducing a pseudo absorption cross-section into the fit which is a NO_2 cross-section, linearly scaled by wavelength and orthogonalised to the actual NO_2 cross-section using the Graham Smith method (see Figure 9.5). By inclusion of this pseudo cross-section in the fit, residuals are significantly reduced over strongly polluted scenes. In addition, the ratio of this AMF-proxy fit coefficient divided by the NO_2 slant column is an indicator of the BL contribution to the NO_2 signal as illustrated in Figure 9.6 for the results obtained on the verification data set. This flag should currently be seen as optional information for users, alerting them that a scene is characterised by large NO_2 amounts in the boundary layer.

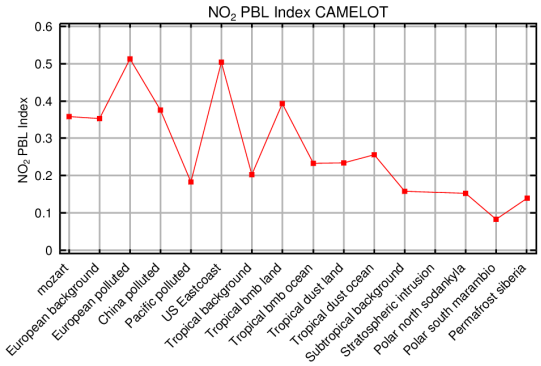

Figure 9.6: Results of the NO_2 BL flag for the S5P synthetic data

9.3.1.3 Post-processing: Spike removal / Destriping / Offset Correction

On synthetic data, no post-processing of slant columns is necessary. However, in real satellite data, a number of problems occur which can be reduced by post-processing. As long as no real S5P observations are available for testing, options to correct for such problems need to be foreseen in the processor.

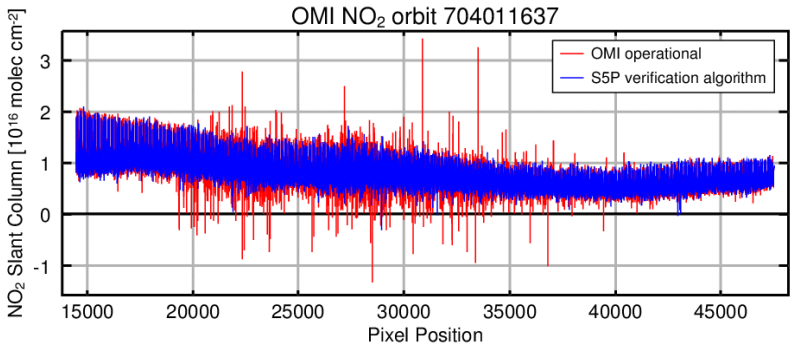

Figure 9.7: Example of the effect of spike correction in an OMI orbit passing through the SAA. For comparison, the operational OMI NO_2 (NASA collection 3) product is also shown. For clarity, the well-known offset in operational OMI NO_2 slant columns has also been applied to the IUP results

Outliers in slant columns retrieved from satellite data can result from **spikes** in the spectra, generated by radiation hitting the detector and electronics of the instrument, in particular in the region of the Southern Atlantic Anomaly (SAA). While some of the spikes can be removed already during lv1 calibration and more are flagged in the data, analysis of fitting residuals can detect and flag smaller spectral spikes, resulting in an iterative fitting procedure and more accurate retrievals. This method is described in Richter et al., 2011 and the effect is illustrated in Figure 9.7 for parts of one orbit of OMI data. As removal of points from the spectrum reduces the information available for the fit, a large fitting window is favourable for spike removal.

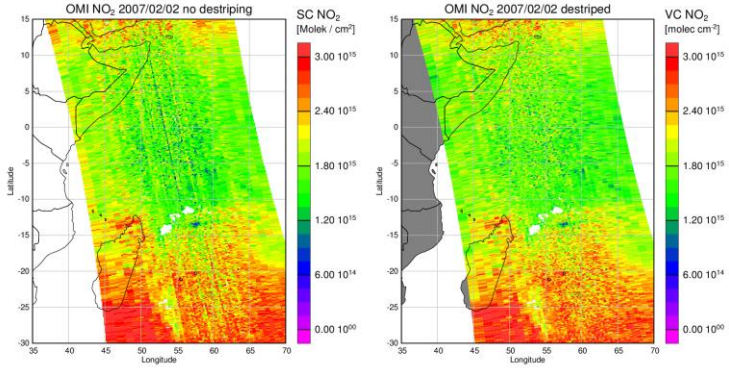

Figure 9.8: Example for the application of destriping in NO_2 fits on OMI data using the S5P verification settings (before destriping: left, after destriping: right).

In DOAS retrievals using measurements from imaging 2d CCD-detectors such as the ones of OMI and S5P, small differences in the properties of the individual CCD-pixels, the dark signal or the irradiance reference spectrum can lead to systematic differences between measurements using different rows which are visible as **stripes** in the retrieved columns. These stripes can be removed by analysing data in regions where no systematic longitudinal variation of the true NO_2 signal is expected and determining row dependent offsets which are then applied for all data. This necessitates correction of differences from radiative transfer (air mass factor) and assumes that there are no systematic changes from photochemistry. An additional problem is that the assumption needs to be made that the average (or median) of all rows gives the correct value which is not necessarily the case. For NO_2, striping is not a very strong effect in OMI data when using the settings of the S5P verification algorithm but application improves consistency. This is illustrated in Figure 9.8. For other species such as HCHO, destriping is essential and a large effect (see section 11).

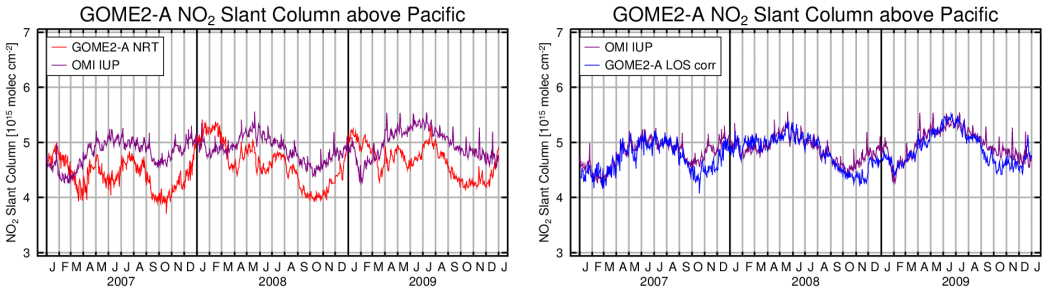

Figure 9.9: Example for the correction of an offset in GOME-2b NO_2 data. The red curve (left figure) is the uncorrected NO_2 slant column, the blue curve (right figure) is the offset corrected curve. The purple curve in both panels is the OMI NO_2 slant column given for comparison.

For the GOME and SCIAMACHY instruments, columns of NO_2 (and other gases) suffer from **offsets** which also vary over time. In cases where no destriping needs to be applied, this offset can be determined for NO_2 by analysing the scan angle dependence of vertical column observations over clean regions, and finding the common offset which produces the smallest scan-angle variation in the vertical columns. An illustration of the results applying this method for GOME-2b data is shown in Figure 9.9.

9.3.1.4 Stratospheric Correction

The stratospheric correction of the verification algorithm is discussed separately in section 9.4. As an alternative to the approach discussed there, stratospheric data from the MACC-III / COPERNICUS system (Flemming et al., 2009) can also be used, which provides operationally several days of forecasts at 0.7° x 0.7° with plans to further improve the spatial resolution. The tropopause can be computed from ECMWF data but is not a critical parameter for NO_2 as the maximum concentrations are at altitudes around 30 km. Based on experience with data from SCIAMACHY, GOME-2, and OMI, an additional offset correction of the model data is needed to improve the consistency with measurements (see Hilboll et al., 2013 for a discussion).

9.3.1.5 Tropospheric Air Mass Factors

After having computed the tropospheric slant column, a tropospheric air mass factor needs to be applied to the retrievals. This depends critically on the a priori information used which is in the following briefly discussed.

9.3.1.5.1 NO2 profiles

Tropospheric NO_2 profiles are taken from the COPERNICUS atmospheric service modelling system. Analysis data is used for normal processing but in principle, forecast data can also be used for NRT processing.

The advantage of the COPERNICUS system is the large amount of atmospheric data assimilated which strongly constrains the fields of some chemical species in the model. It can therefore be expected that the profiles are a good representation of the atmospheric situation. Whether this is the case not only for long-lived molecules such as CO and O_3, but also for short-lived species such as NO_2 which are much less constrained by observations from LEO instruments still needs to be verified. This is a general problem for all global models and probably is one of the largest sources of uncertainty in the tropospheric NO_2 product.

The disadvantage of the COPERNICUS data is the relatively low spatial resolution of 0.7° (expected to improve in the coming year) which is not really appropriate for the S5P spatial resolution. The verification algorithm is therefore written in a way to also accept other model data as input, for example from the regional models also operated in the COPERNICUS system. These could for example provide high spatial resolution a priori data for a European data subset.

Another complication arises as soon as S5P operational data are being assimilated into the COPERNICUS system, as then an impact of the operational S5P NO_2 product on the a priori data used in the verification algorithm can occur. This possibility will have to be investigated once assimilation of S5P data has started.

For scientific use, a more flexible model which can be used for sensitivity runs for example with updated emissions would be preferable but is not available to the verification group at this point.

The interface of the S5P verification processor is flexible with respect to a priori NO_2 profiles, facilitating ingestion of other sources such as regional high resolution models, e.g., from the COPERNICUS atmosphere service.

9.3.1.5.2 Aerosols

In the the verification algorithm, aerosols are not included in the look-up tables for the air mass factors; instead, aerosols are considered in the radiative transfer implicitly via the cloud correction. In future studies, it is foreseen to test the explicit consideration of aerosol information (extinction profile, single scattering profile, simplified phase function) in the look-up table. The a priori information needed for application of these air mass factors could then again come from the COPERNICUS atmospheric service which assimilates aerosol data from all relevant space sensors, or from the climatological data product from the CALIOP measurements. As already discussed for the NO_2 profiles, regional models may instead be used for subsets of data.

9.3.1.5.3 Clouds

The verification algorithm will use the operational S5P cloud product of cloud fraction and cloud top pressure to select for cloud free scenes, using a threshold of 20% geometric cloud fraction. Cloud correction following the independent pixel approximation is implemented in the algorithm as an option. While this option can be switched off if an explicit aerosol correction is used (see the future plans outlined in Section 9.3.1.5.2), it is needed for the implicit aerosol treatment in the current version of the verification algorithm.

9.3.1.5.4 Surface reflectance

As surface reflection data base, the OMLER climatology for the years 2005–2009, which is based on OMI measurements (Kleipool et al., 2008), is used. In the EU funded QA4ECV project, alternatives to this surface reflectance dataset are currently being investigated, and any early results from that will be included in future versions of the verification processor. Of particular interest is the evaluation of BRDF effects (expected to be small with the exception of very large viewing angles) and the applicability of high spatial resolution data sets for the interpolation of high spectral resolution data.

9.3.1.5.5 Digital Elevation Map

The surface altitude for each measurement pixel will be provided by the L1B team as described in Ch. 5 of [RD3]; the current baseline is to use the GMTED2010 dataset (Danielson and Gesch, 2011).

9.3.1.6 Setup of AMF look-up tables

As in the prototype algorithm, the look-up table for the AMF will cover the dimensions solar zenith angle, line-of-sight (i.e., viewing azimuth) angle, relative sun azimuth angle, surface albedo, surface altitude, altitude. Vertical datums (surface altitude, altitude), are given in units of meter. The exact coordinates of the look-up table are given in Table 9.2.

Table 9.2 Nodes in the look-up table for NO_2 air mass factors.

Parameter	# of points	Values
cos(solar zenith angle)	12	0.01, 0.03, 0.05, 0.15, 0.25, 0.3, 0.5, 0.6, 0.7, 0.8, 0.9, 1.0
cos(viewing zenith angle)	6	0.3, 0.5, 0.7, 0.8, 0.9, 1.0
Relative sun azimuth angle	13	0°, 15°, 30°, …, 165°, 180°
Surface albedo	7	0.00, 0.05, 0.10, 0.20, 0.50, 0.80, 1.00
Surface altitude	5	0km, 1km, 2km, 5km, 10km
Altitude	171	0.00km, 0.05km, 0.15km, …, 9.85km, 9.95km, 10.5km, 11.5km, …, 58.5km, 59.5km, 61km, 63km, …, 97km, 99km
Wavelength	1	440nm

9.3.1.6.1 Correction of the temperature-dependence of the NO2 cross-section

The NO_2 absorption cross-section's dependence on temperature is corrected for a-posteriori, i.e., during the application of the tropospheric altitude-resolved air mass factor. This correction uses the approach by Boersma et al., 2004, using temperature scaling factors derived as in Nüß et al., 2006.

9.3.1.6.2 Nonlinearities at very large NO2 columns

One of the basic assumptions in DOAS evaluations is that spectral retrieval of the slant column and the radiative transfer calculations for the air mass factors used to compute vertical columns can be separated. One prerequisite is the assumption of an optically thin atmosphere where the NO_2 absorption is so small, that its effect on the overall radiation field can be neglected. For most situations, this assumption is well justified in the case of NO_2 retrievals between 400 and 500 nm. However, in heavily polluted regions, the NO_2 absorption can reach several percent and the air mass factors become dependent on the assumed amount of NO_2 in the boundary layer. This is illustrated in Figure 9.10 where the relative change in AMF for boundary layer NO_2 is shown as a function of NO_2 amount. Already at columns of a few 10^{16} molec cm^{-2}, the AMF decreases by several percent and starts showing spectral features linked to NO_2 absorption bands. At a NO_2 column of 10^{17} molec cm^{-2}, the effect is already larger than 10%.

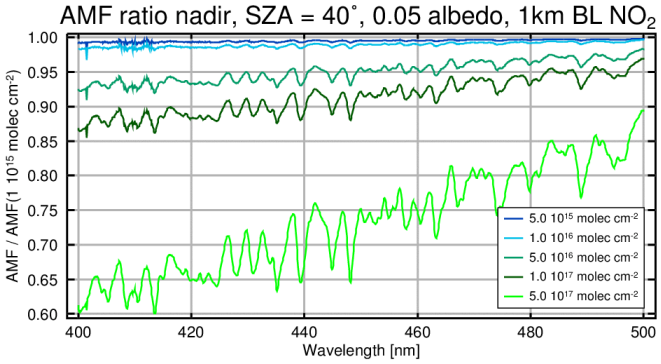

Figure 9.10: Relative change in nadir NO_2 AMF for a 1 km BL layer at different total NO_2 amounts. In the reference scenario, there is a NO_2 column of $1x10^{15}$ molec cm^{-2}.

In the DOAS fit, both the absolute value of the AMF and the fitting interference with the spectral structures in the AMF contribute to the slant column retrieved. The difference between the retrieved SC and the value expected based on simple application of the optically thin AMF to the vertical column is therefore even larger than the change in AMF itself. This is shown in Figure 9.11 where the results for a series of DOAS fits in the two fitting windows used by the verification algorithm and the prototype algorithm are shown relative to the value expected from multiplying the AMF derived for $1x10^{15}$ molec cm^{-2} with the vertical column. In both cases, the NO_2 amounts are underestimated at large NO_2 column to a similar degree. The differences seen at small NO_2 columns are linked to the temperature dependence of the NO_2 cross-section which has a wavelength dependent effect depending on the ratio between cold stratospheric and warm tropospheric NO_2 amounts.

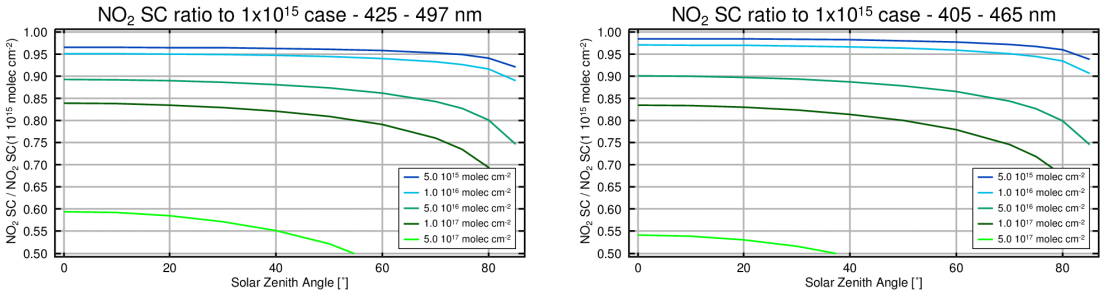

Figure 9.11: Comparison of the overall effect of column dependent AMF for the verification fitting window (left) and the operational fitting window (right). In the optically thin case where the AMF does not depend on NO_2 amount, all values would be on the 1.0 line.

In order to correct for this effect which can be larger than 10% over China during pollution events, the verification algorithm will include a correction term in the final application of the AMFs which will be based on tabulated factors between AMF and NO_2 slant column.

9.3.2 Main differences to prototype algorithm

The differences between the NO_2 prototype and verification algorithms have already been highlighted in the previous sections. In summary, the main differences are

- Use of a wider and shifted fitting window to reduce noise, improve sensitivity to BL absorption, and facilitate computation of a NO_2 BL flag
- Use of NO_2 profiles from the COPERNICUS assimilation system for the air mass factor calculation instead of TM5, either on a climatological or on a daily basis, to have the best possible a priori NO_2 profiles
- Use of the SCIATRAN radiative transfer model for AMF calculations
- Use of a saturation correction for large NO_2 columns
- Use of a cloud-screening approach without further residual-cloud correction

9.3.3 Error analyses

Most of the relevant uncertainties of the verification algorithm as described here are identical to those in the prototype algorithm (see Boersma et al., 2004 and Boersma et al. 2011 for a discussion), and the same estimates apply for the verification algorithm. The main error sources are

- Random noise in the spectra
- Systematic spectral residuals, for example from imperfect radiometric calibration
- Spectroscopic interference in the DOAS retrieval

- Uncertainty on the NO_2 cross-section (see Vandaele et al., 1998)
- Uncertainty on the temperature correction on the NO_2 column
- Imperfect correction of the stratospheric NO_2 column (see section 9.4)
- Uncertainty in the tropospheric AMF and Averaging Kernels from
    - Cloud effects
    - Surface reflectance uncertainty including BRDF effects and shadows
    - A priori NO_2 profile uncertainty including effects of low model resolution
    - Uncertainty in a priori aerosol fields and effects

9.3.4 Verification Results

9.3.4.1 Slant Column Verification using Synthetic Data

The set-up of the synthetic data used for the verification exercise is described in section 8.

In two independent steps, first the fits performed by operational and verification algorithms on simulated spectra without noise are compared to each other and to the slant column densities (SCDs) as simulated by SCIATRAN for the individual fitting windows, the AMF being averaged over all wavelengths. Here, there is one SCD per algorithm per viewing geometry per atmospheric scenario, and these SCDs are directly compared to each other.

Secondly, the fit results of operational and verification algorithms performed on noisy simulated spectra are compared. In this second comparison, the distributions of the SCDs retrieved by one algorithm for the 9 noisy spectra for one viewing geometry / atmospheric scenario pair are compared between operational and verification algorithms.

For the NO_2 data product, the operational algorithm from KNMI (405–465 nm), the verification algorithm from IUP-UB (425–497 nm), and the linear DOAS algorithm from MPIC (430–450 nm) could be compared.

In polluted cases, all algorithms' SCD results are below the simulated slant columns by up to 20%. As an example, the polluted European and biomass burning (land) scenarios are shown in Figure 9.12 and Figure 9.13, respectively.

A significant difference can be observed between the different algorithms, both in the fitted and the simulated SCDs. This can be explained by the wavelength dependency of the air mass factor (see Figure 9.4); as the verification algorithm uses the wavelength range 425–497nm, the air mass factor is larger for polluted scenes, leading to larger slant columns for a given atmospheric pollution scenario. While the final output of the retrieval algorithms, i.e., the vertical column densities, should not depend on the fitting window, the impact of the effective AMF has to be considered in the comparison of slant columns.

A second effect relevant for this comparison is the temperature dependence of the NO_2 absorption cross-section. While this is fully treated in the SCIATRAN run, the retrievals usually assume one fixed temperature for the NO_2 cross-section and rely on a correction of the temperature dependence in the AMF. Thus differences are to be expected and should vanish when comparing vertical columns.

Note that within a NO_2 fit intercomparison on common fit settings within the QA4ECV project, perfect agreement was found. The systematic differences between the different algorithms shown in Figure 9.12) are thus caused by the different settings discussed above, but not on the algorithms themselves; in particular, the linearized DOAS analysis works well for NO_2.

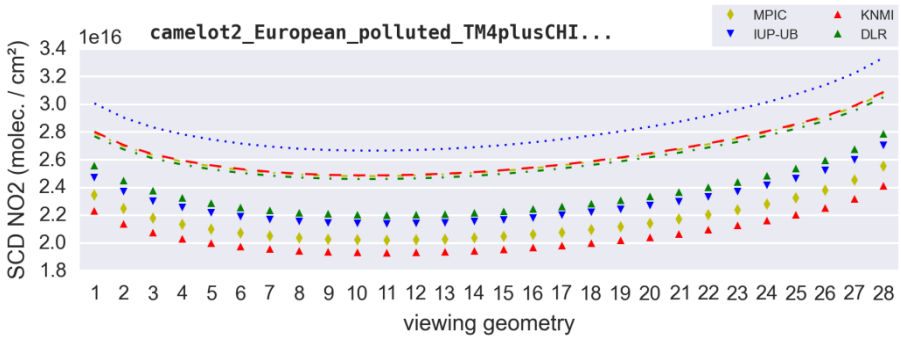

Figure 9.12: NO_2 SCDs fitted by operational (red), verification (blue), and comparison (gold) algorithms, and simulated by SCIATRAN (dotted lines, averaged over the respective algorithm's fitting window), for scenario 2 (Europe polluted / TM4+CHIMERE).

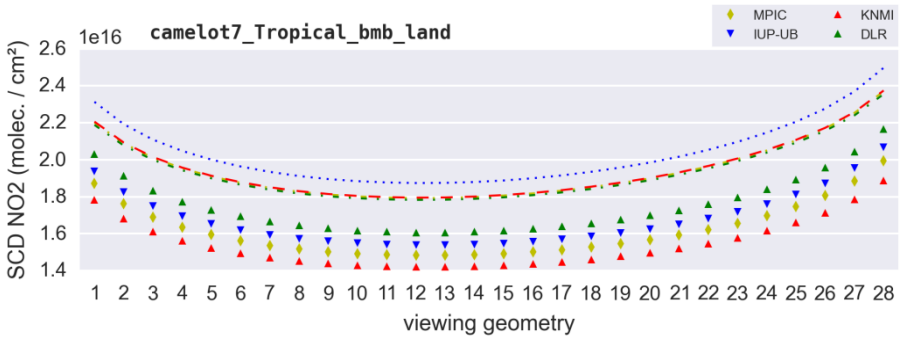

Figure 9.13: NO_2 SCDs fitted by operational (red), verification (blue), and comparison (gold) algorithms, and simulated by SCIATRAN (dotted lines, averaged over the respective algorithm's fitting window), for scenario 7 (biomass burning / land).

In background situations, all three retrieval algorithms' results tend to be slightly below the simulated slant columns. This probably reflects the closer agreement between the various effective AMFs, as the wavelength-dependence of the AMF is negligible in scenes with low tropospheric NO_2. The remaining differences are probably again linked to the temperature dependence of the NO_2 cross-section. Exemplary, Figure 9.14 shows the comparison for the European background scenario.

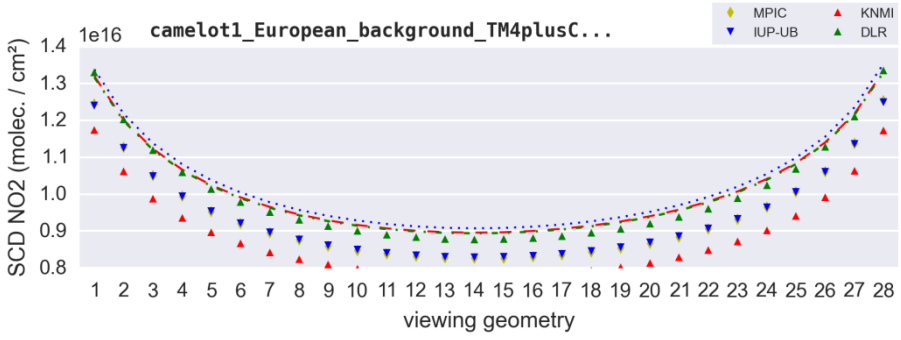

Figure 9.14: NO_2 SCDs fitted by operational (red), verification (blue), and comparison (gold) algorithms, and simulated by SCIATRAN (dotted lines, averaged over the respective algorithm's fitting window), for scenario 1 (European background).

In order to verify that in fact the temperature dependence of the NO2 cross-section is the main reason for the differences between retrieved and simulated slant columns, a dedicated run of SCIATRAN without T-dependence of the NO_2 (i.e., only one NO2 cross-section measured at 220K) was performed and analysed. As can be seen in Figure 9.15 when compared to Figure 9.12, the differences between retrievals and model are reduced but not completely gone in polluted cases. As a comparison of Figure 9.16 with Figure 9.13 shows, these remaining differences are almost completely removed in unpolluted scenarios. This suggests that the differences between fitted and simulated SCDs, as observed in Figure 9.15, result from the wavelength-dependency of the tropospheric air mass factor.

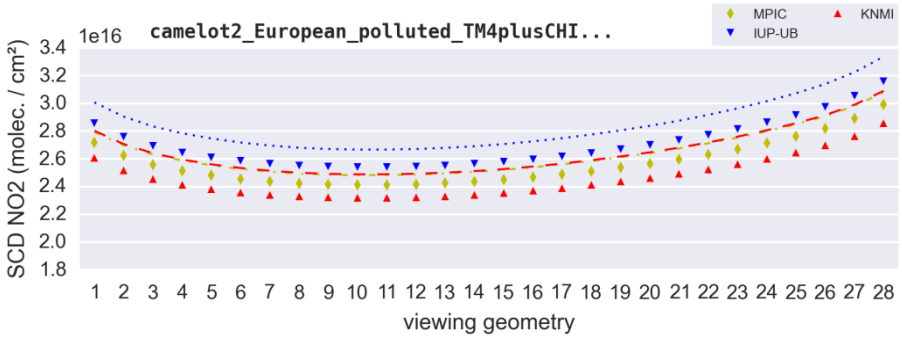

Figure 9.15: NO_2 SCDs fitted by verification (blue), and comparison (gold) algorithms, and simulated by SCIATRAN (dotted lines, averaged over the respective algorithm's fitting window), for scenario 2 (Europe polluted / TM4+CHIMERE). In this test, the temperature dependence of the NO_2 cross-section was switched off in the SCIATRAN calculations

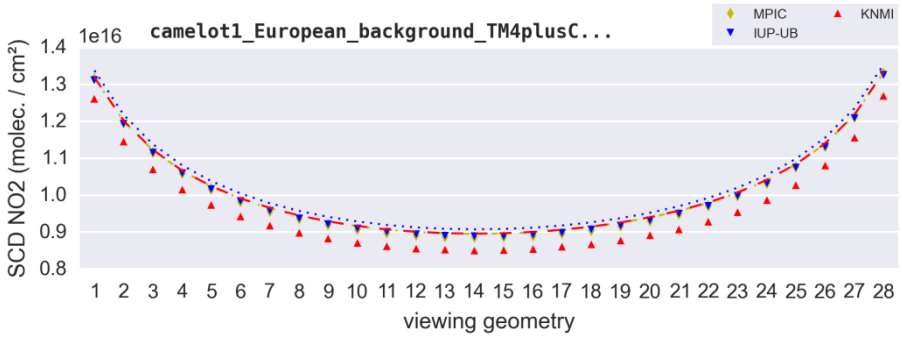

Figure 9.16: NO_2 SCDs fitted by verification (blue), and comparison (gold) algorithms, and simulated by SCIATRAN (dotted lines, averaged over the respective algorithm's fitting window), for scenario 1 (Europe background / TM4+CHIMERE). In this test, the temperature dependence of the NO_2 cross-section was switched off in the SCIATRAN calculations

When investigating the response of the individual algorithms to noisy spectra, the operational algorithm and verification algorithms show very similar results, although with significant variations between individual viewing directions. As an example, Figure 9.17 shows the distributions of the fit results of noisy spectra for all viewing geometries. The variation between viewing directions is the result to the different noise spectra calculated and the relatively small number of noisy spectra used (9).

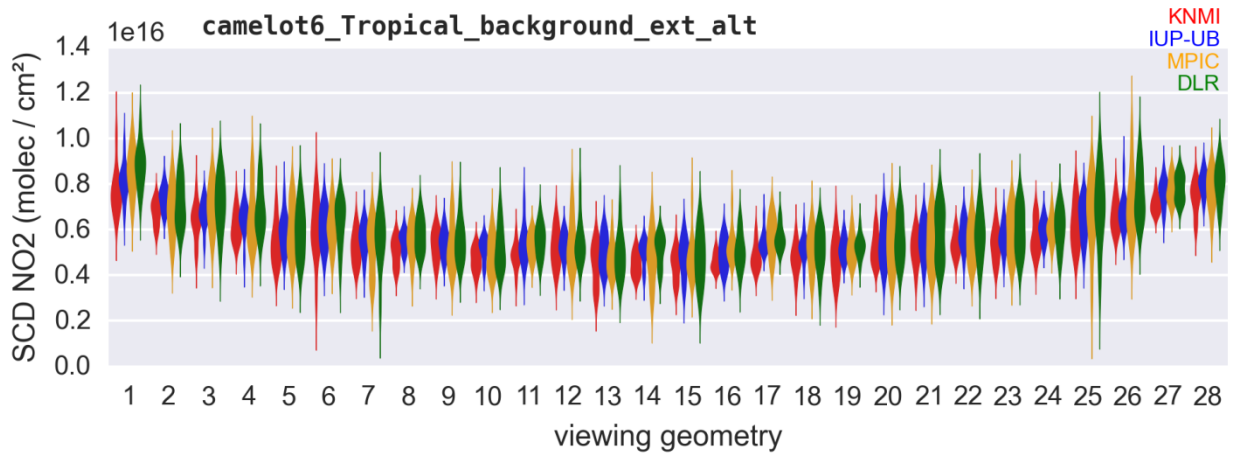

Figure 9.17: Violin plot of the NO_2 SCD fit results of noisy input spectra from operational (red) and verification (blue and yellow) algorithms, for each viewing geometry, for scenario 6 (tropical background). (Vertically, the violin plot is a box plot, while the horizontal extent represents the kernel density, showing the probability density.)

Another way of evaluating the agreement between the algorithms are scatter plots of the retrieved SCDs. The fits not influenced by noise show perfect correlation between the two algorithms, with the already mentioned slightly higher values by the verification algorithm visible in polluted scenarios. The fit results on noisy data show good correlation, but as the fitting windows do not agree, the noise affects the two results in different ways. Two exemplary situations are shown in Figure 9.18.

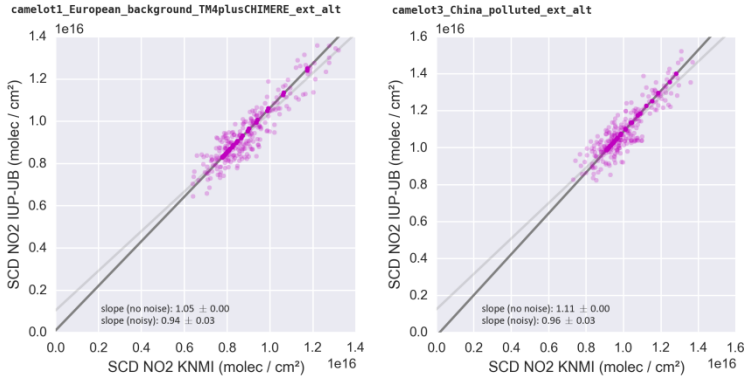

Figure 9.18: Scatter plots of NO_2 SCDs derived from the operational and verification algorithms, for scenarios 1 (European background, left) and 3 (China polluted, right). Those fits not influenced by noise are shown in solid colour, while fits on noisy data are transparent.

9.3.4.2 Slant Column Processing Chain Verification using OMI data

An extensive comparison of the processing chains of the prototype and verification algorithms has been conducted. For this intercomparison exercise, a common set of DOAS fit parameters has been agreed upon according to Table 9.3; the goal of this exercise was to ensure that the software implementation of the prototype algorithm behaves as expected in a large set of realistic measurement scenarios.

Table 9.3: Common DOAS fit settings for NO_2 for the verification of the prototype processing chains using OMI data.

Parameter	Value
Wavelength window	405.0 – 465.0 nm
Fit method	Optical depth
Polynomial degree	4 (i.e., 5 coefficients)
O_3 cross-section	Serdyuchenko et al., 2013, 243K
O_4 cross-section	Thalman et al., 2013, 293K
NO_2 cross-section	Vandaele et al., 1998, 220K
H_2O_{vap}	Rothman et al., 2013 (HITRAN2012)
Ring cross-section	Wagner et al., 2009 (SCIATRAN)
Solar Atlas	Sao2010_solref_vac.dat
Convolution	Per row, i.e., use of 60 slit functions
Background	Mean sun
Intensity offset	None (prototype) / Constant (verification)
Error weighting	Off
Post processing	none
Wavelength calibration	Shift & squeeze on solar spectrum

In general, the correlation between the prototype and verification processors' outputs is excellent. As can be seen in Figure 9.19, the correlation between the two datasets is >0.99 everywhere (yellow and green curves). The regression slope's deviation from 1.00 is always <3.5%. However, a significant, variable offset between the two processors of ~2E14 molec cm^{-2} can be identified.

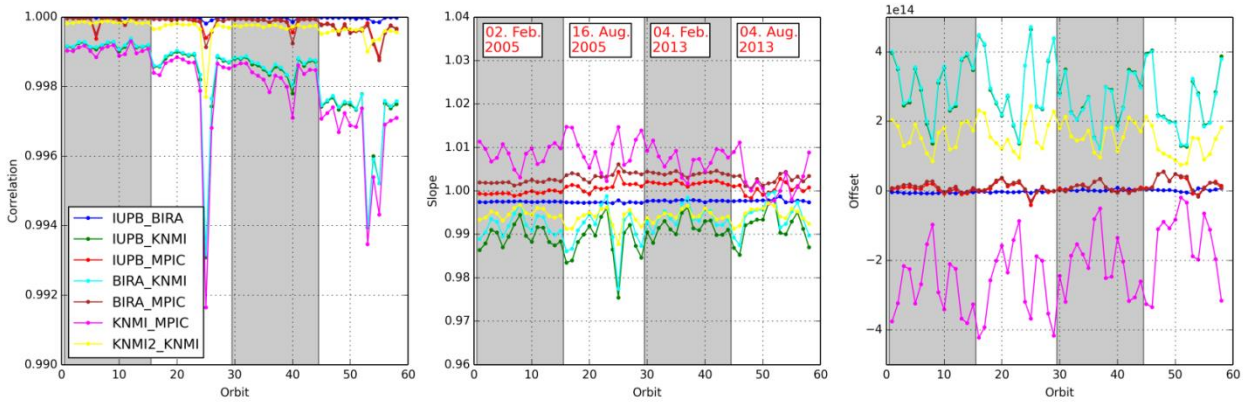

Figure 9.19: Comparison of verification processor and prototype processor with intensity fit method (green) and between prototype with optical depth and with intensity fit methods (yellow), for OMI measurements from 02 Feb 2005, 16 Aug 2005, 04 Feb 2013, and 04 Aug 2013. Pearson correlation coefficient (left), slope of the regression line (centre), and offset of the regression line (right).

During the comparison exercise, it became apparent that significant differences between the processors can be identified in cases of very high intensities where saturation effects of the detector become relevant, i.e., over very bright surfaces/clouds (see Figure 9.20). However, since these pixels will usually not be considered for operational data analysis due to the high cloud cover and the associated uncertainties, this issue is deemed not critical.

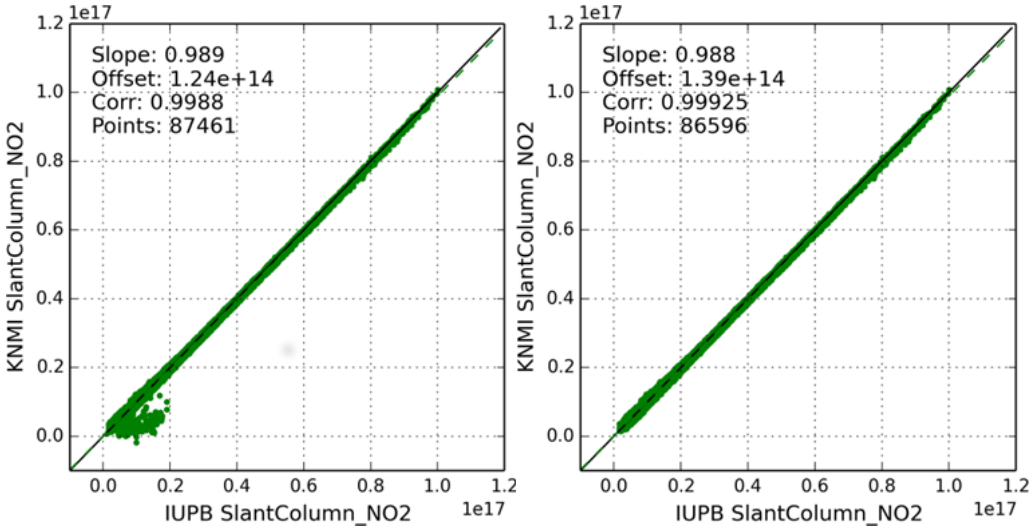

Figure 9.20: Correlation between prototype and verification results for OMI orbit OMIL2_2005m0202t0339, including all pixels with SZA<88° (left), and including only those pixels with SZA<88° and intensity<1.1E14 W m^{-2} nm^{-1}.Harmonized settings were used.

When considering the spatial distribution of the differences between prototype and verification processor, it becomes obvious that differences seem to be larger over bright surfaces, as cloud patterns show up in the mapped differences (see Figure 9.21). Also, there seems to be an across-track dependence in the differences, as the Eastern edge of an orbit often shows a different sign than the rest of the orbit. This leads to the speculation that there might be implementation differences regarding the row-dependent instrument functions between the two processors.

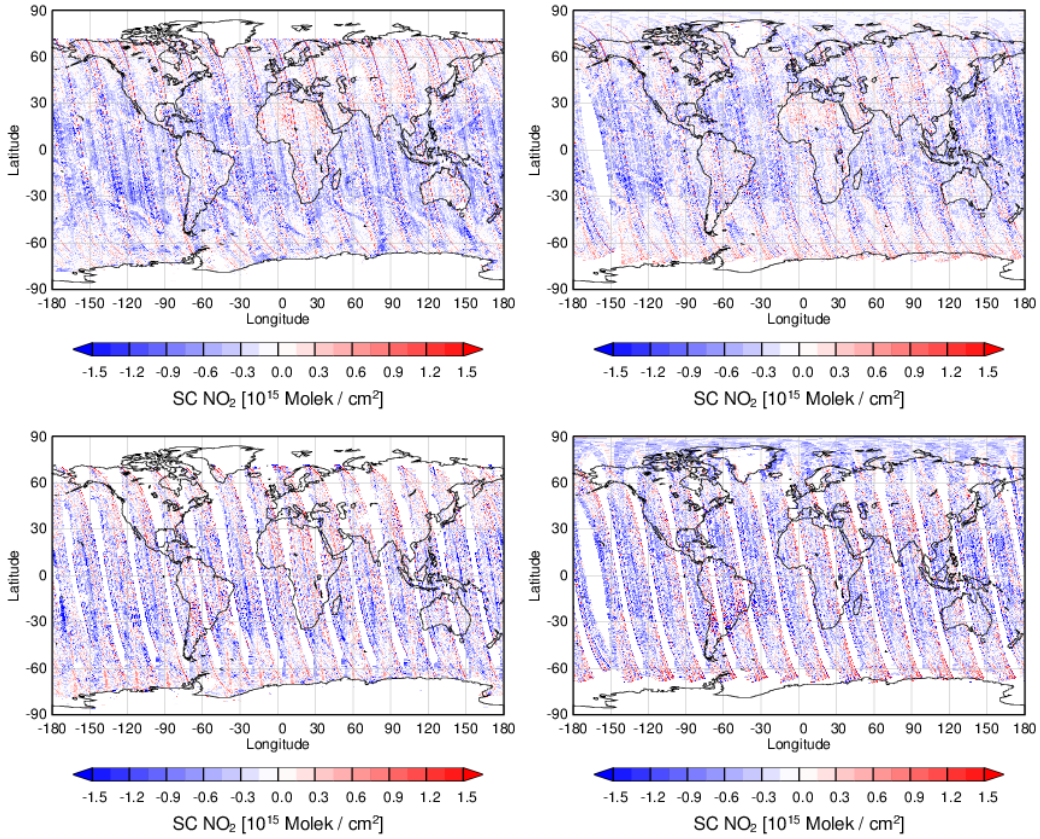

Figure 9.21: Difference of NO_2 SCDs from verification and prototype processors, for four days of OMI measurements: 02 Feb 2005 (top left), 16 Aug 2005 (top right), 04 Feb 2013 (bottom left), and 04 Aug 2013 (bottom right). .Harmonized settings were used.

Finally, when relating the observed differences in retrieved SCDs to the fit uncertainty, it can be concluded that, while considerable differences are present between the prototype and verification processors' output, these differences are smaller than the expected fit uncertainty virtually everywhere over land (see Figure 9.22); over ocean surfaces, significant differences between the processors remain, mostly following cloud patterns. In particular, the processor differences are negligibly small over the areas of interest (tropospheric pollution from anthropogenic and biogenic sources).

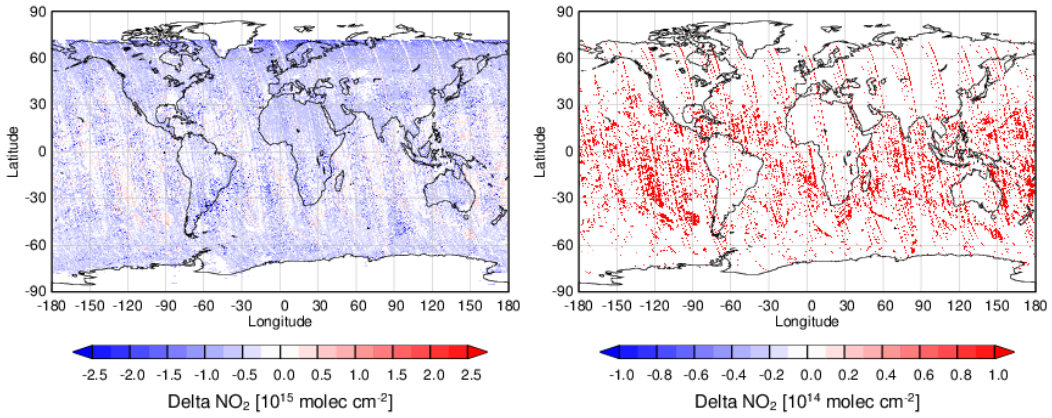

Figure 9.22: Difference between SCD difference and the fit error (from verification algorithm), for OMI data from 2 Feb 2005. The left plot shows all data, while the right plot only shows those pixels where the SCD difference is larger than the fit uncertainty (in a different colour scale). Harmonized settings were used.

9.3.4.3 Slant Column Verification using OMI data

When comparing NO_2 SCDs from the prototype and verification algorithms using non-harmonized settings, differences for individual pixels are larger as expected and can reach up to several 1E15 molec cm^{-2} (see Figure 9.23). In particular, the verification algorithm yields considerably higher SCDs over polluted regions; however, this is to be expected as the wavelength windows differ and lead to different effective sensitivities to boundary layer pollution of 10-15%. Also, the typical clear water ocean regions in the subtropical Pacific show up with larger differences; this might be due to different handling of the intensity offset (1/I vs. $1/I_0$) or possible interferences with vibrational Raman scattering in ocean waters.

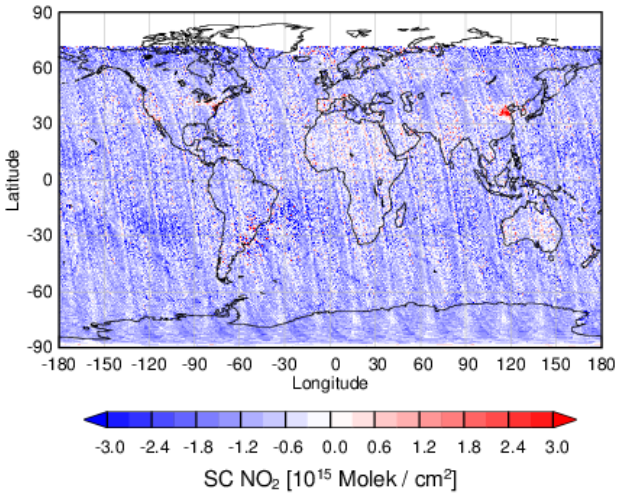

Figure 9.23: Difference between verification and prototype algorithm results, for OMI measurements from 02 Feb 2005. Preferred settings were used.

The correlation between prototype and verification SCDs is excellent (>0.995), with the regression line having slope >0.99 and an offset of ~9E14 for a given example orbit (see Figure 9.24). As expected, the agreement between the two algorithms is not as good as when only comparing the processors with identical fit settings; the spread around the 1:1 line is visibly larger.

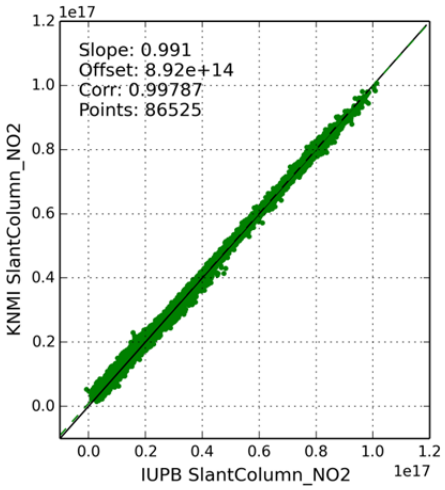

Figure 9.24: Correlation between prototype and verification algorithm results for OMI orbit OMIL2_2005m0202t0339. Preferred settings were used.

When comparing the full verification dataset of four days of OMI measurements, the excellent correlation between prototype and verification algorithms is confirmed (see Figure 9.25). The correlation is >0.98 for all orbits; when excluding orbits affected by the Southern Atlantic Anomaly, the correlation is always >0.99. The correlation is better early in the sensor's lifetime compared to recent years, arguably because differences in the treatment of data affected by the OMI row anomaly. The slope of the regression line is between 0.98 and 1.00 for all orbits, showing very good agreement. However, a significant offset of ~1E15 molec cm^{-2} can be observed between the prototype and verification algorithms, which does not change during the sensor's lifetime. However, this offset can probably be explained to a large extent by the significantly different fitting windows.

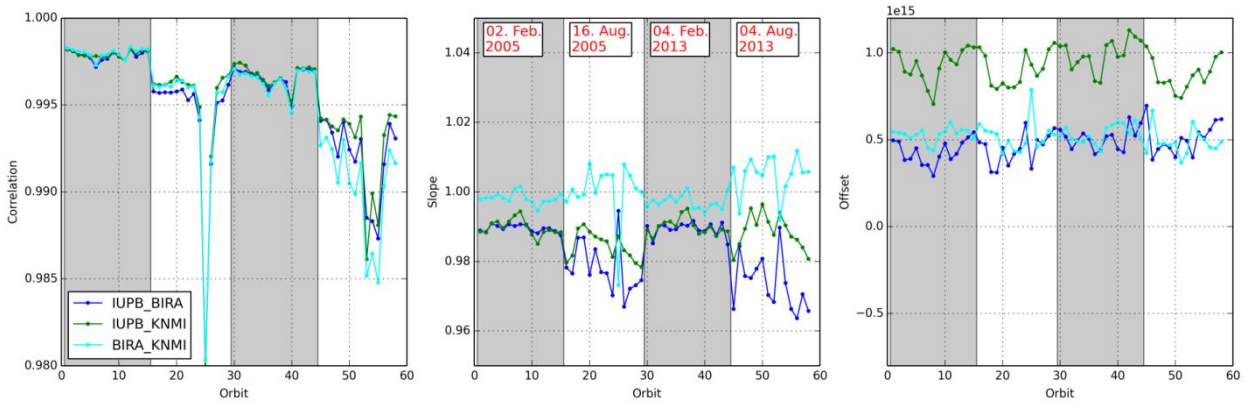

Figure 9.25: Comparison of verification and prototype algorithms (green line), for OMI measurements from 02 Feb 2005, 16 Aug 2005, 04 Feb 2013, and 04 Aug 2013. Pearson correlation coefficient (left), slope of the regression line (centre), and offset of the regression line (right).Preferred settings were used.

9.3.4.4 Verification of tropospheric air mass factors[5]

9.3.4.4.1 Comparison of radiative transfer models

As a first comparison, we investigated top-of-atmosphere (TOA) reflectances as well as the total and ozone optical thickness between the radiative transfer models (RTMs). Additionally to the RTMs from the prototype processor (DAK) and the verification algorithm (SCIATRAN), two other research groups participated with their respective models (BIRA-IASB with LIDORT and MPI-C with McArtim).

Figure 9.26 shows that the spectral dependency of TOA reflectances is generally well reproduced by the RTMs. TOA reflectance increase towards shorter wavelengths as a consequence of the stronger Rayleigh scattering at shorter wavelengths. Reflectances between the models agree to within 0.7% for most geometries, and mean differences between all 4 models are at most 6.4% (maximum difference is 11% between DAK and McArtim) for extreme viewing geometries and short wavelengths.

[5] This Section is based on Lorente Delgado et al. (in prep.)

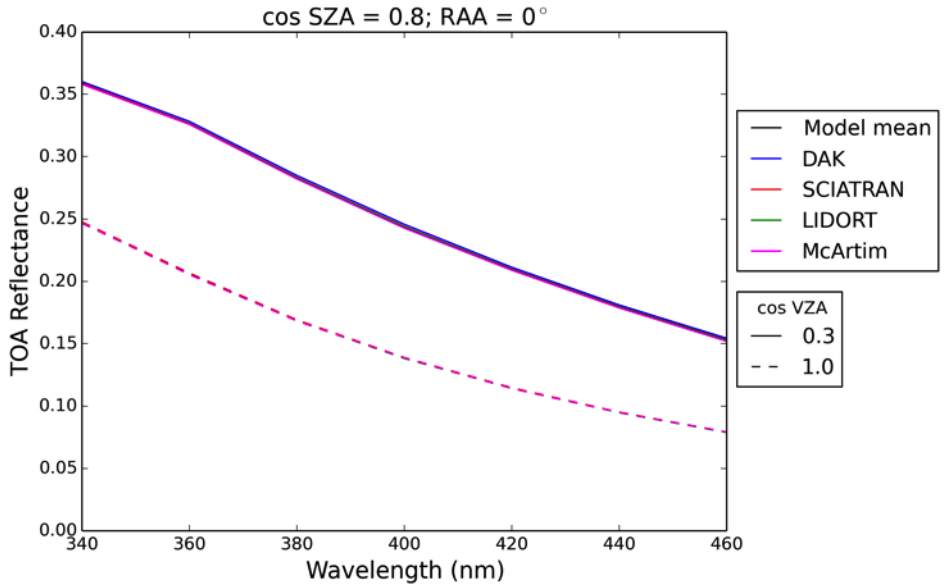

Figure 9.26 TOA reflectances simulated by 4 RTMs for a viewing geometry with θ_0=37° (μ_0=0.8), a nadir viewing angle (dashed lines, θ=0°, μ_0=1.0) and off-nadir viewing angle (θ=72°, μ=0.3) as a function of wavelength (in 20 nm steps). Additionally to the prototype processor (DAK, in blue) and the verification algorithm (SCIATRAN, in red), two other RTMs (LIDORT and McArtim) contributed to this comparison exercise.

These differences are unlikely to be the result of differences in scattering and absorption between the models. The comparison of total and ozone (vertical) optical thickness shown in Figure 9.27 indicates that total optical thickness, the result of extinction through scattering and absorption, is generally consistent to within 0.001 (<0.15%) for all wavelengths except 340 nm, where the differences amount to 0.003 (<0.5%). The right panel of figure 2.5.2 shows the comparison of the ozone optical thickness as a function of wavelength. Higher ozone optical thicknesses are found at 340 nm compared to the longer wavelengths, in line with stronger O_3 absorption in the UV. Absolute differences are very small, ~10^{-5} at 340 nm and 10^{-7} for longer wavelengths. Mean relative differences are 0.25% at 340 nm and 0.4% at 440nm, and are highly variable at intermediate wavelengths with very low ozone optical thickness.

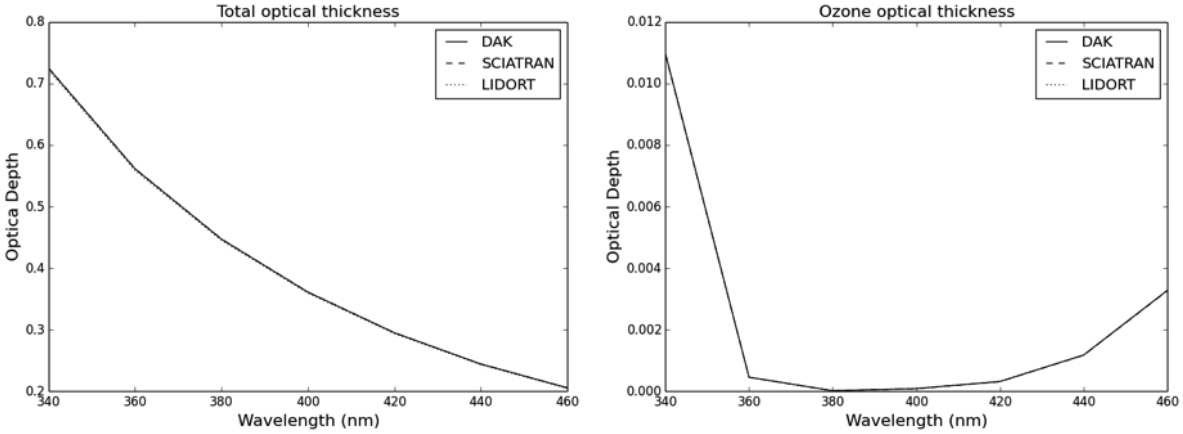

Figure 9.27 Modelled total (vertical) optical thickness (left) and ozone optical thickness (right) as a function of wavelength (left) for 3 RTMs. Additionally to the prototype processor (DAK) and the verification algorithm (SCIATRAN), one other RTM (LIDORT) contributed to this comparison exercise.

The two panels of Figure 9.28 show the dependency of the TOA reflectance at 440 nm (left panel) and on the SZA, and the corresponding absolute relative differences. All models simulate increasing reflectances with decreasing solar zenith angle, and absolute relative differences (defined as $100\% \cdot \left|\left(R(a) - R(b)\right)/R(a)\right|$ with *R(a)* the reflectance from model a) between the models are generally <1%, except for large solar zenith angles. The mean relative difference for the most extreme viewing geometry (μ_0=0.05, μ_0=0.3) is 3.2%, with a standard deviation of 0.042 (2.8% of model mean reflectance). For lower SZA, the standard deviation is lower than 0.005 (i.e. < 0.9%), indicating very good consistency of reflectance calculations in most common retrieval scenarios.

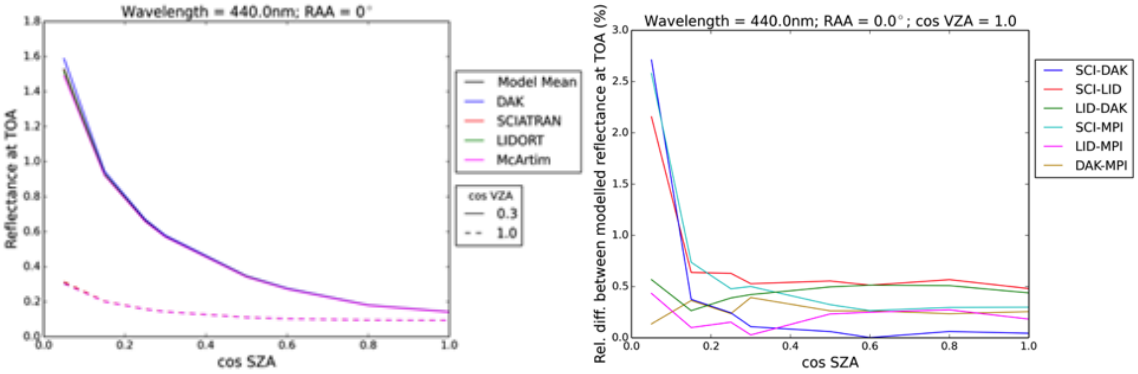

Figure 9.28 TOA reflectances (left) and their absolute relative difference (right), simulated at 440 nm as a function of SZA for a nadir viewing angle (dashed lines, μ=1.0) and off-nadir viewing angle (θ=72°, solid lines, μ=0.3). Additionally to the prototype processor (DAK, in blue) and the verification algorithm (SCIATRAN, in red), two other RTMs (LIDORT and McArtim) contributed to this comparison exercise.

In summary, we can conclude that the differences between the raditative transfer models themselves are negligibly small (below 1% in most typical measurement scenarios). They are larger for high viewing angles and do not strongly depend on the solar elevation.

9.3.4.4.2 Comparison of the air mass factor look-up tables

In a next step, the radiative transfer models were used to calculate look-up tables of altitude-resolved air mass factors (or box air mass factors, BAMF) for a common set of parameters. Again, in addition to the RTMs from the prototype processor (DAK) and the verification algorithm (SCIATRAN), two other research groups participated with their respective models (BIRA-IASB with LIDORT and MPI-C with McArtim). All models were used to create look-up tables of NO_2 box air mass factors for a common set of parameters.

The left panel of Figure 9.29 shows that the models agree well on the vertical shape of NO_2 AMFs at 440 nm for a clear-sky scene. The vertical profile by McArtim (pink line) shows a wavering line due to the model's Monte Carlo nature. This scatter could easily be reduced if more photons were used for the simulations. The right panel shows relative differences between models for a specific surface albedo and surface height, for a wide range of solar and viewing geometries ($0.15 \le \mu_o \le 1.0$, $0.3 \le \mu \le 1.0$). Mean relative differences between the operational and verification algorithms' models are within 2% for all the geometry combinations.

The visible discontinuity in the relative differences at the surface and at 270 hPa (~10 km) is due to differing vertical discretizations in these altitude ranges due to technical limitations of the models.

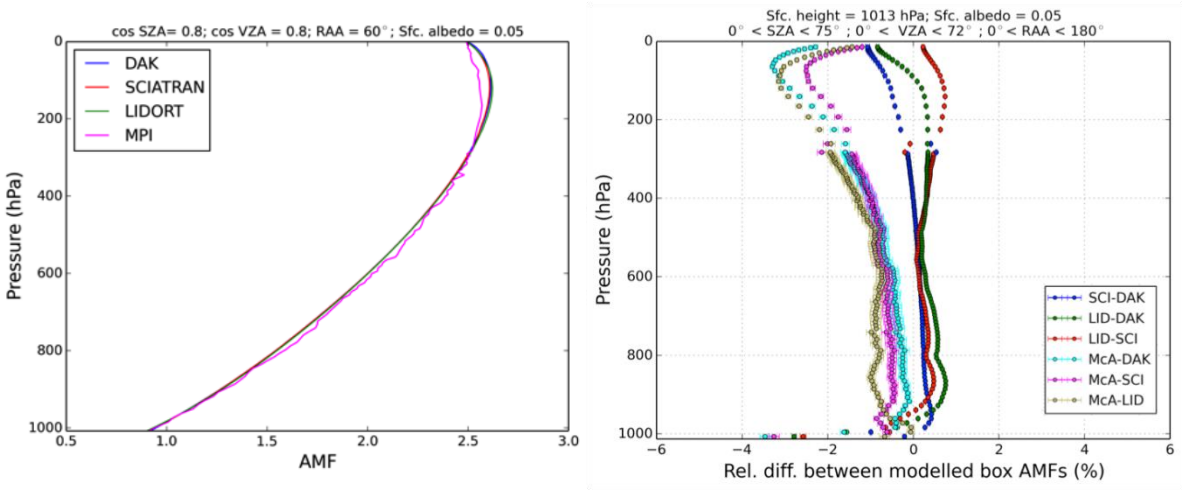

Figure 9.29: Left panel: vertical profile of NO_2 box AMFs calculated by prototype (DAK, blue) and verification (SCIATRAN, red) RTMs for SZA = VZA ≈ 37° ($\mu = \mu_o = 0.8$), RAA = 60°, surface albedo = 0.05 and surface height 1013 hPa. Right panel: vertical profile of relative differences between NO_2 box air mass factors from the different RTMs for a wide range of viewing and solar geometry, surface albedo = 0.05 and surface height 1013 hPa. Bold lines indicate the mean relative difference averaged over all combinations of viewing geometries. Additionally to the prototype processor and the verification algorithms, two other RTMs (LIDORT and McArtim) contributed to this comparison exercise.

Figure 9.30 shows the NO_2 box AMF dependency on the parameters surface albedo, viewing geometry, and surface pressure at 950 hPa. This pressure level is especially relevant because this is where NO_2 is found in many polluted situations. We see a strong sensitivity to albedo (with a 2-4-fold increase in AMF within the range of albedos that are naturally occurring), and this albedo-dependency is well captured by all RTMs. The box AMFs generally increase with surface albedo and the increase is particularly strong for low values of surface albedo. This reflects the rapid increase in the number of photons reflected at the surface, so that more photons traverse the polluted boundary layer, leading to higher sensitivity (and thus AMF values) to NO_2 in the polluted boundary layer. Box AMFs at 950 hPa show a relatively weak dependency on viewing zenith and relative azimuth angle (±10% differences over the range of possible values), and a somewhat stronger dependency on solar zenith angle, but again, all RTMs agree very well on viewing geometry-dependent box AMFs. Panel (e) in Figure 9.30 shows that box AMFs in the lower troposphere (here at 787 hPa) are very sensitive to surface pressure. For the particular geometry shown, the sensitivity of the box AMF to surface pressure is not as strong as to surface albedo, but still substantial (20% for surface pressures between 1000-900 hPa). This dependency is well reproduced by all RTMs. The box AMF is lower for lower surface pressure (i.e. higher surface height). When the surface height is higher, the amount of light scattered and reflected from below 787 hPa decreases. Consequently, the photons experienced fewer scattering events, which tends to reduce the box AMF at that level.

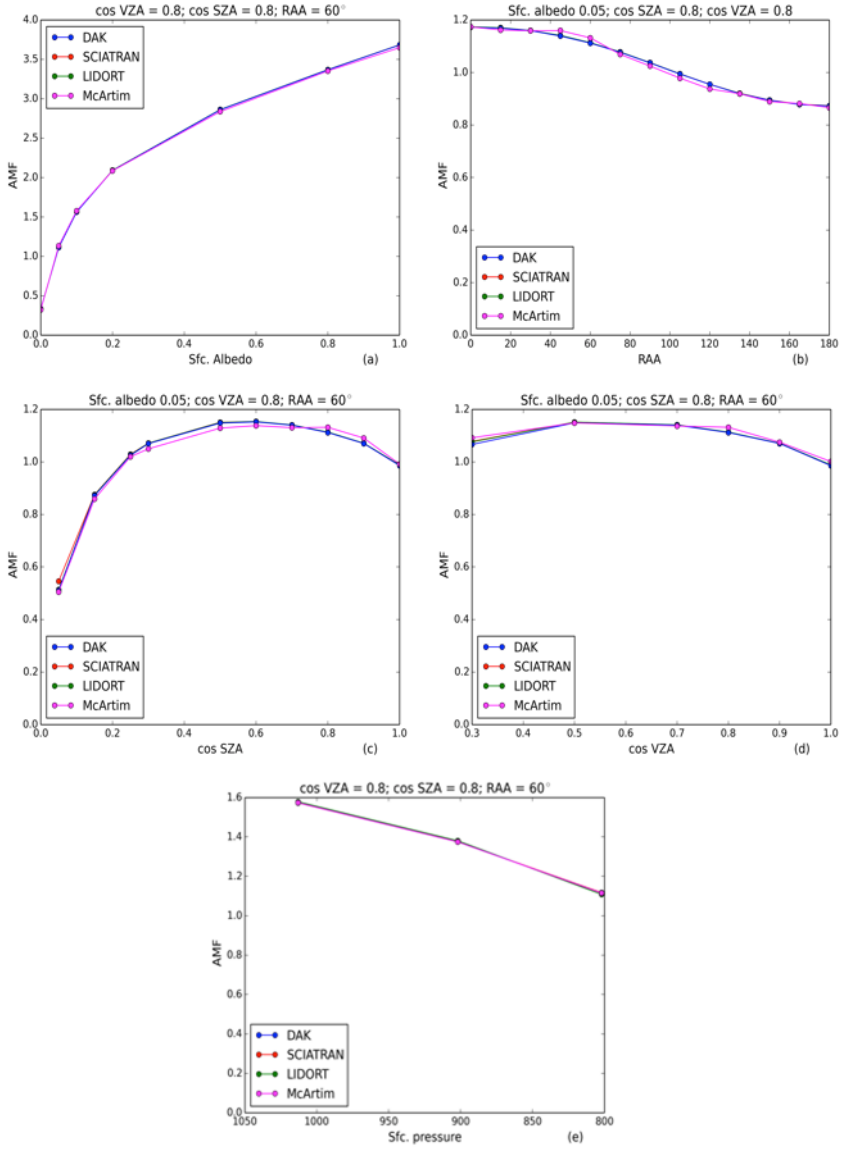

Figure 9.30: Dependency of (950 hPa) NO_2 box AMF to various parameters: (a) surface albedo, (b) RAA, (c) cosine of SZA, (d) cosine of VZA, and (e) surface pressure (at 787 hPa). Additionally to the prototype processor (DAK, in blue) and the verification algorithm (SCIATRAN, in red), two other RTMs (LIDORT and McArtim) contributed to this comparison exercise.

The comparison of the NO_2 box AMFs calculated by the prototype and verification RTMs DAK and SCIAMACHY indicates that for most viewing geometries, box AMFs are consistent to well within 1%.

9.3.4.4.3 Comparison of the air mass factor processing chain

Similar to the comparison of the slant column processing chains in Section 9.3.4.2, we conducted a comparison of the air mass factor processing chains. Using identical choices for input and ancilliary data, box air mass factors and the resulting tropospheric air mass factors have been computed for four typical OMI measurement pixels (two in polluted regions, southern Beijing and South Korey, and and two over pristine, remote regions of the Pacific).

The selected day for comparison is 2 Feb 2005, early in the lifetime of the sensor (orbit lv1 filename OMI-Aura_L2-OMDOMINO_2005m0202t0339-o02940_v003). Figure 9.31 shows an example of box NO_2 AMFs calculated for pixel I, with temperature correction. We can observe a high agreement in the vertical profile between the different groups.

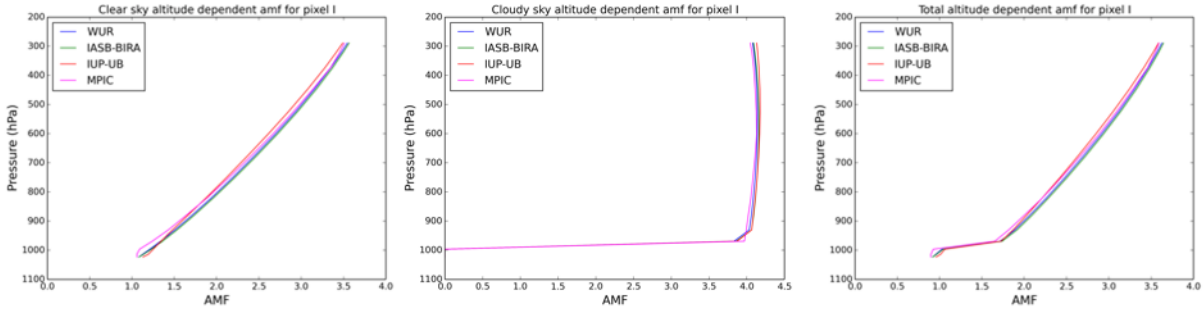

Figure 9.31: Clear-sky (left panel), cloudy-sky (middle panel) and total (right panel) altitude dependent NO_2 air mass factor for pixel I with the following parameters: SZA = 56.7°, VZA = 57.7°, RAA = 64.1°, sfc. Pressure = 1026.3 hPa, surface albedo = 0.079, cloud pressure = 984 hPa, cloud fraction =0.046. Additionally to the prototype processor (labelled WUR, in blue) and the verification algorithm (labelled IUP-UB, in red), two other research groups (BIRA-IASB and MPI-C) contributed to this comparison exercise.

Table 9.4 presents a comparison of total tropospheric AMFs calculated by the prototype and verification algorithms, with temperature correction. In the polluted pixels tropospheric AMFs agree within 0.7%, whereas in the clean remote pixels the agreement is better than 0.4%. The observed differences are within the acceptable values based on the differences found in the previous comparisons of the LUT, and show that slight differences in vertical interpolation schemes between the groups do not result in strong discrepancies.

Table 9.4 Total tropospheric AMFs calculated by each group with temperature correction for the four selected pixels.

	Prototype algorithm	Verification algorithm
Pixel I	1.261	1.270
Pixel II	0.874	0.868
Pixel III	1.889	1.894
Pixel IV	1.731	1.737

9.3.5 Summary of verification results

- All three algorithms retrieve NO_2 slant columns on synthetic data which are close (within 10%) to those modelled by SCIATRAN.
- The largest part of the differences is linked to different effects of NO_2 temperature dependence which are usually accounted for in the AMFs not applied during this test. To quantify these effects, synthetic data without NO_2 temperature dependence have been analysed. In these scenarios, the agreement is better than 5% in all cases and better than 1% for clean scenarios.
- The remaining differences for polluted scenes are linked to differences in tropospheric AMF for the fitting windows used and have to be treated in the AMF step.
- Evaluation of the data with noise shows larger scatter and differences between individual realisations of the noise model. Even with noisy data, none of the retrievals results in negative slant columns even for background stations.
- No significant differences in performance could be found so far between the operational and the two verification algorithms, indicating good maturity of the prototype SC fit.
- Using a set of selected OMI data covering different seasons and sensor ages, excellent agreement was found between verification and prototype results if all settings are harmonized.

- When using the preferred settings of the two algorithms on the OMI data, larger differences of several $1x10^{15}$ molec cm^{-2} are found, mainly linked to the different fitting windows and different treatment of intensity offset.
- Radiative transfer models used by verification and prototype algorithm show excellent agreement for radiances and box air mass factors. The latter can vary by up to 6% if different vertical layering schemes are used, highlighting the need for careful evaluation of this parameter.

9.4 Stratospheric NO2 correction

9.4.1 Algorithm description

STREAM, the STRatospheric Estimation Algorithm from Mainz, was developed at MPI for Chemistry as TROPOMI verification algorithm. Below, we summarize the algorithm design and present the results of TROPOMI verification. Further details on the algorithm, sensitivity studies, and comparisons to other algorithms are provided in a dedicated STREAM manuscript within the TROPOMI special issue in AMT (Beirle et al. 2015).

9.4.1.1 Approach

STREAM is a modified reference sector method. That is, the stratospheric column density of NO_2 is estimated from the total column measurements in regions where tropospheric NO_2 is assumed to be negligible. In addition to such “clean” regions, also satellite measurements over clouds, where the tropospheric column is shielded, are considered.

The derived stratospheric field is smoothed and interpolated globally, based on the assumption that the stratospheric pattern of NO_2 does not feature strong spatial gradients.

Our approach is, in general, similar to the algorithm used in the recent update of NASA’s operational OMI NO_2 product, as described in Bucsela et al. (2013). However, with respect to the concrete implementation, the applied algorithms are significantly different.

9.4.1.2 Realization

9.4.1.2.1 NO_2 columns: Total and stratospheric column densities and tropospheric residues

Starting point of STREAM are total vertical column densities (VCDs) of NO_2 V, which are calculated from the SCDs (resulting from the DOAS analysis) by applying a stratospheric AMF. This procedure eliminates the dependencies of SCDs on SZA and VZA, and is appropriate for regions/cloud conditions with negligible tropospheric (slant) columns. These observations are used for the estimation of the stratospheric VCD V_{Strat}. We define the Tropospheric Residue (TR) T as

$$T = V - V_{Strat} \tag{17}$$

The tropospheric VCD (TVCD), which is the final tropospheric product, is then given as

$$TVCD = T * \frac{AMF_{Strat}}{AMF_{Trop}} \tag{18}$$

Within the following discussion of stratospheric correction, we focus on the TR instead of the TVCD for the following reasons:

- possible biases in the stratospheric estimate are directly related (factor -1) to biases in the TR

- the comparison of TRs among different algorithms isolates the effect of the different stratospheric estimation schemes, but excludes the differences of tropospheric AMFs (see section 9.3.4.4)
- the TR can be determined (and is of high interest for the evaluation of algorithm performance) over clouded pixels with very low tropospheric AMFs.

However, the application of a stratospheric AMF has to be kept in mind when interpreting the tropospheric residue. For regions with tropospheric pollution, the TR will be generally lower than the TVCD, as the tropospheric AMF is smaller than the stratospheric AMF in most cases.

9.4.1.2.2 Characterisation of "clean" and "polluted" pixels by weighting factors

As in all kinds of stratospheric estimation schemes using reference regions, sufficiently "clean" pixels have to be identified which represent the stratospheric column. Typically, observations over remote regions without significant tropospheric NO_x sources are considered. As demonstrated in Leue et al. (2001) and Bucsela et al. (2013), also satellite pixels for cloudy conditions directly provide information on the stratospheric column, as long as the cloud is sufficiently high to shield tropospheric pollution, but not too high so that convection of tropospheric NO_x and production of lightning NO_x can be neglected.

In contrast to Bucsela et al. (2013) (and other modified reference sector methods before), STREAM does not simply flag potentially polluted pixels. Instead, weighting factors are assigned to each individual satellite pixel determining how far these measurements affect the stratospheric estimate. Over regions with regular tropospheric pollution (as derived from a multiannual mean of tropospheric VCDs), weights are low, while observations over mid-altitude clouds are assigned with a high weight.

The weighting factors are multiplicative, such that the cloud weight can overrule the pollution weight for low average pollution levels. The detailed definition of weighting factors is given in section 9.4.1.2.4.

9.4.1.2.3 Weighted convolution

Global daily maps of the stratospheric column density are derived by applying a "weighted convolution", i.e., a spatial convolution which takes the individual pixel weights into account. Here we describe the general approach; the detailed STREAM settings for weights and convolution are given in the next sections.

The algorithm is implemented as follows:

a) A lat/lon grid is defined with 1° resolution. Each satellite pixel is sorted into the matching grid pixel according to its centre coordinates.

At the j^{th} latitudinal/i^{th} longitudinal grid position, there are K satellite pixels with the total columns V_{ijk} (k=1..K) and the weights w_{ijk}. We define

$$C_{ij} ::= \sum V_{ijk} w_{ijk} \tag{19}$$

and

$$e_{ij} := \sum w_{ijk} \tag{20}$$

The weighted mean VCD for each grid pixel is then given as

$$V_{ij} = \frac{C_{ij}}{W_{ij}} \tag{21}$$

b) A convolution kernel G is defined (e.g., a 2D Gaussian; see Section 9.4.1.2.5). Convolution is applied to both C and W:

$$C^{smooth} := G \otimes \mathrm{C} \quad (22)$$

$$W^{smooth} := G \otimes \mathrm{W} \quad (23)$$

The VCD from weighted convolution is then defined as

$$V_{ij}^{smooth} := \frac{C_{ij}^{smooth}}{W_{ij}^{smooth}} \quad (24)$$

This approach is an extension of the "normalized convolution" presented in Knutson and Weston (1993). By this weighted convolution, the stratospheric field is smoothed and interpolated at the same time.

The procedure of weighted convolution is illustrated for a constructed example in Figure 9.32.

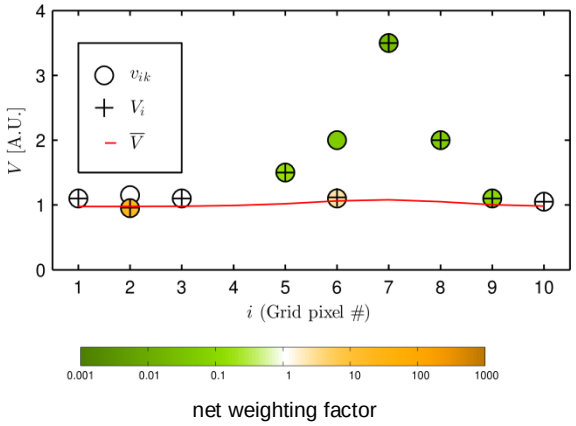

Figure 9.32: Illustration of the concept of weighted convolution for a constructed example over clean (i=1-3, 10) and polluted (i=5-9) regions. Circles represent the individual V for each satellite pixel. Weighting factors are color-coded. The weighted mean VCD in each grid pixel is indicated by a "+". In cases of multiple satellite pixels per grid (i=2,6), the weighted mean is dominated by the "clouded" satellite pixel with high weighting factor. The estimated stratospheric pattern V resulting from weighted convolution is shown in red.

9.4.1.2.4 Weighting factors

The individual weighting factor for each satellite pixel results from the product of the weighting factors w_{pol} (pollution), w_{cld} (cloud), and w_{TR} (trop. residue), which are explained in detail below. A high weighting factor (>1) is associated with observations which are expected to represent the stratospheric column, while a low weighting factor (<1) indicates that the observation is likely affected by tropospheric pollution.

a) Pollution weight w_{pol}

The pollution weight is assigned to measurements over regions with high likelihood for tropospheric pollution. This information is taken from a climatology P of tropospheric NO_2 TVCDs. Here, the MPI-C SCIAMACHY NO_2 product is used (Beirle and Wagner, 2012).

The pollution weight is derived in 3 steps: 1. A threshold of 1 (all units below: 10^{15} molec/cm^2) is applied to the NO_2 climatology P; P is set to NaN where values are below this threshold. 2. The remaining values are smoothed with a 2D-Gaussian with □=2°. By this procedure, also the spatial extent of the area where P is defined is increased. 3. Values of P below 1 are set to 1 (except NaNs). By this operation, a "safety margin" of *potentially* polluted areas is created.

w_{pol} is then defined as

$w_{pol}=0.1/P^3$ where P is defined, and as

$w_{pol}=1$ elsewhere.

Figure 9.33 shows the resulting map of w_{pol}.

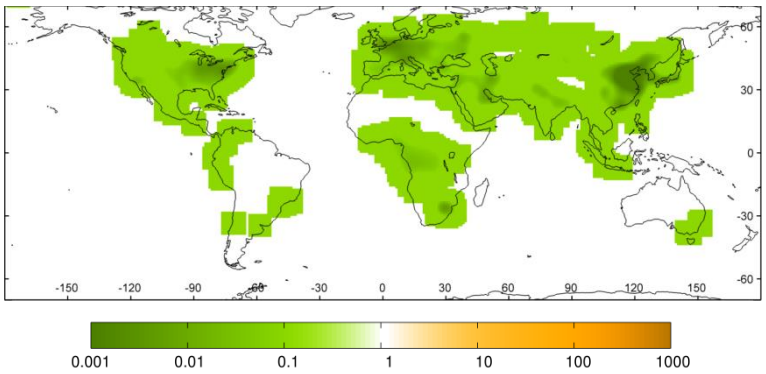

Figure 9.33: Map of the pollution weight w_{pol} derived from a climatology of tropospheric NO_2 from SCIAMACHY.

b) Cloud weight w_{cld}

Most continental regions are assigned with a low weight w_{pol} due to tropospheric pollution. In order to minimize the potential artefacts which might occur if the stratospheric field is interpolated over such large regions, our algorithm makes use of cloudy pixels which shield the tropospheric column. Depending on cloud fraction and cloud height, w_{cld} can compensate a low pollution weight.

In addition, also over “clean” regions, cloudy observations are preferred over cloud free situations. Thus, STREAM is expected to provide a direct estimate of the stratospheric column, and does not require an additional correction of the (small) tropospheric background column, like other reference-region methods.

A high cloud weight should only be assigned to clouds at altitudes high enough to shield the lower troposphere, while clouds at low altitudes should not be considered due to their opposing effects on AMFs (albedo increase, multiple scattering). On the other hand, very high clouds should also be skipped as they might be related to lightning NO_x, or lifting of boundary layer pollution in the upper troposphere by deep convection.

w_{cld} is thus defined as

$w_{cld}=10^{2*C*P}$ with

$C=f^4$ (f: Cloud radiance fraction) and

$P=\exp(-0.5*(p-p_{ref})^4/\square_p^4)$ (p: Cloud pressure; p_{ref}: reference pressure; $\square_p$: width)

C reflects the dependency on the cloud radiance fraction (CRF). Due to the exponent of 4, only pixels with large CRF reach a high weighting factor and contribute strongly to the stratospheric estimation. P describes the dependency on cloud pressure (CP). It is basically a modified Gaussian (with exponent 4 instead of 2, making it flat-topped) centered at p_{ref}=500 hPa with a width of $\square_p$ = 150 hPa. As both C and P yield values in the range from 0 to 1, the resulting value for w_{cld} is within the range of 1 to 100.

The dependencies of w_{cld} on CRF and CP are shown in Figure 9.34, and the resulting map for w_{cld} is exemplarily shown in Figure 9.35 based on CRF and CP from OMI for 1 January 2005.

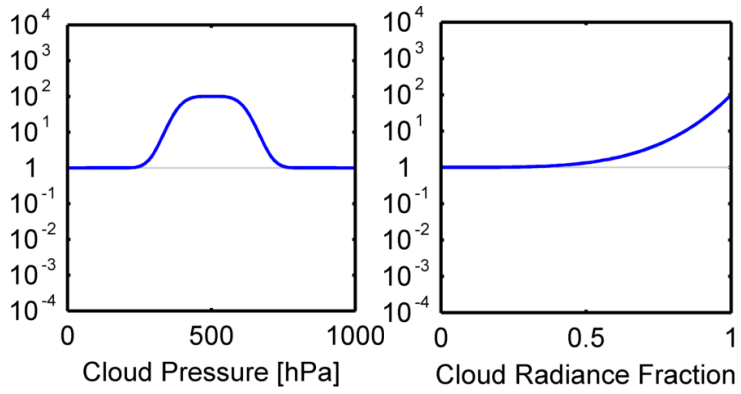

Figure 9.34: Dependency of w_{cld} on CP (left, for a CRF of 1), and on CRF (right, for a CP of 500 hPa).

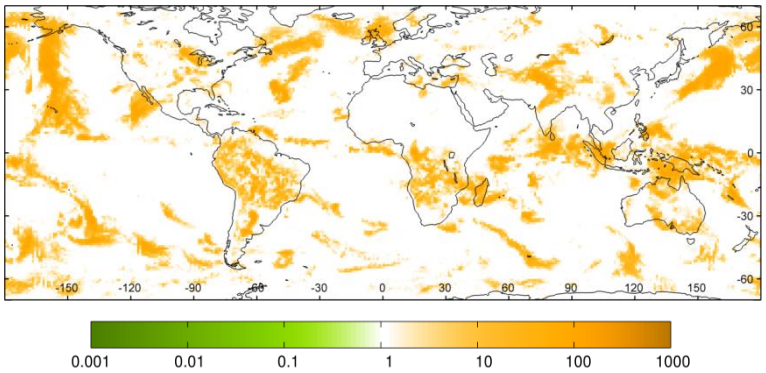

Figure 9.35: Spatial distribution of w_c for 1st of January 2005 for OMI measurements.

c) Tropospheric Residue weight w_{TR}

The tropospheric residue is determined as the difference of total and estimated stratospheric column. Such a subtraction of two quantities of the same order of magnitude with non-negligible errors results in a statistical distribution of estimates that will include negative values. Note that although negative tropospheric column densities (and thus TRs) are unphysical, they are required to keep means unbiased.

However, whenever the stratospheric VCD is *systematically* overestimated such that it exceeds the mean total VCD, the resulting TR becomes systematically negative. In order to avoid (or minimize) such unphysical results, the additional weighting factor w_{TR} is defined such that pixels with (significantly) negative TR get higher weights in the stratospheric estimation. The updated stratospheric estimate will be lower, and, consequently, the updated TR will be higher. This procedure could be done once or iterated several times. In the current implementation, a single iteration is performed.

In order to avoid low biased stratospheric columns which might be caused by individual noisy pixels with negative TR, w_{TR} is calculated based on the mean TR per grid pixel (in contrast to the other weights, which are calculated for each satellite pixel). Only if the mean TR of all satellite ground pixels within a grid pixel is significantly negative (below $-0.5*10^{15}$ molec/cm^2), all these pixels are assigned with a weight w_{TR} in the next iteration. In addition, also the mean TR of adjacent grid pixels is demanded to be negative. Thus, a single noisy satellite measurement with low VCD can never trigger w_{TR}.

In analogy, w_{TR}, is also defined for pixels with systematically *enhanced* tropospheric residues over regions defined as potentially polluted ($w_{pol}<1$). The respective observations obtain lower weights in the next iteration of the stratospheric estimation procedure.

w_{TR} is thus defined as

$w_{TR}=10^{-2T}$ if $|T|>0.5$ (for the grid pixel of interest and adjacent pixels), and $w_{TR}=1$ else.

(T in units of 10^{15} molec/cm^2).

Figure 9.36 displays the dependency of w_{TR} on T.

Figure 9.37 displays w_{TR} for 1st of January 2005 for OMI measurements after the initial run of the weighted convolution algorithm based on w_{pol} and w_{cld} alone.

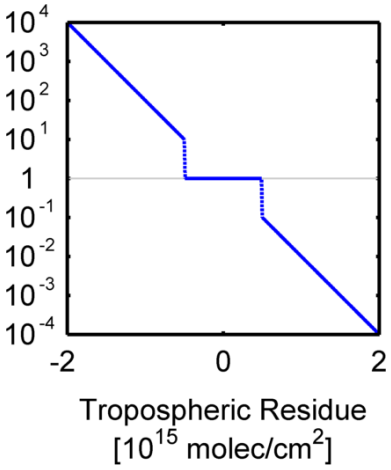

Figure 9.36: Dependency of w_{TR} on the tropospheric residue of the initial stratospheric estimate.

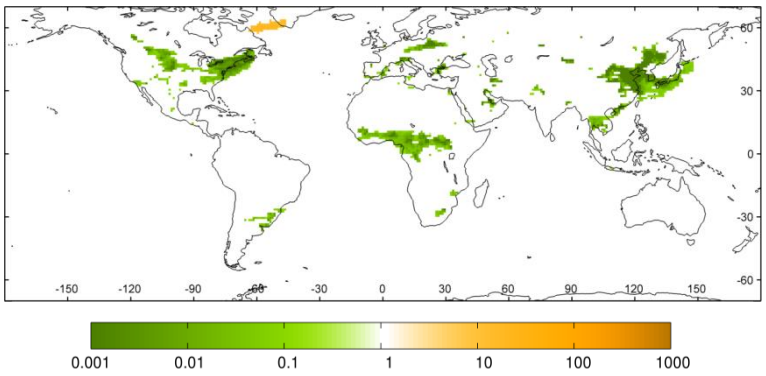

Figure 9.37: Spatial distribution of w_{TR} for 1st of January 2005 for OMI measurements. The weights are increased over the Labrador Sea, where the strong NO_2 gradient due to the polar vortex causes an overestimation of the stratospheric columns for the initial run of the algorithm. Over the US, Eastern Asia and China, the high TR results in low w_{TR}. Over Europe, total VCDs are quite low on that day (compare Figure 9.39).

A total weight defined as $w= w_{pol}\times w_{cld}\times w_{TR}$, is assigned to each satellite pixel. Figure 9.38 displays w for 1st of January 2005 for OMI measurements.

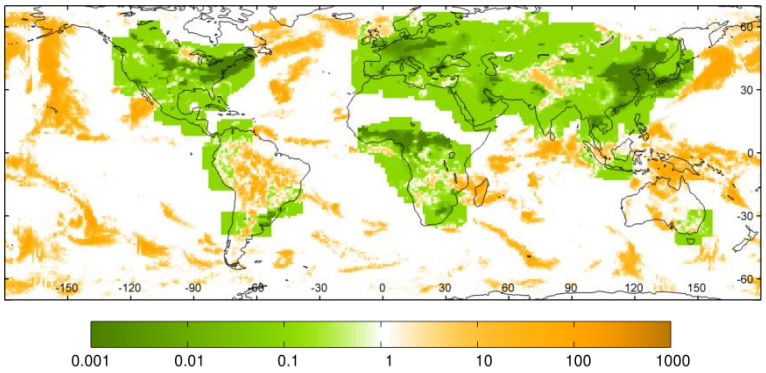

Figure 9.38: Spatial distribution of the final weights w for 1st of January 2005 for OMI measurements.

9.4.1.2.5 Convolution

The stratospheric field is derived from total columns and the weighting factor w for each satellite pixel by weighted convolution as described above. The convolution kernel has to be chosen such that gaps (e.g. China) are appropriately interpolated, while true stratospheric gradients (particularly meridional) are conserved. Thus, the 2D convolution Kernel is defined as a Gaussian with σ_{lat} smaller than σ_{lon}.

Convolution is performed for 2 different convolution Kernels:

1. σ_{lat}=5°, σ_{lon}=10°, and

2. σ_{lat}=10°, σ_{lon}=50°.

The small Kernel conserves strong gradients, e.g. at the polar vortex, while the large Kernel appropriately smooths the stratospheric fields over potentially polluted regions like central Africa. Thus, the final stratospheric field V_{strat} is defined as the weighted sum of the stratospheric fields for the 2 convolutions:

$$V_{strat} = \cos^2(lat) x V_1 + \sin^2(lat)\, x\, V_2 \qquad (25)$$

i.e. at high latitudes a smaller convolution Kernel is applied than at low latitudes.

9.4.1.3 A-priori information

The proposed stratospheric correction scheme requires the following additional information:

9.4.1.3.1 NO_2 climatology

For the definition of w_{pol}, a climatology of tropospheric NO_2 is required. This can be taken from CTMs or satellite measurements, based on annual or monthly means. In STREAM, a mean climatology from SCIAMACHY is used. This can easily be updated with data from e.g. OMI.

9.4.1.3.2 Cloud data

The calculation of cloud weights requires information on cloud pressure and cloud radiance fraction. This is typically derived operationally from radiance measurements and the analysis of O_2 or O_4 absorption. For OMI measurements, we use the operational cloud data provided within the NASA NO_2 product (OMNO2 v3/SP 2, using the OMCLDO2 cloud product).

9.4.1.3.3 Additional datasets (possible future extension)

If further weighting factors should be defined, additional datasets like fire or lightning counts etc. would be required.

9.4.1.3.4 Tropospheric background

The classical reference region approaches (e.g. Richter and Burrows, 2002; Martin et al., 2002) assume that the total column represents the stratospheric column in the clean reference regions. Over these regions, the mean tropospheric residue is thus by definition 0, and the tropospheric product has to be interpreted as excess column relative to the reference region. This small bias can be corrected, if required, by adding the tropospheric background columns, as e.g. provided by CTMs, over the “clean” regions.

In the case of STREAM, however, the emphasis of clouded observations, where the tropospheric background is shielded, allows a direct estimate of the actual stratospheric column, such that an additional tropospheric background correction is obsolete.

9.4.2 Main differences to prototype algorithm

The stratospheric correction proposed in the prototype algorithm is based on assimilating (Eskes et al., 2003) the satellite measurements of NO_2 total column densities into a CTM (Dirksen et al., 2011). While both schemes are flexible in their screening of polluted regions and eventually base the stratospheric estimate on the satellite measurements themselves, the proposed verification algorithm follows a different approach and is independent from chemical transport models.

The main advantages of STREAM are that the method is relatively simple, robust, and fast (~2.5 minutes per one day of OMI measurements), and requires only almost no a-priori data. As the stratospheric field is determined from the measurements themselves, any changes of the instrumental performance, which potentially affect the retrieved trace gas column densities systematically, are intrinsically corrected.

9.4.3 Error analyses

The proposed algorithm is based on the parameterizations of weights for individual pixels and the spatial smoothing by a convolution kernel. This implies the following types of possible errors:

9.4.3.1 Pollution weight

The pollution weight w_{pol} is needed to assign low weights to pixels which are probably affected by tropospheric pollution, according to long-year experience (e.g., a climatology from satellite observations).

If w_{pol} is defined too high (i.e., polluted regions are only moderately down-weighted), this may result in actually polluted pixels which still contribute significantly to the estimated stratospheric field during weighted convolution. Consequently, the stratospheric estimation scheme will partly correct for tropospheric enhancements as well, and the tropospheric residue will be biased low over/close to polluted regions.

If, on the other hand, w_{pol} is defined too low (i.e., polluted regions are strongly down-weighted), this impact of tropospheric pollution on the stratospheric estimation is avoided, but large regions (like whole continents) will be free of any observation with sufficiently high weight. Consequently, the stratospheric patterns in polluted regions will be determined by interpolation only. The occurring interpolation errors can cause the tropospheric residue to be biased either high or low, depending on the actual gradients of the stratospheric field. In particular at high latitudes in winter, this can cause biases of up to some 10^{15} molec/cm^2 (compare Beirle et al., 2010).

9.4.3.2 Cloud weight

The cloud weight w_{cld} is introduced to assign higher weight to cloudy pixels, if the tropospheric column can be considered to be shielded.

Clouds with low altitude should not be included, as they might even increase the tropospheric signal due to multiple scattering and their high albedo.

At the same time, also high altitude clouds should be treated with care, as they may indicate deep convection, which could uplift pollution from the boundary layer into the upper troposphere. Also NO_x produced by lightning might interfere.

But even clouds with medium heights might contain NO_2, as has been regularly observed in long range transport events (Zien et al., 2014). The affected regions are already partly dampened by the pollution and tropospheric residue weight. An additional identification of such special events might be added in future.

The value for w_{cld} has to be defined in a balanced way relative to w_{pol}. If w_{cld} is generally too low, clouded pixels are not considered at all. If too high, they will dominate the stratospheric estimation.

9.4.3.3 Negative and positive tropospheric residue weight

The algorithm can be performed iteratively, introducing the negative/positive tropospheric residue weights w_{TR}. This increases the weight of pixels yielding negative tropospheric residues for the next iteration. This helps to remove or reduce unphysical results, which tend to appear regularly (but not only) in the polar vortex. Analogously, pixels with positive tropospheric residues are assigned low weights for the next iteration, as they probably represent tropospheric pollution. Again, the values for w_{TR} have to be defined in a balanced way. If too low, they have no effect, but if too high, they generally bias the stratospheric field, and thus the tropospheric residue. In particular, one has to avoid that the stratospheric estimate becomes biased just as a consequence of the noise of individual ground pixels. In order to minimize this effect, w_{TR} is calculated based on mean tropospheric residues within 1° grid boxes instead of individual satellite pixels.

9.4.3.4 Convolution kernel

The global maps are smoothed by convolution. If the width of the convolution kernel (i.e., the □ of a Gaussian) is too narrow, the stratospheric pattern is allowed to reflect strong spatial gradients. However, this can easily eliminate tropospheric features, as they might be interpreted as stratospheric.

If the kernel width is too wide, however, spatial gradients (e.g., at the polar vortex or also at stratospheric filaments at moderate latitudes) can no longer be resolved.

This conflict is inevitable for any reference region approach, and it is probably impossible to separate tropospheric transport events from stratospheric filaments automatically, if they reveal similar spatial patterns. Thus, we prefer a wider kernel which might smooth out possible small-scale stratospheric patterns on daily basis, but should reproduce the stratospheric column appropriately on average, and thus preserves tropospheric features.

Note that the operational NASA product follows a generally similar approach for the estimation of the stratospheric column (Bucsela et al., 2013). However, it applies only little smoothing such that even strong gradients can be represented in the stratospheric fields. This removes small scale structures resulting from stratospheric dynamics at higher latitudes, and other patterns like cloud interferences, and generally leads to very smooth tropospheric residues. However, we see the danger that tropospheric transport events, like reported in Stohl et al. (2003) or Zien et al. (2014), are misclassified as stratospheric feature.

9.4.3.5 Error quantification

In order to quantify possible errors due to the STREAM parameter settings, we have systematically varied the definitions for weighting factors and convolution. The details of these sensitivity studies are presented in Beirle et al. (2015).

Summarized, STREAM has been found to perform robust with respect to parameter settings. Variations of the definitions for the weights w_{pol} and w_{cld}, both varied by factors of 0.1 and 10, only cause marginal changes in TR of the order of 0.05-0.1*10^{15} molec/cm^2. This weak dependency on w_{pol} and w_{cld} is partly caused by the additional application of w_{TR} which stabilizes the algorithm.

Largest (but still comparably small) dependencies were found on convolution settings: If the wide convolution Kernel is applied globally, the performance is significantly worsened at high latitudes, where TR over clean regions are still about 0 on average, but reveal a much larger variability. If, on the other hand, the narrow convolution Kernel is applied globally, TR over continents decreases by about 0.1*10^{15} molec/cm^2.

9.4.4 Validation

For validation, STREAM was applied to synthetic data, where the “true” TR is known. In addition, comparisons to stratospheric corrections from SCIAMACHY based on limb measurements, which provide independent data, were performed. Below, we summarize the main findings, while further details are provided in Beirle et al. (2015).

9.4.4.1 Application of STREAM to synthetic data

Synthetic total NO_2 columns V were constructed as the sum of modelled stratospheric VCDs (from the CTM EMAC, sampled at the AURA overpass, Jöckel et al., 2015) and synthetic tropospheric residues T. The latter is defined as

$T=TVCD \times AMF_{trop}/AMF_{strat}$ based on the TVCDs and tropospheric AMF provided by DOMINO v2.

STREAM is applied to the synthetic $V(=V_{strat}+T)$. The resulting TR can then be compared to the a-priori “truth” based on TM4.

The error in T, i.e. the estimated minus a-priori TR, was found to be small: Over the Pacific, STREAM TR was found to be on average biased low by -0.05*10^{15} molec/cm^2. Monthly mean TR from STREAM and a-priori agree within ±0.1*10^{15} molec/cm^2 for 70% of the globe, and exceed ±0.3*10^{15} molec/cm^2 only regionally (2% of the globe).

9.4.4.2 Application of STREAM to SCIAMACHY

We applied STREAM to VCDs from SCIAMACHY and compared the resulting TR to the MPI-C SCIAMACHY product (Beirle and Wagner, 2012) based on a stratospheric correction by limb-nadir matching (Beirle et al., 2010). This allows a validation of STREAM against independent stratospheric measurements.

Again, a very good overall agreement of monthly means within ±0.1*10^{15} molec/cm^2 is found over 83% of the globe, and deviations of more than ±0.3*10^{15} molec/cm^2 are only found over 0.3% of the globe.

9.4.5 Verification Results

9.4.5.1 Description of test data used

STREAM was applied to measurements of the satellite instruments GOME, SCIAMACHY, GOME-2, and OMI. Within TROPOMI verification, we focus on results for OMI, as the TEMIS DOMINO product (v2, Boersma et al., 2011) can be considered as proxy for the TROPOMI prototype.

Here we present STREAM results for OMI and comparison to the prototype (DOMINO) for two days (1st of January and 1st of July 2005) as well as the respective monthly means. As a starting point, we use total slant column densities of NO_2 as provided in NASA hdf files (version OMNO2.003), and derive total VCDs V by applying the stratospheric AMFs provided ibidem. We use the NASA product instead of DOMINO as input to STREAM for two reasons:

- The NASA slant columns are already de-striped, while the DOMINO de-striping is done a-posteriori. While the DOMINO stratospheric fields are smooth, as the assimilation procedure de-stripes the stratospheric fields intrinsically, the total column is not. I.e. the tropospheric residues, which are key quantities for evaluating the performance of the stratospheric estimation, are fully affected by the OMI stripe pattern if based on DOMINO input for V. For TROPOMI, we thus strongly recommend that a de-striping algorithm is applied before the stratospheric estimation.
- Within DOMINO, AMFs are provided up to SZAs of 80°. The NASA dataset provides stratospheric VCDs and AMFs for SZAs up to 88°. This enables the application of STREAM up to higher latitudes.

9.4.5.2 Presentation and discussion of results

Figure 9.38 displays V for 1st of January and July 2005. Figure 9.40 to Figure 9.42 show the resulting tropospheric residues of different algorithms, i.e.,

1. a “classical” reference sector method (RSM), where stratospheric fields are estimated over the remote Pacific and are assumed to be zonally constant, has been included for comparison (Figure 9.40).
2. STREAM, as described in detail above, including one iteration with w_{TR} (Figure 9.41).
3. Assimilation, as provided by DOMINO (Figure 9.42). Note that the stratospheric columns are directly taken from the DOMINO v2 product, while tropospheric residues are calculated as the difference of total VCDs from NASA (as these are de-striped) and the DOMINO stratospheric column. This might introduce some small systematic biases ($<0.05*10^{15}$ molec/cm^2 on average) in the tropospheric residues caused by e.g. different temperature corrections in the NASA and DOMINO algorithms.

TRs are displayed for January (left) and July (right) 2005 for the first day of the month (top) and the monthly mean (bottom). All column densities are given in 10^{15} molec/cm^2.

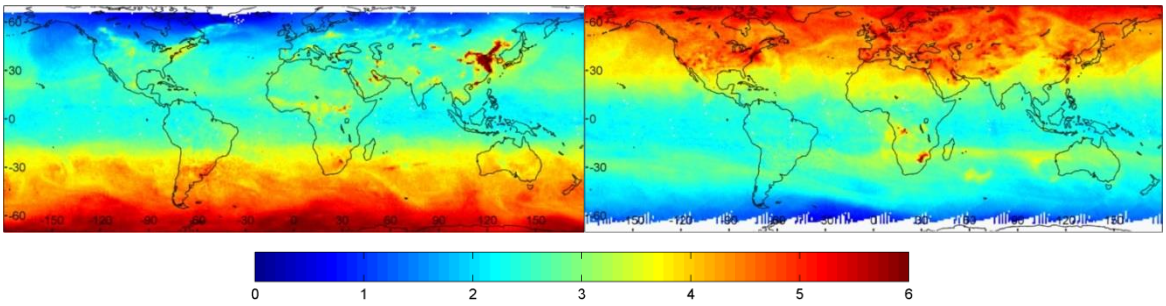

Figure 9.39: Total NO_2 VCD from OMI for 1st of January (left) / July (right) 2005.

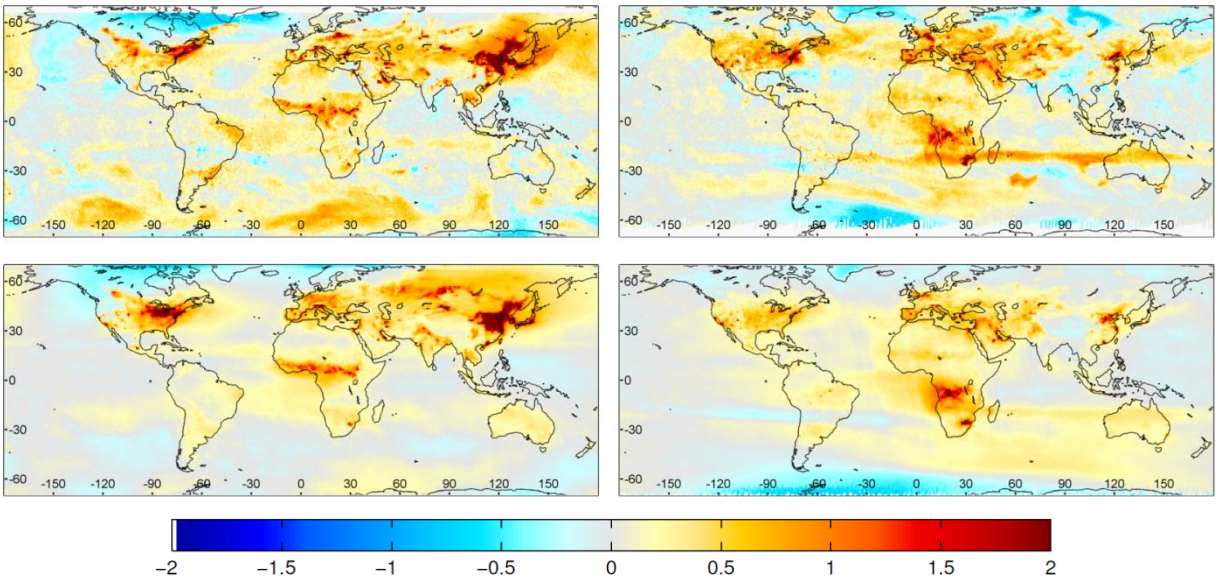

Figure 9.40: OMI NO_2 tropospheric residues based on RSM for January (left) / July (right) 2005 for the first day of the month (top) and the monthly mean (bottom).

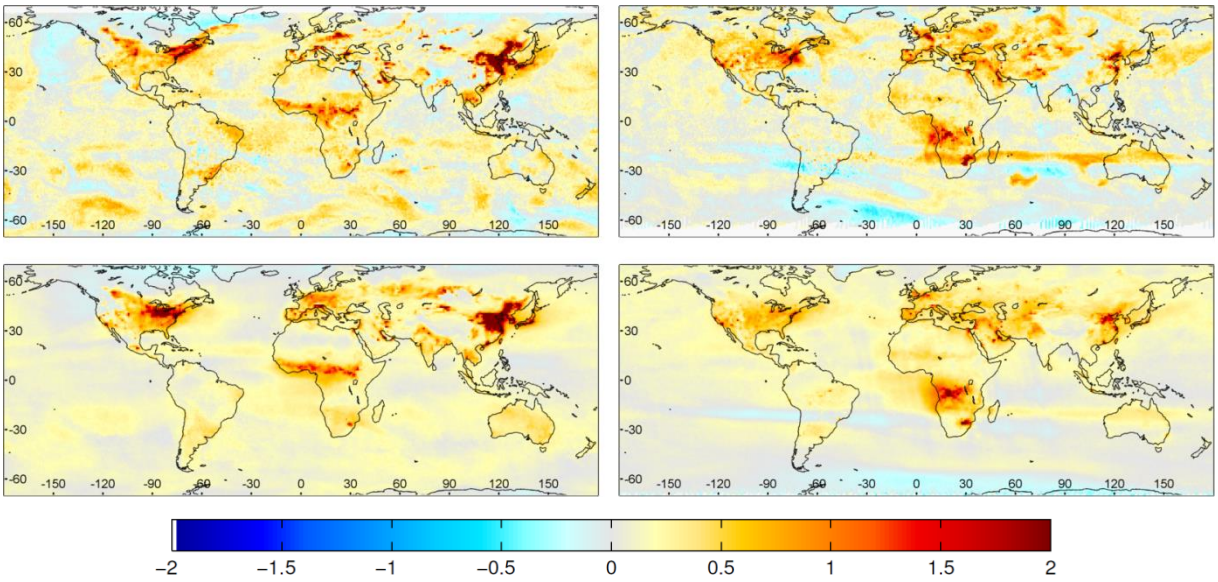

Figure 9.41: OMI NO_2 tropospheric residues based on STREAM for January (left) / July (right) 2005 for the first day of the month (top) and the monthly mean (bottom).

Note that the tropospheric residues are based on stratospheric AMFs. I.e., the real tropospheric VCDs are higher than TR by a factor of about 1 (over clean regions at low latitudes)up to 4 (at higher latitudes and/or in presence of tropospheric pollution), as the tropospheric AMFs are usually lower than the stratospheric AMFs.

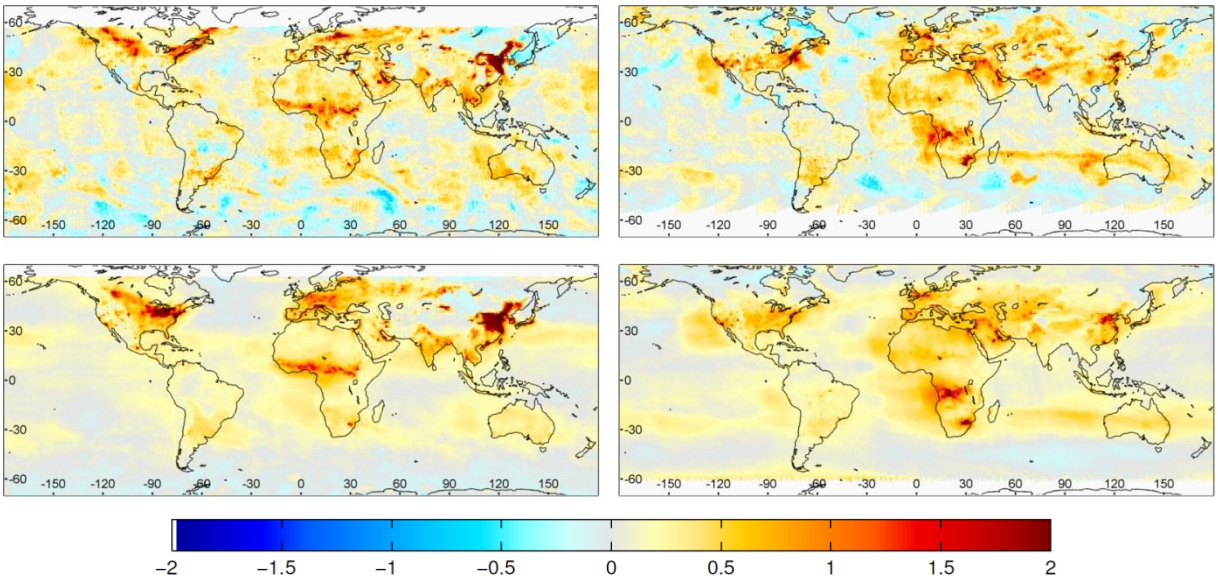

Figure 9.42: OMI NO_2 tropospheric residues based on assimilation (DOMINO v2) for January (left) / July (right) 2005 for the first day of the month (top) and the monthly mean (bottom).

Figure 9.43 summarizes the statistical distribution of TR from the different algorithms over different regions of the world, i.e., the Pacific (40°S-40°N, 180°W-140°W), remote regions (40°S-40°N, 140°W-180°E, w_{pol}=1), high latitudes (polewards from 55°N (Jan)/45°S (Jul), w_{pol}=1), and polluted (w_{pol}<1). As the TR is expected to be low in clean regions, high values for TR (median as well as variability) indicate shortcomings of the respective algorithm. Note that in Figure 9.43, only coincident measurements are included where TR is provided by each algorithm.

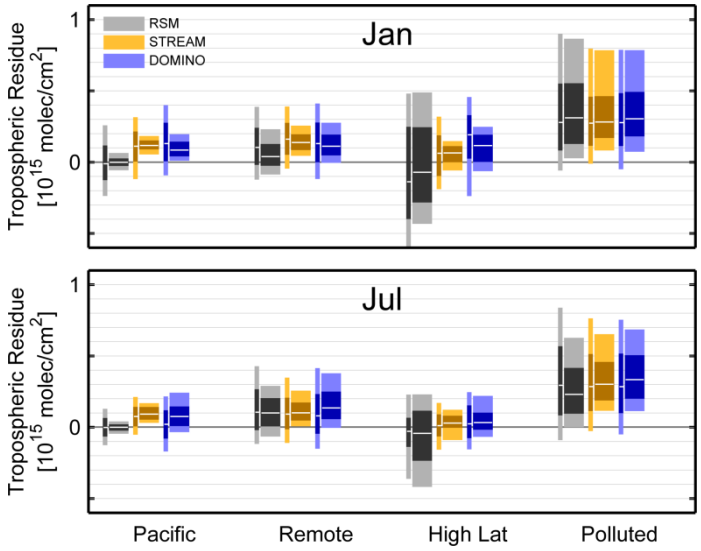

Figure 9.43: Statistics of OMI tropospheric residues TR from different algorithms (colour coded) for different regions of the globe (as defined in the text) for January (top) and July (bottom) 2005. Light and dark bars reflect the 10th-90th and 25th-75th percentiles, respectively. The median is indicated in white. Narrow bars show the statistics for the first day of the month, wide bars those of the monthly means.

Figure 9.40 illustrates the limitations of a simple RSM, in particular at high latitudes. Due to the polar vortex, negative TRs are derived over North America, on 1st of January as well as in the monthly mean. This is significantly improved by STREAM (Figure 9.41), and the spread of TR at high latitudes, as expressed by percentiles in Figure 9.43, is drastically decreased for STREAM. Also for unpolluted regions at low latitudes (outside the Pacific), STREAM TRs show a smaller variability than RSM.

While the problems caused by the polar vortex mostly affect winter months, the stratospheric estimation can also be challenging in summer months. On 1 July 2005, the “slanted” filament of enhanced NO_2 over the Pacific cannot be appropriately reflected by the assumption of longitudinal homogeneity of the simple RSM. Consequently, RSM shows a large “stripe” in the Indian Ocean on 1 July 2005, which is dampened, but still present in the monthly mean. As STREAM uses a wide convolution kernel at low latitudes, STREAM cannot fully resolve these structures as well.

Note that over the Pacific, TRs from RSM is 0 by construction (Figure 9.43), whereas STREAM results in a mean TR of about $0.1*10^{15}$ molec/cm^2. This is a consequence of the emphasis of clouded observations which actually provide measurements of the stratospheric column. An additional correction of the tropospheric background is thus not needed within STREAM.

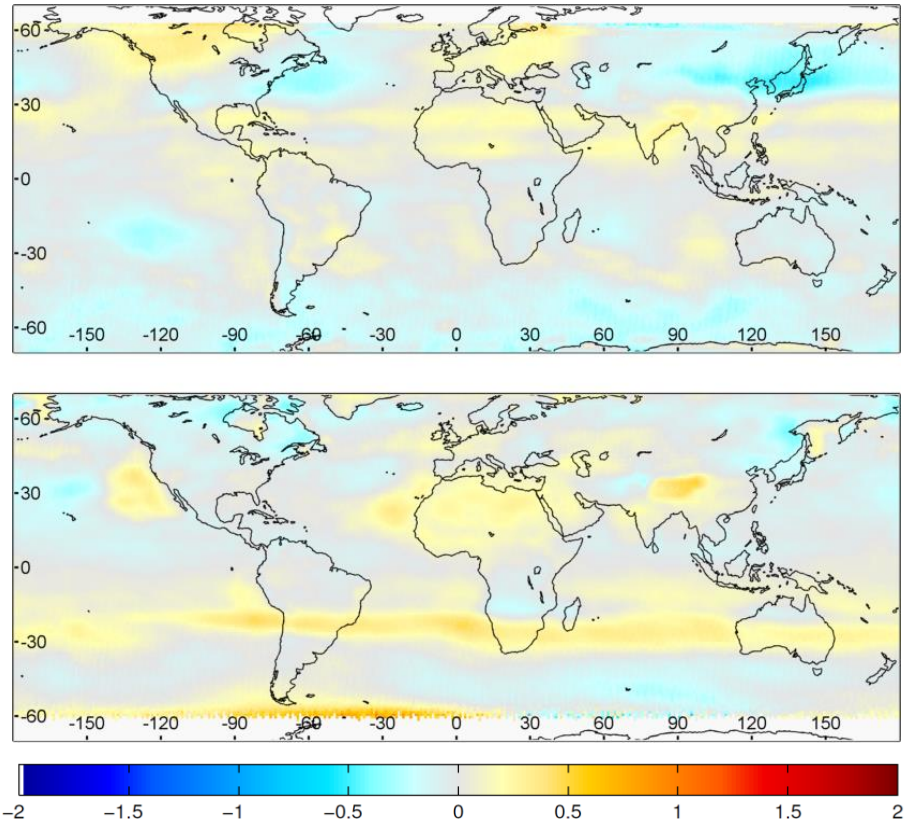

Figure 9.44: Difference of the tropospheric residues derived by DOMINO v2 and STREAM for January (top) and July (bottom) 2005.

Figure 9.44 displays the difference of monthly mean tropospheric residues from STREAM and DOMINO for January and July 2005.

DOMINO and STREAM show on average similar performance (medians and variability) over remote as well as over polluted regions (Figure 9.43). Daily tropospheric residues from STREAM (Figure 9.41) and DOMINO (Figure 9.42), however, look a bit patchy (up to about $\pm 0.5*10^{15}$ molec/cm^2), reflecting the small-scale patterns already present in the total columns (Figure 9.38) which are not resolved by neither STREAM nor DOMINO due to smoothing in the stratospheric estimate. It has to be investigated how far part of these structures are related to the spectral analysis (e.g., interferences with Ring effect etc.)

In the monthly means, these effects are at large part averaged out. Remaining differences between DOMINO and STREAM, as displayed in Figure 9.44, are generally low (within $\pm 0.1*10^{15}$ molec/cm^2 for most parts (70%) of the world, and above $\pm 0.3*10^{15}$ molec/cm^2 in only 3% of the globe). Deviations between prototype and verification algorithm are thus consistent with the estimated uncertainty of stratospheric estimation from assimilation of $\sigma = 0.15*10^{15}$ molec/cm^2 (Boersma et al., 2007).

But still, the systematic spatial patterns of deviations in TR indicate systematic shortcomings of either algorithm, providing a helpful hint for investigations of further algorithm improvement.

Below we shortly list the most striking differences:

- In July, both algorithms see a band of enhanced tropospheric NO_2 in the Indian Ocean west of Australia, but with different width and amplitude. The associated band at 30°S around the globe dominates the difference plot in July and covers South America, South Africa, and Australia (i.e. regions associated with NO_x emissions from soils, biomass burning and lightning.)
- DOMINO TRs are enhanced over the Sahara, which is not found by STREAM.
- West of the US and over the Himalaya, the DOMINO stratosphere shows a minimum, which does not occur in the monthly mean total columns resulting in enhanced tropospheric residues.

9.4.6 Summary of verification results and consequences for the prototype

Both algorithms (verification: STREAM (modified reference region); prototype: assimilation, similar to DOMINO v2.0) work generally well and could both be used for operational correction of the stratospheric column density. Differences are generally below 1 (typical) to 3 (regional) $x10^{14}$ molec/cm^2 (for monthly means, stratospheric AMF) in agreement with estimated uncertainties of stratospheric estimates. The remaining systematic spatial patterns need further investigations and might help to further improve either algorithm in the future.

From the investigations within TROPOMI verification, we conclude the following recommendations for the prototype:

1. Within TROPOMI, the destriping should be performed as first step after the spectral analysis, before the stratospheric estimation.
2. Large SZAs (up to 88°, as in the NASA product, instead of 80° in DOMINO v2) have also to be considered for the assimilation algorithm. Even if these observations might have only limited information content on tropospheric columns directly, they still affect the tropospheric residues significantly, as they strongly improve the stratospheric estimation at high latitudes. The comparison of stratospheric fields from different algorithms allows us to provide realistic estimates of the total tropospheric product caused by the stratospheric estimation, and to indicate particular problematic regions/months.

While the impact of the stratospheric estimation is negligible for most studies over regions with high tropospheric pollution, like China, Europe, or the US, it can still become highly important if small signals over extended areas are investigated, like NO_2 from soil emissions, biomass burning, or lightning (compare the tropospheric residues of the different products over e.g. the Sahara, Australia, or Siberia).

9.5 Total column algorithm

9.5.1 Algorithm description

The verification algorithm for total NO_2 vertical column density (VCD) is based on a standard Differential Optical Absorption Spectroscopy (DOAS) approach.

9.5.1.1 Slant Column Retrieval

The fitting window used in the slant column retrieval of the total column verification algorithm is 425-450 nm. A single NO_2 cross-section reference spectrum at 240K is used (Vandaele et al., 2002). Additionally, cross-sections of the interfering trace gases O_3, O_2-O_2 (Greenblatt et al., 1990) and H_2O HITRAN (Rothman et al., 2003) are included as well as a simulated Fraunhofer Ring spectrum to account for the filling-in of spectral lines ("Ring Effect") by inelastic rotational Raman scattering (RRS).

As the NO_2 absorption cross-section shows a distinct temperature dependence, this has to be taken into account to improve the retrieved column density. This correction is considered during air mass factor (AMF) calculations.

9.5.1.2 Tropospheric column calculation

The tropospheric NO_2 column algorithm of the total column verification algorithm consists of the following steps:

1. Calculation of an initial total NO_2 VCD
2. Estimation of the stratospheric component of the NO_2 column using a spatial filtering approach.
3. Conversion of the residual tropospheric SCD into a tropospheric VCD using an accurate tropospheric air mass factor.

In addition, the initial total NO_2 VCD is corrected for the tropospheric component under polluted conditions, to provide a more accurate total vertical column.

9.5.1.3 AMF and initial total VCD computation

To convert the NO_2 slant column densities (SCD) to vertical column densities (VCD), an initial total VCD is calculated at first. The needed AMF depends on the vertical NO_2 profile and different parameters like viewing geometry, surface albedo, clouds and aerosols.

As NO_2 is an optically thin absorber in the evaluated wavelength region, the radiative transfer calculations can be decoupled from the NO_2 profile shape. The final AMF can then be determined via altitude dependent and temperature corrected air mass factors for individual layers. These calculations are done with the Radiative Transfer Model (RTM) LIDORT (Spurr et al., 2001).

The initial total VCD is computed under the assumption that the troposphere is not polluted. Therefore, the air mass factor is based on stratospheric NO_2 profiles only, whereas the tropospheric NO_2 amount is assumed to be negligible. This approach is valid over large parts of the earth, but in areas with significant tropospheric NO_2, the total column densities are underestimated and need to be corrected. To incorporate the seasonal and latitudinal variation in stratospheric NO_2 in the air mass factor calculations, a harmonic climatology of stratospheric NO_2 profiles is used (Lambert and Granville, 2004). The climatology used for the surface albedo (including mean snow and ice cover) is derived from TOMS and GOME Lambert-equivalent reflectivity (LER) measurements at 380 and 440 nm (Boersma et al., 2004).

9.5.1.4 Stratospheric Estimation

After calculating the initial total NO_2 column, the stratospheric component of the initial total VCD can be estimated. This stratosphere-troposphere separation (STS) is based on the observation that stratospheric NO_2 has a smooth spatial behaviour and tropospheric contributions occur near source regions on smaller geographic scales. The STS algorithm uses a spatial filtering method:

At first, a global map has to be constructed from the initial total NO_2 columns by binning the last 24 hours of data on a spatial grid of 2.5º latitude × 2.5º longitude. To minimize tropospheric biases in the stratospheric field, a global mask is applied to eliminate areas with potentially high amounts of tropospheric NO_2. This pollution mask is derived from MOZART-2 model results: the areas in the model with monthly mean tropospheric NO_2 columns larger than 1.0×10^{15} molec/cm² are masked as polluted.

After pollution masking, the stratospheric NO_2 column is determined by low-pass filtering the initial NO_2 columns in the zonal direction (30º boxcar filter). This is done in two steps, where first the unmasked measurements with initial total VCD exceeding the (preliminary) stratospheric NO_2 column by more than one standard deviation are identified and excluded from the final analysis. Unmasked polluted measurements can occur when pollution events are missed by the model, for instance during transient pollution events. Finally, the stratospheric NO_2 is interpolated between latitude bands in order to avoid jump artefacts associated with a discrete latitude grid.

A limitation of the spatial filtering approach used here is that it will also take up background NO_2 in the free troposphere with smooth spatial behaviour. To correct for this effect, a simple correction will be applied: A fixed background NO_2 column (0.1×10^{15} molec/cm²) is subtracted from the derived vertical stratospheric NO_2 column. This offset for the background NO_2 column is derived from tropospheric NO_2 fields for the (unpolluted) Pacific region, as provided by the MOZART-2 model.

Compared to a simple Pacific Reference Sector method, this spatial filtering approach can better cope with longitudinal variations in mid and high latitudes. A disadvantage of this STS approach is that the stratospheric NO_2 column over some polluted regions is overestimated by the stratospheric correction procedure, which may result in an underestimation of the tropospheric NO_2 column.

9.5.1.5 Tropospheric Air Mass Factors

After the STS procedure, the tropospheric VCD V_t can be determined as follows:

$$V_t = (S - V_s M_s)/M_t \quad (26)$$

Here, S is the SCD calculated in slant column retrieval of the DOAS fit. V_s is the stratospheric component, as calculated with the previous spatial filtering method. M_s is the stratospheric air mass factor, already used for the calculation of the initial total VCD, and M_t is a tropospheric air mass factor calculated with an a priori tropospheric NO_2 profile. The tropospheric air mass factor depends on the same forward model parameters as the stratospheric air mass factor and is calculated equally.

After the calculation of the tropospheric column, a corrected total VCD $V_c=V_s+V_t$ can be calculated, if the initial total VCD exceeds the estimated stratospheric component V_s.

The a priori NO_2 profiles are obtained from a run of the global chemistry transport model (CTM) MOZART-2 (Horowitz et al., 2003). For the computation of the monthly average profiles are used (Nüß et al., 2006).

In the figure below the output of the retrieval algorithm is exemplarily shown for one day of GOME-2 data on MetOp-A.

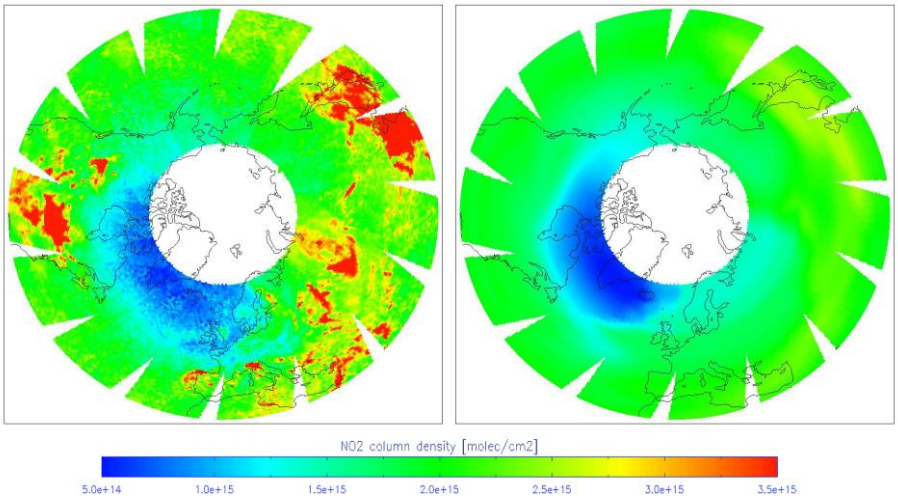

Figure 9.45: Total NO_2 distribution from GOME-2A (left) and the corresponding stratospheric NO2 distribution (right) for 22 February 2008.

9.5.1.6 Clouds

For the verification algorithm, the operational S5P cloud product can be used. The cloud data will be used in the AMF calculation to account for cloudy pixels. Here, the AMF can be expressed by the linear combination of a completely cloud free AMF (M_{clear}) and a completely cloudy AMF (M_{cloud}) using independent pixel approximation (IPA):

$$M = (1 - w)M_{clear} + wM_{clear} \quad (27)$$

The cloud weighted radiance fraction w can be calculated by the S5P cloud fraction c_f and the backscattered radiances for cloud-free (I_{clear}) and cloud-covered (I_{cloud}) conditions:

$$W = \frac{c_f I_{cloud}}{((1 - c_f)I_{clear} + c_f I_{cloud})} \quad (28)$$

9.5.2 Main differences to prototype algorithm

- Use of a different fitting window (425-450 nm instead of 405-465 nm)
- No liquid water absorption included in the fit
- Use of the LIDORT radiative transfer model for AMF calculations
- Use of climatological a priori NO_2 profiles from MOZART-2 instead of daily TM5 profiles

9.5.3 Error analyses

Basic error sources of the verification algorithm are the same as those occurring in the prototype algorithm. For OMI data, no detailed error analysis of the verification algorithm could be realised as yet. For GOME-2 data a detailed error analysis and description of the different error sources can be found in Valks et al. (2011).

9.5.4 Verification results

For the verification of the prototype algorithm, the NO_2 total column verification algorithm has been applied to the synthetic data. Slant column densities have been calculated for the different CAMELOT scenarios to compare with the results of the prototype and verification algorithms (see Section 9.3.4.1).

As the total column verification algorithm has not yet been fully implemented for OMI data and also for the prototype algorithm only slant column densities can be provided, a comparison based on the available SCD results has been performed for chosen OMI orbits, also used in the QA4ECV (Quality Assurance for Essential Climate Variables) project.

As the prototype algorithm cannot provide OMI total column data yet, results based on DOMINO v2.0 data of the current OMI product are used.

9.5.4.1 Comparison of NO_2 OMI SCD

To test the quality of the DOAS NO_2 slant column fit on OMI spectra, prototype and verification algorithm have been used to retrieve NO_2 slant column amounts for selected days, also used in the QA4ECV project (02.02.2005/16.08.2005/04.02.2013/04.08.2013). For the comparison, orbits over central Europe have been chosen and retrieved slant column densities have been plotted versus latitude as shown in the figures below.

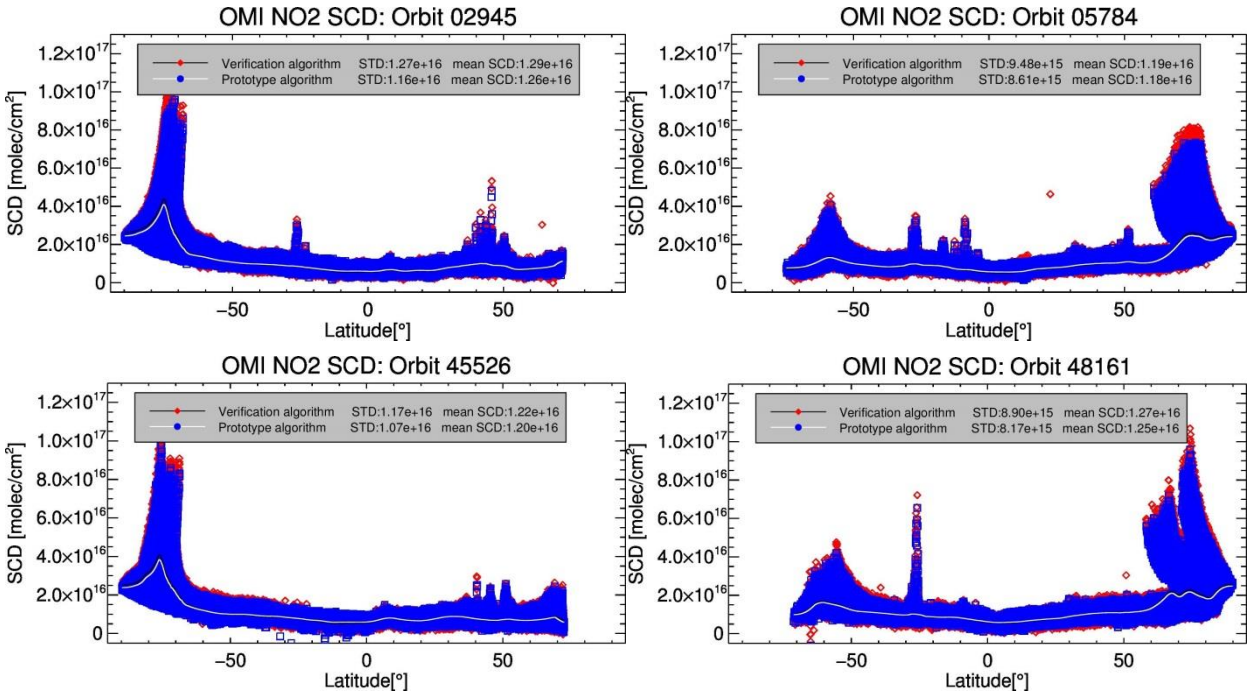

Figure 9.46: NO_2 SCD comparison of OMI orbits 2945 (2.2.2005) 5784 (16.8.2005), 45526 (4.2.2013), and 48161 (4.8.2013). Only measurements with SZA<88° have been chosen. Blue and red symbols represent individual measurements. White and black lines illustrate values averaged over 5° latitude bands. Also the mean slant column density and the standard deviation over the orbits have been calculated.

The comparison of the NO_2 slant columns of both algorithms shows overall good agreement, whereas the scatter of the slant columns of the prototype algorithm is about 10% below the verification algorithm. This may be issued from a slightly larger fitting window and the resulting better signal to ratio of the prototype algorithm.

Especially for high latitudes, the verification algorithm gives slightly higher values than the prototype algorithm. This could be explained by the temperature dependency of the NO_2 absorption cross-section, which will only be accounted for in a later retrieval step (see above).

The mean slant column densities for all orbits are in overall good agreement, but are slightly lower (~1-2%) than the prototype SCD.

When calculating the correlation between the verification and the prototype algorithm of the chosen orbits for the four days, a correlation coefficient larger than 0.99 is achieved and also the regression slope is close to 1. The offset between verification and prototype algorithm is always around $1x10^{15}$ molec/cm².

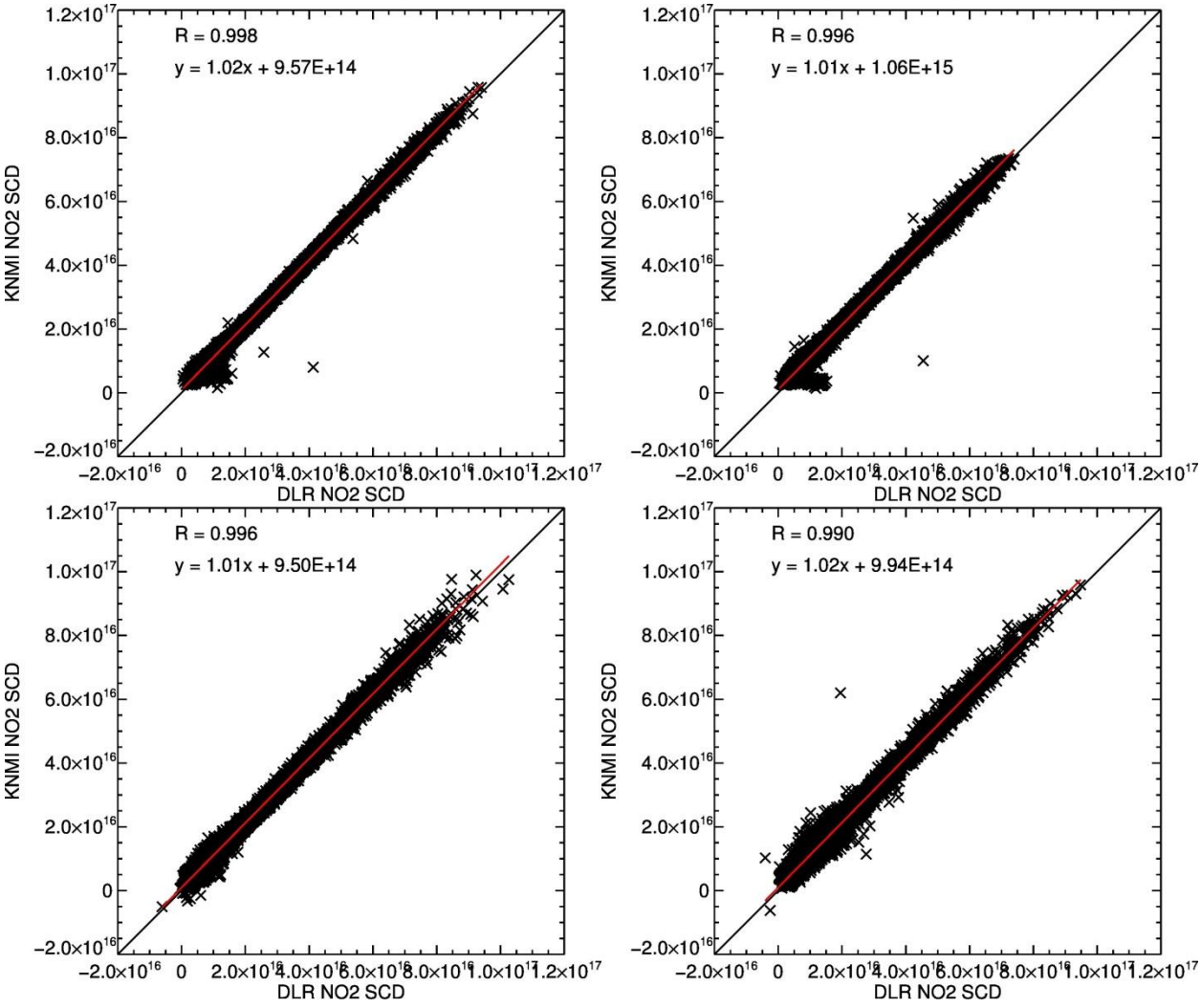

Figure 9.47: Correlation between prototype and verification algorithm for two comparison orbits over Central Europe. Top left: Orbit 2945 (2.2.2005) Top right: Orbit 5784 (2.8.2005) Bottom left: Orbit 45526 (4.2.2013) Bottom right: Orbit 48161(4.8.2013)

The overall agreement between the prototype and the verification algorithm is very good and only small differences can be observed.

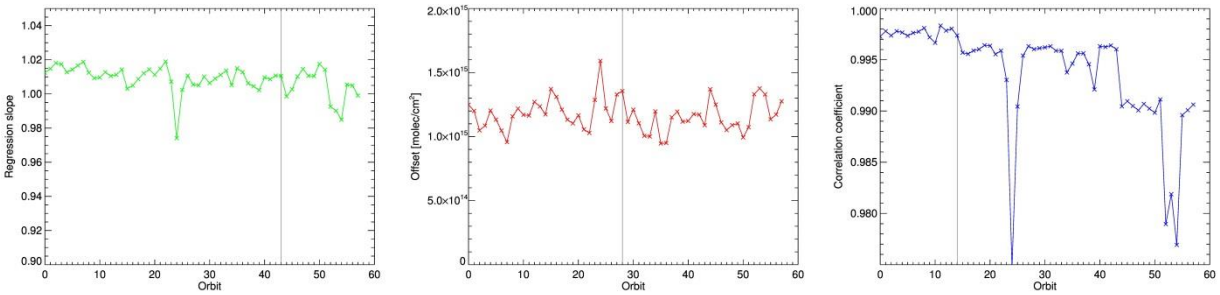

Figure 9.48: Correlation results for all comparison the days (2.2.2005 | 16.8.2005 | 4.2.2013 | 4.8.2013). Shown are correlation coefficient (left: blue), offset (middle: red), regression slope (right: green)

Deviations can be explained by the different settings of the slant column retrieval (cross-sections, fitting window, polynomial degree) and the different fitting method (prototype algorithm: non-linear/verification algorithm: linear).

9.5.5 Summary of verification results

The total column verification algorithm has been extensively tested on GOME-2 satellite data and gives good results. The slant column part of the algorithm has been adapted to OMI data and compared to first results of the prototype algorithm for individual orbits. The results are in very good agreement, whereat the prototype algorithm gives slightly better results with less scatter of data. Apart from the overall good correlation, larger deviations have to be considered only regarding offset.

9.6 References

Beirle, S., Kühl, S., Puķīte, J. and Wagner, T.: Retrieval of tropospheric column densities of NO_2 from combined SCIAMACHY nadir/limb measurements, Atmos. Meas. Tech., 3(1), 283–299, doi:10.5194/amt-3-283-2010, 2010.

Beirle, S. and T. Wagner: Tropospheric vertical column densities of NO_2 from SCIAMACHY, Available from: http://www.sciamachy.org/products/NO2/NO2tc_v1_0_MPI_AD.pdf, 2012.

Beirle, S., Sihler, H., and Wagner, T.: Linearisation of the effects of spectral shift and stretch in DOAS analysis, Atmos. Meas. Tech., 6, 661-675, doi:10.5194/amt-6-661-2013, 2013

Beirle et al., The STRatospheric Estimation Algorithm from Mainz (STREAM), to be submitted to AMT (TROPOMI special issue), 2015.

Boersma, K.F., H.J. Eskes and E.J. Brinksma, Error Analysis for Tropospheric NO_2 Retrieval from Space, *J. Geophys. Res.* **109** D04311, doi:10.1029/2003JD003962, 2004

Boersma, K. F., Eskes, H. J., Veefkind, J. P., Brinksma, E. J., van der A, R. J., Sneep, M., van den Oord, G. H. J., Levelt, P. F., Stammes, P., Gleason, J. F. and Bucsela, E. J.: Near-real time retrieval of tropospheric NO_2 from OMI, Atmos. Chem. Phys., 7(8), 2103–2118, 2007.

Boersma, K. F., Eskes, H. J., Dirksen, R. J., van der A, R. J., Veefkind, J. P., Stammes, P., Huijnen, V., Kleipool, Q. L., Sneep, M., Claas, J., Leitão, J., Richter, A., Zhou, Y., and Brunner, D.: An improved tropospheric NO2 column retrieval algorithm for the Ozone Monitoring Instrument, *Atmos. Meas. Tech.*, **4**, 1905-1928, doi:10.5194/amt-4-1905-2011, 2011

Bogumil, K., Orphal, J., Homann, T., Voigt, S., Spietz, P., Fleischmann, O. C., Vogel, A., Hartmann, M., Bovensmann, H., Frerick, J., and Burrows, J. P.: Measurements of molecular absorption spectra with the SCIAMACHY pre-flight model: instrument characterization and reference data for atmospheric remotesensing in the 230–2380 nm region, J. Photochem. Photobiol. A, 157, 157–167, 2003.

Bucsela, E. J., Krotkov, N. A., Celarier, E. A., Lamsal, L. N., Swartz, W. H., Bhartia, P. K., Boersma, K. F., Veefkind, J. P., Gleason, J. F. and Pickering, K. E.: A new stratospheric and tropospheric NO_2 retrieval algorithm for nadir-viewing satellite instruments: applications to OMI, Atmospheric Measurement Techniques, 6(10), 2607–2626, doi:10.5194/amt-6-2607-2013, 2013.Chance, K. and Kurucz, R.: An improved high-resolution solar reference spectrum for earth's atmosphere measurements in the ultraviolet, visible, and near infrared, Journal of Quantitative Spectroscopy and Radiative Transfer, 111, 1289–1295, 2010.

Danielson, J. J., and D. B. Gesch, Global Multi-Resolution Terrain Elevation Data 2010 (GMTED2010), Open-File Report, U.S. Geological Survey, 2011. http://pubs.usgs.gov/of/2011/1073/pdf/of2011-1073.pdf.

Dirksen, R. J., Boersma, K. F., Eskes, H. J., Ionov, D. V., Bucsela, E. J., Levelt, P. F. and Kelder, H. M.: Evaluation of stratospheric NO_2 retrieved from the Ozone Monitoring Instrument: Intercomparison, diurnal cycle, and trending, J. Geophys. Res.-Atmos., 116, D08305, doi:10.1029/2010JD014943, 2011.

Eskes, H. J., Velthoven, P. F. J. V., Valks, P. J. M. and Kelder, H. M.: Assimilation of GOME total-ozone satellite observations in a three-dimensional tracer-transport model, Q.J.R. Meteorol. Soc., 129(590), 1663–1681, doi:10.1256/qj.02.14, 2003.

Flemming, J., Inness, A., Flentje, H., Huijnen, V., Moinat, P., Schultz, M. G., and Stein, O.: Coupling global chemistry transport models to ECMWF's integrated forecast system, Geosci. Model Dev., 2, 253–265, doi:10.5194/gmd-2-253-2009, 2009.

Greenblatt, G. D., Orlando, J. J., Burkholder, J. B., and Ravishankara, A. R.: Absorption measurements of oxygen between 330 and 1140 nm, Journal of Geophysical Research, 95, 18 577–18 582, 1990

Hilboll, A., Richter, A., Rozanov, A., Hodnebrog, Ø., Heckel, A., Solberg, S., Stordal, F., and Burrows, J. P.: Improvements to the retrieval of tropospheric NO2 from satellite – stratospheric correction using SCIAMACHY limb/nadir matching and comparison to Oslo CTM2 simulations, *Atmos. Meas. Tech*., **6**, 565-584, doi:10.5194/amt-6-565-2013, 2013

Kleipool, Q. L., Dobber, M. R., De Haan, J. F., and Levelt, P. F, Earth surface reflectance climatology from 3 years of OMI data. J. Geophys. Res., 113(D18308), 2008

Knutsson, H. and Westin, C.-F.: Normalized and differential convolution, in , 1993 IEEE Computer Society Conference on Computer Vision and Pattern Recognition, 1993. Proceedings CVPR '93, pp. 515–523., 1993.

Lambert, J.-C., and J. Granville, Harmonic climatology of stratospheric NO2, BIRA-IASB, Brussels, 2004.

Leue, C., Wenig, M., Wagner, T., Klimm, O., Platt, U. and Jähne, B.: Quantitative analysis of NO_x emissions from Global Ozone Monitoring Experiment satellite image sequences, J. Geophys. Res., 106(D6), 5493–5505, 2001.

Lorente Delgado, A., et al (in prep.): Evaluation of radiative transfer models for reflectance and air mass factor calculation.

Nüß, H. Richter, A., Valks, P., and Burrows, J. P., Improvements of the NO2 Total Column Retrieval for GOME-2. O3M SAF Visiting Scientist Activity, Final Report. Universität Bremen, 2006.

Richter, A., Begoin, M., Hilboll, A., and Burrows, J. P.: An improved NO2 retrieval for the GOME-2 satellite instrument, *Atmos. Meas. Tech.*, **4**, 1147-1159, doi:10.5194/amt-4-1147-2011, 2011

Rozanov, V. V., Rozanov, A.V., Kokhanovsky, A.A., and Burrows, J.P., Radiative Transfer through Terrestrial Atmosphere and Ocean: Software Package SCIATRAN., Journal of Quantitative Spectroscopy and Radiative Transfer, doi:10.1016/j.jqsrt.2013.07.004, 2014

Serdyuchenko, A. et al., High spectral resolution ozone absorption cross-sections – Part 2: Temperature dependence. *Atmos. Meas. Tech. Discuss.*, 6(4), pp.6613–6643, 2013

Spurr, R. J. D., T. P. Kurosu, and K. V. Chance (2001), A Linearized discrete Ordinate Radiative Transfer Model for Atmospheric Remote Sensing Retrieval, J. Quant. Spectrosc. Radiat. Transfer, 68, 689-735.

Stohl, A., Huntrieser, H., Richter, A., Beirle, S., Cooper, O. R., Eckhardt, S., Forster, C., James, P., Spichtinger, N., Wenig, M., Wagner, T., Burrows, J. P. and Platt, U.: Rapid intercontinental air pollution transport associated with a meteorological bomb, Atmos. Chem. Phys., 3(4), 969–985, 2003.

Thalman, R. and R. Volkamer. Temperature Dependant Absorption Cross-Sections of O_2-O_2 Collision Pairs between 340 and 630 nm at Atmospherically Relevant Pressure, 2013, Physical Chemistry Chemical Physics, 15(37), 15371-15381, doi: 10.1039/C3CP50968KVandaele, A., Hermans, C., Simon, P., Carleer, M., Colin, R., Fally, S., Mérienne, M., Jenouvrier, A., and Coquart, B.: Measurements of the NO2 absorption cross-section from 42 000 cm-1 to 10 000 cm-1 (238–1000 nm) at 220 K and 294 K, Journal of Quantitative Spectroscopy and Radiative Transfer, 59, 171–184, 1998

Vandaele, A., Hermans, C., Simon, P., Carleer, M., Colin, R., Fally, S., Mérienne, M., Jenouvrier, A., and Coquart, B.: Measurements of the NO2 absorption cross-section from 42 000 cm-1 to 10 000 cm-1 (238–1000 nm) at 220 K and 294 K, Journal of Quantitative Spectroscopy and Radiative Transfer, 59, 171–184, 1998

Valks P., Pinardi G., Richter A., Lambert J.-C., Hao N., Loyola D., Van Roozendael M., Emmadi S. Operational total and tropospheric NO2 column retrieval for GOME-2, Atmospheric Measurement Techniques, vol. 4, pp. 1491-1514, 2011.

Vountas, M., Rozanov, V.V., and Burrows, J.P.: Ring Effect: Impact of rotational Raman Scattering on Radiative Transfer in Earth's Atmosphere, J. Quant. Spec. Rad. Transf., 60(6), 943-961, 1998

Vountas, M., Richter, A., Wittrock, F., and Burrows, J. P.: Inelastic scattering in ocean water and its impact on trace gas retrievals from satellite data, Atmos. Chem. Phys., 3, 1365-1375, 2003

Zien, A. W., Richter, A., Hilboll, A., Blechschmidt, A.-M., and Burrows, J. P.: Systematic analysis of tropospheric NO_2 long-range transport events detected in GOME-2 satellite data, Atmos. Chem. Phys., 14, 7367-7396, doi:10.5194/acp-14-7367-2014, 2014.

10 SO_2 Column

Authors: Christoph Hörmann (MPIC), Pascal Hedelt (DLR-IMF)

10.1 Document changes

Changes in issue 2.0:

- General revised version of issue 1.0.2
- Final comparison of Verification/Prototype Algorithm results for real data

10.2 Verification approach

The S5P SO_2 verification algorithm is based on the Differential Optical Absorption Spectroscopy (DOAS) technique in the UV wavelength range and retrieves SO_2 columns from boundary layer and anthropogenic pollution up to strong explosive eruptions of volcanoes. In contrast to other commonly used approaches, the verification algorithm uses a combination of different evaluation fit windows to correct for non-linear effects that appear for very high SO_2 concentrations during volcanic eruptions.

DOAS was found to be fast and reliable in the UV in order to retrieve atmospheric SO_2. The method chosen by the verification team is similar to the one used for the prototype algorithm in terms of using a combination of different fit windows. However, since different settings and assumptions are made, a verification exercise is still useful. Especially for scenarios with high SO_2 loads (e.g. volcanic eruptions), it is expected that the usage and combination of different fit ranges for prototype and verification algorithm will lead to discrepancies.

The SO_2 verification algorithm is subdivided into 2 major parts:

- Spectral retrieval of the SO_2 SCDs (MPIC)
- Radiative transfer simulations and conversion to VCDs (DLR-IMF)
- The verification approach is twofold:
- First, both the operational Prototype and the Verification algorithms are applied to a set of synthetic spectra. Then, in a second step the retrieval algorithms are applied to real measured data from OMI.

10.3 Algorithm description

10.3.1 Approach

In order to retrieve SO_2 slant columns, a classical DOAS approach is used. The algorithm takes advantage of the narrow-band SO_2 absorption features in the wavelength range between 312.1 and 324nm (SO_2 standard retrieval – SO_2 SR).

To prevent non-linear effects in the SO_2 retrieval during major volcanic eruptions with very high concentrations of SO_2 in the corresponding volcanic plumes, two additional fitting windows are used within the Verification Algorithm:

1) SO_2 MR (SO_2 medium retrieval : 318.6 – 335.1 nm)
2) SO_2 AR (SO_2 alternative retrieval : 323.1 – 335.1 nm)

Using both alternative fitting windows allows a smooth transition between the SO_2 slant column density (SCD) retrieved in case of major volcanic eruptions.

Alternative evaluation schemes at different wavelength regions have recently been developed and evaluated in Bobrowski et al. (2010) and the combination of two optimised fitting ranges has been applied for major volcanic eruptions in Hörmann et al. (2013). Although approaches have been reported in the literature which correct for non-linear effects iteratively based on models, the usage of such a combined retrieval is a sufficient and in particular comparably fast method, which will be able to handle increased data traffic as expected from S5P.

10.3.2 Realization

10.3.2.1 SO_2 slant column density

The standard SO_2 DOAS retrieval includes absorption cross-sections for SO_2 (Bogumil et al., 2003), O_3 (Brion et al., 1983), an inverse reference spectrum (to correct for possible spectrographic straylight) as well as a Ring spectrum (calculated by using the daily solar reference spectrum). Furthermore, the approach by Puķīte et al. (2010) has been included in the fitting routine, where the effects of the strongly non-linear O_3 absorptions in the UV are minimized by including two pseudo-absorption cross-sections of O_3 (one scaled by wavelength and the other one squared) in addition to the regularly used O_3 cross-section. For the alternative retrieval, the evaluation scheme additionally includes a cross-section for BrO (Wilmouth et al., 1999). While the presence of stratospheric BrO typically has no significant influence on the resulting SO_2 SCDs or the general fit quality, large amounts of volcanic BrO may appear for major volcanic eruptions as has been shown in Theys et al. (2009) and Hörmann et al. (2013).

Due to spectral interferences between the SO_2 and O_3 cross-sections and a possible remaining instrumental bias, an empirical offset correction is needed and applied to the SCDs of all three fit windows. This correction accounts for systematic biases in the SO_2 SCD and is currently estimated from a reference area over the Pacific Ocean (± 10°N, 105-135°W), where the SO_2 vertical column is expected to be close to zero due to the absence of significant emission sources. No additional correction is applied for a possible latitudinal dependence. The normalization algorithm includes the correction for the so-called ‘striping effect’ that is mainly caused by hot and transient pixels in the instrument‘s two-dimensional CCD as well as elevated dark current signals. The offset is calculated for each pixel row individually, in contrast to the application on one-dimensional detectors (e.g. like GOME-2A/B). Like for other two-dimensional CCD detectors (e.g., as used in the OMI instrument, see Figure 10.1), the striping effect is also expected for S5P data.

Furthermore a temperature correction is applied to the retrieved SO_2 SCDs since the retrieval is performed using a SO_2 cross-section taken at a fixed temperature of 203K which is appropriate for a volcanic SO_2 plume at 15km. Since volcanic plumes (and also anthropogenic emissions in the planetary boundary layer) occur at different altitudes, a scaling is performed to correct for this.

SCD_SR_Tcorr=SCD_AR*([2.39E-3 * T] + 0.511)

SCD_MR_Tcorr=SCD_MR*([2.41E-5 * T^2] – [6.11E-3 * T] + 1.25)

SCD_AR_Tcorr=SCD_AR*([4.28E-3 * T] + 0.131),

where T is the temperature at the given plume height or surface altitude (cf. Section 10.3.2.3).

The background- and temperature corrected SCDs are then subsequently converted to total vertical column densities (VCD).

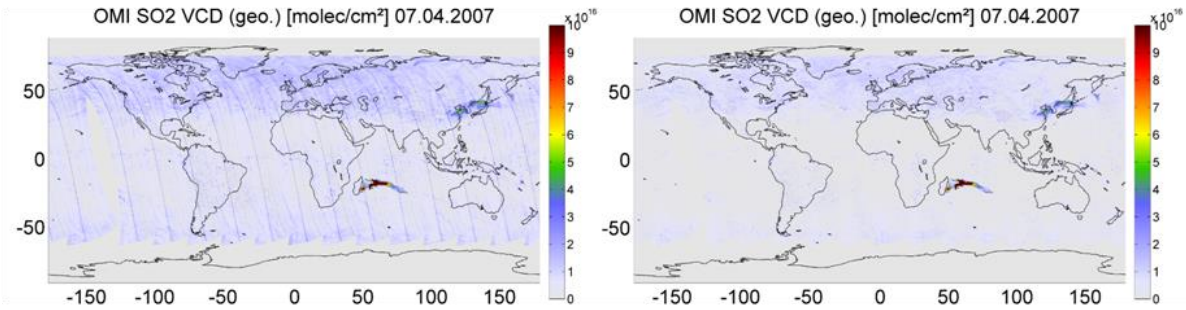

Figure 10.1: SO_2 VCD (geometrical AMF) retrieved from OMI. Left: raw data without striping correction. Right: Same data after application of a de-striping algorithm.

10.3.2.2 Combination approach for SO_2 SCDs from the SR, MR and AR

Initially, the approach by Hörmann et al. (2013) has been mainly used to merge the SO_2 SCDs from both evaluation schemes into one final "combined SO_2 product", where all SO_2 SCDs from the SR that exceed a threshold of $1 \cdot 10^{18}$ molec/cm² are replaced by the corresponding SCDs from the SO_2 AR. However, first results from the analysis of synthetic test data and real data (OMI/GOME-2) showed that this approach may lead to inconsistencies whenever the SO_2 concentration is too high to be accurately retrieved from the SR, but still too low for an accurate retrieval in the proposed alternative evaluation range.

The current approach uses different transition criteria for the combination of SO_2 SR, MR and AR, based on the results of the synthetic spectra scenarios of volcanic plumes (see Section 10.7.2). As the final criteria will always be a compromise between instrumental sensitivity, the consistency of data and a priori assumptions, final fit window transition criteria for S5P may slightly differ once first real measurements will be analysed.

The fit-window transition criteria are:

1) SR SCDs $\leq 4 \times 10^{17}$ molec/cm²

   → SO_2 SR

2) SR SCDs $> 4 \times 10^{17}$ molec/cm² and $< 9 \times 10^{17}$ molec/cm²:

   → $SO_2\ SR \cdot [1 - SO_2\ SR/9 \times 10^{17}] + SO_2\ MR \cdot [SO_2\ SR/9 \times 10^{17}]$

3) SO_2 SR $\geq 9 \times 10^{17}$ molec/cm² and SO_2 MR $\leq 2.4 \times 10^{18}$ molec/cm²

   → SO_2 MR

4) MR SCDs $\geq 2.4 \times 10^{18}$ molec/cm² and $< 4.6 \times 10^{18}$ molec/cm²:

   → $SO_2\ MR \cdot [1 - SO_2\ MR/4.6 \times 10^{18}] + SO_2\ AR \cdot [SO_2\ MR/4.6 \times 10^{18}]$

5) AR SCDs $\geq 4.6 \times 10^{18}$ molec/cm²

   → SO_2 AR

As it is indicated by criteria 2) and 4), the algorithm tries to allow for a slow and smooth transition between SO_2 SR/MR and SO_2 MR/AR by linearly decreasing the weight of the former fit window and at the same time increasing the weight of the following fit window.

Note that the SO_2 vertical columns are first calculated for each fitting window separately and then combined and weighted accordingly to provide the final VCD.

10.3.2.3 SO_2 vertical column density

In order to convert the retrieved SO_2 slant columns into vertical columns, a single-wavelength Air Mass Factor (AMF) for each of the three fitting windows (SO_2 SR, MR and AR) is calculated using the radiative transfer model LIDORT LRRS v2.3 (Spurr, 2008). The AMF depends on the viewing angles and illumination, surface and cloud conditions as well as on the O_3 total column, which is taken from the O_3 total column retrieval. A cloudy and clear-sky AMF is calculated using temperature dependent cross-sections for SO_2 (Bogumil et al., 2003) and O_3 (Brion et al., 1983):

$$\mathrm{AMF}(\lambda) = \frac{\ln\left(\frac{I_{+SO2}}{I_{-SO2}}\right)}{\tau_{SO2}} \tag{29}$$

with $(\mathrm{I}_{+\mathrm{SO2}})$ and $(\mathrm{I}_{-\mathrm{SO2}})$ being simulated Earthshine spectra with and without including SO_2 as a trace gas, respectively. Both AMFs are combined using the cloud fraction information.

The US standard atmospheric profile was used as well as TOMS v7 O_3 profiles. For volcanic eruption scenarios a Gaussian shaped vertical SO_2 distribution with a FWHM of 2.5 km was used. Since the SO_2 plume height is unknown at the time of the measurement, an AMF for three different plume heights is calculated which represents the full range of volcanic eruption events: a 2.5 km plume height which represents passive degassing of low volcanoes and anthropogenic emissions, a 6 km plume height for effusive volcanic eruptions or passive degassing of high volcanoes and a 15 km plume height for explosive eruptions. The corresponding atmospheric temperatures for the temperature correction are T=273, 243, 203 K, respectively (see Section 10.3.2.1)

For the three fitting windows (SO_2 SR, MR and AR) the verification algorithm calculates the AMF at the following wavelength and a-priori SO_2 vertical columns:

1) SR: 313nm, VCD=$4\text{x}10^{17}$ molec/cm²
2) MR: 318nm, VCD=$2\text{x}10^{18}$ molec/cm²
3) AR: 323nm, VCD=$7\text{x}10^{18}$ molec/cm²

Please note that the wavelengths are chosen close to the corresponding major SO_2 absorption band, although they are slightly below the fit range for the SO_2 MR/AR. For each fit window the VCD is calculated and then the final SO_2 VCD is determined using the selection and weighting criteria as described before.

10.4 Main differences to prototype algorithm

The verification algorithm uses three different fitting windows, since it was found in a previous version of the verification report that with only two fitting windows a smooth transition was not possible. Note that the wavelength ranges of the fitting windows are slightly different:

- Prototype algorithm:
  - 312-327nm / 325-335nm / 360-390nm
- Verification algorithm:
  - 312.1-324nm / 318.6-335.1nm (SO2 MR) / 323.1-335.1nm (SO2 AR)

Especially the alternative fit windows (SO_2 MR/AR) strongly differ from the ones that are used for the Prototype Algorithm, so the differences between both algorithms are more distinct (see also Section 10.7.2 and 10.7.3).

The Prototype algorithm uses a SCD background correction based on the O_3 SCD retrieved in the main SO_2 fit window and a latitude-dependent correction for the two alternative fit windows. In the verification algorithm an empirical offset correction over the Pacific Ocean is applied to all fitting windows (see Section 10.3.2.1).

The prototype algorithm uses box-AMFs in order to convert slant columns to vertical columns for volcanic profiles, whereas Gaussian-shaped profiles are considered in the verification algorithm.

Especially for high SO_2 concentrations, the different algorithms will differ because of the different treatment of radiative transfer effects:

- different fitting window ranges
- different background correction schemes
- different temperature correction schemes
- different AMF calculation scheme
- different a-priori profiles for volcanic eruptions
- cloud impact and correction

Furthermore, differences will depend on the specific criteria that are used for the combination process of resulting SO_2 SCDs from the fitting windows.

10.5 Error analyses

One of the main uncertainties for the SO_2 vertical column retrieval is the typically unknown SO_2 profile. This is especially the case during volcanic eruptions. Due to the lack of plume height information, the AMF calculation can usually only be made using a priori SO_2 profiles that are associated with different scenarios (e.g. anthropogenic emissions/degassing volcanoes, minor volcanic eruptions, major volcanic eruptions).

The influence of volcanic aerosols/ash on the SO_2 retrieval for both evaluation ranges is another uncertainty that is currently still under investigation. It was found that large amounts of ash might have a large impact on the SO_2 SCD, especially if the corresponding spectra were recorded at large viewing zenith angles. First case studies also showed that this effect is not equally strong for different SO_2 evaluation schemes (SR, MR and AR).

The approach to merge the results from all three SO_2 evaluation schemes into one “combined” SO_2 product may lead to inconsistencies, whenever the SO_2 concentration is too high to be accurately retrieved from one evaluation scheme, but still too low for an accurate retrieval in the proposed alternative evaluation range. However, a detailed analysis of the processed synthetic test data results showed that current transition criteria allow a smooth transition between all used fitting windows (see Section 10.7.1).

10.6 Definition of test data

The following data have been used as test data:

1) Synthetic data:

- Synthetic data for an extensive simulation of several volcanic scenarios at different altitude regimes (boundary layer, free troposphere and lower stratosphere) and various total vertical column amounts.
- Synthetic data based on atmospheric profiles from the CAMELOT study (data already available within the project), including different scenarios for a wide range of conditions such as anthropogenic pollution over China, Europe or the US East coast as well as one volcanic scenario (Mt. Etna).

Note that it turned out that the pre-defined CAMELOT scenarios include quite low SO_2 amounts (even for the volcanic scenario), such that a successful SO_2 retrieval could not be performed by both the prototype and verification algorithms. Therefore, the volcanic scenario has been modified by upscaling of the original SO_2 amount by factors of 10, 50, 100, 300, 500 and 1000 (see Section 10.6.3).

- Synthetic data for an extensive simulation of several volcanic scenarios at different altitude regimes (boundary layer, free troposphere and lower stratosphere) and various total vertical column amounts (see Section 10.6.5).

2) Real data:

- OMI is chosen as a source of real data, as the instrumental design of OMI and TROPOMI is similar. In particular, measurements that were not affected by the "row anomaly" (before June 2007) were analysed by the verification algorithm that has been successfully adapted for the OMI and GOME-2 A/B instruments

Note that the application of the verification of synthetic data has been initially used to test and finalize the verification algorithm.

10.7 Verification Results

10.7.1 Results of SO_2 box-profiles scenarios

By analyzing the SO_2 box-profile scenarios it was found that the SO_2 MR fit window optimizes the transition from SO_2 SR to SO_2 AR results, especially for moderate VCDs that are already affected by non-linear effects for the SO_2 SR, but yet too low to be adequately detected within the SO_2 AR fit range.

As a first test scenario, a near-nadir geometry has been analysed (SZA=26.89°, LOS=2.22° and AZIM=67.09°). The retrieved SO_2 VCDs were found to be closest to the "real" VCD when applying AMFs at 313 nm (SO_2 SR), 318 nm (SO_2 MR) and 323 nm (SO_2 AR). The results for the 10-11 km SO_2 layer height are presented for all three fit windows in Figure 10.2 - Figure 10.4.

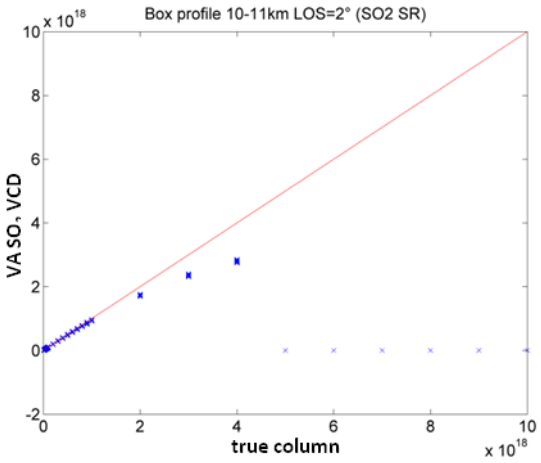

Figure 10.2: SO_2 SR VCDs for a near-nadir SO_2 box scenario (SZA=26.89°, LOS=2.22° and AZIM=67.09°) and homogeneous SO_2 layer at 10-11km, using an AMF at 313 nm and known SO_2 VCD. The red slope indicates the "true" SO_2 VCD. For large VCDs, the usage of the AMF at a single wavelength is not sufficient to correct for non-linear effects. For VCDs > 4E18 molec/cm² the algorithm fails to calculate SCDs due to missing convergence of the fit.

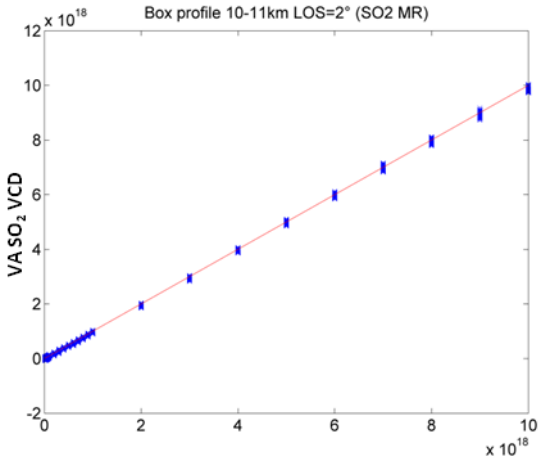

Figure 10.3: SO_2 MR VCDs for a near-nadir SO_2 box scenario (SZA=26.89°, LOS=2.22° and AZIM=67.09°) and homogeneous SO_2 layer at 10-11km, using an AMF at 318 nm and known SO_2 VCD. The red slope indicates the "true" SO_2 VCD. The main uncertainty can be estimated by the standard deviation of all noisy realisations for a given VCD (retrieved VCDs on the y-axis consist of 200 individual retrievals for spectra at a SNR of 1000).

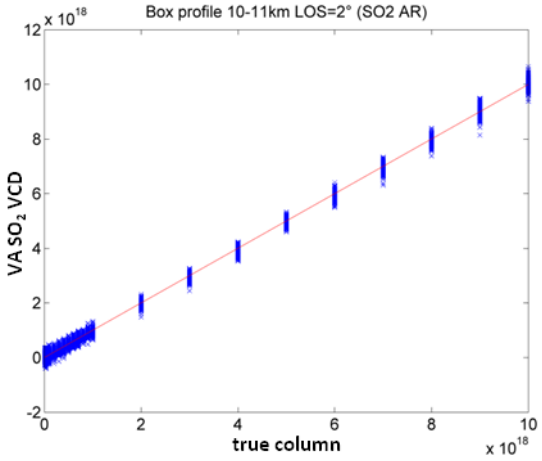

Figure 10.4: SO_2 AR VCDs for a near-nadir SO_2 box scenario (SZA=26.89°, LOS=2.22° and AZIM=67.09°) and homogeneous SO_2 layer at 10-11km, using an AMF at 323 nm and known SO_2 VCD. The red slope indicates the "true" SO2 VCD. Due to the reduced sensitivity of the SO2 AR fit window, all retrieved VCDs show increased variability with respect to the "true" VCD.

For this first rather simple test scenario, it was found that it is crucial to choose a SO_2 cross-section at a temperature that fits the atmospheric temperature of the regarded layer height. Therefore, a SO_2 cross-section at 223K was included for the retrieval of a 10-11 km layer, at 273K for a 5-6 km layer and 293K for a 1-2 km layer.

Figure 10.5 illustrates the large differences that are found for an inappropriate selection of the SO_2 cross-section temperature. Instead of the SO_2 cross-section at 223K, the cross-section at 293K was included for the retrieval of the SO_2 MR for the near nadir scenario and a plume height of 10-11km (cf. Figure 10.3). Large differences occur, especially for large SO_2 VCDs, and can be up to 40% when compared to the results when using the cross-section at 223K. Further comparisons showed that the usage of a SO_2 cross-section at too low temperatures will lead to SO_2 VCDs that underestimate the 'real' VCD, while using a SO_2 cross-section at too high temperatures will lead to an overestimation.

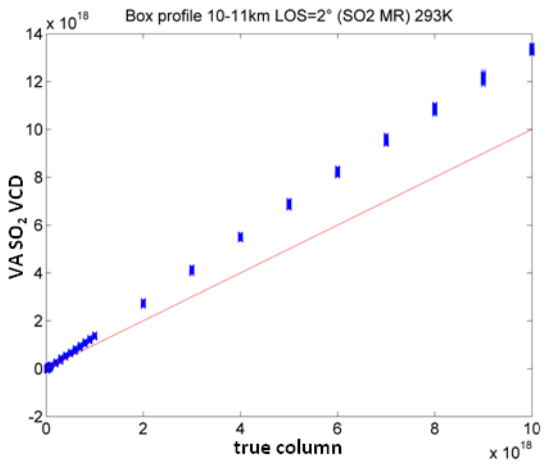

Figure 10.5: SO_2 MR VCDs for a near-nadir SO_2 box scenario (SZA=26.89°, LOS=2.22° and AZIM=67.09°) and homogeneous SO_2 layer at 10-11km, using an AMF at 318 nm and known SO_2 VCD, this time using the SO_2 cross-section at 293K instead of the one at 223K. Large differences occur (especially for large VCDs) that may be up to 40% compared to the results using the 223K SO_2 cross-section.

According to the results in Figure 10.2 - Figure 10.4, the optimized verification algorithm is clearly capable to calculate accurate SO_2 VCDs if the actual VCD is known. In reality, however, the “true” VCD is usually unknown.

Figure 10.6 - Figure 10.8 show the results for all three tested box-profile scenarios covering a wide range of LOS angles.

- SZA=26.89°, LOS=2.22°, AZIM=67.09°
- SZA=26.13°, LOS=29.13°, AZIM=77.38°
- SZA=26.4°, LOS=58.27°, AZIM=94.33°

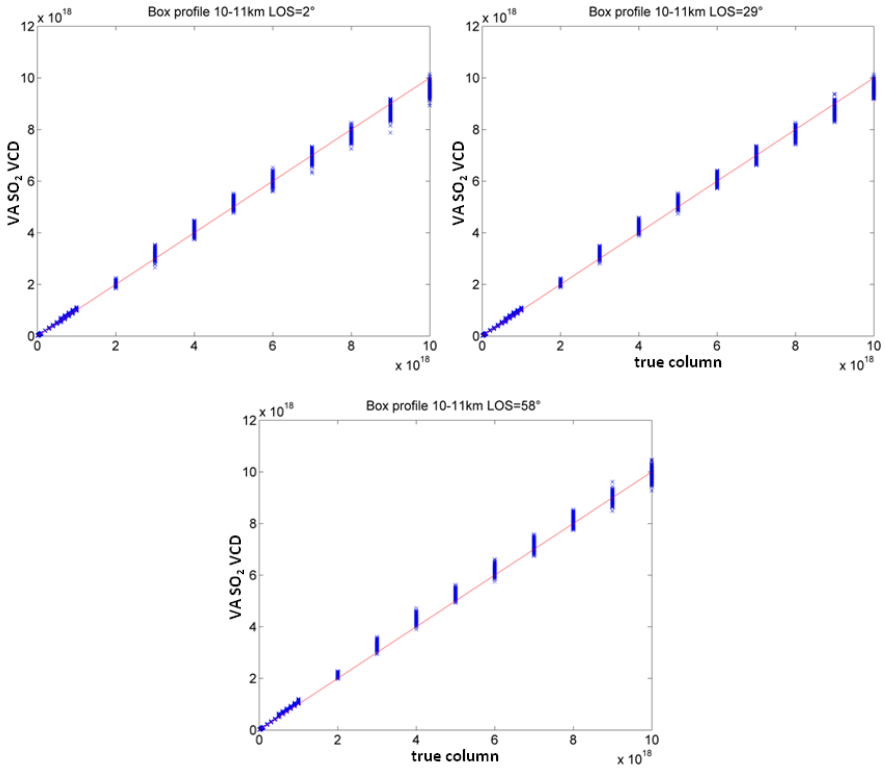

Figure 10.6: Verification algorithm SO_2 VCDs for all three LOS box-profile scenarios (LOS=2°, 29° and 58°) and a SO_2 layer height of 10-11km. Although the algorithm sometimes slightly overestimates the "true" VCD, the mean retrieved VCDs are very close to the correct ones.

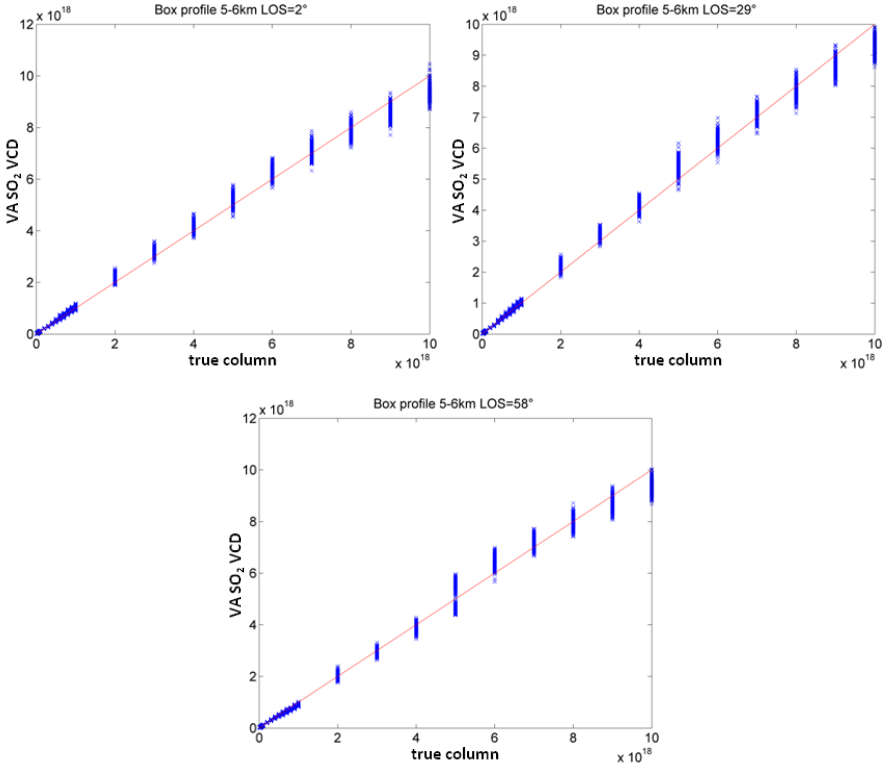

Figure 10.7: Verification algorithm SO_2 VCDs for all three LOS box-profile scenarios (LOS=2°, 29° and 58°) and a SO_2 layer height of 5-6km. The mean retrieved VCDs are very close to the correct VCD for all three LOS scenarios. However, as the sensitivity for SO_2 decreases for lower layers, the variability for a certain "true" VCD scenario increases (and therefore the associated uncertainty).

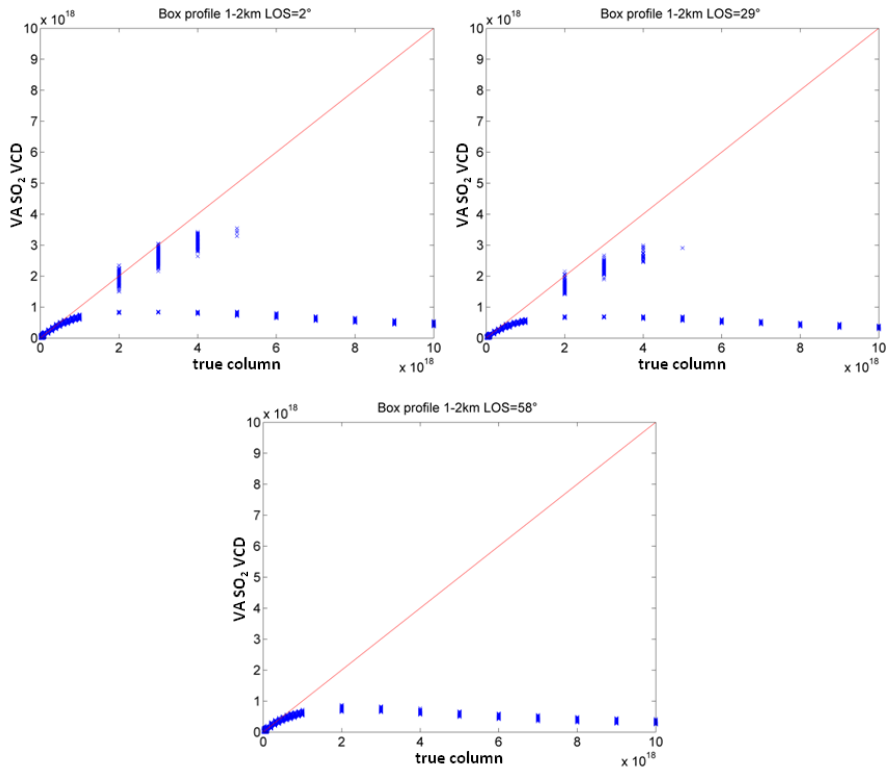

Figure 10.8: Verification algorithm SO_2 VCDs for all three LOS box-profile scenarios (LOS=2°, 29° and 58°) and a SO_2 layer height of 1-2km. The algorithm clearly fails to give an accurate estimation of the "true" VCD, especially for VCDs > $1 \cdot 10^{18}$ molec/cm². Due to the low sensitivity to the layers close to the ground, the transition criteria are missed for most measurements. Low VCDs (as they are typically expected for anthropogenic pollution scenarios), however, can still be accurately retrieved within the SO_2 SR fit window.

Figure 10.7 and Figure 10.8 indicate that the verification algorithm is clearly capable to reproduce the correct SO_2 VCDs for different LOS angles in case of a presumed SO_2 layer at 5-6 km or 10-11 km altitude. For very low layer heights (1-2 km) the algorithm clearly fails at retrieving the "true" VCD accurately, especially at VCDs ≥ 1×10^{18} molec/cm². Furthermore, the predefined criteria for the transition from the SO_2 SR to the SO_2 MR/AR fit windows are not fulfilled for most of the measurements because of the low sensitivity to layers close to the ground and the associated low SO_2 SCDs.

However, most of the investigated cases for a 1-2 km SO_2 layer height represent quite unrealistic scenarios, as the SO_2 VCDs for areas affected by anthropogenic emissions are typically lower than 1×10^{17} molec/cm² as indicated by ground-based measurements (and are certainly not well described by a homogeneous layer of 1 km thickness). Furthermore, most active volcanoes are 3-5 km high, so that even very strong SO_2 degassing will produce layers at higher altitudes for most of the time. The application of the SO_2 MR/AR fit windows will be probably only necessary during minor/major volcanic eruptions, typically causing SO_2 plumes at moderate to high altitudes.

It should be emphasized that neither clouds nor aerosols are included for all analysed synthetic scenarios. Especially the presence of clouds is expected to have a large influence on the retrieved SO_2 SCDs and therefore probably on the transition criteria for different fit windows.

10.7.2 Results of modified volcanic CAMELOT scenario analysis

As for the synthetic SO_2 box profile scenarios, all synthetic CAMELOTx16 volcanic scenario spectra were reanalysed using a further improved Verification Algorithm. In contrast to former results where both Prototype and Verification Algorithm showed significant discrepancies to the expected "real" SO_2 VCDs, both algorithm were this time able to reproduce the predefined SO_2 VCDs accurately.

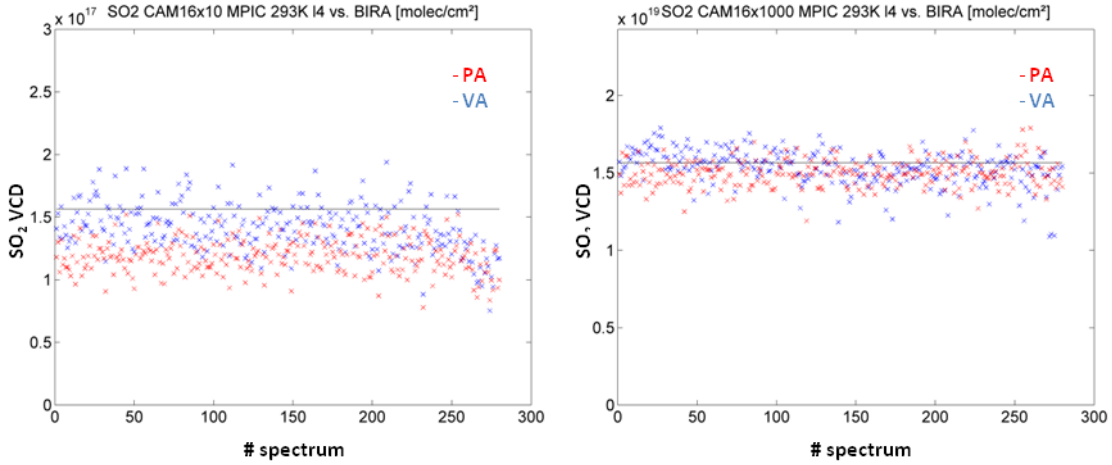

Figure 10.9: SO_2 Verification (blue) and Prototype (red) VCDs for the modified CAMELOT16x10 (left) and CAMELOT16x1000 (right) scenario. The black line indicates the "true" SO_2 VCD. Both algorithms are able to reproduce the predefined SO_2 VCDs accurately.

Figure 10.9 shows the resulting SO_2 VCDs for both algorithms, compared to the expected "true" SO_2 VCD for the CAMELOT16 volcanic scenario including low (CAMELOT16x10, left) and extreme SO_2 concentrations (CAMELOT16x1000, right). Generally, both algorithms are clearly capable to reproduce the predefined SO_2 VCDs accurately (within 15 %), although the Prototype Algorithm slightly underestimates the weakly enhanced SO_2 columns for the CAMELOT16x10 scenario (while the Verification Algorithm shows an increased scattering of the SO_2 SCD/VCDs). However, it is important to note that both algorithms only use resulting SO_2 SCDs from the lowest/highest fitting window exclusively for the CAMELOT16x10 and x1000 scenarios.

For moderate and moderately high SO_2 VCDs, the predefined transition criteria for the now combined SO_2 product might lead to inconsistencies. Figure 10.10 again shows the resulting SO_2 VCDs for both algorithms and the expected "true" SO_2 VCD, but this time for the CAMELOT16 volcanic scenarios including moderate (CAMELOT16x50, left) and moderately high SO_2 concentrations (CAMELOT16x500, right). While the combination of SO_2 SR/MR enables the Verification Algorithm to reproduce the predefined SO_2 VCDs well, the Prototype Algorithm seems to slightly underestimates the SO_2 columns for the CAMELOT16x50 scenario (probably due to non-linear absorption) by using the results from the standard fit windows and mismanages the combination of these results with some of the intermediate fitting window (that additionally shows increased data scattering due to lower sensitivity). For the CAMELOT16x500 scenario (Figure 10.10, right), both algorithms essentially retrieve the "true" VCD accurately by using a combination of second and third fitting window (318.6-335.1/323.1-335.1 nm for the Verification and 325-335/360-390 nm for the Prototype Algorithm). Since the 360-390 nm fitting window of the Prototype Algorithm is less sensitive for the moderately high SO_2 concentrations in the CAMELOT16x500 scenario compared to the SO_2 AR of the Verification Algorithm (323.1-335.1 nm), the Prototype data show increased data scattering.

However, it has to be pointed out that the 360-390 nm fitting window of the Prototype Algorithm will probably be more robust against underestimation of the true SO_2 VCD for major volcanic eruption scenarios including extreme SO_2 concentrations.

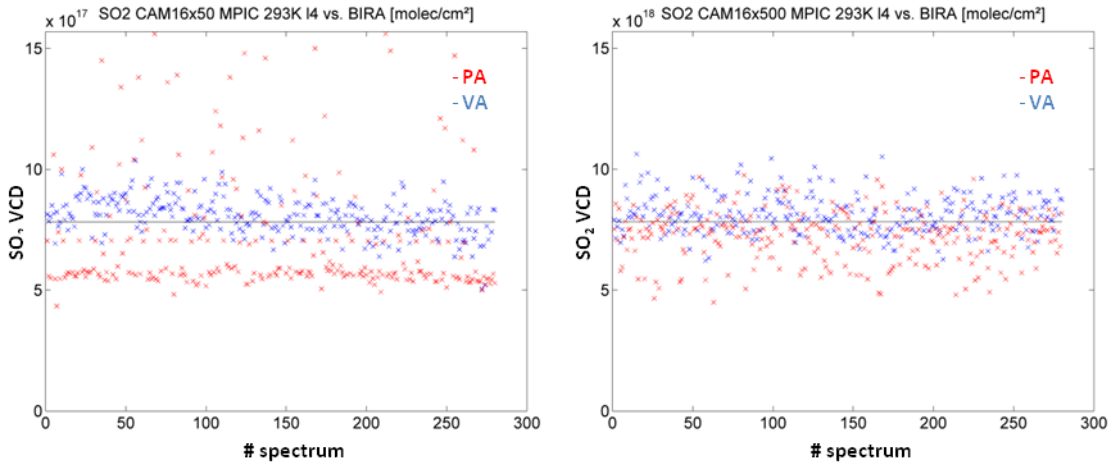

Figure 10.10: SO_2 Verification (blue) and Prototype (red) VCDs for the modified CAMELOT16x50 (left) and CAMELOT16x500 (right) scenario. The black line indicates the "true" SO_2 VCD. Especially for the case of moderate SO_2 VCDs, inconsistencies might appear for the combination of two different SO_2 evaluation fitting windows.

10.7.3 Results of real data analysis (Ozone Monitoring Instrument)

For a final intercomparison, Prototype and Verification Algorithm were applied to real data from the Ozone Monitoring Instrument (OMI). Resulting SO_2 VCDs for single orbits during different days in 2005, 2008 and 2014 will be presented in the following in order to cover different kinds of SO_2 scenarios during the last 10 years of OMI measurements. As the final SO_2 VCD significantly depend on the presumed SO_2 profile for the AMF calculation and both algorithms use a similar scenario for a SO_2 plume located at 15 km altitude, only results for this assumption are used to minimise the influence of differences in the a priori settings. Main deviations between Prototype and Verification Algorithm are therefore expected to be caused by the usage of different fit windows, determining their sensitivity, fit error and especially the corresponding transition criteria.

1.1.1.1 **May 1, 2005**

The considered OMI orbit on May 1, 2005 covers two main scenarios:

1) Moderately enhanced volcanic SO_2 VCDs caused by an ongoing eruption of the Anatahan volcano (Northern Mariana Islands). The eruptive phase lasted several months and clearly enhanced SO_2 columns were observed by OMI during whole 2005.
2) Strongly enhanced anthropogenic SO_2 VCDs caused by the Norilsk copper smelter (Russia), one of the strongest non-volcanic point source polluters on Earth.

Case 1: Moderate volcanic SO_2 enhancement (Anatahan volcano)

Figure 10.11 shows the resulting maps of the SO_2 VCD for the Verification Algorithm (VA – upper panel) and the Prototype Algorithm (PA – lower panel). The colorbar for this (and all of the following) example(s) has been scaled to the maximum SO_2 VCD from both algorithms (i.e., in the Anatahan case, the maximum SO_2 VCD was found to be 5.6×10^{17} molec/cm² by the PA). As can be seen from Figure 10.13, both algorithms result in similar SO_2 VCDs, however, a closer look reveals that the location of the maximum VCD is seen closer to the volcano at the eastern end of the plume for the PA, while it appears to be further downwind for the VA.

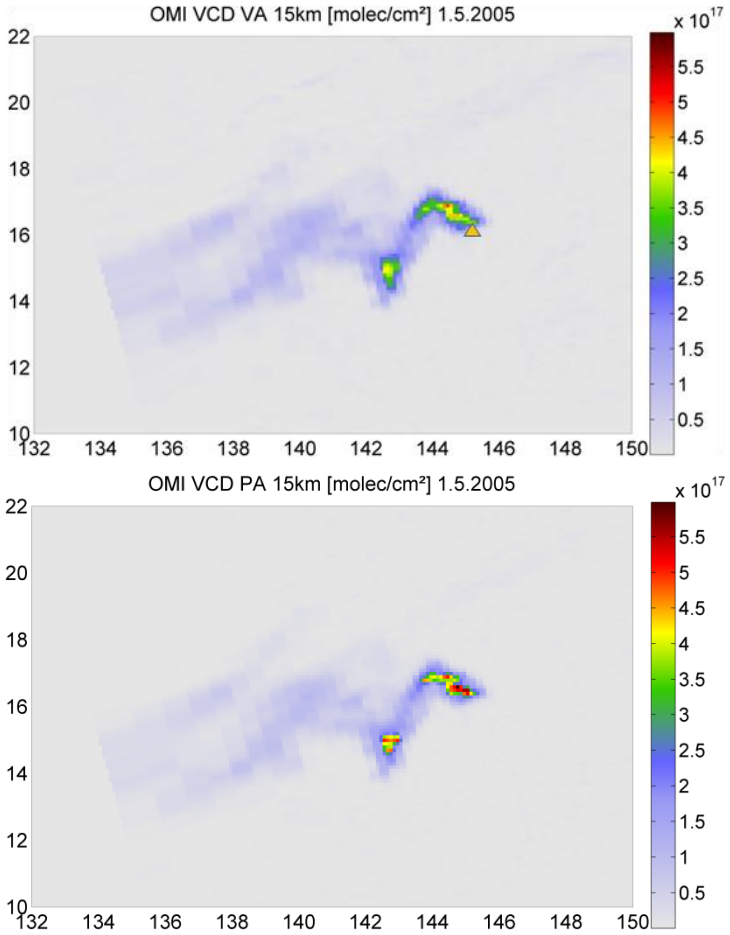

Figure 10.11 OMI SO_2 VCD for the Verification (upper panel) and Prototype Algorithms (lower panel) during the Anatahan eruption on May 1, 2005. The location of the maximum is seen closer to the volcano (orange triangle in the upper panel) for the PA, while it appears to be further downwind the plume for the VA.

This effect can be explained by the corresponding fit windows used for both algorithms as shown in Figure 10.12. Generally, both algorithms use three different fit windows (see also Section 10.4). However, while the PA uses strictly separated results from the individual fit windows, the VA tries to allow a smooth transition whenever resulting SO_2 SCDs are found to be located in between subsequent fit ranges.

Figure 9.13 (upper panel) shows the colour-coded fit windows for the Verfication Algorithm (white: no data, blue: SO_2 SR, purple: SO_2 SR/MR, green: SO_2 MR, orange: MR/AR and red: SO_2 AR). The lower panel indicates the corresponding fit windows for the Prototype Algorithm (white: no data, blue: Window 1, green: Window 2, and red: Window 3). While the VA uses a combination of SO_2 SR and MR for main parts of the volcanic plume, the PA uses a single fit window (Window 2; 325-335 nm) that is comparable to the VA SO_2 AR fit window (323.1-335.1 nm, here indicated in red as fit window 5).

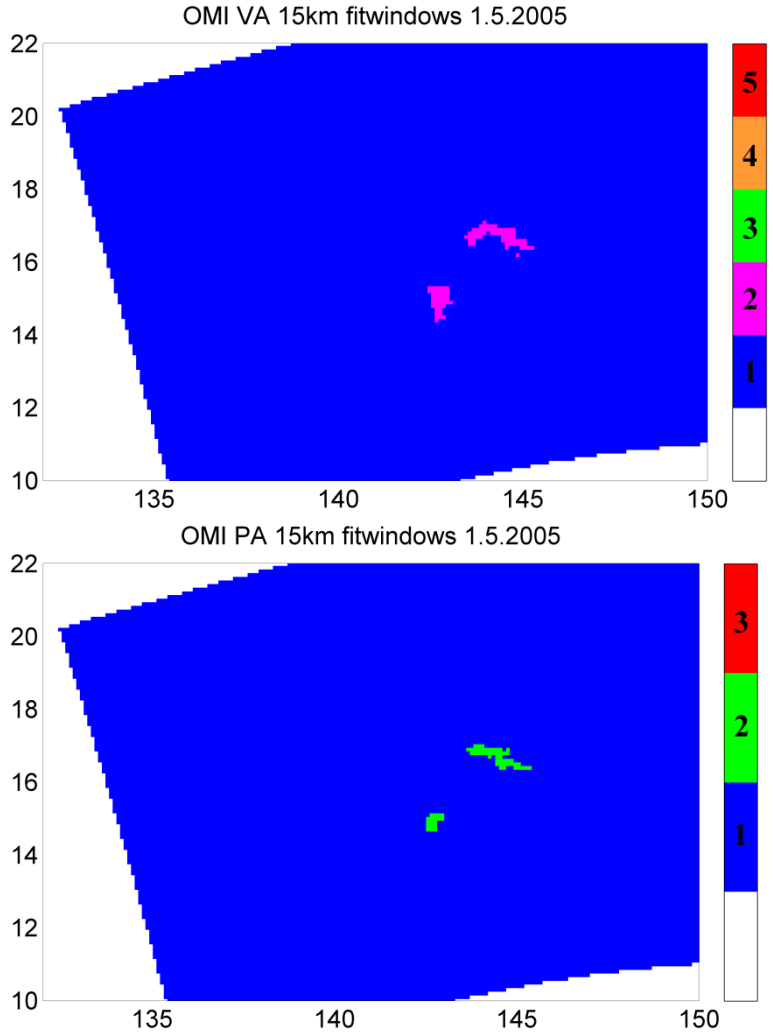

Figure 10.12: The upper panel shows the colour-coded fit windows for the Verification Algorithm (0 - white → no data, 1 - blue → SO_2 SR, 2 – purple → SO_2 SR/MR, 3 - green → SO_2 MR, 4 – orange → SO_2 MR/AR and 5 - red → SO_2 AR). Corresponding colour-coded fit windows for the Prototype Algorithm are shown in the lower panel (0 - white → no data, 1 - blue → 312-327 nm, 2 – green → 325-335 nm, and 3 – red → 360-390 nm). While the VA uses a combination of SO_2 SR and MR for main parts of the volcanic plume, the PA uses a single fit window (325-335 nm) that is comparable to the VA SO_2 AR fit window (323.1-335.1 nm).

These differences of the SO_2 VCDs for the main part of the volcanic plume can also be seen from Figure 10.13, where results from both algorithms are shown as a function of latitude (VA in blue, PA in red). However, the figure further indicates that both algorithms agree generally well when all measurements are taken into account (r^2=0.93). Outside the volcanic plume (e.g., > 20°N), the Prototype Algorithm is less affected by data scattering for low or SO_2 free measurements than the Verification Algorithm (see also atmospheric background scenario in Section 9.5.5.2).

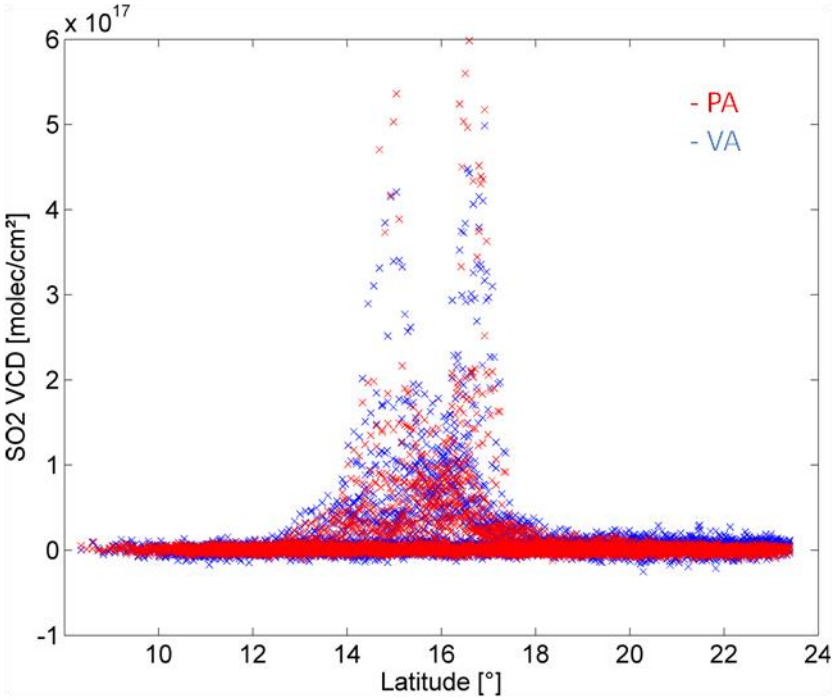

Figure 10.13: OMI SO_2 VCD for Verification (blue) and Prototype Algorithm (red) for the Anatahan eruption on May 1, 2005 as a function of latitude. While both algorithms mainly agree (r^2=0.93), certain differences can be found because of different used fit windows.

Figure 10.14 finally tries to illustrate how different choices of the SO_2 fit windows may result in deviating SO_2 VCDs for both algorithms, especially for SO_2 scenarios where the best choice is difficult to assess. While the SO_2 VCDs in the left panel are colour-coded according to different fit windows used for the Verification Algorithm (blue: SO_2 SR, purple: SO_2 SR/MR), the right panel shows the same data, but this time colour-coded for the fit windows of the Prototype Algorithm (blue: 312-327 nm, green: 325-335 nm; see also Figure 10.12). Both algorithms mainly agree for the lowest fit windows, but the VA shows a larger data scatter close to zero and a steeper slope than the PA. While the reason for the generally observed steeper slope of the VA for moderate SO_2 VCDs is yet unclear, the SO_2 VCDs around $2x10^{17}$ molec/cm² according to the PA seem to be slightly affected by saturation effects. On the other hand, the largest SO_2 VCDs (> $3x10^{17}$ molec/cm²) show an increased scattering for both algorithms. While it cannot be certainly decided which algorithm is closer to the actual SO_2 VCDs, the combined fit windows of the VA probably are better suited for such scenarios as the SO_2 cross-section is generally stronger for lower wavelength (< 325 nm) when compared to the intermediate fit window of the PA. This can also be seen from the standard deviation of the SO_2 VCDs over a SO_2-free area (e.g., the Pacific Ocean) for the different fit windows. While the standard deviation of SO_2 SR and the first PA fit range (312.1-324 / 312-327 nm) as well as for SO_2 AR and the second PA fit range (323.1-335.1 nm / 325-327 nm) are similar (~ 3-5$x10^{15}$ molec/cm² and ~ 1$x10^{17}$ molec/cm², respectively), they differ significantly for the SO_2 MR and the upper PA fit window (318.6-335.1 nm / 360-390 nm) with $\sigma_{360\text{-}390nm}$ ~ 5 $x10^{17}$ molec/cm².

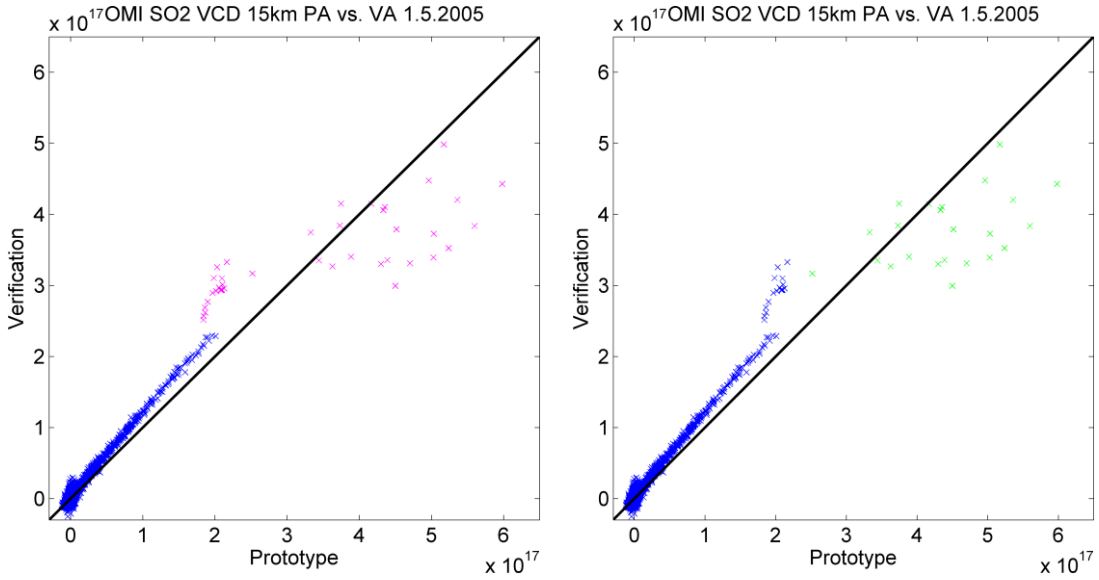

Figure 10.14: OMI SO_2 VCD scatter plot for PA (x-axis) and VA (y-axis) during the Anatahan eruption on May 1, 2005. The different used fit windows for both algorithms are colour-coded (PA – left: SO_2 SR, purple: SO_2 SR/MR; VA – right: blue: 312-327 nm, green: 325-335 nm). The combination of SO_2 SR/MR within the VA is probably better suited for some of the measurements, as the PA seems to be affected by non-linear radiative transfer effects (indicated by the strong bend for VCDs at ~ 2 x10^{17} molec/cm²).

However, in case of extreme SO_2 concentrations the upper PA fit range is expected to be significantly less affected by non-linear radiative transfer effects than all evaluation schemes of the VA (as shown for the Bardabunga case study – see Case 1 on September 4, 2014, p. 187).

Case 2: Strong anthropogenic SO_2 emissions (Norilsk copper smelter)

As an example for strong anthropogenic SO_2 emissions, Figure 10.15 shows the maps of the SO_2 VCD for VA (upper panel) and PA (lower panel) over the Norilsk copper smelter on the same day. Again, both algorithms result in similar SO_2 VCDs, but this time the maximum VCD is seen by the VA and comparably high VCDs appear at different locations of the main SO_2 plume.

Like for the Anatahan case, the VA uses a combination of SO_2 SR and MR for several measurements of the plume, while the PA again uses the single fit window between 325 and 335 nm (see Figure 10.16).

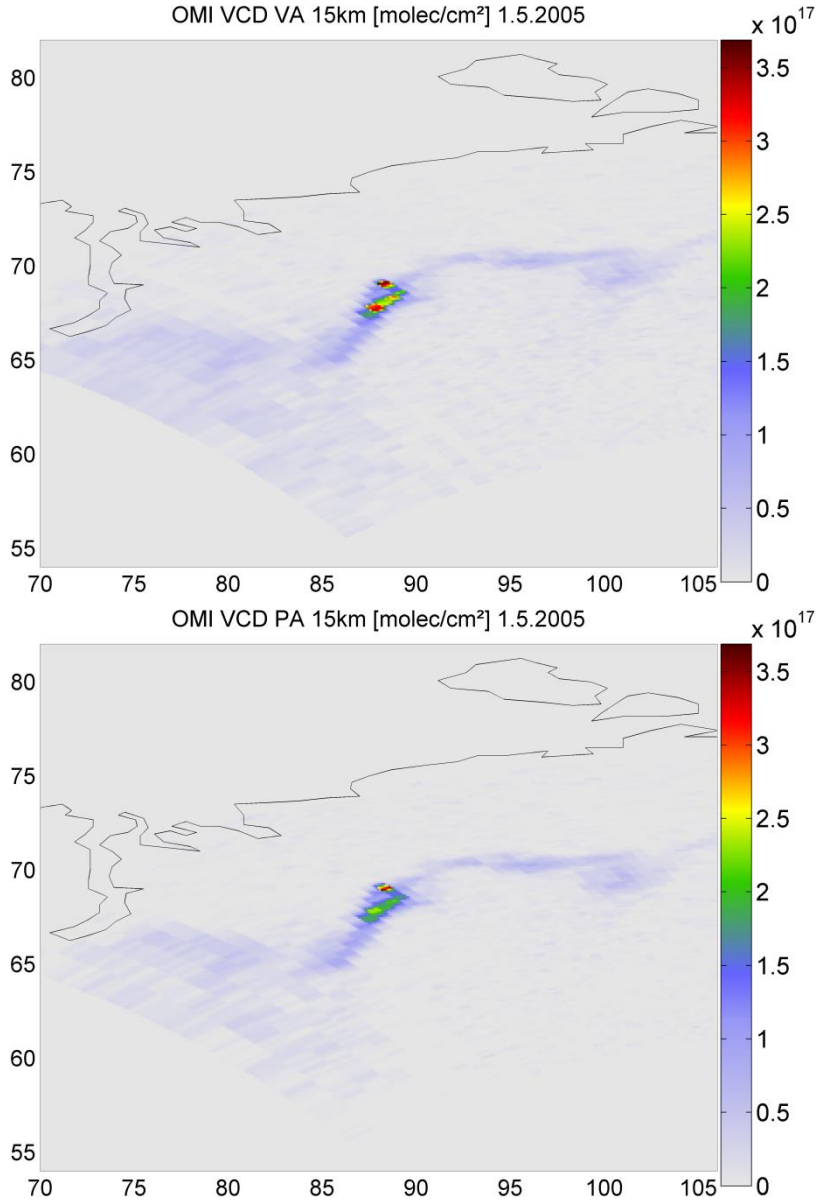

Figure 10.15: OMI SO_2 VCD for the Verification (upper panel) and Prototype Algorithm (lower panel) over the Norilsk copper smelter on May 1, 2005. The maximum VCD is seen by the VA and comparably high columns show up at different locations of the main plume, where the PA VCDs are significantly lower.

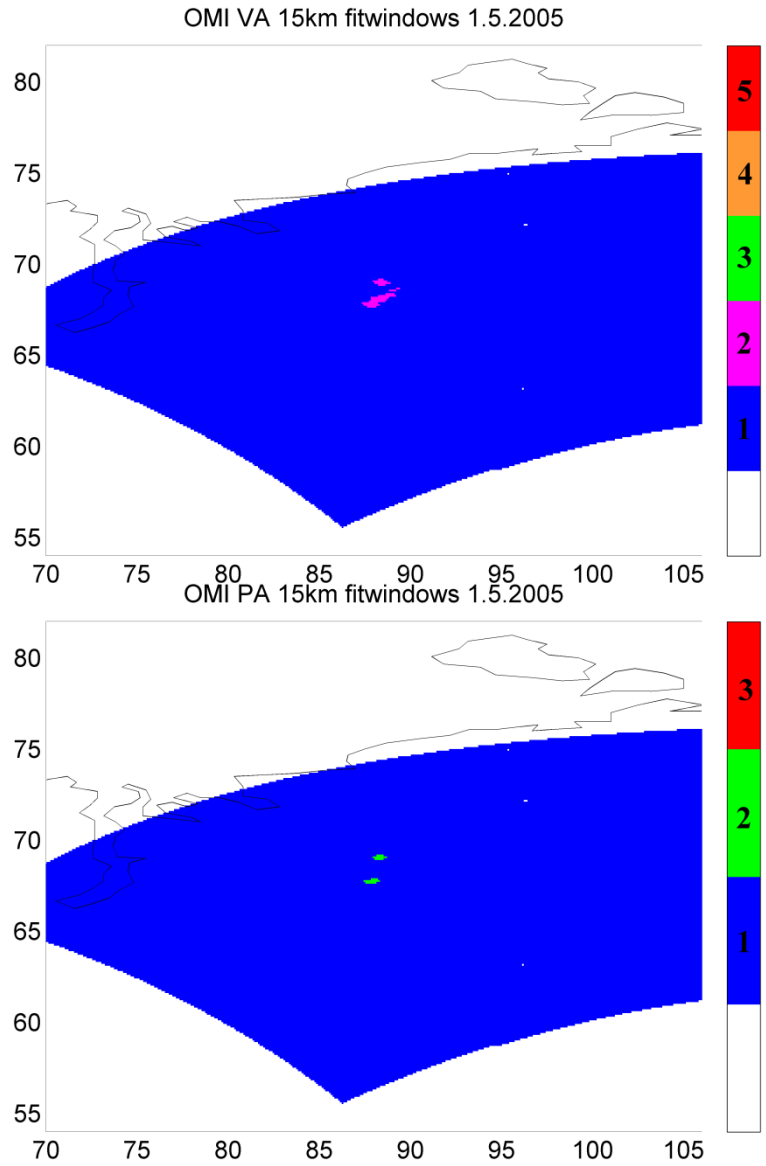

Figure 10.16: Colour-coded fit windows for the Norilsk scenario for VA (upper panel) and PA (lower panel). Like for the Anatahan case, the PA uses a combination of SO_2 SR and MR for some measurements of the plume (indicated in purple), while these measurements are retrieved using the lower or intermediate fit window for the PA.

A comparison of the SO_2 VCDs for both algorithms as a function of latitude (Figure 10.17) illustrates that the results mainly agree (r^2=0.92), but again especially the differences for the highest VCDs and the increased scattering of the VA for lower VCDs can be clearly identified. Furthermore, the VA VCDs at the south-western part of the plume show a slight positive offset compared to the ones from the PA, probably because of the simple empirical background correction for the interference with enhanced O_3 concentrations.

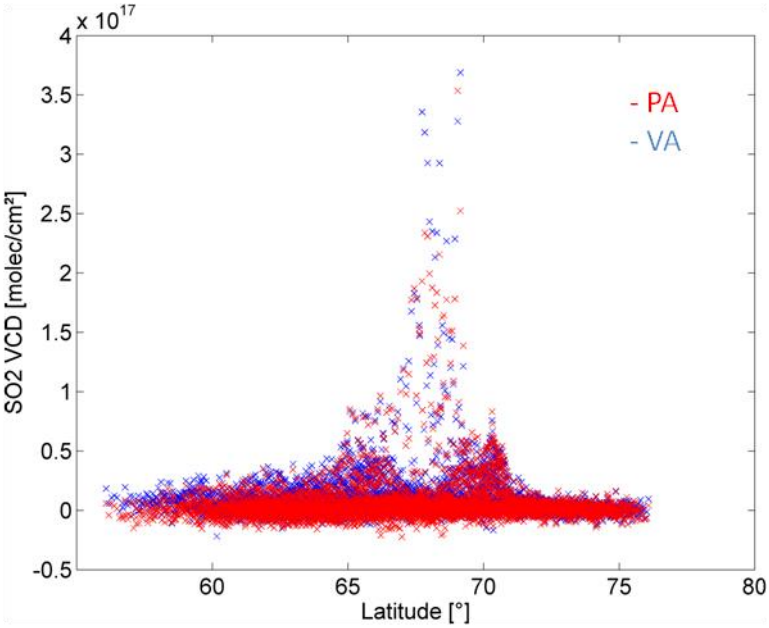

Figure 10.17: OMI SO_2 VCD for Verification (blue) and Prototype Algorithm (red) over Norilsk on May 1, 2005 as a function of latitude. The results from both algorithms agree very well (r^2=0.92), but again certain differences can be found because of different used fit windows for the plume centre around 67°N.

The colour-coded scatter plots in Figure 10.18 finally confirm that both algorithms lead to almost identical SO_2 VCDs whenever the lowest fit window is chosen and the VCD is <1.5x10^{17} molec/cm². For VCDs >1.5x10^{17} molec/cm², PA and VA mainly differ because of the different fit windows used. While the VA again uses a combination of SR and MR (left panel, purple), the PA partly uses the lower or the intermediate fit window (green). As for the Anatahan case, it is expected that the fit windows of the PA are probably better suited for this specific case because of the higher sensitivity of the SO_2 MR when compared to the intermediate VA fit range.

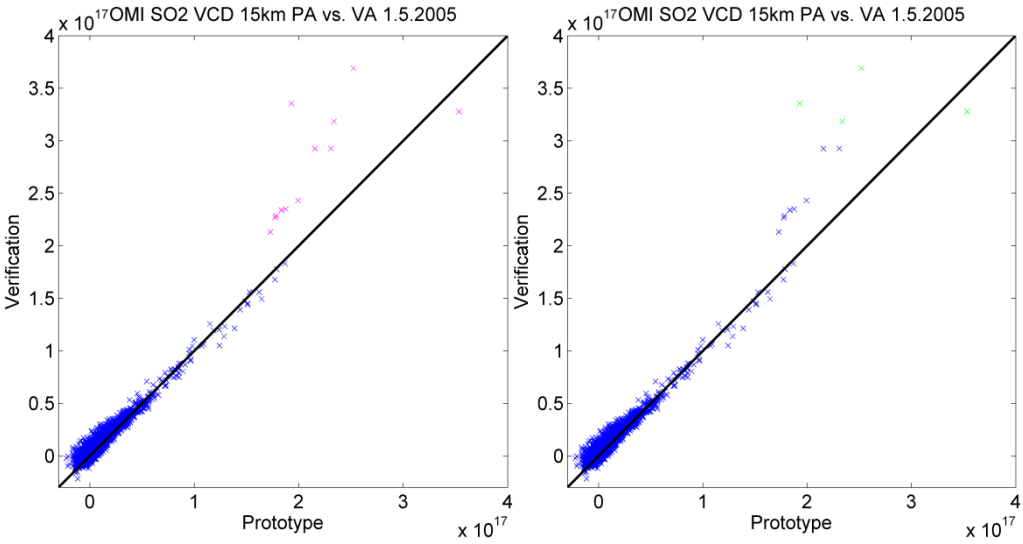

Figure 10.18: OMI SO_2 VCD scatter plot for PA (x-axis) and VA (y-axis) over Norilsk on May 1, 2005. Both algorithms are close to the 1:1 slope for the lower used fit range (blue), while differences occur for results from the SO_2 SR/MR combination of the PA (left panel, purple) and the intermediate fit window of the PA (right panel, green).

10.7.3.1 August 8, 2008

The considered OMI orbit on August 8, 2008 covers three different main scenarios:

1) An unpolluted, presumably SO_2 free area over the Pacific Ocean. Mainly affected by possible spectral interference with tropospheric/stratospheric ozone.
2) Moderately enhanced SO_2 VCDs caused by increased volcanic activity (Kilauea, Hawaii). The volcanic plume height is supposed to be about 2-3 km.
3) Large to extreme SO_2 VCDs caused by the major eruption of the Kasatochi volcano. All three fitting windows of the Prototype/Verification Algorithm are used for the SCD retrieval.

Figure 10.19 shows the resulting OMI SO_2 VCD map for all data on August, 8th 2008 as retrieved by the Verification Algorithm. All three cases are indicated by red circles and numbered in flight direction of the satellite instrument.

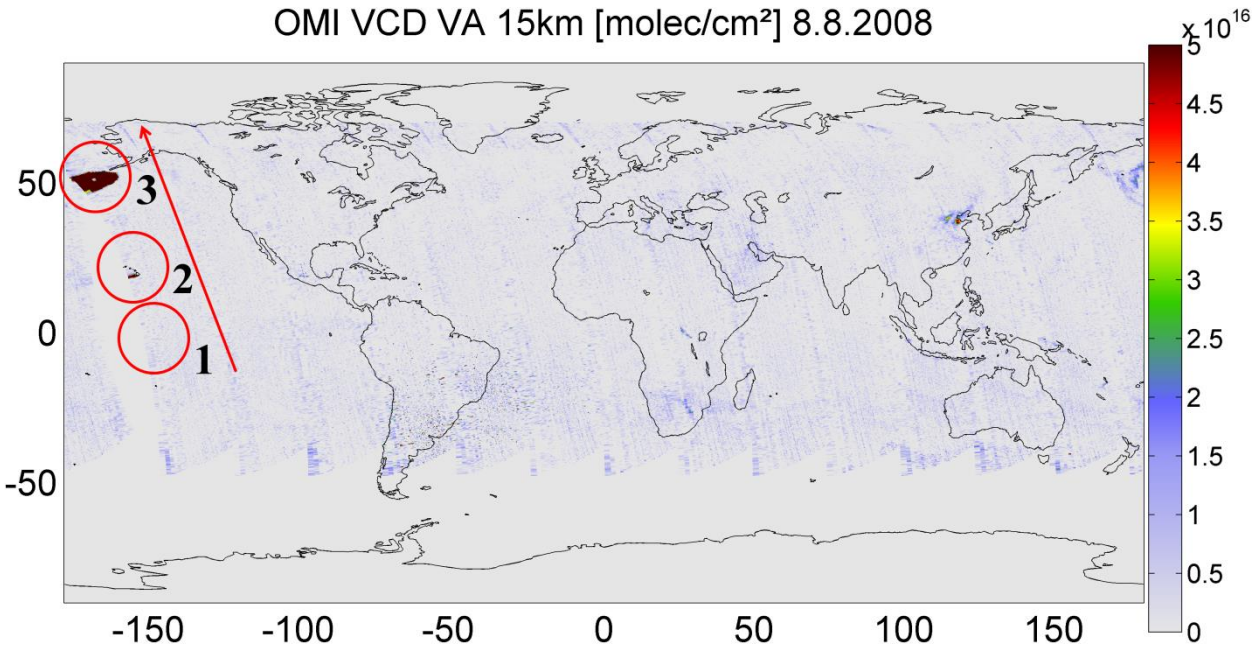

Figure 10.19: OMI SO_2 VCDs for the Verification Algorithm during the first day after the eruption of the Kasatochi volcano (3). The satellite orbit that includes the Kasatochi SO_2 plume additionally covers the moderately enhanced SO_2 VCDs over the Kilauea volcano on Hawaii (2) and a presumably SO_2 free area over the Pacific Ocean (1).

Case 1: SO_2 free area over the Pacific Ocean

In order to investigate the quality of the SO_2 standard evaluation of both algorithms over a presumably SO_2 free area, all measurements of the considered satellite orbit close to the equator (± 10° N) were analysed and compared to each other.

Figure 10.20 shows the corresponding data for the Prototype Algorithm SO_2 VCDs in red, for the Verification Algorithm in blue. The direct comparison of the VCDs as a function of latitude (Figure 10.20, left) indicates that although both algorithms generally show similar SO_2 VCDs scattered around zero, the PA is slightly less affected by data scattering (σ_{PA}=6.9x10^{15} vs. σ_{VA}=7.9 x10^{15} molec/cm^2). A similar behaviour was found as well over other regions, so that the PA seems to be generally better suited in case of close to zero SO_2 VCDs. Possible reasons for this discrepancies are probably differences in the treatment of the empirical offset/destriping correction of both algorithms as well as the different lower spectral range that is used. One main difference is that the PA offset correction bases on the calculation of averaged SO_2 data on an ozone slant column grid (Theys et al., 2015), while the VA uses a very simple averaging process near the equator. Thereby, the PA seems to better prevent the influence of spectral interference between SO_2 and tropospheric/stratospheric ozone. However, the right panel of Figure 10.20 also indicates that the VA VCDs are generally higher than the PA VCDs (slope >1). While this seems to be a general behaviour of the VA (and could already be seen in previous examples), this cannot be explained by the increased scattering. One possible explanation could be a different approach for the temperature correction of the used SO_2 cross-section, but the reason remains unclear and could not be clarified yet.

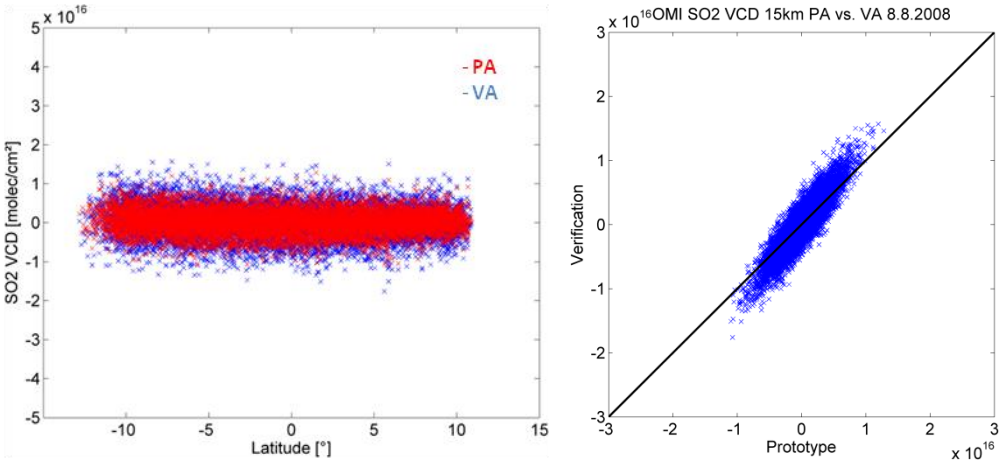

Figure 10.20: OMI SO_2 VCDs for the Prototype (red) and Verification Algorithm (blue) for a presumably SO_2 free area over the Pacific Ocean on 8th August 2008. Both algorithms show similar SO_2 VCDs scattered around zero, but the PA is less affected by data scattering (σ_{PA}=6.9x10^{15} vs. σ_{VA}=7.9 x10^{15} molec/cm^2). The VA, however, shows a steeper slope as can be additionally seen from the scatter plot (right). One possible explanation could be a different approach for the temperature correction of the used SO_2 cross-section.

Case 2: Moderate volcanic SO_2 VCD enhancement (Kilauea, Hawaii)

The Kilauea volcano showed strongly increased activity during March-October 2008 (Beirle et al., 2014), leading to moderately enhanced SO_2 VCDs during almost each day of the OMI measurements within this time period. As can be seen by the corresponding maps, both algorithms show similar results, although the VA VCDs (Figure 10.21, upper panel) are up to almost 20% larger than the PA (lower panel) for the highest SO_2 columns, and both algorithms use the lowest fit range. However, a generally good agreement of the SO_2 distribution can be once again found for both algorithms.

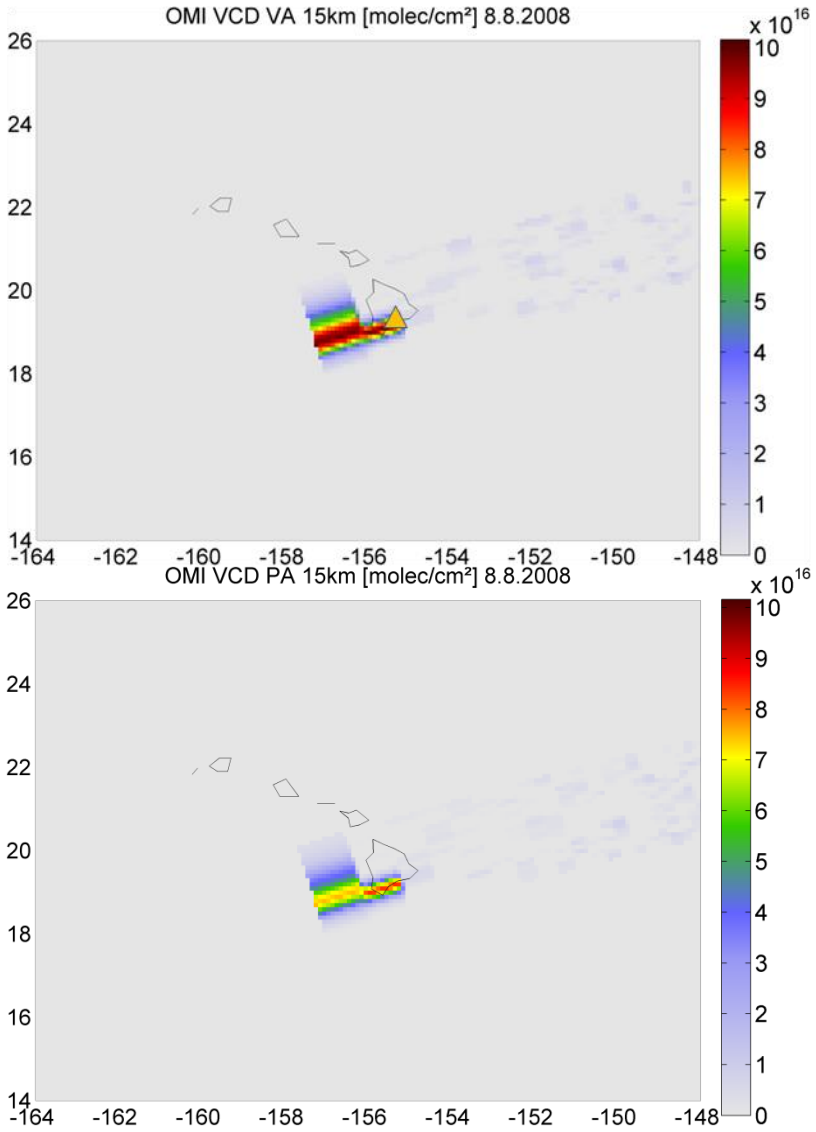

Figure 10.21: Maps of OMI SO_2 VCDs for Verification (upper panel) and Prototype Algorithm (lower panel) for moderately enhanced SO_2 concentrations over the Kilauea volcano (Hawaii) on August 8, 2008. Both algorithms lead to similar results, although the Verification Algorithm tends to slightly higher SO_2 VCDs (+20 %) close to Big Island.

Like for the SO_2-free scenario, both algorithms exclusively use the lowest fit range for the DOAS fit. However, when compared directly to each other (Figure 10.22), it becomes clear that the higher SO_2 VCDs of the Verification Algorithm mainly result from the steeper slope (right panel) that was already noticed in previous examples and possibly results from differences in the temperature correction of the used SO_2 cross-section. This is further indicated by a rather high correlation coefficient of r^2=0.96 as well as the direct comparison of the VCDs as a function of latitude (left panel).

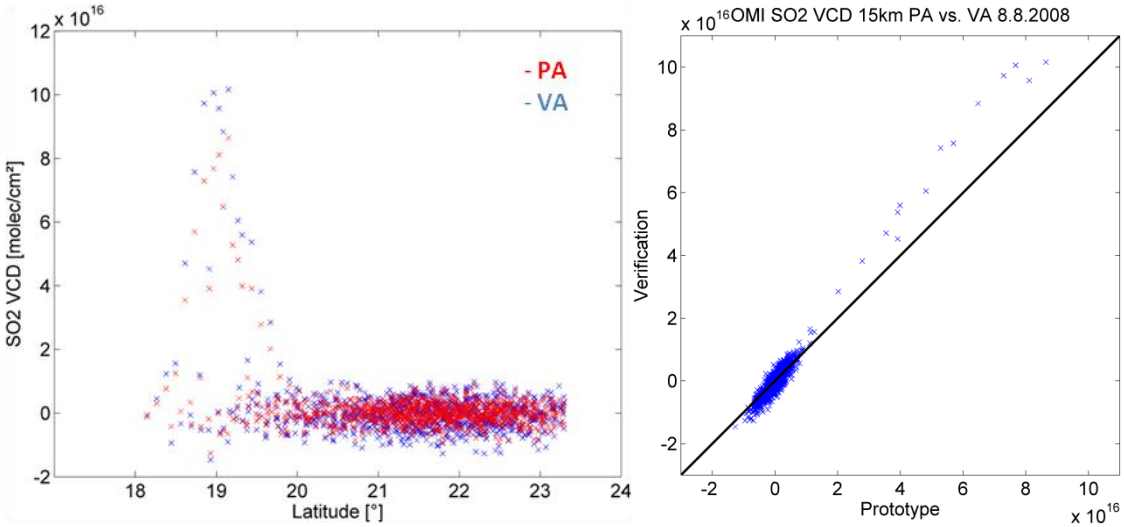

Figure 10.22: OMI SO_2 VCD (geo.) for the Prototype (red) and Verification Algorithm (blue) for moderately enhanced SO_2 concentrations over the Kilauea volcano (Hawaii) on 8th August 2008. Both algorithms lead to similar results, although the Verification Algorithm tends to slightly higher SO_2 VCDs (+15 %) and shows a general steeper slope (right panel). Resulting SO_2 VCDs, however, agree widely within the uncertainties as indicated by data scattering close to zero for measurements outside of the volcanic plume.

Case 3: Strongly enhanced SO_2 VCD (Kasatochi, Aleutian Islands):

In contrast to the SO_2 free and Kilauea case, the Kasatochi plume on August 8, 2008 provides a large range of measurements affected by low to extremely high SO_2 contamination. While the former cases allowed to use mainly the standard SO_2 evaluation fit windows (312.1-324 nm for the Verification, 312-327 nm for the Prototype Algorithm), the DOAS retrieval for the Kasatochi plume requires all three used fit windows to prevent systematic underestimation of the resulting SO_2 SCDs due to non-linear absorption caused by very high SO_2 concentrations within the volcanic plume.

Figure 10.23 shows maps of the final SO_2 VCDs for all three different fitting windows of both, Verification (upper panel) and Prototype Algorithm (lower panel) for the Kasatochi plume. Despite the generally good agreement at first glance, it is important to notice that especially the specific SO_2 distribution seems similar for both algorithms, including the location of the maximum SO_2 VCD. This finding clearly proves that the VA is capable to retrieve strongly enhanced SO_2 concentrations without being too much affected by saturation effects during major volcanic eruptions, although the corresponding SCDs are retrieved at shorter wavelengths when compared to the PA.

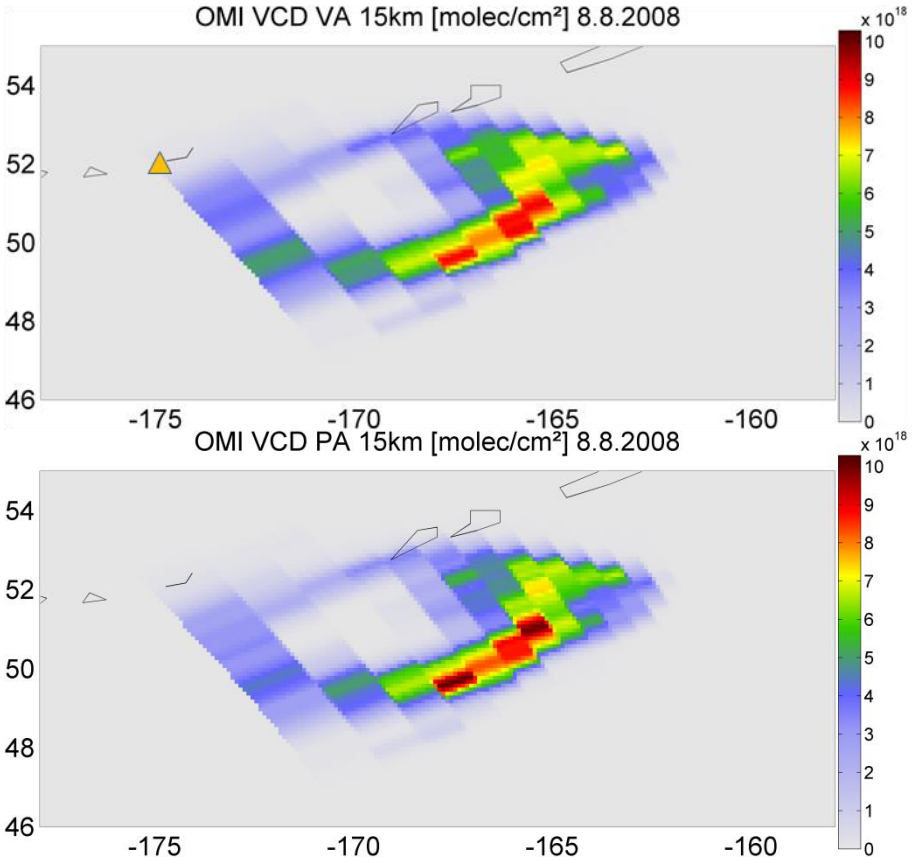

Figure 10.23: OMI SO_2 VCD map for Verification (upper panel) and Prototype Algorithm (lower panel) for the volcanic plume of Kasatochi on August 8, 2008. Both algorithms lead to similar results, although the maximum SO_2 VCDs are retrieved for completely different fit windows.

Figure 10.24 (upper panel) shows the corresponding colour-coded fit windows for the Verfication Algorithm (0 - white → no data, 1 - blue → SO_2 SR, 2 – purple → SO_2 SR/MR, 3 - green → SO_2 MR, 4 – orange → SO_2 MR/AR and 5 - red → SO_2 AR). This time, all three fit windows (SO_2 SR, MR and AR) are used for the retrieval, including the combination of SR/MR and MR/AR in case of SCDs fulfilling the predefined transition criteria (see Section 9.3.2.2).

The lower panel indicates the corresponding fit windows for the Prototype Algorithm (0 - white → no data, 1 - blue → 312-327 nm, 2 – purple → 325-335 nm, and 3 – green → 360-390 nm). Like for the Verification Algorithm, all three fit windows are used for the DOAS retrieval. In contrast to the VA, results from different fit ranges are not combined for intermediate SO_2 SCDs.

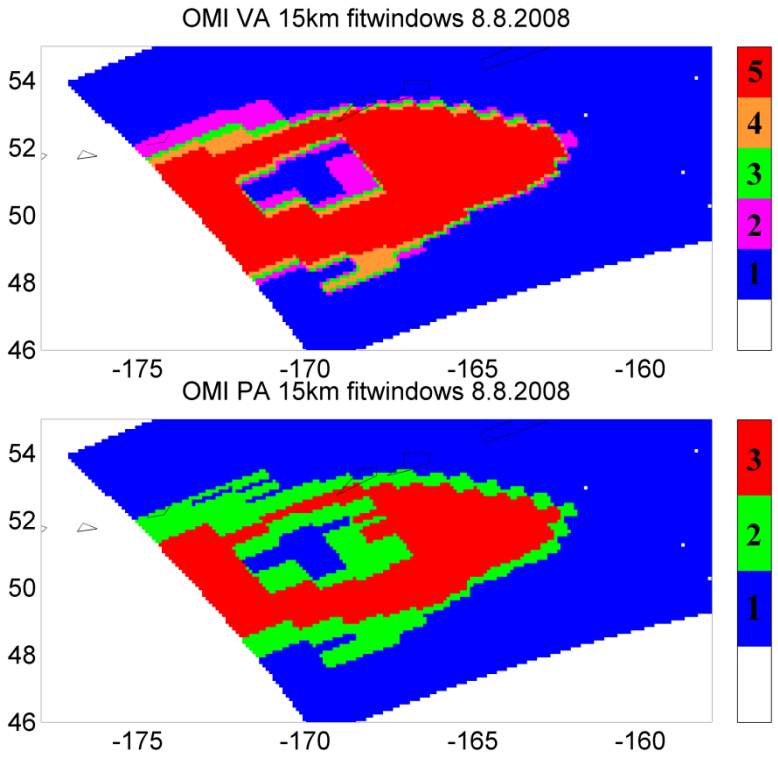

Figure 10.24: Colour-coded fit windows for the Kasatochi plume on August 8, 2008. Both algorithms use all three fit windows for the SCD retrieval. While the Verification Algorithm (upper panel) additionally uses a combination of SO_2 SR/MR and MR/AR (0 - white → no data, 1 - blue → SO_2 SR, 2 – purple → SO_2 SR/MR, 3 - green → SO_2 MR, 4 – orange → SO_2 MR/AR and 5 - red → SO_2 AR), the corresponding colour-coded fit windows for the PA (lower panel) indicates that this is not the case for the fit windows of the Prototype (0 - white → no data, 1 - blue → 312-327 nm, 2 – purple → 325-335 nm, and 3 – green → 360-390 nm).

The differences of both algorithms can only be vaguely discerned by the direct comparison of the VCDs as a function of latitude (Figure 10.25), but become more clear when the colour-coded scatter plots are further analysed (Figure 10.26). At first glance, differences between the SO_2 VCDs more or less seem to compensate each other for different used fit ranges. While the VA once again shows higher values for SO_2 VCDs < $3x10^{18}$ molec/cm², this time essentially for all three fit windows as indicated in the left panel, the slope flattens for VCDs retrieved within the upper fit range of the PA (red crosses, right panel).

For the maximum VCDs according to the Prototype, it seems like the Verification Algorithm might be already slightly affected by an underestimation of the SO_2 VCD caused by non-linear radiative transfer effects in the SO_2 AR fit window.

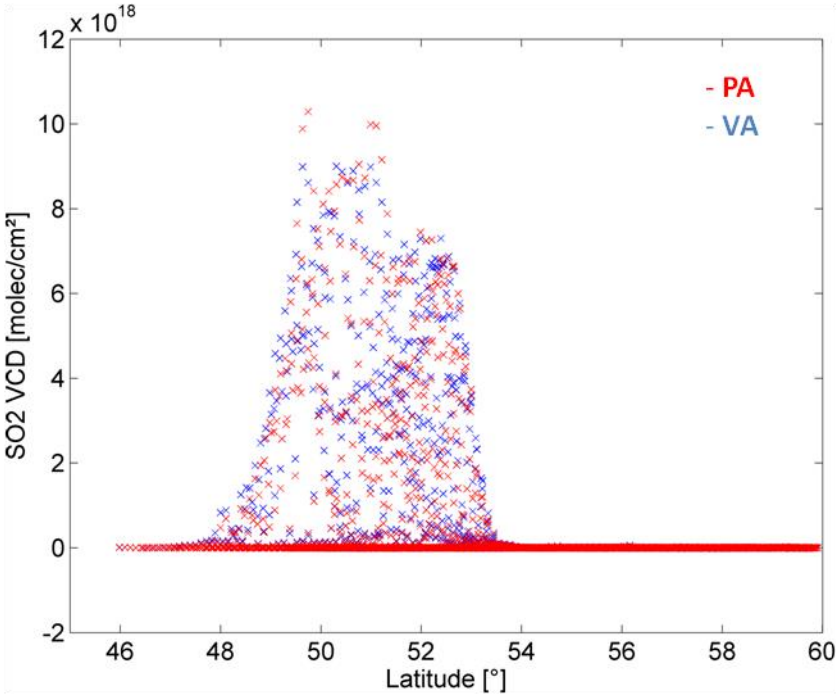

Figure 10.25: OMI SO_2 VCD for Verification (blue) and Prototype Algorithm (red) during the Kasatochi eruption on August 8, 2008 as a function of latitude. Although all three different fit windows are this time used within both algorithms, the results agree very well (r^2=0.99).

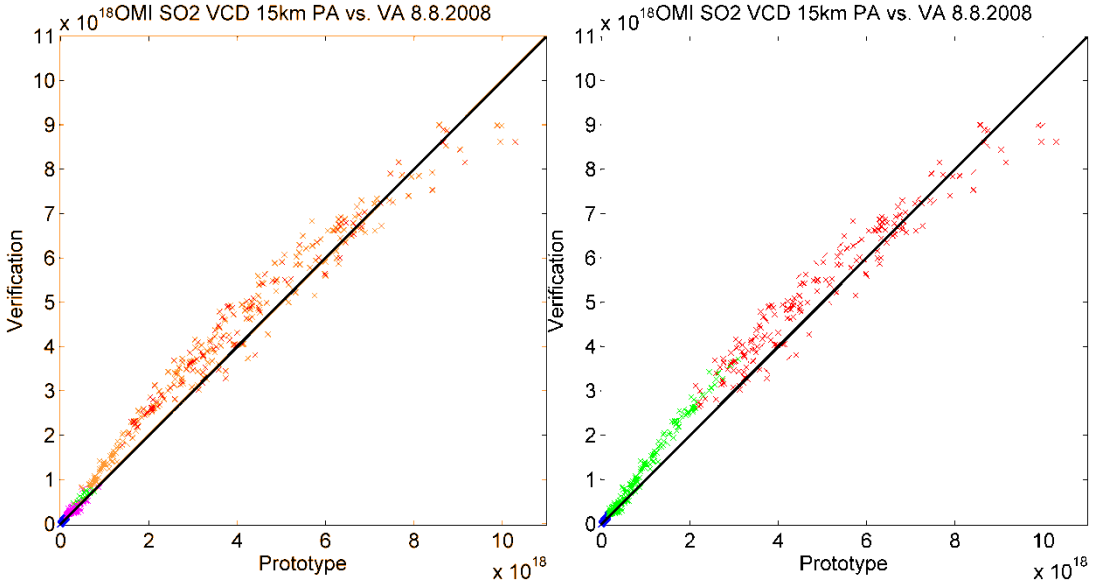

Figure 10.26: OMI SO_2 VCD scatter plot for PA (x-axis) and VA (y-axis) during the Kasatochi eruption on August 8, 2008. Different used fit windows for both algorithms are colour-coded according to the description in Figure 10.24 (left panel – VA, right panel – PA) . At first glance, differences between the SO_2 VCDs more or less seem to compensate each other for different used fit ranges.

To better illustrate the certain effects of the different used fit windows, Figure 10.27 shows the same data as Figure 10.26, but this time scaled to a maximum SO_2 VCD of $1x10^{18}$ molec/cm². While the PA here only uses the first two fit windows (right panel, blue and green), the VA tries to compensate the transitions between SO_2 SR (left panel, blue crosses) and MR (left panel, green crosses) and the SO_2 MR/AR by using combined results of these fit ranges (left panel, purple and orange crosses).

The main differences most likely result from the lower sensitivity of the intermediate PA fit window when compared to the MR (or the combined SR/MR) of the Verification Algorithm. The large scatter of the combined SR/MR VCDs from the VA (purple crosses in left panel) is mainly caused by the scattering of the 325-335 nm fit range of the PA (green crosses in right panel), as the uncertainty is here about one order of magnitude higher for the intermediate PA fit range.

A comparably strong effect can be seen for the SO_2 AR results when compared to the 360-390 nm fit range of the PA, but is partly compensated by the robustness of the PA against saturation effects for high SO_2 concentrations.

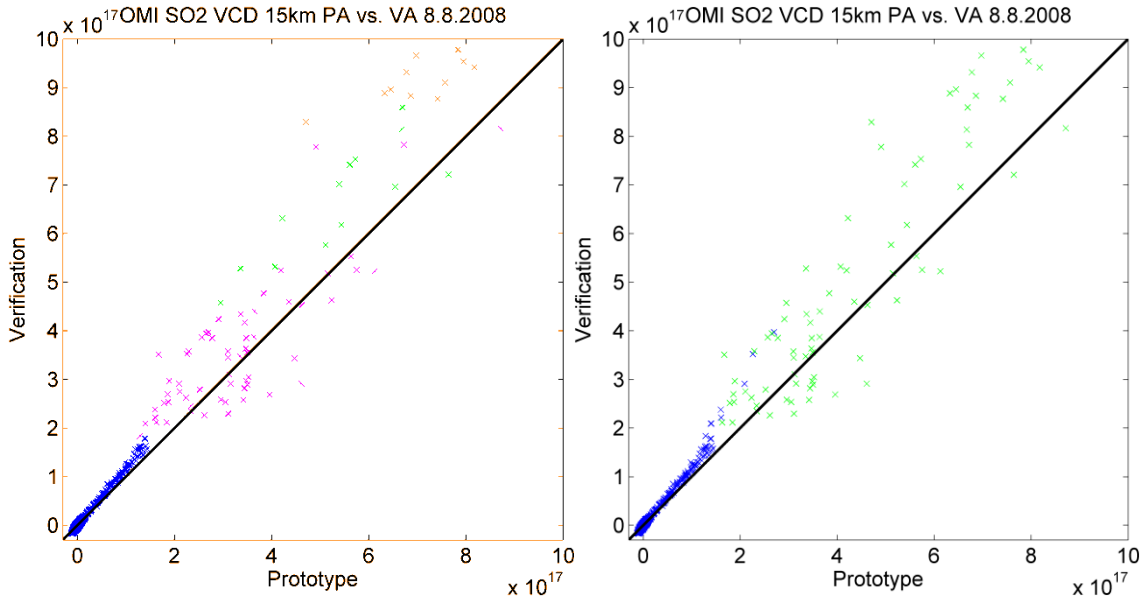

Figure 10.27: Same data as for Figure 10.26:, but this time scaled to a maximum of $1x10^{18}$ molec/cm² in order to illustrate the transition effects of different used fit windows. While the PA only uses the lower fit windows (right panel, blue and green), the VA tries to compensate the transitions between SO_2 SR (left panel, blue crosses), MR (left panel, green crosses) and AR by combined results of these fit ranges (left panel, purple and orange crosses).

1.1.1.2 ***September 4, 2014***

The considered OMI orbit on September 4, 2014 is only used for the illustration of one main scenario:

<u>Case 1: Extremly high volcanic SO_2 concentrations (Bárðarbunga, Iceland):</u>

Figure 10.28 shows maps of the final SO_2 VCDs for both algorithms over Iceland during the Bárðarbunga eruption, where SO_2 has been noticeable for several months in the OMI measurements in late summer 2014. The volcano showed extraordinary large SO_2 emissions to low altitudes (most of the time 2-3 km) when compared to other eruptions during recent years. Because both maps (left panel – VA, right panel – PA) are scaled to the maximum SO_2 VCD of the PA and the volcanic plume features a strong gradient of the VCDs, only the maximum VCDs can be noticed within the maps. Please note that only VCDs for a presumed SO_2 plume altitude of 15 km are shown – the true SO_2 VCDs are typically much higher due to the lower plume altitude. While both algorithms detect the maximum VCD directly at the location of the volcano, the maximum PA SO_2 VCD is almost a factor of 2 higher than the one resulting from the VA.

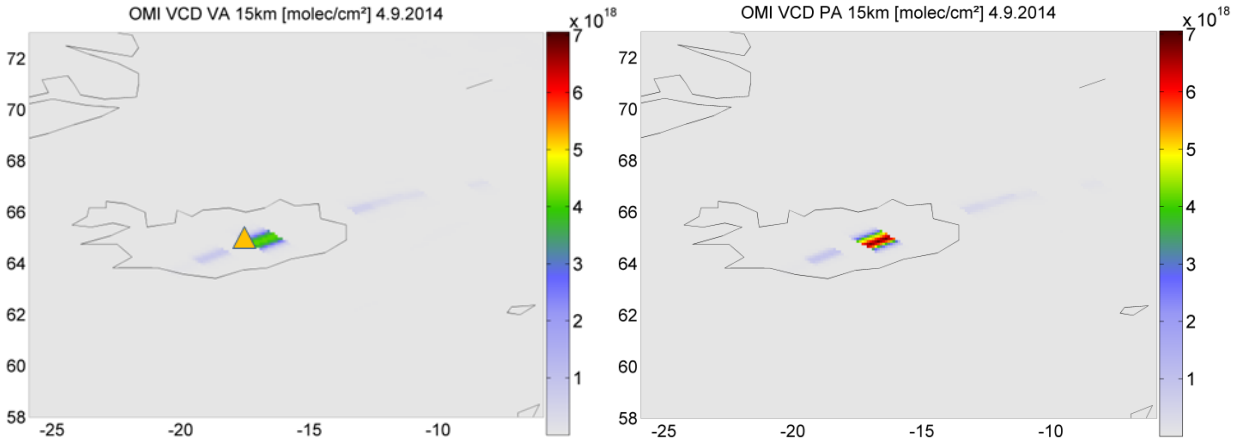

Figure 10.28: OMI SO_2 VCD map for the Prototype (red) and Verification Algorithm (blue) for the volcanic plume of Kasatochi on 8th August 2008. Both algorithms lead to similar results and are able to clearly identify the overall extent of the plume (left). Certain differences can be identified in the corresponding

Figure 10.29 reveals that mainly two fit windows are used by both algorithms, but all three fit windows available are taken into account. While the Verification Algorithm mostly uses the combined SO_2 SR/MR (left panel, purple) and the AR (left panel, red), the main plume is detected by the intermediate and upper fit window of the Prototype (right panel, green and red). Furthermore it should be noted that several white stripes occur in latitudinal direction, indicating data gaps caused by OMI measurements that are affected by the so-called “row anomaly” and that are left out for the verification exercise.

The individually used fit windows in comparison to the final SO_2 VCDs for both algorithms shown in Figure 10.30 this time clearly indicates that the SO_2 AR Verification Algorithm (left panel, red crosses) suffers from an underestimation and saturation of the true SO_2 column, as the VCDs for VA and PA more and more differ. The 360-390 nm fit window of the Prototype Algorithm (right panel, red crosses) is therefore better suited for an adequate retrieval of the SO_2 VCD in case of extremely high SO_2 concentrations that may occur for sporadic volcanic eruptions. However, it is expected that the higher spatial resolution of the TROPOMI instrument will lead to an increase of measurements that are affected by such high SO_2 concentrations, as well as lead to generally higher SO_2 VCDs maxima

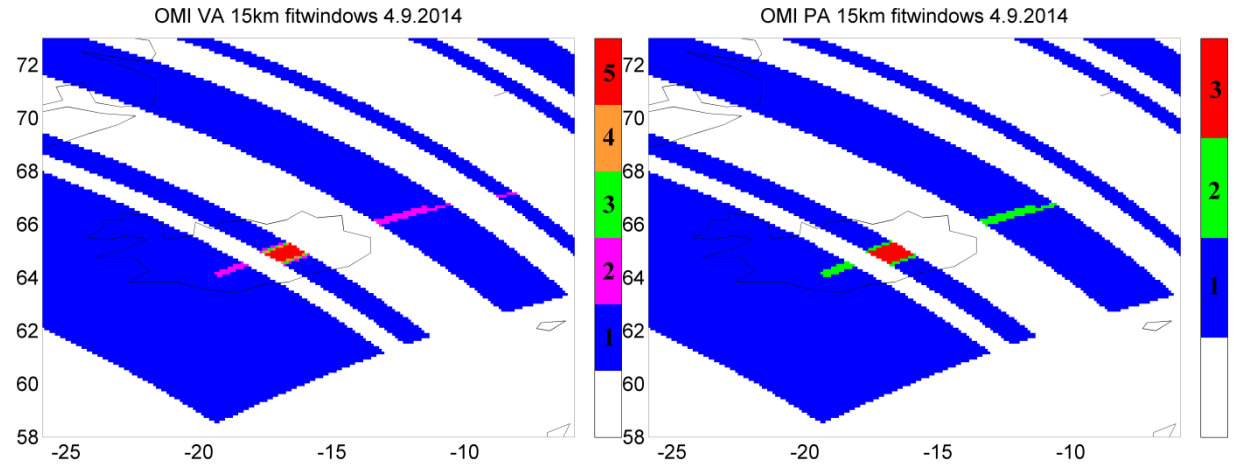

Figure 10.29: Colour-coded fit windows for one day during the Bárðarbunga on September 4, 2014. Both algorithms use all three fit windows for the SCD retrieval. The Verification Algorithm (left panel) mainly uses a combination of SO_2 SR/MR (2 – purple → SO_2 SR/MR) and AR (5 - red), while the Prototype detects the main plume for the intermediate (2 – purple → 325-335 nm) and upper (3 – red → 360-390 nm) fit window.

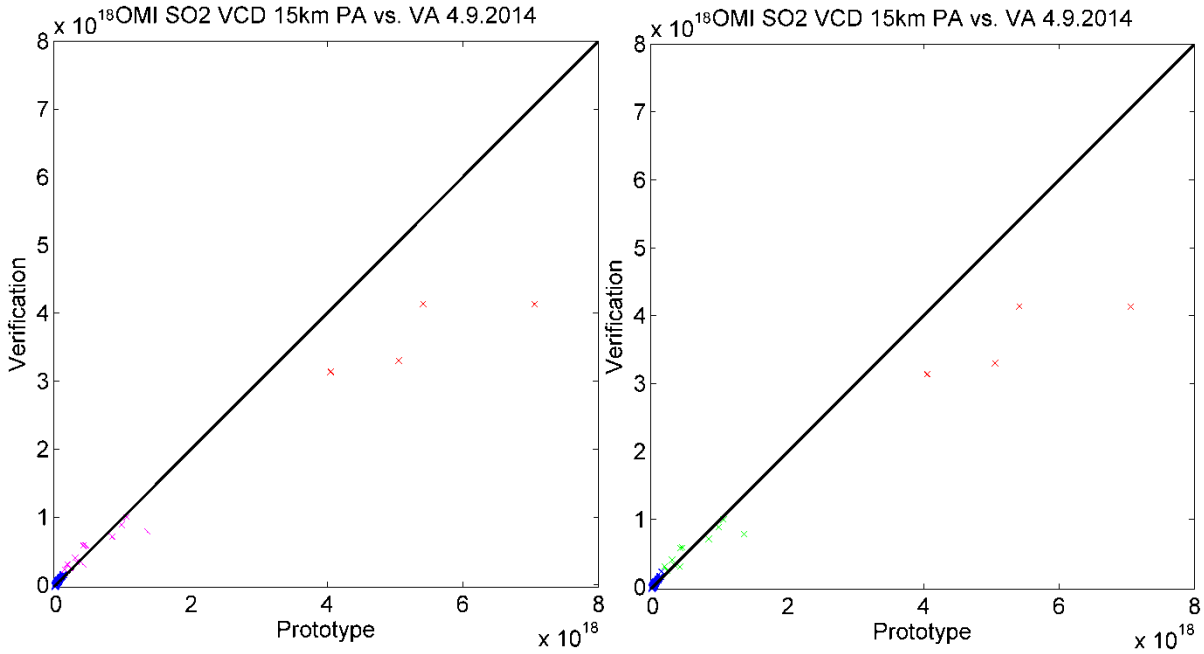

Figure 10.30: OMI SO_2 VCD scatter plot for PA (x-axis) and VA (y-axis) for the volcanic plume during the Bárðarbunga eruption on September 4, 2014. Different used fit windows for both algorithms are colour-coded according to the description in Figure 10.24 (left panel – VA, right panel – PA). While both algorithms show similar VCDs up to ~1x10^{18} molec/cm², the VA is clearly affected by strong underestimation of the SCD/VCD for extreme SO_2 concentrations. In contrast, the upper fit window of the PA (right panel – red crosses) seems to be much better suited for this specific scenario.

10.8 Summary of verification results

The prototype and verification algorithms use a similar DOAS approach in order to retrieve SO_2 vertical column densities from both anthropogenic and especially volcanic origin and show very good agreement for the vast majority of investigated synthetic and real data scenarios. Especially for very low (close to zero) SO_2 concentrations, the Prototype Algorithm does an excellent job on the retrieval of the corresponding VCDs, while the Verification Algorithm suffers from increased data scattering.

The most significant differences between Prototype and Verification Algorithm were found for certain cases, where different wavelength ranges were used for the retrieval of the SO_2 slant column densities. While both algorithms use three different fit ranges, the strength of the additional fit windows chosen for the Prototype lies in the adequate retrieval of SO_2 VCDs caused by extreme SO_2 concentrations. For such scenarios, the additional fit windows of the Verification Algorithm show signs of being affected by non-linear radiative transfer effects that may lead to significant underestimation of the “true” SO_2 SCD/VCD.

However, while such problems were not noticed for the synthetic SO_2 verification scenarios, it was shown from different case studies using real data from the Ozone Monitoring Instrument that the fit windows of the Verification Algorithm might have the advantage of higher sensitivity in case of moderate to high SO_2 concentrations, while the intermediate and upper fit window of the Prototype might suffer from increased data scattering caused by a comparatively lower SO_2 absorption.

It is finally emphasised that former operational DOAS based SO_2 retrieval algorithms for satellite instruments were entirely lacking of a comparably easy and particularly fast approach to deal with radiative transfer effects occurring due to high SO_2 concentrations as typically present in volcanic plumes. The Prototype as well as the Verification Algorithm are therefore an important step forward towards an adequate retrieval of the total SO_2 amount that is regularly injected into the Earth’s atmosphere during volcanic eruptions.

10.9 References

Beirle, S., Hörmann, C., Penning de Vries, M., Dörner, S., Kern, C., and Wagner, T.: Estimating the volcanic emission rate and atmospheric lifetime of SO_2 from space: a case study for Kīlauea volcano, Hawai`i, Atmos. Chem. Phys., 14, 8309-8322, 2014

Bobrowski, N., Kern, C., Platt, U., Hörmann, C., and Wagner, T.: Novel SO_2 spectral evaluation scheme using the 360–390 nm wavelength range, Atmos. Meas. Tech., 3, 879-891, doi:10.5194/amt-3-879-2010, 2010.

Hörmann, C., H. Sihler, N. Bobrowski, S. Beirle, M. Penning de Vries, U. Platt, and T. Wagner, Systematic investigation of bromine monoxide in volcanic plumes from space by using the GOME-2 instrument, Atmos. Chem. Phys., 13, 4749-4781, doi:10.5194/acp-13-4749-2013, 2013.

Pukite, J., Kühl, S., Deutschmann, T., Platt, U., and Wagner, T.: Extending differential optical absorption spectroscopy for limb measurements in the UV, Atmos. Meas. Tech., 3, 631-653, doi:10.5194/amt-3-631-2010, 2010.

Spurr, R. (2008), LIDORT and VLIDORT: Linearized pseudo-spherical scalar and vector discrete ordiate radiative transfer models for use in remote sensing retrieval problems, in Light Scattering Reviews 3, edited by A. Kokhanovsky, pp. 229–275, Springer, Berlin, doi:10.1007/978-3-540-48546-9_7

Theys, N., Roozendael, M. V., Dils, B., Hendrick, F., Hao, N., and Mazíre, M. D.: First satellite detection of volcanic bromine monoxide emission after the Kasatochi eruption, Geophys. Res. Lett., 36, 4 pp., doi:10.1029/2008GL036552, 2009a.

Theys, N., De Smedt, I., van Gent, J. Danckaert, T., Wang, T., Hendrick, F., Stavrakou, T. Bauduin, S. Clarisse, L., Li, C., Krotkov, N. Yu, H. Brenot, H. and Van Roozendael, M.: Sulfur dioxide vertical column DOAS retrievals from the Ozone Monitoring Instrument: Global observations and comparison to ground-based and satellite data, J. Geophys. Res. Atmos., 119, doi:10.1002/2014JD022657, 2015

11 HCHO Column

Authors: Andreas Richter, Andreas Hilboll, and Enno Peters (IUP-UB), Isabelle de Smedt (BIRA-IASB)

11.1 Document changes

Changes in issue 2.0:

- Verification af AMF added

11.2 Verification approach

The verification approach taken for HCHO is comparison of the prototype algorithm with the DOAS retrieval developed at IUP Bremen. The two algorithms agree in principle but use different approaches in many of the detailed analysis settings. It is therefore expected that this comparison will lead to an improved understanding and an optimisation of the prototype algorithm.

The overall approach to HCHO verification is

1. Comparison of HCHO slant columns as derived from synthetic spectra. Details on the approach and settings used are given in section 8. The expected outcome of this exercise is to ensure that the slant column retrievals agree within uncertainties between each other and with the “true” values
2. Comparison of box AMFs for simple scenarios. The expected outcome is to establish agreement between the different radiative transfer models used and the input applied.
3. Comparison of slant column and vertical column retrievals on OMI data. The expected outcome is a quantification of differences and uncertainties between the two retrievals, identification of shortcomings of the two approaches and optimisation of retrieval settings in the prototype algorithm.

As the signal to noise ratio for HCHO columns is relatively low, comparisons on real data have to be done mainly on monthly averages.

11.3 Verification algorithm description

The IUP-UB HCHO product is derived from satellite spectra in a similar procedure as described for NO_2 in section 9.3. It is a classical DOAS retrieval separating spectral fitting of the HCHO signature from radiative transfer.

It follows the usual steps of DOAS retrievals:

1. Slant column retrieval
2. Post processing (spike removal, destriping, offset correction)
3. Application of air mass factors for conversion to vertical columns

11.3.1 Slant Column Retrieval

The settings applied for the HCHO DOAS retrieval are summarised in Table 11.2. A single large fitting window (328.5 – 359.0 nm) is applied as default setting.

Correction of Ozone non-linearities has not been applied in the GOME, SCIAMACHY, and GOME-2 versions of the IUP-UB HCHO retrievals, but tests from the prototyping team indicate improvements on real data when the Pukite et al. (2010) correction is applied.Special attention has to be given to the choice of Ring cross-section. Here, a SCIATRAN calculation is used which is based on a scenario excluding HCHO. Previous experience shows that this reduces artefacts from interference between HCHO and Ring fits.

As the HCHO retrieval is well known for its susceptibility to offsets and other artefacts from spectral interference from other absorbers but also instrument effects, it is expected that final adjustments of the retrieval settings can only be done once real S5P-data is available.

11.3.2 Post-processing: Spike removal / Destriping / Offset Correction

As mentioned in section 9.3, active spike removal can strongly reduce the noise in the region of the Southern Atlantic Anomaly, and for HCHO, this is even more important than for NO_2. Therefore, the HCHO verification algorithm includes spike removal in the DOAS fit

Experience on OMI data has shown that HCHO columns exhibit clear striping and it is expected that a similar problem might also occur in S5P data. Therefore, destriping will be applied to the data in combination with the offset correction described in the next paragraph.

As mentioned above, HCHO columns are affected by spectral interference and offsets in a similar way as SO_2 (see section 10.3.2.1), only more so. Therefore, a similar normalisation is applied by using all measurements over the Pacific sector (180 – 220°E), computing daily averages of the slant columns per detector row, binning in latitude bins, and then subtracting the interpolated values from all measurements of the day. In order to avoid data gaps, the reference values are stored and continuously updated as new data come in. This approach accounts for both striping and latitudinal dependent biases. The optimum resolution of the latitude binning will depend on the quality of the S5P slant columns and is currently set to 5°.

11.3.3 Tropospheric Air Mass Factors

From the post-processed HCHO slant columns, vertical columns are retrieved using the standard DOAS approach of AMF lookup-tables in combination with a priori HCHO profiles.

11.3.3.1 HCHO profiles

Tropospheric HCHO profiles are taken from the COPERNICUS atmospheric service modelling system. Analysis data will be used for normal processing but in principle, forecast data can also be used for NRT processing.

As discussed for NO_2, the advantage of the COPERNICUS system is the large amount of atmospheric data assimilated which strongly constrains the fields of some chemical species in the model. It can therefore be expected that the profiles are a good representation of the atmospheric situation. The disadvantage of the COPERNICUS data is the relatively low spatial resolution of 0.7° (expected to improve in the coming year) which is not really appropriate for the S5P spatial resolution. The verification algorithm is therefore written in a way to also accept other model data as input, for example from the regional models also operated in the COPERNICUS system. These could for example provide high spatial resolution a priori data for a European data subset.

11.3.3.2 Aerosols

In this version of the verification algorithm, aerosols are not included in the look-up tables for the air mass factors. As for NO_2, the implementation of an option to include parameterized aerosol information (extinction profile, single scattering profile, simplified phase function) into a future version of the look-up tables is foreseen using either climatologies or COPERNICUS data as input.

11.3.3.3 Clouds

The verification algorithm will use the operational S5P cloud product of cloud fraction and cloud top pressure to select for cloud free scenes, using a threshold of 20% geometric cloud fraction. While cloud correction is implemented in the algorithm as an option, the current baseline is to apply only cloud screening. Whether or not to switch to cloud correction will depend on the outcome of studies on real data investigating the consistency of cloud correction schemes at small cloud fractions.

11.3.3.4 Surface reflectance

As surface reflection data base, the OMLER climatology for the years 2005–2009, which is based on OMI measurements (Kleipool et al., 2008) is used. In the EU funded QA4ECV project, alternatives for this surface reflectance dataset are being investigated, and any early results from that can be added as last minute changes to the processor. Of particular interest will be the evaluation of BRDF effects (expected to be small with the exception of very large viewing angles) and the applicability of high spatial resolution data sets for the interpolation of high spectral resolution data.

11.3.3.5 Digital Elevation Map

The surface altitude for each measurement pixel will be provided by the L1B team as described in Ch. 5 of [RD3]; the current baseline is to use the GMTED2010 dataset (Danielson and Gesch, 2011).

11.3.3.6 Setup of AMF look-up tables

As in the prototype algorithm, the look-up table for the AMF covers the dimensions solar zenith angle, line-of-sight (i.e., viewing azimuth) angle, relative sun azimuth angle, surface albedo, surface altitude, altitude. Vertical data (surface altitude, altitude) are given in units of meter. The exact coordinates of the look-up table are given in Table 11.1.

Table 11.1 Nodes in the look-up table for HCHO air mass factors.

Parameter	# of points	Values
cos(solar zenith angle)	12	0.01, 0.03, 0.05, 0.15, 0.25, 0.30, 0.50, 0.60, 0.70, 0.80, 0.90, 1.00
cos(viewing zenith angle)	6	0.3, 0.5, 0.7, 0.8, 0.9, 1.0
Relative sun azimuth angle	13	0°, 15°, 30°, …, 165°, 180°
Surface albedo	7	0.00, 0.05, 0.10, 0.20, 0.50, 0.80, 1.00
Surface altitude	5	0km, 1km, 2km, 5km, 10km
Altitude	171	0.00km, 0.05km, 0.15km, …, 9.85km, 9.95km, 10.5km, 11.5km, …, 58.5km, 59.5km, 61km, 63km, …, 97km, 99km
Wavelength	1	341nm

11.3.3.7 Main differences to prototype algorithm

The physical basis for the retrieval of tropospheric HCHO and the fundamental approach taken is similar in the verification and prototype algorithm. The main differences are with the choice of fitting region, the treatment of interfering species (application of pre-fitting of BrO in the prototype) and the climatologies used for the AMF calculations.

11.4 Error analyses

Most of the relevant uncertainties of the verification algorithm as described here are identical to those in the prototype algorithm (see de Smedt et al., 2008 and de Smedt et al., 2012 for a discussion), and the same estimates apply for the verification algorithm. The main error sources are

- Random noise in the spectra
- Systematic spectral residuals, for example from imperfect radiometric calibration
- Spectroscopic interference in the DOAS retrieval
- Uncertainty on the HCHO cross-section (see Meller and Moortgart, 2000)
- Uncertainty on the temperature correction on the HCHO column
- Imperfect correction of the background HCHO column
- Uncertainty in the tropospheric AMF and Averaging Kernels from
    - Cloud effects
    - Surface reflectance uncertainty including BRDF effects and shadows
    - A priori HCHO profile uncertainty including effects of low model resolution
    - Uncertainty in a priori aerosol fields and effects

11.5 First Verification Results on synthetic spectra

The set-up of the synthetic data used for the verification exercise is described in section 8.

In two independent steps, first the fits performed by operational and verification algorithms on simulated spectra without noise are compared to each other and to the slant column densities (SCDs) as simulated by SCIATRAN for the respective fitting windows. Here, there is one SCD per algorithm per viewing geometry per atmospheric scenario, and these SCDs are directly compared to each other. Secondly, the fit results of operational and verification algorithms performed on noisy simulated spectra are compared. In this second comparison, the distributions of the SCDs retrieved by one algorithm for the 9 noisy spectra for one viewing geometry / atmospheric scenario pair are compared between operational and verification algorithms.

For the HCHO data product, the operational algorithm from BIRA could be compared to the verification algorithm from IUP-UB. A direct comparison of the settings used in this verification exercise is given in Table 11.2. It should be noted that the use of a Ring spectrum based on the CAMELOT 5 scenario in the verification algorithm intrinsically provides a better representation of the Ring effect for these simulations which might not be the case for real data.

Table 11.2: Settings used for the HCHO verification exercise. Some of the settings differ from the settings foreseen for the final processor to simplify interpretation of the verification results

Quantity	Prototype Algorithm	Verification Algorithm
fitting window	328.5-346 nm	328.5 – 359.0 nm
degree of polynomial	5	4
prefitting of BrO in window	328.5 – 359.0 nm	--
HCHO x-section	Meller & Moortgart et al., 293 K	Meller & Moortgart et al., 293 K
O3 x-section	Gorshelev et al. & Serdyuchenko et al., 223K + 243K	Gorshelev et al. & Serdyuchenko et al., 223K + 243K
NO2 x-section	Vandaele et al. 220K	Vandaele et al. 220K
O4 x-section	Greenblatt et al., 296K	Greenblatt et al., 296K
BrO x-section	Fleischmann et al., 223K	Fleischmann et al., 223K
Ring x-section	2 Ring cross-sections calculated in an ozone containing atmosphere for low and high SZA, using LIDORT_RRS (Spurr et al., 2008b) and a standard atmosphere (CAMELOT European Pollution atmospheric profile), according to Vountas et al., 1998.	SCIATRAN CAMELOT5, no HCHO absorption included + second Ring, scaled by wavelength
O3 non-linearity correction	Non-linear O3 absorption effect: 2 pseudo-cross-sections from the Taylor expansion of the wavelength and the O3 optical depth (Puķīte et al., 2010).	-
additive offset	linear	constant

In the fitting of HCHO, a strong discrepancy between the operational algorithm on one hand and the verification algorithm and the simulated slant columns on the other hand can be observed. In most scenarios, the operational algorithm yields HCHO SCDs which are about 50-80% higher than both the verification algorithm's and the simulated HCHO SCDs. This is exemplarily shown for scenarios 5 (U.S. east coast) and 7 (biomass burning / land) in Figure 11.1 and Figure 11.2, respectively.

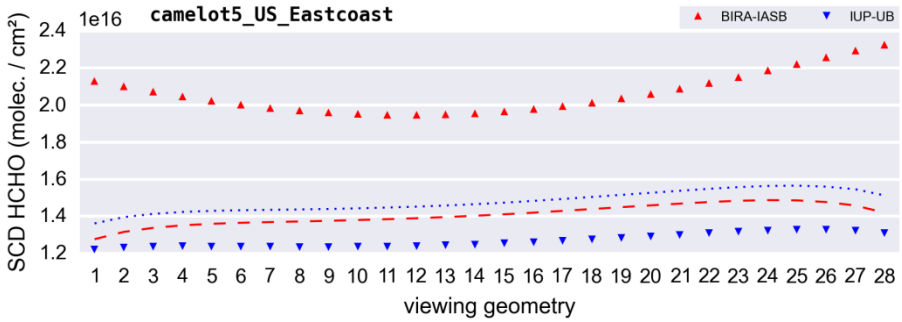

Figure 11.1: HCHO SCDs fitted by operational (red) and verification (blue) algorithms, and simulated by SCIATRAN (dotted lines, averaged over the respective algorithm's fitting window), for scenario 5 (U.S. east coast).

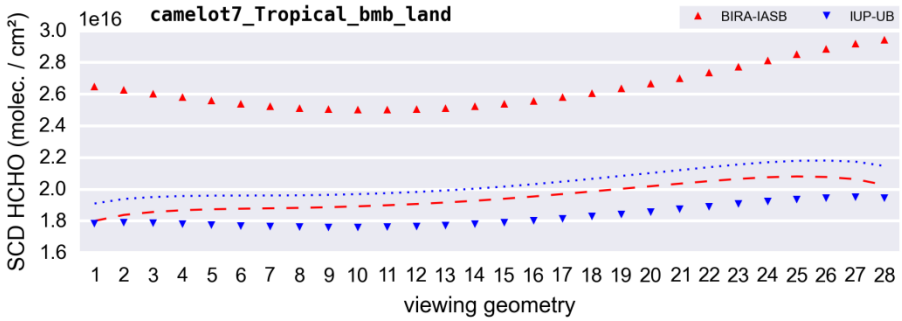

Figure 11.2: HCHO SCDs fitted by operational (red) and verification (blue) algorithms, and simulated by SCIATRAN (dotted lines, averaged over the respective algorithm's fitting window), for scenario 7 (biomass burning / land).

Apart from the obvious difference between the two algorithms, the following issues can be identified:

- The operational algorithm leads to a line-of-sight dependency opposite to that visible in the simulated slant columns.
- The verification algorithm generally underestimates the simulated slant columns but to a lesser degree.
- The verification algorithm has a weaker dependency on the line-of-sight compared to the simulated slant columns.

Some work has been undertaken trying to reduce the large discrepancy between the operational and verification algorithms. While the operational algorithm can be tuned to closer reproduce the verification algorithm and the SCIATRAN simulations, this comes at the cost of reduced fit quality. At this point, it is doubtful if these tunings are actually desirable. Rather, further investigation has to be undertaken to analyse the reasons behind the large discrepancy and why fit residuals increase when the results are closer to the truth.

Generally, both operational and verification algorithms are very sensitive to changes in the retrieval settings, especially to the choice of pseudo cross-section used to consider the effect of rotational Raman scattering in the atmosphere (Ring effect). Further investigation were needed to identify reasons for the strong difference between the two retrieval algorithms and the simulated slant columns (see next section).

Figure 11.3 shows the influence of the Ring effect on the retrieved SCDs; the atmospheric scenario is the same as in Figure 11.2, but the synthetic spectra do not include the Ring effect. Clearly, the discrepancy between the operational algorithm and the simulated data is reduced in this case, but the Ring effect alone cannot explain the large differences. The verification algorithm actually performs worse than with Ring effect, possibly due to some mis-assignment of HCHO signals to the Ring cross-section.

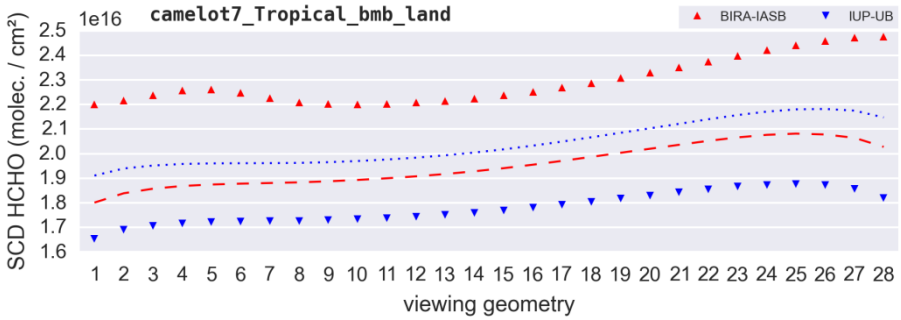

Figure 11.3: HCHO SCDs fitted by operational (red) and verification (blue) algorithms, and simulated by SCIATRAN (dotted lines, averaged over the respective algorithm's fitting window), for scenario 7 (biomass burning / land). The simulated spectra on which these fits were performed did not include the Ring effect.

The spread in the fit results caused by noisy input spectra is shown in Figure 11.4. In almost all scenarios, the scatter in the operational algorithm is larger than in the verification algorithm. Often, the lower extremes are reasonably close to each other, while the upper extreme values are higher in the operational algorithm. Sensitivity tests have shown that the larger scatter in the prototype algorithm results is related to the inclusion of the "O_3 Pukite" cross-sections.

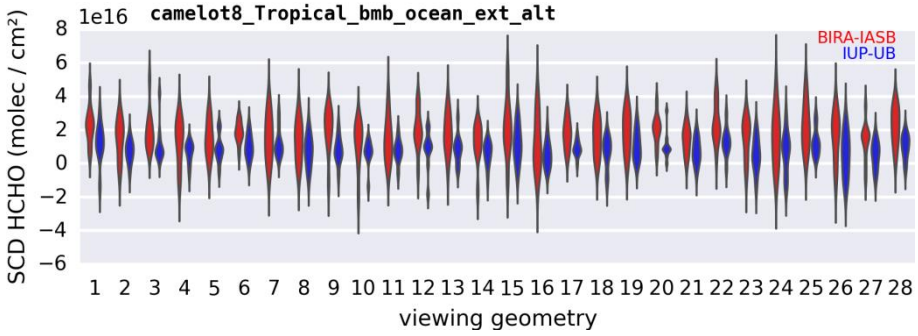

Figure 11.4: Violin plot of the HCHO SCD fit results of noisy input spectra from operational (red) and verification (blue) algorithms, for each viewing geometry, for scenario 8 (tropical biomass burning / ocean). (Vertically, the violin plot is a box plot, while the horizontal extent represents the kernel density).

When directly comparing the fitted SCDs from operational and verification algorithms, those fits not influenced by noise show perfect correlation. However, the verification algorithm yields significantly lower SCDs, which shows in a low slope of the regression line. The noisy fits also show good correlation, with a higher (but still significantly lower than 1) slope of the regression line. Examples are shown in Figure 11.5.

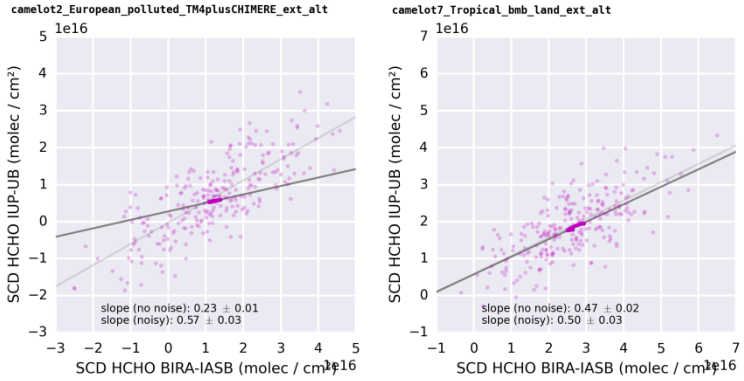

Figure 11.5: Scatter plots of HCHO SCDs derived from the operational and verification algorithms, for scenarios 2 (European polluted, left) and 7 (tropical biomass burning / land). Those fits not influenced by noise are shown in solid colour, while fits on noisy data are transparent.

11.6 Sensitivity tests performed with the prototype algorithm

In order to understand the initial problems faced with the HCHO slant column verification, sensitivity tests were performed with the prototype algorithm to investigate the uncertainties on HCHO slant column retrievals under geometries typical of TROPOMI observations. Simulated spectra have been provided by IUP Bremen using the SCIATRAN model. The set-up of the synthetic data used for the verification exercise is described in section 8. In the most realistic case, simulations include all known effects, i.e., realistic profiles for all known trace gases absorbing in the wavelength range of interest, temperature dependent cross-sections for all gases, radiances accounting for inelastic rotational Raman scattering effects (Ring effect). In addition, in an attempt to disentangle sources of biases in the retrievals, tests are performed using various levels of simplification as described below.

We start from an analysis of the HCHO slant columns (SCDs) obtained using the prototype “baseline configuration”, i.e., the configuration proposed for the prototype as described in the ATBD (see results shown in section 11.5). To get a better view of the uncertainties, we have included in our sensitivity tests 3 fitting intervals and two different Ring corrections (see Table 11.3). In each case, we compare results obtained using as reference spectrum (1) the solar irradiance used as an input for the simulations, and (2) a simulated radiance obtained in the equatorial Pacific (CAMELOT 6 scenario), for a small viewing angle. This second case is more representative of prototype retrievals which are performed against a reference spectrum acquired in the background Pacific Ocean. Note that the approach foreseen in the prototype algorithm goes even one step further, using (1) a different reference spectrum for each detector/viewing angle, and (2) including a post-processing normalization of the slant columns (latitude and row dependent reference sector normalization, see details in the ATBD) which further minimizes row-dependent errors.

In order to simulate realistic retrievals, we use own absorption cross-sections (i.e. cross-sections chosen and processed at BIRA). These cross-sections may differ from the “true cross-sections” used in simulations as to (1) their origin (see Table 11.3) and (2) the pre-processing applied (convolution and interpolation might be applied differently).

In all cases discussed below, the true SCDs are displayed using black filled squares. True SCDs have been obtained by multiplying the known input HCHO VCDs by calculated air mass factors (AMFs) averaged over the fitting interval.

Table 11.3: Overview of the retrieval settings used for the different HCHO sensitivity tests performed with the prototype processor.

Test settings		
Interval 1	**328.5-359 nm**	**First interval used in the prototype algorithm to fit BrO – also corresponds to the verification interval.**
Interval 2	**328.5-346 nm, with BrO pre-fitted in interval 1.**	**Prototype algorithm**
Interval 3	**336.5-359 nm**	**Interval recommended for ground-based MAXDOAS measurements of HCHO in Pinardi et al., 2013.**
DOAS reference spectrum		
Upper panels	Sun spectrum used in the SCIATRAN simulations	
Lower panels	Simulated radiance in the reference sector (equatorial Pacific): camelot6, Tropical background, SZA=29.34, LOS=2.22, AZIM=67.05. In this case an estimation of the HCHO slant column contained in the reference sector has been added to the HCHO columns ($0.5x10^{15}$ molec.cm^{-2}).	
Ring correction		
Plain Markers	2 Ring cross-sections calculated in an ozone containing atmosphere for low and high SZA, using LIDORT_RRS (Spurr et al., 2008b) and a standard atmosphere (CAMELOT European Pollution atmospheric profile), according to Vountas et al., 1998.	
Empty Markers	2 Ring cross-sections calculated by simple convolution of the solar irradiance by RRS cross-sections: Ring + Ring*wavelength (LRing). The second cross-section accounts for the wavelength dependence of the RRS probability.	
Absorption cross-sections		
HCHO	Meller and Moortgat (2000), 298K	
Ozone	Gorshelev et al. (2013) and Serdyuchenko et al. (2013), 223K and 243K.	
BrO	Fleischmann et al. (2004), 223K	
NO_2	Vandaele et al. (1998), 220K	
O_4 (O_2-O_2)	Greenblatt et al. (1990)	
Non-linear O_3 absorption effect	2 pseudo-cross-sections from the Taylor expansion of the wavelength and the O_3 optical depth (Puķīte et al., 2010).	

11.6.1 Analysis of full SCIATRAN simulations

In a first step, the different retrieval settings are applied to spectra simulated with all possible effects. This includes Rotational Raman Scattering (RRS) and the temperature dependence of all absorption cross-sections is taken into account in the SCIATRAN calculations.

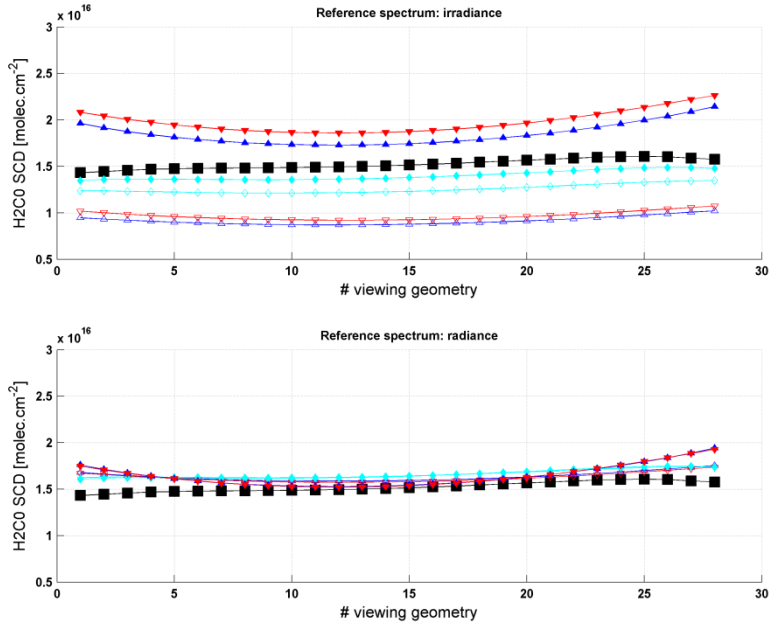

Figure 11.6: HCHO SCDs fitted using different DOAS retrieval settings (see Table 11.3). True SCDs are indicated with black squares. They correspond to the CAMELOT scenario 5 (US East coast). The upper panel shows results obtained using the solar irradiance as reference spectrum, while results in the lower panel are obtained using a simulated radiance in the reference Pacific sector (scenario 6). Simulations include all possible effects, in particular RRS and temperature dependencies for all absorbers.

Results are displayed in Figure 11.6:

- Variable and large offsets are observed on the resulting HCHO SCDs when using the sun irradiance as reference. These offsets largely cancel when a radiance spectrum is used in the retrievals instead of the solar irradiance (lower panel). In the latter case, the SCDs still show a dependency on the viewing angle (VZA). Note that in actual retrievals using the S5P baseline described in the ATBD, these differences would also cancel since S5P retrievals will use different reference spectra for each position along the TROPOMI swath.
- The HCHO SCDs obtained using the simple “Fraunhofer only” Ring correction are always lower than those obtained using the baseline “ozone-containing” Ring correction. This indicates that at least part of the observed offsets is related to the Ring effect (see 11.6.2).
- The 2 intervals starting at 328.5 nm are more sensitive to the choice of the Ring correction method than the third interval (336.5-359). They also show a larger VZA dependency.

11.6.2 Analysis of elastic simulations: impact of the Ring effect

These tests are based on simplified elastic simulations, where RRS is not included. All other effects are treated in the same way as for the full simulations (in particular the temperature dependence of the absorption cross-sections). For these elastic cases, Ring cross-sections have been removed from the DOAS settings.

Results are displayed in Figure 11.7:

- It is obvious that offsets are greatly reduced, as well as the VZA dependency.

- However the 328.5-346 nm interval still shows a small positive offset, which is likely due to a persisting ozone misfit (see section 11.6.4)

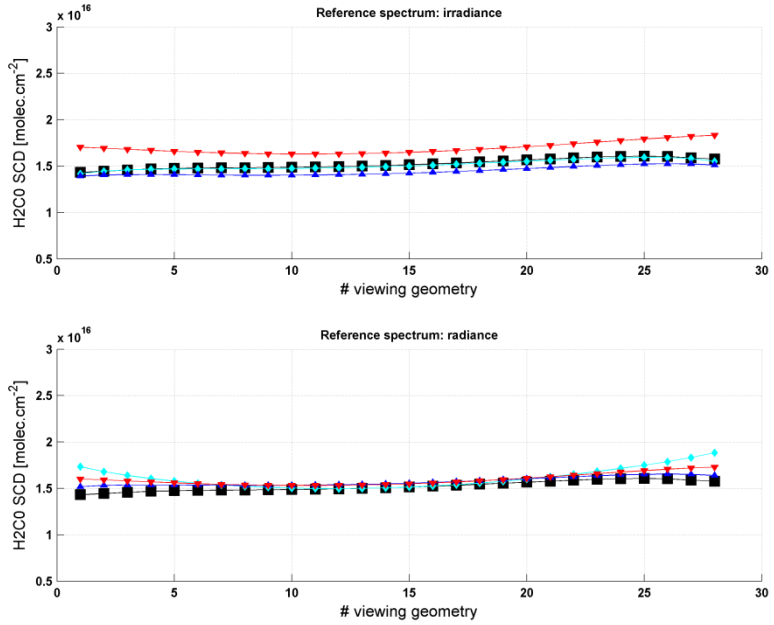

Figure 11.7: HCHO SCDs fitted using different DOAS retrieval settings (see Table 11.3). True SCDs are indicated with black squares. They correspond to the CAMELOT scenario 5 (US East coast). The upper panel shows results obtained using the solar irradiance as reference spectrum, while results in the lower panel are obtained using a simulated radiance in the reference Pacific sector (scenario 6). The simulated spectra are elastic, i.e. they do not include RRS, however temperature dependencies are considered for all absorbers.

11.6.3 Impact of the temperature dependence of ozone absorption cross-sections

In this case, simulations include RRS but the temperature dependence of the absorption cross-sections is de-activated (arbitrarily set to 223°K).

Results are displayed Figure 11.8:

- In comparison to Figure 11.6, one can see that biases are reduced in all cases except those making use of the simple “Fraunhofer only” Ring correction (which are still biased negatively, especially in the 328.5-346 nm interval). Additional tests not shown here indicate that the impact of the temperature dependence of gases other than ozone is negligible.
- These results indicate that (1) the imperfect correction of the temperature dependence of the ozone cross-section may introduce biases on HCHO, and (2) the molecular contribution to the Ring effect needs to be taken into account in the analysis, especially at shorter wavelengths where the ozone absorption is stronger.
- Like in Figure 11.6, biases are comparatively smaller at long wavelength (336.5-359 nm) than at short wavelength (328.5-359 nm), most probably because of the reduced interference by ozone absorption in this region.

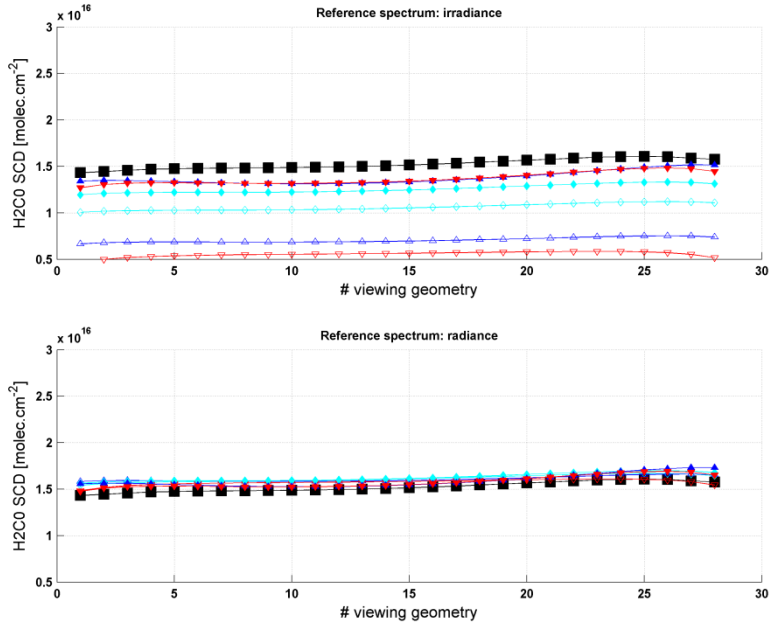

Figure 11.8: HCHO SCDs fitted using different DOAS retrieval settings (see Table 11.3). True SCDs are indicated with black squares. They correspond to the CAMELOT scenario 5 (US East coast). The upper panel shows results obtained using the solar irradiance as reference spectrum, while results in the lower panel are obtained using a simulated radiance in the reference Pacific sector (scenario 6). The simulated spectra include RRS, but all cross-sections are assumed to be independent of the temperature.

11.6.4 Analysis of elastic spectra with temperature-independent cross-sections

These tests represent a further step in the simplification of the problem. In this case, RRS is not included (elastic simulations) and the temperature dependence of the cross-sections is de-activated. Like in section 11.6.2, Ring cross-sections have been removed from the DOAS fit.

Results are displayed in Figure 11.9:

- As can be seen, in this very simplified simulation, the obtained offsets are negligible in all cases and for all viewing angle positions.
- We conclude that the two main effects affecting the DOAS HCHO fits are uncertainties in the Ring effect correction and misfits due to imperfect correction of the temperature dependence of the ozone absorption. A simple attempt to minimize the latter effect is presented in the next section.

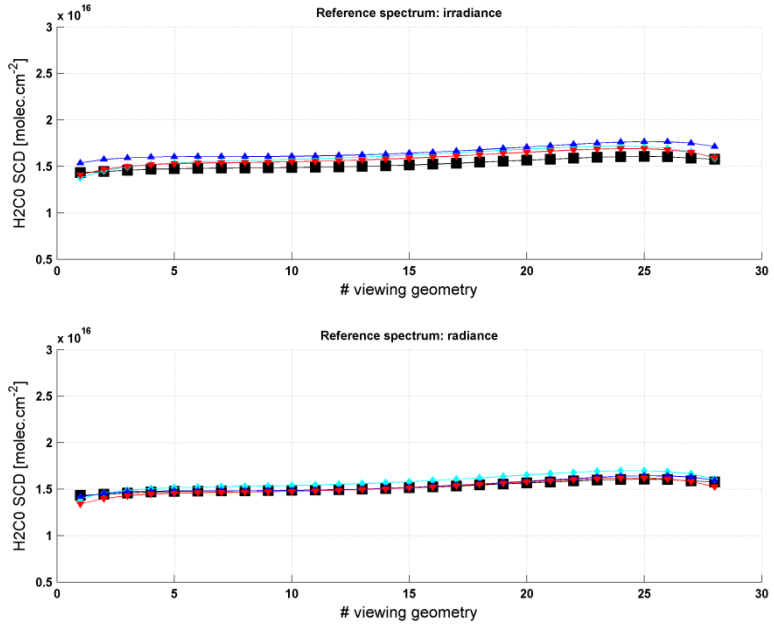

Figure 11.9: HCHO SCDs fitted using different DOAS retrieval settings (see Table 11.3). True SCDs are indicated with black squares. They correspond to the CAMELOT scenario 5 (US East coast). The upper panel shows results obtained using the solar irradiance as reference spectrum, while results in the lower panel are obtained using a simulated radiance in the reference Pacific sector (scenario 6). The simulated spectra do not include RRS, and the absorption cross-sections are assumed to be independent of the temperature.

11.6.5 Effect of adding correction terms for ozone absorption, following Pukite et al.

In addition to the already included pseudo-cross-sections from the Taylor expansion of the wavelength and the O_3 optical depth ($O3_{223}$*lambda and $O3_{223*}$ $O3_{223}$, Pukīte et al., 2010), we successively tested the addition of the following pseudo cross-sections, which are meant to explicitly treat temperature effects in the Taylor expansion terms:

- $(O3_{243}\text{-}O3_{223})*O3_{223}$
- $(O3_{243}\text{-}O3_{223})$*lambda
- $(O3_{243}\text{-}O3_{223})*(O3_{243}\text{-}O3_{223})$

Simulations include RRS and temperature dependent cross-sections for all absorbers.

Results are displayed in Figure 11.10:

- Compared to Figure 11.6, a clear – while still imperfect – improvement is obtained when including the 3 additional cross-sections (see also SO_2 results in Chapter 10).
- As to be expected, the addition of the ozone correction terms has no impact on the results using the “Fraunhofer only” Ring correction.
- Note that a significant viewing angle dependency is still present in results obtained using an earthshine radiance as reference (lower panel). This suggests that temperature effects still play a role, probably at the level of the ozone contribution to the Ring effect.
- Again like in cases 1 and 3, biases are less pronounced in the long wavelength interval (336.5-359 nm) than at 328.5-359 nm due to smaller interference by ozone.

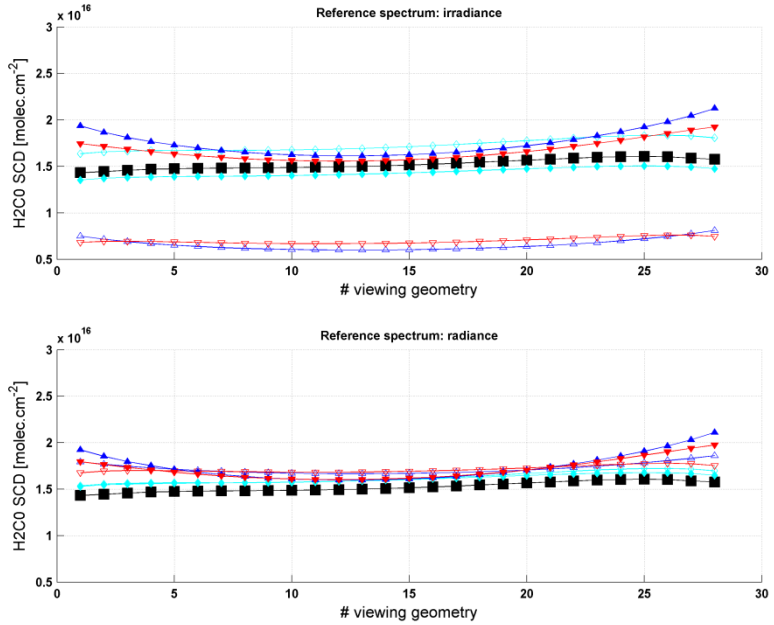

Figure 11.10: HCHO SCDs fitted using different DOAS retrieval settings (see Table 11.3). True SCDs are indicated with black squares. They correspond to the CAMELOT scenario 5 (US East coast). The upper panel shows results obtained using the solar irradiance as reference spectrum, while results in the lower panel are obtained using a simulated radiance in the reference Pacific sector (scenario 6). The simulated spectra include RRS, and temperature dependencies are considered for all absorbers. Additional ozone correction terms are applied in the DOAS fits (see text for details).

11.6.6 Impact of the spectral resolution: simulations at 0.2 nm FWHM

Additional simulations have been performed using SCIATRAN in order to check the impact of the spectral resolution on HCHO SCD fitting results. Two cases are compared, spectra at the resolution of 0.54 nm (TROPOMI resolution) and at the resolution of 0.2 nm (similar to the resolution of the SCIAMACHY instrument). These simulations are for the CAMELOT 5 scenario and they include RRS and temperature dependent cross-sections for all absorbers.

Results are displayed in Figure 11.11:

- Comparing the results shown in the upper panel (0.54 nm) to those in the lower panel (0.2 nm) it is clear that the spread of the retrieved HCHO SCDs is significantly reduced in the high resolution case.
- In particular these results suggest that the sensitivity of the HCHO retrieval to inaccuracies in the Ring effect treatment might be reduced at high resolution, which could be related to the fact that the frequency of the Ring effect structures significantly increases at high resolution, allowing for better de-correlation with trace gas absorption structures.

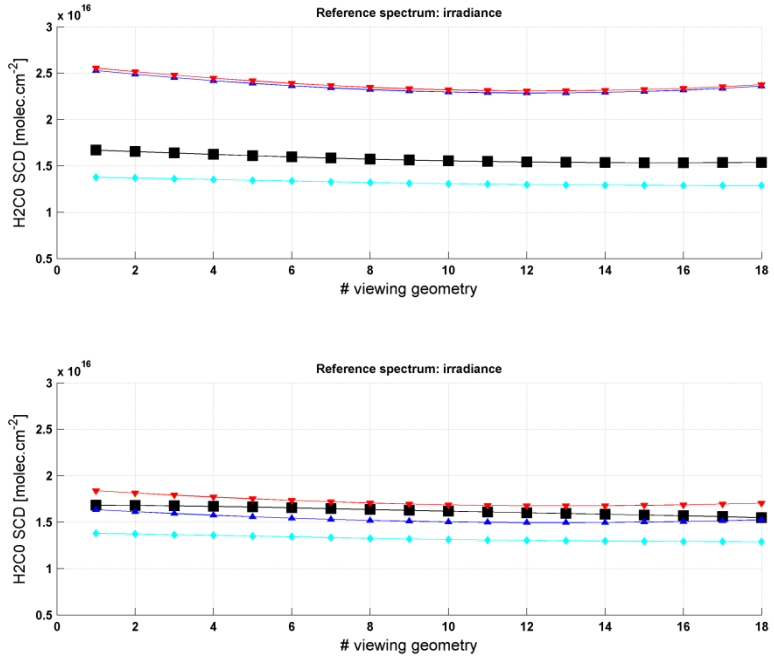

Figure 11.11: HCHO SCDs fitted using different DOAS retrieval settings (see Table 11.3). True SCDs are indicated with black squares. They correspond to the CAMELOT scenario 5 (US East coast). The upper panel shows results obtained with simulated spectra at the resolution of 0.54 nm, while lower panels shows results obtained at higher resolution (0.2 nm). The simulated spectra include RRS, and temperature dependencies are considered for all absorbers.

11.6.7 Conclusions from sensitivity studies

Based on the simulations performed in this study, one can conclude that:

- HCHO slant columns retrieved from realistic nadir radiance simulations, using DOAS settings successfully applied to sensors like GOME, SCIAMACHY, GOME-2, and OMI, can display significant and variable offsets in comparison to true HCHO columns.
- Those offsets are understood as being due to spectral interferences related to imperfect correction of the Ring effect and of the temperature-dependent ozone absorptions.
- Such spectral interferences have a smaller impact on simulations at 0.2 nm (representative of previous sensors) than at 0.54 nm.
- To correct for the Ring effect, it is important to take into account the molecular Ring effect (in particular ozone effects) in addition to the solar lines contribution.
- In all cases, the use of a radiance spectrum selected in the background Pacific (baseline approach proposed for HCHO retrieval from TROPOMI) allows to mitigate a large part of the observed interferences. In addition it is expected that the zonal reference sector normalization will largely correct for remaining latitude-dependent offsets. Such effects have been experimentally demonstrated in actual retrievals from GOME, SCIAMACHY, GOME-2, and OMI.
- All test cases investigated in this study based on noise-free spectra indicate that HCHO retrievals are less affected by ozone and Ring effect related biases when performed at long wavelength (336.5-359 nm). It must however be stressed that this interval has been shown to be less favourable in real situations when noise is taken into consideration, due to several reasons:

- The spectral interference between BrO and HCHO is significant in this region and leads to enhanced noise on HCHO columns due cross-talk effect.
- This interval includes a strong O_2-O_2 band not well measured in the laboratory and of which the temperature dependence is currently poorly understood. Experience has shown that uncertainties in this O_2-O_2 absorption introduce biases on HCHO in actual retrievals. This effect is minimized in the 328.5-346 nm interval (TROPOMI ATBD baseline).
- Finally this interval cannot be applied to SCIAMACHY spectra due to a strong polarization anomaly around 360 nm (Woods anomaly in the ruled grating used in the SCIAMACHY channel 2). Also in the case of GOME-2, polarisation structures in this interval have stronger effects than in the in the 328.5-346 nm interval. So it could not be used to generate consistent harmonised HCHO data sets from multiple sensors

- More tests on real data from the TROPOMI instrument will be needed to come to final decisions on the settings to be used for prototype and verification algorithms.

11.7 Verification of the prototype processing chain using OMI data

As with the NO_2 verification, also in the HCHO case, an extensive comparison of the processing chains of the prototype and verification algorithms has been conducted. For this intercomparison exercise, a common set of DOAS fit parameters has been agreed upon according to Table 11.4. The goal of this exercise was to ensure that the software implementation of the prototype algorithm behaves as expected in a large set of realistic measurement scenarios.

Table 11.4: Common DOAS fit settings for HCHO for the verification of the prototype processing chains.

Parameter	Value
Wavelength window	328.5 – 359.0 nm
Polynomial degree	5 (i.e., 6 coefficients)
HCHO cross-section	Meller and Moortgat, 2000, 298K
O_3 cross-section	Serdyuchenko et al., 2013, 223 + 243K
BrO cross-section	Fleischmann et al., 2004, 223K
O_4 cross-section	Thalman et al., 2013, 293K
NO_2 cross-section	Vandaele et al., 1998, 220K
Ring cross-section	Chance and Spurr, 1997
Solar Atlas	Chance and Kurucz, 2011
Calibration	1 calibration window (328 – 359 nm)
Convolution	Per row, i.e., use 60 slit functions
Background	Mean sun
Intensity offset	Linear slope
Error weighting	Off
Post processing	Background correction + de-striping
Wavelength calibration	Shift & squeeze on solar spectrum

The fit results from the prototype, verification, and comparison processing chains have been compared for a total of 6 representative days (2 Feb 2005, 12 Jun 2005, 16 Aug 2005, 21 Jun 2011, 04 Feb 2013; a total of 88 orbits) of OMI measurements.

An overview of the comparison of the raw SCDs is shown in Figure 11.12. The correlation of prototype and verification processing chains is extremely high (~1.0) in most cases; it is > 0.998 for all orbits. The slope of the regression line between prototype and verification results is close to 1.0; however, there is a consistent offset of ~10^{15} molec/cm². The mean SCDs of both prototype and verification algorithms are negative (which is not worrying because this is before application of the background correction); the 1-sigma variability and the mean RMS of both prototype and verification algorithms are virtually identical.

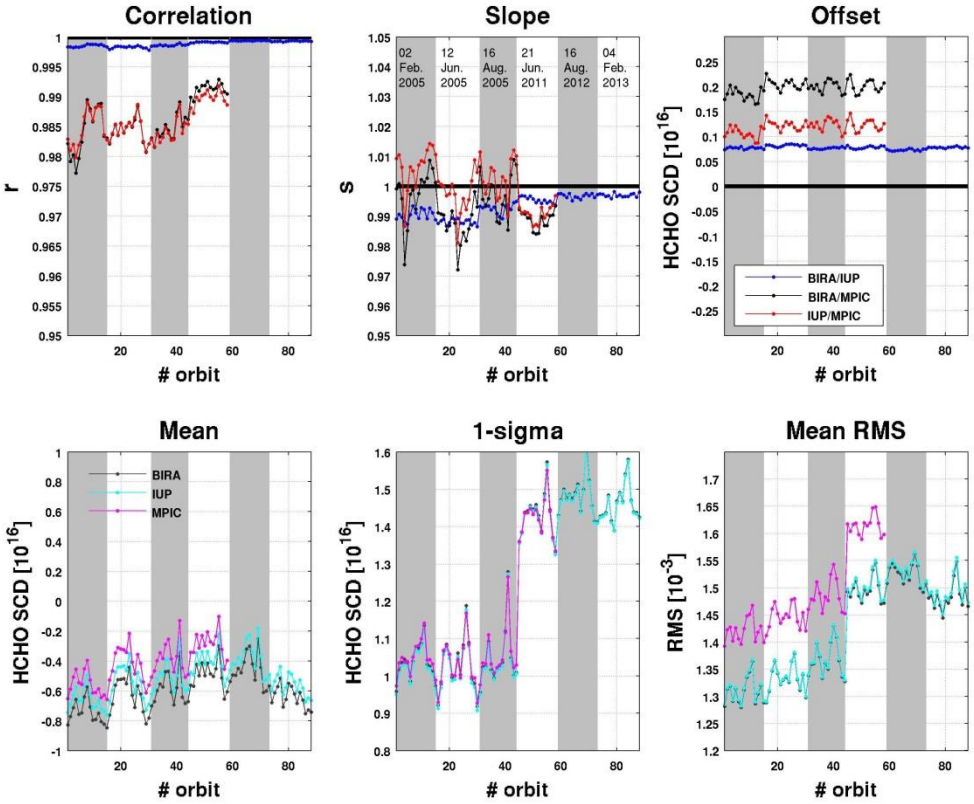

Figure 11.12: Comparison of key fit parameters from HCHO fits using harmonized fit settings (see Table 11.4measurements, before application of the background correction.

The analogous comparison of background-corrected SCDs is shown in Figure 11.13 As expected, the offset between prototype and verification results becomes negligibly small after the background correction (less than 5% of the slant column errors). However, for some orbits (those with slopes < 0.99, mainly on 21 Jun 2011), the correlation coefficient between prototype and verification processors drops to 0.96. This is most probably due to slight implementation differences regarding the background correction between the processing chains, which have not yet been identified. However, the achieved correlation is nonetheless > 0.96, so this issue is not deemed critical. The mean SCDs are now around zero. Note also the reduction of the standard deviations (1-sigma), particularly for years 2011 and onwards, thanks to the destriping correction.

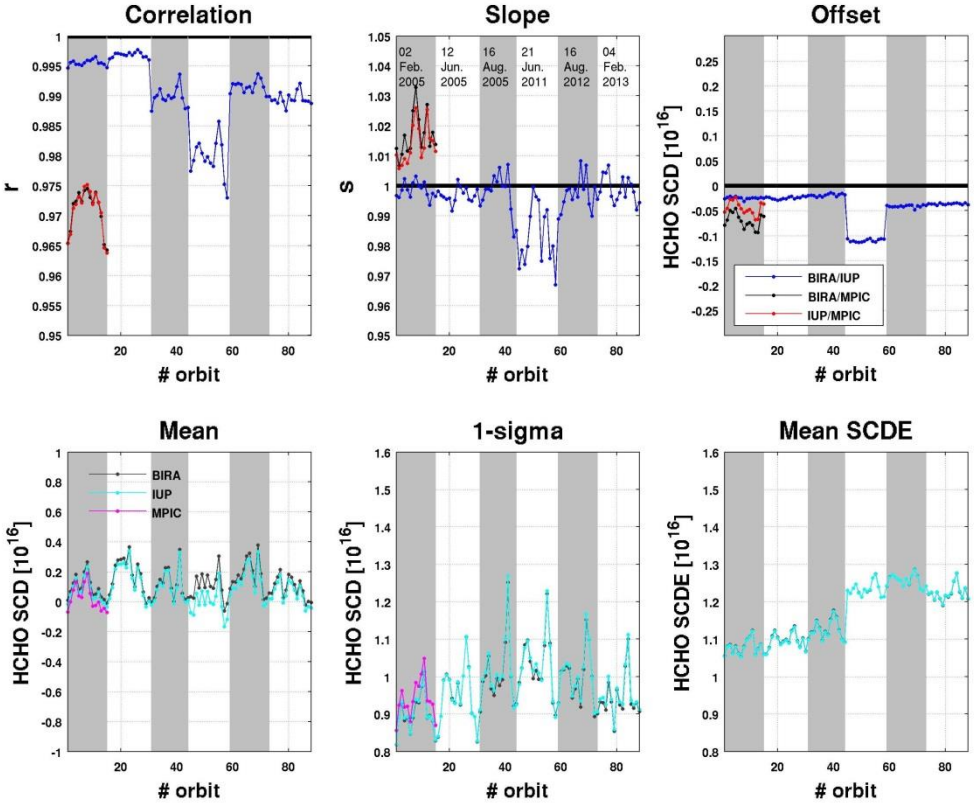

Figure 11.13: As Figure 11.12, but after application of the background correction, and showing SCDE instead of RMS.

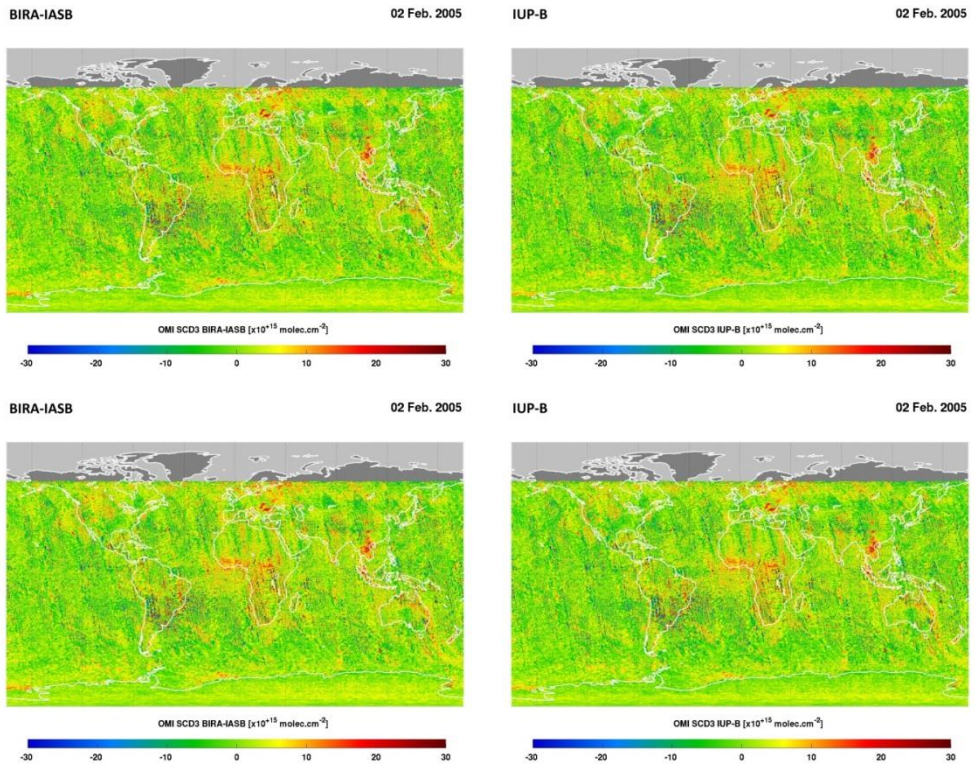

Figure 11.14 finally shows mapped HCHO SCDs (after background correction) from prototype and verification processing chains for 2 Feb 2005. It is apparent that the two processing chains yield very similar results; all major sources regions (e.g., Africa, SE-Asia) are clearly visible in both maps. The spatial patterns of HCHO SCDs are extremely similar.

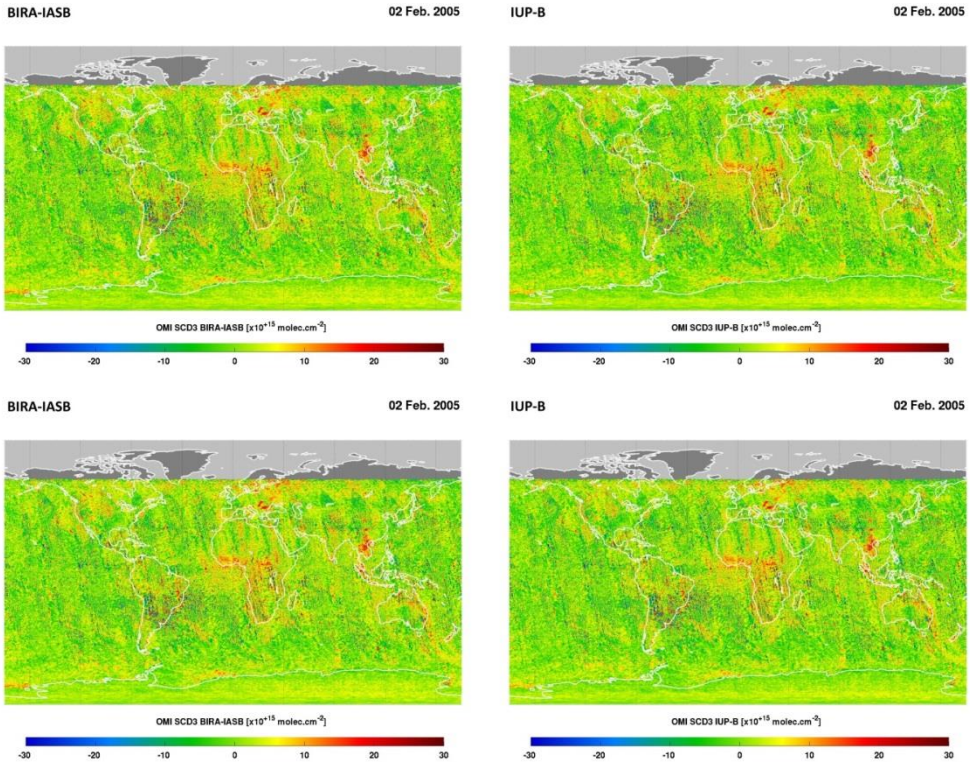

Figure 11.14: Background corrected HCHO SCDs retrieved from OMI measurements on 2 Feb 2005, using the prototype (left) and verification (right) algorithms.

During this intercomparison, various issues in both the prototype and verification processing chains could be identified, for example an across-track dependency of the fitting RMS. Initial comparison of the prototype (BIRA) fit results to output from both the verification (IUP-UB) and the additional comparison (MPIC) algorithms showed a row-dependency in the RMS in the prototype results. This row-dependency could be fully attributed to interpolation errors in the wavelength calibration procedure, due to inadequate spectral sampling of the pre-convoluted solar atlas (undersampling issue). As a solution, the convolutions will be performed on a high-resolution spectral grid (0.01nm). The same baseline is also used in the verification algorithm. Details are shown in Figure 11.15.

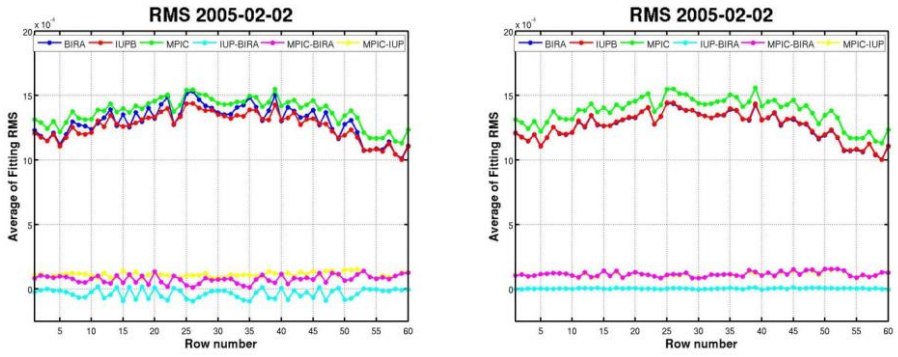

Figure 11.15: Across-track variability of fit RMS for one orbit on 2 Feb 2005, before (left) and after (right) identification of the interpolation issue in the prototype processor.

Additional aspects of the algorithms which turned out to need fine tuning were convolution with the row dependent slit function, treatment of the intensity offset and spectral calibration. Sensitivity studies have shown that fitting an intensity offset as $1/I_{sun}$ instead of 1/I produces HCHO results of equivalent precision, with a gain in processing time. This option was therefore selected as a baseline in both prototype and verification algorithms. The Fraunhofer wavelength calibration has been slightly modified in the prototype algorithm. Radiances are now interpolated on the original (level-1) irradiance wavelength grid. The optimized irradiance wavelength grid (derived as part of the level-2 pre-processing) is then used for both radiance and irradiance spectra. This reduces the amplitude of the shifts between I and I_{sun} to be fitted during the DOAS fit, with an improvement at the edges of the OMI scans.

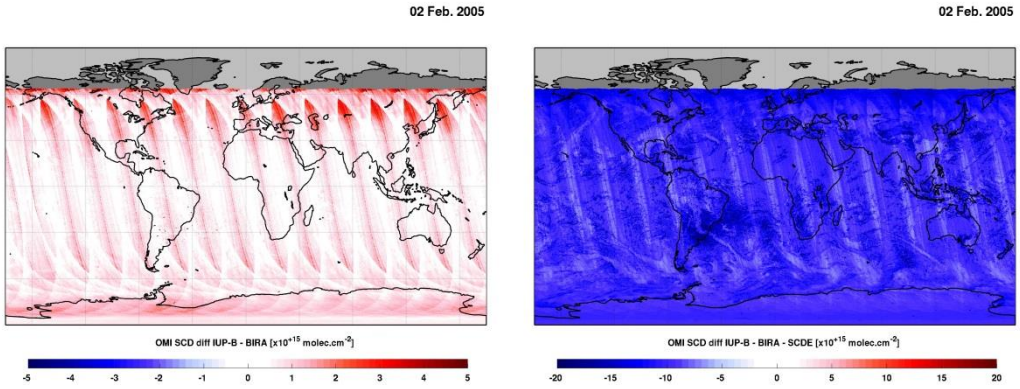

Figure 11.16: Difference of HCHO SCDs from verification and prototype processors (left) and difference between SCD difference and the fit error from verification algorithm (right), for OMI data on 02 Feb 2005. Harmonized settings were used.

Figure 11.16 (left panel) shows the spatial distribution of the remaining SCD differences between prototype and verification processor. These differences do not follow geophysical parameters, but are mainly across-track dependent, with a maximum amplitude at the centre rows of the scan. They are thought to be caused by remaining implementation differences regarding the Fraunhofer wavelength calibration. Finally, when relating the observed differences in retrieved SCDs to the fit uncertainty, it can be concluded that the differences between the prototype and verification results are much smaller than the expected fit uncertainty everywhere (see right panel of Figure 11.16). Note the different scales between left and right panels.

11.8 Air mass factors[6]

11.8.1 Comparison of radiative transfer models

The two panels of Figure 11.17 show the dependency of the TOA reflectance at 340 nm on the SZA (left panel), and the corresponding absolute relative differences. The mean relative difference between the models is 6.4% for the most extreme viewing geometry (μ_0=0.05, μ_0=0.3; not shown in the Figure), with a standard deviation of 0.086 (5.7% of model mean reflectance). For lower SZA, the standard deviation is lower than 0.011 (i.e., <1.2%), indicating good consistency of reflectance calculations in most common retrieval scenarios.

[6] This Section is based on Lorente Delgado et al. (in prep.)

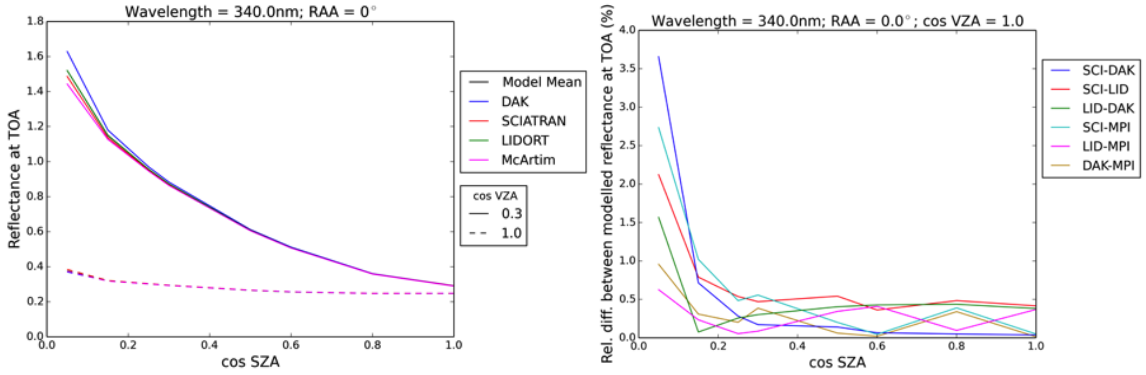

Figure 11.17 TOA reflectances (left) and their absolute relative difference (right), simulated at 340 nm as a function of SZA for a nadir viewing angle (dashed lines, μ=1.0) and off-nadir viewing angle (θ=72°, solid lines, μ=0.3). Additionally to the prototype processor (LIDORT, in green) and the verification algorithm (SCIATRAN, in red), two other RTMs (DAK and McArtim) contributed to this comparison exercise.

Overall, the differences between the radiative transfer models are negligibly small, even though they are larger than in the visible wavelength range (see Section 9.3.4.4.1).

11.8.2 Comparison of air mass factor look-up tables

HCHO Box AMFs have been calculated with LIDORT, SCIATRAN, and DAK. Calculations are done at three different wavelengths: 338, 341, and 344 nm, in order to test the box AMF dependency on wavelength.

The left panel of Figure 11.18 shows the vertical profile of AMFs for a specific geometry configuration at 338 nm. Even though the profile shape is well reproduced by all the models, differences are clearly larger than for NO_2, the verification RTM (SCIATRAN) showing discontinuities in the box AMFs close to 270 hPa (caused by an inhomogeneity in the vertical layering at this altitude). The right panel of Figure 11.18 shows relative differences between models for a specific surface albedo and surface height, for a wide range of solar and viewing geometries ($0.15 < \mu_o < 1.0$, $0.3 < \mu < 1.0$). This panel indicates that the relative differences between the HCHO box AMFs are somewhat larger than for NO_2, (cf. Section 9.3.4.4.2) especially in the lowest layer (1007 hPa) and in the lower troposphere. Mean relative differences are within 6% for all geometries, with exception of the lowest pressure level (mean relative difference of -6.5%). As in the NO_2 case, the peak around 270 hPa is due to inconsistent vertical discretizations at this altitude. The highest relative differences are found for large viewing and solar zenith angles. If those angles are not taken into consideration ($0.25 < \mu_o < 1.0$, $0.5 < \mu < 1.0$), relative differences drop to below 2% (without taking into account the lowest pressure level).

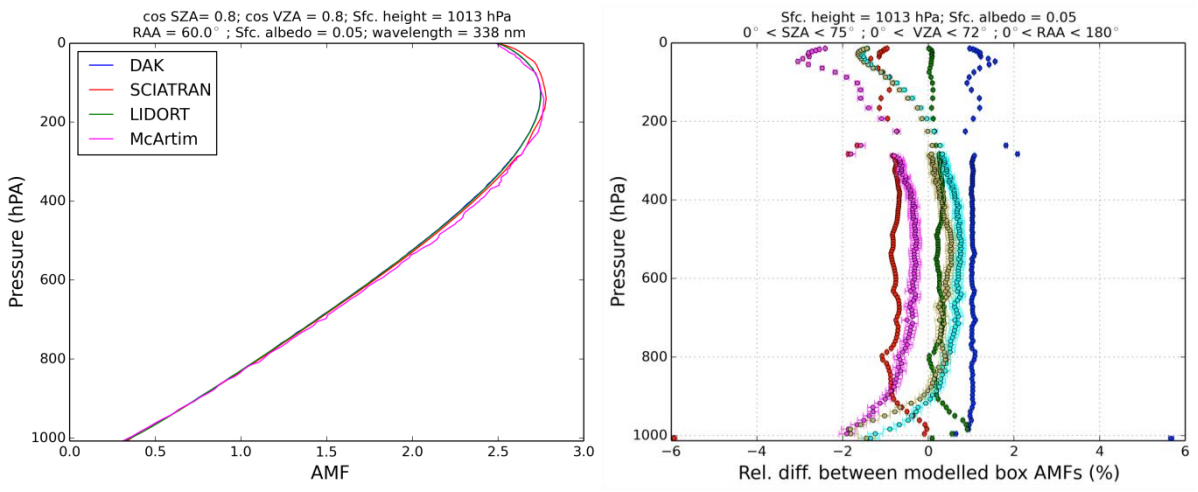

Figure 11.18 Left panel: vertical profile of HCHO box AMFs calculated by protype (LIDORT, green) and verification (SCIATRAN, red) RTMs for SZA = VZA ≈ 37° ($\mu = \mu_o = 0.8$), RAA = 60°, surface albedo = 0.05, surface height 1013 hPa at 338 nm. Right panel: vertical profile of relative differences between HCHO box AMFs calculated by the different RTMs for a wide range of viewing and solar geometries, surface albedo = 0.05, surface height 1013 hPa at 338 nm. Bold lines indicate mean relative difference averaged over all viewing geometries. In addition, two other RTMs (DAK, and McArtim) contributed to this comparison exercise.

Figure 11.19 (a) shows the 950 hPa HCHO box AMF dependency on surface albedo. The figure shows a clear, almost linear dependence of the box AMF on surface albedo. Compared to NO_2 (Figure 9.30), the HCHO box AMFs show a weaker (2-3-fold) and more gradual increase with albedo, reflecting the lower probability of 338nm photons reaching the surface in the first place. The dependency is well captured by both RTMs. Similar to NO_2, the HCHO box AMF dependency on geometry is relatively weak for viewing zenith angle and relative azimuth angle (Figure 11.19 (b)), and more relevant for SZA (Figure 11.19 (c)). Figure 11.19 (e) shows the dependency of the 787 hPa box AMF dependency to surface pressure (at 1013, 902, and 802 hPa). For the particular geometry shown, the sensitivity of the box AMF to surface pressure is not as strong as for surface albedo, but still substantial (20-30% for surface pressures between 1000-900 hPa) and relatively stronger than for NO_2. This dependency is well reproduced by the four RTMs.

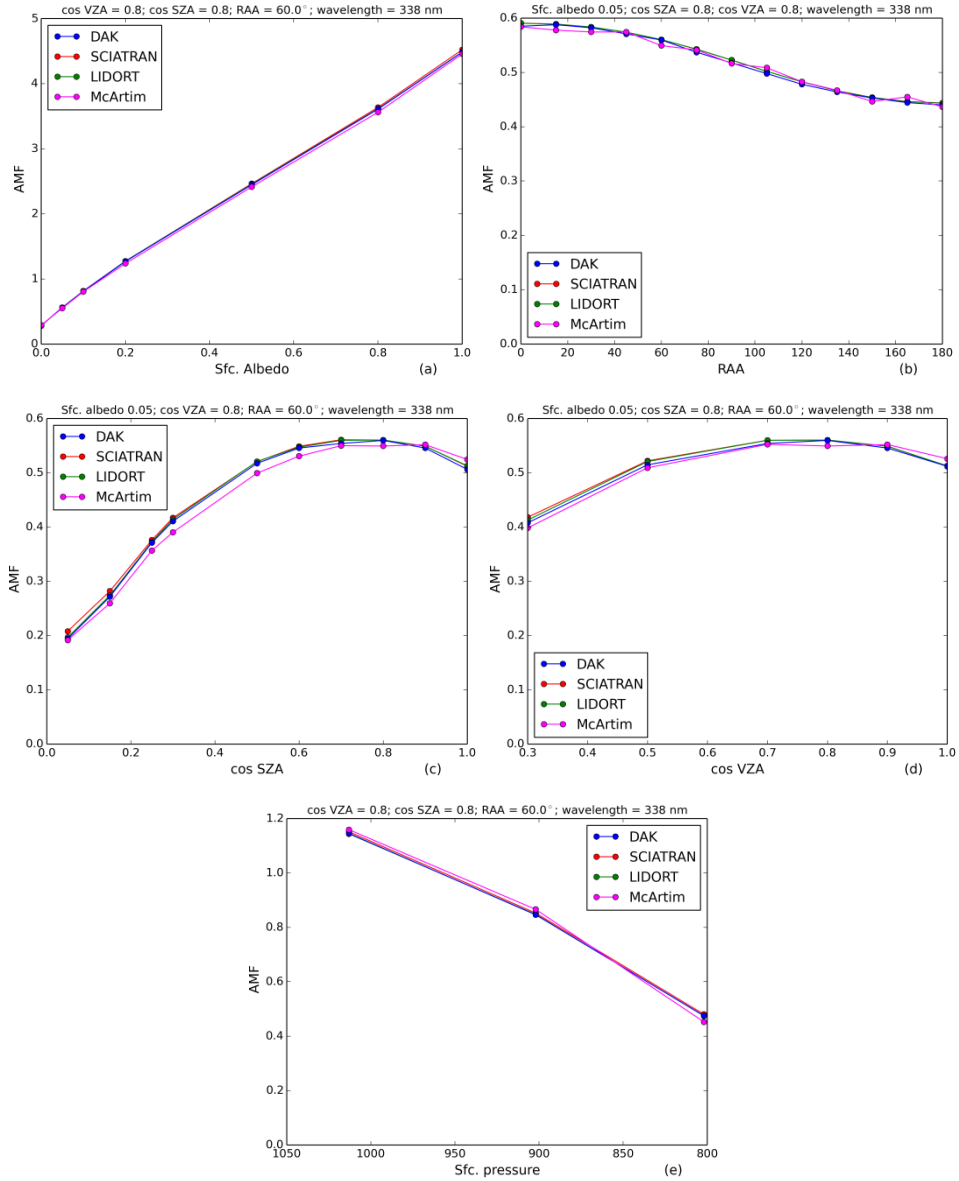

Figure 11.19: (a) Dependency of 950 hPa HCHO box AMF to surface albedo, (b) RAA, (c) cosine of SZA, (d) cosine of VZA, and (e) surface pressure for SZA = VZA ≈ 37° ($\mu = \mu_o = 0.8$), RAA = 60° and surface height 1013 hPa at 338 nm. In addition to the prototype (LIDORT, green) and verification (SCIATRAN, red) RTMs, two other RTMs (DAK and McArtim) contributed to this comparison exercise.

The above comparison indicates that for most viewing geometries, the HCHO box AMFs are consistent to within 1%.

11.8.3 Comparison of the air mass factor processing chain

As for NO_2 (see Section 9.3.4.4.3), we conducted a comparison of the air mass factor processing chains using identical choices for input an ancillary data. The selected day for comparison is 02 Feb 2005, early in the lifetime of the sensor (orbit lv1 filename OMI-Aura_L2-OMDOMINO_2005m0202t0339-o02940_v003). Details of the measurement scenes are given in Table 11.5.

Table 11.5: Scene parameters and total AMF results for the four exemplary pixels.

	Pixel 1	**Pixel 2**	**Pixel 3**	**Pixel 4**
Longitude (°)	116.2126	127.5450	138.8448	138.7013
Latitude (°)	39.67700	37.35957	15.01003	15.73464
SZA (°)	56.567	55.947	40.090	40.604
VZA (°)	57.602	3.410	42.245	42.246
RAA (°)	64.112	64.335	133.300	132.629
Albedo	0.079	0.057	0.068	0.068
Surface pressure (hPa)	1026.335	1011.726	1011.610	1012.031
Cloud fraction	0.0460	0.0260	0.1440	0.0550
Cloud pressure (hPa)	984.00	610.00	812.00	842.00
Total AMF (BIRA / IUP-UB)	0.808 / 0.854	0.634 / 0.643	1.327 / 1.340	1.266 / 1.221
Total AMF relative difference	-5.5%	-1.4%	-1.0%	+3.6%

Figure 11.20 shows the HCHO box AMFs calculated for the four pixels. We can observe a high agreement in the vertical profile between the different groups. The AMF profiles show mostly excellent agreement, with exceptions of the upper troposphere and around the cloud altitudes. The latter difference is caused by slight differences in the vertical interpolation schemes employed in the two algorithms, and can be identified with the largest contribution to the small differences in the total AMFs (see Table 11.5).

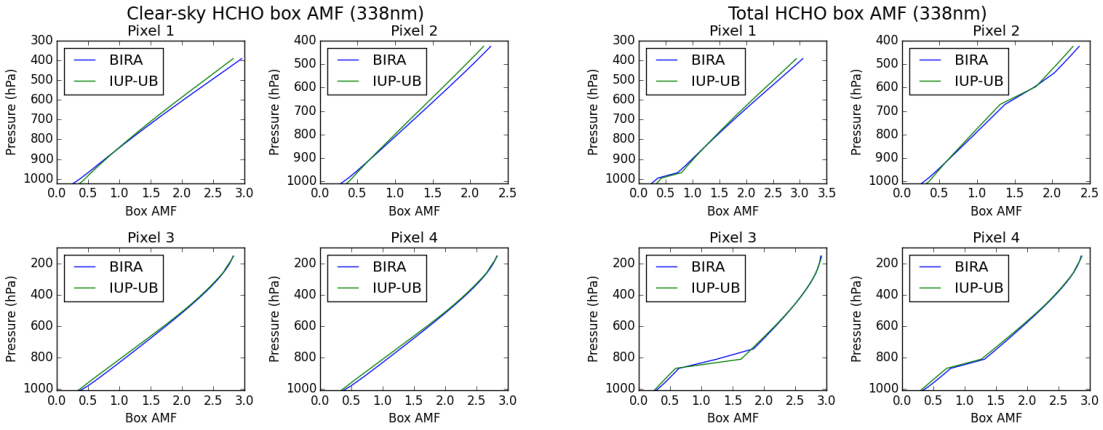

Figure 11.20: Clear-sky (left panel) and total (right panel) altitude dependent HCHO air pass factors for four exemplary pixels from OMI orbit 2940 (02 Feb 2005), from prototype (blue) and verification (green) processors.

11.9 Summary of verification results

The main results of the HCHO verification activities are

- Initially, large discrepancies between slant columns from the prototype, the verification algorithm and the “true” values were found when using synthetic spectra
- The problems could be traced down to a combination of
  - Spectral interference from the Ring effect
  - Spectral interference from the temperature dependence of the O_3 cross-sections

  - The reduced spectral resolution of TROPOMI when compared to GOME, SCIAMACHY, and GOME-2

- The problems can be reduced to acceptable levels by
  1. Using earth shine background spectra
  2. Including the Pukite et al. (2010) correction approach
  3. Changing the lower end of the fitting window

  While the first and second approach is already implemented in the prototype, the third point has proven to be problematic in real data and will have to be revisited in the verification on real TROPOMI data.

- Comparison of prototype and verification algorithm on OMI data shows very good agreement in HCHO slant columns before normalisation and excellent agreement after normalisation.
- Several aspects of the algorithms (convolution with slit function, treatment of offset correction, calibration on Fraunhofer atlas) have proven to be of importance in the HCHO retrieval on OMI data and these points have been improved in both algorithms.
- Radiative transfer models used by verification and prototype algorithms show excellent agreement for radiances and box air mass factors. As in the NO_2 case, special care must be taken regarding the vertical layering, as this strongly affects the calculated box AMFs.

11.10 References

Chance, K., & Kurucz, R. L. (2010). An improved high-resolution solar reference spectrum for earth's atmosphere measurements in the ultraviolet, visible, and near infrared. Journal of Quantitative Spectroscopy and Radiative Transfer, 111(9), 1289–1295. http://doi.org/10.1016/j.jqsrt.2010.01.036

Chance, K. V., & Spurr, R. J. D. (1997). Ring effect studies: Rayleigh scattering, including molecular parameters for rotational Raman scattering, and the Fraunhofer spectrum. Applied Optics, 36(21), 5224–5230. http://doi.org/10.1364/AO.36.005224

De Smedt, I., Müller, J.-F., Stavrakou, T., van der A, R., Eskes, H., & Van Roozendael, M. (2008). Twelve years of global observations of formaldehyde in the troposphere using GOME and SCIAMACHY sensors. Atmos. Chem. Phys., 8(16), 4947–4963. http://doi.org/10.5194/acp-8-4947-2008

De Smedt, I., Van Roozendael, M., Stavrakou, T., Müller, J.-F., Lerot, C., Theys, N., … van der A, R. (2012). Improved retrieval of global tropospheric formaldehyde columns from GOME-2/MetOp-A addressing noise reduction and instrumental degradation issues. Atmospheric Measurement Techniques, 5(11), 2933–2949. http://doi.org/10.5194/amt-5-2933-2012

Gorshelev, V., Serdyuchenko, A., Weber, M., Chehade, W., & Burrows, J. P. (2013). High spectral resolution ozone absorption cross-sections – Part 1: Measurements, data analysis and comparison with previous measurements around 293 K. Atmospheric Measurement Techniques Discussions, 6, 6567–6611. http://doi.org/10.5194/amtd-6-6567-2013

Greenblatt, G. D., Orlando, J. J., Burkholder, J. B., & Ravishankara, A. R. (1990). Absorption measurements of oxygen between 330 and 1140 nm. Journal of Geophysical Research, 95(D11), 18577–18582. http://doi.org/10.1029/JD095iD11p18577

Kleipool, Q. L., Dobber, M. R., Haan, J. F. de, & Levelt, P. F. (2008). Earth surface reflectance climatology from 3 years of OMI data. Journal of Geophysical Research, 113, D18308. http://doi.org/10.1029/2008JD010290

Fleischmann, O. C., Hartmann, M., Orphal, J., & Burrows, J. P. (2000). UV absorption cross-sections of BrO for stratospheric temperatures (203-293K) recorded by a Time-resolved Rapid Scan FTS method. Bremen: Institute of Remote Sensing, University of Bremen. Retrieved from http://www.iup.physik.uni-bremen.de/gruppen/molspec/bro2_page.html

Lorente Delgado, A., et al. (in prep.): Evaluation of radiative transfer models for reflectance and air mass factor calculation.

Meller, R., & Moortgat, G. K. (2000). Temperature dependence of the absorption cross-sections of formaldehyde between 223 and 323 K in the wavelength range 225–375 nm. Journal of Geophysical Research: Atmospheres, 105(D6), 7089–7101. http://doi.org/10.1029/1999JD901074

Pukite, J., Kühl, S., Deutschmann, T., Dörner, S., Jöckel, P., Platt, U., & Wagner, T. (2010). The effect of horizontal gradients and spatial measurement resolution on the retrieval of global vertical NO2 distributions from SCIAMACHY measurements in limb only mode. Atmospheric Measurement Techniques, 3(4), 1155–1174. http://doi.org/10.5194/amt-3-1155-2010

Serdyuchenko, A., Gorshelev, V., Weber, M., Chehade, W., & Burrows, J. P. (2013). High spectral resolution ozone absorption cross-sections – Part 2: Temperature dependence. Atmospheric Measurement Techniques Discussions, 6, 6613–6643. http://doi.org/10.5194/amtd-6-6613-2013

Spurr, R. (2008). LIDORT and VLIDORT: Linearized pseudo-spherical scalar and vector discrete ordinate radiative transfer models for use in remote sensing retrieval problems. In A. A. Kokhanovsky (Ed.), Light Scattering Reviews 3 (pp. 229–275). Berlin: Springer.

Thalman, R., & Volkamer, R. (2013). Temperature dependent absorption cross-sections of O2–O2 collision pairs between 340 and 630 nm and at atmospherically relevant pressure. Physical Chemistry Chemical Physics, 15(37), 15371–15381. http://doi.org/10.1039/C3CP50968K

Danielson, J. J., & Gesch, D. B. (2011). Global multi-resolution terrain elevation data 2010 (GMTED2010) (Open-File Report No. 2011–1073) (p. 26). U.S. Geological Survey. Retrieved from http://pubs.usgs.gov/of/2011/1073/pdf/of2011-1073.pdf

Vandaele, A. C., Hermans, C., Simon, P. C., Carleer, M., Colin, R., Fally, S., … Coquart, B. (1998). Measurements of the NO2 absorption cross-section from 42 000 cm−1 to 10 000 cm−1 (238–1000 nm) at 220 K and 294 K. Journal of Quantitative Spectroscopy and Radiative Transfer, 59(3-5), 171–184. http://doi.org/10.1016/S0022-4073(97)00168-4

Vountas, M., Rozanov, V. V., & Burrows, J. P. (1998). Ring effect: Impact of rotational Raman scattering on radiative transfer in Earth's atmosphere. Journal of Quantitative Spectroscopy and Radiative Transfer, 60(6), 943–961. http://doi.org/10.1016/S0022-4073(97)00186-6

12 CO columns and XCH4

Authors: Thomas Krings, Maximilian Reuter, Michael Buchwitz, Michael Hilker (IUP-UB)

12.1 Document changes

Major changes in issue 2.0:

- Added results for the viewing zenith angle and azimuth angle investigations for the XCH_4 verification
- Added results for the viewing zenith angle and azimuth angle investigations for the CO verification
- Added investigations regarding the column averaging kernels for CO
- Added a chapter showing comparisons of simulated spectra (relating to both the CO and CH_4 prototype)

12.2 Verification approach

The purpose of this chapter is to describe the verification activities with respect to the retrieval of the column-average dry-air mole fraction of atmospheric methane (XCH_4) and carbon monoxide (CO) vertical columns from the Sentinel-5 Precursor satellite mission. This chapter also describes in detail the Bremen optimal EStimation DOAS algorithm BESD used for the retrieval and verification.

Both institutes, IUP-UB (responsible for the scientific verification algorithm) and SRON (responsible for the prototypes) have long-standing experience in retrieving XCH_4 and CO columns using real SCIAMACHY satellite data (see Schneising et al., 2011, Buchwitz et al., 2007, Vidot et al., 2012 and Butz et al., 2012, and references given therein). Both groups are therefore well aware of many critical aspects which need to be considered when dealing with real satellite data. Both groups have also carefully analysed simulated measurements, e.g., within the context of algorithm optimization and error analysis. This ensures that both groups are aware of many real world potential issues and this will help to avoid surprises after launch when using the real S5P data.

A critical first step was to perform a careful analysis of simulated observations. The goal was to perform a statistically robust analysis to estimate the random error (precision), systematic error (accuracy) for a range of critical or potentially critical parameters such as different amounts and types of aerosols, high (thin) cirrus and low lying (thin or sub-pixel) water clouds, surface albedos, solar zenith angles (SZA), observation viewing angles, etc.

The performance of the optimized version of BESD was compared with the corresponding performance of the prototypes. This required coordination with the prototype developers in terms of harmonization of the geophysical and observational scenarios to be studied. The results of this comparison led to further improvements of BESD while the prototypes were refined. The corresponding activities were the focus of the activities carried out.

Once it was shown that an acceptable performance had been achieved for BESD and for the prototypes a next step was the exchange of the simulated S5P spectra generated by “the other” institute. This verification step was very time consuming as it required a significant amount of harmonization for the many relevant input parameters used for the radiative transfer programs etc. (note that the two radiative transfer models use different aerosol parameterizations, etc., which complicated the analysis)

12.3 Introduction

Parts of this chapter are compiled from text and figures of the publications of Krings et al. (2013b) and Reuter et al. (2010, 2011). Reuter et al. (2010) describe the first release of BESD for the retrieval of column averaged dry-air mole fractions of carbon dioxide (XCO_2) and is a theoretical study based on simulated measurements. The application to real-world SCIAMACHY measurements is described by Reuter et al. (2011). Adjustments and first sensitivity studies for retrieval of XCH_4 and CO from the future satellite mission Sentinel-5 Precursor (S-5P) are presented by Krings et al. (2013b).

Methane (CH_4) is after carbon dioxide the most important anthropogenic greenhouse gas. To better assess the impact on the climate system a close monitoring of CH_4 emissions is necessary. While there are airborne instruments available that are able to accurately monitor emissions on local scales (Krings et al., 2013a), global coverage can only be achieved using satellite instruments. After the decommissioning of SCIAMACHY (Burrows et al., 1995; Bovensmann et al., 1999) onboard ENVISAT, GOSAT (Kuze et al., 2009; Yoshida et al., 2013) is the only remaining satellite in orbit measuring CH_4 with sensitivities down to the surface where most sources are located. While GOSAT has higher horizontal resolution of about 10 km it is lacking complete coverage due to gaps of about 260 km between individual measurements (Kuze et al., 2009, Crisp et al., 2012).

The next upcoming satellite mission providing global coverage of measurements of CH_4 sensitive down to the lowest atmospheric layers is ESA's Sentinel-5 Precursor (S-5P) mission scheduled for launch in 2016. S-5P is a single instrument mission with the absorption spectrometer TROPOMI (TROPOspheric Monitoring Instrument) measuring in the ultraviolet (UV), the visible (VIS), the near-infrared (NIR) and the shortwave infrared (SWIR) spectral range. With a swath of 2600 km and a horizontal nadir resolution of 7 km × 7 km in the SWIR band, where CH_4 is measured, TROPOMI has daily global coverage (Veefkind et al., 2012). The SWIR channel of TROPOMI was designed to retrieve carbon monoxide (CO) which is an important atmospheric pollutant impacting air quality. The retrieval of precise and accurate CH_4 information from this band is more challenging, for example, due to higher accuracy and precision requirements (see below).

Generally, scattering related errors are a major source of uncertainty for satellite retrievals for trace gases. For example, undetected cirrus clouds with a cloud optical thickness (COT) below 0.1 can result in retrieval errors of about 8% for XCO_2 using O_2 as a proxy (Schneising et al., 2008b). The same would be true for a retrieval of XCH_4 using O_2 as a proxy.

Originally BESD aimed to significantly reduce scattering related errors of SCIAMACHY retrieved XCO_2. In that version it uses SCIAMACHY nadir data at 0.76 and 1.6 µm and explicitly considers scattering by an (optically thin) ice cloud layer and aerosols assuming a default profile.

Due to the different spectral channels compared to SCIAMACHY, no XCO_2 can be retrieved from of S-5P. Instead, BESD has been adjusted to retrieve XCH_4 and CO using spectral information at 0.76 and 2.3 µm with a resolution of 0.38 nm and 0.25 nm, respectively. Hence, while for SCIAMACHY XCH_4 is retrieved using CO_2 as a proxy gas (Schneising et al., 2008a), this is not possible for S-5P.

12.4 Overview of the verification algorithm BESD

BESD was originally designed to analyse near-infrared nadir measurements of the SCIAMACHY instrument in the CO_2 absorption band at 1580 nm and in the O_2-A absorption band at around 760 nm. For the verification activities in preparation of the upcoming Sentinel-5 Precursor mission with the TROPOMI instrument, BESD has been adjusted to analyse the CH_4 and CO bands at 2.3µm instead of the CO_2 band at 1580 nm.

The algorithm is a so-called full physics algorithm which explicitly accounts for scattering in an optically thin cirrus cloud layer and at aerosols of a default profile. The scattering information is mainly obtained from the O_2-A band and a merged fit windows approach enables the transfer of information between the O_2-A and the CH_4/CO bands. This technique makes BESD relatively insensitive with respect to unknown scattering properties. Via the optimal estimation technique, the algorithm is able to account for a priori information to further constrain the inversion.

12.4.1 Physical Basis

BESD retrieves several independent parameters from (simulated) S-5P/TROPOMI measurements in the spectral region dominated by CH_4, CO and H_2O absorption from 2305 nm to 2385 nm and also from measurements in the spectral region of the O_2-A band from 755 nm to 775 nm (in the following referred to as the "O_2 fit window"). The list of retrieval parameters such as CH_4 and CO mixing ratio, surface pressure, cloud top height, albedo, etc., defines the state vector.

Each of these parameters influences the spectrum of reflected solar radiation measured by the satellite instrument. The partial derivatives of the measured radiation with respect to a parameter is called the weighting function (or Jacobian) of this parameter. Of course, it is only possible to retrieve those parameters having a unique weighting function, sufficiently different from all other weighting functions in terms of the instrument's accuracy. Very similar weighting functions can result in ambiguities of the retrieved corresponding parameters.

Figure 12.1 shows for exemplary atmospheric conditions with moderate aerosol load and one thin ice cloud layer the weighting functions of three different scattering related parameters under a typical observation geometry in S-5P's spectral resolution. Additionally, the figure shows the XCH_4, CO, and H_2O weighting functions which give the change of radiation when increasing the columnar concentration by 1 ppb for CH_4, 1 % for CO or 1 ‰ for H_2O respectively. For this example, the magnitude of spectral signature of CH_4 is comparable to a change of the cloud top height (CTH) by 0.1 km, the cloud water/ice path (CWP) by 0.05 g/m^2, or to a change of the aerosol load by 25%. There are significant correlations between the curves, especially between the aerosol profile scaling (APS) and the cloud water/ice path weighting function as well as between the cloud top height and the XCH_4 and H_2O weighting function. CO absorption is also correlated with cloud top height but this is less visible due to the weaker absorption.

This means, it is challenging to discriminate XCH_4 or CO variations from changes of the given scattering parameters, i.e., uncertainties of the scattering parameters will always result in uncertainties of the retrieved XCH_4 and CO columns when solely analysing measurements from this fit window.

As Figure 12.1, Figure 12.2 shows for identical atmospheric conditions the weighting functions of the same scattering parameters but for the O_2 fit window. Additionally, it shows the weighting function with respect to surface pressure p_s which can be used to derive the total number of dry air molecules within the atmospheric column by applying the hydrostatic assumption. The similarities between the weighting functions are less pronounced in this fit window. This applies especially when comparing the surface pressure weighting function to the weighting functions of the given scattering parameters. This is the result of much stronger absorption lines in this fit window. As width and depth of absorption lines depend on the ambient pressure, saturation effects differ much stronger with height within this spectral region. Nevertheless, there are still similarities that are not negligible e.g. between the cloud top height and aerosol profile scaling weighting function. Therefore, it can be expected that independent information on the given scattering parameters can be extracted from this fit window simultaneously with information about the surface pressure.

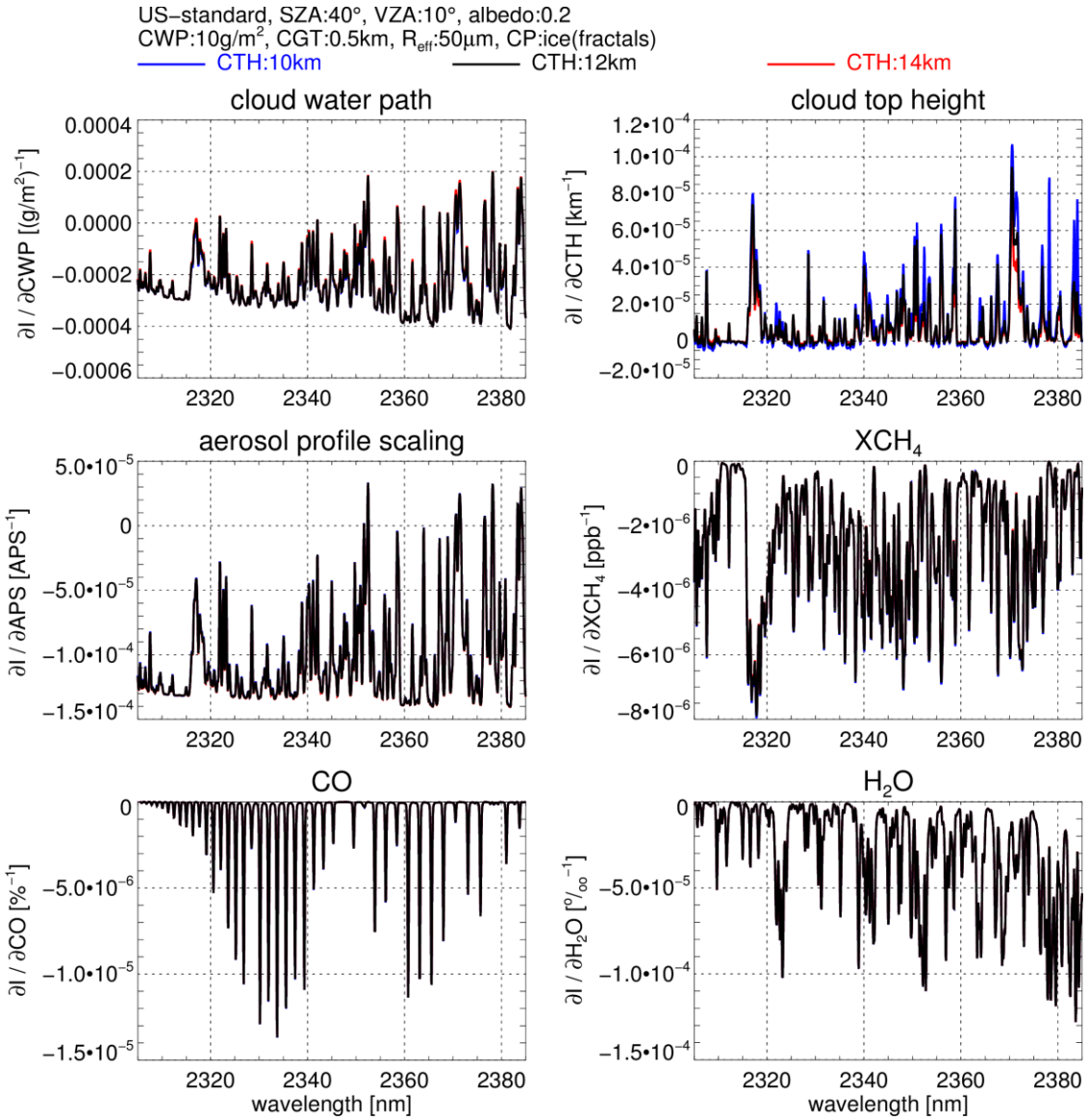

Figure 12.1: Weighting functions in the CH_4 and CO fit window for three cloud scenarios based on a US-standard atmosphere including an optically thin ice cloud with a cloud top height of 10 km (blue), 12 km (black), and 14 km (red): cloud water/ice path (top/left), cloud top height (top/right), scaling of the aerosol profile (middle/left), XCH_4 (middle/right), CO (bottom/left) and H_2O (bottom/right). The weighting functions are calculated with the SCIATRAN 3.1 radiative transfer code and are convolved with the S-5P slit function.

The large differences of the three illustrated cloud top height weighting functions show that the radiative transfer can become non-linear in respect to this parameter. Additionally, the spectral similarity of the CTH and the CWP weighting function strongly depends on the scenario (large differences for the cloud at 12 km, minor diifferences for the cloud at 10 km). This means that, depending on the individual scene, ambiguities may be more or less pronounced. In this context, also the selected surface albedo has strong influence.

Section 12.5 will describe how the information on scattering parameters, which can be derived from the O_2 fit window, is transported to the CH_4 and CO fit window.

12.5 BESD Mathematical Algorithm Description

12.5.1 Retrieval method

BESD uses an optimal estimation based inversion technique to find the most probable atmospheric state given a measurement and some prior knowledge. Nearly all mathematical expressions given in this algorithm description as well as their derivation and notation can be found in the text book of Rodgers (2000). A list of used symbols is given by Table 12.1.

The forward model **F** is a vector function which calculates for a given (atmospheric) state simulated measurements, i.e., simulated S-5P spectra. The input for the forward model are the state vector **x** and the parameter vector **b**. The state vector consists of all unknown variables that shall be retrieved from the measurement (e.g., CH_4). Parameters which are assumed to be exactly known but affecting the radiative transfer (e.g., viewing geometry) are the elements of the parameter vector. The measurement vector **y** consists of (simulated) radiances of two merged fit windows concatenating the measurements in the CH_4/CO and O_2 fit window. The difference of measurement and corresponding simulation by the forward model is given by the error vector **ε** comprising inaccuracies of the instrument and of the forward model:

$$\mathbf{y} = \mathbf{F}(\mathbf{x}; \mathbf{b}) + \boldsymbol{\varepsilon} \qquad (30)$$

According to Eq. 5.3 of Rodgers (2000), BESD aims to find the state vector **x** which minimizes the cost function χ^2:

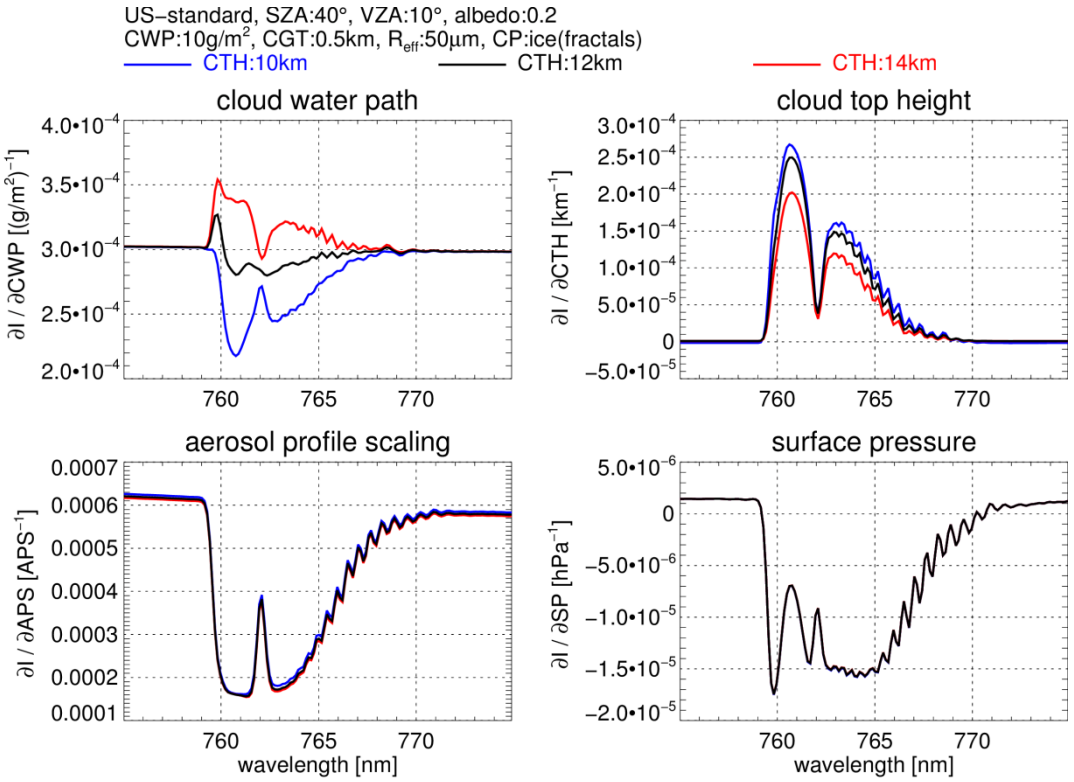

Figure 12.2: Weighting functions in the O_2 fit window for three cloud scenarios based on a US-standard atmosphere including an optically thin ice cloud with a cloud top height of 10 km (blue), 12 km (black), and 14 km (red): cloud water/ice path (top/left), cloud top height (top/right), scaling of the aerosol profile (bottom/left), and surface pressure (bottom/right). The weighting functions are calculated with the SCIATRAN 3.1 radiative transfer code and are convolved with the S-5P slit function.

$$\chi^2 = (\mathbf{y} - \mathbf{F}(\mathbf{x}, \mathbf{b}))^T \mathbf{S}_\varepsilon^{-1} (\mathbf{y} - \mathbf{F}(\mathbf{x}, \mathbf{b}))$$

$$+ (\mathbf{x} - \mathbf{x}_a)^T \mathbf{S}_a^{-1} (\mathbf{x} - \mathbf{x}_a) \quad (31)$$

Here, $\mathbf{S}_\varepsilon$ is the error covariance matrix corresponding to the measurement vector, $\mathbf{x}_a$ is the a priori state vector which holds the prior knowledge about the state vector elements and $\mathbf{S}_a$ is the corresponding a priori error covariance matrix which specifies the uncertainties of the a priori state vector elements as well as their cross correlations.

Even though the number of state vector elements (36) is smaller than the number of measurement vector elements (1111), the inversion problem is generally under-determined. The weighting functions of some state vector elements show quite large correlations under certain conditions. This especially applies to the weighting functions corresponding to the ten-layered CH_4 and CO profile but also to some of the weighting functions shown in Figure 12.1 and Figure 12.2. For this reason BESD uses a priori knowledge further constraining the problem and making it well-posed. However, for most of the state vector elements the used a priori knowledge gives only a weak constraint and is therefore not dominating the retrieval results. Furthermore, only static a priori knowledge of XCH_4 and CO is used.

Table 12.1: List of used symbols, corresponding dimensions and short descriptions.

Symbol	Dimension	Description
A	n × n	Averaging kernel matrix
B	n_b × 1	Parameter vector
d_l	1	Degree of non-linearity
d_s	1	Degree of freedom for signal
ε	m × 1	Measurement and forward model error
F	m × 1	Forward model
G	n × m	Gain matrix
K	m × n	Weighting function matrix
H	1	Information content in bits
m	1	Size of measurement vector (= 1111)
n	1	Size of state vector (= 36)
n_b	1	Size of parameter vector
n_{CH4}	1	CH_4 profile layers (= 10)
n_{CO}	1	CO profile layers (= 10)
ps	1	Surface pressure
$\mathbf{r}_\sigma$	n × 1	Uncertainty reduction
$\hat{\mathbf{S}}$	n × n	Covariance matrix of retrieved state
S_a	n × n	A priori covariance matrix
$\mathbf{S}_\varepsilon$	m × m	Measurement error covariance matrix
w	n × 1	Layer weighting vector
x	n × 1	State vector
$\mathbf{x}_0$	n × 1	First guess state vector
$\mathbf{x}_a$	n × 1	a priori state vector
$\mathbf{x}_t$	n × 1	True state vector
$\hat{\boldsymbol{x}}$	n × 1	Retrieved state vector
χ^2	1	Cost function (Eq. 2)
y	m × 1	Measurement vector

BESD uses a Levenberg-Marquardt method described in Eq. 5.36 of Rodgers (2000) to iteratively find the state vector $\hat{\boldsymbol{x}}$ which minimizes the cost function.

$$\mathbf{x}_{i+1} = \mathbf{x}_i + \hat{\mathbf{S}}\left[\mathbf{K}_i^T \mathbf{S}_\varepsilon^{-1}\left(\mathbf{y} - \mathbf{F}(\mathbf{x}_i, \mathbf{b})\right) - \mathbf{S}_a^{-1}(\mathbf{x}_i - \mathbf{x}_a)\right] \quad (32)$$

$$\hat{\mathbf{S}} = (\mathbf{K}_i^T \mathbf{S}_\varepsilon^{-1} \mathbf{K}_i + (1+\gamma)\mathbf{S}_a^{-1})^{-1} \quad (33)$$

Within this equation, **K** is the Jacobian or weighting function matrix consisting of the derivatives of the forward model in respect to the state vector elements $\mathbf{K} = \partial \mathbf{F}(\mathbf{x}, \mathbf{b}) / \partial \mathbf{x}$. In the case of convergence, $\mathbf{x}_{i+1}$ is the most probable solution given the measurement and the prior knowledge and is then denoted as maximum a posteriori solution $\hat{\boldsymbol{x}}$ of the inverse problem. $\hat{\mathbf{S}}$ is the corresponding covariance matrix consisting of the variances of the retrieved state vector elements and their correlations.

The damping factor γ adjusts the step size of the iteration in a way which ensures that each (successful) step further minimizes the cost function. This requires the ratio *R* of the change of the cost function computed properly to that computed with the linear approximation of the forward model:

$$R = \left(\chi_i^2 - \chi_{i+1}^2\right) / \left(\chi_i^2 - \chi'^{\,2}_{i+1}\right) \quad (34)$$

$$\chi'^{\,2}_{i+1} = \left(y - F'(x_{i+1}, b)\right)^T S_\varepsilon^{-1} \left(y - F'(x_{i+1}, b)\right) + (x_{i+1} - x_a)^T S_a^{-1} (x_{i+1} - x_a) \quad (35)$$

$$F'(x_{i+1}, b) = F(x_i, b) + K_i (x_{i+1} - x_i) \quad (36)$$

R is unity if the forward model can perfectly be described by its linear approximation. In the case χ^2 has increased rather than decreased, *R* becomes negative and the iteration step is rejected. The following strategy is used to find a value of which restricts $\mathbf{x}_{i+1}$ to lie within the linear range, i.e., the so called "trust region" of $\mathbf{F}(\mathbf{x}_i, \mathbf{b})$: if $R > 0.75$ then reduce γ by a factor of 2, if $R < 0.25$ then enhance γ by a factor of 2, otherwise make no changes.

The iteration starts with γ = 1 and the first guess state vector $\mathbf{x}_0$. Often, $\mathbf{x}_0$ is set to $\mathbf{x}_a$, even though this is mathematically not mandatory and also not done here for some state vector elements. Referring to Eq. 5.29 of Rodgers (2000), BESD tests for convergence by relating the changes of the state vector to the error covariance $\hat{\mathbf{S}}$ after each iteration. If the value of $(\mathbf{x}_i - \mathbf{x}_{i+1})^T \hat{\mathbf{S}}^{-1} (\mathbf{x}_i - \mathbf{x}_{i+1})$ falls below the number of state vector elements (36), convergence is achieved and the iteration is stopped. As it is theoretically possible that convergence is never achieved, iteration also stops after several unsuccessful steps. However, typically, the convergence criterion is fulfilled after about 1-10 iterations.

Subsequently, some terms are used also given by Rodgers (2000) to compute the gain matrix **G** (Eq. 2.45), the averaging kernel matrix **A** (Eq. 3.10), the degree of freedom for signal ds (Eq. 2.80), and the information content *H* (Eq. 2.80). The gain matrix corresponds to the sensitivity of the retrieval to the measurement and is given by:

$$\mathbf{G} = (\mathbf{K}^T \mathbf{S}_\varepsilon^{-1} \mathbf{K} + \mathbf{S}_a^{-1}) \mathbf{K}^T \mathbf{S}_\varepsilon^{-1} \quad (37)$$

Having the gain matrix, the averaging kernel matrix can be computed which is the sensitivity of the retrieval to the true state:

$$\mathbf{A} = \mathbf{GK} \quad (38)$$

The degree of freedom for signal corresponds to the number of independent quantities that can be derived from the measurement and is given by the trace of **A**:

$$d_{\boldsymbol{S}} = \mathrm{tr}(\mathbf{A}) \quad (39)$$

The information content gives the number of different atmospheric states that can be distinguished in bits:

$$H = -\frac{1}{2}\ln(|\mathbf{I} - \mathbf{A}|) \tag{40}$$

The degree of freedom as well as the information content can be calculated for arbitrary sub sets of state vector elements by taking only corresponding elements of the averaging kernel matrix into account. Comparing the variances of the retrieved state vector elements with the corresponding a priori variances, the uncertainty reduction $\mathbf{r}_\sigma$ of the j^{th} state vector element is defined by:

$$\mathbf{r}_{\sigma j} = 1 - \sqrt{\hat{\mathbf{S}}_{jj}/\mathbf{S}_{ajj}} \tag{41}$$

Note: using merged fit windows instead of performing the retrieval in two separate fit windows has two main advantages when retrieving state vector elements which have sensitivities in both fit windows. 1) These elements are better constrained because simultaneous fitting implicitly utilizes the knowledge that the retrieved quantity (e.g. the atmospheric temperature) must be identical in both fit windows. 2) If there are state vector elements with strong ambiguities in one fit windows (e.g. surface pressure and scattering parameters in the CH_4 fit window), the information come mainly from the fit window with less ambiguities. Merging the fit windows makes this information available in both fit windows.

12.5.2 Forward Model

As forward model, BESD makes use of the SCIATRAN 3.1 radiative transfer code (Rozanov et al., 2014) in discrete ordinate mode. As final part of the forward calculation, the resulting spectra are convolved with a Gaussian slit function. NASA's tabulated absorption cross-section database HITRAN 2008 (Rothman) is used.

The radiative transfer calculations are performed on up to 60 model levels, even though the state vector includes only a ten-layered CH_4 and CO mixing ratio profile. This profile is expanded to the model levels before each forward calculation. In the case of liquid water droplets, phase function, extinction, and scattering coefficient of cloud particles are calculated with Mie's theory assuming gamma particle size distributions.

In the case of ice crystals, corresponding calculations are performed with a Monte Carlo code, assuming an ensemble of randomly aligned fractal or hexagonal particles. The volume scattering function is the product of phase function and scattering coefficient. Figure 12.3 illustrates the volume scattering functions of several cloud particles.

In order to prepare the exchange of data on the spectral level with the prototypers, efforts have been made to harmonize the absorption cross-sections between the different radiative transfer models. To accomplish this, SRON provided tabulated cross-section data for CH_4, CO, H_2O and O_2 for the relevant wavelength ranges. The radiative transfer model SCIATRAN was then modified to handle this new data type differing significantly from the online computation of cross-sections at runtime as used so far. As an additional advantage, this will speed up the BESD retrieval.

The functionality to utilize tabulated cross-section was implemented into an up to date version of SCIATRAN. This necessitated an upgrade to SCIATRAN version 3.3. However, tests showed no significant differences to version 3.1 regarding the algorithm components used for this study. Nevertheless it will always be stated which SCIATRAN version has been used for a given application.

12.6 State Vector

All retrieval results shown in this chapter are valid for a state vector consisting of 36 elements (see Table 12.2). Corresponding weighting functions calculated for exemplary atmospheric conditions are illustrated in Figure 12.4. The a priori uncertainties have been chosen so that they sufficiently constrain the inversion by defining a well-posed problem without dominating the retrieval results.

12.6.1.1 Wavelength Shift, Slit Function FWHM

The state vector accounts for fitting a wavelength shift and the full width half maximum (FWHM) of a Gaussian shaped instrument's slit function separately in the O_2 and CH_4 fit window. This means, the weighting functions are only non-zero in the corresponding fit window.

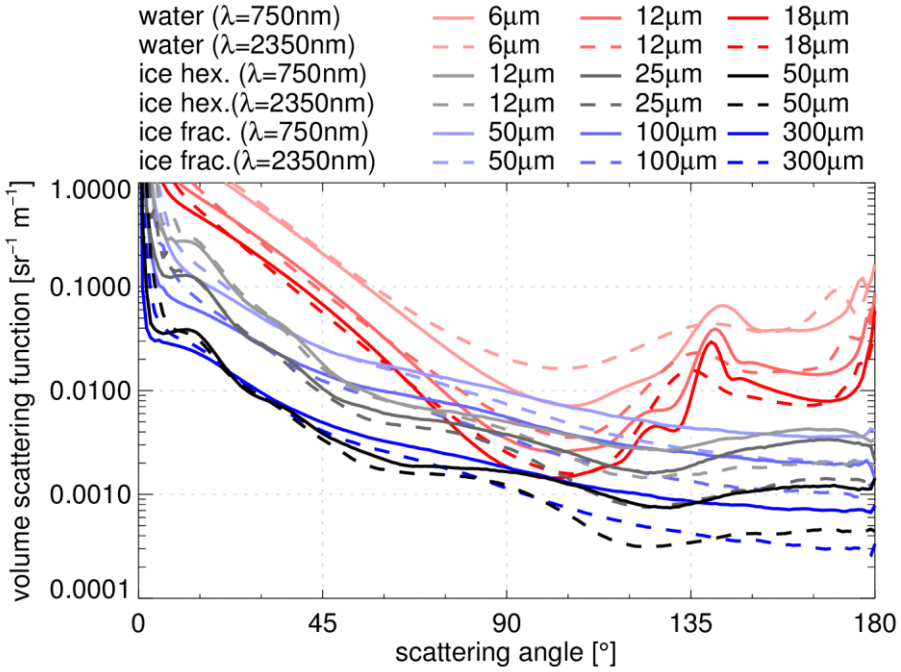

Figure 12.3: Volume scattering functions of cloud particles. The dominant forward peaks are clipped in this figure.

Table 12.2: List of state vector elements and the relevant bands for each element.

Name	O2 (NIR)	CH4, CO (SWIR)
Albedo P0	•	
Albedo P1	•	
Albedo P2	•	
Albedo P0		•
Albedo P1		•
Albedo P2		•
Δλ [nm]	•	
Δλ [nm]		•
FWHM [nm]	•	
FWHM [nm]		•
ΔT [K]	•	•
H2O [‰]	•	•
APS	•	•

CWP [g/m²]	•	•
CTH [km]	•	•
p_s [hPa]	•	•
CH4 L9 [ppm]		•
CH4 L8 [ppm]		•
CH4 L7 [ppm]		•
CH4 L6 [ppm]		•
CH4 L5 [ppm]		•
CH4 L4 [ppm]		•
CH4 L3 [ppm]		•
CH4 L2 [ppm]		•
CH4 L1 [ppm]		•
CH4 L0 [ppm]		•
CO L9 [ppm]		•
CO L8 [ppm]		•
CO L7 [ppm]		•
CO L6 [ppm]		•
CO L5 [ppm]		•
CO L4 [ppm]		•
CO L3 [ppm]		•
CO L2 [ppm]		•
CO L1 [ppm]		•
CO L0 [ppm]		•

12.6.1.2 Albedo

BESD assumes a Lambertian surface with an albedo with smooth spectral progression which can be expressed by a 2nd order polynomial separately within both fit windows. In order to get good first guess and a priori estimates for the 0th polynomial coefficients, the albedo is estimated within a micro window least influenced by gaseous absorption lines in each fit window assuming a cloud free atmosphere with moderate aerosol load.

12.6.1.3 CH_4 and CO Mixing Ratio Profile

The CH_4 and CO mixing ratio is fitted within 10 atmospheric layers, splitting the atmosphere into equally spaced pressure intervals normalized by the surface pressure p_s (0.0, 0.1, 0.2, …, 1.0).

For CH_4 a static a priori statistic in each pressure level was selected that corresponds to the one for CO_2 in the original BESD version. It is based on Carbon-Tracker CO_2 data over land surfaces of the years 2003 to 2005. Thereby, the largest variability is observed in the lowest 10% of the atmosphere with large cross correlations in the boundary layer, the free troposphere, and the stratosphere. Of course this is only a very rough approximation and the analysis of a dedicated a priori statistic for BESD retrieval of CH_4 and CO is foreseen in the future.

As the shape of the CH_4 weighting functions in S-5P resolution shows only minor changes with height, it cannot be expected that there is much information obtainable about the CH_4 profile shape from S-5P nadir measurements.

Therefore, a relatively narrow constraint for the profile shape but simultaneously a rather weak constraint for XCH_4 is used. The a priori uncertainty of 10% on XCH_4 enables the retrieval to put more weight on the measurement and less weight on the a priori information. The XCH_4 a priori is 1780 ppb.

For CO, the a priori vertical column density is $2.386 \cdot 10^{18}$ molecules/cm^2 with an a priori uncertainty of 100%.

12.6.1.4 Atmospheric Profiles and Surface Pressure

When applying BESD to real data, atmospheric profiles of pressure, temperature and humidity provided by ECMWF (European centre for medium-range weather forecasts) will be used for the forward model calculations as part of the parameter vector. Applying the hydrostatic assumption, the surface pressure determines the total number of air molecules within the atmospheric column. Therefore, it is a critical parameter for the retrieval of XCH_4 and CO.

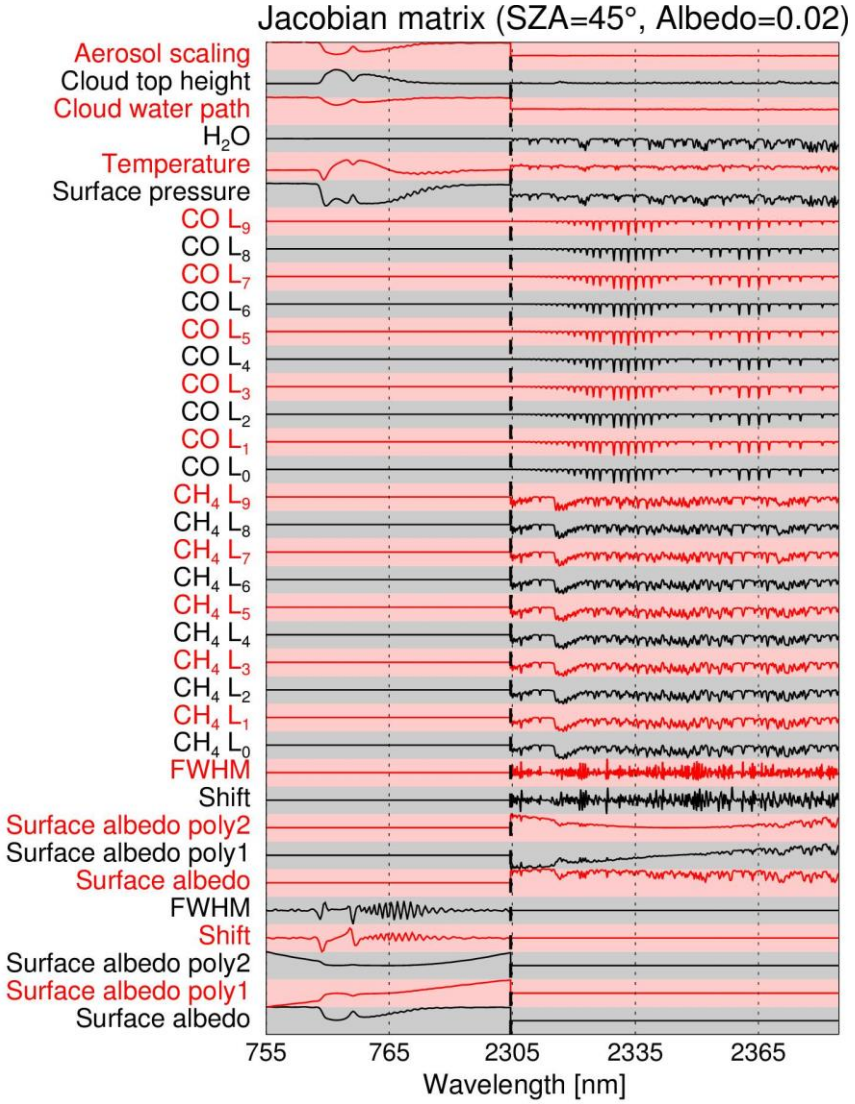

Figure 12.4: Weighting functions (scaled to the same amplitude) calculated with the SCIATRAN 3.1 radiative transfer code (solar zenith angle (SZA): 40°, surface albedo: 0.02).

A dataset of more than 8000 radiosonde measurements of the year 2004 within -70°E to 55°E longitude and -35°N to 80°N latitude has been compared with corresponding ECMWF profiles. Resulting from these comparisons, the standard deviation of the temperature shift between measured and modelled temperature profiles amounts to 1.1 K. The corresponding value for a scaling of the H_2O profile is 32%. The biases are much smaller than the standard deviations. Therefore, unbiased a priori knowledge is used for the temperature profile shift and the scaling of the humidity profile.

The a priori uncertainty of the surface pressure is estimated to be 0.1-0.3%, which strongly constrains the surface pressure retrieval. These values seem to be realistic; King (2003) and Lammert et al. (2008) validated the sea surface pressure of ECMWF model analyses and found much smaller standard deviations of about 1 hPa and 0.5 hPa, respectively.

12.6.1.5 Scattering Parameters

Scattering can cause very complex modifications of the satellite observed radiance spectra and there is nearly an infinite amount of micro and macro physical parameters that are needed to comprehensively account for all scattering effects in the forward model. However, as illustrated in Figure 12.1 and Figure 12.2, it is unlikely possible to retrieve many of these parameters simultaneously from S-5P measurements in the O_2 fit window. The same applies to the CH_4 fit window which contains even less information about these parameters.

Therefore, BESD aims only at three macro physical scattering parameters having a dominant influence on the measured spectra. Their weighting functions contain sufficiently unique spectral signatures which makes them distinguishable from other weighting functions. These parameters are cloud top height (CTH), cloud water/ice path (CWP) where water/ice stands for ice and/or liquid water, and the aerosol scaling factor for a default aerosol profile. All other scattering related parameters are not part of the state vector but only part of the parameter vector and are set to constant values. From these parameters the radiative transfer model SCIATRAN internally computes extinction coefficients and optical thickness as described by Kokhanovsky (2007).

The parameter vector defines that scattering on particles takes place in a plane parallel geometry in one cloud layer with a geometrical thickness of 0.5 km homogeneously consisting of fractal ice crystals with 50 µm effective radius. In addition, scattering happens on a standard LOWTRAN summer aerosol profile with moderate rural aerosol load and Henyey-Greenstein phase function. Both cloud parameters (CTH and CWP) are aimed at optically thin cirrus clouds because on the one hand it is not possible to get enough information from below an optically thick cloud and on the other hand the foregoing cloud screening already filters out the optically thick clouds. Additionally, Schneising et al. (2008b) found that thin cirrus clouds are most likely the reason for shortcomings of the WFM-DOAS 1.0 CO_2 retrieval in the southern hemisphere.

The a priori value of CTH is set to 10 km with a one sigma uncertainty of 5 km. Both values are only rough estimates for typical thin cirrus clouds. Nevertheless, the size of the one sigma uncertainty seems to be large enough to avoid over-constraining the problem as it covers large parts of the upper troposphere where these clouds occur.

All micro physical cloud and aerosol parameters are assumed to be constant and known. This assumption is obviously not true. Scattering strongly depends on the size of the scattering particles, e.g., scattering is more effective at clouds with smaller particles. For this reason, it is not possible to derive the correct cloud water/ice path without knowing the true phase function, scattering, and extinction coefficient of the scattering particles. Hence, the cloud water/ice path parameter, which is part of the state vector, is rather an effective cloud water/ice path corresponding to the particles defined in the parameter vector. As an example, it can be expected that the retrieved CWP will be larger than the true CWP in cases with true particles that are smaller than the assumed particles. Such effects must be considered when choosing the a priori constraints of CWP. Additionally, the constraints must be weak enough to enable cloud free cases with CWP = 0. Therefore, an a priori value for CWP of 10 g/m^2 with a one sigma uncertainty of 10 g/m^2 is used, corresponding to cloud optical depths in the range of about 0 to 0.7. For the aerosol scaling factor an a priori value of 1.0 with a standard deviation of 1.0 is used.

Obviously, three parameters are by far not sufficient to describe all forms of scattering that can influence the measurements so that the retrieved scattering parameters should be treated as effective parameters.

12.6.2 Computation of XCH_4

This section describes how XCH_4 is calculated from the retrieved state vector elements and what implications this calculations have for the error propagation. As mentioned before, the CH_4 mixing ratio profile consists of ten layers with equally spaced pressure levels at (0.0, 0.1, 0.2, …, 1.0)p_s. Under the assumption of hydrostatic equilibrium, each layer consists of approximately the same number of air molecules. The layer weighting vector **w** is defined as fraction of air molecules in each layer compared to the whole column. In this case its value is always 0.1. For all elements that do not correspond to a CH_4 mixing ratio profile element in the state vector, the layer weighting vector is zero. XCH_4 is then simply calculated by:

$$XCH_4 = \mathbf{w}^T \hat{\mathbf{x}} \quad (42)$$

Following the rules of error propagation, the variance of the retrieved XCH_4 is given by

$$\sigma^2_{XCH_4} = \mathbf{w}^T \hat{\mathbf{S}} \mathbf{w} \quad (43)$$

where $\hat{\mathbf{S}}$ denotes the covariance matrix of the retrieved CH_4.

Note: the surface pressure weighting function is defined in a way that a modification of the surface pressure influences the number of molecules in the lowest layer only. This means, after an iteration that modifies the surface pressure, the surface layer will not have the same number of air molecules anymore. The surface pressure weighting function expands or reduces the lowest layer assuming that this layer has a CH_4 mixing ratio given by the latter iteration or the first guess value. Therefore, the surface pressure weighting function influences the mixing ratio which is now a weighted average of the mixing ratio before and after iteration. For this reason, at the end of each iteration, the new non-equidistant CH_4 mixing ratio profile, which now starts at the updated surface pressure, is interpolated to ten equidistant pressure levels whereas XCH_4 is conserved.

The CO total column is computed similarly.

12.7 Differences to prototype algorithms

12.7.1 Methane: Comparison with RemoTeC

Overall, BESD and the prototype algorithm RemoTeC for CH_4 (Butz et al, 2012, Hasekamp et al., 2013) are rather similar as both algorithms will use similar spectral bands and consider scattering effects by selecting appropriate parameters as part of the state vector. Nevertheless, there are many differences when considering the details of each approach, for example: BESD is based on optimal estimation whereas the prototype is based on a Philips-Tikhonov regularization scheme. One important difference between RemoTeC and BESD is the representation of aerosols and clouds. Here, RemoTeC mainly focuses on the effect of aerosols where for BESD the focus lies more on the description of cirrus clouds. Furthermore RemoTeC generally does not retrieve surface pressure. Finally, both algorithms rely on different radiative transfer models. More key differences, e.g., with respect to parameterization are listed in Section 12.9.

12.7.2 Carbon monoxide: Comparison with SICOR

BESD and the CO prototype algorithm SICOR are quite different: While both BESD and SICOR are “Full Physics” (FP) algorithms, BESD is aiming at retrieving scattering parameters primarily from the 0.76 µm spectral region in addition to CO from the SWIR. In contrast, the prototype only uses the 2.3 µm SWIR band and aims at retrieving scattering parameters from methane absorption lines located in this band (Landgraf et al., 2013, Vidot et al., 2012). In addition BESD and the prototype use different radiative transfer models. The prototype has been optimized for speed to process the data in near real time (NRT) whereas the scientific verification algorithm does not have to meet such a requirement. More key differences, e.g., with respect to parameterization are listed in Section 12.9.

12.8 BESD Algorithm Error Characterization

Radiative transfer through a scattering atmosphere can be very complex. Thinking about the almost infinite number of possible ensembles of scattering particles, all with different phase functions, extinction, and absorption coefficients, a set of three scattering related state vector elements is by far not enough to comprehensively describe all possible scattering effects. For this reason, the remaining test scenarios are used to estimate the sensitivity to cloud micro and macro physical parameters which are not part of the state vector but of the parameter vector.

An overview of the results of all test scenarios is given in Table 12.3 and Table 12.4 showing the systematic and stochastic XCH_4 and CO errors of all scenarios for the solar zenith angles (SZA) 20°, 40°, and 60°. Additionally, the systematic and stochastic errors of the scattering parameters and the surface pressure are given for 40° SZA. The apriori uncertainty for surface pressure for this study was set to 0.05% according to Lammert et al. (2008).

Note: The stochastic errors represent the a posteriori errors based on the assumed measurement noise and the assumed a priori error covariance matrix. According to Eq. (3.16) of Rodgers (2000), the systematic errors given in Table 12.3 and Table 12.4 correspond to the smoothing error $(\mathbf{A}-\mathbf{I})(\boldsymbol{x}_t-\boldsymbol{x}_a)$ of the state vector elements. This applies to all scenarios in which only state vector elements but no parameter vector elements are modified. In these cases, errors due to noise, unknown parameter vector elements, and due to the forward model do not exist.

12.8.1 The ‘dry run’ scenario

The true state vector of the ‘dry run’ scenario is almost identical to the first guess state vector which is again identical to the a priori state vector in almost all elements. Only the constant part of the albedo polynomials of the first guess state vector differ slightly from the true state vector as it is estimated by the prior first guess albedo retrieval. Residuals with relative root mean square (RMS) values below 0.01‰_in the NIR(O_2) and SWIR (CH_4/CO) region as well as almost no systematic errors prove that the algorithm is self-consistent (Table 12.3 and Table 12.4).

12.8.2 The ‘met 1σ’ scenario

The meteorological parameters (temperature shift, H_2O scaling, APS, CWP, CTH, p_s , CH_4 and CO mixing ratio) of the true state vector of the ‘met. 1σ’ scenario differ from the corresponding values of the a priori state vector by 1/3 to 1 sigma a priori uncertainty.

The ‘met. 1σ’ scenario serves as basis for several other scenarios which are mainly intended to quantify the retrievals performance under more realistic conditions including also unknown parameter vector elements, i.e., an imperfect forward model.

Table 12.3: Overview of the retrieval performance for 32 test scenarios based on SCIATRAN 3.3 simulations with a modified US-standard atmosphere. For all scenarios, we assume a Lambertian surface with an albedo which is spectrally constant 0.2 except for the 'spectral albedo' scenarios. The table shows the average signal to noise (SNR) and the residuals relative root mean square (RMS) in both fit windows as well as the main retrieval errors of XCH4, scattering parameters (CWP, CTH, APS), and surface pressure. All errors are given with systematic error (bias) ± stochastic error. The scenarios are based on the 'dry run' scenario (♣), the 'met. 1σ' scenario (♦), and the 'no cloud' scenario (♥). Some scenarios are intended to quantify the retrieval's capability of reproducing modifications of state vector elements (o). The other scenarios are intended to additionally quantify the retrieval's sensitivity to parameter vector elements (□) (i.e. to an imperfect forward model).

Scenario	SNR		RMS [‰]		SZA 40°					SZA 20°	SZA 60°
	NIR	SWIR	NIR	SWIR	p_s [hPa]	CWP [g/m^2]	CTH [km]	APS	XCH_4 [%]	XCH_4 [%]	XCH_4 [%]
dry run ♣,o	2827	568	0.00	0.00	0 ± 0	0.0 ± 0.1	0.0 ± 0.1	0.0 ± 0.1	0.01 ± 0.09	0.01 ± 0.09	0.01 ± 0.14
met. 1σ ♣,o	2992	528	0.36	1.50	1 ± 0	-0.4 ± 0.1	-0.3 ± 0.1	1.3 ± 0.2	-0.94 ± 0.10	-0.27 ± 0.09	-0.83 ± 0.16
calibration ♣,□	3109	625	0.37	1.66	-1 ± 0	1.2 ± 0.1	0.6 ± 0.1	-0.9 ± 0.1	-0.23 ± 0.09	-0.44 ± 0.09	-0.05 ± 0.13
CH_4 profile											
plus 0.3σ ♣,o	2827	566	0.00	0.02	0 ± 0	-0.0 ± 0.1	-0.0 ± 0.1	0.0 ± 0.1	-0.06 ± 0.09	-0.05 ± 0.09	-0.06 ± 0.14
plus 1σ ♣,o	2827	560	0.00	0.03	0 ± 0	-0.0 ± 0.1	0.0 ± 0.1	0.0 ± 0.1	-0.06 ± 0.09	-0.05 ± 0.09	-0.09 ± 0.14
Spectral albedo											
sand ♣,o	4102	1249	0.01	0.03	0 ± 0	-0.0 ± 0.1	0.0 ± 0.1	-0.0 ± 0.1	-0.03 ± 0.07	-0.03 ± 0.07	-0.03 ± 0.07
soil ♣,o	2047	833	0.00	0.01	0 ± 0	0.0 ± 0.1	-0.0 ± 0.1	0.0 ± 0.1	-0.06 ± 0.08	0.07 ± 0.08	-0.06 ± 0.11
deciduous ♣,o	3847	161	0.01	0.03	0 ± 0	-0.0 ± 0.1	0.0 ± 0.1	-0.0 ± 0.1	-0.07 ± 0.23	-0.07 ± 0.20	-0.03 ± 0.50
conifers ♣,o	2818	148	0.00	0.02	0 ± 0	-0.0 ± 0.1	0.0 ± 0.1	-0.0 ± 0.1	-0.07 ± 0.27	-0.06 ± 0.21	-0.04 ± 0.61
rangeland ♣,o	2776	447	0.00	0.01	0 ± 0	-0.0 ± 0.1	0.0 ± 0.1	-0.0 ± 0.1	0.08 ± 0.10	-0.01 ± 0.10	-0.07 ± 0.17
snow ♣,o	11916	125	0.03	0.56	0 ± 0	-0.0 ± 0.1	0.0 ± 0.1	0.0 ± 0.0	0.12 ± 0.40	-0.05 ± 0.30	0.19 ± 0.76
ocean ♣,o	791	83	0.00	0.03	0 ± 0	0.0 ± 0.1	0.0 ± 0.1	-0.0 ± 0.2	-0.09 ± 1.05	-0.07 ± 0.84	-0.10 ± 1.61
Macro physical cloud properties											
no cloud ♣,o	2678	616	0.09	0.08	0 ± 0	0.0 ± 0.1	-0.0 ± 5.0	0.0 ± 0.1	0.05 ± 0.11	0.04 ± 0.10	0.07 ± 0.13
CWP 0.3 ♣,o	2681	615	0.07	0.08	0 ± 0	-0.0 ± 0.1	1.2 ± 2.1	-0.0 ± 0.1	0.02 ± 0.11	0.04 ± 0.10	0.01 ± 0.13
CWP 3.0 ♣,o	2713	600	0.00	0.01	0 ± 0	0.0 ± 0.1	0.0 ± 0.3	-0.0 ± 0.1	-0.04 ± 0.10	0.00 ± 0.10	0.07 ± 0.13
CWP 30.0 ♣,o	3303	509	0.01	0.05	0 ± 0	0.0 ± 0.1	0.0 ± 0.0	-0.0 ± 0.1	-0.03 ± 0.09	-0.07 ± 0.08	0.09 ± 0.22
CTH 3 ♣,o	2804	566	0.08	0.40	0 ± 0	-2.4 ± 1.2	0.4 ± 0.2	-0.1 ± 0.1	0.02 ± 0.10	-0.00 ± 0.10	0.41 ± 0.15
CTH 6 ♣,o	2812	567	0.03	0.22	0 ± 0	0.0 ± 0.3	0.0 ± 0.2	-0.1 ± 0.1	0.04 ± 0.10	0.02 ± 0.09	0.01 ± 0.14
CTH 12 ♣,o	2833	569	0.00	0.01	0 ± 0	0.0 ± 0.1	0.0 ± 0.1	-0.0 ± 0.1	0.02 ± 0.09	0.01 ± 0.09	0.02 ± 0.13
CTH 21 ♣,o	2851	569	0.01	0.05	0 ± 0	0.0 ± 0.1	-0.1 ± 0.4	-0.0 ± 0.1	0.00 ± 0.10	-0.00 ± 0.09	0.02 ± 0.15
CGT ♦,□	2985	527	0.55	2.31	3 ± 0	-0.5 ± 0.1	-2.0 ± 0.1	1.4 ± 0.2	-1.02 ± 0.10	-0.24 ± 0.08	-0.74 ± 0.15
Micro physical cloud properties											
ice frac. 100 ♦,□	2718	576	0.52	2.25	-1 ± 0	-13.0 ± 0.1	-1.3 ± 0.5	0.6 ± 0.1	-0.08 ± 0.10	-0.24 ± 0.10	-0.58 ± 0.14
ice frac. 300 ♦,□	2702	581	0.56	2.48	-1 ± 0	-14.0 ± 0.1	-1.5 ± 1.2	0.5 ± 0.1	-0.03 ± 0.11	-0.22 ± 0.11	-0.44 ± 0.14
ice hex. 25 ♦,□	2767	553	1.21	8.31	-4 ± 0	-4.0 ± 0.1	7.7 ± 1.1	-0.6 ± 0.1	0.58 ± 0.11	-0.90 ± 0.09	0.31 ± 0.15
ice hex. 50 ♦,□	2761	559	1.02	10.21	-3 ± 0	-4.2 ± 0.0	35.0 ± 4.0	-1.0 ± 0.1	0.28 ± 0.10	-0.74 ± 0.09	0.17 ± 0.15
water 6 ♦,□	3149	673	1.82	4.92	-1 ± 0	12.5 ± 0.5	1.8 ± 0.1	-1.9 ± 0.1	-4.05 ± 0.10	-4.39 ± 0.09	-4.37 ± 0.13
water 12 ♦,□	2936	622	0.88	8.15	-2 ± 0	3.6 ± 0.2	3.0 ± 0.1	-1.9 ± 0.1	-2.19 ± 0.10	-2.15 ± 0.09	-0.99 ± 0.14
water 18 ♦,□	2857	602	0.69	7.93	-1 ± 0	0.2 ± 0.1	4.7 ± 0.2	-1.4 ± 0.1	-1.40 ± 0.11	-1.21 ± 0.10	-0.30 ± 0.14
Aerosol											
OPAC background ♥,□	2684	617	0.06	0.13	0 ± 0	0.0 ± 0.1	0.8 ± 4.9	-0.2 ± 0.1	0.03 ± 0.11	0.00 ± 0.10	0.02 ± 0.13
OPAC urban ♥,□	2576	608	1.39	0.38	0 ± 0	0.0 ± 0.1	-1.4 ± 5.0	-0.2 ± 0.1	0.12 ± 0.11	-0.24 ± 0.10	0.00 ± 0.13
OPAC desert ♥,□	2669	616	0.09	0.20	1 ± 0	5.2 ± 0.7	-8.3 ± 0.1	-0.1 ± 0.0	-0.28 ± 0.11	-0.41 ± 0.10	0.07 ± 0.13
extreme in BL ♥,□	2675	550	0.37	1.94	0 ± 0	2.7 ± 0.3	-4.9 ± 0.4	-0.4 ± 0.1	0.66 ± 0.11	0.37 ± 0.10	3.18 ± 0.20

Table 12.4: Overview of the retrieval performance for 32 test scenarios similar to Table 12.3 but for CO. The table has been computed using an a priori uncertainty of about 25% for CO.

Scenario	SNR		RMS [‰]		SZA 40°					SZA 20°	SZA 60°
	NIR	SWIR	NIR	SWIR	p_s [hPa]	CWP [g/m^2]	CTH [km]	APS	CO [%]	CO [%]	CO [%]
dry run ❍	2827	568	0.00	0.00	0 ± 0	0.0 ± 0.1	0.0 ± 0.1	0.0 ± 0.1	-0.01 ± 1.06	-0.01 ± 0.92	-0.01 ± 1.48
met. 1σ ❍	2992	528	0.36	1.50	1 ± 0	-0.4 ± 0.1	-0.3 ± 0.1	1.3 ± 0.2	-0.51 ± 1.15	0.00 ± 0.98	-0.10 ± 1.65
calibration ♣,❑	3109	625	0.37	1.66	-1 ± 0	1.2 ± 0.1	0.6 ± 0.1	-0.9 ± 0.1	-0.40 ± 0.99	-0.59 ± 0.86	-0.20 ± 1.35
CO profile											
plus 0.3σ ♣,❍	2827	566	0.00	0.02	0 ± 0	-0.0 ± 0.1	-0.0 ± 0.1	0.0 ± 0.1	-0.39 ± 1.08	-0.38 ± 0.94	-0.41 ± 1.50
plus 1σ ♣,❍	2827	560	0.00	0.03	0 ± 0	-0.0 ± 0.1	0.0 ± 0.1	0.0 ± 0.1	-0.36 ± 1.09	-0.34 ± 0.95	-0.40 ± 1.52
Spectral albedo											
sand ♣,❍	4102	1249	0.01	0.03	0 ± 0	-0.0 ± 0.1	0.0 ± 0.1	-0.0 ± 0.1	-0.30 ± 0.47	-0.31 ± 0.41	-0.29 ± 0.64
soil ♣,❍	2047	833	0.00	0.01	0 ± 0	0.0 ± 0.1	-0.0 ± 0.1	0.0 ± 0.1	-0.39 ± 0.72	0.36 ± 0.61	-0.40 ± 1.00
deciduous ♣,❍	3847	161	0.01	0.03	0 ± 0	-0.0 ± 0.1	0.0 ± 0.1	-0.0 ± 0.1	-0.42 ± 4.40	-0.41 ± 3.85	-0.41 ± 5.86
conifers ♣,❍	2818	148	0.00	0.02	0 ± 0	-0.0 ± 0.1	0.0 ± 0.1	-0.0 ± 0.1	-0.43 ± 4.89	-0.42 ± 4.29	-0.42 ± 6.47
rangeland ♣,❍	2776	447	0.00	0.01	0 ± 0	-0.0 ± 0.1	0.0 ± 0.1	-0.0 ± 0.1	0.38 ± 1.36	-0.00 ± 1.21	-0.41 ± 1.93
snow ♣,❍	11916	125	0.03	0.56	0 ± 0	-0.0 ± 0.1	0.0 ± 0.1	0.0 ± 0.0	0.40 ± 6.56	0.04 ± 5.84	1.40 ± 8.29
ocean ♣,❍	791	83	0.00	0.03	0 ± 0	0.0 ± 0.1	0.0 ± 0.1	-0.0 ± 0.2	-0.37 ± 10.32	-0.40 ± 9.41	-0.37 ± 12.16
Macro physical cloud properties											
no cloud ♣,❍	2678	616	0.09	0.08	0 ± 0	0.0 ± 0.1	-0.0 ± 5.0	0.0 ± 0.1	0.14 ± 1.00	0.26 ± 0.90	0.27 ± 1.19
CWP 0.3 ♣,❍	2681	615	0.07	0.08	0 ± 0	-0.0 ± 0.1	1.2 ± 2.1	-0.0 ± 0.1	-0.02 ± 1.00	0.14 ± 0.90	-0.16 ± 1.21
CWP 3.0 ♣,❍	2713	600	0.00	0.01	0 ± 0	0.0 ± 0.1	0.0 ± 0.3	-0.0 ± 0.1	-0.29 ± 1.02	-0.07 ± 0.90	0.23 ± 1.25
CWP 30.0 ♣,❍	3303	509	0.01	0.05	0 ± 0	0.0 ± 0.1	0.0 ± 0.0	-0.0 ± 0.1	-0.42 ± 1.48	-0.39 ± 1.17	0.46 ± 2.63
CTH 3 ♣,❍	2804	566	0.08	0.40	0 ± 0	-2.4 ± 1.2	0.4 ± 0.2	-0.1 ± 0.1	-0.13 ± 1.01	-0.08 ± 0.87	-0.22 ± 1.45
CTH 6 ♣,❍	2812	567	0.03	0.22	0 ± 0	0.0 ± 0.3	0.0 ± 0.2	-0.1 ± 0.1	0.01 ± 1.04	-0.00 ± 0.89	-0.00 ± 1.50
CTH 12 ♣,❍	2833	569	0.00	0.01	0 ± 0	0.0 ± 0.1	0.0 ± 0.1	-0.0 ± 0.1	0.15 ± 1.06	-0.01 ± 0.93	0.10 ± 1.46
CTH 21 ♣,❍	2851	569	0.01	0.05	0 ± 0	0.0 ± 0.1	-0.1 ± 0.4	-0.0 ± 0.1	0.00 ± 1.07	-0.01 ± 0.94	-0.01 ± 1.42
CGT ♦,❑	2985	527	0.55	2.31	3 ± 0	-0.5 ± 0.1	-2.0 ± 0.1	1.4 ± 0.2	0.20 ± 0.93	0.57 ± 0.78	0.87 ± 1.35
Micro physical cloud properties											
ice frac. 100 ♦,❑	2718	576	0.52	2.25	-1 ± 0	-13.0 ± 0.1	-1.3 ± 0.5	0.6 ± 0.1	0.11 ± 0.82	0.20 ± 0.73	-0.04 ± 1.03
ice frac. 300 ♦,❑	2702	581	0.56	2.48	-1 ± 0	-14.0 ± 0.1	-1.5 ± 1.2	0.5 ± 0.1	0.35 ± 0.81	0.33 ± 0.73	0.28 ± 1.00
ice hex. 25 ♦,❑	2767	553	1.21	8.31	-4 ± 0	-4.0 ± 0.1	7.7 ± 1.1	-0.6 ± 0.1	1.20 ± 0.86	0.21 ± 0.77	0.97 ± 1.09
ice hex. 50 ♦,❑	2761	559	1.02	10.21	-3 ± 0	-4.2 ± 0.0	35.0 ± 4.0	-1.0 ± 0.1	1.23 ± 0.85	0.72 ± 0.77	0.90 ± 1.07
water 6 ♦,❑	3149	673	1.82	4.92	-1 ± 0	12.5 ± 0.5	1.8 ± 0.1	-1.9 ± 0.1	-5.68 ± 0.71	-5.94 ± 0.60	-5.95 ± 1.05
water 12 ♦,❑	2936	622	0.88	8.15	-2 ± 0	3.6 ± 0.2	3.0 ± 0.1	-1.9 ± 0.1	-2.70 ± 0.77	-2.32 ± 0.67	-0.81 ± 1.05
water 18 ♦,❑	2857	602	0.69	7.93	-1 ± 0	0.2 ± 0.1	4.7 ± 0.2	-1.4 ± 0.1	-1.62 ± 0.80	-1.07 ± 0.71	0.04 ± 1.04
Aerosol											
OPAC background ♥,❑	2684	617	0.06	0.13	0 ± 0	0.0 ± 0.1	0.8 ± 4.9	-0.2 ± 0.1	0.27 ± 0.99	-0.02 ± 0.91	-0.02 ± 1.21
OPAC urban ♥,❑	2576	608	1.39	0.38	0 ± 0	0.0 ± 0.1	-1.4 ± 5.0	-0.2 ± 0.1	-0.06 ± 1.02	-0.02 ± 0.90	0.04 ± 1.23
OPAC desert ♥,❑	2669	616	0.09	0.20	1 ± 0	5.2 ± 0.7	-8.3 ± 0.1	-0.1 ± 0.0	-0.09 ± 0.96	-0.09 ± 0.87	0.14 ± 1.21
extreme in BL ♥,❑	2675	550	0.37	1.94	0 ± 0	2.7 ± 0.3	-4.9 ± 0.4	-0.4 ± 0.1	0.85 ± 1.07	0.51 ± 0.91	2.66 ± 1.65

12.8.3 Calibration

To account for spectrally smooth variations of the surface albedo and for calibration errors causing a scaling of the sun-normalized radiance the albedo is fitted with a 2nd order polynomial. The ‘calibration’ scenario estimates the influence of calibration errors that cause an intensity scaling. For this purpose, the simulated intensity of the ‘dry run’ was scaled by a factor of 10%. This primarily affects the retrieved 0th order albedo polynomials which are approximately 10% too large. The weighting function of the 0th order albedo polynomial shows similarities with other weighting functions (see Figure 12.4) affecting the retrieval errors of other parameters. The resulting systematic errors of XCH_4 and CO are below 0.5%.

12.8.4 CH_4 and CO profile

The two scenarios for CH_4 (and CO respectively) differ from the ‘dry run’ scenario only by a modified (true) CH_4 (or CO) profile. The ‘plus 0.3 σ’ scenario has a true CH_4 profile which differs from the a priori profile by an enhancement of 0.3σ a priori uncertainty in each layer. The resulting XCH4 has a bias of -0.06% and a stochastic error of 0.09% for 40° SZA (Table 12.4). For CO the corresponding error is -0.39±1.08%.

12.8.5 Spectral Albedo

Unfortunately, the spectral albedo cannot be assumed to be constant within the O_2 and CH_4/CO fit window. In the worst case, the spectral shape of the albedo would be highly correlated with the surface pressure or CH_4 and CO weighting function. In this case, errors of the retrieved surface pressure or CH_4 and CO mixing ratios would be unavoidable. However, this is most unlikely in reality.

As illustrated in Figure 12.7, the albedo of typical surface types is spectrally smooth and only slowly varying within the fit windows. This applies especially to satellite pixels with large foot print size consisting of a mixture of surface types. Therefore, it has been assumed that the albedo can be approximated within each fit window with a 2nd order polynomial. In order to make a perfect retrieval with no remaining residuals theoretically possible, a 2nd order polynomial is fitted in both fit windows to the spectral albedos. These polynomials have been used as true spectral albedo for the albedo scenarios 'sand', 'soil', 'deciduous', 'conifers', 'rangeland', 'snow', and 'ocean'. All other elements of the state vector are identical to those of the 'dry run' scenario. Table 12.3 and Table 12.4 show that the systematic XCH_4 errors of these scenarios are in the range of -0.09% and +0.19%. For CO the error range is from -0.43% to +1.40%.

According to the large differences of the tested albedos, SNR values vary from 791 to 11916 in the NIR fit window and from 83 to 1249 in the SWIR fit window. The lowest stochastic errors for CH_4 and CO are found for the 'sand' scenarios. These scenarios have a relatively high albedo of about 0.3 in the NIR and 0.45 in the SWIR fit window. For this reason the corresponding SNR values are also relatively large, which is essential for low stochastic errors.

The largest SNR values are observed in the NIR fit window for the 'snow' scenario because of the high reflectivity of snow in this spectral region. The 'ocean' scenario has the lowest albedo and therefore the lowest SNR value in both fit windows respectively. Consequently, the largest stochastic errors of about 1.6% for CH_4 and 12% for CO are observed here.

These albedo scenarios have also been used in Section 12.9.1.

12.8.6 Macro physical cloud parameters

Within the scenarios 'no cloud', 'CWP 0.3' to 'CWP 30.0', the retrieval's ability to retrieve CWP of an ice cloud of fractal particles with 50 µm effective radius (as defined in the parameter vector) has been tested. All other state vector elements are defined as in the 'dry run' scenario. As implied by the name of these scenarios, the ice content of the analyzed clouds amounts to 0.0g/m^2, 0.3g/m^2, 3.0g/m^2, and 30.0g/m^2. The corresponding cloud optical thicknesses of these scenarios are about 0.00, 0.01, 0.10, and 1.00. Note, in this context, specifying only the optical thickness is not appropriate to describe the scattering behaviour of a cloud. Knowledge about phase function, extinction, and absorption coefficients is required in order to make the optical thickness a meaningful quantity. The SNR values of the 'no cloud' and 'CWP 0.3' scenarios is almost identical and there are only weak differences to the 'CWP 3.0' scenario. This indicates that the clouds of these cases are extremely transparent and most likely not visible for the human eye. In contrast to this, the SNR of the 'CWP 30.0' scenario increases within the NIR fit window. Within the SWIR fit window, the effect of enhanced backscattered radiation is balanced by the strong absorption of ice in this spectral region. Nearly no systematic errors of the retrieved surface pressure can be observed.

The CWP retrieval is bias free for all analysed solar zenith angles. The same applies to the retrieved CTH of the 'CWP' scenarios except for 'CWP 0.3'. For the 'no cloud' scenario, the unmodified a priori value is retrieved without any error reduction which is reasonable. The stochastic CTH error reduces for CWP values greater than 3.0 g/m^2. The systematic absolute XCH_4 error of these scenarios is less or equal 0.09% whereas the stochastic error is less than 0.22%.

Analog to the ‘CWP’ scenarios, the ‘CTH’ scenarios are identical to the ‘dry run’ scenario except for the cloud top height which varies between 3 km, 6 km, 12 km, and 21 km. CWP and CTH are retrieved nearly bias free for the ‘CTH 6’, ‘CTH 12’, and ‘CTH 21’ scenario. The systematic XCH_4 error of these scenarios is also comparatively low with values between 0.0% and 0.04% (for CO 0.0% and 0.15%). Only the ‘CTH 3’ scenario produces larger systematic errors of CWP and CTH. Additionally, the systematic XCH_4 error of this scenario is slightly larger with values up to 0.41% (and -0.22% for CO). This behaviour may be explained by the fact that APS, and especially CTH and CWP weighing functions become more and more similar for low clouds.

Up to this point, solely the retrieval’s ability to reproduce modifications to state vector elements has been tested. However, and as mentioned before, especially in respect to scattering, three state vector elements are by far not enough to entirely define the radiative transfer. For this reason, also the retrieval’s sensitivity to parameter vector elements has been analysed with the following scenario. At this, the focus has been put on properties of thin cirrus clouds. In the context of macro physical cloud parameters the retrieval’s sensitivity to cloud geometrical thickness (“CGT” scenario) has been estimated. This scenario is based on the ‘met. 1σ’ scenario.

The ‘CGT’ scenario differs from this reference scenario only by the cloud geometrical thickness that is 2.5 km compared to 0.5 km for the reference scenario. The results of this scenario are very similar to the reference results for XCH_4. Solely, the retrieved CTH is systematically 1.7km lower. Due to the larger geometrical thickness and identical ice content at the same time, the particle density is lower. For this reason, the effective penetration depth in this cloud is larger which can explain the differences of the retrieved CTH. For CO the errors are somewhat higher but stay rather low between 0.2% and 0.87%.

12.8.7 Micro physical cloud parameter

Within this section the retrieval’s sensitivity to cloud micro physical properties is estimated. This means, BESD is confronted with clouds consisting of particles differing from those defined in the parameter vector.

The information about the three retrieved scattering parameters CWP, CTH, and APS can nearly entirely be attributed to the O_2 fit window in the NIR. Scattering properties are defined within the state vector solely by these three parameters. The whole micro physical cloud and aerosol properties like phase function, extinction, and absorption coefficients are only defined in the parameter vector. Unfortunately, these micro physical properties are not known and also not constant in reality and the values that are defined in the parameter vector are obviously only a rough estimate.

Let us first consider only the O_2 fit window and assume that extinction and absorption coefficients as well as phase function of the scattering particles are constant in this spectral region. Let us now assume two clouds having phase functions which differ only by a factor (or an offset within a logarithmic plot) outside the forward peak. In such case, the CWP retrieval would be ambiguous in respect to the micro physical properties and consequently, correct CWP values are only retrievable if the scattering particles are known. Referring to Figure 12.3, the volume scattering functions within the O_2 fit window of e.g. fractal ice crystals of different size show such similarities. This means that in the case of unknown particles, it is hardly possible to retrieve the true CWP from measurements in the O_2 fit window only. The retrieved CWP is then rather an effective CWP under the assumption of specific particles. Its value does not have to correspond to the true CWP. Note: The same applies to APS and also to some extend to CTH. As long as the true geometrical thickness is known and defined in the parameter vector, the retrieved CTH corresponds to the true CTH. Nevertheless, in reality the true cloud geometrical thickness is unknown and therefore, only an effective CTH can be retrieved under the assumption of a cloud with 0.5 km geometrical thickness. This corresponds to the CTH results of the ‘CGT’ scenarios in Table 12.3 and Table 12.4.

However, the effective scattering parameters are mainly retrieved from the O_2 fit window without knowledge of the actual micro physical properties. Therefore, the retrieved parameters may not be appropriate for the usage in the CH_4 and CO fit window under some conditions. Particularly, this depends on the relation of the absorption coefficients and volume scattering functions within the O_2 fit window compared to the CH_4/CO fit window. It can be expected that the retrieved parameters are applicable if this relation is similar for the true particles and those particles that are assumed within the parameter vector.

Assuming here a static relation is only a rough estimate, because methods like that of Nakajima and King (1990) are based on the fact that liquid water droplets have a stronger absorption at, e.g., 2350 nm compared to, e.g., 750 nm with nearly no absorption. This results in differences of the reflection at clouds in both wavelengths which can be used to derive the cloud optical thickness and simultaneously the particle's effective radius. However, this method may fail for very thin clouds under conditions with unknown spectral albedo. Additionally, ice particles usually have non-spherical shapes influencing the corresponding phase functions. For these reasons, it was not considered to retrieve the cloud particle effective radius simultaneously.

The clouds which have been used for the scenarios of this section, consist of fractal ice particles with 100 µm and 300 µm effective radius ('ice frac. 100' and 'ice frac. 300' scenarios), hexagonal ice particles with 25 µm and 50 µm effective radius ('ice hex. 25' and 'ice hex. 50' scenario), and water droplets with a gamma particle size distribution and an effective radius of 6 µm, 12 µm, and 18 µm, respectively ('water 6', 'water 12', and 'water 18' scenarios). These scenarios are based on the 'met. 1σ' reference scenario. The corresponding volume scattering functions are given in Figure 12.3. For the most common shapes of cloud particles, a decreasing particle size results in an increasing optical thickness and a decreasing forward peak of the phase function. For this reason different true CWP values have been used for these scenarios: 3 g/m^2 for the 'water' scenarios, 8 g/m^2 for the 'ice hex.' scenarios, and 15 g/m^2 for the "ice frac." scenarios. Additionally different CTH values have been used: 3 km for the 'water' scenarios and 15 km, otherwise.

The SNR values in the O_2 fit window confirm, that more radiation is scattered back from smaller particles. In these cases, the enhanced or reduced back scattered radiation is mainly misinterpreted as albedo effect. Given a true albedo of 0.20 within both fit windows, the retrieved albedo varies between about 0.19 and 0.26 within both fit windows.

Results in CWP and APS show large biases indicating that clouds can be misinterpreted as aerosol by the retrieval. The systematic errors of the retrieved XCH_4 are in the range of -4.4% and -0.2% for 20° SZA, −4.1% and 0.6% for 40° SZA, and -4.4% and 0.3% for 60° SZA. For CO, the systematic errors are in the range of -5.9% and 0.7% for 20° SZA, -5.7% and 1.2% for 40° SZA, and 6.0% and 1.0% for 60° SZA.

12.8.8 Aerosol

In analogy to the cloud scenarios, the influence of aerosol properties which are not part of the state vector have been estimated. For this purpose, BESD has been confronted with four aerosol scenarios which are described in detail by Schneising et al. (2008b). Their profile, class of particles, and their phase function differ from the default aerosol scenario. The 'OPAC background' scenario consists of continental relatively clean aerosol in the boundary layer and the free troposphere; the 'OPAC urban' scenario has continental polluted aerosol in the boundary layer and continental average aerosol in the free troposphere; the 'OPAC desert' scenario consists of desert aerosol in the boundary layer and the continental clean aerosol type in the free troposphere; the 'extreme in BL' scenario has strongly enhanced urban aerosol in the boundary layer with a visibility of only 2 km and relative humidity of 99%. The 'no cloud' scenario serves as basis.

The systematic absolute errors are below 0.3% for XCH_4 and below 0.4% for CO for the OPAC scenarios. In contrast to this, the extreme scenario produces larger systematic errors up to 3.2% (XCH_4) and 2.7% (CO).

12.9 Verification results

The first step in the verification process is the comparison of retrieval results for well-defined atmospheric scenarios between prototype and verification algorithm. As a precondition, the sun spectra and noise model between the algorithms have been harmonized so that signal to noise ratio is approximately 100 in the continuum for a dark scene (albedo = 0.05) and low sun (solar zenith angle of 70°). This corresponds to the threshold requirement. For bright scenes, the signal to noise ratio is accordingly higher. In the following, initial results will be shown for comparisons between the verification algorithm BESD and the prototype algorithms RemoTeC for CH_4 and SICOR for CO respectively.

12.9.1 Methane

For an initial comparison several test scenarios have been chosen to assess the retrieval noise (precision) and the errors caused by cirrus clouds and spectrally varying surface spectral reflectance. While cloud location in the radiative transfer model that is used for BESD (SCIATRAN) is defined by cloud top height and geometrical thickness, the according parameters for RemoTeC are cloud centre altitude and full width at half maximum. Furthermore also the microphysical representation differs in the two radiative transfer models, so that optical thickness is the most important, comparable parameter in case of cloud impacts on the retrieval algorithms. All scenarios were computed using a viewing zenith angle of 0° that is directly nadir looking.

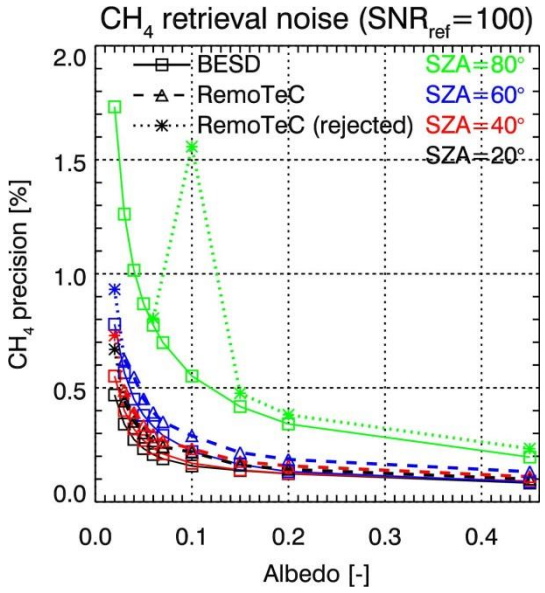

Figure 12.5: Retrieval noise (precision) of the XCH_4 result for different SWIR albedos and solar zenith angles (SZA). Generally the precision is below the random error requirement of 1% for both retrieval algorithms. Note that solar zenith angles of greater than 70°, retrieved albedos of lower than 0.02 and optical thickness of greater than 0.3 will be rejected for operational RemoTeC CH_4 retrievals and are shown here only for comparison. The discontinuity in precision for SZA=80° and albedo=0.1 is caused by the fact that RemoTeC has a flexible determination of the regularization strength. For this point a weaker regularization has been selected which causes a discontinuity in the precision.

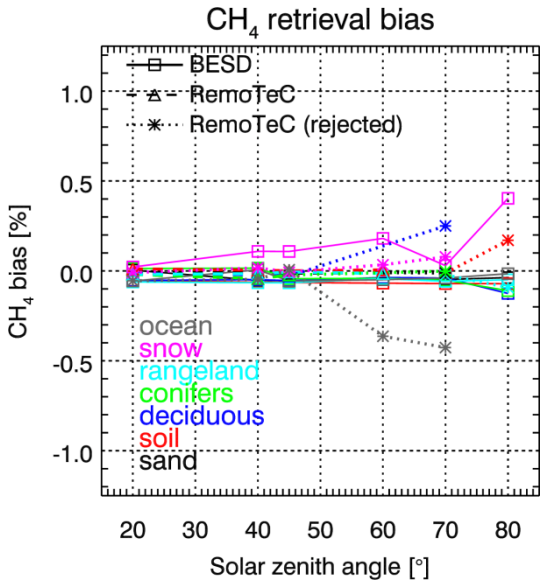

Figure 12.6: Retrieval bias induced by spectrally varying albedo in the SWIR channel for different solar zenith angles. RemoTeC results for snow are not shown.

The first scenario (Figure 12.5) tests the retrieval noise (precision) for different solar zenith angles and a background aerosol scenario (optical thickness at 765nm is 0.1292 and optical thickness at 2345nm is 0.017 for BESD). No cloud was inserted for this scenario. The NIR albedo was fixed at 0.2 and the SWIR albedo was varied according to the x-coordinate but constant within the respective wavelength bands. The precision is generally well below (i.e., better than) the random error requirement of 1%, except for solar zenith angles of 80°. Note, that for RemoTeC scenarios with SZA greater than 70° and retrieved albedos lower than 0.02 will be filtered out and are shown here only for comparison.

For the second scenario (Figure 12.6) the impact of a varying albedo in the NIR and SWIR band was investigated. The influence of the wavelength dependence of the surface albedo cannot be completely accounted for by a second order polynomial as used in both retrievals. The induced bias for different cloud free albedo scenarios is shown in Figure 12.7. For BESD, the bias is generally well below 0.1% except for high solar zenith angles over snow which generally have a very low albedo in the SWIR spectral range. The same is true for RemoTeC when high solar zenith angles and low albedos are neglected that would be filtered out. Nevertheless, all errors are well below the systematic error requirement of 1%.

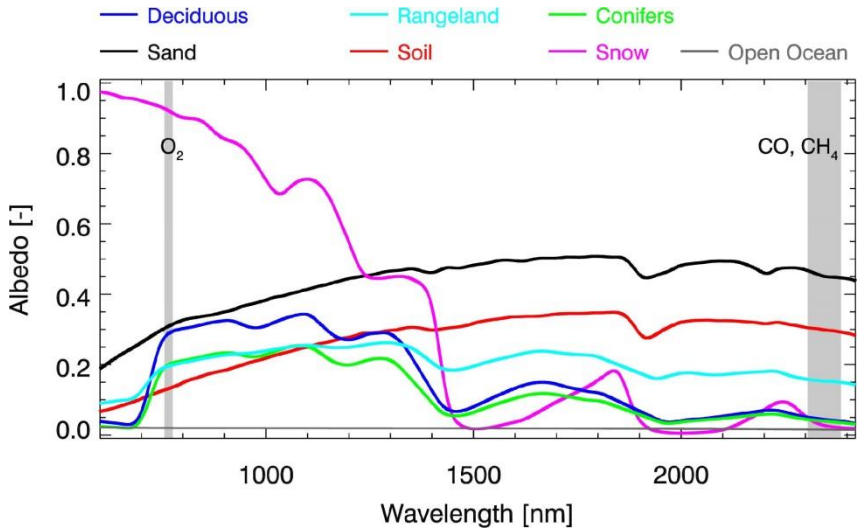

Figure 12.7: Spectrally varying albedo as used for the test scenarios. Albedo values are based on the ASTER Spectral Library through the courtesy of the Jet Propulsion Laboratory, California Institute of Technology, Pasadena, California (©1999, California Institute of Technology) and the Digital Spectral Library 06 of the US Geological Survey in the same manner as used by Reuter et al. (2010).

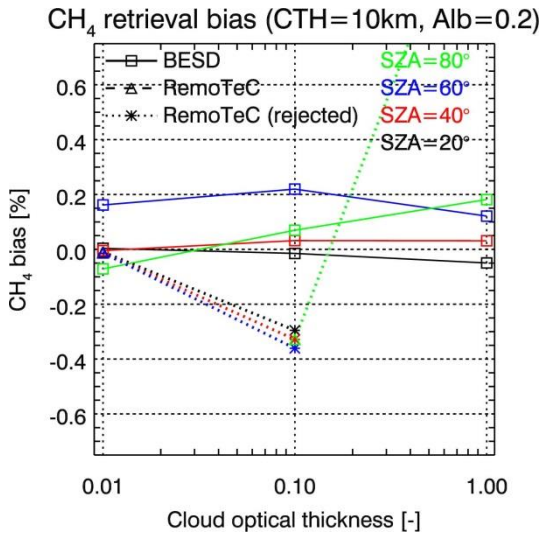

Figure 12.8: Retrieval bias induced by clouds of different cloud optical thicknesses depending on solar zenith angle.

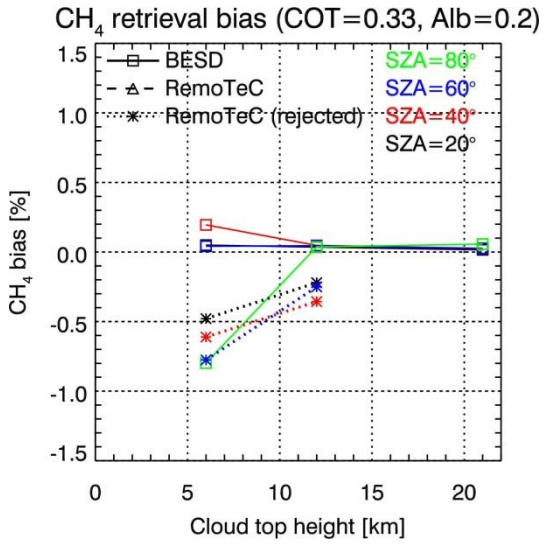

Figure 12.9: CH_4 retrieval bias induced by clouds at varying altitudes. For RemoTeC, cloud optical thickness of 0.33 would be filtered in operational use and results are shown only for comparison.

The associated spectral albedo scenarios are based on the ASTER Spectral Library through the courtesy of the Jet Propulsion Laboratory, California Institute of Technology, Pasadena, California (©1999, California Institute of Technology) and the Digital Spectral Library 06 of the US Geological Survey in the same manner as used by Reuter et al. (2010). The spectrally varying albedos for different surface types are displayed in Figure 12.7.

For the third scenario, the impact of (thin) clouds has been studied (Figure 12.8). Clouds generally can have a strong impact on trace gas retrievals. This is somewhat mitigated due to the explicit accounting of scattering in the BESD retrieval algorithm. Figure 12.8 shows the introduced retrieval bias based on a simulated cirrus cloud at 10 km altitude applying a surface albedo of 0.2 and different solar zenith angles for varying cloud optical thickness of 0.01, 0.1, and 1.0 where forward model and simulation use a consistent cloud model. For BESD XCH_4 the error is below about 0.25%.

The RemoTeC algorithm is not specifically designed to account for clouds but focusses mainly on the effect of aerosols on the retrieval. This approach will also work for very thin clouds (COT ≤ 0.05), but pixels with thicker clouds will be filtered out. More specifically, scenes with high COT (greater than 0.3) will be filtered out in a pre-processing step. Furthermore, an a posteriori filter based on retrieved scattering properties filters out high layers with large scattering particles (i.e. clouds). With this filter, effectively cirrus clouds with an optical thickness larger than 0.05 are filtered out.

Nevertheless the retrieval bias is very low for optically thin clouds.

Additionally to the cloud optical thickness also the cloud top height was varied from 6 km to 21 km for different solar zenith angles (see Figure 12.9). In this case, high solar zenith angles in combination with low clouds can lead to large biases. Generally, however, the introduced retrieval bias for BESD is below 0.05% for CH_4 with an exception for a very low cloud.

For RemoTeC, convergence problems were encountered for scenes with high clouds (21 km) and high COT (1.0). This could be explained by the fact that the forward model in the retrieval is inconsistent with the simulation (one particle type in retrieval, two in simulation) in contrast to BESD. Furthermore, it can be seen in Figure 12.8 and Figure 12.9 that RemoTeC indeed filters out scenes with cloud contamination, which demonstrates that the proposed filtering approach works properly.

In the fourth scenario, several aerosol types depending on location were defined (see Table 12.5). Since the aerosol parameterization is very different for the radiative transfer simulation model of RemoTeC and BESD, the common parameters used for the comparison were aerosol optical thickness and albedo in the NIR and SWIR wavelength range as well as cloud optical thickness, cloud top height, cloud geometrical thickness and viewing geometry (solar zenith angle, viewing zenith angle, azimuth angle). While for RemoTeC the particles are explicitly defined, for BESD simulated data only the aerosol type (e.g., maritime, rural, urban, desert) can be defined and was selected according to the regional location of the test site. The vertical distribution of aerosols is also not perfectly harmonized due to the differing parameterization types.

For both retrievals, simulation and forward model were not consistent, i.e., the parameterization significantly differed. Since the implementation of these aerosol scenarios cannot be made 100% consistent between the simulation for RemoTeC and the simulation for BESD (different parameterization, see above), and due to the fact the degree of inconsistency between forward model and simulation model is hard to quantify, the difference in obtained systematic errors should be evaluated with care but nevertheless can give a good indication for uncertainties to be expected.

Figure 12.10 shows the results for these aerosol scenarios. The resulting biases in XCH_4 for BESD and RemoTeC are in the same order of magnitude while RemoTeC performs somewhat better for most aerosol cases. The errors are generally below 0.3%. For the Germany case, the errors for BESD are somewhat higher. This could be due to the high solar zenith angle. The better performance of RemoTeC might be explained by the facts that RemoTeC is optimised for coping with aerosol and that surface pressure is not retrieved (in contrast to BESD) but assumed to be known.

Table 12.5: List of aerosol scenarios for the XCH_4 verification. SZA denotes the solar zenith angle, AOT the aerosol optical thickness and ALB the albedo in the respective wavelength windows.

Latitude	Longitude	Type	Location	SZA	AOT (NIR)	AOT(SWIR)	ALB (NIR)	ALB (SWIR)	Scenario name
23.72°N	11.25°E	Desert	Sahara	37.3°	0.12	0.08	0.47	0.48	sahara_sza37
26.51°S	115.31°E	Coastal	West-Australia	24.9°	0.13	0.10	0.22	0.25	australia_sza24
40.46°N	109.69° W	Rural	Utah (USA)	49.4°	0.09	0.36	0.21	0.22	utah_sza49
37.67°N	120.94° W	Urban	California (USA)	49.7°	0.09	0.01	0.19	0.14	california_sza49
51.63°N	8.44°E	Rural	Germany	60.6°	0.07	0.04	0.27	0.10	germany_sza60
46.045° N	106.88°E	Rural	Mongolia	55.0°	0.09	0.04	0.23	0.27	mongolia_sza55

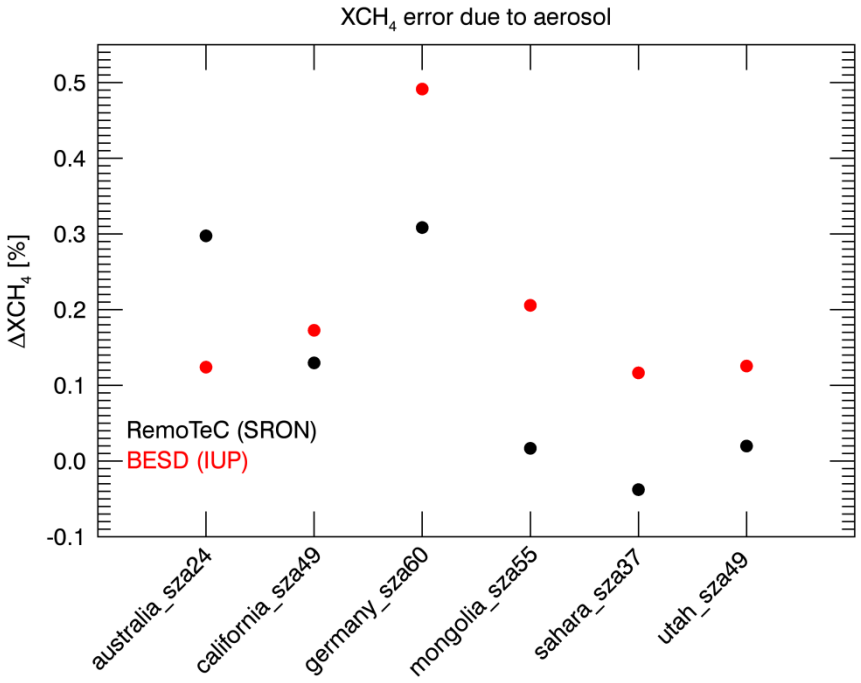

Figure 12.10: XCH_4 bias for different aerosol scenarios for the simulated data and an inconsistent aerosol model for the retrieval forward model.

Based on the Utah aerosol scenario, the influence of the viewing geometry on the CH_4 retrievals was investigated. For that the viewing zenith angle was varied between 0° (nadir) and 50° and the azimuth angle between 0° (looking towards the sun) and 180°. As shown in Figure 12.11 the results for BESD and RemoTeC are very similar for azimuth angles of 0° and 90°. In the case of 180°, biases in the RemoTeC retrieval are somewhat larger but remain in all cases well below the requirement of 1%. Note that the BESD results are slightly different from the aerosol scenario result in Figure 12.10. This is due to the fact that the algorithm was modified by disabling the Levenberg-Marquardt step size control to avoid convergence issues (compare also Section 12.9.2). This leads to results that are not identical but do not significantly differ with respect to their random errors as can be seen from Figure 12.11.

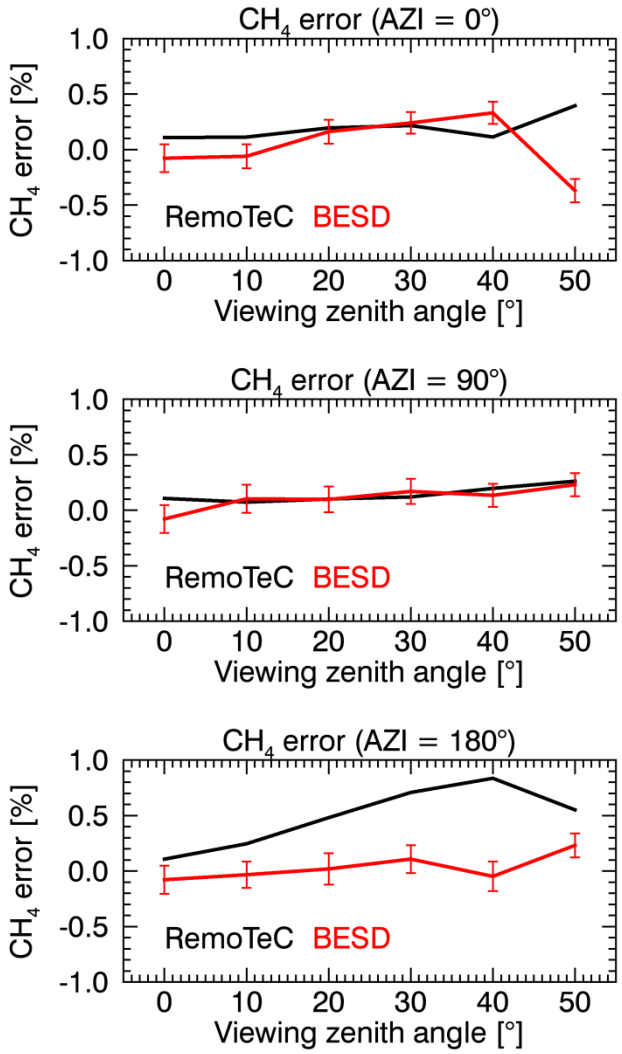

Figure 12.11: Comparison of the viewing zenith angle dependence for BESD and RemoTeC. Shown are the biases between retrieved and true CH_4 column as well as the random errors as error bars for BESD. The azimuth angle (AZI) is given in the title of each plot.

12.9.2 Carbon monoxide

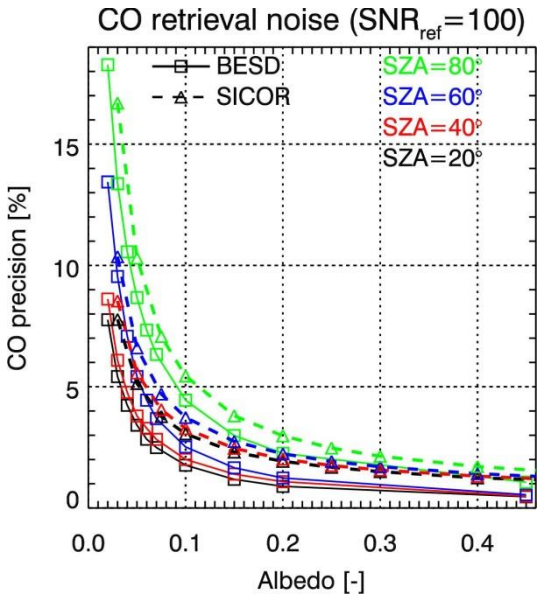

Figure 12.12: Retrieval noise (precision) of the CO results for different SWIR albedos and solar zenith angles (SZA). Generally the precision is below the random error requirement of 8% for both retrieval algorithms for albedos larger than 0.05 and solar zenith angles lower than 80°.

The initial test scenarios for the comparison of CO retrieval results for prototype and verification algorithm comprise investigations of the retrieval noise based on albedo and solar zenith angle and simulations regarding the impact of cirrus cloud optical thickness. For these scenarios the viewing zenith angle was set to 40° and the azimuth angle to 60°. The prototype algorithm SICOR uses a CH_4 pre-fit to filter for clouds. More specifically, measurements with CH_4 pre-fits that are biased by more than 25% from the a priori will be disregarded for the CO retrieval. These pre-fits are simplified non-scattering retrievals. Retrieval results that would have been rejected for operational processing are indicated in the figures.

Figure 12.12 shows the retrieval precision as a function of albedo and solar zenith angle. The albedo in the NIR band (that is used only for BESD) was set to 0.2. The precision threshold requirement of 8% is generally met by both retrievals. Only for very low albedos below 0.05 and high solar zenith angles of 80° this threshold is exceeded. The BESD precision is overall slightly better compared to SICOR most likely due to the fact that a broader wavelength range was used at a much higher computational expense.

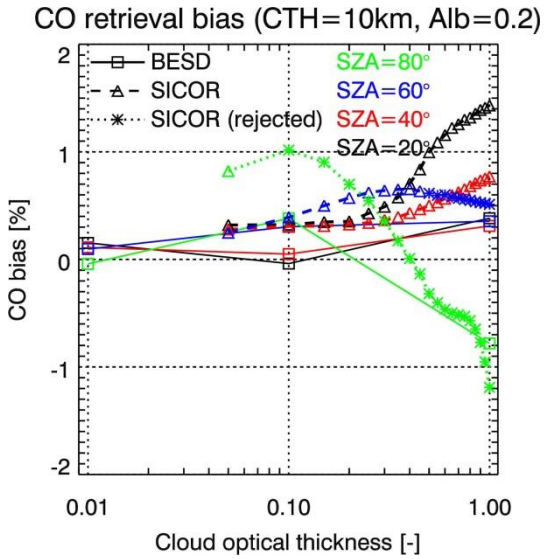

Figure 12.13: CO retrieval bias induced by clouds of different cloud optical thicknesses depending on solar zenith angle. SICOR results that are rejected due to the CH4 pre-fit criterion are indicated with stars.

The results for the cloud optical thickness scenario are shown in Figure 12.13. For low solar zenith angles and optical thicknesses the retrieval bias is for both algorithms very low (i.e., good) and always well below the 8% threshold requirement for retrieval biases. Towards optically thicker clouds BESD performs slightly more stable.

Another important atmospheric influence on the CO retrieval is based on the aerosol load of the probed atmosphere. To better assess the impact on the different retrievals, an aerosol scenario was defined by the prototypers consisting of a background aerosol with exponentially decreasing vertical distribution (~ $(0.9998)^z$, where z is given in meters) and an optical thickness of 0.1 at 2300nm. Additionally an urban aerosol layer of 1km thickness and a layer top height of 5km were introduced. The optical thickness at 2300nm of this block layer was varied from 0.0 to 1.0. Furthermore, the solar zenith angle was constant at 50° for a nadir viewing geometry. Since also a strong dependence on surface reflection is to be expected, the albedo was varied between 0.03 and 0.6.

Since the forward model aerosol parameterization for the verification algorithm BESD significantly differs from SICOR, an exact match of scenarios between the forward models cannot be accomplished. However, the scenarios were matched as closely as possible.

For the simulated scenario for BESD (using SCIATRAN), the aerosol types for the exponential and block layer both had to be set to an urban type. While the exact spectral dependence of the aerosol optical thickness cannot be matched, the optical thickness in the NIR and SWIR band centre wavelengths were manually set to be equal in the two forward models. This may to some degree lead to an unrealistic behaviour for the SCIATRAN simulation (e.g., unrealistic Ångström coefficients) adding further complexity for the retrieval. Note, that the aerosol parameterisation in the simulation (based on OPAC scenarios) and in the forward model (based on MODTRAN) are highly inconsistent anyway.

Originally BESD was not designed for these optically rather thick aerosol layers, reflected in the a priori value and constraints for the default aerosol scaling parameter of 1 ± 1 (see Chapter Scattering Parameters). To allow the retrieval also to cope with the circumstances at hand, the aerosol scaling parameter priori information was relaxed to 2 ± 6. It appears that this rather lose constraint could be chosen also in the default retrieval. A comparison of the results for error Table 12.3 and Table 12.4 for the two different settings did not exhibit significant differences.

Detailed results for the synthetic BESD retrievals applying an albedo of 0.1 are shown in Figure 12.14, where BESD is shown in black and available SICOR data in red. Relevant data is shown depending on the optical thickness τ of the block aerosol layer.

With a few exceptions (e.g., at an optical thickness of 0.2), the results for CO error (or bias) and precision for the two algorithms are very similar. Results for SICOR show a somewhat smoother behaviour with less variation than BESD. Generally for both algorithms, the bias is well below 2% and the precision varies between 3% and 9%, depending on the aerosol optical thickness.

For BESD several other retrieval results and diagnostic parameters are shown. The scattering at the aerosol layer is not completely considered by the aerosol parameter, but partly also by the cloud parameters where the cloud top height matches closely the aerosol layer top height. This shows that for BESD the scattering parameters should mainly be interpreted as effective parameters.

The NIR albedo is rapidly decreasing with increasing aerosol, indicating that there is only little information originating from the surface. This is less pronounced in the SWIR where aerosol optical thickness is less than in the NIR. Since there is less information from the layers below the aerosol block layer, also the uncertainty reduction decreases. Here it should be noted, that for these tests, the a priori uncertainty for CO was set to about ±25%.

Pressure is rather strongly constrained and therefore only deviates little from the true value.

What is striking however is the very large value of gamma (γ, see Chapter 12.5.1) before the retrieval converges. High values of γ effectively mean a steepest descent technique with a step size tending to zero. This happens also when the convergence criterion is relaxed. Generally, large gammas will also impact for example the averaging kernels so that this feature needs to be investigated further. Potentially a further relaxation of the convergence criterion can resolve this issue and even accelerate the retrieval.

To avoid further issues with too large damping factors gamma, the Levenberg-Marquardt step size control has been disabled for the following studies, i.e. effectively setting gamma to zero (compare Section 12.5.1) favouring a Gauss-Newton approach. Furthermore the SCIATRAN radiative transfer model version has been upgraded from 3.1 to 3.3.

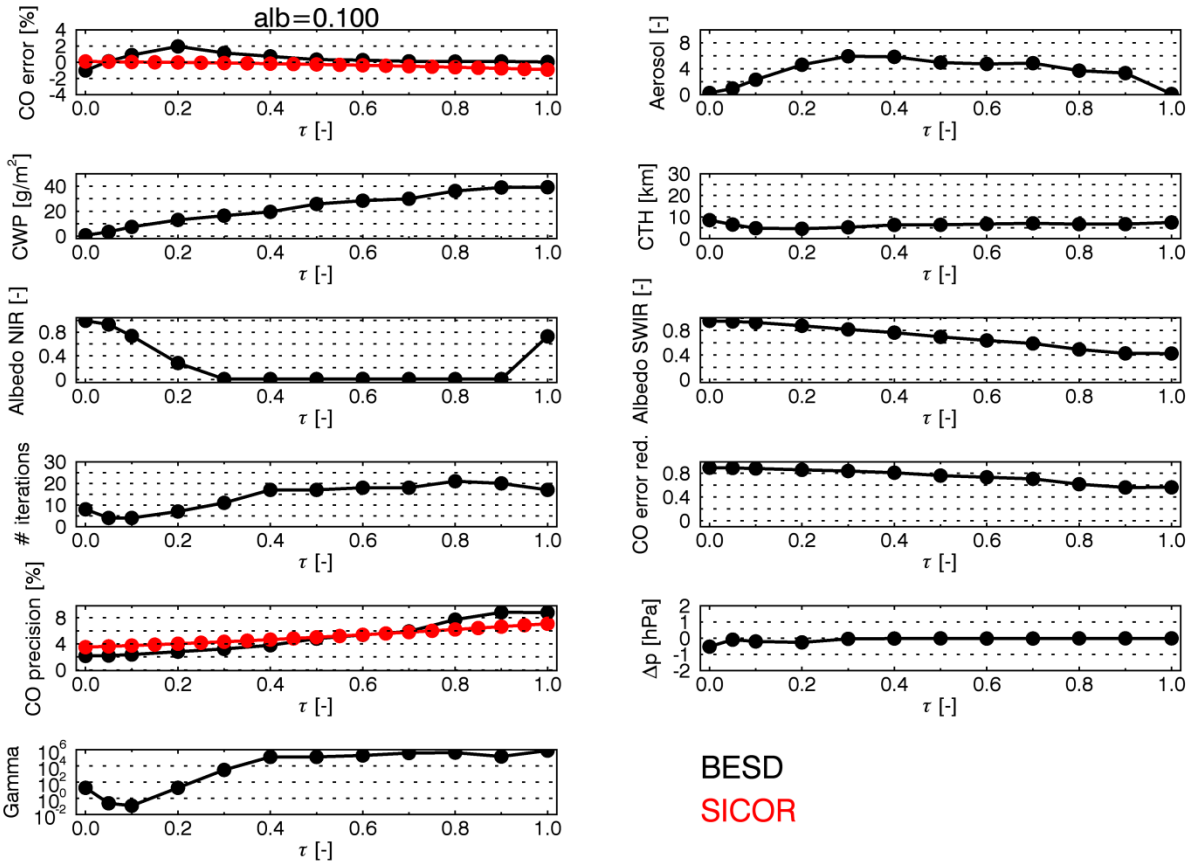

Figure 12.14: Overview of the retrieval performance for 32 test scenarios similar to Table 12.3 but for CO. The table has been computed using an a priori uncertainty of about 25% for CO.

The influence of the viewing geometry in terms of viewing zenith angle impact on the CO retrievals has also been examined and the results are shown in Figure 12.15. Thereby the viewing zenith angle was varied between 0° (looking directly nadir) and 50° and the azimuth angle was varied from 0° (looking towards the sun) to 180° (looking away from the sun). The solar zenith angle was constant at 45°. The baseline scenario included the aerosol from the Utah case (see Table 12.5), but no clouds and an albedo ob 0.05 in the SWIR and for BESD an albedo of 0.2 in the NIR. From Figure 12.15 it can be concluded that the biases resulting from the viewing geometry variation are rather low and with respect to the much larger random error negligible. The random error for BESD is somewhat lower than for SICOR as already explained earlier (see also Figure 12.12).

A last comparison comprised the column averaging kernels of the two algorithms which are a measure for the sensitivity to changes in the CO amounts at different altitude levels. The test scenario included again the Utah aerosol but additionally also cirrus clouds at the heights of 4km, 7km, and 10km with varying optical depth (0.1, 0.3, 0.6, and 1.0 at 500 nm). The viewing direction was nadir with a solar zenith angle of 45° and an azimuth of 0°. The surface albedo was again 0.05 in the SWIR and 0.2 in the NIR (for BESD). Results are shown in Figure 12.16. For a column retrieval, uniform column averaging kernels close to unity for all altitude levels are generally desired. However, if there is a cloud present, the sensitivity below the cloud is typically decreased due to a shielding effect. This can be seen in Figure 12.16 from the steps in the column averaging kernels at the cloud height. For an optical thickness of 0.1 (black curves), the column averaging kernels are hardly impacted, but the higher the cloud optical thickness is, the stronger the difference in the averaging kernels below and above the cloud becomve. Generally for BESD the averaging kernels are more uniform indicating a more even sensitivity throughout the column. The introduced CO column differences for the respective scenarios are for both algorithms rather low. For SICOR, the differences are below 1% and for BESD below 2%.

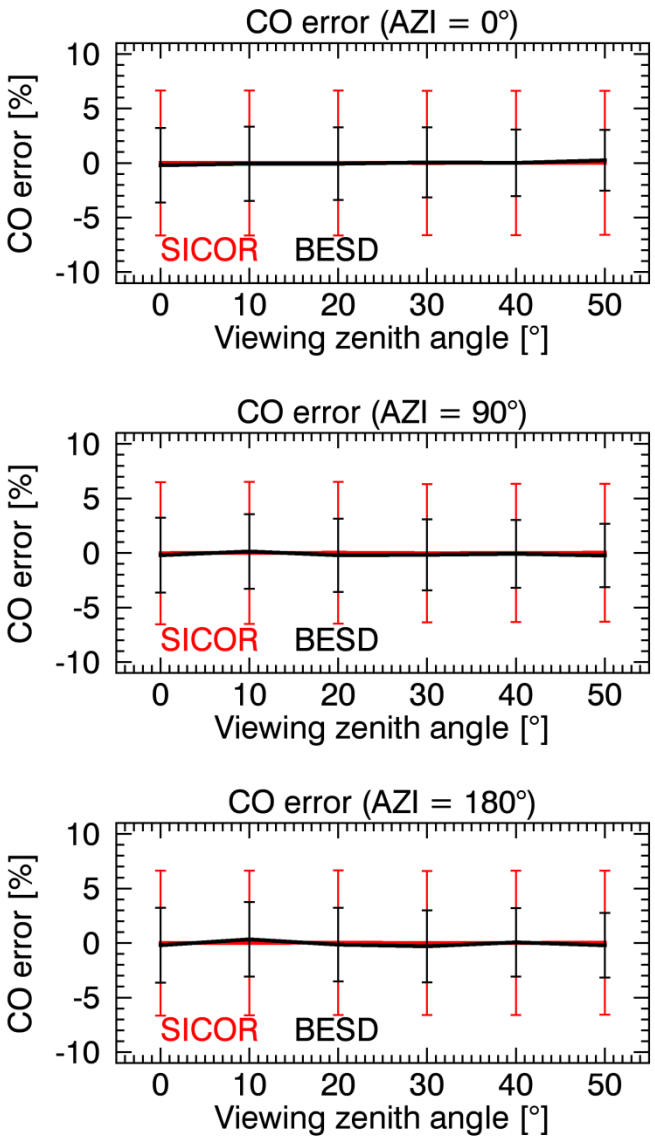

Figure 12.15: Comparison of the viewing zenith angle dependence for BESD and SICOR. Shown are the differences between retrieved and true CO column as well as the random errors as error bars. The azimuth angle (AZI) is given in the title of each plot.

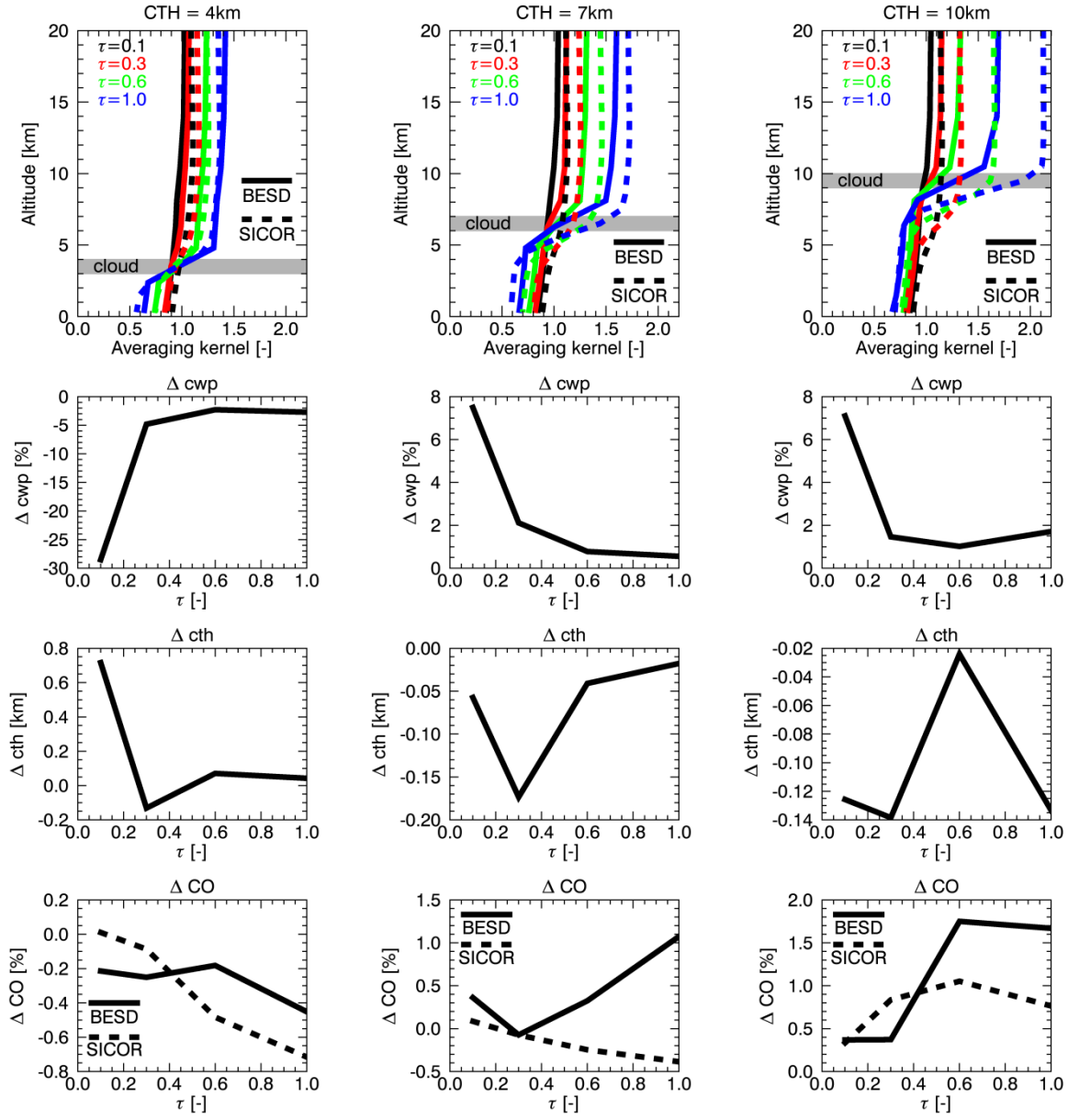

Figure 12.16: Comparison of column averaging kernels. The columns denote from left to right the different cloud top heights 4km, 7km and 10km. the first rows show the column averaging kernels for different optical thicknesses. The second and third row show the differences between retrieved and true column in the retrieved cloud water path and cloud top height for BESD. The last row gives the biases as a function of the optical thickness for the two algorithms.

12.9.3 Comparison of spectra

To compare also the underlying radiative transfer models between the two prototype algorithms and the verification algorithm, a comparison of spectra was conducted. A lot of effort was needed to harmonize the respective radiative transfer models. SCIATRAN was modified to accept the tabulated cross-sections that were provided by the prototypers. Nevertheless, there still remain inconsistencies (see below). As an additional effect, the modifications speeded up the retrieval by about a factor of 3 yielding a computation time of a few minutes per retrieval for BESD.

Furthermore, the atmospheric profiles were harmonized and a scenario was selected that included no scattering (no clouds, no aerosol, no Rayleigh scattering). The radiative transfer models of the prototypers were already harmonized to a very high degree (differences for the convoluted spectra are in the range of 0.001% of the continuum in the NIR and 0.01% of the continuum in the SWIR), so that the comparison between SCIATRAN and the prototype radiative transfer model was conducted with the RemoTeC high-resolution model spectra spectra only. To avoid errors from slightly different convolutions, the convolution with a Gaussian was performed for both with the same routine by the verification team

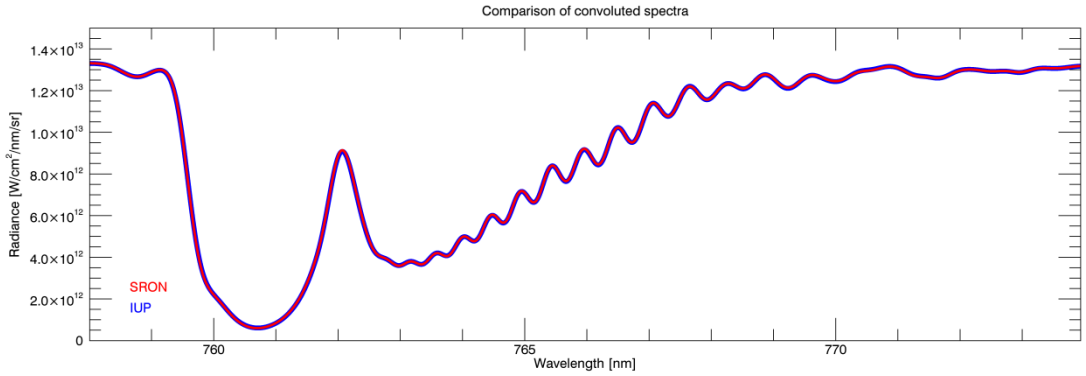

Figure 12.17: Comparison of simulated spectra in the NIR spectral range, SCIATRAN (IUP) in blue and SRON in red.

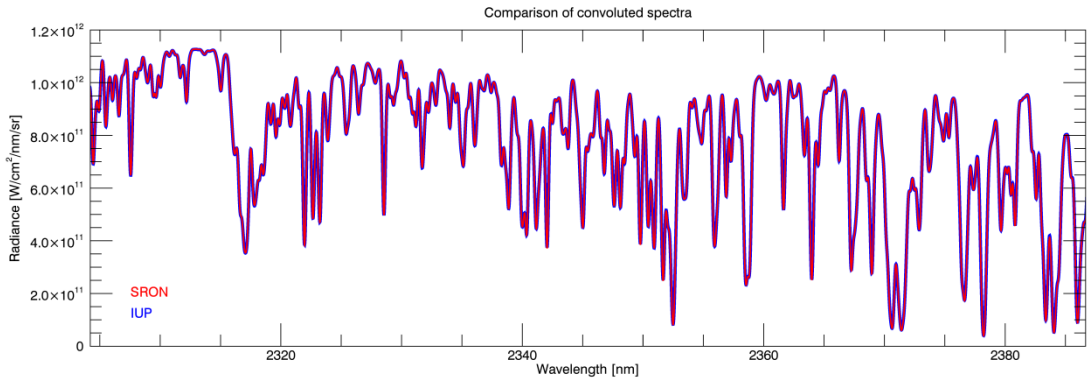

Figure 12.18: Comparison of simulated spectra in the SWIR spectral range, SCIATRAN (IUP) in blue and SRON in red.

In principal, the spectra in the NIR and SWIR are very similar (see Figure 12.17 and Figure 12.18) but for a closer inspection the differences are additionally plotted. The differences between the RemoTeC radiative transfer model and SCIATRAN are shown in Figure 12.19 for the NIR and in Figure 12.20 for the SWIR relative to the continuum. The grey shaded area denotes the range of the random error based on the instrument noise model. In the NIR case, the difference reach a value of about -0.06% which is significantly higher than the inter-prototype comparison but still lower than the noise. Additionally there appears to be an offset of about 0.06%. Since in principal in both radiative transfer models no scattering was involved this is surprising. However, the reasons for this difference are currently unclear.

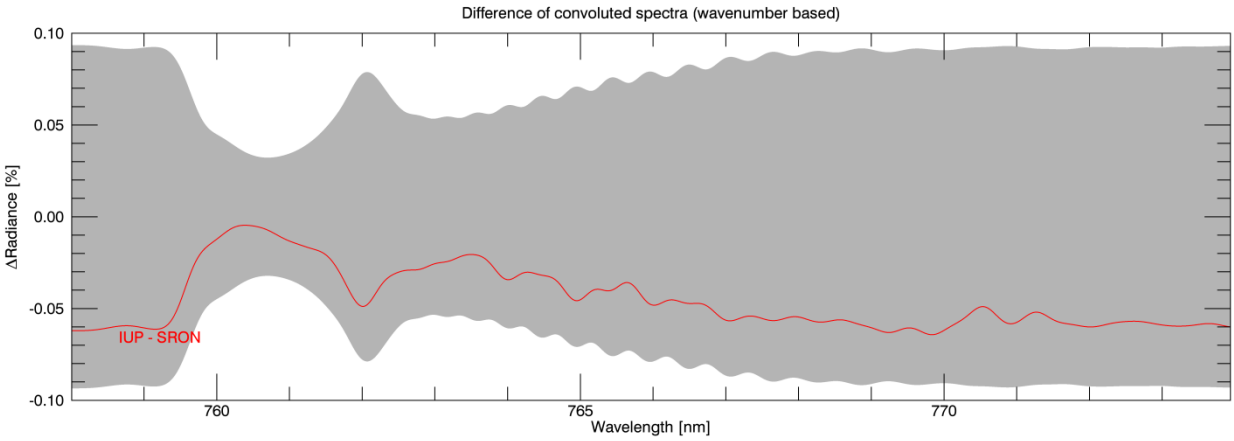

Figure 12.19: Comparison of the spectrum between SCIATRAN (IUP Bremen) and RemoTeC (SRON) relative to the continuum in the NIR spectral range. The grey shaded area denotes the instrument noise on the spectrum.

For the SWIR spectral range, the relative differences reach about 0.5% which is also in the range of the noise level. The residuals show some features that resemble the water vapour absorption lines (compare Figure 12.1). This is most likely due to the fact that the RemoTeC model spectra were computed using the water vapor self-broadening (Frankenberg et al., 2013), which was not implemented for SCIATRAN

For both the NIR and the SWIR the differences between SCIATRAN and RemoTeC are more than an order of magnitude larger than the inter-prototype comparison. Reasons for this could be for example differences in the interpolation schemes for the tabulated cross-sections and also for the atmospheric profiles.

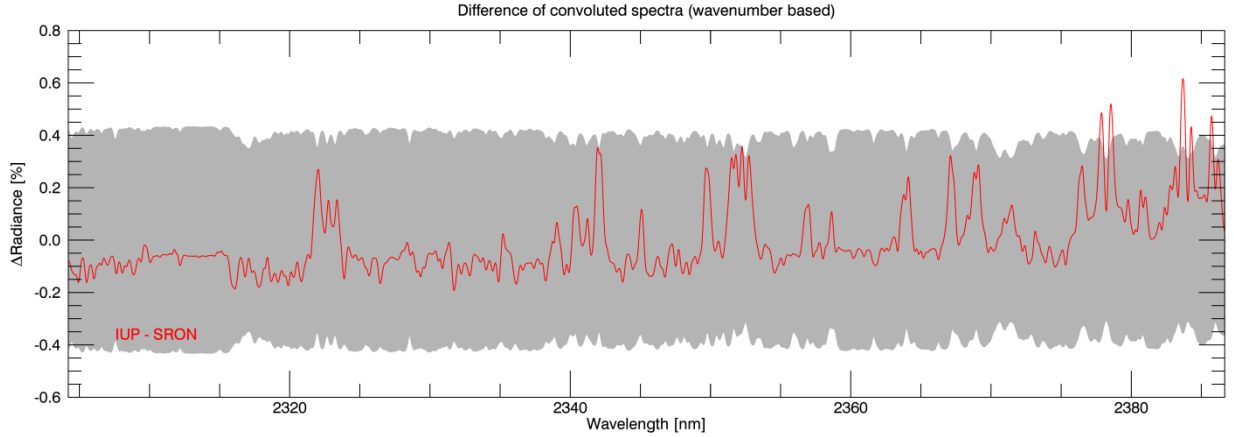

Figure 12.20: Comparison of the spectrum between SCIATRAN (IUP Bremen) and RemoTeC (SRON) relative to the continuum in the SWIR spectral range. The grey shaded area denotes the instrument noise on the spectrum.

12.10 Summary of verification results

This chapter gave a detailed overview of the verification activities regarding the retrieval of column averaged dry air mole fractions of methane (XCH_4) and vertical columns of carbon monoxide (CO) using simulated data from the upcoming satellite mission Sentinel-5 Precursor. The mathematical design of the Bremen optimal EStimation DOAS (BESD) verification algorithm was described in detail and differences to the prototype algorithms RemoTeC (for XCH_4) and SICOR for (CO) were pointed out.

The second part of this chapter dealt with results of the verification. The comparison between verification and prototype algorithms showed, that results are essentially similar for precision and accuracy and typically well within the requirements.

Test scenarios for comparisons between the XCH_4 verification and prototype algorithm included simulations with varying albedo and solar zenith angle to assess the retrieval noise. Furthermore, the impact of clouds of various altitudes and optical thicknesses as well as spectrally varying albedos and different aerosol scenarios on the retrievals were investigated.

Also different viewing geometries with changing viewing zenith angle and azimuth angle relative to the sun were analysed.

For CO the retrieval noise was investigated as well as biases due to clouds of varying optical thickness. Furthermore, aerosol scenarios with two aerosol layers of different distribution for varying surface albedo were analysed.

Similar to the CH_4 verification also the viewing geometry was analysed, and additionally the column averaging kernels.

To compare also the underlying radiative transfer models, the computed spectra were compared for simplified atmospheric conditions.

The verification algorithm is computationally very expensive, but including the tabulated cross-sections speeded up the retrieval by about a factor of 3.

As an outcome of the undertaken verification efforts, it can be concluded that with respect to the investigated test scenarios both the prototype for the CH_4 retrieval (RemoTeC) and the prototype for the CO retrieval (SICOR) perform very well and generally much better than demanded by the requirements. Albeit much slower, also the verification algorithm BESD fulfils the requirements on random and systematic errors.

The comparison of spectra revealed differences which are mostly lower than the noise level and included offsets as well as features that resemble the spectral signature of H_2O. Since differences in an inter-prototype comparison proved to be much smaller, it is likely that the observed differences are due to remaining challenges in the harmonization of radiative transfer models like, for example, differences in the interpolation scheme for absorption cross-sections and atmospheric parameters. The differences with water vapour signature in the SWIR were traced back to the water vapour self-broadening which is implemented for the prototypes but not for SCIATRAN.

12.11 References

Bovensmann, H., Burrows, J. P., Buchwitz, M., Frerick, J., Noël, S., Rozanov, V. V., Chance, K. V., and Goede, A.: SCIAMACHY – Mission Objectives and Measurement Modes, Journal of the Atmospheric Sciences, 56, 127–150, 1999.

Burrows, J. P., Hölzle, E., Goede, A. P. H., Visser, H., and Fricke, W.: SCIA-MACHY – Scanning Imaging Absorption Spectrometer for Atmospheric Char-tography, Acta Astronautica, 35, 445–451, 1995.

Butz, A., Galli, A., Hasekamp, O., Landgraf, J., Tol, P. and Aben, I.: TROPOMI aboard Sentinel-5 Precursor: Prospective performance of CH4 retrievals for aerosol and cirrus loaded atmospheres, Remote Sensing of Environment, 120, 267-276, 2012

Crisp, D., Fisher, B. M., O'Dell, C., Frankenberg, C., Basilio, R., Bösch, H., Brown, L. R., Castano, R., Connor, B., Deutscher, N. M., Eldering, A., Grif-fith, D., Gunson, M., Kuze, A., Mandrake, L., McDuffie, J., Messerschmidt, J., Miller, C. E., Morino, I., Natraj, V., Notholt, J., O'Brien, D. M., Oyafuso, F., Polonsky, I., Robinson, J., amd V. Sherlock, R. S., Smyth, M., Suto, H., Taylor, T. E., Thompson, D. R., Wennberg, P. O., Wunch, D., and Yung, Y. L.: The ACOS CO2 retrieval algorithm - Part II: Global XCO2 data characterization, Atmos. Meas. Tech., 5, 687–707, doi:10.5194/amt-5-687-2012, 2012.

Frankenberg, C., Wunch, D., Toon, G., Risi, C., Scheepmaker, R., Lee, J.-E., Wennberg, P., and Worden, J.: Water vapor isotopologue retrievals from high-resolution GOSAT shortwave infrared spectra, Atmos. Meas. Tech., 6, 263-274, doi: 10.5194/amt-6-263-2013, 2013.

Hasekamp, O., Hu, H., Galli, A., Tol, P., Landgraf, J., and Butz, A.: Algorithm Theoretical Baseline Document for Sentinel-5 Precursor methane retrieval, 2013.

King, J.: Validation of ECMWF sea level pressure analyses over the Bellingshausen Sea, Antarctica, Weather Forecasting, 18, 536–540, 2003.

Kokhanovsky, A. A.: Local optical characteristics of mixed clouds: Simple parameterizations, Atmospheric Research, 84, 42–48, 2007.

Krings, T., Gerilowski, K., Buchwitz, M., Hartmann, J., Sachs, T., Erzinger, J., Burrows, J. P., and Bovensmann, H.: Quantification of methane emission rates from coal mine ventilation shafts using airborne remote sensing data, Atmos. Meas. Tech., 6, 151–166, doi:10.5194/amt-6-151-2013, 2013a.

Krings, T., Reuter, M., Buchwitz, M., Heymann, J., Hilker, M., Bovensmann, H., and Burrows, J.: Sensitivity studies for methane and carbon monoxide retrievals from Sentinel-5 Precursor, Conference proceedings ESA Special Pub-lication SP-722, ESA Living Planet Symposium, Sept 9-13, 2013, Edinburgh, UK, 2013b.

Kuze, A., Suto, H., Nakajima, M., and Hamazaki, T.: Thermal and near infrared sensor for carbon observation Fourier-transform spectrometer on the Greenhouse Gases Observing Satellite for greenhouse gases monitoring, Appl. Opt., 48, 6716–6733, doi:10.1364/AO.48.006716, 2009.

Lammert, A., Bruemmer, B., Ebbers, I., and Mueller, G.: Validation of ECMWF and DWD model analyses with buoy measurements over the Norwegian Sea, Meteorology and Atmospheric Physics, 102, 87–96, doi:10.1007/s00703-008-0008-1, 2008.

Landgraf, J., Vitas, N., Borsdorff, T., aan de Brugh, J., Sheepmaker, R. A., Houweling, S., and Hasekamp, O. P.: Algorithm Theoretical Baseline Document for Sentinel-5 Precursor: Carbon Monoxide Total Column Retrieval, 2013.

Nakajima, T. and King, M. D.: Determination of optical thickness and effective particle radius of clouds from reflected solar radiation measurements. Part I: Theory, Journal of the Atmospheric Sciences, 47, 1878-1893, 1990

Reuter, M., Buchwitz, M., Schneising, O., Heymann, J., Bovensmann, H., and Burrows, J. P.: A method for improved SCIAMACHY CO2 retrieval in the presence of optically thin clouds, Atmospheric Measurement Techniques, 3, 209–232, doi:10.5194/amt-3-209-2010, URL http://dx.doi.org/10.5194/ amt-3-209-2010, 2010.

Reuter, M., Bovensmann, H., Buchwitz, M., Burrows, J. P., Connor, B. J., Deutscher, N. M., Griffith, D. W. T., Heymann, J., Keppel-Aleks, G., Messer-schmidt, J., and et al.: Retrieval of atmospheric CO2 with enhanced accuracy and precision from SCIAMACHY: Validation with FTS measurements and comparison with model results., Journal of Geophysical Research, 116, doi:10.1029/2010JD015047, URL http://dx.doi.org/10.1029/2010JD015047,2011.

Rodgers, C. D.: Inverse Methods for Atmospheric Sounding: Theory and Practice, World Scientific Publishing, Singapore, 2000.

Rothman, L., Gordon, I., , Barbe, A., Benner, D., Bernath, P., Birk, M., boudon, V., Brown, L., Campargue, A., Champion, J.-P., Chance, K., Coudert, L., Dana, V., Devi, V., Fally, S., Flaud, J.-M., Gamache, R., Goldman, A., Jacquemart, D., Kleiner, I., Lacome, N., Lafferty, W., Mandin, J.-Y., Massie, S.,Mikhailenko, S., Miller, C., Moazzen-Ahmadi, N., Naumenko, O., Nikitin, A., Orphal, J., Perevalov, V., Perrin, A., Predoi-Cross, A., Rinsland, C., Rotger, M., Simĕckoýa, M., Smith, M., Sung, K., Tashkun, S., Tennyson, J., Toth, R., Vandaele, A., and Auwera, J. V.: The HITRAN 2008 molecular spectroscopic database, J. Quant. Spectr. Radiat. T., 110, 533–572, doi:10.1016/j.jqsrt.2009.02.013, 2009.

Rozanov, V., Rozanov, A., Kokhanovsky, A., and Burrows, J.: Radiative transfer through terrestrial atmosphere and ocean: Software package SCIATRAN, Journal of Quantitative Spectroscopy and Radiative Transfer, 133, 13–71, doi:http://dx.doi.org/10.1016/j.jqsrt.2013.07.004, URL http://www.sciencedirect.com/science/article/pii/S0022407313002872, 2014.

Schneising, O., Buchwitz, M., Burrows, J. P., Bovensmann, H., Bergam-aschi, P., and Peters, W.: Three years of greenhouse gas column-averaged dry air mole fractions retrieved from satellite - Part 2: Methane, Atmospheric Chemistry and Physics Discussions, 8, 8273–8326, URL http://www.atmos-chem-phys-discuss.net/8/8273/2008/, 2008a.

Schneising, O., Buchwitz, M., Burrows, J. P., Bovensmann, H., Reuter, M., Notholt, J., Macatangay, R., and Warneke, T.: Three years of greenhouse gas column-averaged dry air mole fractions retrieved from satellite - Part 1: Carbon dioxide, Atmospheric Chemistry and Physics, 8, 3827–3853, URL http://www.atmos-chem-phys.net/8/3827/2008/, 2008b.

Veefkind, J. P., Aben, I., McMullan, K., Hörster, H., de Vries, J., Otter, G., Claas, J., Eskes, H. J., de Haan, J. F., Kleipool, Q., van Weele, M., Hasekamp, O., Hoogeveen, R., Landgraf, J., Snel, R., Tol, P., Ingmann, P., Voors, R., Kruizinga, B., Vink, R., Visser, H., and Levelt, P. F.: TROPOMI on the ESA Sentinel-5 Precursor: A GMES mission for global observations of the atmospheric composition for climate, air quality and ozone layer applications, Remote Sensing of Environment, 120, 70–83, doi:10.1016/j.rse.2011.09.027, 2012.

Vidot, J., Landgraf, J., Hasekamp, O. P., Buth, A., Galli, A., Tol, P., and Aben, I.: Carbon monoxide from shortwave infrared reflectance measurements: a new retrieval approach for clear sky and partially cloudy atmospheres, Remote Sensing of Environment, 120, 255–266, doi:10.1016/j.rse.2011.09.032, 2012.

Yoshida, Y., Kikuchi, N., Morino, I., Uchino, O., Oshchepkov, S., Bril, A., Saeki, T., Schutgens, N., Toon, G. C., Wunch, D., Roehl, C. M., Wennberg, P. O., Griffith, D. W. T., Deutscher, N. M., Warneke, T., Notholt, J., Robinson, J., Sherlock, V., Connor, B., Rettinger, M., Sussmann, R., Ahonen, P., Heikkinen, P., Kyrö, E., Mendonca, J., Strong, K., Hase, F., Dohe, S., and Yokota, T.: Improvement of the retrieval algorithm for GOSAT SWIR XCO2 and XCH4 and their validation using TCCON data, Atmospheric Measurement Techniques, 6, 1533–1547, doi:10.5194/amt-6-1533-2013, 2013.

13 Clouds

Authors: Holger Sihler, Thomas Wagner (MPIC), Maarten Sneep, Piet Stammes, Ping Wang (KNMI), Luca Lelli (IUP-UB)

13.1 Document changes

Changes in issue 2.0:

Cloud fraction:

- description of algorithm for the determination of the lower threshold
- comparison of results with prototype algorithm using GOME-2 data
- removal of discussion of upper threshold determination
- update on discussion and summary

Cloud top height and optical thickness:

- updated RTM comparisons
- added verification on GOME-2 data
- added description of synthetic data

13.2 Verification approach

For the determination of the effective cloud fraction, the following verification strategy is applied:

HICRU (HICRU Iterative Cloud Retrieval Utilities, Grzegorski et al, 2006) provides an algorithm for the determination of the effective cloud fraction of satellite observations. Its original design is limited to observations at small viewing zenith angles. Therefore a completely new, enhanced HICRU algorithm (also denoted by the abbreviation HICRU in the following) for the retrieval of effective cloud fractions based on radiometric measurements has been developed specifically for satellite measurements featuring large viewing zenith angles. The result is an independent data set for cloud fractions because prototype and verification algorithm are based on different assumptions and are implemented differently.

The comparison of HICRU and the prototype algorithm OCRA (Optical Cloud Recognition Algorithm, Loyola and Ruppert, 1998) is performed using GOME-2 measurements alone, because GOME-2 provides both a sufficient large swath needed to evaluate the performance of both algorithms at large viewing zenith angles and a spectral bandwidth sufficiently broad for the OCRA algorithm. For the comparison four days of GOME-2 data are selected, whereas data of the entire measurement period between April 2008 and June 2013 are required as algorithm input for HICRU. Systematic differences between verification and prototype algorithm are investigated. Especially small cloud fractions are critical because errors therein have a strong impact on the accuracy of tropospheric trace-gas retrievals requiring the cloud fraction as input. Small cloud fractions strongly depend on the lower threshold (i.e. a cloud-free albedo map) but only weakly depend on the definition of the cloud model determining the upper threshold. Hence, the comparison of low cloud fractions is less biased by the applied cloud model.

The verification algorithm for cloud properties is subdivided into 2 major parts which are described separately in the next sections:

- Determination of the effective cloud fraction (HICRU, MPIC)
- Determination of the cloud albedo, geometric cloud top height, geometric cloud base height and cloud optical depth (SACURA, IUP-Bremen)

13.3 Verification – cloud fraction

The S5P cloud fraction prototype algorithm is OCRA. For its verification, OCRA results are compared to cloud fractions determined using the HICRU algorithm. It was decided that the verification of the cloud fractions will solely be performed applying real data from existing missions. Prototype and verification teams decided on using GOME-2A PMD data for this comparison, because the instrument characteristics of GOME-2 are sufficiently close to S5P with respect to spatial and spectral resolution in order to provide meaningful results. The initial idea to use OMI data for the comparison was rejected because its spectral bandwidth is not sufficient for the RGB OCRA algorithm.

HICRU has been previously applied to PMD measurements performed by the GOME and SCIAMACHY instruments. The HICRU algorithm for measurements from these instruments takes advantage of some simplifications justified by the specific instrument design. Most notably, the influence of the scan angle on the measured radiance in the red spectral range was assumed to be minor and the image sequence algorithm neglected the influence of the geometry. This approximation is not valid any more for the larger VZA featured by GOME-2, OMI, and also TROPOMI. Furthermore, OMI does not provide measurements for wavelengths above 500nm. Therefore, the approach as published by Grzegorski et al. (2006) needed to be enhanced and reimplemented as described in the next section. The following sections proceed with the description of the verification of OCRA using the enhanced HICRU algorithm.

13.3.1 Description of the enhanced HICRU algorithm

The effective cloud fraction retrieved by HICRU depends on the geometric cloud fraction and on the brightness of the cloud (i.e., its albedo). It is noted that the HICRU effective cloud fraction is a radiometric cloud fraction as opposed to a geometric cloud fraction, which applies subpixel information from a complimentary instrument. The definition of the effective cloud fraction is based on the experience that clouds almost always have a higher reflectivity than the underlying Earth surface in the UV/vis spectral region. Exceptions to this rule are very bright surfaces like those covered by snow and ice for which the proposed algorithm is not applicable.

The input data for the HICRU algorithm are intensities at a narrow wavelength band centred at λ, from which the top-of-atmosphere (TOA) reflectance is calculated. The TOA reflectance is defined as

$$R = \frac{\pi I}{E_0 \cos(SZA)} \tag{44}$$

where I is the measured intensity at wavelength λ, E_0 is the solar irradiation at wavelength λ, and SZA is the solar zenith angle at the surface. Assuming that the upper and lower reflectance thresholds R_{max} and R_{min}, respectively, are known, the effective cloud fraction can be computed by

$$CF = \frac{R - R_{min}}{R_{max} - R_{min}} \tag{45}$$

using the independent pixel approximation (IPA). The main challenge for the proposed algorithm is the determination of R_{max} and R_{min}. R_{max} represents a pixel entirely covered by bright clouds, it depends on λ, observation geometry defined by SZA, viewing zenith angle (VZA) at the surface, solar relative azimuth (RAZ) angle, and the a-priori assumed cloud properties (OD, cloud model). R_{min} represents a pixel completely devoid of clouds. Compared to R_{max}, R_{min} also depends on time and location as additional parameters because it strongly depends on surface albedo, temporal albedo variations (seasonal and short-term), and possible instrumental degradation. Therefore, the determination of R_{min} is particularly important in order to enable HICRU to accurately retrieve small effective CF. It is noted that the bidirectional reflectance distribution function (BRDF) model needs to be considered instead of the Lambertian reflector model for a more accurate model for the description of the surface reflectivity. This is especially the case for large VZA.

On the one hand, a particular strength of HICRU compared to other retrievals for CF is that it retrieves R_{min} from the measurements themselves instead of using prescribed surface albedo/BRDF maps. On the other hand, the generation of empirical background TOA reflectance maps requires access to a sufficiently large data set in which there are at least some cloud free observations for every location on the globe.

13.3.1.1 Determination of lower threshold

In general, the lower threshold R_{min} depends on wavelength, surface BRDF, and atmospheric Rayleigh scattering. Furthermore, R_{min} needs to be retrieved as a function of geolocation. The choice of input parameters like spatial resolution, temporal resolution, and empirical threshold levels are instrument dependent and thus require careful adjustment. Here, we present the enhanced HICRU accumulation point algorithm for the lower threshold, which is now applicable to observations with swaths much wider than those of GOME and SCIAMACHY (GOME/SCIAMACHY: 960km, GOME-2: 1920km, OMI/TROPOMI: 2600km). It is noted that using the lower accumulation point renders HICRU more robust against outliers compared to an algorithm that searches for the absolute minimum reflectance which may be significantly below the true background albedo, e.g., due to solar eclipses, cloud shadows, or measurement noise.

The image sequence approach of the classical HICRU is replaced by a series of three retrieval steps, which are further detailed below:

1. Analysis of the VZA-dependence of R_{min} in large geospatial ensembles
2. Parameterisation of the VZA-dependence of R_{min} using the nadir SZA
3. Empirical determination of a time dependent minimum nadir reflectance for all geolocation bins

The results are time dependent lower threshold maps of the TOA reflectance R_{min}, as for classical HICRU. For the steps 1 and 3, the threshold method applied in HICRU is extended by fitting a linear model to the input data between each minimising iteration, as illustrated in Figure 13.1. In step 1, a polynomial is applied to model the VZA-dependence, whereas in step 3, a combination of polynomial and Fourier expansion terms are used to model the temporal evolution of the lower threshold. Furthermore, a 3σ-cutoff is introduced to improve the robustness towards lower outliers.

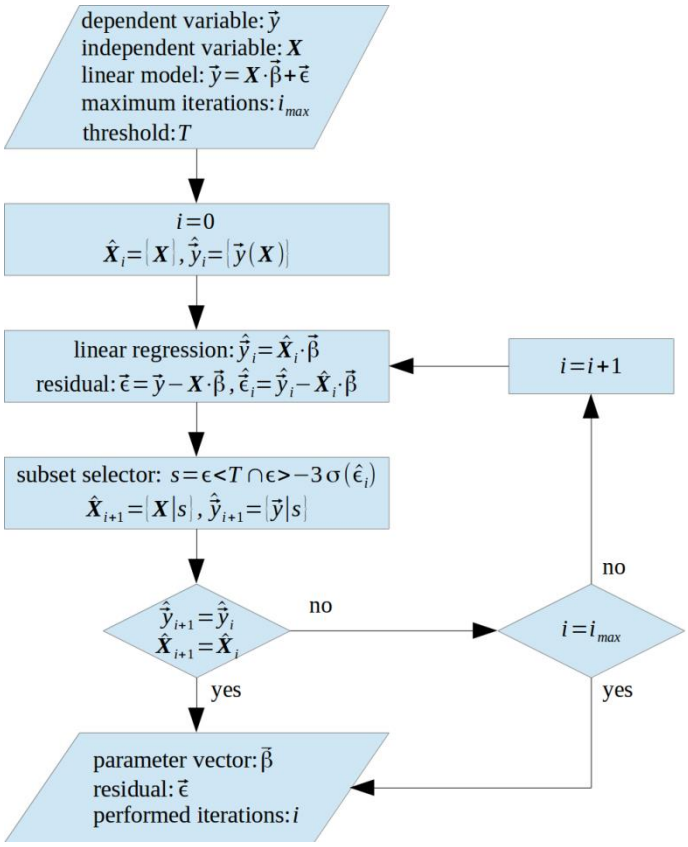

Figure 13.1: Flowchart of the extended HICRU threshold method to find the lower accumulation point within a given set of reflectance measurements R depending on a generalized linear model.

The main idea behind the correction of the VZA-dependence is to use the VZA as a proxy for all possible observation geometries and BRDF constellations instead of applying a 3D parameterization using SZA, VZA, and RAZ because (1) R_{min} depends mainly and systematically on VZA, (2) SZA and RAZ are nearly constant at a given latitude for any VZA for a sufficiently small tempo-spatial domain, and (3) the statistical analysis is more robust for a 1D parameterization compared to approaches in higher dimensions. Therefore, the determination of the average VZA-dependence is the first retrieval step.

In order to determine the average VZA-dependence, monthly aggregates of reflectance measurements within 20°x1° bins are analysed (cf. Figure 13.2(b)). The VZA-dependence of the lower threshold is then approximated by a quadratic model (parabola)

$$R = a\,VZA^2 + b\,VZA + R_0 \tag{46}$$

using the HICRU threshold method in Figure 13.1. The residual reflectances of this procedure are exemplary depicted for GOME-2 PMD-PP measurements at 519nm (channel 10) in Figure Figure 13.2(c). The resulting parabola is transformed into an apex-curvature form with apex-position VZA_s=-$b/2a$ and curvature C=a.

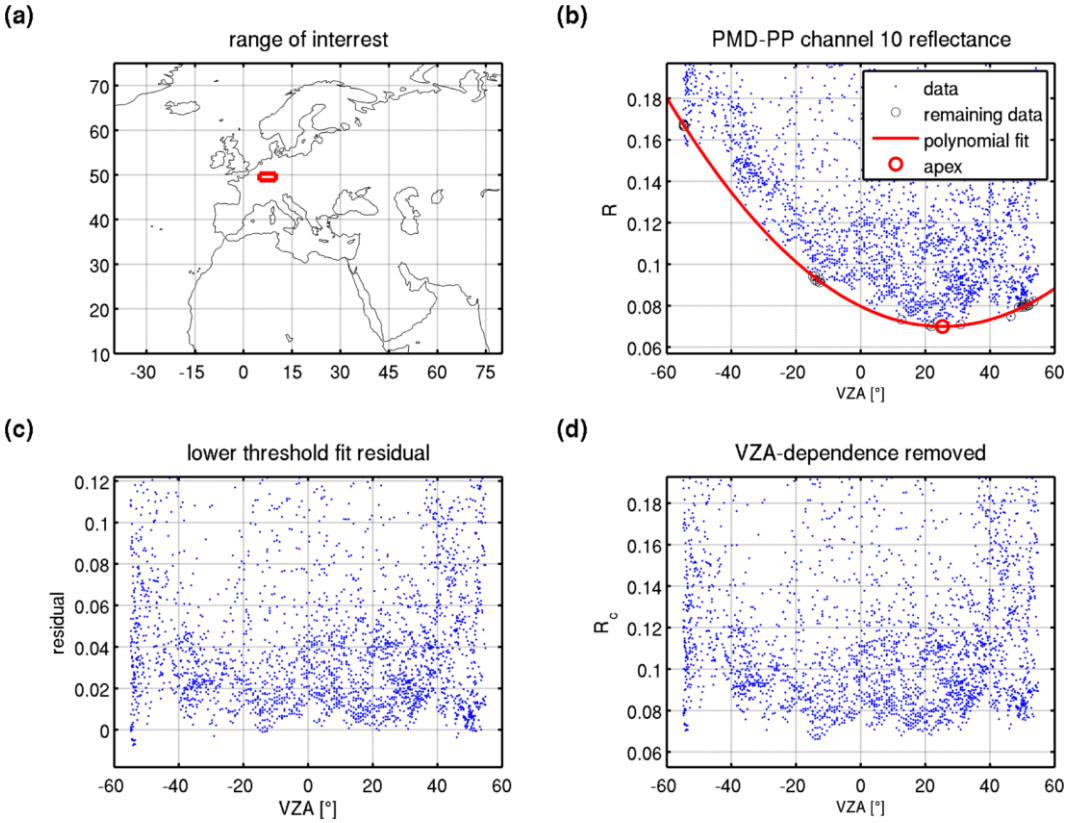

Figure 13.2: : Different steps of the VZA-dependence correction method applying GOME-2 PMD-PP channel 10 (519nm) data of April 2009: (a) definition of geospatial range, (b) reflectance data of this particular spatio-temporal subset with polynomial VZA-parameterisation of the lower threshold, (c) reflectance residual after removing the polynomial fit result, and (d) data after the VZA-dependence is removed by applying the averaged parameterisation of the VZA-dependence shown in Figure 13.3 (see text)

All retrieved VZA_s and C are then sorted by the corresponding average SZA in nadir direction (VZA=0) after filtering insignificant results. The resulting dependence of VZA_s and C on the nadir SZA for GOME-2 PMD-PP channel 10 (519nm) is shown in Figure 13.3. Even though both plots show a natural scatter in y-direction, the linear and cubic least-squares fits of VZA_s and C, respectively, appeared to be sufficiently accurate for the computation of lower threshold maps. For example, Figure 13.2(d) shows the radiance measurements in Figure 13.2(b) after removing the VZA-dependence using the average VZA_s and C parameterisation shown in Figure 13.3.

After removing the VZA-dependency of every measurement, the seasonality of the lower threshold is derived on a 0.5°x0.5° grid. The temporal evolution of the lower threshold R_{min} is modelled by a combination of a polynomial, to correct for a possible degradation trend, and a Fourier series expansion to account for the seasonality:

$$R_q(t) = a_q + \sum_{k=1..n} a_k t^k + \sum_{j=1..m} (b_j \cos j\omega t + c_j \sin j\omega t) \qquad (47)$$

where q denotes the bin index (geolocation), n is the polynomial degree, and m is the order of Fourier polynomials. For GOME-2 PMD channels, $n=3$ and $m=3$ are chosen. The frequency ω is fixed to 1/365.25d.

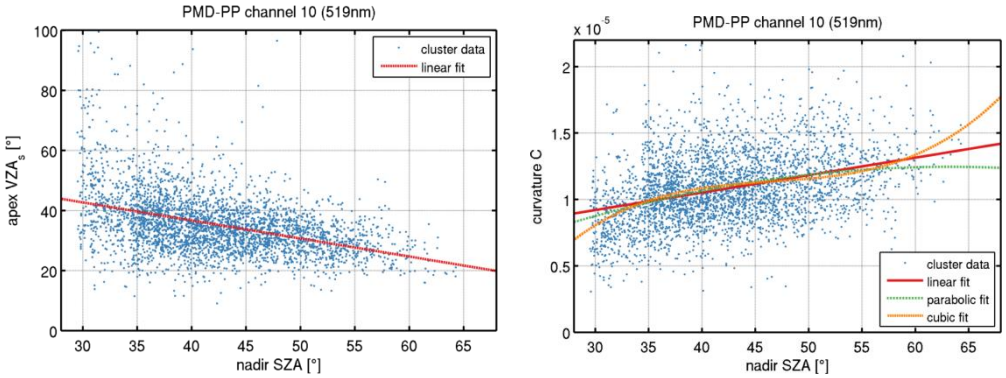

Figure 13.3: The averaged parameterisation of the VZA-dependence of the lower threshold for GOME-2 PMD-PP channel 10 (519nm): (left) the VZA of the apex and (right) the SZA-dependence of the curvature *C*. The individual data points represent single lower threshold fits (cf. Figure 13.2(b)) of monthly spatio-temporal subsets of all measurement between April 2008 and June 2013 (see text).

In order to derive the time dependent lower threshold in one 0.5°x0.5° bin, all measurements with removed VZA-dependence within this bin and its neighbouring bins (2x1 over land, 8x2 over ocean) over the same surface type (land or ocean) are considered to fit a common Fourier series model (with coefficients b_j and c_j) and common trend (a_k) in all bins (to improve statistics) and individual offset TOA albedos a_q. Figure 13.4 shows an example of the time dependent lower threshold fit for GOME-2 PMD measurements at 519nm.

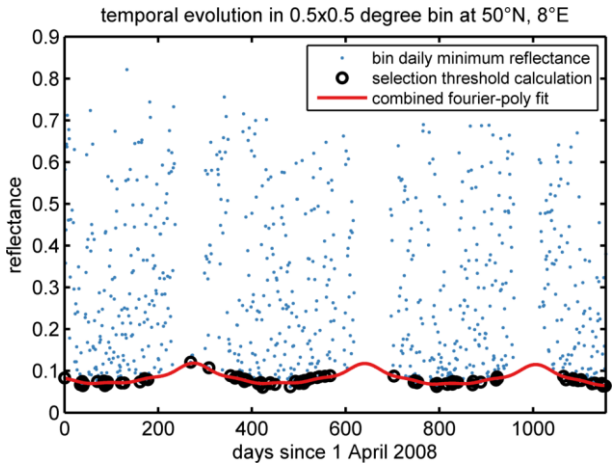

Figure 13.4: Temporal evolution of the lower threshold between April 2008 and June 2013 within a 0.5°x0.5° bin centred at 50°N, 8°E (approx. Mainz, Germany) retrieved from GOME-2 PMD-PP channel 10 measurements at 519nm. The lower threshold is parameterised using a combination of a 3rd order polynomial trend and a 3rd order Fourier series with individual phase and amplitude. The blue dots represent daily minimum values measured within this bin. Data gaps in winter are due to filtering measurements potentially affected by snow.

After performing the lower threshold fit in all 0.5°x0.5° bins, it is possible to compute the lower TOA reflectance threshold at any time in any bin. Figure 13.5 shows the lower threshold maps for 1 April 2009 00:00 UTC using GOME-2 PMD-PP reflectance measurements at 382nm (channel 7) and 519nm (channel 10), respectively. The figure illustrates that the TOA reflectance at 382nm depends much less on surface type compared to 519nm. Therefore, larger interferences with surface reflectivity can be expected for HICRU at 519nm compared to 382nm.

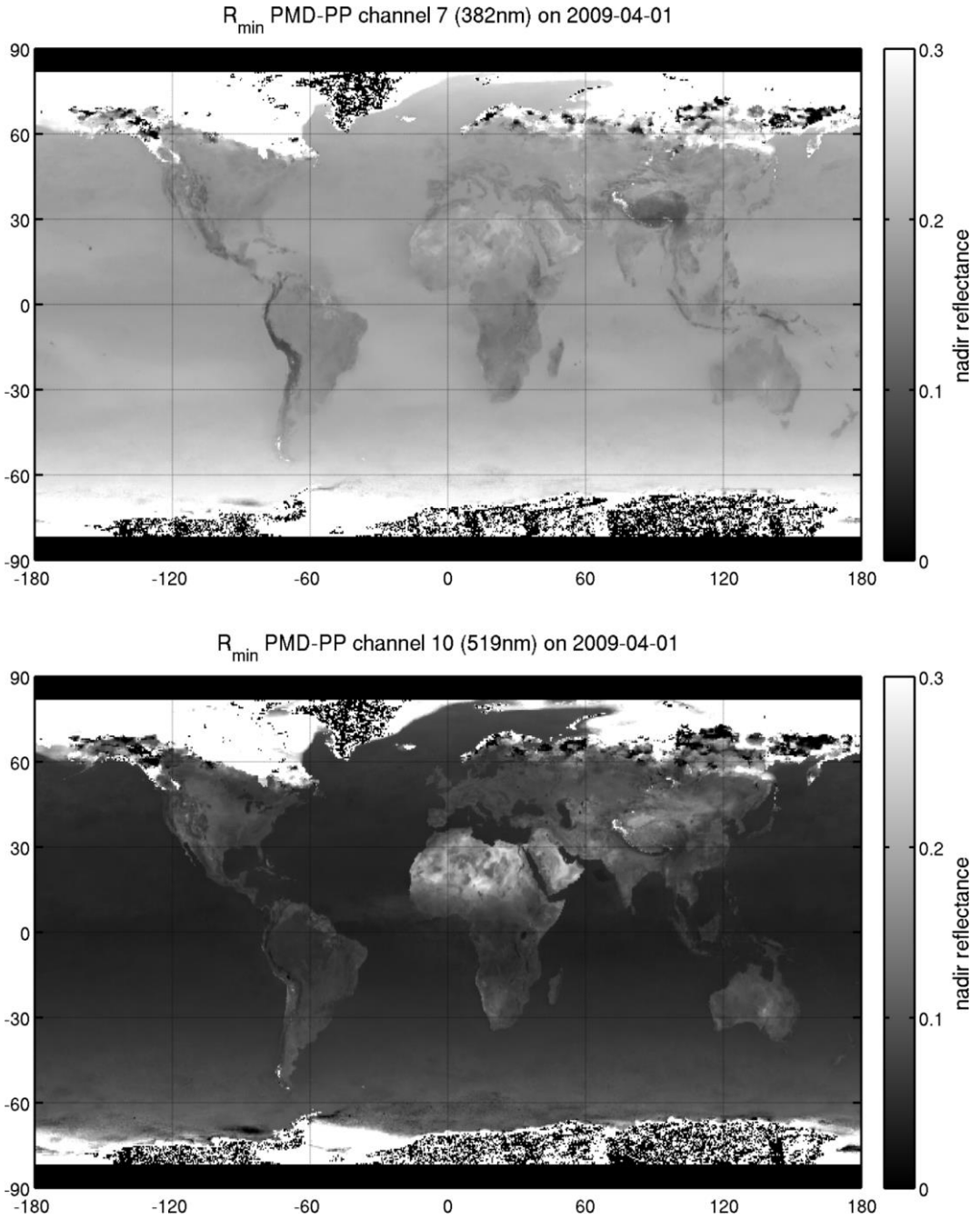

Figure 13.5: Global maps of the lower threshold retrieved from GOME-2 measurements and derived for 1 April 2009. Input data are (above) channel 7 (382nm) and (below) channel 10 (519nm) PMD-PP measurements between April 2008 and June 2013, respectively. Black-white artefacts in higher latitudes are caused by interferences with snow and ice. Areas in black denote regions without data.

13.3.1.2 Determination of the upper threshold

The second input parameter needed to compute the HICRU effective cloud fraction is the upper reflectance threshold R_{max}. This threshold represents a pixel completely covered by an optically thick cloud. In the HICRU implementation for GOME as published by Grzegorski et al. (2006), R_{max} is retrieved from the measurements as well. However, it is also feasible to use a radiative transfer model (RTM) to compute the upper threshold as implemented in HICRU for SCIAMACHY (Grzegorski, 2009).

Two fundamentally different cloud models are possible: (1) reflecting clouds using a Lambertian surface, and (2) scattering cloud particles parameterized using Mie theory. In the first case, usually an albedo of 0.8 is assumed, whereas in the second case a cloud optical thickness (COT) of at least 50 with a single scattering albedo of 1 and a Henyey-Greenstein parameter g=0.85 is assumed. For the second case of scattering clouds it is even possible to implement a heterogeneously distributed Mie scattering volume in order to model realistic cloud shapes. Also ice phase functions might be used for the upper cloud layers.

In the S5P verification cloud fraction algorithm, the Lambertian cloud model is implemented. The Lambertian cloud model has the advantage of requiring fewer input parameters than the Mie model. It is noted that the choice of the upper threshold only has a weak effect on small cloud fractions, which are most important for trace gas retrievals.

Look-up tables (LUTs) for the upper threshold are computed using the McArtim3 RTM (Deutschmann et al., 2011). The LUTs are parameterized by the three observation angles cos(SZA), cos(VZA), and RAZ (cf. Section 14.3.1.2). The nodes are defined on an equidistant grid. The reflecting (Lambertian) cloud surface is set to an altitude of 10km and an albedo of 0.8.

13.3.1.3 Error description

Possible errors are mainly due to uncertainties in the determination of upper and lower thresholds. Specifically, the accuracy of the enhanced HICRU algorithm depends on the choice of a number of parameters (wavelength, instrument, channels, threshold values, spatio-temporal sampling, etc.) which need to be determined through empirical research and, hence may not be ideal.

For the minimum reflectance, there are several influences: aerosols may alter the radiance of pixels assumed as cloud-free, shadows from clouds in neighbouring pixels (see section below), as well as shadows due to topography may decrease the radiance. Furthermore, short-term fluctuations of the surface BRDF (e.g., snowfall or changing vegetation) and the approximated VZA-dependence parameterisation reduce the accuracy of the derived parameterization of R_{min}.

For the upper threshold, the choice of cloud model has a significant influence. In any case, it will not be possible to treat 3D effects comprehensively, due to the large number of free parameters (shape, distribution, direction). As a baseline, the definition of the HICRU effective cloud fraction includes the application of a Lambertian cloud model, which needs to be considered when interpreting the data and possible preceding processing steps as well.

In general, the retrieved effective cloud-fractions are assumed to be accurate within a few per cent. The proposed algorithm is assumed especially accurate for small cloud fractions as lower thresholds are determined at close spatio-temporal proximity from measurements by the same instrument. This approach intends to minimize systematic biases.

13.3.1.4 Differences to prototype algorithm

The prototype algorithm for fractional cloud cover is based on OCRA - the Optical Cloud Recognition Algorithm (Loyola and Ruppert, 1998). The main expected differences with respect to the proposed enhanced HICRU algorithm are: (1) the prototype is proposed to use a cloud-free composite reflectance data set either from GOME-2 or OMI, which is successively replaced by S5P data during mission, whereas HICRU produces a cloud-free composite from the S5P data themselves provided that the data basis is sufficiently large, (2) the algorithms use different spectral ranges, and (3) the definition of the upper threshold is not the same. (1) may have an impact on the agreement of small cloud fractions between both algorithms for S5P observations (but is not important for the comparison presented below), whereas (2) and (3) have an impact on medium to large cloud fractions.

13.3.2 Results using GOME-2 data

This section aims at a comprehensive verification of the S5P prototype cloud fraction algorithm OCRA by comparing its results to HICRU cloud fractions gained from the algorithm described in the previous section. This verification is performed using 4 days of GOME-2A PMD data: 1 January, 1 April, 1 July, and 1 October 2009. OCRA cloud fractions *CF_OCRA* are results from averaged GOME-2 PMD-PP and PMD-SP channel radiances. In analogy to the definition of *CF_OCRA*, HICRU cloud fractions *CF_HICRU* are determined from radiances averaged from both polarization directions from GOME-2 PMD channels 7 (382nm) and 10 (519nm), respectively.

13.3.2.1 HICRU cloud fraction

Before comparing HICRU and OCRA results, CF_HICRU for channel 7 and channel 10 are compared in order to estimate the consistency of the algorithm and to illustrate the differences at the two different wavelengths. The plots in Figure 13.6 show the correlation of both HICRU results on 1 April 2009 for all data and different subsets (|VZA|<20, surface type). The squared correlation coefficient is always >0.99. The plots also include bivariate fits. The positive offsets indicate that HICRU applied to measurements at 519nm slightly overestimates the CF for small CF. The slope is always below 1 indicating that real clouds are at 382nm, on average, brighter than the applied Lambertian cloud model compared to their reflectivity at 519nm.

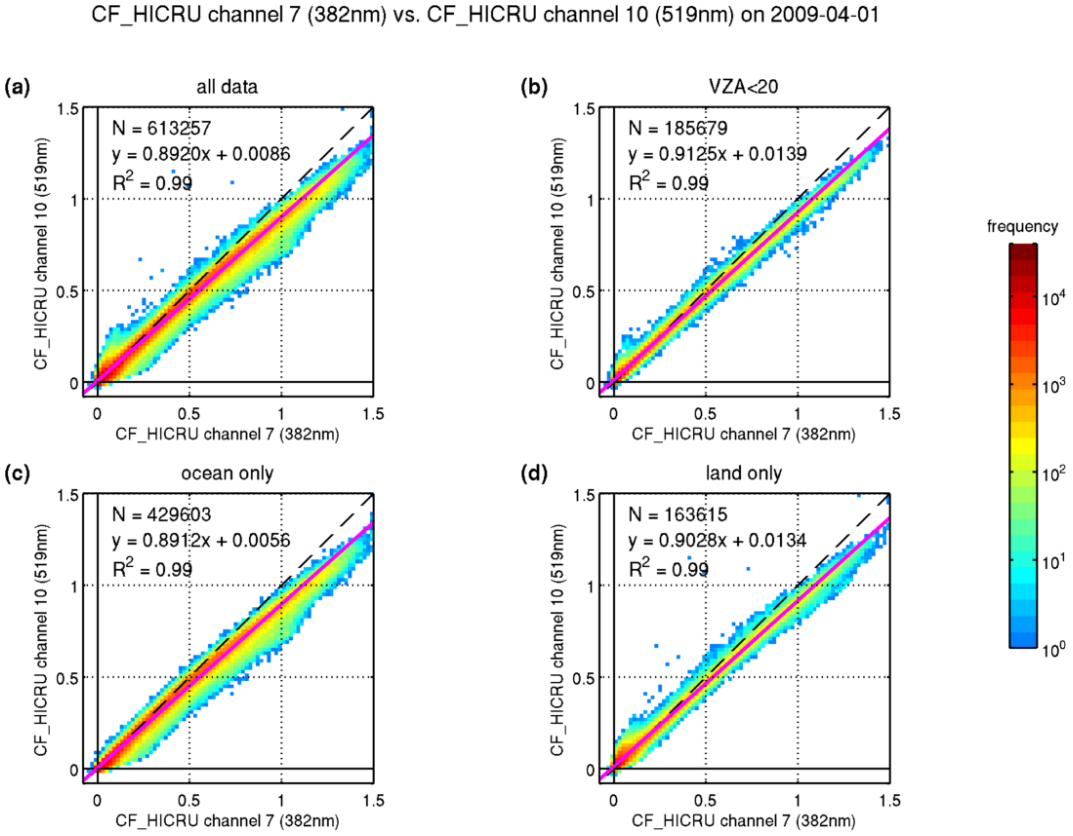

Figure 13.6: Correlation plots with bivariate linear fits of HICRU effective cloud fractions obtained from GOME-2 PMD measurements of 1 April 2009 at 382nm (channel 7) and 519nm (channel 10), respectively. (a) all data (see text for preselection criteria), (b) viewing zenith angles smaller 20°, (c) only over ocean, and (d) only over land. Clouds brighter than a Lambertian surface with an albedo of 0.8 result in CF>1.

Maps of the same data are shown in Figure 13.7. First of all, these images illustrate the subset for which HICRU has been applied: areas possibly affected by sunglint (reflection angle >36° over water), snow (8-day MODIS snow concentration >5%), and sea-ice (latitudes >60°N and <55°S) are removed from the study in order to minimise interferences and improve the accuracy of the comparison over land.

Figure 13.7 reveals that for small CF and under certain circumstances, HICRU retrieves significantly higher CF at 519nm than at 382nm. For example, the CF map at 519nm over Northern Africa reveals several structures that are not visible in the CF map at 382nm. The reason is that the comparatively bright and structured surface of the Sahara desert affects the accuracy with which HICRU can determine the lower threshold. This area appears in slightly bluish colours in the bottom panel in Figure 13.7 indicating that HICRU results in larger CF at 519nm compared to 382nm.

Furthermore, the difference map also reveals that the VZA-dependence correction is not always sufficient for HICRU at the swath edge of GOME-2 at 382nm. Red colours at the western swath edge indicate that HICRU CF at 382nm over ocean may overestimate the CF up to 10%.

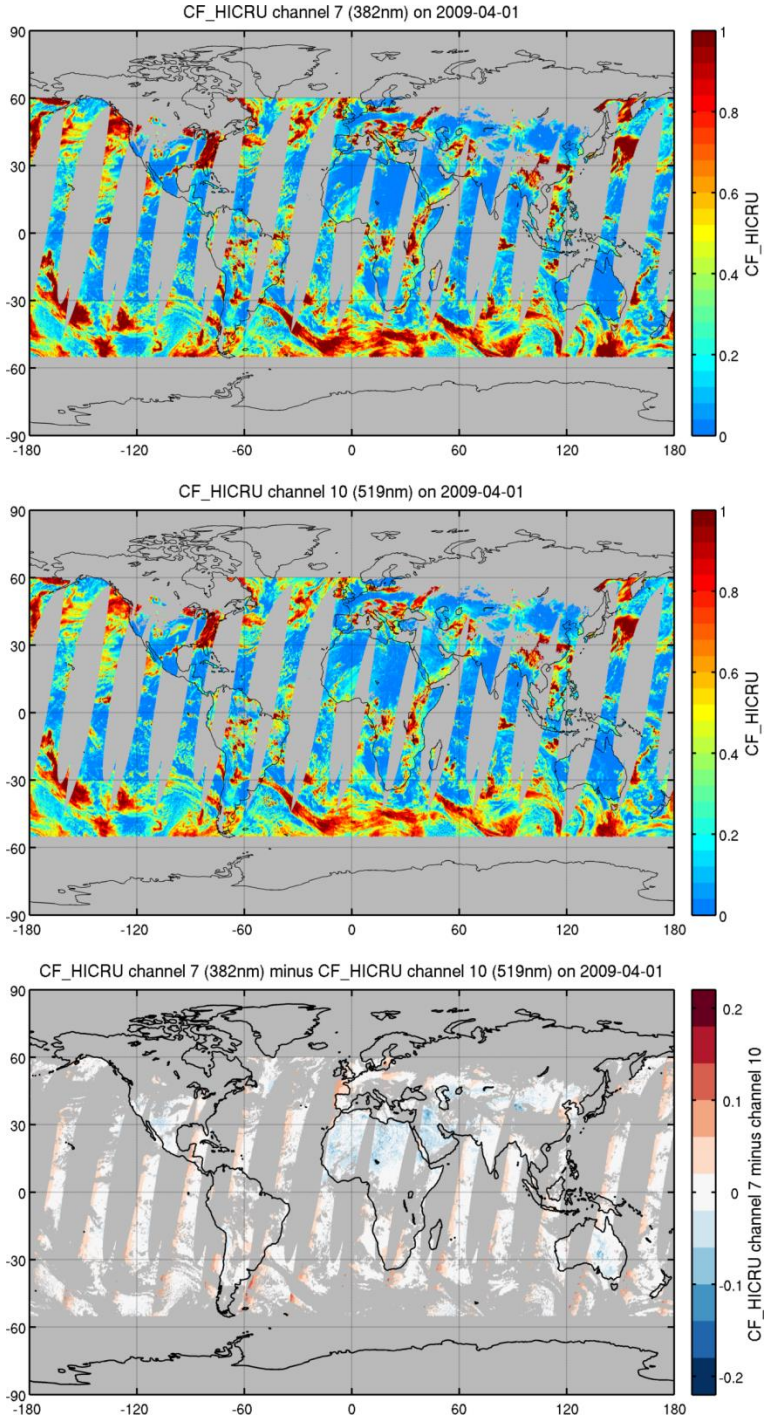

Figure 13.7: Maps of HICRU cloud fraction obtained from GOME-2 PMD measurements of 1 April 2009 at two different wavelengths: (a) 382nm (PMD channel 7), (b) 519nm (channel 10), and (c) difference of (a) and (b). Areas in gray denote regions without data. (c) shows only cloud fractions between -0.2 and 0.2.

13.3.2.2 Correlation between OCRA and HICRU

In this section, OCRA and HICRU results are compared in a similar way as above. To start off, Figure 13.8 shows the correlation between *CF_OCRA* and *CF_HICRU* at 382nm obtained from GOME-2 measurements of 1 April 2009. The coefficient of correlation is always >0.9, which is, however, significant considering that both algorithms apply different cloud models. The slopes of the bivariate fits is always below one indicating that the reflecting cloud model of HICRU potentially underestimates the reflectivity of clouds compared to OCRA, which applies a cloud model based on cloud whiteness.

The plots furthermore reveal that OCRA crops its cloud fractions to the [0,1]-interval. HICRU, however, outputs also CF<0 (statistically probable) and CF>1 (clouds brighter than R_{max}). The normalization by OCRA renders the results of the bi-variate fit less significant. The negative offset, however, indicates that OCRA overestimates small cloud fractions compared to HICRU at 382nm. This behavior of OCRA is furthermore indicated by the color-coded measurement frequency: At small cloud fractions over land (Figure 13.8(d)), the red and orange colors below the 1:1 line reveal that OCRA cloud fractions are often larger, when HICRU cloud fractions are close to zero.

For HICRU at 519nm, the results are similar (Figure 13.9). The correlation coefficients are even higher and the offsets of the bi-variate fits are all <1% cloud fraction. Hence, the differences at small CF are much smaller in this wavelength range.

It is noted that the same analysis has also been performed using data of 1 January, 1 July, 1 October, respectively, but no significant seasonality was observed (R^2 changes by less than 0.02 between days).

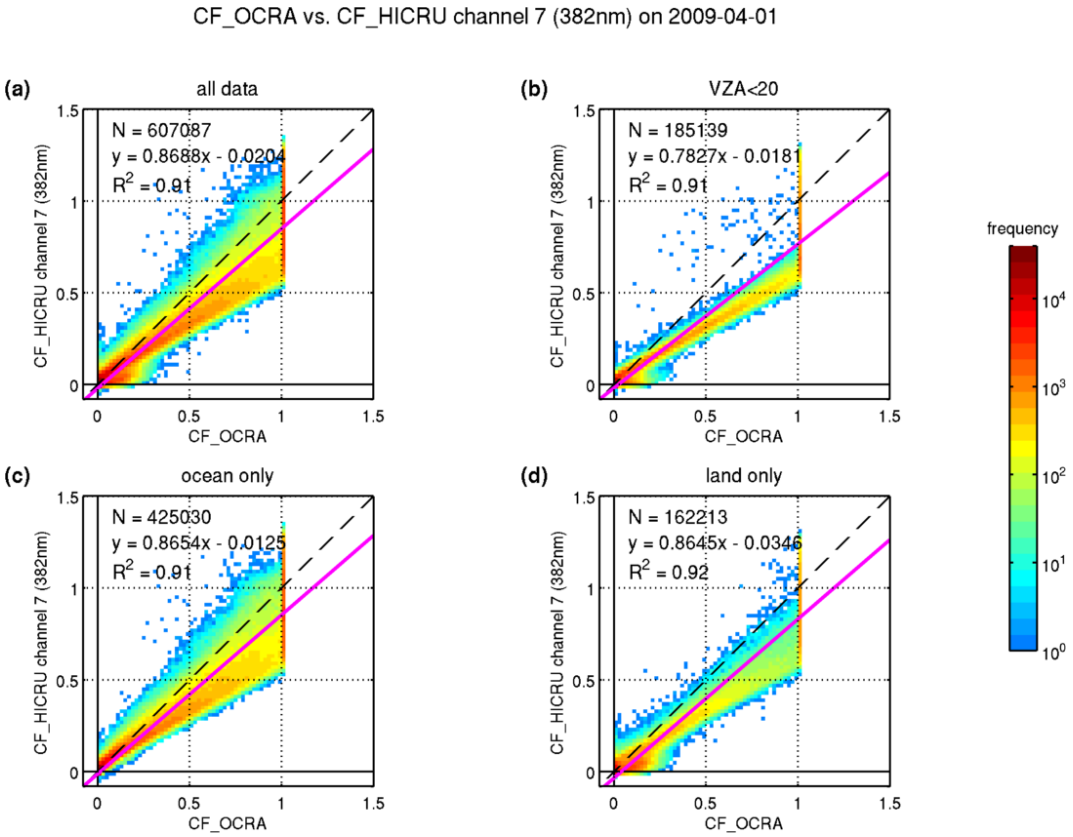

Figure 13.8: Correlation plots with bivariate linear fits of OCRA versus HICRU effective cloud fractions obtained from GOME-2 PMD measurements of 1 April 2009 at 382nm (channel 7). (a) all data (see text for preselection criteria), (b) viewing zenith angles smaller 20°, (c) only over ocean, and (d) only over land.

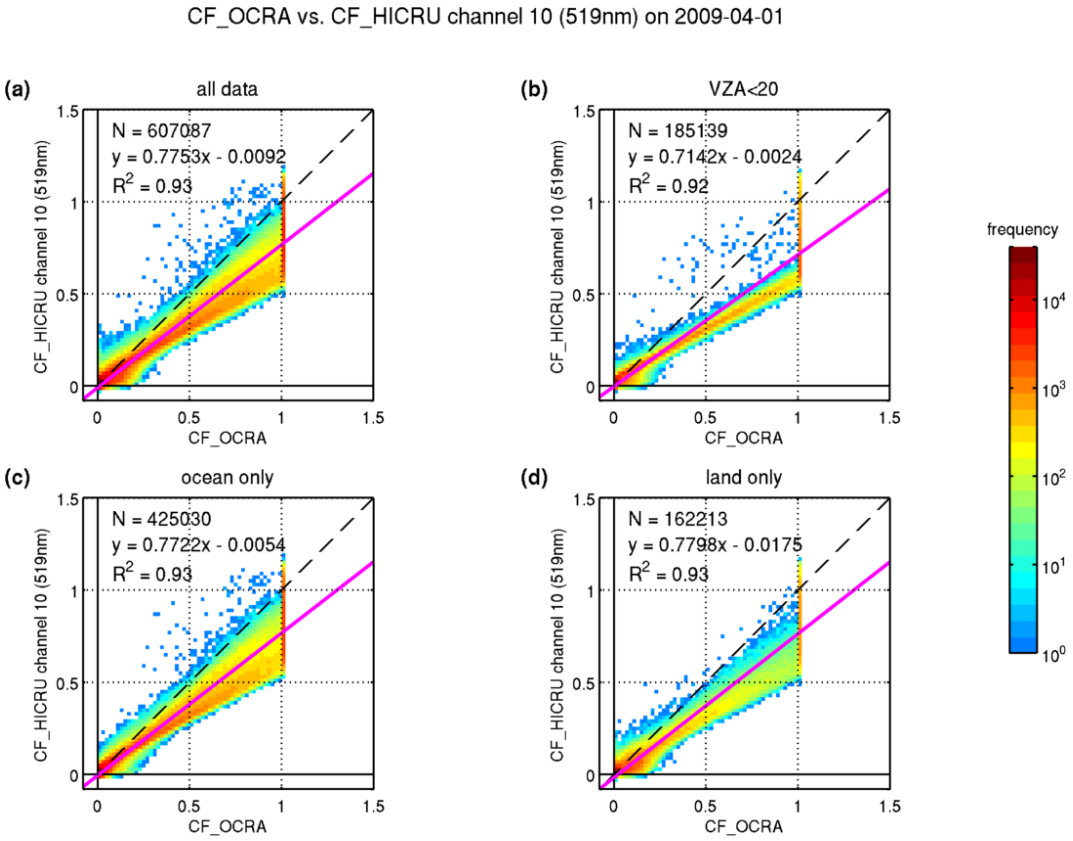

Figure 13.9: Same as Figure 13.10 but using HICRU effective cloud fractions obtained at 519nm (PMD-PP channel 10).

13.3.2.3 Comparison at very small cloud fractions

This section presents a more specific comparison between *CF_OCRA* and *CF_HICRU* for small CF<0.05. Table 13.1 and Table 13.2 compile the statistics of OCRA versus HICRU using GOME-2 PMD channel 7 and 10, respectively. For each of the four selected days in 2009, the cloud fraction statistics (mean, median, and standard deviation) of one algorithm are computed using the data filtered for CF<5% of the other algorithm and vice versa. Then, averages of all four days are computed.

In summary, the mean and median HICRU CF corresponding to OCRA CF<5% are larger than the corresponding OCRA values. The CF spread indicated by the standard deviation behaves the other way round. The spread of OCRA CF at small HICRU CF is significantly larger than vice versa. E.g., at 382nm, the standard deviation of HICRU is 0.0268, the corresponding figure of OCRA is 0.0384. At 519nm, however, mean and median values are generally smaller, whereas the spread of small cloud fractions is smaller (Table 13.2).

Table 13.1: Across-algorithm cloud fraction mean, median, and standard deviation for CF<0.05 for four days in 2009. OCRA and HICRU results are averages of PMD channels PP and SP, HICRU results obtained at 382nm (channel 7).

382nm	*day*	*mean*	*median*	*std*
$CF_{HICRU}(CF_{OCRA}<0.05)$	2009-01-01	0.0382	0.0321	0.0313
	2009-04-01	0.0261	0.0218	0.0231
	2009-07-01	0.0315	0.0265	0.0260
	2009-10-01	0.0315	0.0260	0.0269
	average	**0.0318**	**0.0266**	**0.0268**
$CF_{OCRA}(CF_{HICRU}<0.05)$	2009-01-01	0.0218	0.0055	0.0341
	2009-04-01	0.0319	0.0142	0.0435
	2009-07-01	0.0264	0.0083	0.0398
	2009-10-01	0.0269	0.0104	0.0360
	average	**0.0268**	**0.0096**	**0.0384**

Table 13.2: Same as Table 13.1 but using HICRU results obtained at 519nm (channel 10).

519nm	*day*	*mean*	*median*	*std*
$CF_{HICRU}(CF_{OCRA}<0.05)$	2009-01-01	0.0293	0.0249	0.0253
	2009-04-01	0.0257	0.0217	0.0218
	2009-07-01	0.0295	0.0250	0.0247
	2009-10-01	0.0295	0.0251	0.0245
	Average	**0.0285**	**0.0242**	**0.0241**
$CF_{OCRA}(CF_{HICRU}<0.05)$	2009-01-01	0.0221	0.0096	0.0304
	2009-04-01	0.0293	0.0148	0.0377
	2009-07-01	0.0214	0.0064	0.0330
	2009-10-01	0.0238	0.0090	0.0310
	Average	**0.0242**	**0.0099**	**0.0330**

13.3.2.4 Spatial differences between OCRA and HICRU

Figure 13.11 compiles the cloud fraction maps of OCRA and HICRU for two HICRU channels on 1 April 2009. The images on top illustrates that OCRA provides a much larger coverage compared to HICRU, because it allows also measurements at high latitudes and in areas potentially affected by sunglint. HICRU does not provide this information and, hence, the quality of OCRA in these areas may not be assessed.

The difference maps (bottom row in Figure 13.11) again illustrate the differences of the respective figures above. Red colors indicate that *CF_OCRA>CF_HICRU*. At both wavelengths and over land, OCRA yields larger CF in the western half of the swath, whereas HICRU results are slightly larger in the eastern part of the swath (blue colors over Sahara).

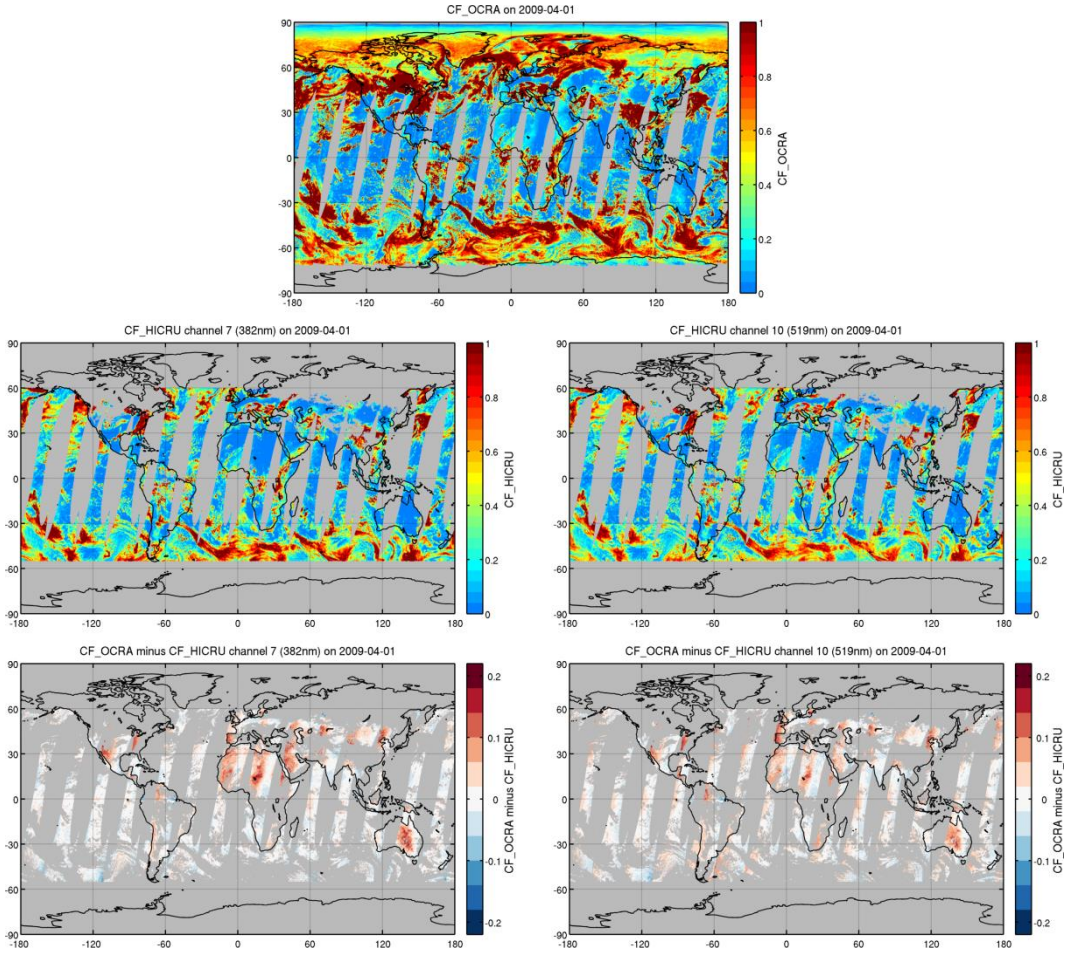

Figure 13.11: Maps of OCRA and HICRU cloud fraction obtained from GOME-2 PMD measurements of 1 April 2009: (top) OCRA cloud fraction, (middle-left) HICRU cloud fraction at 382nm, (middle-right) HICRU cloud fraction at 519nm, and (bottom) difference of (top) and (middle). Areas in grey denote regions without data. Difference maps (bottom) show only cloud fractions between -0.2 and 0.2.

In order to investigate whether the scan angle dependence of the OCRA/HICRU differences are seasonally dependent, Figure 13.12 compiles all four difference maps for both HICRU channels, respectively. This figure reveals a significant seasonality of the differences depending on scan angle. During the northern winter, HICRU produces significantly larger CF at both swath edges in the northern hemisphere compared to OCRA, whereas OCRA provides larger values in the centre of the swath.

In April and July, however, the differences between OCRA and HICRU are less symmetric. In these months OCRA results are significantly larger in the western part of the swath than in the eastern part, where differences to HICRU are much smaller. Furthermore, the differences in July also seem to depend on latitude (more intense red between 30°N and 60°N).

On 1 October 2009, however, differences between OCRA and HICRU are significantly smaller than on the other three exemplary days (bottom row in Figure 13.12). Here, overland OCRA cloud fractions are increased in the swath centre at low latitudes and towards the western swath edge above 30°N.

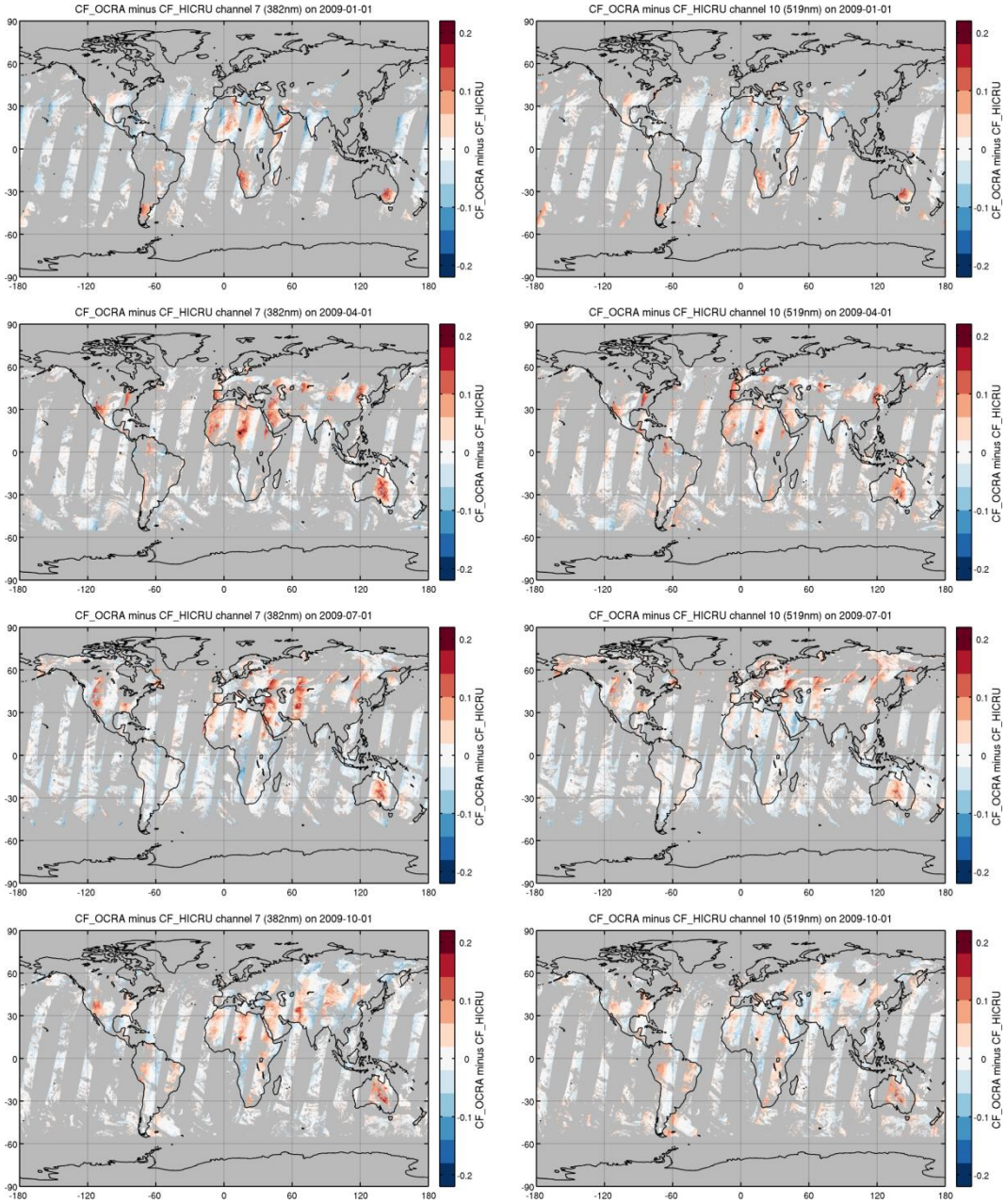

Figure 13.12: Compilation of OCRA-HICRU cloud fraction differences: (left) HICRU results at 382nm, (right) HICRU results at 519nm. The seasonal evolution is mapped from top to bottom: 1 January, 1 April, 1 July, and 1 October 2009. Areas in grey denote regions without data or |CF|>0.2.

13.3.2.5 Zoom on residual viewing angle dependency over continents

In the previous section, a significant deviation between OCRA and HICRU cloud fractions was found for 1 July in northern mid-latitudes. Figure 13.13 zooms into this particular region. In both orbits over Northern America, OCRA finds a large “hazy” area (CF on the order of 0.2) in the western half of the swath, which is not found by HICRU. Furthermore, the OCRA cloud fractions reveal a discontinuity where two orbits begin to overlap in the north around -115°E longitude.

Figure 13.13 furthermore reveals another difference between both algorithms: The difference plot changes hue between land and ocean at the coast of Pacific and Gulf of Mexico. Over land, OCRA cloud fractions are larger compared to HICRU and over ocean the polarity is changed (blue instead of red colour).

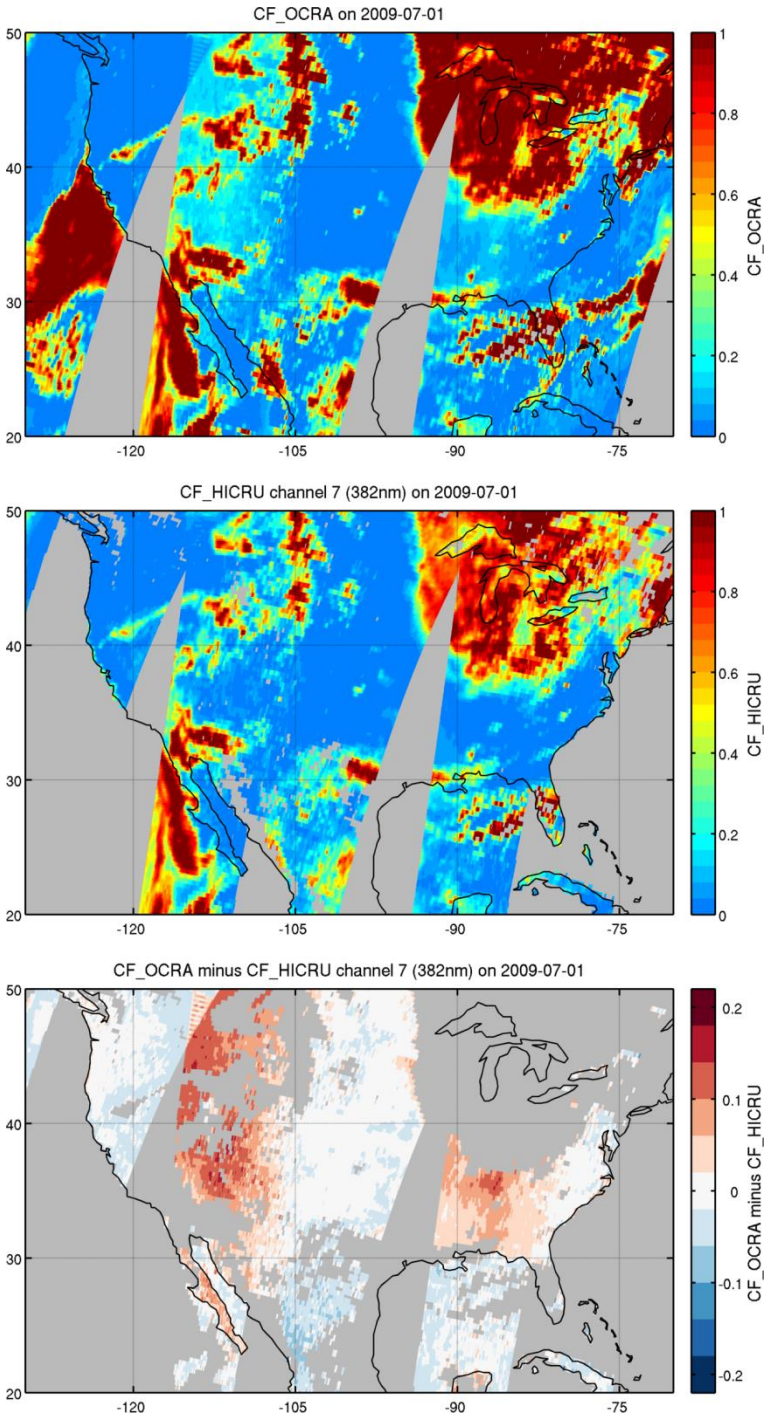

Figure 13.13: Same as left column in Figure 13.11, but zoomed on Northern America. Areas in gray denote regions without data. The cloud fraction difference map (bottom) shows only cloud fractions between -0.2 and 0.2. See text for explanation.

13.3.3 3D RT effects and cloud edges

Gound pixels of TROPOMI will be so small that 3D effects like cloud shadow, which have been ignored so far, become important for the retrieval of both cloud fraction and also trace gas column densities. The RT model McArtim is applied here to calculate reflectances and 2D box air-mass factors (boxAMF), which are a measure for the sensitivity to trace-gas absorption at a particular height and horizontal position. The simulations are performed at 440nm.

Figure 13.14 sketches the geometry of the model setup. In a plane-parallel world, the sensor is placed 800km above the surface with a field-of-view (FOV) of 7km at the surface in nadir (θ=0°) direction. The sun is on the right side of the scene with an SZA=50° corresponding to the geometry at equinox noon in Mainz, Germany. The reference lower threshold for the retrieval of effective cloud fraction is simulated using a Rayleigh atmosphere. The upper threshold is calculated with an infinite cloud with an optical density of 50 between 5 and 6km altitude. A cloud front with OD=10 is inserted into the scene at different cloud positions *p* as indicated in Figure 13.14.

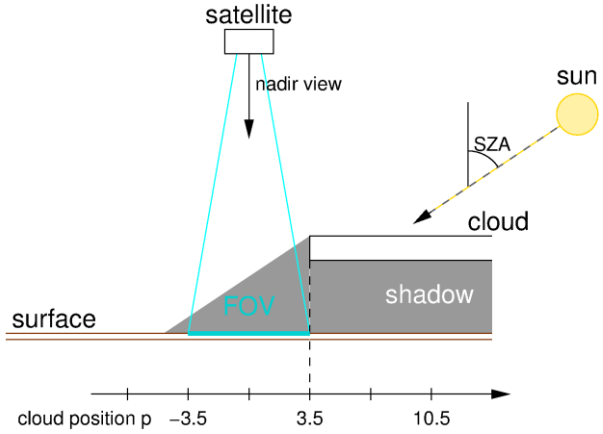

Figure 13.14: Geometry sketch of RT model set-up. The instrument's field of view (FOV) from 800km above the ground is 7km wide. The solar zenith angle is 50°. The cloud between 5 and 6km altitude with an optical thickness of 10 expands from the edge at cloud position *p* to infinity.

Figure 13.15 summarises the retrieved effective cloud fractions depending on the location of the cloud front's edge. Clearly, the intensity and thus the retrieved effective cloud fraction (y-axis) are affected even though the geometrical cloud fraction is zero (denoted #1). The increase of intensity within the FOV due to the brighter cloud approximately compensates for the darker shadow at 10% geometric cloud fraction (denoted #2).

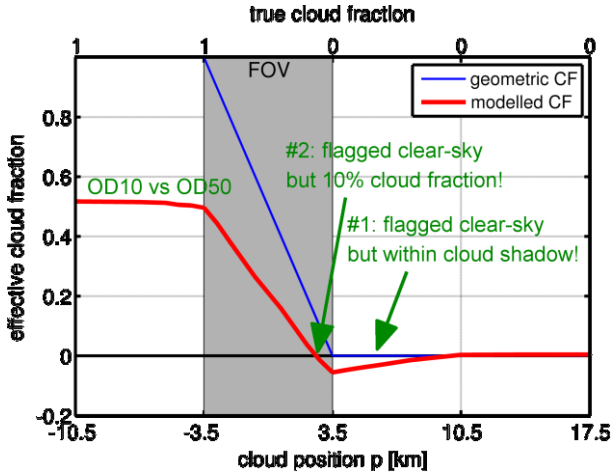

Figure 13.15: Summary of RT model results at 440nm for a cloud optical density (OD) of 10, whereas OD=50 is chosen for the definition of the upper threshold.

The horizontal and vertical sensitivity distributions for three selected cases are illustrated in Figure 13.16. The clear-sky case is shown in subplot (a). The sensitivity towards trace-gas absorption is largest (cyan colours) within the instruments FOV as expected. There is, however, a corona of slightly elevated AMFs (less dark blue colours) ranging ±15km at an altitude around 6km. The inset on the right shows horizontal integrals of the 2D-boxAMF showing 1D boxAMF profiles.

Figure 13.16b shows the same properties but for case denoted #1 in Figure 13.15: the FOV is influenced by a cloud shadow and would be flagged clear-sky because its reflectance is smaller than the pure Rayleigh case. The 2D boxAMF illustrates, that the sensitivity is not evenly distributed within the FOV. The bottom inset shows vertical averages of the boxAMF within the lowest 200m and 1km. It is shown, that the sensitivity within the cloud shadow is reduced to less than a third compared to the shadow-free part.

At a geometric cloud fraction of 10% (Figure 13.16c) the brightening effect of the cloud top cancels the darkening effect of the cloud shadow. The retrieved effective cloud fraction is 0%, but the sensitivity to trace-gas absorption within the lowest 1km of the atmosphere is significantly reduced.

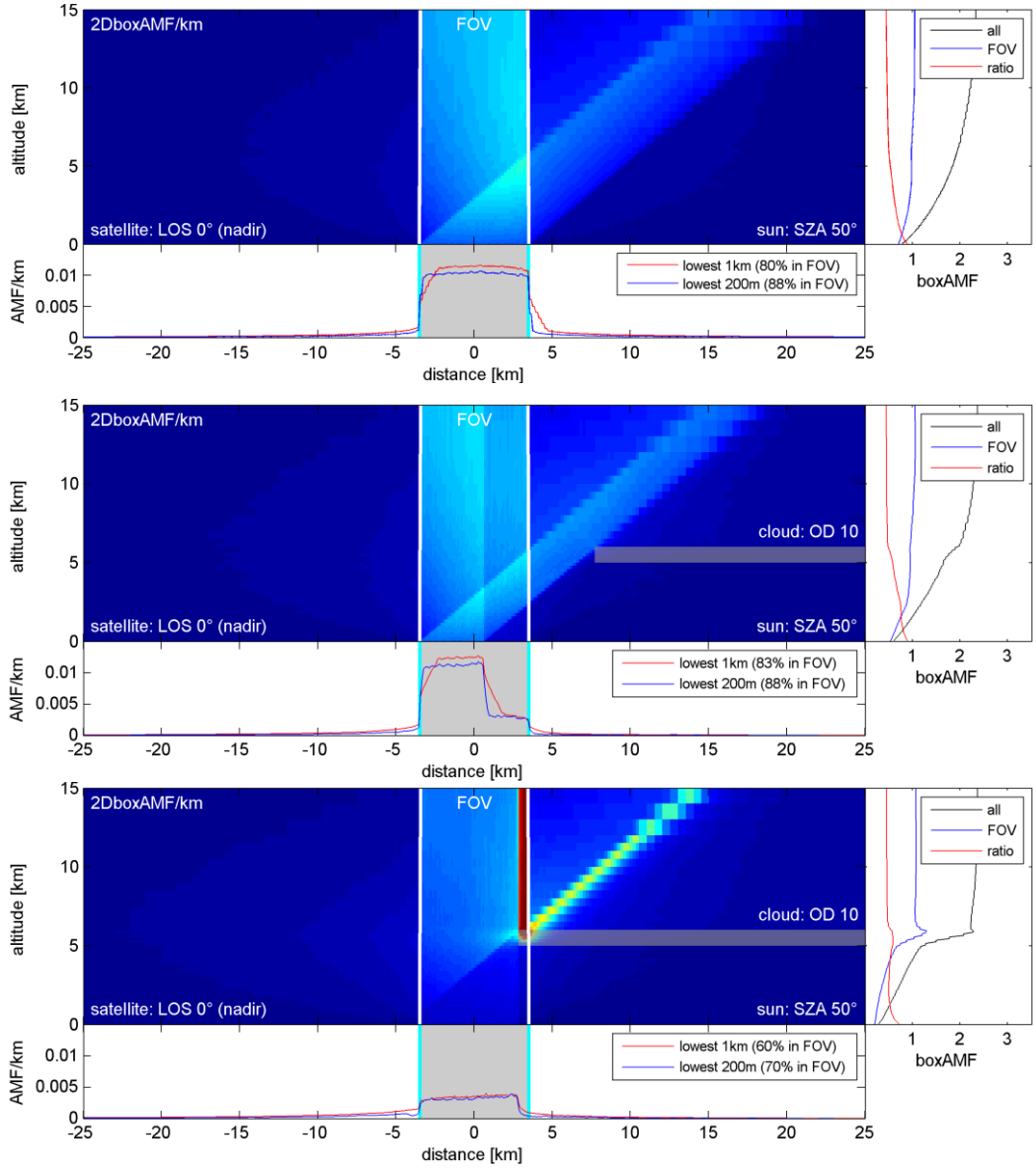

Figure 13.16: RT model results at 440nm for cloud scenes highlighted in Figure 13.15 The main panel displays 2D-boxAMFs as a measure for measurement sensitivity. Horizontal integrals corresponding to classical 1D-boxAMFs are shown on the right; below are vertical integrals to illustrate the horizontal heterogeneity of the measurement sensitivity. (a) clear-sky; (b) geometrical cloud fraction of 60% in neighbouring pixel towards the sun; (c) geometric cloud fraction of 10% and the neighbouring pixel towards the sun completely cloud-covered.

Another aspect shall be noted here. There is also a VZA-dependence of the geometric cloud fraction itself because clouds are vertically extended. Minnis (1989) illustrates several cloud constellations leading to larger cloud fractions at larger VZA as is shown by coincident GOES observations. At very large VZA, partly cloudy scenes may, in fact, be classified as fully cloudy (Liang and Di Girolamo, 2013).

13.3.4 Discussion and Conclusion

The HICRU cloud fraction algorithm has been enhanced to be applicable to observations at large viewing angles. The consequence of this enhancement is a significant complexity increase of HICRU, which now provides a continuous spatio-temporal model of the TOA albedo and VZA-parameterisation. An important parameter of HICRU effective CF algorithm is the wavelength at which the input reflectances are measured. The most important constraint is to avoid interference with optically thick absorbers. Furthermore, on the one hand, the influence of Rayleigh scattering and hence the VZA-dependency of reflectance is weaker at longer wavelengths compared to shorter wavelengths. On the other hand, the presented results show that the gradients of the lower threshold are much stronger already at 519nm imposing various artefacts on the retrieved HICRU cloud fractions. The VZA-dependence of R_{min} is parameterized by a parabola. This simplification introduces artificially increased CF at large viewing angles in some cases. For the upper threshold, a simple Lambertian cloud model was chosen in order to limit the number of free parameters.

The comparison between OCRA and HICRU was performed on GOME-2 PMD data featuring a comparatively high spatial resolution. GOME-2 does not provide a swath as wide as OMI and S5P/TROPOMI, but GOME-2 was preferred over OMI because of the additional spectral information in the red and the higher spatial resolution. The overall comparison between OCRA and HICRU shows a very high consistency between both algorithms. Without knowing the truth it is difficult to provide quantitative figures. The comparison of particularly small cloud fractions, however, indicates that HICRU at 382nm is more accurate for cloud fractions <5% than OCRA. The comparison of spatial patterns of cloud fractions <20% reveal that both algorithms have a residual viewing angle dependence, which, in turn, depends on surface type, season, latitude, and geography. For specific dates, geolocations and observation geometries, OCRA clouds fractions <20% can be more than 10% larger than HICRU cloud fractions. In these extreme cases, the consistency of OCRA cloud fractions is significantly reduced where two GOME-2 swaths overlap.

Three dimensional RT studies are performed in order to study cloud effects which were negligible in similar satellite missions of the past due to their inferior horizontal resolution compared to TROPOMI. For TROPOMI, 3D features become more important since the horizontal and vertical dimension of probed troposphere become similar. At smaller pixel sizes, the influence of cloud shadows will inevitably increase. At the same time, the resolution of TROPOMI may not be sufficient to identify cloud edges using image analysis techniques. It is shown that even clouds in neighbouring pixels influence the sensitivity to trace-gases close to the surface. Furthermore, the near-surface slant column at a wavelength of 440nm, which is representative for NO_2 retrievals, can be reduced to less than one third by a geometric cloud fraction of 10% but zero effective cloud fraction. This sensitivity reduction is possible, but will not be detectable by the proposed algorithm and also those cloud algorithms based on similar input quantities. However, these effects are too complex to be accounted for in operational cloud products, but it is still important to keep these effects and the potential impact on trace gas retrievals in mind. TROPOMI measurements will allow investigating these effects empirically.

13.3.5 Summary of verification results

- Cloud fraction verification results are obtained using a newly implemented, enhanced HICRU algorithm. The agreement with the OCRA prototype processor based on four days of GOME-2A PMD data is very good (R^2>0.9).
- The correlation is mostly limited by the application of different definitions of the upper threshold. This property is, however, of minor importance for the tropospheric trace gas retrievals requiring small cloud fractions at high accuracy.
- There are indications that, in specific situations and for cloud fractions <20%, HICRU is more accurate than OCRA (cf. Figures 13.17 and 13.18). For cloud fractions <5%, the standard deviation of OCRA cloud fractions is larger compared to HICRU (cf. Tables 13.3 and 13.4).
- Both algorithms reveal systematic biases depending on scan angle. These biases furthermore depend on season, latitude, and surface type. On the one hand, OCRA regularly retrieves larger cloud fractions than HICRU in the western half swath at northern mid-latitudes. On the other hand, HICRU overestimates the cloud fractions at the outermost swath edge up to 10% depending on season and SZA.
- Effects of 3D clouds are investigated. They have the potential to adversely affect the retrieval for both retrievals of cloud fractions and, hence, column densities of tropospheric trace gases.

13.4 Verification – cloud top height and optical thickness

In the framework of the verification activity for Sentinel-5 Precursor, the L2WG for cloud and aerosol groups agreed on the generation of a synthetic data set, portraying a representative combination of geophysical scenarios with varying atmospheric, cloud, and surface properties as well as sensing geometries. The data set is ingested in the retrieval algorithms of the involved teams and the first differences can be assessed, along with retrievals from real data. The dataset is generated with SCIATRAN (IUP-UB, Rozanov et al. 2014). As first step a synchronization of the radiative transfer models is needed. DISAMAR (KNMI) is used as forward model, representative of the TROPOMI instrument. Then SCIATRAN is tuned for the least residual achievable and as last independent verification of the RT modelling, simulations using VLIDORT (Spurr R.J.D., 2006; used in the prototype cloud retrieval algorithm from DLR) are carried out.

13.4.1 Atmospheric model, spectroscopy and instrument specifications

For this purpose two spectra calculated with DISAMAR have been provided: a cloud/aerosol-free case and a cloudy case, both for a dark (surface albedo 0.0) and a bright (surface albedo 0.5) ground, in nadir view for a solar zenith angle of 60 degrees. The Top-Of-Atmosphere (TOA) reflectance is defined as

$$R = \frac{\pi I}{\cos(sza)\, E_0} \tag{48}$$

where Eo is the solar irradiance and I is the first element of the Stokes vector {I,Q,U,V}. All runs are in vectorial mode. The calculations are performed line-by-line.

The atmospheric model comprises a mid-latitude summer temperature profile, surface pressure 1013.25 hPa, for an aerosol free atmosphere containing only N_2, O_2, Argon, and CO_2. Rayleigh scattering is described by Bodhaine (1999) and the depolarization term for the calculation of the Rayleigh cross-sections (i.e., the King factor) has been weighted with the abundances of the respective atmospheric gaseous constituents (N_2, O_2, Ar, and CO_2) (Bates, 1984). Considered gases in the cloudy spectrum are: O_3, H_2O, O_2, NO_2, SO_2. T, p, and gas profiles and mole fractions are consistent both in DISAMAR and SCIATRAN, as well as E_0, which is taken from the delivered TROPOMI spectrum.

Spectroscopy database used: HITRAN 2008 without line mixing and collisional-induced absorption. Molecular lines have been cut off at 300 cm^{-1} from the line centre. The spectral features of TROPOMI bands are summarised in Table 13.5. The S/N ratio values are taken from Veefkind et al. (2012), while all other parameters have been taken from the L1B ATBD.

Table 13.5: TROPOMI spectral specifications used in the RTM synchronization

BandID	**3**	**4**	**5**	**6**
Spectral range [nm]	320-405	405-500	675-725	725-775
Spectral resolution [nm]	0.5	0.5	0.5	0.5
Spectral dispersion [nm/pixel]	0.2	0.2	0.12	0.12
Signal to noise	1000-1500	1500	500	100-500

The convolution is done for 2.7 sigma at both sides of the slit function. In SCIATRAN, the internal equidistant step equals 0.001nm. The instrument response function is assumed to be a flat-topped Gaussian function as

$$f(\lambda, \lambda_c, a, w) = a\, 2^{-\left(\frac{\lambda_c - \lambda}{w}\right)^4} \tag{49}$$

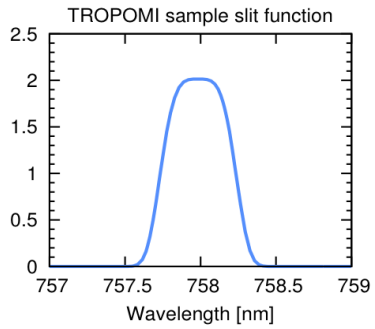

Figure 13.19: Flat-topped Gaussian as TROPOMI sample slit function

In the following comparison, the relative residual Δ [%] is defined as

$$\Delta = 100 \frac{R_s - R_d}{R_d} \tag{50}$$

where the subscripts “s” denote quantities from SCIATRAN and VLIDORT and “d” from DISAMAR, respectively.

13.4.2 Results

13.4.2.1 Clear sky case

The focus is on the Rayleigh scattering signal. The formulae used in SCIATRAN for the representation of the scattering cross-sections come from Bodhaine, 1999 (with refractive indexes from Peek & Reeder, 1972). The weighted King factor includes N_2, O_2, Ar, and CO_2 with the respective following PVC (percent volume concentration) of 78.084, 20.946, 0.934, and 0.036, respectively. These settings coincide with those used in DISAMAR and VLIDORT.

Figure 13.20 shows the comparison for band 3 and 4. Dark and bright surfaces are considered in the left and right plot, respectively. The bias above dark surface is negative and within 0.1 % in the whole window for SCIATRAN while VLIDORT shows a positive bias of approx 0.2%. Moreover, the broadband residual oscillations have been found in either two RTM as compared with DISAMAR.

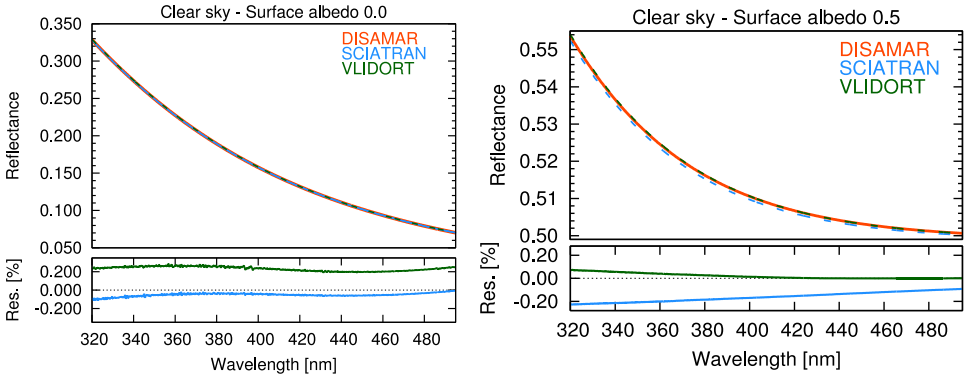

Figure 13.20: Three-way comparison among the RTM involved in the verification of cloud products for a clear sky atmosphere with underlying dark (left plot) and bright (right plot) surface. The lower panels show the relative residuals (%) of SCIATRAN (blue) and VLIDORT (green) with respect to DISAMAR (red).

The layering of the atmosphere between DISAMAR and SCIATRAN differs. However, having set the top-of-atmosphere at 60 km, after comparison of two identical runs with the respective height grids (DISAMAR 381 layers, SCIATRAN 60 layers), no significant differences have been found for the clear sky case. It can be concluded that the all three RTM models calculate the Rayleigh molecular signal to a reasonable degree of accuracy.

13.4.2.2 Cloudy case

The cloudy spectrum was generated for a cloud with Henyey-Greenstein phase function, single-scattering albedo 1, and asymmetry parameter 0.8. This implies that a non-absorbing cloud has been considered. Cloud top and bottom altitudes are set to 5 and 4 km. Cloud optical thickness is set to 20.

Band 6 is chosen for comparison because almost all algorithms retrieve cloud properties (cloud top height, cloud optical thickness and cloud fraction) inside and around the oxygen A-band centred at approx. 761 nm. The comparison for band 6 above a dark surface between SCIATRAN and DISAMAR is shown in Figure 13.21, together with the corresponding clear-sky case. Here, the cloud deck is assumed to be Lambertian. This assumption implies that the TOA reflectance is mainly dominated by light scattered at the cloud top and that the additional oxygen absorption due to enhanced multiple scattering throughout the cloud is not fully taken into account. This might be the reason for the discrepancy found around 761 nm, where a relative bias greater than 2.5% (with a maximum of 4.7%) has been found, when compared to the 1% bias for the clear-sky case at the same wavelength.

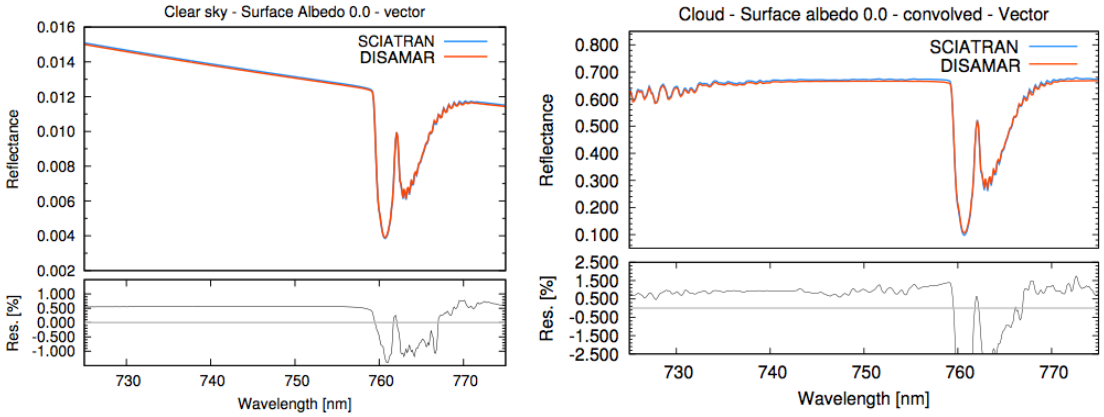

Figure 13.21: Comparison of modelled oxygen A-band between SCIATRAN and DISAMAR for (left) a clear sky case and (right) Lambertian cloud at height 5 km, optically thick 20 and with geometrical thickness 1 km.

In order to understand the reason of the discrepancies, a high-resolution wavelength grid of the A-band has been provided, together with associated weights and the monochromatic intensities used for the integration of the signal within the spectral bins. The spectrum represents a cloud-free atmosphere and no convolution is performed. In Figure 13.22 the monochromatic Earth-shine radiances from DISAMAR and SCIATRAN are plotted for two different bandwidths. The relative residuals in the continuum amounts to less than 0.001%, whereas in the region of strong absorption a mean residual of -0.8% with peaks up to -5% have been found.

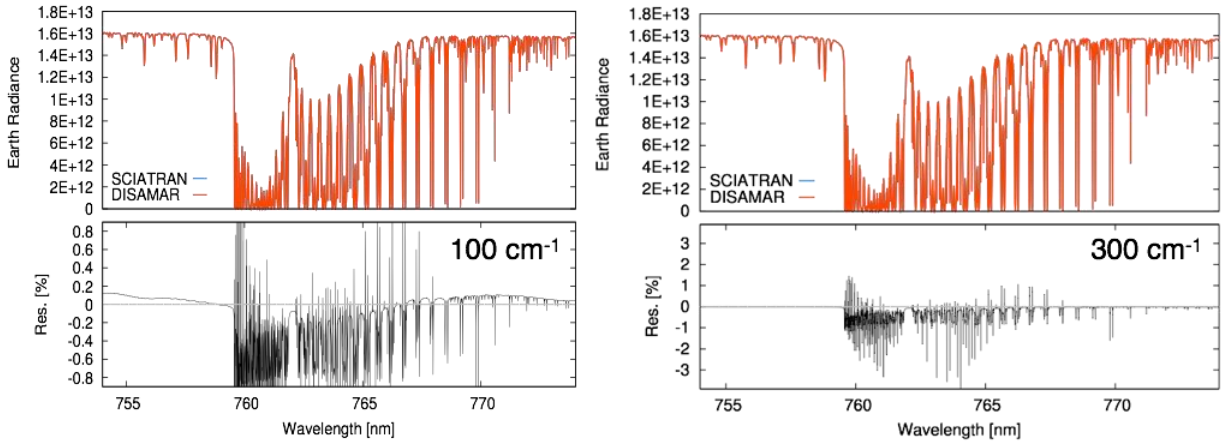

Figure 13.22: High-resolution oxygen spectra from SCIATRAN and DISAMAR for a clear-sky atmosphere and two different intervals (given in cm^{-1}) of individual line contribution to the line-by-line calculations. The respective bandwidths amount to 5.745 nm (left) and 17.236 nm (right), at 758 nm.

It has to be noted that DISAMAR and SCIATRAN differ in the integration method. The high resolution spectral grid implemented in SCIATRAN is equidistant, whereas DISAMAR uses a non-equidistant distribution of spectral points (i.e., repeated Gaussian), in order to take into account the position of strong absorption lines. This different scheme may cause the RTM to calculate different oxygen cross-sections, biasing the results of the comparison.

Other sources of error are the treatment of molecular absorption line shapes as well as the levels at which the calculation of the oxygen cross-sections are performed. It is known that molecular line shifts and line widths are proportional to the atmospheric gas pressure. This implies that if two RTM do not take into account either parameterizations, the results can be biased. This is indeed the case, because SCIATRAN does not take into account oxygen line shifts, as opposed to DISAMAR.

Conversely, oxygen spectra calculated by SCIATRAN and VLIDORT are not expected to be impacted by such biases due to the same equidistant spectral integration method shared by both RT models. To prove this effect, oxygen spectroscopy has been taken from HITRAN 2012 (Rothman et al., 2013) and spectra of a Mie scattering cloud (see Table 13.6 for the cloud microphysical model), consisting of polydispersed spherical water droplets, with an optical thickness of 10 and placed at 5 km, have been calculated for a dark and a bright underlying Lambertian surface taking into account polarization (i.e., in vector mode).

Figure 13.23 and Figure 13.24 show results of two different runs. While both RT models agree very well in the continuum outside strong oxygen absorption, thus providing almost identical results for the molecular scattering signal, the residuals of Figure 13.23, amounting to up to 3% at 761 nm, can be systematically cut down to less than 0.5% across the whole band. The main reason of discrepancy between Figure 13.23 and Figure 13.24 is the different treatment of the layered total optical thicknesses of the gas species considered in the forward modelling, namely O_2 and H_2O.

Table 13.6: Local optical characteristics of the Mie scattering cloud model used for the computation of synthetic TOA reflectances in the O_2-A band. Phase-matrix expansion coefficients calculated for the non-absorbing wavelength = 758 nm.

Parameter [unit]	***Value***
Size distribution of water droplets	Gamma, a= 6.0, b=0.1111
Effective radius, volume [micron, micron^3]	6, 0.111
Refractive index	1.328 ± 0.0i
Asymmetry parameter	0.846
Single-scattering albedo	0.999

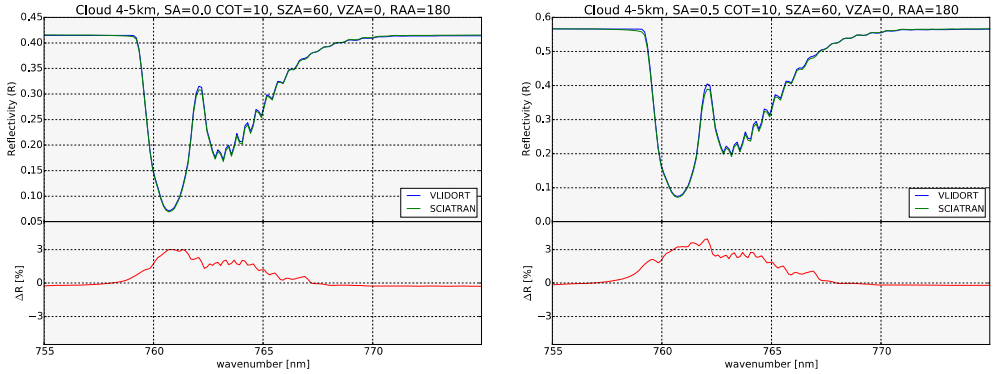

Figure 13.23: Sun-normalized TOA intensities in oxygen absorption at nominal TROPOMI resolution from SCIATRAN and VLIDORT. A single-layer cloud of 1 km height and having an optical thickness of 10, of spherical Mie scatterers is placed at 5 km, above a dark (surface albedo 0.0, left) and a bright (surface albedo, 0.5) ground. The lower panel displays the respective relative residuals [%], defined as VLIDORT – SCIATRAN.

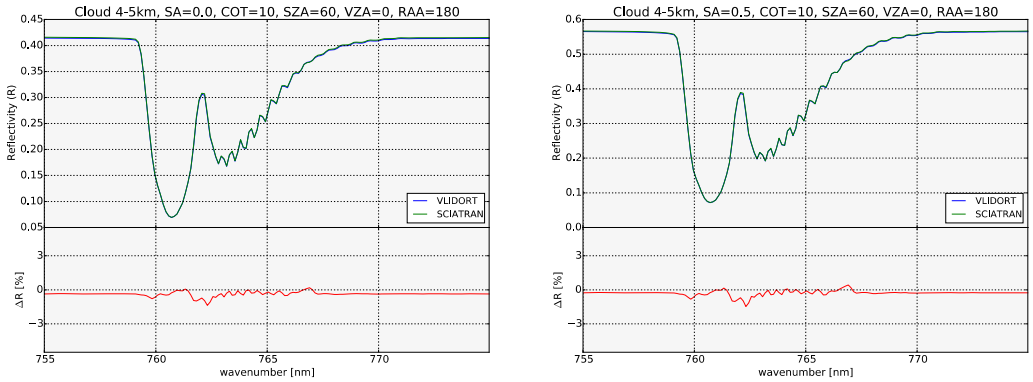

Figure 13.24: As the previous figure, but for SCIATRAN and VLIDORT sharing the same total gaseous optical thicknesses. Oxygen and water vapour extinction cross-sections are considered. No aerosols are present and the surface is assumed to be Lambertian

It is worth noting that, despite the relatively high cloud optical thickness, surface radiative effects can still influence the radiative transfer especially in the strong absorption lines of oxygen, due to multiple scattering between the cloud bottom and the ground. The scattering cloud model is, therefore, more representative of real situations than a pure Lambertian cloud, which would not only screen the lowest layers of the atmosphere, but also hamper the transmission of unpolarized incident sunlight throughout the cloud deck and suppress polarization effects by both molecules and polydispersed cloud scatterers (either water droplets, ice crystals, or mixed-phase elements), due to the strong forward peak component of scattering for large particles. The second Stokes vector Q (not shown here) and its respective residuals between SCIATRAN and VLIDORT behave similarly to the cases shown in Figure 13.23 and Figure 13.24 for the intensity I. Even though TROPOMI has been designed as a polarization insensitive instrument, in view of the fact that in real experiments clouds are often composed not only of pure water but also of mixtures of ice and water, differences in the respective phase functions of water and ice can introduce effects which shall be taken into account in the forward modelling.

13.4.2.3 Real test data: July 2009 and November 2009 from GOME-2

GOME-2 spectra from July and November 2009 have been selected to investigate the performance of the respective cloud retrieval algorithms involved in the verification activity. They are the prototype algorithm ROCINN - DLR (Loyola D.G., 2004; DLR, 2015), the verification algorithm SACURA – IUP/UB (Rozanov and Kokhanovsky, 2004; Lelli et al., 2012) and the FRESCO – KNMI (Wang et al., 2008). ROCINN provides cloud height, optical thickness, and albedo. SACURA, in addition, gives information also on the bottom height of the cloud deck. The FRESCO algorithm delivers cloud height and fraction instead. The ROCINN prototype algorithm is provided in two different versions (V.3 and V.4). While in its version 3, ROCINN handles Clouds as Lambertian Reflecting Boundaries (CRB), the updated variant V.4 offers also the option of treatment of Clouds As scattering Layers (CAL).

It is necessary to stress upfront that while all three retrieval schemes employ the Independent Pixel Approximation (IPA, Marshak et al. 1995) to scale, with the local cloud fraction value, the measured TOA reflectance between the cloud-free, radiatively surface-dominated part of the ground pixel with the cloudy part of the scene, the actual retrieval of cloud height (and for ROCINN and SACURA cloud optical thickness) is based on different assumptions and technical implementations of radiative transfer and cloud modelling. This makes the verification not only a challenging exercise, but also the interpretation of retrievals difficult and not straightforward, because different parts of the cloudy atmosphere will be sensed.

Physically, this can be understood acknowledging that the oxygen molecule, due to the different spectral penetration depths, will be sensitive to different atmospheric layers and cloud parts. Differences in the provided cloud products have to be expected when multiple scattering between 755 and 775 nm is not taken fully into account, if surface is differently treated and if the cloud local optical model differs among the algorithms. Technical implementations can also give rise to additional numerical residuals. As an example, the most common approach to retrieve cloud parameters is to synthetically generate *look-up-tables* (LUT), which consist of exactly pre-calculated reflectances for all the physically meaningful combinations of instrument, geometry, cloud, surface and atmospheric parameters. The retrieval is then carried out looking for the best interpolation point inside the array that matches the actual measured reflectance. Either a polynomial approach (Fischer and Grassl, 1991) or a neuronal network technique (Loyola, 2004) can be devised.

In the case of ROCINN, LUTs are calculated with VLIDORT, while SACURA deploys a semi-analytical approach to derive cloud parameters. Since the uncertainty of such analytical approximations of radiative transfer (Kokhanovsky et al., 2003; Kokhanovsky and Rozanov, 2004, Kokhanovsky and Nauss, 2006) grows beyond 20% for COT less than 4 at non-absorbing wavelengths, SACURA is currently being modified with LUTs for thin clouds (see section about the analysis of the synthetic cloud data set).

GOME-2 Level 1-b data have been used to generate cloud properties for the month July and November 2009, together with the versioning of the three algorithms, is given in Table 13.7. While ROCINN and FRESCO L1b data are in their reprocessed stage (5.3, R_O), SACURA ingested near-real time data (4.2, N_O). The main difference between the two versions is the spatial aliasing of the ground pixels, which may result in slightly shifted latitude and longitude data between different L1b versions and, therefore, need careful co-registration.

Table 13.7: Algorithm and their versioning used in the comparison of GOME-2 retrievals.

Algorithm	***Version***
ROCINN	V.3 (CRB), GDP 4.8, L1b: 5.3
SACURA	OCRA cloud fraction GDP 4.5, L1b: 4.2
FRESCO	V.6, L-1b: 5.3, Software: 1.28, Algorithm: 0.06

Figure 13.25 displays the mean cloud height (left column) and its standard deviation (right column) for ROCINN V.3 (top row), SACURA (mid row) and FRESCO (bottom row) for July 2009. The respective statistics, together with November 2009, are given in Table 13.8.

Table 13.8: Statistics of cloud height of GOME-2 retrievals for July and November 2009. In brackets the minimum and maximum values of the sample are given.

. Algorithm	***July 2009***	***November 2009***
ROCINN	3.64 ± 2.01 km (0.004 – 14.99)	3.73 ± 1.63 km (0.03 - 14.99)
SACURA	5.01 ± 2.52 km (1.200 – 16.78)	5.16 ± 2.45 km (1.20 - 15.32)
FRESCO	3.46 ± 2.48 km (0.002 – 15.00)	3.32 ± 1.61 km (0.17 - 13.02)

As can be seen from Figure 13.25, all three algorithms can reproduce the large-scale cloud patterns. The prototype cloud product (ROCINN), in its V.3 (ROCINN CRB) shows consistency with the FRESCO cloud product for the average CTH values. This similarity is rooted in the similar treatment of a cloud in the forward modelling: both algorithms assume clouds as pure Lambertian cloud surfaces, neglecting oxygen absorption throughout the cloud deck. It is known that this assumption leads to the underestimation of cloud altitude, because higher oxygen absorption is misinterpreted as a lower cloud. For this reason, a new version of ROCINN (V4.0) which treats clouds as scattering layers has been developed for the processing of TROPOMI data.

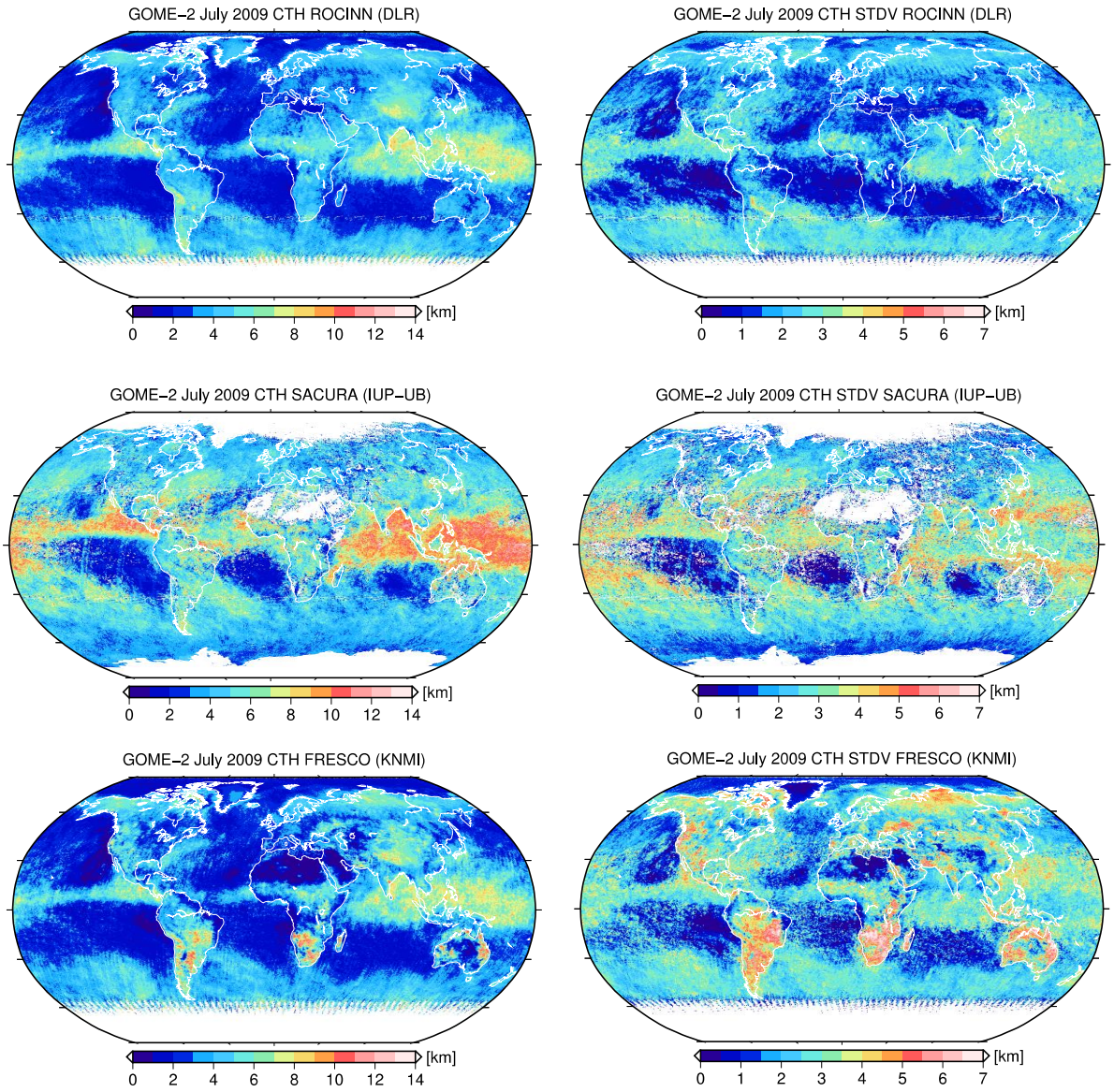

Figure 13.25: Average (left column) and standard deviation (right column) for cloud height from GOME-2 measurements for July 2009 derived with ROCINN (top row), SACURA (middle row) and FRESCO (bottom row) algorithms.

The right column of Figure 13.25 reveals different results for the CTH standard deviation of the three cloud products. While SACURA and FRESCO seem to capture the cloud variability in the subsidence latitudinal belts off the equator, this being especially clear over the Western Pacific, ROCINN CTH shows less variability. Conversely, FRESCO CTH exhibits strong variability over land surfaces such as South America, the African continent and almost all of Australia. This FRESCO behaviour might be an indication of aerosol misclassification, as it is already synthetically known (Wang et al. 2012) that, at λ = 760 nm, the FRESCO algorithm handles cloud and aerosol radiances similarly, as long as the layer is optically thicker than 5. Additionally, the fractional cover will be systematically underestimated in the presence of aerosol events.

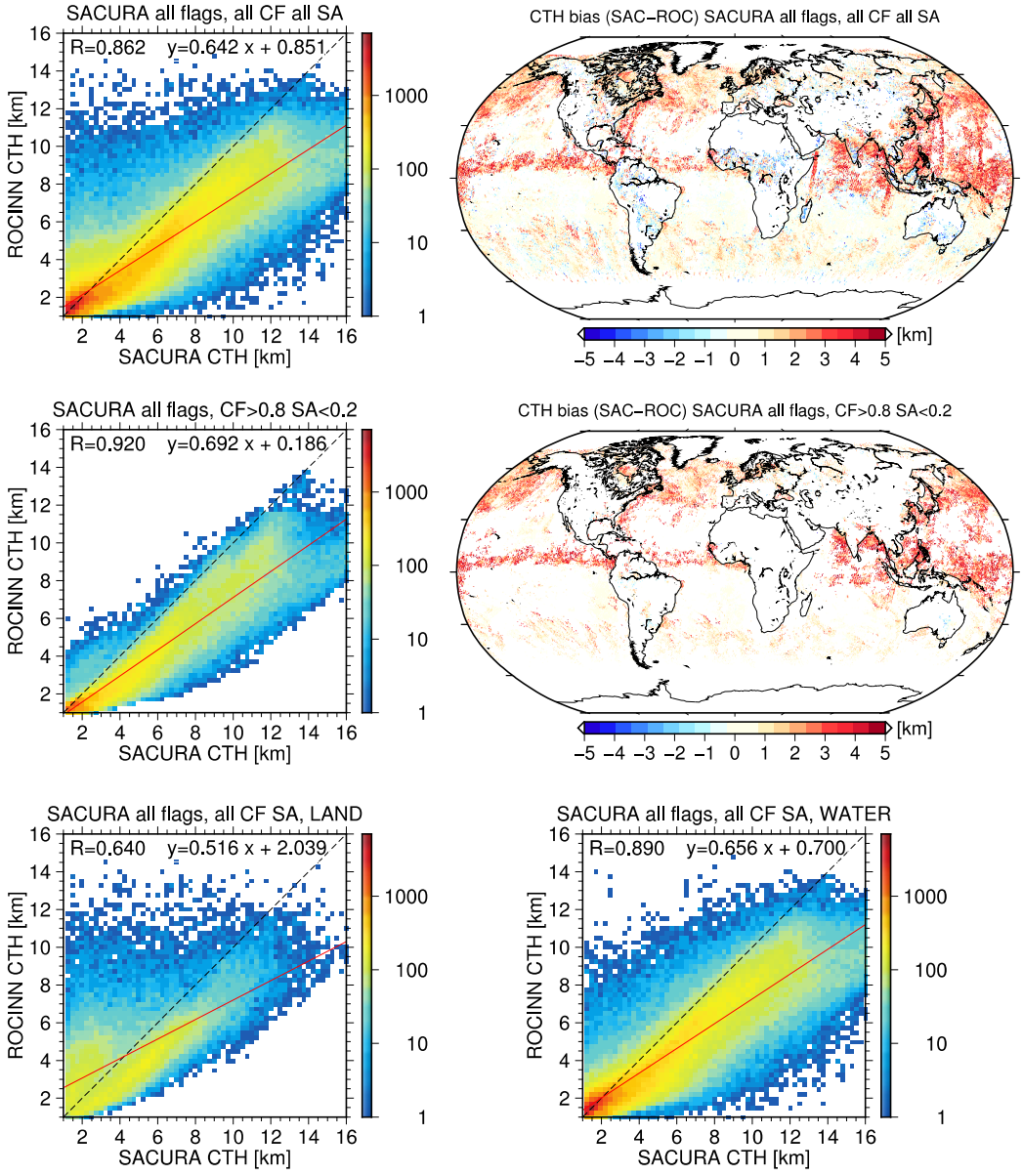

Figure 13.26: Scatterplots (left column) and mapped cloud height bias (in km, right column) between SACURA and ROCINN for July 2009. The bottom row displays the break-up of retrievals over land and water masses.

Since SACURA makes use of a Mie scattering cloud and the atmosphere-weighted single-scattering albedo of oxygen is calculated in the forward model, it is expected that comparison of the CTHs will show an underestimation for ROCINN and FRESCO. This is indeed the case, when looking at Figure 13.26 and Figure 13.27, where SACURA retrievals have been collocated respectively with ROCINN (Figure 13.26) and FRESCO (Figure 13.27) and biases in cloud height have been globally mapped. Moreover, the scatterplots have been subset for underlying land and water masses (bottom rows of the respective Figures).

Focusing on Figure 13.27, it is clear that cloud height bias (defined as SACURA CTH – ROCINN CTH) is mostly emerging from regions of optically thick clouds, such as the ICTZ and the western Pacific warm pool. These cloud structures are typically vertically extended and heterogeneity (i.e., multi-layer clouds) is to be expected, especially for such a coarse sensor as GOME-2. While increasing the spatial resolution of the instrument, as with TROPOMI, will be beneficial to reduce discrepancies, the effect of light penetration through optically thick clouds and the consequently increased oxygen absorption has to be taken into account.

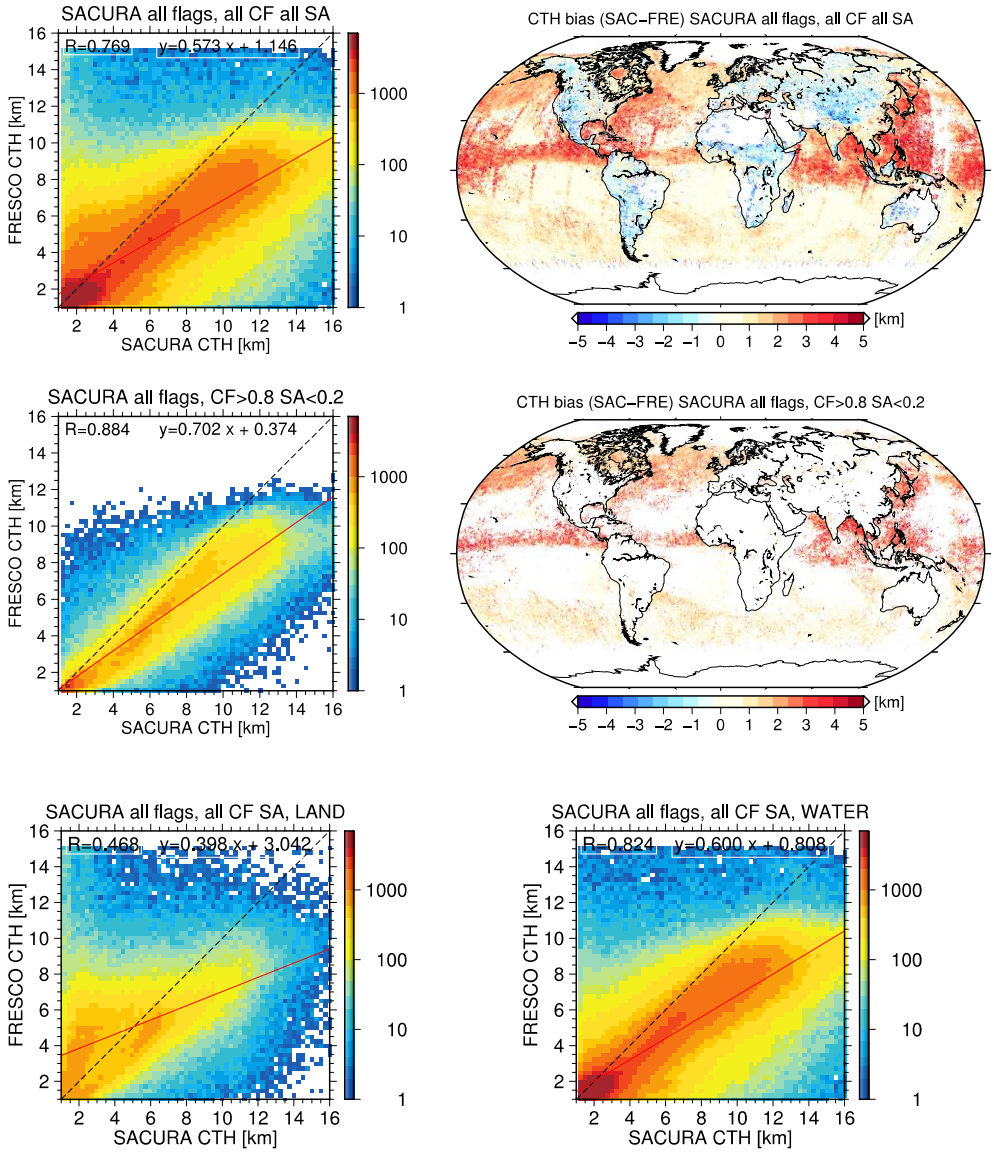

Figure 13.27: Scatterplots (left column) and mapped cloud height bias (in km, right column) between SACURA and FRESCO for July 2009. The bottom row displays the break-up of retrievals over land and water masses.

Additionally, it must be noted that the accuracy of cloud fraction (CF) can also influence the accuracy of derived cloud products. Since both ROCINN and SACURA ingest the radiometric OCRA CF and since the two OCRA versions differ for the cloud products in their actual versions, it can be expected that errors in CF will propagate into cloud albedo and cloud optical thickness. CTH will be also impacted, but to a lesser extent, as already shown by Lelli et al., 2012 when analysing GOME data.

In order to prove this effect, cloud height biases and correlation coefficients between SACURA and ROCINN/FRESCO are binned as function of the local cloud fraction and the underlying surface albedo, both provided by the respective algorithms, as separately plotted in Figure 13.28 and Figure 13.29, for both July and November 2009.

Focusing on the evaluation of ROCINN V.3 (top row), it is clear that surface albedo values will impact cloud top height retrievals for CF less than 0.8, as can be seen in the increased scatter among different symbols for the same CF bin. For CF greater than 0.8, the diminished scatter between symbols of different SA values points to a physically consistent effect: the increasing screening of the underlying surface by a cloudier scene. In fact, for CF = 1, the influence of the surface is very limited and the points almost overlap. This is not the case for the FRESCO height product (bottom row), which exhibits a constant scatter between points of different SA across all the CF bin range, provided that CF is not smaller than 0.6. Moreover, a positive bias stands for SACURA cloud height higher than the compared algorithm. This again signifies that the difference in the cloud model cannot be neglected and oxygen absorption needs to be taken into account when looking at the altitude of clouds. .

Figure 13.28 illustrates also the dependency of the biases in cloud height on the brightness of the surface. The impact of the cloud model is clearly to be seen for dark scenes (dark blue crosses) and exhibits almost no dependence on CF. When the brightness of the underlying ground increases, then compensations between the radiation fields emerging from the cloud deck and the surface take place. Apparently, this effect is more evident for the FRESCO cloud product than for ROCINN. Indeed, FRESCO cloud heights increase already for SA > 0.1, as can be seen in the slope of the light-blue crosses for decreasing CF in Figure 13.28 over land masses. Above these, likely vegetated, surfaces ROCINN cloud height retrievals are less affected by SA and this explains the lower standard deviation in the maps of Figure 13.25 (top row).

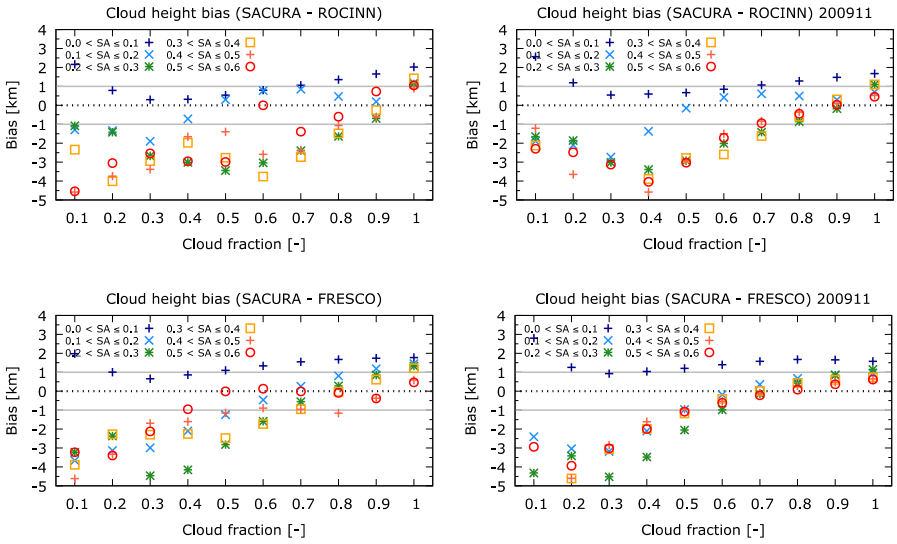

Figure 13.28: Bias in cloud height for July 2009 (left column) and November 2009 (right column) for ROCINN (top row) and FRESCO (bottom row) against SACURA. The biases are binned as function of cloud fraction and brightness of the underlying surface, provided by the respective compared algorithm.

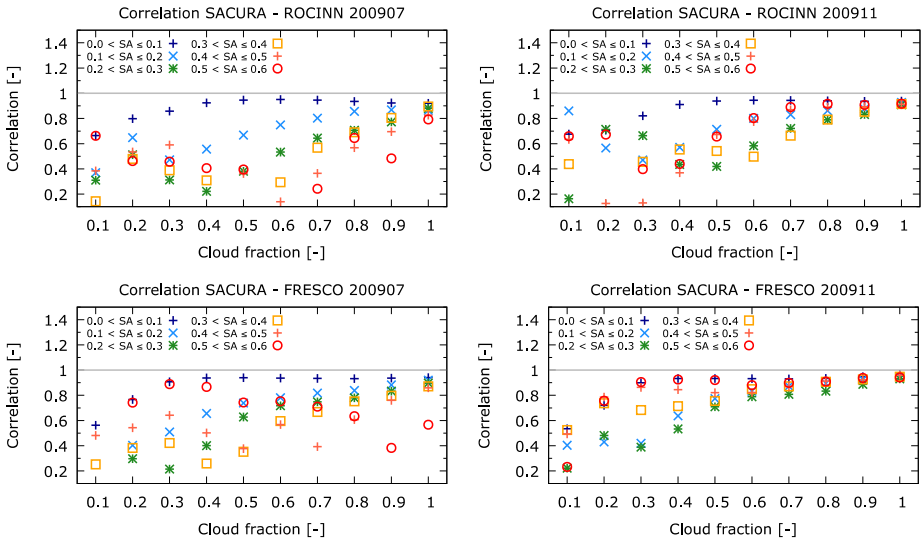

Figure 13.29: Correlations of cloud height for July 2009 (left column) and November 2009 (right column) for ROCINN (top row) and FRESCO (bottom row) against SACURA. As in Figure 13.28, the values are binned as function of cloud fraction and brightness of the underlying surface, provided by the respective compared algorithm. Synthetic cloud data set

13.4.2.4 Synthetic cloud data set

Although the algorithms involved in the verification of cloud products theoretically should produce identical results if the same input measurements are used, this is often not the case, as seen in the previous section. Disagreements may arise due to different assumptions with respect to the cloud fraction, to the refractive index of particles, to the type of cloud water droplets and possible inclusion of ice crystals, different surface albedo treatments, atmospheric state, and eventually radiative transfer models deployed in the forward calculations. Therefore, there is a need for understanding and quantifying differences among the algorithms.

To this end, a data set of spectra of the oxygen A-band (755 – 775 nm) has been calculated with the RT model SCIATRAN (Rozanov et al., 2014) in its version 3.4.5, accounting for multiple scattering and polarization for a plane parallel atmosphere. It contains intensities I (i.e., the first element of the Stokes vector) of scenarios representing a complete set of all permutations of typical geophysical parameters such as cloud properties, surface albedo, and geometrical configuration of the experiment (e.g., the relative positions of Sun, Earth, and spacecraft). The set of considered scene parameters is given in Table 13.9, amounting to a total of 158760 spectra.

Table 13.9: Space of geophysical parameters covered in the calculation of synthetic cloud spectra in the oxygen A-band (755 – 775 nm)

Parameter [unit]	***Value***
Surface albedo [-]	0, 0.2, 0.4, 0.6, 0.8, 1.0
Cloud bottom height [km]	1.0, 4.0, 9.0
Cloud top height [km]	2.0 – 15.0, with 1.0 km step
Cloud optical thickness [-]	1.0, 2.0, 5.0, 10.0, 30.0, 50.0
Solar zenith angle [deg]	0, 5, 15, 30, 45, 60, 75
Viewing zenith angle [deg]	0, 5, 15, 30, 45, 60, 75
Relative azimuth [deg]	0, 45, 90, 135, 180

13.4.2.5 Synthetic data: cloud height

In contrast to the previous section, whose focus is on retrievals from GOME-2 data, where ROCINN V.3 (CRB, Cloud as Reflecting Boundaries) has been evaluated, the synthetic data set has been ingested in ROCINN V.4 (CAL, Cloud As scattering Layers). For a selected subset of provided spectra representing low-, mid- and high-level clouds, the retrieved values of cloud altitude have been plotted against the assumed input values for a black underlying surface, near- and off-nadir observation angles (i.e., viewing zenith at satellite smaller/greater than 5 degrees) and plotted in Figure 13.30. The statistics are given in Table 13.10. ROCINN V.4 values correlate the best with the input truth (correlation is close or equal to 1.0 in both observational settings) for all cases, showing a slight overestimating tendency of retrieved cloud height as function of altitude. In general, the description of clouds as scattering layers reduces the bias seen in the previous sections, where the ROCINN cloud heights from GOME-2 measurements were lower than the SACURA corresponding values. The standard deviation of all three products also increases as function of altitude, being the lowest for clouds at lower altitudes. Figure 13.30 also displays the well-known result that clouds treated as Lambertian reflectors are not captured closer to their physical top height, but somewhere close to their middle, radiative height, also termed the optical centroid of the cloud body. This is the case for the FRESCO product, which shows a systematic underestimation amounting to approximately -1.42 km on average.

It has to be noted that the total number of evaluated spectra differ, so have the mean values of CH reported in Table 13.10, due to different settings and quality flagging of the three algorithms. For instance, the SACURA retrievals are filtered for cloud optical thicknesses smaller than 5 and attained full convergence only for cloud height (and not for cloud bottom height and optical thickness), while the FRESCO retrievals have been performed with LUTs pre-calculated for the GOME-2 viewing geometries, which do not match some of the cases of the synthetic cloud data set of Table 13.9. Given these limitations, down-sampling all three cloud products to the minimum set of common properties would have degraded each respective statistics. Thus, the choice has fallen on comparing the same cloud property space instead, while maximizing the statistics for each algorithm, where possible.

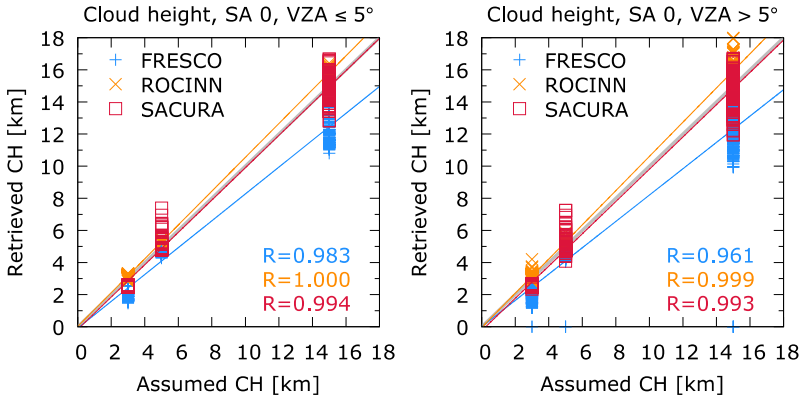

Figure 13.30: Scatter plots of retrieved cloud height versus the true input value for a dark underlying surface and near-nadir (left) and off-nadir (right) observation angles.

Table 13.10: Statistics of Figure 13.30 for the comparison of the three cloud products derived from the synthetic data set. Note that the respective mean properties of the "true" input cloud fields differ due to different quality flagging schemes of the algorithms, which extract different subsets. Fit fields: S = Slope, I = Intercept, R = correlation coefficient, N = number of observations.

	Near-nadir (VZA ≤ 5°)			***Off-nadir (VZA > 5°)***		
Cloud product	***Mean ± Stdv [km]***	**Bias [km]**	***Fit (S,I,R,N)***	***Mean ± Stdv [km]***	**Bias [km]**	***Fit (S,I,R,N)***
ROCINN	8.93 ± 5.68	+0.47	1.054; +0.009; 1.000; 1050	8.93 ± 5.74	+0.51	1.065; -0.047; 0.999; 2608
SACURA	9.42 ± 5.45	-0.10	1.007; -0.166; 0.994; 409	9.38 ± 5.43	-0.19	1.005; -0.241; 0.993; 955
FRESCO	6.72 ± 4.52	-1.43	0.836; -0.093; 0.983; 572	6.47 ± 4.47	-1.42	0.821; -0.002; 0.961; 1103

In Figure 13.31, the biases in cloud heights are plotted as function of cloud altitude and cloud optical thickness in the left and right plot, respectively. ROCINN retrievals reside between the ±1 km error bars for almost all cases under consideration, being more accurate for low-level than high-level clouds. However, a slight dependency of the biases on the viewing zenith angle can be expected, with a general tendency of overestimation of cloud altitudes, irrespective of their optical thicknesses. This effect can be seen when looking at the right plot of Figure 13.31, where the orange ROCINN retrievals, plotted for VZA > 5 degrees (that is, off-nadir) not only exhibit more scatter but almost all reside above the thick grey line. Figure 13.32 also proves that off-nadir geometries might have an impact on the accuracy of cloud altitudes, especially above dark and moderately bright surfaces.

To investigate this effect, the accuracy of the retrievals is plotted as function of scattering angle in Figure 13.33. The scattering angle is defined as the angle between the direction of incident and scattered solar radiation, in the scattering plane. Given any geometry, the solar zenith Θ_0, the viewing zenith Θ and the relative azimuth angle φ, the scattering angle ξ can be calculated with the following equation

$$cos\xi = \cos\Theta * \cos\Theta_0 + \sin\Theta * \sin\Theta_0 * \cos\phi \quad (51)$$

As can be seen, both plots illustrate the effect of a suboptimal microphysical description of cloud droplets in the forward modelling, because the highest scatter emerges in proximity of primary and secondary rainbow angles, that is, in the range 100°-130° for the geometry under consideration.

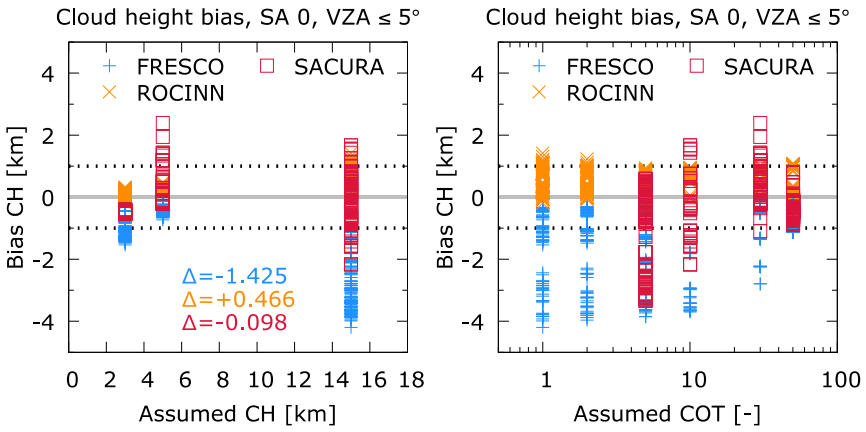

Figure 13.31: Bias in retrieved cloud height as function of altitude (left plot) and cloud optical thickness (right) for the near-nadir cases and black underlying surface.

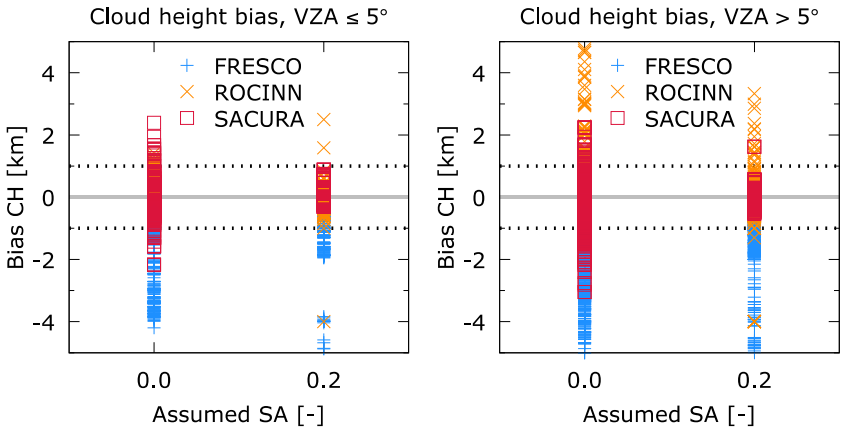

Figure 13.32: Bias in retrieved cloud height as function of brightness of the underyling surface, for near-nadir (left) and off-nadir (right) geometries.

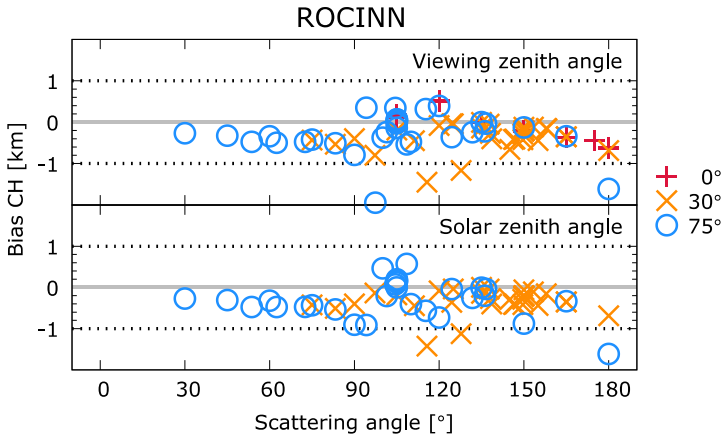

Figure 13.33: ROCINN V.4 bias in retrieved cloud height as function of the scattering angle for varying viewing zenith (top plot) and solar zenith (bottom plot) angles.

13.4.2.6 Synthetic data: cloud optical thickness

The retrieval of cloud optical thickness (COT) can follow two distinct pathways. Assuming that at near-infrared wavelengths the absorption by water droplets is negligible, then the amount of light scattering attenuation throughout a cloud (modelled as a semi-infinite layer) can be described as function of cloud transmissivity, photon diffusion efficiency, and the asymmetry parameter, which in turns depends on the chosen cloud phase function. Then, the non-absorbing gaseous wavelength 758 nm is used to analytically calculate COT. This is the approach of SACURA, which borrows the technique described by King (1978). The advantage of speed of calculations is counterbalanced by increasing residuals for COT < 5 and greater sensitivity to viewing geometry. Conversely, ROCINN V.4 bases its retrieval on a Tikhonov-regularized least-square fit between the measurement and a set of pre-calculated LUT, being the output the two-parameter state vector of cloud top height and optical thickness (Schüssler et al. 2014). Therefore, it can be expected that residuals in retrieved COT will be due to the interpolation errors when looking for the global minimum of the cost function within the LUT. This approach has been adopted also for SACURA in order to deal with COT smaller than 5. The results for the retrieved COT of the three algorithms are presented in Figure 13.34. The synthetic measurements are subset for brightness of the underlying surface (dark and otherwise) for a viewing zenith angle ≤ 5°, that is, near-nadir geometry.

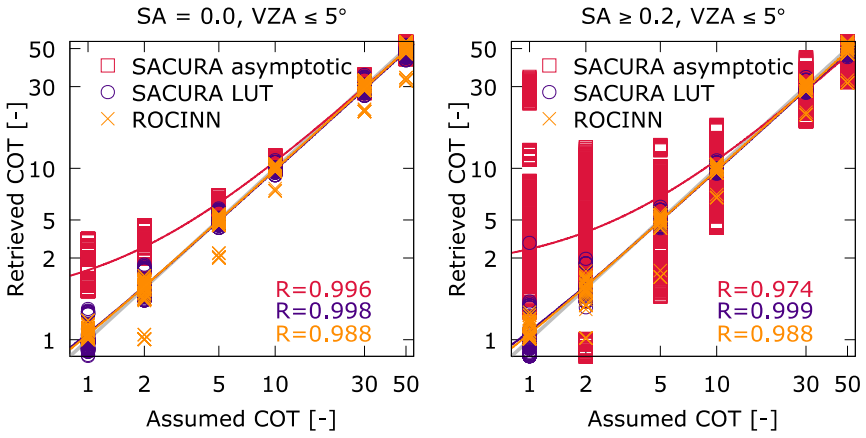

Figure 13.34: Scatterplots of retrieved optical thickness of clouds at a near-nadir geometry (i.e. VZA ≤ 5°) over a black (left) and bright (right) surface for the prototype algorithm ROCINN and two implementations of the verification algorithm SACURA (with asymptotic equations and with Look-Up-Tables).

In both subset samples of Figure 13.34, the input mean COT amounts to 15 and the retrieved mean COT for a dark surface (left) amount to 14.1 for ROCINN, 15.3 for SACURA LUT, and 16.5 for SACURA asymptotic. Over bright surfaces ROCINN yields 12.4, SACURA LUT 13.04, and its asymptotic version 16.4. However, while COT retrievals based on exact RT (ROCINN and SACURA LUT) yield stable results in terms of standard deviation, the approximate solutions of the original verification algorithm produce notable spread across the diagonal.

The relative errors in retrieved COT, corresponding to Figure 13.34, are plotted in Figure 13.35. The errors that can be expected from ROCINN are in general within the ±15% envelope for all optical thicknesses, except for few outliers. This holds for dark underlying surfaces, whereas, for bright surfaces, the relative residuals for thin clouds (COT = 1) are almost all positive, with values clustering about +25%. Moreover, Figure 13.35 shows the well-known effect that thicker clouds (COT > 5) tend to effectually screen the surface and the reflected light by it, such that their COT can be retrieved with a mean accuracy of ±10%.

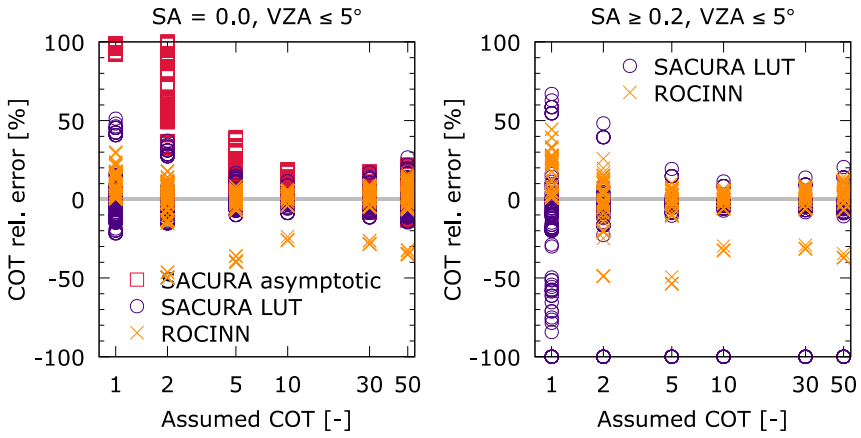

Figure 13.35: Relative errors of retrieved COT at a near-nadir geometry (i.e. VZA ≤ 5°) over a bark (left) and bright (right) surface for the prototype algorithm ROCINN and two implementations of the verification algorithm SACURA (with asymptotic equations and with LUT). Residuals from SACURA asymptotic are omitted from the right plot for readability.

Before focusing on off-nadir geometries, it must be noted that in the context of a plane-parallel atmosphere, it holds (Chandrasekhar, 1960):

$$\mu_0 I(\mu, \phi, \tau) F(\mu, \phi) = \mu I'(\mu_0, \phi_0, \tau) F'(\mu_0, \phi_0) \quad (52)$$

where I is the upwelling radiance in direction of the cosine of VZA and SZA (μ and μ_0 respectively) and azimuth angle φ, F is the downwelling solar irradiance, and τ is the optical depth of the sensed atmosphere. The prime symbol expresses the time lag at which two different measurements are taken. Since F is approximated and cancels out, the above equation indicates that the same radiance is observed if μ and μ_0 are interchanged and average quantities are sensed (Di Girolamo et al. 1998). The above equation is also deemed the *reciprocity principle*. Due to this principle, the relative errors of Figure 13.34 in retrieved COT by ROCINN, plotted as function of SZA (x-axis) and VZA (y-axis), are symmetric about the diagonal.

The first row of Figure 13.36 shows COT relative errors for an optically thin and mid-level cloud, above a moderately bright surface (i.e., COT 1, CH 6 km, SA 0.2) for the five different relative azimuth angles. The found residuals are always positive, ranging from +3% up to 30% at a relative azimuth of 135°. Conversely, the bottom row of Figure 13.36 displays the residuals for an optically thick and high-level cloud, above a dark surface (i.e., COT 30, CH 15 km, SA 0.0). In this case, for geometries resembling latitude belts close to the Equator (i.e., SZA < 50°) in nadir, the residuals are in the range 0% and +15%, while an underestimation of COT can be expected only for a relative azimuth of 180°. Interestingly, the patterns change sign as function of relative azimuth angle but also rotate clockwise from 0° to 180°, signifying that the residuals are also dependent on the scattering angle (forward-to-backward peak of the cloud phase function) in the scattering plane, that is, across-track of the TROPOMI swath.

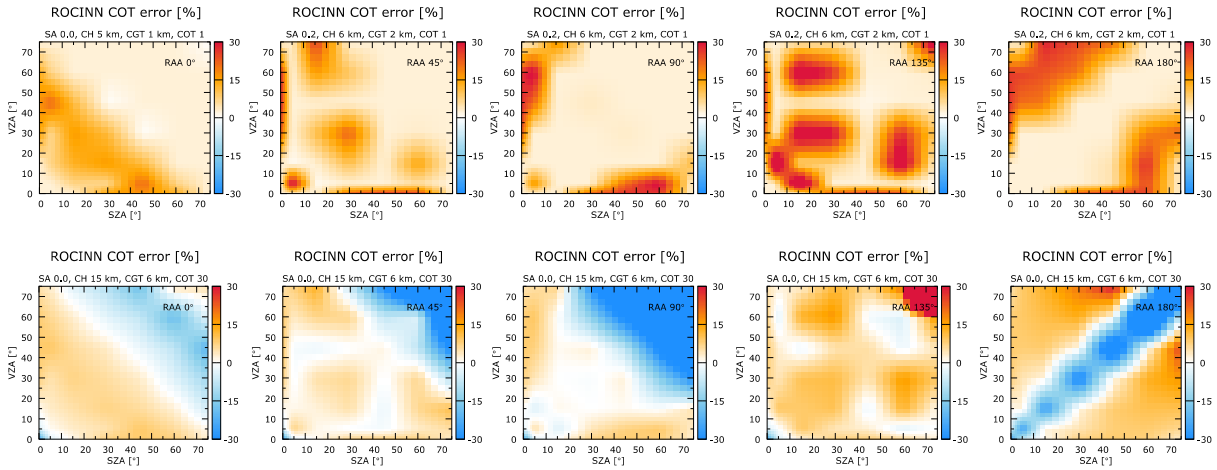

Figure 13.36: Relative error (%) in retrieved COT for (top row) a optically thin mid-level cloud above a moderate bright surface (i.e., COT 1, CH 6 km, SA 0.2) and (bottom row) a optically thick high-level cloud above a black surface (i.e., COT 30, CH 15 km, SA 0.0) as function of solar zenith (x-axis), viewing zenith (y-axis) and relative azimuth angles (color-coded surface), the latter ranging from 0° (leftmost column) to 180° (rightmost column).

13.4.3 Summary of verification results

It has been shown that RT models with the same solution procedure (both SCIATRAN and VLIDORT are based on discrete-ordinate-method solvers for an equidistant spectra integration grid) can agree up to a systematic relative residual of less than 0.5% in the strong absorption of oxygen. While this value can still be improved when high-resolution fine tuning is desirable, the actual radiometric bias has been judged adequate for the optical closure experiment of the cloud verification part. This preparation step has enabled the generation of a synthetic cloud data set, generated with SCIATRAN, whose evaluation has supported the unambiguous assessment of the performances of the cloud retrieval algorithms.

As for real test data, taken from GOME-2 measurements of July 2009 and November 2009, it has been proven that the altitude of clouds treated as Mie scattering layers can be higher by as much as 3 km when compared to cloud heights calculated treating clouds as pure Lambertian reflective layers. This effect is even more important when optically thick clouds are sensed. A reprocessing, encompassing both cloud fraction (new OCRA version), together with cloud height and optical thickness with a new cloud model is expected to deliver more accurate results and improve the overall comparison. Also, the SACURA cloud product, being reprocessed with the most recent OCRA cloud fraction data provided by DLR and with the surface database of the MERIS black sky albedo (Popp et al. 2011), employed in the ROCINN processing, will lessen the discrepancies found over land masses, especially for the cloud height product.

The treatment of clouds as scattering layers by ROCINN has provided more accurate cloud altitudes than the ones retrieved with the Lambertian model, as proved in the analysis of real and synthetic data sets together, delivering an average bias lower than ±1 km for all case studies. ROCINN cloud heights are accurate also with respect to the underlying surface albedo and optical thickness, given a near-nadir observational geometry. However, cloud height and cloud optical thickness retrievals at off-nadir extreme geometries can be affected mostly by differences between the prescribed microphysical cloud model used for the generation of the LUTs and the actual local one.

The verification of cloud optical thickness has shown that low and mid-level clouds, especially for the thin cases, will be overestimated by an average of approximately 15% for all TROPOMI geometries. Due to the analytical treatment of radiative transfer for optically thin clouds of SACURA, a necessary update in terms of Look-Up-Tables has been implemented, delivering consistent results with the ROCINN prototype. Additionally, accuracy in retrieved COT can be expected to vary both for optically thin and thick clouds, depending on the local side of the TROPOMI swath, in the off-nadir geometries, due to changes of scattering planes on the azimuthal plane (backward to forward scattering). To this end, change in signs of the COT retrievals can be expected especially for high-level and thick clouds, with relative residuals amounting up to ±25% for extreme angles (SZA and VZA greater than 70°).

However, having in mind the plausibility of the verification results when using real data, it must be stressed that the SCIATRAN cloud phase function has intentionally not been tuned with VLIDORT for the specific exercise of the synthetic retrievals, so that the differences in the RT calculations (likely greater than the residuals of 0.5% found in the optical closure exercise) will possibly mimic those differences arising from the unavoidable deviations of a forward model atmosphere and the actual sensed one.

13.5 References

Bates DR, Rayleigh scattering by air. Planet. Space Sci. 32(6): 785–90, 1984.

Bodhaine BA, Wood NB, Dutton EG, Slusser JR. On Rayleigh optical depth calculations. J Atmos. Ocean. Tech., 1999;16:1854–61.

Chandrasekhar, S.: Radiative transfer, Oxford, Clarendon Press (UK), 1950. Reprinted, Dover publica- tions (New York), 1960.

Deutschmann, T., S. Beirle, U. Frieß, M. Grzegorski, C. Kern, L. Kritten, U. Platt, C. Prados-Román, J. Pukite, T. Wagner, B. Werner, and K. Pfeilsticker, The Monte Carlo atmospheric radiative transfer model McArtim: introduction and validation of Jacobians and 3-D features, J. Quant. Spectrosc. Ra., 112, 1119– 1137, doi:10.1016/j.jqsrt.2010.12.009, 2011.

Di Girolamo, L., Várnai, T., and Davies, R.: Apparent breakdown of reciprocity in reflected solar radiances, J. Geophys. Res., 103, 8795–8803, doi:10.1029/98JD00345, 1998.

DLR (2015), ATBD for GOME-2 Total Columns of O3, NO2, BrO, HCHO, SO2, H2O and Cloud Properties, Doc. No.: DLR/GOME-2/ATBD/01, Rev: 3/A, Date: 30 March 2015

Fischer, J. and Grassl, H.: Detection of cloud-top height from reflected radiances within the oxy- gen A band, part 1: Theoretical studies, J. Appl. Meteor., 30, 1245–1259, doi:10.1175/1520-0450(1991)030<1245:DOCTHF>2.0.CO;2, 1991.

Grzegorski, M., M. Wenig, U. Platt, P. Stammes, N. Fournier, T. Wagner, The Heidelberg iterative cloud retrieval utilities (HICRU) and its application to GOME data, Atmos. Chem. Phys., 6, 4461-4476, 2006.

Grzegorski, M., Cloud retrieval from UV/VIS satellite instruments (SCIAMACHY and GOME), PhD-thesis, University of Heidelberg, 2009.

King, M. D.: Determination of the scaled optical thickness of clouds from reflected solar radiation measurements, J. Atmos. Sci., 44, 1734–1751, doi:10.1175/1520- 0469(1987)044<1734:DOTSOT>2.0.CO;2, 1987.

Kleipool, Q. L., M. R. Dobber, J. F. de Haan, and P. F. Levelt, Earth surface reflectance climatology from 3 years of OMI data, J. Geophys. Res., 113, D18308, doi:10.1029/2008JD010290, 2008.

Kokhanovsky, A. A. and Rozanov, V. V.: The physical parameterization of the top-of-atmosphere reflection function for a cloudy atmosphere–underlying surface system: the oxygen A-band case study, J. Quant. Spectrosc. Rad. Tran., 85, 35–55, doi:10.1016/S0022-4073(03)00193-6, 2004.

Kokhanovsky, A. A., Rozanov, V. V., Zege, E. P., Bovensmann, H., and Burrows, J. P.: A semianalytical cloud retrieval algorithm using backscattered radiation in 0.4–2.4 μm spectral region, J. Geophys. Res., 108, 4008, doi:10.1029/2001JD001543, 2003.

Kokhanovsky, A. A. and Nauss, T.: Reflection and transmission of solar light by clouds: asymptotic theory, Atmos. Chem. Phys., 6, 5537–5545, doi:10.5194/acp-6-5537-2006, 2006.

Kokhanovsky, A. A., Mayer, B., von Hoyningen-Huene, W., Schmidt, S., and Pilewskie, P.: Retrieval of cloud spherical albedo from top-of-atmosphere reflectance measurements performed at a single observation angle, Atmos. Chem. Phys., 7, 3633–3637, doi:10.5194/acp-7-3633-2007, 2007.

Lelli, L., Kokhanovsky, A. A., Rozanov, V. V., Vountas, M., Sayer, A. M., and Burrows, J. P.: Seven years of global retrieval of cloud properties using space-borne data of GOME, Atmos. Meas. Tech., 5, 1551-1570, doi:10.5194/amt-5-1551-2012, 2012.

Liang, L., and L. Di Girolamo, A global analysis on the view-angle dependence of plane-parallel oceanic liquid water cloud optical thickness using data synergy from MISR and MODIS, J. Geophys. Res. Atmos., 118, 2389–2403, doi:10.1029/2012JD018201, 2013.

Loyola, D., and T. Ruppert, A new PMD cloud-recognition algorithm for GOME, ESA Earth Observation Quarterly, 58, 45-47, 1998.

Loyola, D. G.: Automatic cloud analysis from polar-orbiting satellites using neural network and data fusion techniques, in: IEEE T. Geosci. Remote Symposium, vol. 4, pp. 2530–2534, doi:10.1109/IGARSS.2004.1369811, 2004.

Marshak, A., Davis, A., Wiscombe, W., and Titov, G.: The verisimilitude of the independent pixel approximation used in cloud remote sensing, Rem. Sens. Environ., 52, 72–78, doi:10.1016/0034- 4257(95)00016-T, 1995.

Minnis, P., Viewing zenith angle dependence of cloudiness determined from coincident GOES East and GOES West data. J. Geophys. Res., 94, 2303–2320, doi:10.1029/JD094iD02p02303, 1989.

Peck ER, Reeder K. Dispersion of air. J. Opt. Soc. Am., 1972;62:958–62.

Popp, C., P. Wang, D. Brunner, P. Stammes, Y. Zhou, and M. Grzegorski, MERIS albedo climatology for FRESCO+ O2 A-band cloud retrieval, Atmos. Meas. Tech., 4, 463-483, doi:10.5194/amt-4-463-2011, 2011.

Rothman, L.S. et al. (2013) The HITRAN 2012 Molecular Spectroscopic Database. Journal of Quantitative Spectroscopy and Radiative Transfer, 130, pp. 4-50. Elsevier. DOI: 10.1016/j.jqsrt.2013.07.002. ISSN 0022-4073.

Rozanov, V. V. and Kokhanovsky, A. A.: Semianalytical cloud retrieval algorithm as applied to the cloud top altitude and the cloud geometrical thickness determination from top-of-atmosphere reflectance measurements in the oxygen A band, J. Geophys. Res., 109, 4070, doi:10.1029/2003JD004104, 2004.

Rozanov, V.V. and Rozanov, A.V. and Kokhanovsky, A.A. and Burrows, J.P. (2014) Radiative transfer through terrestrial atmosphere and ocean: Software package SCIATRAN. Journal of Quantitative Spectroscopy & Radiative Transfer, 133 . pp. 13-71

Schüssler, O, Loyola, D., Doicu, A. and Spurr, R.:Information Content in the Oxygen A-Band for the Retrieval of Macrophysical Cloud Parameters. IEEE Transactions on Geoscience and Remote Sensing, 52 (6), pp. 3246-3255. IEEE Geoscience and Remote Sensing Society. DOI: 10.1109/TGRS.2013.2271986, 2014.

Spurr, R.J.D.:VLIDORT: A linearized pseudo-spherical vector discrete ordinate radiative transfer code for forward model and retrieval studies in multilayer multiple scattering media, Journal of Quantitative Spectroscopy and Radiative Transfer, 102, 2, 316-342, http://dx.doi.org/10.1016/j.jqsrt.2006.05.005, 2006

Stöckli, R., Vermote, E., Saleous, N., Simmon, R., Herring, D., The Blue Marble Next Generation - A true color earth dataset including seasonal dynamics from MODIS, NASA Earth Observatory, 2005.

Wang, P., Stammes, P., van der A, R., Pinardi, G., and van Roozendael, M.: FRESCO+: an improved O2 A-band cloud retrieval algorithm for tropospheric trace gas retrievals, Atmos. Chem. Phys., 8, 6565-6576, doi:10.5194/acp-8-6565-2008, 2008.

Wang, P., Tuinder, O. N. E., Tilstra, L. G., De Graaf, M., and Stammes, P.: Interpretation of FRESCO cloud retrievals in case of absorbing aerosol events, Atmos. Chem. Phys., 12, 9057–9077, doi:10.5194/acp- 12-9057-2012, 2012.

14 Aerosols

Authors: Marloes Penning de Vries (MPIC), Marco Vountas and Luca Lelli (IUP-UB)

14.1 Document changes

Changes in issue 2.0:

- UVAI: Update of Table 14.1; new LUTs were calculated
- UVAI: Three-way comparison of RTM radiances at 340 nm and 380 nm repeated with improved results
- UVAI: Verification of prototype algorithm and comparison with operational data from four days of GOME-2 data
- Aerosol layer height: verification results for Icelandic volcano added

14.2 Verification approach

The verification algorithm is subdivided into 2 major parts:

- Calculation of the UV Aerosol Index (UVAI) (MPIC)
- Retrieval of the Aerosol Optical Depth (AOD) and Aerosol Layer Height (ALH) (IUP-UB)

Both are discussed in the following sections.

14.2.1 Verification of UVAI

The following verification activities were planned:

- Detailed investigation of remaining inconsistencies between RTM radiances at large viewing angles; these were found to be largely due to LUT-interpolation errors. This was remedied by adopting a new LUT approach for the verification algorithm (see Sect. 14.3.1.2).
- Calculation of UVAI from synthetic test data and comparison with results from prototype algorithm.
- Calculation of UVAI from selected GOME-2 and OMI orbits and comparison with results from the prototype algorithm and operational products. Prototype and verification UVAI from four days of GOME-2 data have been compared; UVAI from two of these days were additionally compared with operational TEMIS data. Two months of TEMIS data were compared to UVAI from the verification algorithm. As the prototype team did not evaluate OMI data, these could not be used for verification.

An intercomparison of RTM radiances was performed to assess how large the differences in UVAI due to the use of different RTMs and LUT approaches are. These were expected to be minor (and in fact, an offset of 0.1-0.2 units was found; see below) for nadir measurements, but increase with viewing angle. This intercomparison should be continued in a future study to clarify what causes the observed deviations.

The synthetic test data were prepared by L. Lelli (IUP-Bremen) and represent different aerosol and cloud scenes with five viewing directions (nadir, extremes (±60°), and in between) and four SZAs. Several aerosol types from the AERONET climatology (Dubovik et al., 2002) are included, as well as different surface types (dark and bright). One test data set is based on data presented in (Torres et al., 1998), and one data set represents different cloud scenes.

This data set suffers from angle incompatibilities (as discovered during the intercomparison exercise described above) and needs to be recalculated, therefore it could not be used for verification of the UVAI algorithms.

In the second verification step UVAI was calculated from GOME-2 data, allowing a comparison between the operational (TEMIS/KNMI) product and the verification algorithm. The prototype algorithm is nearly identical to the operational product.

The agreement between prototype and verification UVAI algorithms is expected to be excellent, as UVAI is not a retrieved but a derived quantity. Differences will most probably only arise from differences in the respective RTMs, which are usually small, but may become noticeable at large viewing angles. The mission requirement of (absolute) accuracy is 0.25 UVAI units.

14.2.2 Verification of Aerosol layer height

The following verification activities were planned:

- Selection of real data and inter-comparison of the results provided by the prototype and verification algorithms with an independent validation data set;
- As the layer height of aerosols from passive nadir-looking, moderately spectrally-resolved instruments is a novel product, the main outcome of this activity is first to establish the physical retrieval framework and then to explore the feasibility of the respective approaches, with respect to the height and the optical thickness of the aerosols.

It is expected that such algorithms, exploiting the absorption features of oxygen, can retrieve the height of elevated and relatively thick aerosol layers accurately, whereas difficulties are likely to arise for thin and low aerosol layers.

14.3 UV Aerosol Indices

14.3.1 Description of Verification Algorithm

14.3.1.1 Definition of the UV Aerosol Indices

The UV Aerosol Index (UVAI) is a semi-quantitative measure of aerosols. Originally called "residue" r_λ, UVAI is determined by relating the observed radiance R at two wavelengths in the UV range, λ and λ_0, with radiances from radiative transfer (RT) calculations of the corresponding Lambert-equivalent surface reflector (Herman et al., 1997; Torres et al., 1998):

$$r_\lambda = -100\left(\log_{10}\left(\frac{R_\lambda}{R_{\lambda_0}}\right)^{\text{meas}} - \log_{10}\left(\frac{R_\lambda}{R_{\lambda_0}}\right)^{calc}\right) \quad (53)$$

The albedo of the Lambert Equivalent Reflector (LER) used in the radiance calculations is derived from the measured radiance at λ_0, so that $R_{\lambda 0}^{meas} = R_{\lambda 0}^{calc}$. Hence:

$$r_\lambda = -100\log_{10}\left(\frac{R^{meas}}{R^{calc}}\right) \quad (54)$$

The minus sign was introduced so that a positive r_λ (UVAI) is found for cases when $R_\lambda^{meas} < R_\lambda^{calc}$, which occurs for aerosol types that absorb UV radiation (assuming that $\lambda_0 > \lambda$, as originally proposed by Herman and co-workers (Herman et al., 1997)). The positive part of UVAI is commonly defined as the Absorbing Aerosol Index (AAI); the negative part was recently defined as SCattering Index (SCI) (Penning de Vries et al., 2009), such that:

- AAI = UVAI for UVAI ≥ 0, undefined for UVAI < 0
- SCI = UVAI for UVAI ≤ 0, undefined for UVAI > 0

The UVAI have been (or are being) determined from TOMS, GOME, SCIAMACHY, GOME-2, OMI, and OMPS data.

14.3.1.2 Calculation of UVAI

Look-up-tables

The most important step in the calculation of UVAI is determining the surface albedo that matches the measured radiance at λ_0. For the calculation of UVAI, look-up tables (LUTs) are constructed that contain radiances at λ and λ_0 for a Rayleigh atmosphere. The LUTs include values for all possible combinations of line-of-sight (LOS) and solar zenith angles to take into account the dependence of radiance on scattering angle. Topography (i.e., surface height) needs to be accounted for and an ozone column needs to be included (see below). In the previous version of the verification algorithm, the calculation of UVAI was performed by interpolating a LUT that contained radiances at λ and λ_0 for a Rayleigh atmosphere with surface albedo varying between 0 and 1. It was found, however, that the high dimensionality of the LUT (6, i.e., SZA x LZA x RAZ x ozone column x surface altitude x albedo) led to unacceptably large interpolation errors. The current version of the UVAI verification algorithm instead follows the approach used by KNMI (de Graaf et al., 2005b; Tilstra et al.,2012) of parameterizing the RAZ and albedo dependence of the reflectance. This reduces the number of LUT dimensions to 4. The LUT entries and ranges are based on our own studies and on work by Tilstra et al. (2012); they are listed in Table 14.1. To constrain the size of the LUT – which has four dimensions per wavelength – the step size of the various entries is chosen as large as possible without compromising on accuracy. For the calculation of UVAI, the LUT is first interpolated in the angle dimensions (SZA and LZA) and subsequently interpolated linearly in the surface pressure and ozone column dimensions.

Table 14.1: Look-up-table entries for calculation of UVAI

	Range	**Step***
Solar zenith angle	0°-87°	Δcos = 0.05
LOS zenith angle	0°-70°	Δcos = 0.025
Surface height	0, 1.4, 3.0, 4.8, 7.0 km	variable
Ozone column density	100-500 DU	100 DU
Wavelength pairs	340 and 380 nm 354 and 388 nm	40 nm 34 nm

*Δcos indicates angular steps expressed in radians

The LUTs of the verification algorithm are calculated using the Monte Carlo RT model McArtim (Deutschmann et al., 2009), which is fully spherical and is therefore accurate for all solar and LOS geometries. Polarization plays an important role in RT in the UV range (Graaf et al., 2005) and is, therefore, included in the calculations.

The UVAI is calculated for two wavelength pairs: 1) the “classical” pair 340/380 nm, used for the first TOMS sensor, both GOME instruments, SCIAMACHY, and OMI, and 2) the alternative pair 354/388 nm, which was adopted for OMI for the sake of collocation (340 and 380 nm radiances are measured by different channels, leading to more UVAI noise due to imperfect collocation).

Viewing angle dependence

Due to anisotropy of the Rayleigh scattering phase function, top-of-atmosphere radiances in the UV strongly depend on solar zenith angle (SZA), viewing zenith angle (VZA), and relative azimuth angle (RAZ); therefore, the angles need to be sufficiently sampled in the LUT. If aerosols and clouds are present in the scene, UVAI becomes viewing angle dependent due to the combined effects of the phase functions of particles and molecules. This was investigated by Graaf et al. (2005b) for a modelled scene with moderately absorbing aerosols at 3-4 km altitude. It was found that "values of [UVAI] increase quickly for solar zenith angles and [LOS] zenith angles larger than 60°"; a difference of 2 index points was seen if the VZA was changed from nadir to 60° at large SZA (60°) and small RAZ angle (0°).

We recently performed a more comprehensive study of the viewing angle effect on UVAI (Penning de Vries et al., 2014) and found that the effect can be quite large for high-altitude plumes, even at a relatively small SZA of 20°. Aerosols that do not or only slightly absorb UV radiation show negative UVAI values throughout most of the swath. High positive UVAI may, however, be found in the easternmost pixels (VZA>45) if the aerosol layer is at altitudes > 10km. The magnitude of the viewing angle dependence scales with aerosol optical depth (AOD) but does not depend on single-scattering albedo (SSA).

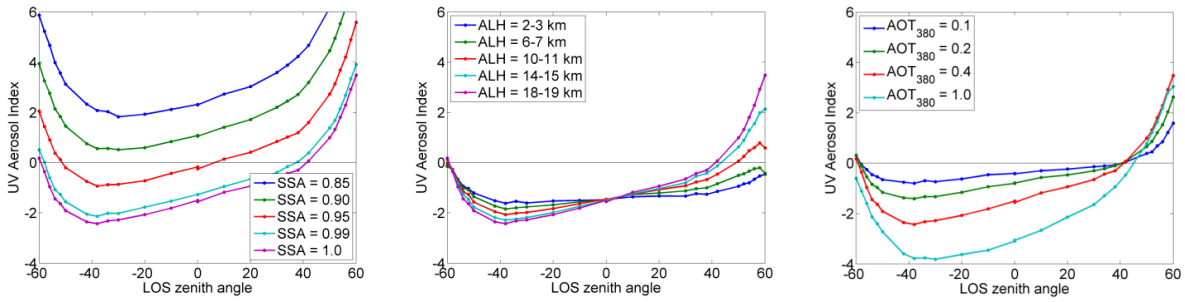

Figure 14.1: Modelled line-of-sight dependence of UVAI for various aerosol scenarios. RTM calculations were performed with McArtim; solar zenith angle was set to 20° and surface albedo 0.1. Aerosols have g=0.6 and Ångström coefficient 1.5 (AOD given at 380 nm). Left, Aerosols with AOD 0.4, SSA=1.0 and varying layer altitude; middle, Aerosols with SSA = 1.0 at 18-19 km with varying AOD; right, Aerosols with AOT=0.4 at 18-19 km with varying SSA. Figures from supplementary information to Penning de Vries et al. (2014).

Different cloud scenarios were also tested. The cloud phase function was parameterized with a Henyey-Greenstein asymmetry parameter of 0.87 and cloud optical thickness values between 1 and 50 were investigated. The viewing angle dependence of clouds is less pronounced than for aerosols.

In contrast to GOME(-2) and SCIAMACHY, OMI measures at viewing angles up to 60° and recently provided a good example of the viewing angle dependence of UVAI, described in detail in Penning de Vries et al. (2014) and summarized here:

An eruption plume from the Nabro volcano (Eritrea) was detected during two consecutive OMI overpasses on June 14, 2011. The high-altitude plume, consisting mainly of non-UV-absorbing sulphate aerosols, was viewed from the East during orbit 36772, whereas the viewing direction was opposite for the following orbit 36773. The difference in viewing direction caused the sign of UVAI to change from negative to positive, as shown in Figure 14.2, panels A-D. As the clouds directly north of the volcanic plume somewhat muddy the picture, we selected only those pixels that have SO_2 columns larger than 1.5 DU for panels C and D of Figure 14.2. Despite the fact that not all selected plume pixels contain a pronounced aerosol signal, the viewing angle effect can be clearly seen. We performed RTM simulations using the aerosol parameters representative of volcanic sulphate particles and the results of this exercise are shown in panels E and F of Figure 14.2. Although the measurements in panels C and D are not in perfect agreement with the model results, the viewing angle effect is very well reproduced.

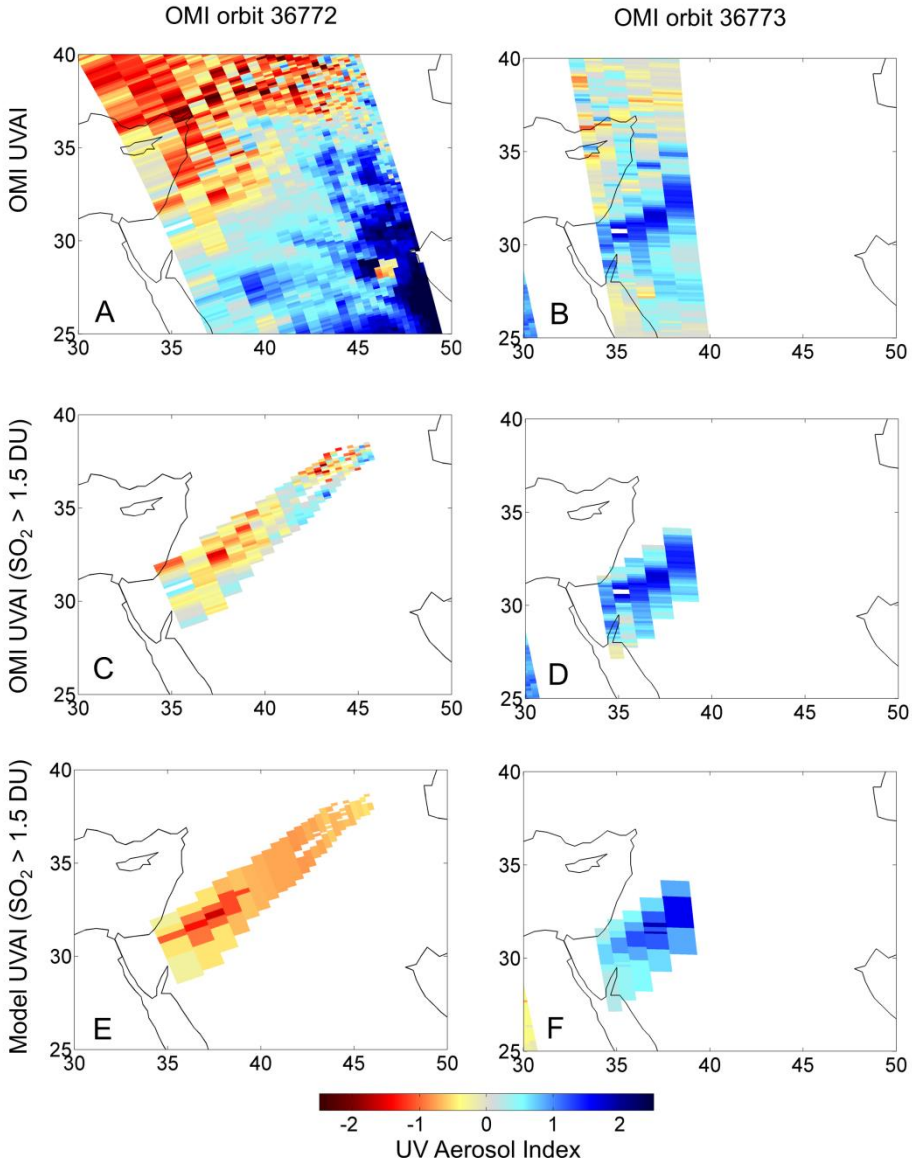

Figure 14.2: UV Aerosol Index from OMI (panels A-D) and from RTM calculations (E-F) for the volcanic plume detected on June 14, 2011. The right panels (A, C, and E) show data from orbit 36772; on the left (panels B, D, and F) data from the following orbit, 36773, are shown. The data in panels C-F are filtered by SO2 vertical column density (> 1.5 DU) to more clearly show the volcanic plume. The UVAI in panels E and F were modelled using McArtim with aerosol parameters representative of sulphate particles at 18-19 km altitude. Figure from Penning de Vries et al. (2014).

Trace gas absorption

Absorption of UV radiation by ozone is explicitly taken into account in the calculation of LUT radiances by varying the ozone total column density. As the radiances at the UVAI wavelengths are nearly independent of the shape of the ozone profile, a mid-latitude summer profile is assumed which is scaled according to a total column density between 200 and 600 DU.

The short-lived collision complex O_2-O_2 also absorbs radiation at the UVAI wavelengths and is therefore included in the RT calculations.

Surface height

For the calculation of UVAI, accurate surface elevation data is essential. The calculation of mean surface height of a satellite pixel is a computationally expensive step in the UVAI algorithm, and it was found that the resolution of ETOPO-4 was sufficient for SCIAMACHY's pixel size (Tilstra et al., 2012). For the small pixels of TROPOMI, a higher-resolved map like GTOPO30, which has 30 arc seconds resolution and is distributed by US Geological Service (used for the determination of SCIAMACHY and GOME-2 UVAI at MPIC) might be more appropriate. However, as pointed out in [RD3], GTOPO is inaccurate in certain areas, therefore the DEM, distributed by NASA (ftp://edhs1.gsfc.nasa.gov/edhs/sdptk/DEMdata), will be used.

14.3.1.3 Prior information

The only external datasets needed for UVAI calculation are a map of surface elevation (see above) and the ozone total column density. Ozone data from the TROPOMI instrument itself is preferred (for reasons of collocation), but in absence of such data, e.g., for online UVAI calculations of a near-real time product, data from a different instrument (e.g., OMI or GOME-2) or a climatology will be used.

For the calculation of the LUT cross-sections of ozone and O_2-O_2 are also required.

14.3.2 Main differences to prototype

The calculation of UVAI is rather straightforward; therefore the verification algorithm is very similar to the prototype algorithm (and to most other UVAI algorithms). The prototype algorithm makes use of the DISAMAR model to calculate Rayleigh radiances, whereas McArtim is used in the verification algorithm. This should not affect UVAI significantly, as the agreement between radiative transfer models is very good if only Rayleigh scattering is included. Other differences are the a priori surface pressure information, which for the prototype algorithm is obtained from ECMWF and is calculated from the surface elevation map in the verification algorithm.

14.3.3 Error analysis

The accuracy of UVAI is difficult to assess, as UVAI is an index of which the absolute value has no unique interpretation. It is known to be very sensitive to calibration errors (e.g., Graaf et al., 2005b) and is, in fact, being used to monitor the degradation of SCIAMACHY and GOME-2. Hence, detector degradation, as encountered with the GOME, SCIAMACHY, and GOME-2 instruments but not with OMI, is a serious problem that needs to be addressed should it occur. For SCIAMACHY, absolute UVAI greater than 0.2-0.3 were deemed reliable (Penning de Vries et al., 2009). This estimate does not include systematic errors that arise from imprecise surface elevation data or incorrect trace gas column densities (mainly ozone).

Inaccuracies from RT calculations are generally much smaller than other error sources, but play a role for the extreme viewing angles of OMI and TROPOMI. In the course of the verification study, it was found that LUT interpolation is a potentially large source of error, which was addressed by decreasing the LUT dimensionality of the verification algorithm from 6 to 4.

Additional errors arise from sun-glint and for scattering angles smaller than 90°. The effect of sun-glint is to create an artificial, potentially high, UVAI signal. This is currently not corrected; instead, sun-glint affected pixels are flagged based on solar and viewing geometry. It is intended to adapt the more accurate sun-glint detection scheme devised by Beirle et al. (2013) to (TROP)OMI data, but the lack of polarization-sensitive channels means that the scheme cannot be implemented in the same way as for GOME-2. The enhanced UVAI signal occurring at scattering angles smaller than 90° is obvious in GOME-2 and OMI data, but the reason for it is not known (Tilstra et al., 2013). Pixels affected by this error are flagged.

14.3.4 Summary of verification results

The development of the UVAI algorithm is complete.

Due to discrepancies in angle definitions in the various data sets used for the verification exercises presented in Version 1.0.0 of this document, the results of those exercises were rather poor. Subsequently, the angle definitions were adjusted and a three-way comparison of UV radiances between the RTMs DAK, SCIATRAN, and McArtim was executed (calculations performed by G. Tilstra (KNMI), L. Lelli, and M. Penning de Vries, respectively). The agreement between the radiances at 340 nm and 380 nm from the three models is very good, as shown in Figure 14.3. However, discrepancies on the order of 0.01 occur at the extreme viewing angles for the studied SZA (37°). This relatively small difference leads to significant UVAI deviations due to the fact that UVAI depends logarithmically on the ratio of two radiances (Sect. 14.3.1.1).

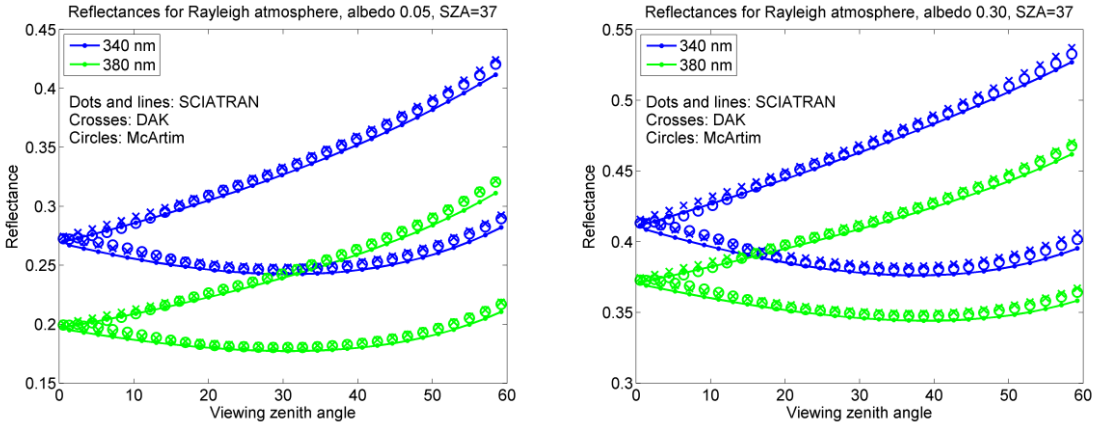

Figure 14.3: Comparison of Rayleigh radiances calculated by SCIATRAN, DAK, and McArtim for an SZA=37° and surface albedo 0.05 (left) or 0.30 (right). VZA and RAZ were chosen to represent realistic OMI viewing geometries

To investigate the influence of deviations in calculated radiances on UVAI directly, UVAI were calculated from DAK Rayleigh radiances using the MPIC verification algorithm for a selection of angles covering the extremes of OMI geometries (SZA 0°-75°, VZA 0°-60°, RAZ 0°-180°). A completely black surface (albedo = 0) was chosen, as then differences in Rayleigh scattering are most pronounced. The results of this investigation are shown in Figure 14.4.

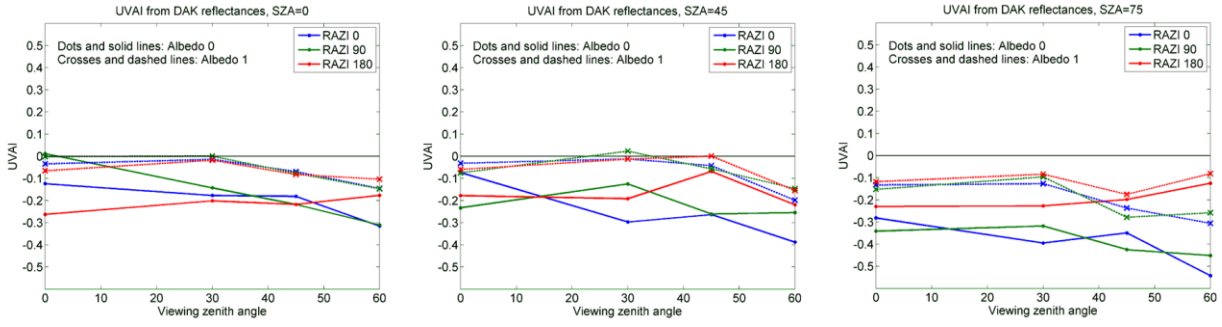

Figure 14.4: UVAI calculated using the MPIC verification algorithm from radiances calculated using the DAK RTM. Various solar and viewing geometries were tested (left, SZA=0°; middle: SZA=45°; right: SZA = 75°), VZA 0°-60°, and RAZ = 0°, 90°, 180° (blue, green, and red lines, resp.); surface albedo was set to 0 (dots and solid lines) or 1 (crosses and dashed lines). Perfect agreement would yield UVAI=0 for all cases

For a perfect agreement between the radiance data sets, zero UVAI would be found for all geometries, because only Rayleigh radiances are used. Here we find an offset of -0.1 to -0.3 for LZA≤45° and no systematic dependence on RAZ. For larger viewing angles the deviations increase in magnitude to -0.3 for overhead sun (leftmost panel) and to -0.6 for SZA=75°. A more pronounced dependence on RAZ is also found at the extreme viewing geometries (except for SZA=0°, where RAZ has no physical meaning). UVAI's deviation from 0 for extreme viewing geometries is suspected to be a result of different parameterizations of Rayleigh scattering, but may also be due to slightly different model set-ups (e.g., profiles of atmospheric state or composition).

A comparison of the UVAI from the MPIC verification algorithm, the KNMI prototype algorithm, and the operational (TEMIS/KNMI) algorithm using measured GOME-2 radiances from one day (February 4, 2008) is shown in Figure 14.5 and Figure 14.6. As expected for a derived quantity like UVAI, the agreement is very good with a slope very close to 1, no appreciable offset, and R^2=0.99 (for comparisons between all three data sets).

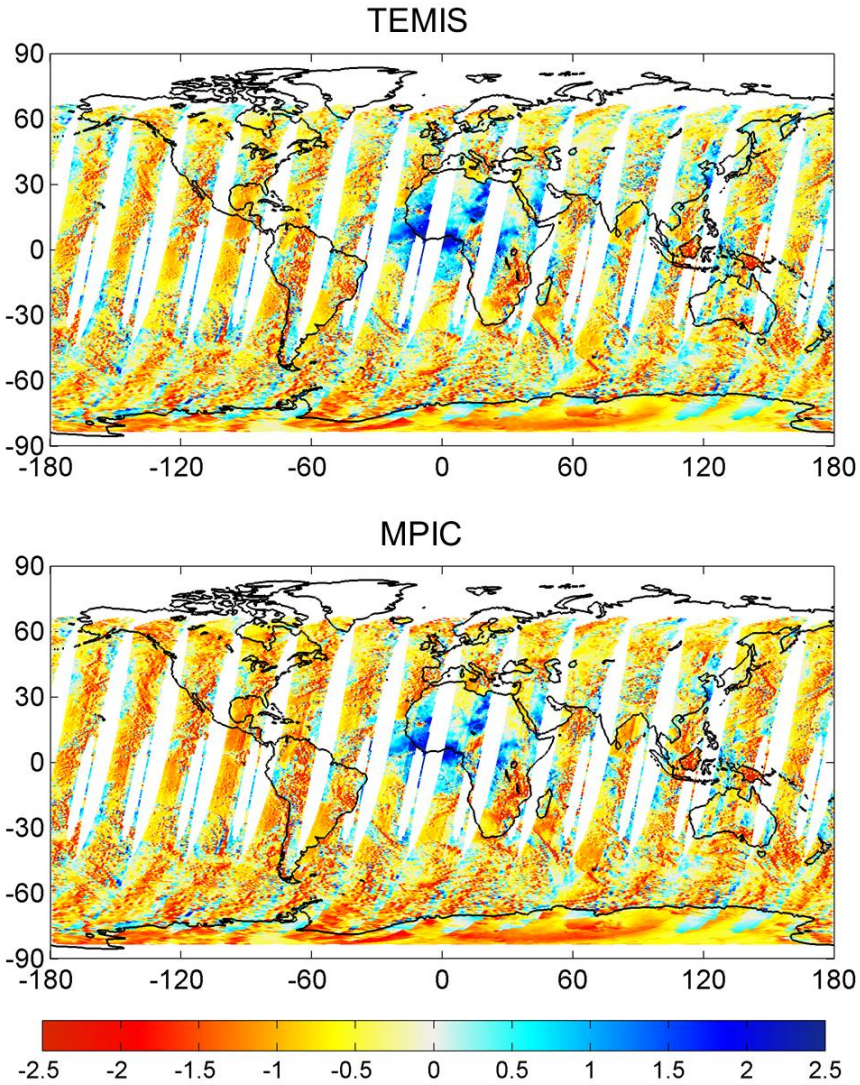

Figure 14.5: UVAI from GOME-2 radiances measured on February 4, 2008. UVAI were determined using the operational (TEMIS/KNMI) algorithm (top panel) or using the MPIC verification algorithm (bottom panel).Due to the high similarity of the results, the global map for prototype UVAI is not shown.

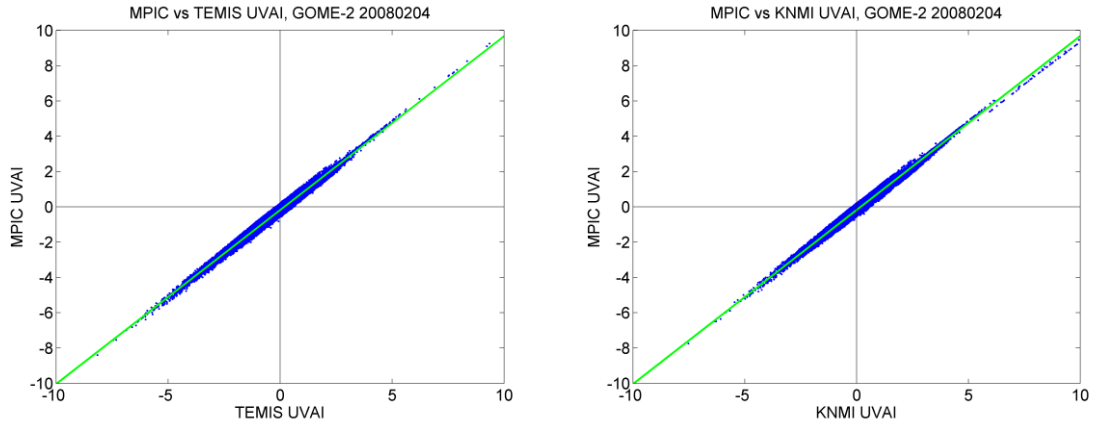

Figure 14.6: Comparison between verification (MPIC) and operational (KNMI/TEMIS, left) or prototype (KNMI) UVAI (right) for one full day of GOME-2 data: February 4, 2008. The green lines present a linear fit to the points. R^2 = 0.99 for both data sets.

The agreement between the prototype and verification algorithms was investigated in more detail by separating the data by SZA and viewing geometry. UVAI from four days of GOME-2 data were sorted into a “small SZA” bin (SZA<45) or a “large SZA” bin (SZA>60) and additionally sorted by viewing angle. Example regression plots of four of these subsets of data are shown in Figure 14.7 and Figure 14.8 for the 340/380 and 354/388 nm wavelength pairs, respectively. The coefficients of a linear fit and corresponding correlation coefficients are given in Table 14.2 for the combined data from February 4, 2008 and August 11, 2008. The other two days considered (August 15, 2012 and February 2, 2013) yield very similar results that are not shown here.

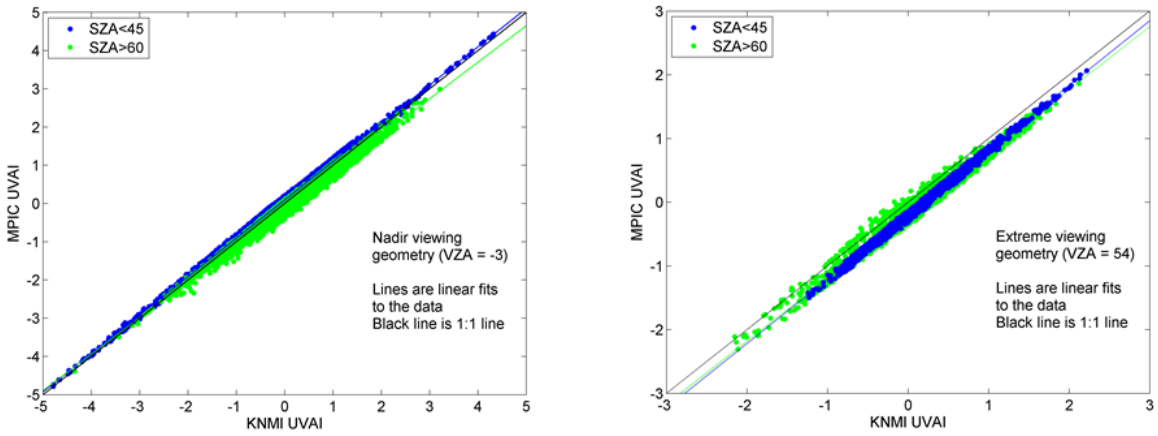

Figure 14.7: Comparison between verification (MPIC, y-axis) and prototype (KNMI, x-axis) 340/380 nm UVAI for SZA<45 (blue) or SZA>60 (green). Left, nadir viewing geometry (LZA = -3); right, extreme viewing geometry (LZA = 54). The agreement between the two data sets is very good (see Table 14.2 for linear fit coefficients and corresponding correlation coefficient).

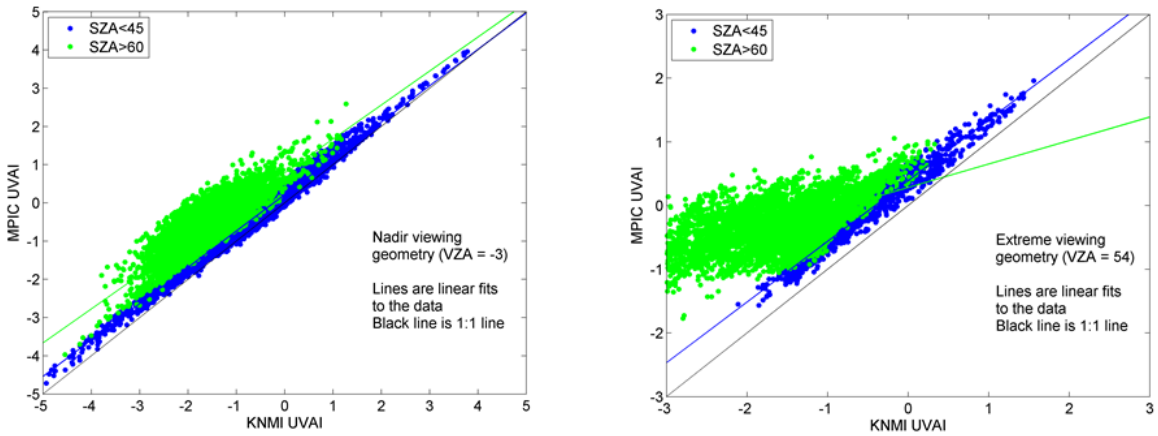

Figure 14.8: Comparison between verification (MPIC, y-axis) and prototype (KNMI, x-axis) 354/388 nm UVAI for SZA<45 (blue) or SZA>60 (green). Left, nadir viewing geometry (LZA = -3); right, extreme viewing geometry (LZA = 54). The agreement between the two data sets is very good under small SZA only; for large SZA and off-nadir viewing angles the correlation deteriorates rapidly (see Table 14.2 for linear fit coefficients and corresponding correlation coefficient).

Figure 14.7 and Table 14.2 show that the agreement between prototype and verification algorithms is excellent for the classical 340/380 nm wavelength pair. The correlation coefficient (R^2) does not fall below 0.97 for any viewing geometry, the slope barely deviates from 1, and the offset rarely exceeds 0.25, which corresponds to the verification goals.

Table 14.2: Comparison between UVAI from the 340/380 nm pair (x-axis) and from the 354/388 nm pair (y-axis). The viewing geometries are SZA<45 and VZA = -3 (best case, blue) or SZA>60 and VZA = 54 (worst case, green). Left, MPIC verification algorithm; right, KNMI prototype algorithm. There is a clear correlation between the two UVAI products under small SZA and VZA, which becomes less under extreme viewing geometry.

SZA<45						SZA>60			
LZA	R^2	a	b	N		R^2	a	b	N
-54	0.9978	0.9907	-0.2107	5469		NaN	NaN	NaN	0
-51	0.9971	0.9904	-0.1876	5964		NaN	NaN	NaN	0
-48	0.9983	0.9933	-0.208	5965		NaN	NaN	NaN	0
-44	0.9986	0.9939	-0.1646	5820		0.9954	1.0085	-0.2441	168
-40	0.999	0.9954	-0.1808	5671		0.9966	1.0067	-0.2935	526
-36	0.9991	0.9984	-0.146	5508		0.9939	1.0131	-0.2432	1150
-31	0.9991	1	-0.1418	5343		0.9947	1.0121	-0.2333	1849
-26	0.9993	0.9972	-0.1391	5169		0.9946	1.0012	-0.2009	2543
-21	0.999	0.9958	-	4986		0.9922	0.986	-	3234

			0.1293					0.1959	
-15	0.9985	0.9964	-0.1667	4793		0.9909	0.9773	-0.2225	3920
-9	0.9976	1.0044	0.0305	4590		0.9902	0.9561	-0.1533	4572
-3	0.9967	1.003	0.0887	4367		0.9858	0.9546	-0.1241	4750
3	0.9905	0.9994	-0.3137	4125		0.9891	0.9881	-0.2867	5595
9	0.995	1.0046	-0.2801	3863		0.9907	0.9869	-0.2731	5717
15	0.9951	1.0031	-0.129	3564		0.9903	0.98	-0.212	5846
21	0.9978	1.0005	-0.1388	3198		0.9874	0.9857	-0.2178	5962
26	0.9983	0.9959	-0.1171	2666		0.9844	0.9846	-0.2152	6071
31	0.9967	0.9966	-0.0955	2181		0.9898	1.0002	-0.2284	6163
36	0.9977	1.0038	-0.1413	2080		0.988	0.9946	-0.2181	6233
40	0.9977	1.0032	-0.1255	1970		0.9904	0.9986	-0.2296	6304
44	0.998	0.9979	-0.093	1853		0.987	0.9995	-0.213	6373
48	0.9955	1.002	-0.14	1727		0.9821	0.9924	-0.213	6440
51	0.9967	0.9973	-0.0863	1587		0.9788	0.9989	-0.1852	6494
54	0.9952	1.0128	-0.1916	1431		0.9822	0.9876	-0.208	6499

Figure 14.8, however, indicates severe disagreement between prototype and verification algorithm for the 354/388 nm wavelength pair. Whereas for overhead sun and near-nadir geometry the agreement is very good (R^2 = 0.96), for large SZA and particularly for large viewing angles, the discrepancy becomes unacceptably large. As this wavelength pair is not part of the operational TEMIS UVAI product, comparison with a third data set from GOME-2 is not possible, hence it is not possible to decide which algorithm performs best from the shown comparison alone. However, significant correlation is expected to exist between the UVAI products from the two wavelength pairs (de Graaf et al., 2005a). This is shown in Figure 14.9, where 354/388 nm UVAI is plotted against 340/380 nm UVAI from the verification (left) and prototype algorithm.

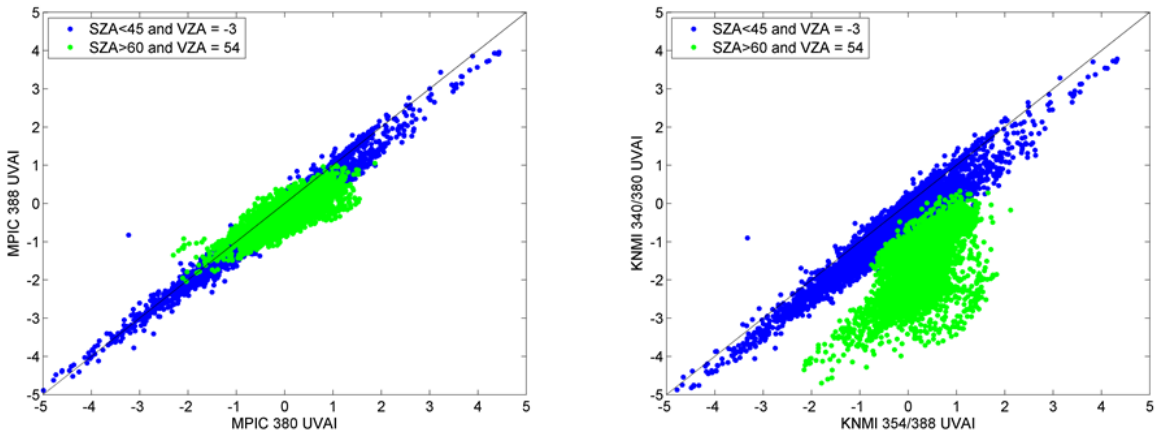

Figure 14.9: Comparison between UVAI from the 340/380 nm pair (x-axis) and from the 354/388 nm pair (y-axis). The viewing geometries are SZA<45 and VZA = -3 (best case, blue) or SZA>60 and VZA = 54 (worst case, green). Left, MPIC verification algorithm; right, KNMI prototype algorithm. There is a clear correlation between the two UVAI products under small SZA and VZA, which becomes less under extreme viewing geometry.

The results in Figure 14.9 point to a problem in the prototype algorithm: whereas the correlation between the UVAI from the two wavelength pairs decreases somewhat for extreme viewing geometry in the verification algorithm, the prototype data show large changes in correlation coefficient, slope, and offset.

14.3.5 Conclusions and recommendations

The agreement between prototype, verification, and operational UVAI algorithms presented in this report leads us to the conclusion that the verification of the UVAI was successful for the classical 340/380 nm wavelength pair. UVAI were computed from four days of GOME-2 data from three different years to investigate the correspondence between UVAI from the prototype and verification algorithms. A correlation coefficient R^2>0.98 was found for all viewing angles when SZA>60 and R^2>0.99 when SZA<45. The slopes are very close to 1 (0.95-1.03 under all sun conditions). There is an offset of -0.3 to -0.2 UVAI units that can be traced back to small differences in radiative transfer settings, as this offset was also found in the study with synthetic data.

The second wavelength pair for which prototype and verification UVAI were calculated, 354 and 388 nm, showed much less agreement. For SZA<45 and near-nadir viewing angles, R^2>0.9, but at larger SZA and more extreme viewing angles, the correlation rapidly deteriorates, the slope decreases and the offset increases. As UVAI is not calculated for these wavelengths on an operational basis from GOME-2 data, a comparison with an independent, third dataset was not performed. The fact that the UVAI from both wavelength pairs shows a good correlation for the verification algorithm, but not for the prototype, points to an error in the radiative transfer calculations used for the LUT of the prototype algorithm.

For the classical 340/380 nm pair, there are no recommendations, as UVAI from the verification and prototype algorithms agree to a very high degree. For the 354/388 pair, however, the error in LUT calculation needs to be corrected and the LUT updated before becoming operational.

14.4 Aerosol Layer Height

14.4.1 Description of the verification algorithm

The height of an aerosol layer (ALH) is determined using top-of-atmosphere (TOA) reflectances in the oxygen A-band, that is, in the range 758-772 nm, at the actual spectral sampling of TROPOMI. The TOA reflectance R is defined as

$$R = \frac{\pi I}{\mu_0 E_0} \tag{55}$$

where I, E_0, and μ_0 are the TOA radiance, irradiance, and the cosine of the solar zenith angle, respectively. The retrieval approach is based on the calculation of the weighting functions W(h) = dR/dh, i.e., the Jacobians of R as function of top and bottom height of the aerosol layer. In this context, the measured TOA reflectance R in a gaseous absorption band can be written, after linearization, as function of the desired top height h as

$$R(h) = R(h_0, h_{b0}, \tau_0) + (h - h_0)W(h_0) + (h_b - h_{b0})W(h_{b0}) + (\tau - \tau_0)W(\tau_0) \tag{56}$$

where h_0 is the a-priori value of h, the subscript b stands for bottom layer height, and tau for the optical thickness of the layer.

The above equation can be simplified assuming that the aerosol layer originates at the ground (h_{b0} = 0) and that the optical thickness of the layer can be calculated from an independent source, such as a non-absorbing channel outside the oxygen A-band. Thus one obtains

$$R(h) = R(h_0) + (h - h_0)W(h_0) \tag{57}$$

and the minimization of the following cost function

$$min|F(\lambda, h)| = |R(h) - R(h_0) - (h - h_0)W(h_0)| \tag{58}$$

between the modelled reflectance $R(h_0)$ and the measured TOA reflectance delivers the ALH, reducing the problem to the calculation of the Jacobian $W(h_0)$ (Rozanov, 2006, Rozanov et al. 2007). The above step is performed iteratively, updating the a-priori value h_0 after each iteration until a pre-defined tolerance value is reached. It must be noted that the local aerosol optical properties, encoded in the scattering matrix, as well as the single-scattering albedo and the aerosol extinction profiles are embedded in $W(h_0)$. For the time being, it is also assumed that these quantities are independent of height inside the aerosol layer.

The auxiliary derivation of aerosol optical thickness τ, necessary for the solution of the minimization problem of the cost function F is accomplished in a similar fashion as above, defining a second problem as

$$min|F(\tau)| = |R(\tau) - R(\tau_0) + (\tau - \tau_0)W(\tau_0)| \tag{59}$$

where explicit expressions for $W(tau_0)$ are given in Rozanov, 2006.

14.4.2 Synthetic data and sensitivity study

The forward TOA reflectances in the oxygen A-band of Figure 14.10 have been simulated with SCIATRAN (Rozanov et al. 2014) for two different aerosol models, namely biomass burning particles and urban aerosols (Dubovik et al 2002). Size distribution is measured to be bimodal lognormal with effective radius r_{eff} between 0.1 and 10 micron. Fine and coarse modes are in the range [0.15 - 0.24] and [2.54 - 3.27] micron, respectively.

It is shown that the oxygen A-band does provide enough sensitivity for the determination of the height of an aerosol layer and that its calculation will be affected by the albedo of the underlying surface.

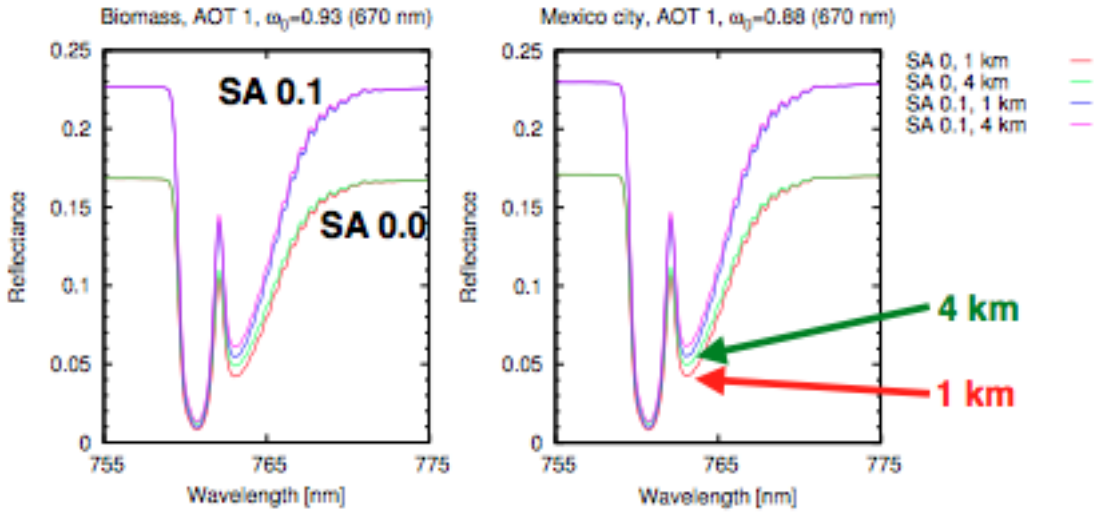

Figure 14.10: Oxygen A-band sensitivity to a change in height of an aerosol layer of optical thickness 1, for biomass burning and urban aerosols and for two different underlying ground reflectivities.

The influence of the assumption of an incorrect a-priori knowledge of ground reflectivity (i.e., surface albedo - SA) is investigated in Figure 14.11 and Figure 14.12, where the retrieval technique described in the former section has been applied to a set of TOA reflectances, with varying optical thickness and height of the layer, in the range [0.25 - 3] and [0.5 - 6] km, respectively.

In Figure 14.11 an underestimation of SA of 10% has been assumed, while in Figure 14.12 an overestimation of 10% has been assumed, as compared to the correct values. A-priori values of optical thickness and layer height have been set to 0.05 and 5 km, respectively, and they are free to vary in the iterative retrieval procedure. The bottom height of the layer is set coincident to the ground height. From the analysis of both figures, one can expect opposite tendencies for the errors in ALH as function of error in SA.

In particular, -10% in SA (Figure 14.11) causes an average bias in ALH of -0.5 km, with decreasing accuracy for thin (AOT < 0.5) and elevated (ALH > 3 km) aerosol layers. AOT is solely overestimated in the range [0 - 20]%, given an AOT of 0.25. The opposite holds true for Figure 14.12. It must be noted that AOT errors are independent of height and monotonically decreasing as function of AOT for the following reasons: first, the layer bottom height has been fixed at the ground and the AOT is scaled to preserve the extinction coefficient along the spatial dimension. Second, SSA is assumed to be known in the forward and inverse problem, which is an ideal case. It has already been shown (Kokhanovsky and Rozanov, 2010) that overestimating (underestimating) the actual SSA (±10% in the NIR spectral range) leads to underestimation (overestimation) of optical thickness of about ±20%, which, in turn, causes an additive positive (negative) bias to ALH of about ± 400 m.

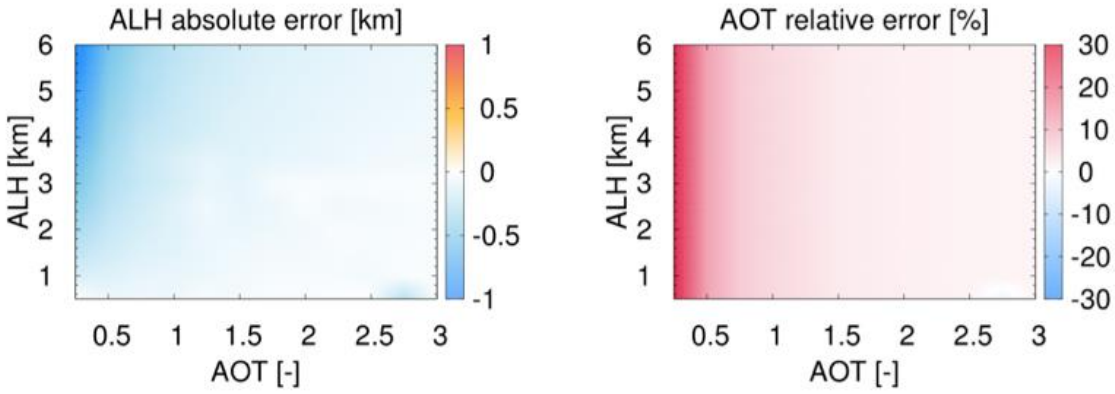

Figure 14.11: Error analysis of a 2-parameter (ALH, AOT) retrieval for biomass burning aerosol model for a-priori SA underestimation of 10%. SSA=0.97 (at 758 nm), radius fine/coarse 0.14, 3.17 micron, bimodal lognormal size distribution. Solar zenith angle is 60°, nadir view.

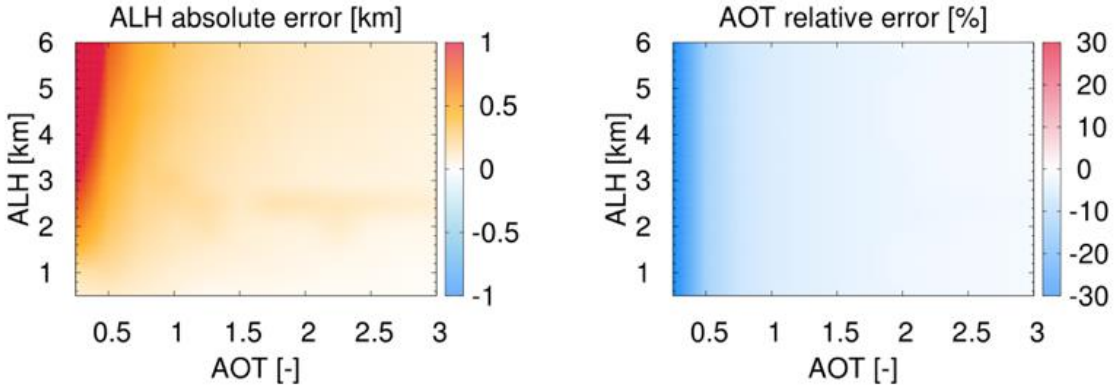

Figure 14.12: Same as Figure 14.11 but now for a-priori SA overestimation of 10%.

14.4.3 Application to real data

In the previous section, the ALH error has been discussed as function of single scattering albedo and ground reflectivity. However, the phase function error dependence was not assessed. To this end, we analyse a real case of the Icelandic Eyjafjallajökull, which erupted twice in spring 2010. A first eruption event took place in April, while a second event produced a major ash plume on May 7, which provided a test bench due to its strong signal. Height retrievals, inferred from GOME-2 TOA radiances, are co-located with retrievals from the Multi-angle Imaging SpectroRadiometer (MISR) instrument aboard NASA's Terra satellite (Kahn and Limbacher, 2012; Nelson et al, 2013), which is here assumed to be the target "truth". Here the analytical approximation of radiative transfer, coded in the Semi-Analytical Cloud Retrieval Algorithm SACURA (Rozanov and Kokhanosvsky, 2004) is employed, owing to the fact that in the geometrical optics limit, the phase function representation is given by the asymmetry parameter g.

The advantage of an algorithm based on the screening of oxygen absorption by a scattering layer can be appreciated not only when clouds are present in the satellite's footprint. Layers generated by dust outbreaks over desert regions or injected in the atmosphere by volcanic eruptions can result in radiances similar to the ones generated by clouds and detected (Boesche et al., 2009, Dubuisson et al., 2009). However, especially for the coarse spatial resolution of GOME-2 and depending on the algorithm's design, one must have at hand the actual value of plume/aerosol fraction in the FOV of the sensor.

Table 14.3: GOME-2 pixels and respective retrievals for different asymmetry parameter and plume cover of Figure 14.13.

Pixel#	Time	Centre	MISR	G2	G2	G2	Geom.PF	FRESCO PF
15398	13:13:48.6865	62.91 - 18.14	4.60	5.05	7.11	6.42	0.45	0.25
367	11:34:03.1460	62.32 - 16.62	5.00	2.47	4.18	5.03	0.66	0.21
398	11:34:08.9585	61.76 - 15.43	4.86	1.70	2.89	6.18	0.50	0.16
430	11:34:14.9585	61.42 - 15.68	4.56	1.56	2.91	4.15	0.70	0.13
557	11:34:38.7710	59.84 - 15.30	2.90	1.23	1.57	1.39	0.25	0.12

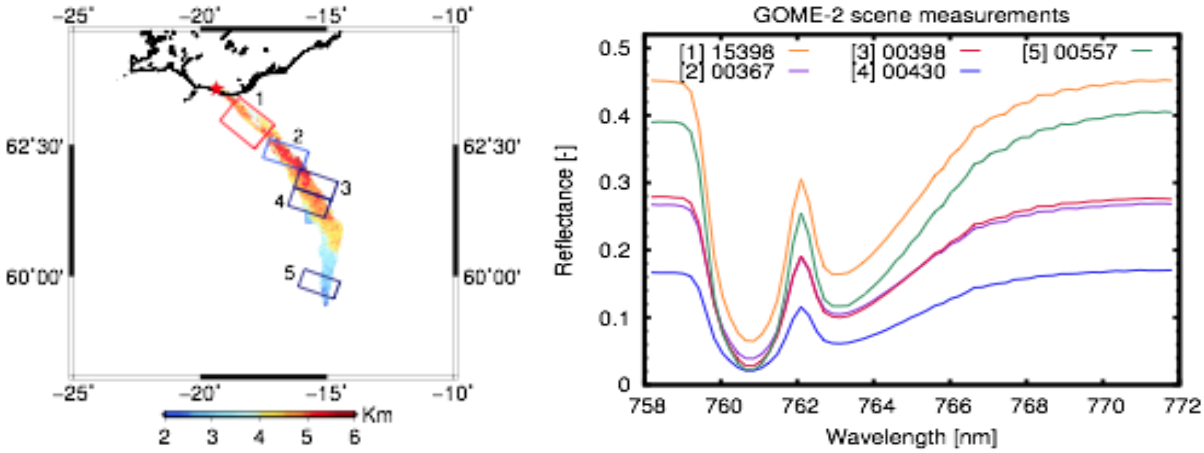

Figure 14.13: (Right) Spectra measured by GOME-2 on May, 7th 2010, mid-morning, and labelled according to ground pixel numbering (left).

To this purpose, we used FRESCO cloud fraction retrievals, delivered in bundle with GOME-2 Level 1b data. Wang et al., 2012 have synthetically shown that at 760 nm the FRESCO algorithm can handle cloud and aerosol radiances similarly, as long as the layer is optically thicker than 5. Additionally, the fractional cover will be systematically underestimated in the presence of a plume instead of a cloud.

In Figure 14.13 five pixels were matched, labelled and plotted as function of distance from the source. After a visual inspection, it was evident that FRESCO underestimates the fractional layer cover of the sensed scene, confirming the results given in Wang et al. (2012). Owing to the fact that MISR outlines the real plume's horizontal extent, due to its better spatial resolution, the geometrical fractional plume cover is recalculated, within each GOME-2 pixel, by intersection of the respective multi-segment polygons. The values are shown in the lower panel of Figure 14.14.

In the upper plot of Figure 14.14, the mean MISR layer height is pictured (black curve) together with the oxygen A-band retrievals and FRESCO plume cover (blue curve). The mean bias amounts to -2.5 km. A second attempt was made with the geometrical plume cover (green curve) and the algorithm was rerun with the updated value. The bias is diminished to -0.76 km. The retrieval can be further refined when taking into account the actual asymmetry parameter of ash particles (g = 0.65, see Bi et al., 2010; Lindqvist et al., 2011), instead of water droplets (g = 0.85). The red curve displays the retrievals which now exhibit a mean bias of -0.03 km. Ground pixels 2 and 4 match almost exactly the MISR heights. These pixels have the highest plume fraction. However, it must be noted that the influence of the aerosol plume fraction on the accuracy of the retrieved geometrical parameters may depend also on the adopted solution of the forward modelling of RT. For instance, in this verification section, the forward problem has used analytical approximations of RT and the concept of IPA have been borrowed from a cloud algorithm. While this approach can be appropriate for clouds, due to their relative high optical density, it may be not completely suitable for aerosol layers, because of their comparably lower optical thickness. At present, this effect is under investigation and first tests show that the accuracy of the OE approach is barely affected by changes in plume fraction.

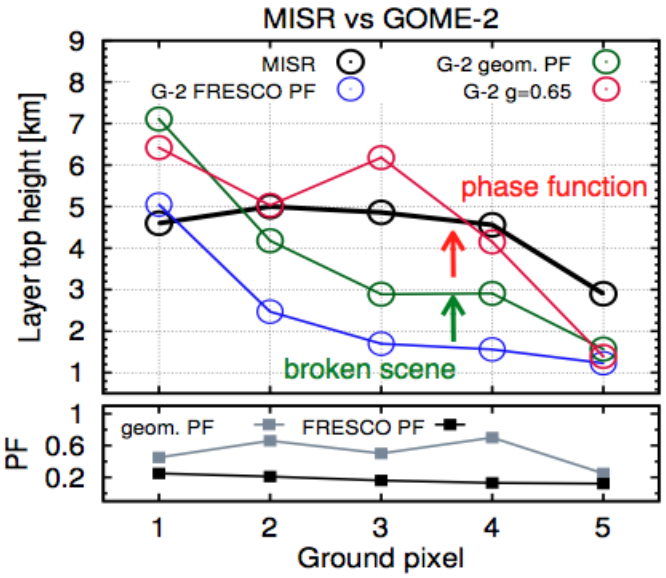

Figure 14.14(Top) Layer height from MISR (black curve) and GOME-2, retrieved with two different fractional layer covers (blue and green curve) and with ash asymmetry parameter (red curve), as function of co-located ground pixels of Figure 14.13 (Bottom) FRESCO and geometrical plume fraction derived intersecting MISR retrievals within GOME-2 pixels

14.4.4 Summary of verification results

The GOME-2 measurements pictured in Figure 14.13 have been ingested in the prototype algorithm (DISAMAR/KNMI) and the results are shown in Figure 14.15. The comparison with the verification algorithm is portrayed in Figure 14.16. In the interpretation of the following results, one has to keep in mind the two main differences between the prototype and the verification algorithms: (i) the local fractional aerosol cover value is needed by the verification, whereas the prototype assumes an aerosol fraction of 1; (ii) due to the different physical retrieval frameworks, the prototype fits the surface albedo value, whereas it is assumed in the verification implementation of the algorithm; (iii) the verification and prototype algorithm have different profile parameterizations.

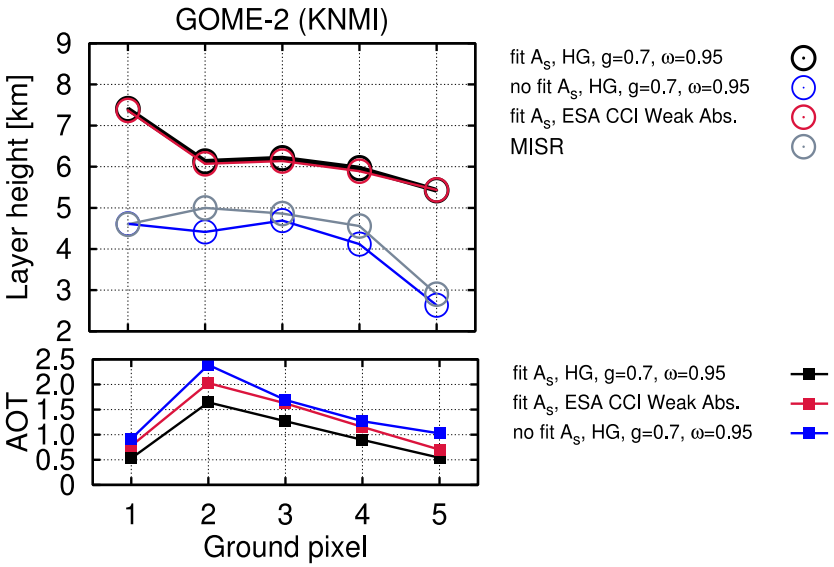

Figure 14.15: (Top) Layer height from MISR (grey curve) and GOME-2, retrieved with the prototype algorithm for three different settings: (black) Henyey-Greenstein aerosol phase function and fitting surface albedo; (red) aerosol parameterization taken from ESA-CCI project and fitting surface albedo; (blue) same as black, but without fitting surface albedo. (Bottom) Retrieved optical depth of the aerosol layer for the three model settings described in the upper panel.

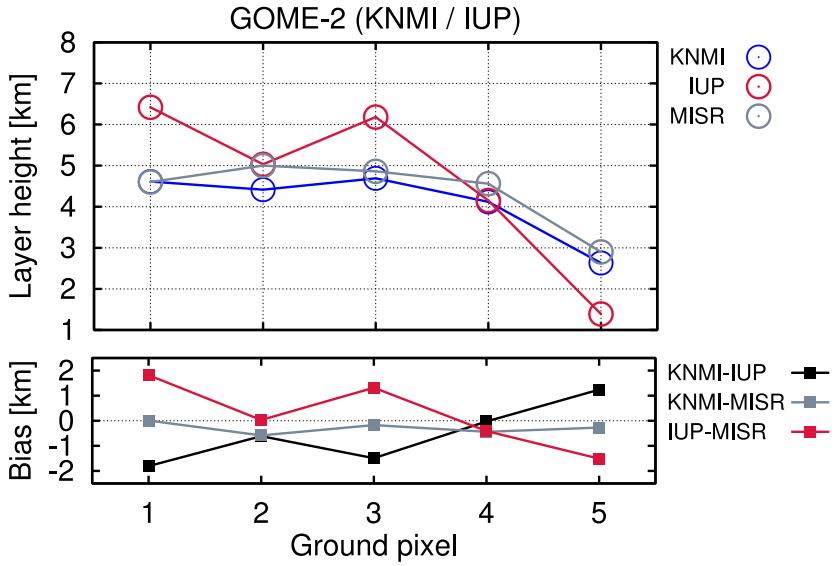

Figure 14.16: (Top) Layer height from MISR (grey curve) and GOME-2, retrieved with the prototype algorithm (blue curve) without fitting surface albedo and verification algorithm (red). (Bottom) Bias (given in km) between prototype and verification algorithms with target values of MISR.

Given that MISR retrievals are inferred with a stereoscopic approach, they can be regarded as the geometrical top height of the plume and have been chosen as the target values for the intercomparison between the prototype and the verification algorithms. The Icelandic eruptive event provides an ideal testbed due to the high aerosol load over a relatively dark ocean surface. However, the impact of cloud contamination on the retrieval of aerosol height is usually high, due to the coarse spatial scale of GOME-2 pixels. But from RGB imagery of the case under study it can be ruled out due to cloud-free conditions at that day.

The analysis of Figure 14.15 mainly shows that the optical parameters of the aerosols have negligible impact on the accuracy of the layer height, whereas surface reflection plays a major role in the retrieval procedure. This effect has already been noted by the prototyping team (as described in the KNMI-ALH-ATBD v. 0.10.0). It must be also underlined that the approach of the prototype differs from the one of the verification algorithm, as applied to this special aerosol event. While the OE approach of DISAMAR provides a stable bias trend w.r.t. MISR, being for almost all cases lower than ca. 600 m (approx. 100hpa), the verification algorithm relies on an analytical approach in the regime of geometrical optics. As such, a higher sensitivity of the verification algorithm on the prescribed optical properties of the local and plume fraction is expected.

In contrast, the AOT values retrieved by the prototype for the corresponding ground pixels barely exhibit dependence on the height of the layer, as expected from the synthetic study of Section 14.6.2. However, a higher sensitivity (up to approx. 20%) to the prescribed aerosol model can be seen, when looking at ground pixel 2.

Three main conclusions can be drawn from Figure 14.16: (i) the assumed aerosol model has only a greater effect on the retrieved height of the verification algorithm than on the one of the prototype, particularly when the surface albedo is not fitted. (ii) However, if the surface albedo is fitted, retrieved heights are biased high (see KNMI-ALH-ATBD v.0.10.0) (iii) If the surface albedo is not fitted and assuming uncertainty on the prescribed aerosol model, the retrieved heights of DISAMAR agree very well with MISR and also with the verification

In summary, the ALH prototype algorithm has been applied to five GOME-2 ground pixels that capture the Icelandic eruption of May 2010. The retrievals have been first verified by the heights derived with the SACURA-IUP algorithm and preliminarily validated against MISR stereoscopic plume height retrievals. Although there are biases, mostly due to different retrieval techniques and physical assumptions among the algorithms, the results suggest a good correlation between the various retrievals.

14.5 References

Beirle, S., Penning de Vries, M., Lang, R., and Wagner, T.: An empirical sun-glint index for GOME-2, Proc. EUMETSAT conference, 2013.

Bi, L., Yang, P., Kattawar, G. W., and Kahn, R.: Modeling optical properties of mineral aerosol particles by using nonsymmetric hexahedra, Appl. Opt. 49, 334-342, doi:10.1364/AO.49.000334, 2010.

Boesche, E. and Stammes, P. and Bennartz, R.: Aerosol influence on polarization and intensity in near-infrared O2 and CO2 absorption bands observed from space, J. Quant. Spectrosc. Rad. Tran., 110, 3, 223–239, doi:10.1016/j.jqsrt.2008.09.019, 2009.

Deutschmann, T., Beirle, S., Frieß, U., Grzegorski, M., Kern, C., Kritten, L., Platt, U., Prados-Roman, C., Puķīte, J., Wagner, T., Werner, B., and Pfeilsticker, K.: The Monte Carlo atmospheric radiative transfer model McArtim:Introduction and validation of Jacobians and 3D features, J. Quant. Spectrosc. Radiat. Trans., 112(6), 1119-1137, 2011.

Dubuisson, P., Frouin, R., Dessailly, D., Duforet, L., Léon, J.-F., Voss, K., and Antoine, D.: Estimating the altitude of aerosol plumes over the ocean from re- flectance ratio measurements in the O2 A-band, Rem. Sens. Environ., 113, 1899-1911, doi:10.1016/j.rse.2009.04.018, 2009.

Dubovik, O., et al. (2006), Application of spheroid models to account for aerosol particle nonsphericity in remote sensing of desert dust, J. Geophys. Res., 111, D11208.

Dubovik, O., Holben, B., Eck, T., Smirnov, A., Kaufman, Y., King, M., Tanré, D., and Slutsker, I.: Variability of absorption and optical properties of key aerosol types observed in worldwide locations, J. Atmos. Sci., 59(3), 590-608, 2002.

Graaf, M. de, Stammes, P., Torres, O., and Koelemeijer, R.B.A.: Absorbing Aerosol Index: Sensitivity analysis, application to GOME and comparison with TOMS, J. Geophys. Res., 110, D01201, 2005a.

Graaf, M. de, Stammes, P., Torres, O., and Koelemeijer, R.B.A.: Absorbing Aerosol Index – Calibration issues and and global results from 2002-2004, Atmos. Chem. Phys., 5, 2385-2394, 2005.

Herman, J.R., P.K. Bhartia, O. Torres, C. Hsu, C. Seftor, E. Celarier: Global distribution of UV-absorbing aerosols from Nimbus 7/TOMS data, J. Geophys. Res., 102, D14, 16,911-16,922, 1997.

Kahn, R. A. and Limbacher, J.: Eyjafjallajökull volcano plume particle-type characterization from space-based multi-angle imaging, Atmos. Chem. Phys., 12, 9459-9477, doi:10.5194/acp-12-9459-2012, 2012.

Kalashnikova, O.V., Garay, M.J., Davis, A.B., Diner, D.J., Martonchik, J.V.: Sensitivity of multi-angle photo-polarimetry to vertical layering and mixing of absorbing aerosols: Quantifying measurement uncertainties, Journal of Quantitative Spectroscopy and Radiative Transfer, 112, 13, 2149-2163, doi:10.1016/j.jqsrt.2011.05.010, 2011

Kokhanovsky, A. A. and Rozanov, V. V.: The determination of dust cloud altitudes from a satellite using hyperspectral measurements in the gaseous absorption band, Int. J. Remote Sens., 31, 2729–2744, doi:10.1080/01431160903085644, 2010.

Lindqvist, H., Nousiainen, T., Zubko, E., and Muñoz, O.: Optical modeling of vesicular volcanic ash particles, J. Quant. Spectrosc. Rad. Tran., 112, 11, 1871-1880, doi:10.1016/j.jqsrt.2011.01.032, 2011.

Nelson, D.L., Garay, M.J., Kahn, R.A., Dunst, B.A.: Stereoscopic Height and Wind Retrievals for Aerosol Plumes with the MISR INteractive eXplorer (MINX). Remote Sens., 5, 4593-4628, 2013.

Penning de Vries, M., Beirle, S., and Wagner, T.: UV Aerosol Indices from SCIAMACHY: introducing the SCattering Index (SCI), Atmos. Chem. Phys., 9, 9555-9567, 2009.

Penning de Vries, M., Dörner, S., Puķīte, J., Hörmann, C., Fromm, M., and Wagner, T.: Characterisation of a stratospheric sulphate plume from the Nabro volcano using a combination of passive satellite measurements in nadir and limb geometry, Atmos. Chem. Phys.14, 8149-8163, doi: 10.5194/acp-14-8149-2014, 2014.

Rozanov, V.V., 2006, Adjoint radiative transfer equation and inverse problems. In Light Scattering Reviews, A.A. Kokhanovsky (Ed.), pp. 339–392 (Berlin: Springer Praxis).

Rozanov, V.V., Rozanov, A.V. and Kokhanovsky, A.A., 2007, Derivatives of the radiative field and their application to the solution of inverse problems. In Light Scattering Reviews, A.A. Kokhanovsky (Ed.), pp. 205–268 (Berlin: Springer-Praxis).

Rozanov, V.V., Rozanov, A.V., Kokhanovsky, A.A., Burrows, J.P.: Radiative transfer through terrestrial atmosphere and ocean: Software package SCIATRAN, Journal of Quantitative Spectroscopy and Radiative Transfer, 133,, 13-71, doi:10.1016/j.jqsrt.2013.07.004., 2014

Rozanov, V. V. and Kokhanovsky, A. A.: Semianalytical cloud retrieval algorithm as applied to the cloud top altitude and the cloud geometrical thickness determination from top-of-atmosphere reflectance measurements in the oxygen A band, J. Geophys. Res., 109, 4070, doi:10.1029/2003JD004104, 2004.

Tilstra, L.G., Graaf, M. de, Aben, I., and Stammes, P.: In-flight degradation correction of SCIAMACHY UV reflectances and Absorbing Aerosol Index, J. Geophys. Res., 117, D6(27), 2012.

Tilstra, L.G., Tuinder, O.N.E., and Stammes, P.: O3MSAF Validation Report, SAF/O3M/KNMI/VR/001, Issue 4, 2013.

Torres, O., P.K. Bhartia, J.R. Herman, Z. Ahmad, J. Gleason: Derivation of aerosol properties from satellite measurements of backscattered ultraviolet radiation: Theoretical basis, J. Geophys. Res., 103, D14, 17,099-17,110, 1998.

Wang, P., Tuinder, O. N. E., Tilstra, L. G., De Graaf, M., and Stammes, P.: Interpretation of FRESCO cloud retrievals in case of absorbing aerosol events, Atmos. Chem. Phys., 12, 9057-9077, doi:10.5194/acp- 12-9057-2012, 2012.